Fat Crystal Networks

ALEJANDRO G. MARANGONI

Fat Crystal Networks

FOOD SCIENCE AND TECHNOLOGY

A Series of Monographs, Textbooks, and Reference Books

1. Flavor Research: Principles and Techniques, *R. Teranishi, I. Hornstein, P. Issenberg, and E. L. Wick*
2. Principles of Enzymology for the Food Sciences, *John R. Whitaker*
3. Low-Temperature Preservation of Foods and Living Matter, *Owen R. Fennema, William D. Powrie, and Elmer H. Marth*
4. Principles of Food Science
   Part I: Food Chemistry, *edited by Owen R. Fennema*
   Part II: Physical Methods of Food Preservation, *Marcus Karel, Owen R. Fennema, and Daryl B. Lund*
5. Food Emulsions, *edited by Stig E. Friberg*
6. Nutritional and Safety Aspects of Food Processing, *edited by Steven R. Tannenbaum*
7. Flavor Research: Recent Advances, *edited by R. Teranishi, Robert A. Flath, and Hiroshi Sugisawa*
8. Computer-Aided Techniques in Food Technology, *edited by Israel Saguy*
9. Handbook of Tropical Foods, *edited by Harvey T. Chan*
10. Antimicrobials in Foods, *edited by Alfred Larry Branen and P. Michael Davidson*
11. Food Constituents and Food Residues: Their Chromatographic Determination, *edited by James F. Lawrence*
12. Aspartame: Physiology and Biochemistry, *edited by Lewis D. Stegink and L. J. Filer, Jr.*
13. Handbook of Vitamins: Nutritional, Biochemical, and Clinical Aspects, *edited by Lawrence J. Machlin*
14. Starch Conversion Technology, *edited by G. M. A. van Beynum and J. A. Roels*
15. Food Chemistry: Second Edition, Revised and Expanded, *edited by Owen R. Fennema*
16. Sensory Evaluation of Food: Statistical Methods and Procedures, *Michael O'Mahony*
17. Alternative Sweeteners, *edited by Lyn O'Brien Nabors and Robert C. Gelardi*
18. Citrus Fruits and Their Products: Analysis and Technology, *S. V. Ting and Russell L. Rouseff*
19. Engineering Properties of Foods, *edited by M. A. Rao and S. S. H. Rizvi*
20. Umami: A Basic Taste, *edited by Yojiro Kawamura and Morley R. Kare*
21. Food Biotechnology, *edited by Dietrich Knorr*
22. Food Texture: Instrumental and Sensory Measurement, *edited by Howard R. Moskowitz*
23. Seafoods and Fish Oils in Human Health and Disease, *John E. Kinsella*

24. Postharvest Physiology of Vegetables, *edited by J. Weichmann*
25. Handbook of Dietary Fiber: An Applied Approach, *Mark L. Dreher*
26. Food Toxicology, Parts A and B, *Jose M. Concon*
27. Modern Carbohydrate Chemistry, *Roger W. Binkley*
28. Trace Minerals in Foods, *edited by Kenneth T. Smith*
29. Protein Quality and the Effects of Processing, *edited by R. Dixon Phillips and John W. Finley*
30. Adulteration of Fruit Juice Beverages, *edited by Steven Nagy, John A. Attaway, and Martha E. Rhodes*
31. Foodborne Bacterial Pathogens, *edited by Michael P. Doyle*
32. Legumes: Chemistry, Technology, and Human Nutrition, *edited by Ruth H. Matthews*
33. Industrialization of Indigenous Fermented Foods, *edited by Keith H. Steinkraus*
34. International Food Regulation Handbook: Policy • Science • Law, *edited by Roger D. Middlekauff and Philippe Shubik*
35. Food Additives, *edited by A. Larry Branen, P. Michael Davidson, and Seppo Salminen*
36. Safety of Irradiated Foods, *J. F. Diehl*
37. Omega3 Fatty Acids in Health and Disease, *edited by Robert S. Lees and Marcus Karel*
38. Food Emulsions: Second Edition, Revised and Expanded, *edited by Kåre Larsson and Stig E. Friberg*
39. Seafood: Effects of Technology on Nutrition, *George M. Pigott and Barbee W. Tucker*
40. Handbook of Vitamins: Second Edition, Revised and Expanded, *edited by Lawrence J. Machlin*
41. Handbook of Cereal Science and Technology, *Klaus J. Lorenz and Karel Kulp*
42. Food Processing Operations and Scale-Up, *Kenneth J. Valentas, Leon Levine, and J. Peter Clark*
43. Fish Quality Control by Computer Vision, *edited by L. F. Pau and R. Olafsson*
44. Volatile Compounds in Foods and Beverages, *edited by Henk Maarse*
45. Instrumental Methods for Quality Assurance in Foods, *edited by Daniel Y. C. Fung and Richard F. Matthews*
46. *Listeria*, Listeriosis, and Food Safety, *Elliot T. Ryser and Elmer H. Marth*
47. AcesulfameK, *edited by D. G. Mayer and F. H. Kemper*
48. Alternative Sweeteners: Second Edition, Revised and Expanded, *edited by Lyn O'Brien Nabors and Robert C. Gelardi*

49. Food Extrusion Science and Technology, *edited by Jozef L. Kokini, ChiTang Ho, and Mukund V. Karwe*
50. Surimi Technology, *edited by Tyre C. Lanier and Chong M. Lee*
51. Handbook of Food Engineering, *edited by Dennis R. Heldman and Daryl B. Lund*
52. Food Analysis by HPLC, *edited by Leo M. L. Nollet*
53. Fatty Acids in Foods and Their Health Implications, *edited by Ching Kuang Chow*
54. *Clostridium botulinum*: Ecology and Control in Foods, *edited by Andreas H. W. Hauschild and Karen L. Dodds*
55. Cereals in Breadmaking: A Molecular Colloidal Approach, *Ann-Charlotte Eliasson and Kåre Larsson*
56. LowCalorie Foods Handbook, *edited by Aaron M. Altschul*
57. Antimicrobials in Foods: Second Edition, Revised and Expanded, *edited by P. Michael Davidson and Alfred Larry Branen*
58. Lactic Acid Bacteria, *edited by Seppo Salminen and Atte von Wright*
59. Rice Science and Technology, *edited by Wayne E. Marshall and James I. Wadsworth*
60. Food Biosensor Analysis, *edited by Gabriele Wagner and George G. Guilbault*
61. Principles of Enzymology for the Food Sciences: Second Edition, *John R. Whitaker*
62. Carbohydrate Polyesters as Fat Substitutes, *edited by Casimir C. Akoh and Barry G. Swanson*
63. Engineering Properties of Foods: Second Edition, Revised and Expanded, *edited by M. A. Rao and S. S. H. Rizvi*
64. Handbook of Brewing, *edited by William A. Hardwick*
65. Analyzing Food for Nutrition Labeling and Hazardous Contaminants, *edited by Ike J. Jeon and William G. Ikins*
66. Ingredient Interactions: Effects on Food Quality, *edited by Anilkumar G. Gaonkar*
67. Food Polysaccharides and Their Applications, *edited by Alistair M. Stephen*
68. Safety of Irradiated Foods: Second Edition, Revised and Expanded, *J. F. Diehl*
69. Nutrition Labeling Handbook, *edited by Ralph Shapiro*
70. Handbook of Fruit Science and Technology: Production, Composition, Storage, and Processing, *edited by D. K. Salunkhe and S. S. Kadam*
71. Food Antioxidants: Technological, Toxicological, and Health Perspectives, *edited by D. L. Madhavi, S. S. Deshpande, and D. K. Salunkhe*

72. Freezing Effects on Food Quality, *edited by Lester E. Jeremiah*
73. Handbook of Indigenous Fermented Foods: Second Edition, Revised and Expanded, *edited by Keith H. Steinkraus*
74. Carbohydrates in Food, *edited by AnnCharlotte Eliasson*
75. Baked Goods Freshness: Technology, Evaluation, and Inhibition of Staling, *edited by Ronald E. Hebeda and Henry F. Zobel*
76. Food Chemistry: Third Edition, *edited by Owen R. Fennema*
77. Handbook of Food Analysis: Volumes 1 and 2, *edited by Leo M. L. Nollet*
78. Computerized Control Systems in the Food Industry, *edited by Gauri S. Mittal*
79. Techniques for Analyzing Food Aroma, *edited by Ray Marsili*
80. Food Proteins and Their Applications, *edited by Srinivasan Damodaran and Alain Paraf*
81. Food Emulsions: Third Edition, Revised and Expanded, *edited by Stig E. Friberg and Kåre Larsson*
82. Nonthermal Preservation of Foods, *Gustavo V. Barbosa-Cánovas, Usha R. Pothakamury, Enrique Palou, and Barry G. Swanson*
83. Milk and Dairy Product Technology, *Edgar Spreer*
84. Applied Dairy Microbiology, *edited by Elmer H. Marth and James L. Steele*
85. Lactic Acid Bacteria: Microbiology and Functional Aspects, Second Edition, Revised and Expanded, *edited by Seppo Salminen and Atte von Wright*
86. Handbook of Vegetable Science and Technology: Production, Composition, Storage, and Processing, *edited by D. K. Salunkhe and S. S. Kadam*
87. Polysaccharide Association Structures in Food, *edited by Reginald H. Walter*
88. Food Lipids: Chemistry, Nutrition, and Biotechnology, *edited by Casimir C. Akoh and David B. Min*
89. Spice Science and Technology, *Kenji Hirasa and Mitsuo Takemasa*
90. Dairy Technology: Principles of Milk Properties and Processes, *P. Walstra, T. J. Geurts, A. Noomen, A. Jellema, and M. A. J. S. van Boekel*
91. Coloring of Food, Drugs, and Cosmetics, *Gisbert Otterstätter*
92. *Listeria*, Listeriosis, and Food Safety: Second Edition, Revised and Expanded, *edited by Elliot T. Ryser and Elmer H. Marth*
93. Complex Carbohydrates in Foods, *edited by Susan Sungsoo Cho, Leon Prosky, and Mark Dreher*
94. Handbook of Food Preservation, *edited by M. Shafiur Rahman*

95. International Food Safety Handbook: Science, International Regulation, and Control, *edited by Kees van der Heijden, Maged Younes, Lawrence Fishbein, and Sanford Miller*
96. Fatty Acids in Foods and Their Health Implications: Second Edition, Revised and Expanded, *edited by Ching Kuang Chow*
97. Seafood Enzymes: Utilization and Influence on Postharvest Seafood Quality, *edited by Norman F. Haard and Benjamin K. Simpson*
98. Safe Handling of Foods, *edited by Jeffrey M. Farber and Ewen C. D. Todd*
99. Handbook of Cereal Science and Technology: Second Edition, Revised and Expanded, *edited by Karel Kulp and Joseph G. Ponte, Jr.*
100. Food Analysis by HPLC: Second Edition, Revised and Expanded, *edited by Leo M. L. Nollet*
101. Surimi and Surimi Seafood, *edited by Jae W. Park*
102. Drug Residues in Foods: Pharmacology, Food Safety, and Analysis, *Nickos A. Botsoglou and Dimitrios J. Fletouris*
103. Seafood and Freshwater Toxins: Pharmacology, Physiology, and Detection, *edited by Luis M. Botana*
104. Handbook of Nutrition and Diet, *Babasaheb B. Desai*
105. Nondestructive Food Evaluation: Techniques to Analyze Properties and Quality, *edited by Sundaram Gunasekaran*
106. Green Tea: Health Benefits and Applications, *Yukihiko Hara*
107. Food Processing Operations Modeling: Design and Analysis, *edited by Joseph Irudayaraj*
108. Wine Microbiology: Science and Technology, *Claudio Delfini and Joseph V. Formica*
109. Handbook of Microwave Technology for Food Applications, *edited by Ashim K. Datta and Ramaswamy C. Anantheswaran*
110. Applied Dairy Microbiology: Second Edition, Revised and Expanded, *edited by Elmer H. Marth and James L. Steele*
111. Transport Properties of Foods, *George D. Saravacos and Zacharias B. Maroulis*
112. Alternative Sweeteners: Third Edition, Revised and Expanded, *edited by Lyn O'Brien Nabors*
113. Handbook of Dietary Fiber, *edited by Susan Sungsoo Cho and Mark L. Dreher*
114. Control of Foodborne Microorganisms, *edited by Vijay K. Juneja and John N. Sofos*
115. Flavor, Fragrance, and Odor Analysis, *edited by Ray Marsili*
116. Food Additives: Second Edition, Revised and Expanded, *edited by A. Larry Branen, P. Michael Davidson, Seppo Salminen, and John H. Thorngate, III*

117. Food Lipids: Chemistry, Nutrition, and Biotechnology: Second Edition, Revised and Expanded, *edited by Casimir C. Akoh and David B. Min*
118. Food Protein Analysis: Quantitative Effects on Processing, *R. K. Owusu- Apenten*
119. Handbook of Food Toxicology, *S. S. Deshpande*
120. Food Plant Sanitation, *edited by Y. H. Hui, Bernard L. Bruinsma, J. Richard Gorham, Wai-Kit Nip, Phillip S. Tong, and Phil Ventresca*
121. Physical Chemistry of Foods, *Pieter Walstra*
122. Handbook of Food Enzymology, *edited by John R. Whitaker, Alphons G. J. Voragen, and Dominic W. S. Wong*
123. Postharvest Physiology and Pathology of Vegetables: Second Edition, Revised and Expanded, *edited by Jerry A. Bartz and Jeffrey K. Brecht*
124. Characterization of Cereals and Flours: Properties, Analysis, and Ap-plications, *edited by Gönül Kaletunç and Kenneth J. Breslauer*
125. International Handbook of Foodborne Pathogens, *edited by Marianne D. Miliotis and Jeffrey W. Bier*
126. Food Process Design, *Zacharias B. Maroulis and George D. Saravacos*
127. Handbook of Dough Fermentations, *edited by Karel Kulp and Klaus Lorenz*
128. Extraction Optimization in Food Engineering, *edited by Constantina Tzia and George Liadakis*
129. Physical Properties of Food Preservation: Second Edition, Revised and Expanded, *Marcus Karel and Daryl B. Lund*
130. Handbook of Vegetable Preservation and Processing, *edited by Y. H. Hui, Sue Ghazala, Dee M. Graham, K. D. Murrell, and Wai-Kit Nip*
131. Handbook of Flavor Characterization: Sensory Analysis, Chemistry, and Physiology, *edited by Kathryn Deibler and Jeannine Delwiche*
132. Food Emulsions: Fourth Edition, Revised and Expanded, *edited by Stig E. Friberg, Kare Larsson, and Johan Sjoblom*
133. Handbook of Frozen Foods, *edited by Y. H. Hui, Paul Cornillon, Isabel Guerrero Legarret, Miang H. Lim, K. D. Murrell, and Wai-Kit Nip*
134. Handbook of Food and Beverage Fermentation Technology, *edited by Y. H. Hui, Lisbeth Meunier-Goddik, Ase Solvejg Hansen, Jytte Josephsen, Wai-Kit Nip, Peggy S. Stanfield, and Fidel Toldrá*
135. Genetic Variation in Taste Sensitivity, *edited by John Prescott and Beverly J. Tepper*

136. Industrialization of Indigenous Fermented Foods: Second Edition, Revised and Expanded, *edited by Keith H. Steinkraus*
137. Vitamin E: Food Chemistry, Composition, and Analysis, *Ronald Eitenmiller and Junsoo Lee*
138. Handbook of Food Analysis: Second Edition, Revised and Expanded, Volumes 1, 2, and 3, *edited by Leo M. L. Nollet*
139. Lactic Acid Bacteria: Microbiological and Functional Aspects: Third Edition, Revised and Expanded, *edited by Seppo Salminen, Atte von Wright, and Arthur Ouwehand*
140. Fat Crystal Networks, *Alejandro G. Marangoni*
141. Novel Food Processing Technologies, *edited by Gustavo V. Barbosa-Cánovas, M. Soledad Tapia, and M. Pilar Cano*

Additional Volumes in Preparation

Fat Crystal Networks

ALEJANDRO G. MARANGONI
Department of Food Science
University of Guelph
Guelph, Ontario, Canada

MARCEL DEKKER NEW YORK

Library of Congress Cataloging-in-Publication Data
A catalog record for this book is available from the Library of Congress.

ISBN: 0-8247-4075-0

This book is printed on acid-free paper.

Headquarters
Marcel Dekker, 270 Madison Avenue, New York, NY 10016, U.S.A.
tel: 212-696-9000; fax: 212-685-4540

Distribution and Customer Service
Marcel Dekker, Cimarron Road, Monticello, New York 12701, U.S.A.
tel: 800-228-1160; fax: 845-796-1772

World Wide Web
http://www.dekker.com

The publisher offers discounts on this book when ordered in bulk quantities. For more information, write to Special Sales/Professional Marketing at the headquarters address above.

Current printing (last digit):

10 9 8 7 6 5 4 3 2 1

PRINTED IN THE UNITED STATES OF AMERICA

Preface

There exists a need for a comprehensive textbook based on fundamental physical and chemical theory that provides a description and explanation of the various levels of structure that exist and influence the macroscopic physical properties of fat crystal networks. This book is intended to fill this need both as a textbook suitable for a graduate level course on fat crystal networks, and as a reference source for researchers and instructors in the area of lipids. The emphasis has been placed on food lipids, since the properties of the fat crystal network formed in many fat-containing foods usually determine many of the organoleptic properties of the food product. Therefore, this book will also serve as a reference for industrial professionals engaged in product development and quality control. Students using this book are expected to have a good working knowledge of second-year undergraduate physics and of undergraduate chemistry.

From a global perspective, this book is relevant to the area of materials science: the emphasis on material science has been changing from semi-conductors and hard materials to soft materials, specifically to the rheological properties of soft materials. The approach taken in this book in relating different levels of structure to macroscopic physical properties is also a strategy that is being applied with increasing popularity to all areas of materials science. The extensive use of soft materials as plastics or foods also establishes this area of endeavor as a priority with industry.

The use of fractal mathematics to characterize the microstructure of fat crystal networks is a new and exciting application of fractal analysis to natural systems. In many ways, the quantification of the microstructure in fat crystal networks represents the missing link in the chain of structural influences on the macroscopic physical properties of fat crystal networks.

This book is organized into 16 chapters. Chapters 1-8 cover the theory behind the study of fat crystal networks, namely crystallization, rheology and microstructure. A quantitative link between the structure of fat crystal networks and mechanical properties is offered here as well. An appealing Chapter 9 describes and discusses the analytical methodologies used in this area of endeavor. This section is richly illustrated and should make these advanced techniques accessible to most scientists and technologists. Chapters 10–14 are devoted to a few applications of the theory and techniques discussed in order to illustrate their usefulness in addressing scientific and technological problems. Chapters 15 and 16 include two stand-alone contributions from Leendert Wesdorp and Jerrold Litwinenko. Leendert Wesdorp's work on the phase behavior of triacylglycerols remains to date the most comprehensive and in-depth study in this area. Jerrold Litwinenko has pioneered the use of 3-dimensional microscopy and microanalysis of fat crystal networks, pointing towards the future of this art. Finally, this book includes a DVD image archive of most of the microscopy carried out in our laboratory. The microstructure of cocoa butter, milkfat, milkfat fractions, palm oil, among others, crystallized statically and dynamically under different conditions is catalogued in this work. All images are provided as high-resolution TIFF files. Also included are macros to carry out particle counting fractal dimension determinations, and image-capture automations. Magnification bars for the different images are provided with instructions on how to add them to the images, if required. It is the hope of the author that this DVD can become a tool and a source of data for further studies on fat crystal network structure. The images can be used for research and educational purposes, and can be published as long as proper acknowledgment is made with respect to their source.

It is the hope of the authors that this book will be used not only as a tool for teaching, but also as a tool by researchers and industry professionals, since it contains a wealth of information on fat crystal networks that is pertinent to current problems in the industry.

Alejandro G. Marangoni

Contents

Contributors

Tarek S. Awad Department of Food Science, University of Guelph, Guelph, Ontario, Canada

Rodrigo Campos Department of Food Science, University of Guelph, Guelph, Ontario, Canada

S. de Jong Unilever Foods Research Centre Vlaardingen, Vlaardingen, The Netherlands

Th. de Loos Department of Applied Thermodynamics, Delft University of Technology, Delft, The Netherlands

A. Don Unilever Foods Research Centre Vlaardingen, Vlaardingen, The Netherlands

I. Gandasasmita Department of Applied Thermodynamics, Delft University of Technology, Delft, The Netherlands

R. v.d. Giessen Unilever Foods Research Centre Vlaardingen, Vlaardingen, The Netherlands

P. A. M. Grootscholten Unilever Foods Research Centre Vlaardingen, Vlaardingen, The Netherlands

K. L. Humphrey Agri-Food Materials Science Centre, Department of Agricultural, Food and Nutritional Science, University of Alberta, Edmonton, Alberta, Canada

Jerrold W. Litwinenko Department of Food Science, University of Guelph, Guelph, Ontario, Canada

Alejandro G. Marangoni Department of Food Science, University of Guelph, Guelph, Ontario, Canada

Suresh S. Narine Agri-Food Materials Science Centre, Department of Agricultural, Food and Nutritional Science, University of Alberta, Edmonton, Alberta, Canada

P. Overbosch Unilever Foods Research Centre Vlaardingen, Vlaardingen, The Netherlands

C. Peters Department of Applied Thermodynamics, Delft University of Technology, Delft, The Netherlands

Michael A. Rogers Department of Food Science, University of Guelph, Guelph, Ontario, Canada

E. Royers Unilever Foods Research Centre Vlaardingen, Vlaardingen, The Netherlands

M. Struik Unilever Foods Research Centre Vlaardingen, Vlaardingen, The Netherlands

J. A. van Meeteren Unilever Foods Research Centre Vlaardingen, Vlaardingen, The Netherlands

L. H. Wesdorp Unilever Foods Research Centre Vlaardingen, Vlaardingen, The Netherlands

1

Crystallography

ALEJANDRO G. MARANGONI
Department of Food Science
University of Guelph
Guelph, Ontario, Canada

1. REVIEW OF CRYSTALLOGRAPHY

The diffraction of waves is the basis of several powerful techniques for the determination of the structures of molecules and solids. X-rays have wavelengths comparable to the spacing of atoms in crystals (about 100 pm), so they are diffracted by crystal lattices.

1.1. Crystal Lattices

Early in the history of modern science it was suggested that the regular external form of crystals (their morphology) implied an internal regularity. Visual inspection of many different crystals led to the realization that they all correspond to

one of only seven regular shapes, collectively called the *seven crystal systems*. The system a crystal belongs to is determined by measuring the angles between its faces, and deciding how many axes are needed to define the principal features of its shape. For example, if three equivalent, mutually perpendicular axes are required, then the crystal belongs to the *cubic system*. If one axis perpendicular to two, making an obtuse angle, are required, then the crystal belongs to the *monoclinic system* (Table 1; Figure 1).

The *crystal systems* can be discussed in terms of the symmetry elements they possess. Operations that leave an object looking the same are called symmetry operations. Symmetry operations include the identity operation (E), rotation about an axis of symmetry (n-fold rotation denoted C_n), reflection in a plane of symmetry or a mirror plane (σ), inversion through a center of symmetry (i), and improper rotation (rotary reflection) about an axis of improper rotation (rotary-reflection axis) (S_n). There is a corresponding symmetry element for each operation: these are the points, lines, and planes with respect to which the symmetry operation is performed. Objects can be classified into symmetry groups by identifying all their symmetry elements. These are essential in the sense that the specified elements must be present for the crystal to belong to the system, but other elements may also be present, in which case they belong to a particular *crystal class* of that crystal system. For example, two crystals belonging to the cubic system can have different rotational symmetry. When these additional

Table 1 The Seven Crystal Systems and Their Structural Characteristics

System	Axes	Angles
Cubic	a=b=c	$\alpha=\beta=\gamma=90°$
Rhombohedral (Trigonal)	a=b=c	$\alpha=\beta=\gamma\neq90°$
Tetragonal	a=b≠c	$\alpha=\beta=\gamma=90°$
Hexagonal	a=b≠c	$\alpha=\beta=90°$, $\gamma=120°$
Orthorhombic	a≠b≠c	$\alpha=\beta=\gamma=90°$
Monoclinic	a≠b≠c	$\alpha=\gamma=90°$, $\beta\neq90°$
Triclinic	a≠b≠c	$\alpha\neq\beta\neq\gamma\neq90°$

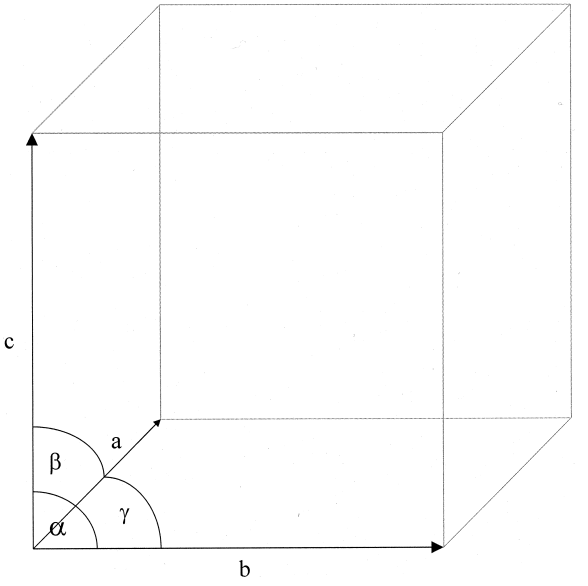

Figure 1 Diagram of a1 unit cell depicting the three crystallographic axes and angles.

symmetry elements are taken into account, it turns out that there are 32 crystal classes, distributed over the seven crystal systems. The classification system used in the discussion of crystal symmetry is the Hermann-Mauguin (or International) system.

The difficulty with the classification procedure is that crystal faces grow at different rates, and so the appearance of the crystal may be distorted. Moreover, in some cases there may be accidental equivalences of axes. Therefore, in order to classify crystals unambiguously, we must do so on the basis of the *internal* symmetry elements they possess.

1.2. Lattices and Unit Cells

A crystal is an orderly array of symmetrically arranged particles. In order to be precise about the internal organization of the crystal, individual units from which the crystal is built

need to be distinguished. We introduce the following definitions:

1. *The Asymmetric Unit*: the particle (ion, molecule) from which the crystal is built
2. *The Space Lattice*: a three-dimensional, infinite array of points, each of which is surrounded in an identical way by its neighbors. The space lattice defines the basic structure of the crystal. In some cases, there may be an asymmetric unit at each lattice point, but that is not necessary. For instance, each lattice point might be at the center of a cluster of three asymmetric units. The space lattice is, in effect, the abstract scaffolding for the crystal structure.
3. The *Crystal Structure*: the association of each lattice point with an assembly of asymmetric units in a symmetrical arrangement that is identical for each lattice point.
4. The *Unit Cell*: the fundamental unit from which the entire crystal may be constructed purely by translational displacements (like a brick in a wall). The unit cell contains all the symmetry elements of the crystal.

A unit cell must possess the overall symmetry of the crystal. It follows that we should expect to be able to account for the external morphology of a crystal in terms of the symmetry of its unit cell. The morphology, however, also depends on the relative rates of growth of the different crystal faces, but the underlying unit cell structure is uniform. Therefore, if we can identify the symmetry elements of the unit cell, we shall have an unambiguous classification of the crystal.

In three dimensions there are fourteen types of unit cells that can stack together and give rise to a space lattice that fills all space: the Bravais lattices. Those with lattice points only at the corners of the unit cell are called primitive (P); a body-centered (I) unit cell has a point at the center, and face-centered (F) unit cells have lattice points on their faces. The Bravais lattices fall into seven groups, which correspond precisely to the seven crystal systems. In other words, the seven crystal systems correspond to the existence of the seven regular internal shapes that may be packed together to fill all

space. Furthermore, the occurrence of the crystal classes reflects the presence of the corresponding symmetry elements in the unit cells. Therefore, a triclinic crystal morphology indicates the presence of a unit cell with triclinic symmetry, and so on.

1.3. The Miller Indices

Even in a rectangular lattice, a large number of planes can be identified. Consider a three-dimensional (3D) rectangular lattice formed from a unit cell of sides a,b (Figure 2). Four sets of planes have been drawn through these lattice points. These planes can be identified according to the projected distances along the a, b, and c axes that a plane covers between two consecutive lattice points. For example, the four sets in the illustration can be denoted respectively (1a, 1b), (3a, 2b), ($-$1a, 1b), and (∞a, 1b). If we agree to quote distances along the axes in terms of the lengths of the unit cells, these planes can be specified more simply as (1,1), (3,2), ($-$1,1), and (∞,1). The lattice in Figure 2 corresponds to the top view of a 3D rectangular lattice in which the unit cell has a length "c" in the z-direction. Thus, all four sets of planes intersect the z-axis at infinity, and therefore, the full labels are (1,1,∞), (3,2,∞),

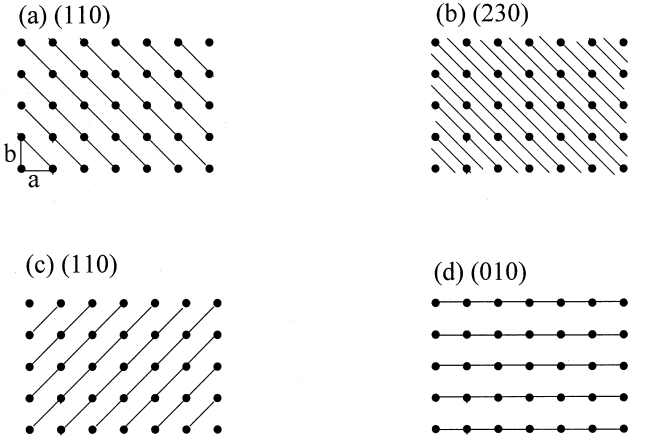

Figure 2 Possible planes through a crystal lattice

$(-1,1,\infty)$ and $(\infty, 1, \infty)$. The appearance of ∞ is inconvenient, and a way of eliminating it is to deal with the reciprocal of the indices. The, so-called, Miller indices are the reciprocals of the numbers in the brackets, with fractions cleared. For example, the (1a, 1b, ∞c) plane, abbreviated as the $(1, 1, \infty)$ plane, becomes (110) in the Miller system. This label is used to refer to the complete set of equally spaced planes parallel to this one. Similarly, the $(3, 2, \infty)$ plane becomes (1/3, 1/2, 0) on taking reciprocals, and (2, 3, 0) upon clearing fractions, and so it is referred to as the (230) plane in the Miller system. Negative indices are written with a bar over the number. The three numbers in the Miller system are denoted as (hkl).

One should remember that the unit cell need not be rectangular; the procedure works equally well when axes are not perpendicular. For that reason, the axes are called a,b,c rather than x,y,z. As well, the smaller the value of h in (hkl), the more nearly parallel the plane to the a-axis (The same applies to k and the b axis and l and the c axis). When $h = 0$, the planes intersect the a-axis at infinity, and so (0,k,l) are parallel to the a-axis. Similarly, (h0l) and (hk0) are parallel to the b and c axis, respectively.

The Miller indices are very useful for expressing the separation of planes (d). From the extension of the Pythagorean theorem to three dimensions, it is possible to show that, for a general orthorhombic lattice (a rectangular, or orthogonal, lattice based on a unit cell with different sizes),

$$\frac{1}{d_{hkl}^2} = \left(\frac{h}{a}\right)^2 + \left(\frac{k}{b}\right)^2 + \left(\frac{l}{c}\right)^2 \tag{1}$$

This equation simplifies for the case of a cubic lattice ($a = b = c$) to

$$\frac{1}{d_{hkl}^2} = \frac{\left(h^2 + k^2 + l^2\right)}{a^2} \tag{2}$$

1.4. Powder X-Ray Diffraction and Bragg's Law

Because x-rays have wavelengths comparable to atomic spacings, they are diffracted when passed through a crystal as a result of the interference between waves. Where their ampli-

tudes are in-phase, the waves augment each other and the intensity is enhanced; where their amplitudes are out-of-phase, they waves cancel each other and the intensity is decreased.

Consider a stack of reflecting lattice planes (Figure 3). The path-length difference between the two rays is 2x, which equals 2dsinθ, where d is the layer spacing and (is the glancing angle. For many glancing angles, the path-length difference is not an integral number of wavelengths, thus resulting in destructive interference. However, when the path-length difference is an integral number of wavelengths (2x = nλ, the reflected waves are in-phase and interfere constructively. It follows that a bright reflection should be observed when the glancing angles fulfill the Bragg condition:

$$n\lambda = 2d \sin\theta \tag{3}$$

In modern crystallography, all reflections are considered to be first order (n = 1), with higher order reflections (n = 2, n = 3, etc.) absorbed into d. Thus, Bragg's law can be rewritten as:

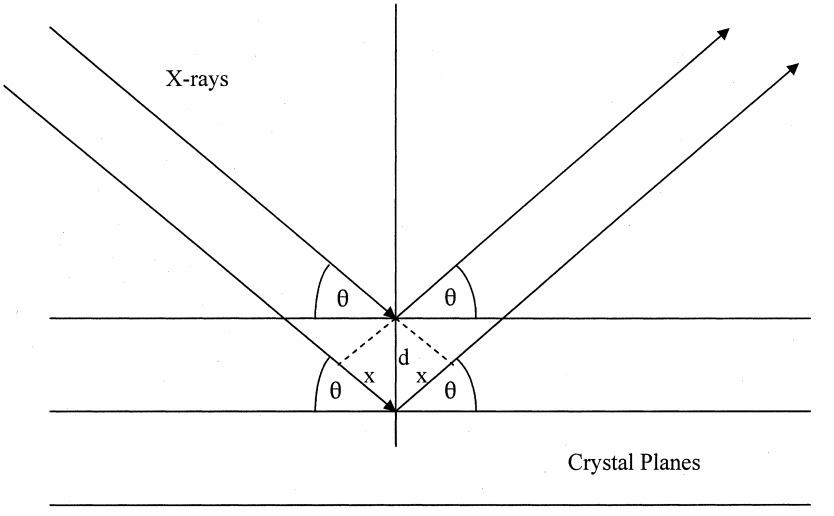

Figure 3 Geometry of the refection of X-rays from crystal planes used in the derivation of Bragg's law.

$$\lambda = 2d_{hkl} \sin\theta \quad (4)$$

In this case, an nth order reflection is considered to arise from the (nh,nk,nl) planes. For example $d_{246} = 1/2\ d_{123}$. In general, increasing the indexes uniformly by a factor of n decreases the separation distance by the same factor (Figure 4).

In most fats and oils work, single-crystal X-ray diffraction (XRD) is not carried out, however, powder XRD does occur. Fats are polycrystalline materials, a randomly oriented heap of tiny crystals. Some of the crystals will, however, be in the correct orientation to satisfy Bragg's law, even for monochromatic radiation. In principle, each set of (h,k,l) planes gives rise to a diffraction cone because some of the randomly orientated crystallites can diffract the incident beam. This powder technique is equivalent to rotating a single crystal over all possible orientations relative to the incident X-ray beam. These days, the major application of powder XRD is to qualitative analysis since many diffraction patterns have been recorded

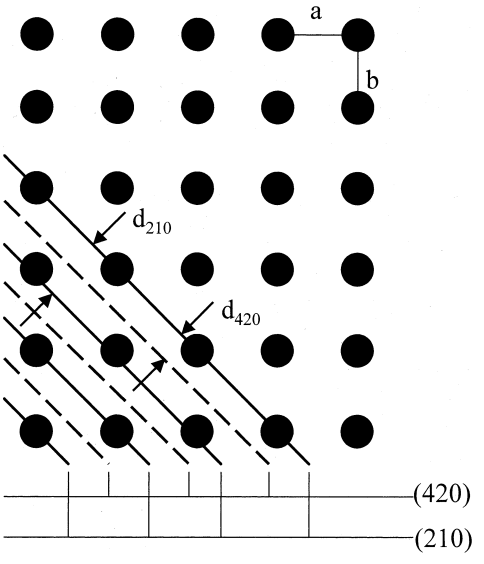

Figure 4 Crystal planes corresponding to first-and second-order reflections.

and can be used as a fingerprint. The powder technique is useful for a qualitative analysis of the sample and for an initial determination of the dimensions and symmetry of the unit cell, but it cannot provide the detailed information about the electron density distribution that is available from single-crystal methods.

1.5. A Typical Powder XRD Setup

Figure 5 depicts a possible configuration for a powder XRD experiment. In this particular setup, the sample is positioned in the middle of the camera and the walls of the camera are lined with photographic film. When Bragg's law is obeyed, the incoming X-ray beam will be diffracted by the crystal planes and leave a burn mark (a line) on the photographic film (Figure 6). Using the distance between the camera and the sample

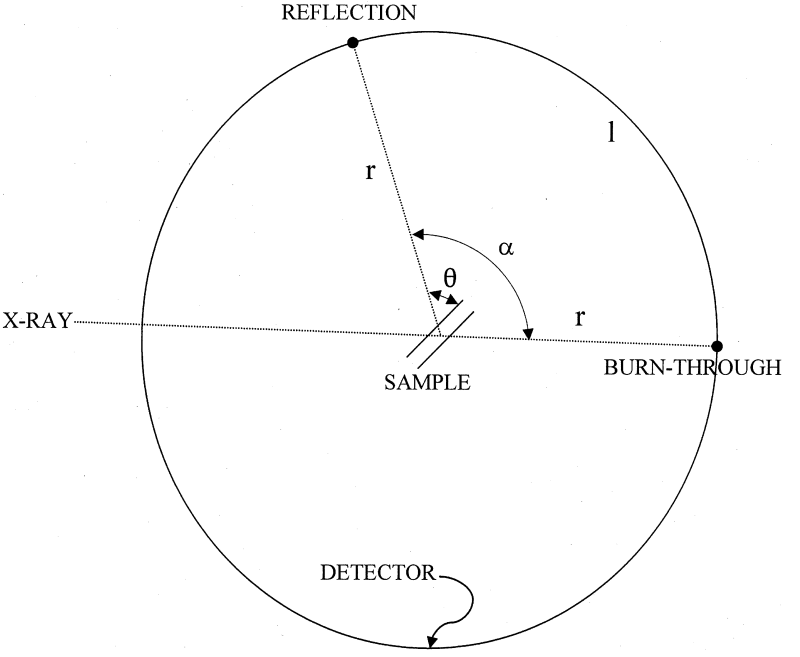

Figure 5 A powder X-ray diffraction experimental setup.

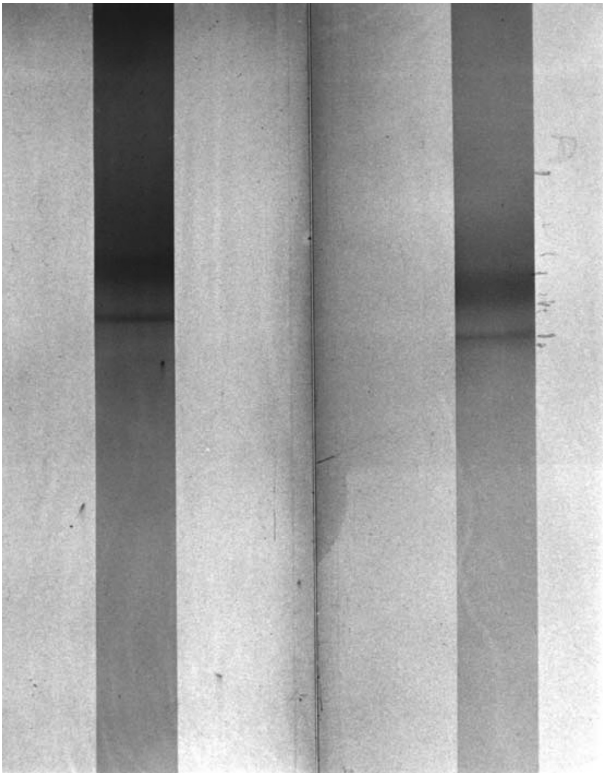

Figure 6 Photographic film used in a powder x-ray diffraction experiment. The lines observed correspond to the wide-angle reflections of milkfat (*left*) and chemically interesterified milkfat (*right*).

(r), as well as the distance between the burn-through and the particular reflection (the length of the arc, l), it is possible to determine the angle α, which is equal to 2θ, using:

$$\alpha = 360^\circ \frac{l}{2\pi r} \tag{5}$$

Since $\alpha = 2\theta$, we can determine the spacing between crystal planes corresponding to that particular reflection using Eqn. 3,

$$d_{hkl} = \frac{\lambda}{2\sin\theta} \tag{6}$$

A densitometric scan of the film will provide an intensity-scattering angle profile for the crystalline material being analyzed. This profile is called the powder-spectrum.

Many other setups are possible. Many modern machines have 2-dimensional charge-coupled device detectors (CCD detectors) that can detect the position and intensity of all reflections simultaneously, as shown in Figure 7. X-rays are usually transmitted through the sample in this setup. These detectors allow for the study of the dynamics of crystallization processes. The detector could also be a scintillation counter that travels and collects intensity data at the different scattering angles, as shown in Figure 8. X-rays are usually reflected from the sample in this setup. The resolution obtained with such setup is very high, however, it takes a fairly long period of time to collect a spectrum that includes both wide-angle and small-angle data (step sizes are in the order of 0.01°). Thus, the dynamics of the

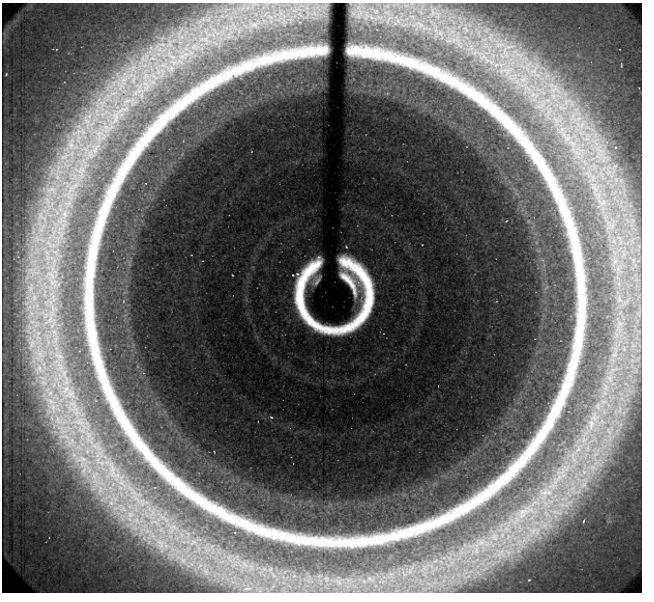

Figure 7 Two-dimensional powder x-ray diffraction spectrum for cocoa butter crystallized isothermically at 20 °C for 35 days.

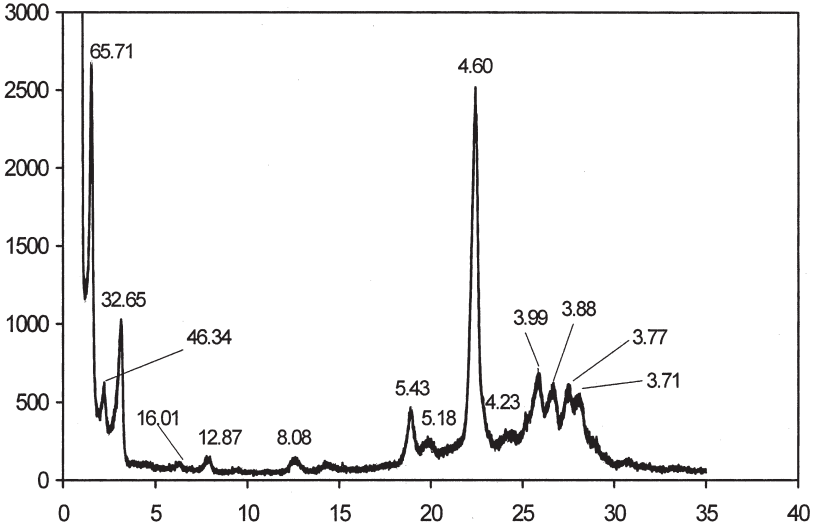

Figure 8 1D powder spectrum of cocoa butter crystallized at 22 °C for 20 days. The numbers correspond to the d-spacings in Angstroms.

crystallization processes are difficult to study. One can envision how the spectrum in Figure 8 would correspond to a cross section of Figure 7.

1.6. Indexing Reflections

By knowing the location of the glancing angle, θ, the values of d_{hkl} can be determined. The dimensions of the unit cell (a, b, and c) can be determined by identifying the d-spacings that correspond to the (100), (010), and (001) planes, respectively. Using this information, it is then straightforward to calculate d spacings corresponding to putative hkl planes and compare them to experimentally determined values. For example, Eqn. 7 can be used to index reflections for the case of a cubic unit cell.

$$d_{hkl} = \frac{a}{\left(h^2 + k^2 + l^2\right)^{\frac{1}{2}}} \tag{7}$$

Some types of unit cells give characteristic and easily recognizable patterns of diffraction lines. Thus, it is possible to gener-

ate characteristic spectra for known unit cell types and compare them with the experimental results.

Of note is that not all (hkl) planes will produce a diffraction line. Consider the (100), (110), and (111) planes of primitive, face-centered, and body-centered cubic lattices. In a face-centered lattice, the (100) and (110) planes sandwich planes sharing the same lattice points. The same is true for the (100) and (110) planes of a body-centered lattice. Reflections from these planes will, therefore, destructively interfere with reflections from the intervening planes. It follows, then, that all three of these planes will produce diffraction lines only in crystals with a structure based on the primitive lattice.

2. CRYSTALLOGRAPHIC STRUCTURE OF FATS

Most of our knowledge on the crystalline structure of fats comes from XRD studies. Fat crystal structure has profound effects on the physical properties of the fat (i.e, consistency, melting point). The adopted crystal structure depends on the type of lipid present, the fatty acid distribution and type on the lipid molecule, lipid purity, and crystallization conditions (temperature, rate of cooling, shear, seeds, solvent).

When a triacylglycerol molecule crystallizes, the chains will align side-by-side to maximize van der Waal's interactions (Figure 9). Indicated on the figure are the (a) and (c) axes of the unit cell. This view of the crystal lattice is along the a–c plane. The (c) axis usually refers to the long axis of the unit cell. The other short axis, (b), would be protruding behind the a–c plane.

In general, long spacings mirror the distance between methyl end groups for triacylglycerols and are usually comprised of two or three chain lengths of the fatty acid (Figure 10). Long spacings for triacylglycerols increase with increasing chain length and decrease with increasing tilt angle. In crystallographic terms, these reflections correspond to separation distances between (001) planes (d_{001}).

2.1 Single Crystal Structures

Very few single-crystal structures have been determined for triacylglycerols. Vand and Bell [1] first attempted to deter-

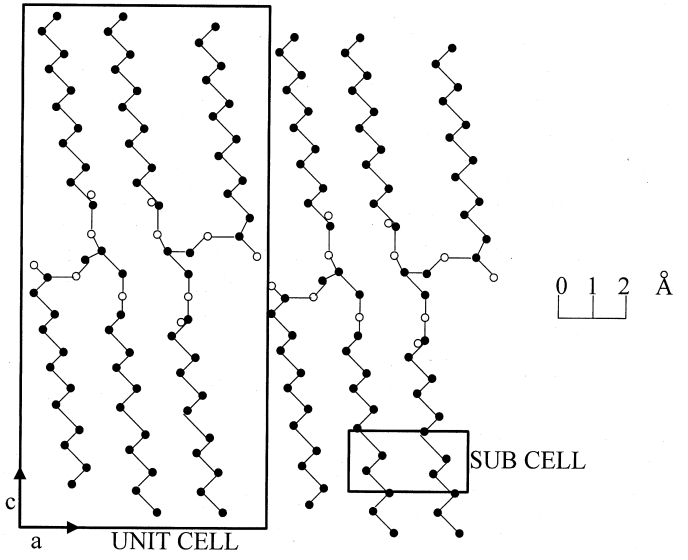

Figure 9 Diagram depicting the unit cell and the subcell of a triacylglycerol.

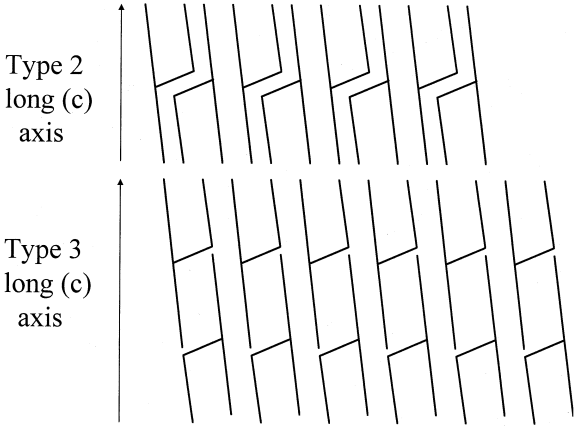

Figure 10 Double and triple chain stacking arrangement of triacylglyerols in a fat crystal.

mine the crystal structure of trilaurin. They came very close, being able to define the structure of the hydrocarbon chains, as well as the dimensions and space group of the unit cell. The first full crystal structure of a triacylglycerols is attributed to, L. H. Jensen and, A. J. Mabis in 1963 [2]. They determined the structure of the β-form of tricaprin. The refinement of their structure appeared in 1966. Shortly after, Larsson [3] reported the complete structure of trilaurin. The account of this work was, unfortunately, published in a somewhat obscure journal. The crystal structure of the β-form of 1,2-dipalmitoyl-3-acetyl-sn-glycerol was reported by Goto et al. in 1992 [4]. Of note are also the reported structures for brominated triaclyglycerols, namely tri-11-bromoundecanoin [3] and 2-11-bromoundecanoyl-1,1′dicaprin [6].

The structure of the β′ form was not reported until the year 2000, mainly due to difficulties in growing a large enough crystal for XRD studies. The structures of the β′ forms of 1,3-dicapryl-2-lauryl-sn-glycerol and 1,2-dipalmitoyl-3-myristoyl-sn-glycerol [7,8] have been determined experimentally.

2.2 Polymorphism

Polymorphic forms of fats are solid phases of the same chemical composition that, upon melting, yield identical liquid phases (like diamond and carbon). In fats and oils research, true polymorphism does not exist. This is because every phase usually also has a different molecular composition. Thus, according to the definition above, this does not constitute true polymorphism. Having qualified this fact, we will continue using the word polymorphism to describe the different crystal forms identified in a particular fat.

In fats and oils work, polymorphism is associated with different packing ***of the hydrocarbon chains*** and their angle of tilt. Three major polymorphic forms have been identified in fats and oils, namely the α, the β′ and the β forms. The alpha form is metastable and will thus transform into more stable forms. Two crystalline forms are called monotropic when one is more stable than the other, and recrystallization will take place in the direction of the more stable form only. Transformation of one polymorphic form into another is possible with

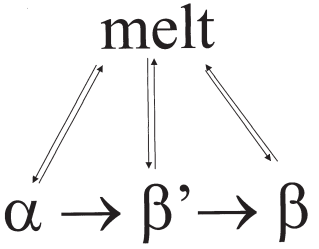

Figure 11 Dynamics of polymorphic crystallization and recrystallization in fats.

or without melting of the solid (melt-mediated vs. solid state). Figure 11 summarizes the possible dynamics of fat crystallization and recrystallization in terms of the polymorphism of the solid state. Notice how the a, β′ and β forms can form directly from the melt. Also evident is the irreversibility of the a to β′ to β transformations (monotropism).

2.2.1 Subcells and Subcell Packing

Subcells are the smallest spatial units of repetition along the chain axes within the unit cell (Figure 9). Methyl and carboxyl groups are not included in the subcell lattice. Ethylene is the smallest unit within the hydrocarbon chain, which constitutes a 3D entity. Diagrams, like the one shown in Figure 12, depict the way in which ethylene groups within the long hydrocarbon chains are arranged relative to each other. The best way to visualize this packing arrangement is through the use of molecular models. These two-dimensional representations of 3D structures are rather poor.

Simple lipids, like alcohols, fatty esters, and esters, show three main chain-packing arrangements that can be described by the chain-packing subcell. The most common subcell structures in fats are the hexagonal (α), triclinic (β or $T_{//}$), and orthorhombic perpendicular (β′ or $O_{\perp}$). In the triclinic (β) packing, there is one ethylene group per subcell, and all zigzag planes are parallel (Figure 12). The orthorombic packing (β′) is also characterized by one ethylene group per subcell; however, the

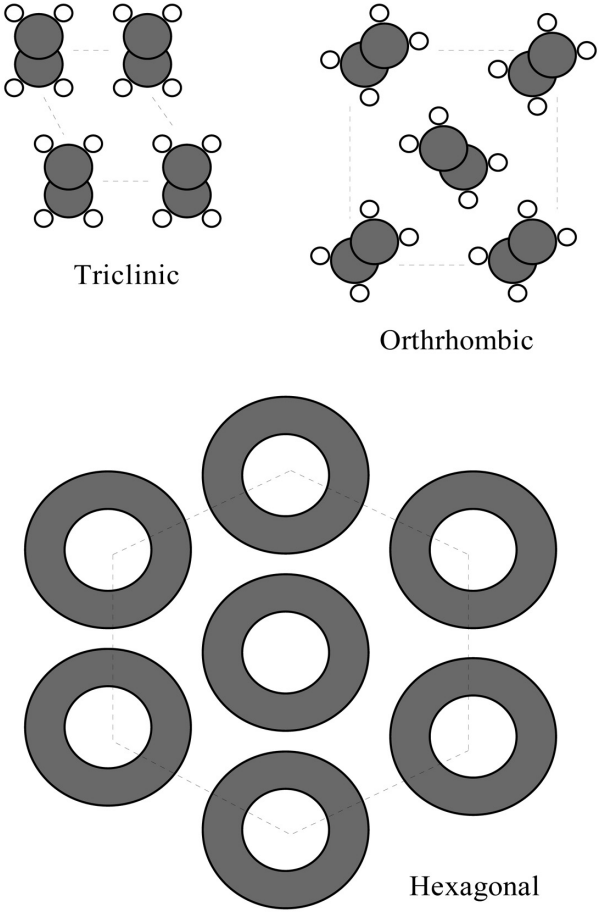

Figure 12 Possible geometric packing arrangements for ethylene groups within the long fatty acid chains of triacylglycerols in fat crystals.

difference between orthorhombic and triclinic is that the crystal planes are perpendicular to their adjacent planes (Figure 12). The hexagonal (α) packing occurs just below the melting point of the acyl chains. The chains are randomly oriented and display rotation about their long axis (Figure 12). Table 2 summarizes some of the characteristics of the different polymorphic forms in fats.

Table 2 Characteristics of the Different Polymorphic Forms in TAGs

Characteristic	α Form	β' Form	β Form
Chain packing	Hexagonal	Orthorhombic	Triclinic
Short spacing(s)	0.415 nm	0.38 and 0.42 nm	0.46 nm
IR Spectrum (-CH_2-) rocking vibration	Singlet at 720 cm^{-1}	Doublet at 727 and 719 cm^{-1}	Singlet at 717 cm^{-1}
Density	Least dense	Intermediate	Most dense
Melting Point	Lowest	Medium	Highest

2.2.2. Energetics of Crystallization as it Relates to Polymorphism

Figure 13 summarizes many of the principles governing the crystallization of fats. Triacylglycerols are relatively large (small) molecules. It takes a relatively long time for the long hydrocarbon chains to align and form a stable crystal form. The driving force for nucleation (and thus crystallization) is the degree of undercooling (or supercooling). When a melt is cooled below its melting point, a driving force for crystallization is established, which is proportional to the extent of this

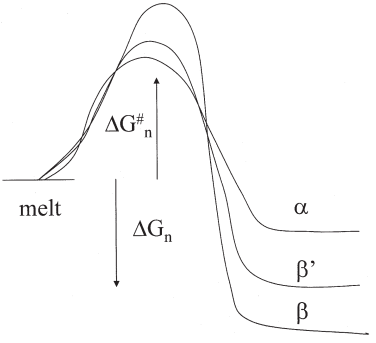

Figure 13 Diagram depicting the free energy of activation (kinetics of formation) for the formation of a particular polymorph as well as the free energy difference between products and reactants (thermodynamic stability).

undercooling (ΔT). Below its melting point, a material is in a metastable region where even though the material is undercooled, it does not crystallize. In this region, molecules are trying to adopt stable packing arrangements for the formation of a crystalline solid and decrease this driving force (the chemical potential between the solid and the melt). Given sufficiently high degrees of supercooling, molecules do not have sufficient time to pack in the most thermodynamically stable configuration and thus tend to crystallize in metastable forms. The key concept here is that the metastable forms have a lower free energy on nucleation ($\Delta G^{\#}$) than the more stable forms (Figure 13). Thus, the metastable forms will form more readily. This is a purely kinetic effect. Also, notice how the free energy of formation (ΔG) of the metastable forms is lower than that of the stable forms, since the free energy of the metastable form is the highest. Thus, even though the mestable forms have a lower thermodynamic stability, they tend to form more readily due to the kinetics of the process. This explains why metastable forms form first even though their melting point is lower than that of the more stable forms.

REFERENCES

1. Vand V, Bell IP. A direct determination of the crystal structure of the β form of trilaurin. Acta Crystallographica 1951; 4:465–469.
2. Jenson LH, Mabis AJ. Crystal structure of β-tricaprin. Nature 1963; 197:681–682.
3. Larsson K. The crystal structure of the β-form of trilaurin. Arkiv Kemi 1964; 23:1–15.
4. Goto M, Kodali DR, Small DM, Honda K, Kozawa K, Uchida T. Single crystal structure of a mixed-chain triacylglycerol: 1,2-Dipalmitoyl-3-acetyl-sn-glycerol. Proc Natl Acad Sci USA 1992; 89:8083–8086.
5. Larsson K. The crystal structure of the 1,3-diglyceride of 3-thiododecanoic acid. Acta Crystallog 1963; 16:741–748.
6. Doyne TH, Gordon JT. The crystal structure of a diacid triglyceride. J Amer Oil Chem Soc 1968; 45:333–334.

7. Sato K, Goto M, Yano J, Honda K, Kodali DR, Small DM. Atomic resolution structure analysis of β′ polymorph crystal of a triacylglycerol: 1,2-dipalmitoyl-3-myristoyl-sn-glycerol. J Lipid Research 2001; 42:338–345.

8. Van Langevelde A, van Malssen K, Driessen R, Goubitz K, Hollander F, Peschar R, Zwart P, and Schenk H. 2000. Structure of $C_nC_{n+2}C_n$-type (n = even) β′-triacylglycerols. *Acta Crystallographica* B56:1103–1111.

2

Crystallization Kinetics

ALEJANDRO G. MARANGONI
Department of Food Science
University of Guelph
Guelph, Ontario, Canada

1. INTRODUCTION TO CRYSTALLIZATION

1.1 Nucleation

When the temperature of a fat melt is decreased below its maximum melting temperature, it becomes supersaturated in the higher-melting triacylglycerol (TAG) species present in the mixture. This so-called undercooling or supercooling (below the melting temperature) represents the thermodynamic driving force for the change in state from liquid to solid. Fats usually have to be undercooled by at least 5–10°C before they begin to crystallize. For a few degrees below the melting point, the melt exists in a so-called metastable region. In this region, molecules begin to aggregate into tiny clusters called embryos.

At these low degrees of undercooling, embryos continuously form and breakdown, but do not persist to form stable nuclei. The energy of interaction between triacylglycerol molecules has to be greater than the kinetic energy of the molecules in the melt so as to overcome Brownian effects. For these flexible molecules, it is not sufficient to simply interact; molecules have to adopt a specific conformation in order to form a stable nucleus. The adoption of this more stable conformation is relatively slow, thus explaining the existence of a metastable region. As the undercooling is increased (i.e., at lower temperatures), stable nuclei of a specific critical size are formed. The Gibbs free energy change associated with the formation of a crystal embryo (ΔG_n) includes contributions from both surface (positive) and volume changes (negative) and is defined by

$$\Delta G_n = A_n \delta - V_n \frac{\Delta \mu}{V_m^s} \quad (1)$$

where A_n is the surface area of a nucleus, δ is the surface free energy per unit area, V_n is the volume of a nucleus, $\Delta\mu$ is the chemical potential difference between solid and liquid (related to the degree of supersaturation) and V_m^s is the molar volume of the solid. The formation of a crystal leads to the creation of a solid–liquid interface, resulting in a positive contribution to the free energy of nucleation (proportional to A_n). On the other hand, the formation of a crystal also leads to a decrease in the chemical potential difference between the solid and liquid (proportional to V_n). Thus, at a critical nucleus size (referred to as a critical radius, r_c, in this discussion) a maximum in the free energy of nucleation profile will be observed, where an increase proportional to A_n is exactly balanced by a decrease proportional to V_n. Beyond r_c, the free energy of nucleation will continuously decrease. In order to minimize their free energy, clusters smaller than r_c will break down while those larger than r_c will continue to grow.

The three most common types of nucleation include primary homogeneous nucleation, primary heterogeneous nucleation, and secondary nucleation. With significant undercooling, primary homogenous nucleation may occur in a melt. Primary homogenous nucleation occurs in pure solutions, in the absence of foreign interfaces. In reality, however, nucle-

ation is usually catalyzed by the presence of foreign particles or interfaces. Primary heterogeneous nucleation requires significantly lower supersaturation than homogeneous nucleation because foreign surfaces reduce the effective surface free energy by decreasing the crystal-melt interfacial tension (δ in equation. 1). "Catalytically active impurities," which can include surface edges, create order in small regions of the melt, thus serving as templates for nucleation. Secondary nucleation, the process where new crystal nuclei form on contact with existing crystals, or crystal fragments, will proceed once primary nucleation has taken place. The number of nuclei needed to induce crystallization in bulk fats is very low (1 per cubic mm or less). In contrast, each droplet in an emulsified fat must contain a nucleus for crystallization to take place. Since the likelihood of each globule containing a nucleus or catalytic impurity is low, emulsified fats require much more undercooling to induce crystallization compared to bulk fat.

1.2 Growth

Crystal growth involves both the diffusion of TAGs from the bulk solution across a boundary layer and the incorporation of TAGs into the crystal lattice of an existing nucleus or crystal. TAG crystal growth depends on a number of factors, including the degree of undercooling, the rate of molecular diffusion to the crystal surface, and the time required for TAG molecules to fit into the growing crystal lattice. Because of the large entropic loss (gain in "order" of the system) associated with the incorporation of a molecule into a crystal lattice, the activation energy for this event is high. Especially at low degrees of supersaturation, incorporation of TAG molecules into the crystal lattice is considered to be the rate-limiting step in fat crystallization rather than diffusion to the crystal surface. Crystallization in a multicomponent fat is especially slow because the supersaturation for each TAG molecule is very small and because of competition between very similar molecules for the same sites in the crystal lattice.

Melt viscosity can also have a significant effect on growth rate, particularly at higher degrees of supersaturation, because it limits molecular diffusion and the dissipation of the

latent heat of crystallization away from a growing crystal face. Growth rate is inversely proportional to melt viscosity, which tends to increase with decreasing temperature.

Compared to nucleation, the driving force required for crystal growth is relatively small. Given that fats have in general large negative entropies of fusion (about 10 times that of water), nucleation events are expected to dominate the crystallization process. As a result, there is likely to be further nucleation during crystal growth. For example, nucleation was observed in tristearin melts throughout the crystallization process [1]. A low reaction-rate constant for growth, relative to the overall rate of crystallization, means that there is enough supercooling in the melt for nucleation to take place throughout the melt, beyond the growing solid–liquid interface. In these cases, the rate of nucleation, rather than the rate of crystal growth, governs the overall rate of solidification [1].

The crystal growth rate and mechanism will depend on both the nature of the crystal–melt interface and structure of the crystal surface [2]. When a surface, at a molecular scale, is rough, there will be many "kink" sites present in the lattice of a growing crystal where approaching molecules may be incorporated. As a result, continuous growth will occur. The growth rate for continuous growth is linearly related to the supersaturation of the system [2,3]. While kinked faces grow continuously, relatively flat crystal faces grow in a layered fashion [4]. A smooth surface makes growth more difficult and, as a result, "layer" growth models predominate [2]. The two models to describe layered growth on crystal surfaces are two-dimensional nucleation and spiral growth [4]. Two-dimensional nucleation is quite rare, but can occur if enough growth units cluster together to form an embryo of stable critical nuclei on a crystal surface. At this point, lateral growth may proceed with further growth units diffusing to the surface and attaching to the nucleus. Because surface nuclei must form on the perfect crystal surface in two-dimensional growth, a relatively high driving force is needed [4,5]. At low degrees of supersaturation, the energy barrier for two-dimensional nucleation is very high. In these cases, the more common spiral growth mechanism will predominate [4].

In the spiral growth mechanism, kinks are produced in the crystal-melt interface by emergent screw dislocations. Growth units then reach these sites by surface diffusion [2,6]. Frank [6] proposed that incoming molecules readily migrate to imperfections, in the form of dislocations, on a growing face because these regions possess a lower surface free energy. This renews the crystal defects which continue to be perpetuated in a spiral manner [7]. Spiral defects in crystal surfaces can lead to continuous growth [3]. At low degrees of supersaturation, steps protrude from the crystal surface and spiral growth occurs [5]. The reaction-rate constant for this type of growth is much lower than the constant for continuous growth [1]. In long-chain compounds, spiral growth is commonly polygonized (as opposed to circular) [8,9]. It has been suggested that polygonized growth may be responsible for the generation of polytypes in materials which demonstrate this behavior [4,10].

van Putte and Bakker [11] found the growth rate of saturated palm oil crystals to follow a screw dislocation mechanism [12]. Crystal growth in the direction of a TAG's hydrocarbon chains is believed to occur via a screw-dislocation mechanism (as reported by Skoda and van den Tempel [13]). In tristearin crystals, the faces which contain the methyl end groups are almost flat because of the asymmetric shape of the TAG molecule and the requirement of close packing in the planes of the methyl groups [14]. In contrast, the lateral crystal faces are rough [15]. Lateral growth of TAG crystals does not seem to be controlled by either a dislocation or surface nucleation mechanism [13]. Surface roughness, particularly at high degrees of supersaturation, makes the initiation of a new layer by two-dimensional nucleation unnecessary [15]. Electron micrographs of milk fat crystals showed rounded ends, while the (100) faces were either flat or somewhat rounded, and the large (001) faces were flat with an occasional sharp step (as reported by Walstra [16]). *n*-paraffin crystals also demonstrate rounded, rather than planar crystal ends, because of increased kinetic roughening (i.e., formation of many small nuclei on the face) of the crystal faces in the (010) direction (as reported by Walstra [16]).

1.3 The Effects of Impurities on Crystallization

Treatises on fat crystallization often include a discussion about the effects of impurities on phase transformations with strong emphasis placed on the review by Boistelle [4]. According to crystallization theory, impurities should increase nucleation and decrease crystal growth rates [4]. Heterogeneous nucleation is controlled by the relationship between the crystal and melt, the crystal and the foreign substance, and the melt and the foreign substance [5]. As an impurity adsorbs onto a nucleus' surface, it can decrease the interfacial tension between the solid crystal and the melt. Thus, the presence of foreign particles in a melt may decrease the free energy of formation of a critical nucleus [2]. As a result, the rate of nucleation should increase [4]. Boistelle [4] reported that the adsorption of impurities and additives should theoretically also increase crystal growth rates. Adsorption of impurities result in a decrease in the edge free energy of the crystal steps which means that the distance between the steps should be decreased with a simultaneous increase in growth rate. In three-dimensional nucleation (i.e., not on an existing crystal surface), however, crystal growth is inhibited by impurity adsorption because kinetic factors decrease more rapidly than thermodynamic factors [4]. Additives may also decrease the growth of crystal faces by partially blocking the surface and hindering the approach and incorporation of new molecules [17]. If an additive affects the growth rate of the crystal's faces differently, a change in shape (habit modification) occurs [17]. While additives may be effective at extremely low concentrations [17], they are generally more effective at increased concentration and also at decreasing supersaturation [4,18,19].

Several examples of impurity effects on crystallization can be found in nature [20]. In kidney or gall stones, for example, organic additives inhibit crystal growth, just as polyvinylsulfonate and polyglutamic acid can retard carbonate precipitation and crystallization in some metals [21,22]. In other examples, impurities have been shown to accelerate phase transitions. For example, some aspartic-rich proteins initiate the growth of calcite crystals [23], just as polyglutamic acid promotes calcium oxalate nucleation at low levels [24].

The reported effects of impurities on crystallization are variable. Impurities may either enhance nucleation or suppress it by interfering with the formation of stable embryos. Likewise, they can retard crystal growth or increase crystal growth rates [24].

The examples cited previously involve "impurities," the structures of which bear little resemblance to the crystallizing molecules. As a result, these molecules will adsorb onto a growing crystal face or a nucleation template [20]. van den Tempel [15] thought that emulsifiers, because of their surface-active nature, may adsorb at active surfaces and prevent heterogeneous nucleation, resulting in a higher supercooling requirement or a longer time for crystallization. He suggested that molecules which adsorb more strongly and become more firmly attached to a growing crystal should exert larger effects on crystallization [15]. In fat systems, we are most commonly dealing with emulsifier-type molecules which demonstrate a high degree of similarity with the crystallizing molecules. It is doubtful that these molecules function as "impurities" in the classical sense. It is more likely that chemical and structural affinity between the "impurity" and crystallizing TAGs results in co-crystallization of the molecules [20].

2. CRYSTALLIZATION KINETICS

2.1. Nucleation

2.1.1. Steady-State Nucleation Theory

The conventional Gibbs-Thomson formulation expresses the overall free energy change resulting from the formation of a spherical nucleus as the sum of a surface term and a volume term,

$$\Delta G_n = 4\pi r^2 \delta - \frac{4}{3}\pi r^3 \frac{\Delta\mu}{V_m^s} \tag{2}$$

where ΔG_n is free energy change associated with the formation of spherical nucleus (J), r is crystal radius (m), δ is the solid-liquid surface free energy per unit area (J m^{-2}), or crystal-melt interfacial tension, $\Delta\mu$ is the chemical potential differ-

ence between the liquid and the solid (J mol^{-1}), while V_m^s is molar volume of the solid (m^3 mol^{-1}).

The creation of a solid–liquid interface requires energy, leading to an increase in the free energy of the sysem; however, the creation of a nucleus also causes a decrease in the free energy of the system, driven by a decrease in the supersaturation of the system upon crystallization. Thus, at a certain critical radius, a maximum in the ΔG_n-r profile will be observed (Figure 1). As discussed above, this ΔG_n maximum corresponds to the critical radius of the nucleus (r_c).

Envision a particular ith TAG component in a fat mixture. If the fat melt is cooled below the melting point of this i^{th} component, it will crystallize until its saturation concentration in the melt is reached and thermodynamic equilibrium reestablished. At this point, the chemical potential of the pure i^{th} solid [$\mu_i^*(s)$] equals the chemical potential of that same i^{th} component dissolved in the melt [$\mu_i(l)$] (along with the other components), namely

$$\mu_i^* = \mu_i(l) \tag{3}$$

The chemical potential of the i^{th} component in the melt equals

$$\mu_i(l) = \mu_i^*(l) + RT \ln a_i(l) \tag{4}$$

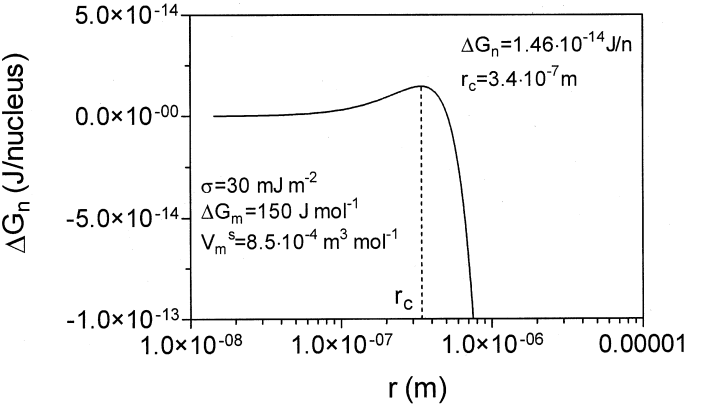

Figure 1 Simulation of changes in the free energy of nucleation with nucleus size. Notice the maximum at the critical radius ($\sqrt{c}$).

where $\mu_l^*(l)$ is the chemical potential of a pure liquid of the i^{th} component, and $a_i(l)$ corresponds to the activity of the i^{th} component in the melt, $a_i(l) = \gamma_i x_i(l)$, where γ_i is the activity coefficient and $x_i(l)$ is the concentration. Thus we can write

$$\mu_i^*(s) = \mu_i^*(l) + RT \ln a_i(l) \tag{5}$$

and therefore

$$\Delta\mu = \mu_i^*(s) - \mu_i^*(l) + RT \ln a_i(l) \tag{6}$$

Consider the Hildebrand equation,

$$\ln a_i(l) = \frac{\Delta H_{f,i}}{R}\left(\frac{1}{T_{f,i}} - \frac{1}{T}\right) = \frac{\Delta H_{f,i}}{RT_{f,i}} - \frac{\Delta H_{f,i}}{RT} \tag{7}$$

where ΔH_f is the enthalpy of fusion, and T_f is the temperature of fusion (melting point). Recall that $\Delta S_f = \Delta H_f/T_f$, and therefore the Hildebrand equation can be rearranged to

$$RT \ln a_i(l) = \frac{T\Delta H_{f,i}}{T_{f,i}} - \Delta H_{f,i} = T\Delta S_{f,i} - \Delta H_{f,i} = -\Delta G_{f,i} \tag{8}$$

Thus, the difference in chemical potential between the pure solid of the ith component and the pure liquid of the ith component is equivalent to the free energy of fusion (ΔG_f),

$$\Delta G_{f,i} = -RT \ln a_i(l) = \mu_s^*(l) - \mu_s^*(s) = \Delta\mu \tag{9}$$

If the solid phase was composed of a mixture of fats, rather than a single component, then we would have to take into account the concentration (activity) of the ith component in the solid as well. Thus, after the material has crystallized and equilibrium has been reestablished, the chemical potential of the solid and the liquid would be equal,

$$\mu_i^*(s) + RT \ln a_i(l) = \mu_i^*(l) + RT \ln a_i(l) \tag{10}$$

The chemical potential difference between the pure i^{th} solid and the pure i^{th} liquid could then be expressed as a function of the concentration (activity) of the i^{th} component in the solid and the liquid,

$$\Delta\mu = \mu_i^*(s) - \mu_i^*(l) = RT \ln a_i(l) - RT \ln a_i(s) = RT \ln \frac{a_i(l)}{a_i(s)} \tag{11}$$

Considering the above, we can rewrite the Gibbs-Thomson equation as

$$\Delta G_n = 4\pi r^2 \delta - \frac{4}{3}\pi r^3 \frac{\Delta G_f}{V_m^s} \tag{12}$$

The change in free energy as a function of radius is given by

$$\frac{\partial \Delta G_n}{\partial r} = 8\pi r \delta - 4\pi r^2 \frac{\Delta G_f}{V_m^s} \tag{13}$$

The formation of a stable crystal nucleus takes place above a critical radius (r_c). This radius corresponds to a maximum in the free energy *versus* nuclei radius profile. At this point,

$$\frac{\partial \Delta G_n}{\partial r} = 0 \tag{14}$$

Equation 13 can then be rearranged to

$$8\pi r_c \delta = 4\pi r_c^2 \frac{\Delta G_f}{V_m^s} \tag{15}$$

and an expression for this critical radius obtained,

$$r_c = \frac{2\delta V_m^s}{\Delta G_f} \tag{16}$$

Substituting r_c for r in the Gibbs-Thompson equation,

$$\Delta G_n^{r_c} = 4\pi \left(\frac{2\delta V_m^s}{\Delta G_f} \right)^2 \delta - \frac{4}{3}\pi \left(\frac{2\delta V_m^s}{\Delta G_f} \right)^3 \frac{\Delta G_f}{V_m^s} \tag{17}$$

and after rearrangement, leads to a useful expression,

$$\begin{aligned} \Delta G_n^{r_c} &= \frac{16\pi\delta^3 (V_m^s)^2}{(\Delta G_f)^2} - \frac{32\pi\delta^3 (V_m^s)^3 \Delta G_f}{3(\Delta G_f)^3 V_m^s} = \frac{16\pi\delta^3 (V_m^s)^2}{(\Delta G_f)^2} - \frac{32\pi\delta^3 (V_m^s)^2}{3(\Delta G_f)^2} \\ &= \frac{48\pi\delta^3 (V_m^s)^2}{3(\Delta G_f)^2} - \frac{32\pi\delta^3 (V_m^s)^2}{3(\Delta G_f)^2} \\ &= \frac{16\pi\delta^3 (V_m^s)^2}{3(\Delta G_f)^2} \end{aligned} \tag{18}$$

Considering that

$$\Delta G_f = \Delta H_f - T\Delta S_f \tag{19}$$

and that since $\Delta G_f = 0$ when $T = T_f$, then

$$\Delta S_f = \frac{\Delta H_f}{T_f} \tag{20}$$

Thus, the free energy of fusion can be expressed as

$$\begin{aligned}\Delta G_f &= \Delta H_f - T\left(\frac{\Delta H_f}{T_f}\right) = \Delta H_f\left(1 - \frac{T}{T_f}\right) = \Delta H_f\left(\frac{T - T_f}{T_f}\right) \\ &= \frac{\Delta H_f(\Delta T)}{T_f}\end{aligned} \tag{21}$$

Substituting equation. 21 into equation. 18 results in the common form of the Gibbs-Thompson equation used in fat crystallization studies,

$$\Delta G_n^{r_c} = \frac{16\pi\delta^3(V_m^s)^2 T_f^2}{3\Delta H_f^2(\Delta T)^2} \tag{22}$$

This free energy of nucleation corresponds to an activation free energy of nucleation—the free energy barrier required to form a spherical nucleus of critical radius r_c.

2.1.2. Theory of Reaction Rates

Absolute reaction rate theory is a collision theory that assumes that chemical activation occurs through collisions between molecules. The central postulate of this theory is that the rate of a chemical reaction is given by the rate of passage of the activated complex through the transition state.

This theory is based on two assumptions, a dynamical bottleneck assumption and an equilibrium assumption. The first asserts that the rate of a reaction is controlled by the decomposition of an activated transition-state complex, and the second one asserts that an equilibrium exists between reactants (A and B) and the transition-state complex, $C^{\#}$, namely

$$A + B \leftrightarrows C^{\#} \rightarrow \text{products.} \tag{23}$$

It is therefore possible to define an equilibrium constant for the conversion of reactants in the ground state to an activated complex in the transition state. For the above reaction,

$$K^{\#} = \frac{[C^{\#}]}{[A][B]} \tag{24}$$

At equilibrium, the rate of the forward reaction (v_1) is equal to the rate of the reverse reaction (v_{-1}), $v_1 = v_{-1}$. Therefore, for the reaction A + B $\leftrightarrows$ $C^{\#}$ at equilibrium,

$$k_1 [A] [B] = k_{-1} [C^{\#}] \tag{25}$$

and therefore

$$K = \frac{[\text{Products}]}{[\text{Reactants}]} = \frac{[C^{\#}]}{[A][B]} = \frac{k_1}{k_{-1}} \tag{26}$$

Since $\Delta G^\circ = -RT\ln K$, the temperature dependence of the logarithm of the equilibrium constant for the standard state equals

$$\frac{d \ln K}{dT} = \frac{\Delta G^o}{RT^2} \tag{27}$$

And since $\ln K = \ln k_1 - \ln k_{-1}$, then

$$\frac{d \ln k_1}{dT} - \frac{d \ln k_{-1}}{dT} = \frac{\Delta G^o}{RT^2} \tag{28}$$

The change in the standard state free energy of a system undergoing a chemical reaction from reactants to products (ΔG°) is equal to the free energy required for reactants to be converted to products minus the free energy required for products to be converted to reactants. Moreover, the energy required for reactants to be converted to products is equal to the difference in energy between the ground state and transition state of the reactants ($\Delta G_1^{\#}$), while the energy required for products to be converted to reactants is equal to the difference in energy between the ground state and transition state of the products ($\Delta G_{-1}^{\#}$) (Figure 2).

Therefore, the change in the free energy of a system undergoing a chemical reaction from reactants to products can be expressed as

$$\Delta G^\circ = G_{products} - G_{reactats} = \Delta G_1^{\#} - \Delta G_{-1}^{\#} \tag{29}$$

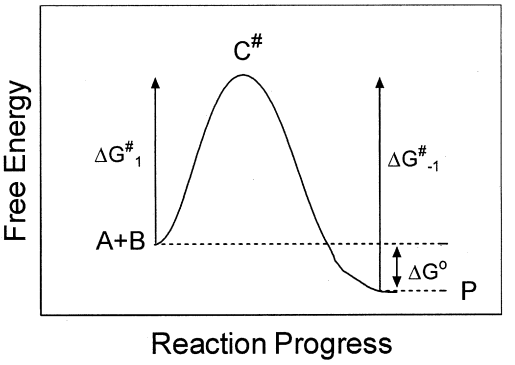

Figure 2 Changes in free energy as a function of the progress of a chemical reaction.

The equation can therefore be expressed as two separate differential equations corresponding to the forward and reverse reactions.

$$\frac{d\ln k_1}{dT} = \frac{\Delta G_1^{\#}}{RT^2} + A \quad and \quad \frac{d\ln k_{-1}}{dT} = \frac{\Delta G_{-1}^{\#}}{RT^2} + A \tag{30}$$

Arrhenius determined that for many reactions, A = 0. Therefore, indefinite integration of the above equation for either the forward or reverse reactions,

$$\int d\ln k_r = \frac{\Delta G^{\#}}{R}\int \frac{dT}{T^2} \tag{31}$$

yields the expression

$$\ln k_r = \ln C - \frac{\Delta G^{\#}}{RT} \quad or \quad k_r = Ce^{-\left(\frac{\Delta G^{\#}}{RT}\right)} \tag{32}$$

where $\Delta G^{\#}$ is the free energy of activation. By using statistical thermodynamic arguments, it is possible to show that the preexponential factor C equals

$$C = \kappa\upsilon \approx \frac{k_B T}{h} \tag{33}$$

where κ is the transmission coefficient (dimensionless) and ε is the frequency (s^{-1}) of the normal mode oscillation of the

transition-state complex along the reaction coordinate—more rigorously, the average frequency of barrier crossing. The transmission coefficient, which can differ dramatically from unity, includes many correction factors, including tunneling, barrier recrossing correction, and solvent frictional effects. This expression can also equal k_BT/h, where k_B is Boltzman's constant (J K^{-1}), while h is Planck's constant (J s).

Thus, an expression for the rate of a first order chemical reaction involving N molecules can have the form

$$v = kN = \frac{Nk_BT}{h} e^{-\frac{\Delta G^{\#}}{k_BT}} \tag{34}$$

where ν is the rate of the reaction (s^{-1}), k is the first order reaction rate constant (s^{-1}), and N is the number of molecules participating in the reaction.

2.1.3. The Fisher-Turnbull Equation

The Fisher-Turnbull equation can be used to quantify the activation free energy of nucleation for a crystallization process, and has been extensively used in the study of fat crystallization.

The Fisher-Turnbull equation can be obtained by considering the activation free energy of nucleation to be a combination of a free energy of activation for diffusion ($\Delta G_d^{\#}$) and the free energy of nucleation for a nucleus of critical radius r_c (ΔG_n^{rc}, equation 22),

$$\Delta G^{\#} = \Delta G_d^{\#} + \Delta G_n^{\sqrt{c}} \tag{35}$$

Substituting equation. 35 into equation. 34 yields

$$v = \frac{Nk_BT}{h} e^{-\frac{\Delta G_d^{\#}}{k_BT}} e^{-\frac{\Delta G_n^{r_c}}{k_BT}} \tag{36}$$

where ν now denotes the rate of nucleation (s^{-1}), and N the number of molecules in the melt participating in the nucleation process.

At relatively low degrees of undercooling, or for a narrow range of temperatures, $\Delta G_d^{\#}$ is assumed to remain constant, and, thus, equation. 36 can be expressed as

$$v = \frac{\alpha N k_B T}{h} e^{-\frac{\Delta G_n^{r^*}}{k_B T}} \tag{37}$$

where

$$\alpha = e^{-\frac{\Delta G_d^{\#}}{k_B T}} \tag{38}$$

The rate of nucleation is approximated by the inverse of the induction time of crystallization (γ),

$$v \sim \frac{1}{\tau} \tag{39}$$

Thus, equation. 37 can be expressed as

$$\frac{1}{\tau} \sim \frac{\alpha N k_B T}{h} e^{-\frac{\Delta G_n^{r_c}}{k_B T}} \tag{40}$$

and

$$\frac{1}{\tau T} \sim \frac{\alpha N k_B}{h} e^{-\frac{\Delta G_n^{r_c}}{k_B T}} \tag{41}$$

Taking the natural logarithm on both sides results in

$$\ln(\tau T) \sim -\ln \frac{\alpha N k_B}{h} + \frac{\Delta G_n^{r_c}}{k_B T} \tag{42}$$

Introducing equation. 22 into equation. 42 yields

$$\ln(\tau T) \sim -\ln \frac{\alpha N k_B}{k} + \frac{\Delta G_n^{r_c}}{k_B T} = -\ln \frac{\alpha N k_B}{k} + \frac{\left(\frac{16\pi\delta^3 (V_m^s)^2 T_f^2}{3\Delta H_f^2 (\Delta T)^2} \right)}{k_B T} \tag{43}$$

After rearrangement, this equation can be expressed as

$$\ln(\tau T) \sim -\ln \frac{\alpha N k_B}{h} + \frac{16\pi\delta^3 (V_m^s)^2 T_f^2}{3 k_B \Delta H_f^2} \left(\frac{1}{T(\Delta T)^2} \right) \tag{44}$$

Thus, a plot of $\ln(\tau T)$ versus $1/[T(\Delta T)^2]$ should yield a straight line with a slope, m (K^3), which equals

$$m = \frac{16\pi\delta^3 (V_m^s)^2 T_f^2}{3 k_B \Delta H_f^2} \tag{45}$$

Since

$$\Delta G_n^{r_c} = \frac{16\pi\delta^3 (V_m^s)^2 T_f^2}{3\Delta H_f^2 (\Delta T)^2} \tag{46}$$

the free energy of nucleation can then be determined from

$$\Delta G_n^{r_c} = \frac{mk_B}{(\Delta T)^2} \tag{47}$$

Figure 3 depicts the Fisher-Turnbull plot for palm oil. Two distinct linear regions can be appreciated above and below 27°C.

Since

$$\Delta G_n^{r_c} = \frac{16\pi\delta^3 (V_m^s)^2 T_f^2}{3\Delta H_f^2 (\Delta T)^2} \tag{46a}$$

the free energy of nucleation can then be determined from

$$\Delta G_n^{r_c} = \frac{mk_B}{(\Delta T)^2} \tag{47a}$$

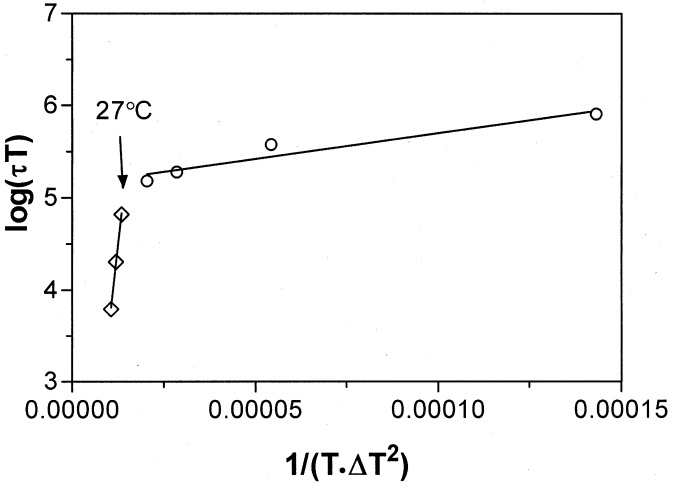

Figure 3 A plot log (ΔT) vs. $1/(T \cdot \Delta T^2)$ yields two distinct linear region slopes that permit the calculation of activation free energies of nucleation of each region. Induction times of crystallization (τ, sec) were determined using a cloud point analyzer.

Results for the palm oil example presented earlier are shown in Figure 4.

This particular example is quite educational. If palm oil was a single-component system, we would expect $\Delta G_n^{r^*}$ to be lower at lower temperatures (increased rate of nucleation). However, the opposite is true. This is explained by the fact

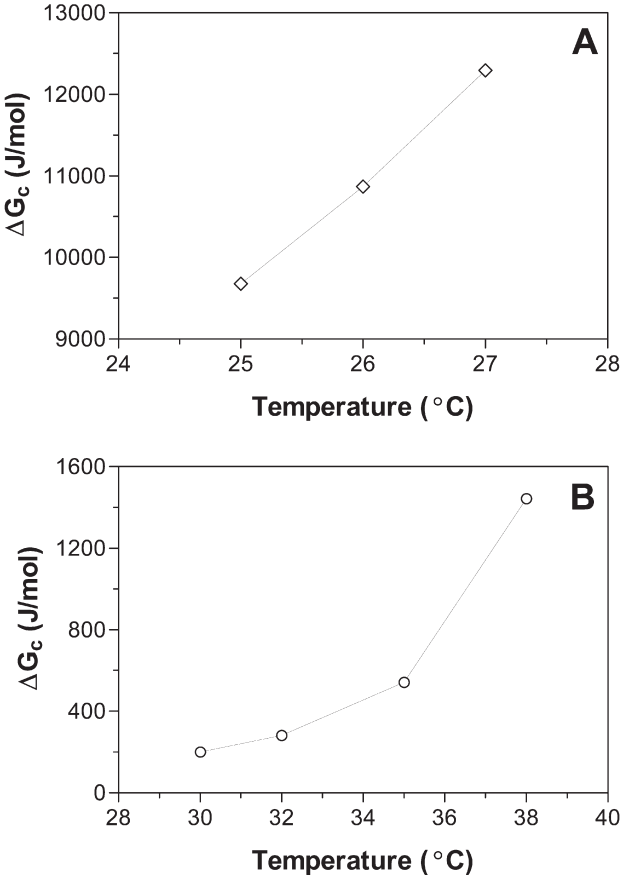

Figure 4 Activation free energies of nucleation (J/mol) vs. temperature (°C) calculated from the slopes of the linear regions in Figure 3, for the fractions crystallizating in the range of (**A**) 25°C to 27C°C and (**B**) 30°C to 38°C.

that the break observed in the Fisher-Turnbull plot is due to the crystallization of two distinct fractions present in the material. Thus, the free energies of nucleation reported are for two distinct materials. The effect of temperature on the crystallization behavior of palm oil is thus different in different temperature ranges.

Another useful application of the Fisher-Turnbull equation is in the determination of the crystal-melt interfacial tension (δ). If reliable calorimetric data for the enthalpy and temperature of fusion are available, and an estimate of the molar volume can be obtained, the solid–melt interfacial tension can be directly calculated from

$$\delta = \left(\frac{3mk_B \Delta H_f^2}{16\pi (V_m^s)^2 T_f^2} \right)^{\frac{1}{3}} \tag{48}$$

2.1.4. Estimates of ΔH_f and V_m^s

Estimates of the enthalphy of fusion should be obtained experimentally using differential scanning calorimetry. It is not possible to predict *a priori* the enthalpy of fusion of a complex mixture of triacylglycerols and minor polar components which have been crystallized, most probably, under dynamic conditions. Knowledge of the complex phase behavior of TAGs crystallized under nonequilibrium, dynamic conditions does not exist yet.

The density of a solid TAG mixture, crystallized under relevant conditions, should also be determined experimentally by picnometry. The molar volume of a fat can then be calculated from density data using

$$molar\ volume\ (m^3 / mol) = \frac{MW(g / mol)}{density(g / ml)} (1 \cdot 10^{-6} m^3 / ml) \tag{49}$$

Experimentally determined melting enthalpies and temperatures, as well as densities, for different pure TAG polymorphs are listed in Appendix Va and Table 10.3, respectively, of Donald Small's book [25]. This data, however, is not very relevant to a complex fat system. Suffice to say, good experimental

data is required for these type of analyses. The nature of the material (multicomponent system, presence of impurities, metastable nucleation, etc.) though, makes it quite difficult to obtain good data.

2.1.5. Metastability and the Free Energy of Nucleation

Even at moderate degrees of undercooling, triacylglycerols do not nucleate in their most stable polymorphic form, but rather nucleate in a metastable form. This can be explained by close inspection of equation 22. Being closer in nature to the liquid state, the α form of TAGs has a lower surface free energy, or crystal-melt interfacial tension. This, in turn will lead to a lower free energy of nucleation, and thus a higher nucleation rate. The crystal-melt surface free energy is the main factor responsible for the metastable nucleation behavior of triacylglycerols and fats. This effect must be enormous. For an α form at a particular temperature, the degree of undercooling (ΔT), melting enthalpy (ΔH_f) and melting temperature (T_f) are lower, and the molar volume (V_m) is higher (lower density), than for more stable crystal forms. This should result in a higher activation free energy for the nucleation of an α form than for more stable crystal forms. However, the opposite is true. The activation free energy of nucleation is actually lower for an α form, resulting in a higher rate of nucleation, than for more stable crystal forms. Close inspection of equation 22 reveals that for this to be the case, the surface free energy term (δ) must be much lower for the α form than for more stable crystalline phases. Future studies should pay more attention to the effects of δ on crystallization behavior.

2.2 Crystal Growth: The Avrami model

The Avrami model [26–28] can be used to quantify crystallization kinetics and provides an indication of the nature of the crystal growth process. Applied to the study of fat crystallization, the Avrami equation has the following form,

$$\frac{SFC}{SFC_{\max}} = 1 - e^{-kt^n} \tag{50}$$

where n is the Avrami exponent (dimensionless), k is the Avrami constant (t^{-n}), SFC corresponds to the solid fat content at a particular time, and SFC_{max} corresponds to the maximum SFC achieved at a particular temperature.

This model was developed to describe the kinetics of liquid–solid phase transitions in metals and its principles were first applied to polymer crystallization in the 1950s [7,29]. The Avrami model is the most commonly used model used in the study of fat crystallization. The equation describes an event in which there is an initial lag period, where crystallization occurs very slowly, followed by a subsequent rapid increase in crystal mass. This model takes into account that crystallization occurs by both nucleation and crystal growth and is based on the assumptions of isothermal transformation conditions, spatially random nucleation, and linear growth kinetics in which the growth rate of the new phase depends only on temperature and not on time. It is also assumed that the density of the growing bodies is constant.

The Avrami parameters provide information on the nature of the crystallization process. The constant, k, represents a crystallization rate constant. It is primarily a function of the crystallization temperature, generally obeys an Arrhenius-type temperature dependency, and takes both nucleation and crystal growth rates into account. Half-times of crystallization, $t_{1/2}$, reflect the magnitudes of k and n according to

$$t_{\frac{1}{2}} = \left(\frac{\ln 2}{k}\right)^{\frac{1}{n}} \tag{51}$$

The Avrami exponent, n, sometimes referred to as an index of crystallization, indicates the crystal growth mechanism. This parameter is a combined function of the time dependence of nucleation and the number of dimensions in which growth takes place. Nucleation is either instantaneous, with nuclei appearing all at once early on in the process, or sporadic, with the number of nuclei increasing linearly with time. Growth either occurs as rods, discs, or spheres in one, two, or three dimensions respectively. Table 1 shows the value of the Avrami exponent, n, expected for various types of nucleation and growth.

Table 1 Values for the Avrami Exponent, n, for Different Types of Nucleation and Growth[a]

N	Type of Crystal Growth and Nucleation Expected
3 + 1 = 4	Spherulitic growth from sporadic nuclei
3 + 0 = 3	Spherulitic growth from instantaneous nuclei
2 + 1 = 3	Disc-like growth from sporadic nuclei
2 + 0 = 2	Disc-like growth from instantaneous nuclei
1 + 1 = 2	Rod-like growth from sporadic nuclei
1 + 0 = 1	Rod-like growth from instantaneous nuclei

[a]Adapted from Ref. 7.

Although n should be an integer, fractional values are usually obtained, even in cases where the model fits the data quite well. Deviations from integer values for n have been explained as simultaneous development of two (or more) types of crystals, or similar crystals from different types of nuclei (sporadic vs. instantaneous). Deviations may also occur in cases where spherical crystals arise from initially rod- or plate-like nuclei. In these situations, n is continually changing. Christian [29] reported that for some cases of metals and alloys in which growth is diffusion-controlled, fractional exponents often correlate with specific growth mechanisms which can be confirmed microscopically.

In the case of fats, we have adopted the philosophy of Christian [29], where specific Avrami exponents are associated with certain growth modes determined by microscopy. For example, for milk fat crystallized at high degrees of supercooling, we would expect a lower free energy of nucleation and a higher rate of nucleation, thus leading to the formation of a large number of nuclei at the onset of the crystallization process (instantaneous nucleation). The rate of crystal growth would also be quite high. This in turn would lead to a more one-dimensional growth. The end result would be a granular microstructure composed of a large number of small crystals (Figure 5).

On the other hand, for milk fat crystallized at low degrees of supercooling, we would expect a higher free energy of nucle-

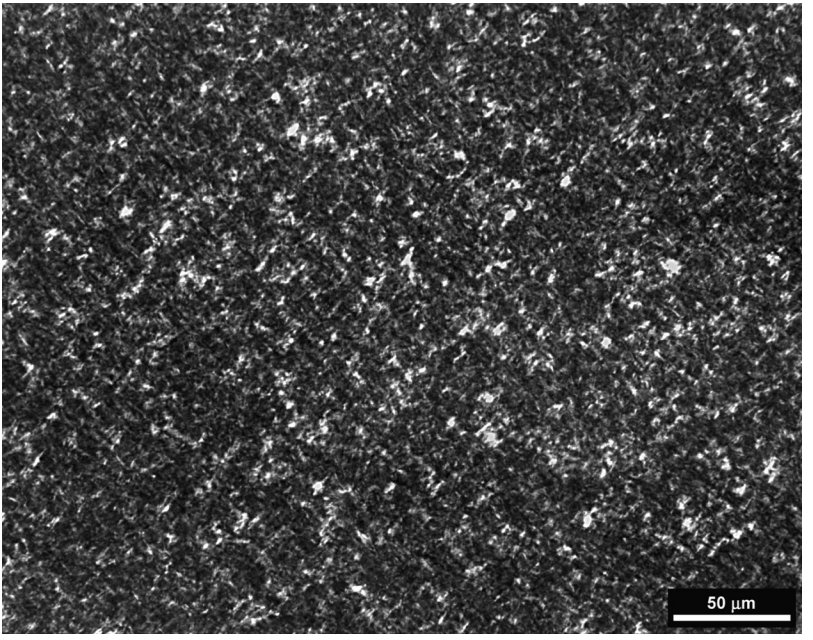

Figure 5 Microstructure of milk fat crystallized isothermally at 5°C. The Avrami index for the crystallization process leading to this microstructure was n = 1.

ation and a lower rate of nucleation, thus leading to the formation of a small number of nuclei, possibly in a sporadic fashion (sporadic nucleation). The rate of crystal growth would also be lower. This in turn would lead to a more multidimensional growth. The end result would be a "clustered" microstructure composed of a small number of large crystals

2.2.1 Derivation of the Model

Abbreviations

A = area through which diffusion takes place (m^2)
A_g = area of the crystal involved in growth (m^2)
c = concentration of supersaturated material
c* = equilibrium saturation concentration of the material
(c–c*) = concentration difference between the amount of supersaturated material at a particular time and the

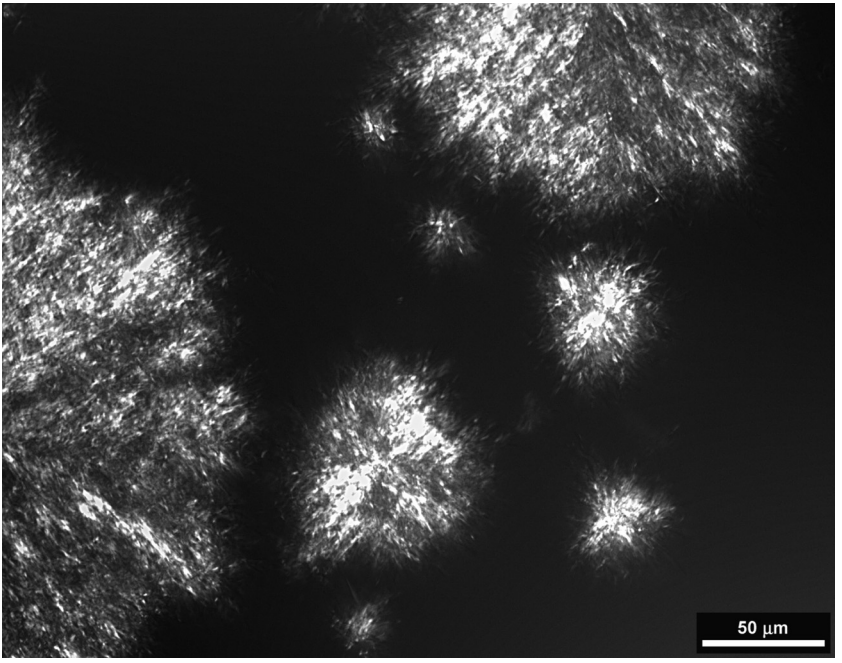

Figure 6 Microstructure of milk fat crystallized isothermally at 25°C. The Avrami index for the crystallization process leading to this microstructure was n = 4.

equilibrium saturation concentration of material at a particular temperature (kg m^{-3})
ΔC = concentration difference across boundary layer (mol m^{-3})
g = growth rate constant for the crystal's radius, length or height (s^{-1})
h = crystal height (m)
j = nucleation rate constant ($m^{-3}s^{-1}$)
k = Avrami constant (s^{-n})
K = mass transfer, or diffusion (D), coefficient (m^2s^{-1})
k_g = rate constant for single crystal growth (combined specific mass transfer coefficient and surface reaction rate constant) (m s^{-1})

κ = surface reaction rate constant ($m^2 s^{-1}$)
l = crystal length (m)
m_c = mass of a single crystal at a particular time (kg)
m_s = total mass of solids present in the system at a particular time (kg)
m_{max} = maximum total mass of solids present in the system at infinite time (kg)
$(m_{max} - m_s)$ = mass of supercooled material that has not crystallized yet (kg)
m_T = total amount of mass in the system (solids plus liquid) (kg)
MW = molecular weight of the diffusing molecules (kg mol^{-1})
N_c = total number of crystals in system
Q = number of moles of material (mol)
r = crystal radius (m)
ρ = crystallite density (m^{-3})
t = crystallization time (s)
V_T = volume of the system (m^3)
Δx = thickness of layer across which diffusion takes place – the boundary layer (m)

The starting point of this treatment is the empirical chemical diffusion equation (Fick's first law in one dimension),

$$\frac{\partial Q}{\partial t} = KA\left(\frac{\Delta C}{\Delta x}\right) \tag{52}$$

The above equation describes the transport of mass per unit area across a concentration gradient. Since the increase in mass of a crystal is a function of the amount of mass that diffuses to the crystal surface, we can write

$$\frac{\partial m_c}{\partial t} = \frac{\partial Q}{\partial t} MW \tag{53}$$

The chemical diffusion equation describing the growth of a single crystal can therefore be written as

$$\frac{\partial m_c}{\partial t} = k_g A_g (c - c^*) \tag{54}$$

where

$$k_g = \left(\frac{1}{K} + \frac{1}{\kappa}\right)^{-1} (\Delta x)^{-1} \tag{55}$$

and

$$(\Delta C)\, MW = (c - c^*) \tag{56}$$

The rate constant for single crystal growth (k_g) accounts for the possibility of diffusion control at small relative velocities and surface reaction control at high relative velocities. K varies with solution properties like viscosity and agitation, but 6 does not. As well, K varies little with temperature, while κ can change dramatically on cooling.

The total increase in solids in the system is the product of the increase in mass of a single crystal times the number of growing crystals in the system,

$$\frac{\partial m_s}{\partial t} = N_c k_g A_g (c - c^*) \tag{57}$$

and since

$$(c - c^*) = \frac{(m_{\max} - m_s)}{V_T} \tag{58}$$

equation. 57 can be expressed as

$$\frac{\partial m_s}{\partial t} = N_c k_g A_g \frac{(m_{\max} - m_s)}{V_T} \tag{58}$$

The number of crystals per unit volume in the system is defined as

$$\rho_c = \frac{N_c}{V_T} \tag{59}$$

Considering equation. 59, and after variable separation, equation. 58 can be rearranged to

$$\frac{\partial m_s}{(m_{\max} - m_s)} = k_g \rho_c A_g \partial t \tag{60}$$

This is the basic equation that can be used to derive the final form of the Avrami equation for different growth geometries and types of nucleation.

2.2.1.1 Spherical Growth with Instantaneous Nucleation

The surface area of a spherical crystal involved in crystal growth is

$$A_g = 4\pi r^2 \tag{61}$$

The linear growth rate of the crystal radius in time is expressed as

$$r = gt \tag{62}$$

Introducing equation 62 and 61 into equation 60 results in

$$\frac{\partial m_s}{(m_{\max} - m_s)} = k_g \rho_c 4\pi g^2 t^2 \partial t \tag{63}$$

Integration of the above expression for the boundary conditions $m_s = 0$ at $t = 0$, and m_s at t,

$$\int_0^{m_s} \frac{\partial m_s}{(m_{\max} - m_s)} = 4\pi k_g \rho_c g^2 \int_0^t t^2 \partial t \tag{64}$$

results in the equation

$$\ln\left(\frac{m_{\max}}{m_{\max} - m_s}\right) = \frac{4}{3}\pi k_g \rho_c g^2 t^3 \tag{65}$$

This expression can be transformed and rearranged to:

$$\frac{m_s}{m_{\max}} = 1 - e^{-\frac{4}{3}\pi k_g \rho_c g^2 t^3} \tag{66}$$

Moreover, the mass fraction (m_s/m_{max}) can be expressed as the ratio of solid fat contents, namely

$$\frac{m_s}{m_{\max}} = \frac{\frac{m_s}{m_T}}{\frac{m_{\max}}{m_T}} = \frac{SFC}{SFC_{\max}} \tag{67}$$

Thus, the Avrami equation describing the growth of a spherical crystal under conditions of instantaneous nucleation can be expressed as

$$\frac{SFC}{SFC_{\max}} = 1 - e^{-k_A t^3} \tag{68}$$

where

$$k_A = \frac{4}{3}\pi k_g \rho_c g^2 \tag{69}$$

2.2.1.2 Spherical Growth with Sporadic Nucleation

The treatment starts with equation 63, shown here again for the sake of clarity,

$$\frac{\partial m_s}{(m_{\max} - m_s)} = k_g \rho_c 4\pi g^2 t^2 \partial t \tag{63}$$

For sporadic nucleation, the change in the number of nuclei as a function of time is given by

$$\rho_c = \frac{N_c}{V_T} = jt \tag{70}$$

Introducing equation 70 into equation 63 results in

$$\frac{\partial m_s}{(m_{\max} - m_s)} = k_g j 4\pi g^2 t^3 \partial t \tag{71}$$

Integration of the above expression for the boundary conditions $m_s = 0$ at $t = 0$ and m_s at t,

$$\int_0^{m_s} \frac{\partial m_s}{(m_{\max} - m_s)} = 4\pi k_g j g^2 \int_0^t t^3 \partial t \tag{72}$$

results in the equation

$$\ln\left(\frac{m_{\max}}{m_{\max} - m_s}\right) = \pi k_g j g^2 t^4 \tag{73}$$

which can be transformed and rearranged to

$$\frac{m_s}{m_{\max}} = 1 - e^{-\pi k_g j g^2 t^4} \tag{74}$$

Thus, the Avrami equation describing the growth of a spherical crystal under conditions of sporadic nucleation can be expressed as

$$\frac{\mathrm{SFC}}{\mathrm{SFC}_{\max}} = 1 - \mathrm{e}^{-\mathrm{kt}^4} \tag{75}$$

where

$$\mathrm{k_A} = \pi \mathrm{k_g j g^2} \tag{76}$$

2.2.1.3 Plate-Like Growth with Instantaneous Nucleation

Consider a rectangular plate growing in the X–Y plane, but not in the Z-plane. The area involved in crystal growth is therefore

$$A_g = 4lh \tag{77}$$

where the dimension l is increasing linearly in time according to

$$l = gt \tag{78}$$

Introducing equations 77 and 78 into equation 60 results in

$$\frac{\partial m_s}{(m_{\max} - m_s)} = k_g \rho_c 4gth\partial t \tag{79}$$

Integration of the above expression for the boundary conditions $m_s = 0$ at $t = 0$, and m_s at t,

$$\int_0^{m_s} \frac{\partial \mathrm{m_s}}{(\mathrm{m_{max}} - \mathrm{m_s})} = 4\mathrm{hk_g}\rho_\mathrm{c}\mathrm{g}\int_0^{t} \mathrm{t}\partial \mathrm{t} \tag{80}$$

results in the equation

$$\ln\left(\frac{m_{\max}}{m_{\max} - m_s}\right) = 2hk_g\rho_c g t^2 \tag{81}$$

which can be transformed and rearranged to

$$\frac{m_s}{m_{\max}} = 1 - e^{-2hk_g\rho_c g t^2} \tag{82}$$

Thus, the Avrami equation describing the growth of a plate-like crystal under conditions of instantaneous nucleation can be expressed as

$$\frac{SFC}{SFC_{\max}} = 1 - e^{-k_A t^2} \tag{83}$$

where

$$k_A = 2hk_g\rho_c g \tag{84}$$

2.2.1.4 Plate-Like Growth with Sporadic Nucleation

The treatment starts with equation 79, shown here again for the sake of clarity,

$$\frac{\partial m_s}{(m_{\max} - m_s)} = 4hk_g\rho_c gt\partial t \tag{79}$$

For sporadic nucleation, the change in the number of nuclei as a function of time is given equation 70, shown here again for the sake of clarity,

$$\rho_c = \frac{N_c}{V_T} = jt \tag{70}$$

Introducing equation 70 into equation 79 results in

$$\frac{\partial m_s}{(m_{\max} - m_s)} = 4hk_g jgt^2\partial t \tag{85}$$

Integration of the above expression for the boundary conditions $m_s = 0$ at $t = 0$, and m_s at t,

$$\int_0^{m_s} \frac{\partial m_s}{(m_{\max} - m_s)} = 4hk_g jg\int_0^t t^2\partial t \tag{86}$$

results in the equation

$$\ln\left(\frac{m_{\max}}{m_{\max} - m_s}\right) = \frac{4}{3}hk_g jgt^3 \tag{87}$$

which can be transformed and rearranged to

$$\frac{m_s}{m_{\max}} = 1 - e^{-\frac{4}{3}hk_g jgt^3} \tag{88}$$

Thus, the Avrami equation describing the growth of a plate-like crystal in two dimensions under conditions of sporadic nucleation can be expressed as

$$\frac{SFC}{SFC_{\max}} = 1 - e^{-kt^3} \tag{89}$$

where

$$k_A = \frac{4}{3} h k_g j g \tag{90}$$

2.2.1.5 Rod-Like Growth with Instantaneous Nucleation

Consider a cylinder growing in length, but not in cross-section. The area involved in crystal growth is therefore

$$A_g = 2\pi r^2 \tag{91}$$

Introducing equation 91 into equation 60 results in

$$\frac{\partial m_s}{(m_{\max} - m_s)} = k_g \rho_c 2\pi r^2 \partial t \tag{92}$$

Integration of the above expression for the boundary conditions $m_s = 0$ at $t = 0$, and m_s at t,

$$\int_0^{m_s} \frac{\partial m_s}{(m_{\max} - m_s)} = 2\pi r^2 k_g \rho_c \int_0^t \partial t \tag{93}$$

results in the equation

$$\ln\left(\frac{m_{\max}}{m_{\max} - m_s}\right) = 2\pi r^2 k_g \rho_c t \tag{94}$$

which can be transformed and rearranged to

$$\frac{m_s}{m_{\max}} = 1 - e^{-2\pi r^2 k_g \rho_c t} \tag{95}$$

Thus, the Avrami equation describing the growth of a rod-like crystal in one dimension under conditions of instantaneous nucleation can be expressed as

$$\frac{SFC}{SFC_{\max}} = 1 - e^{-k_A t} \tag{96}$$

where

$$k_A = 2\pi r^2 k_g \rho_c \tag{97}$$

2.2.1.6 Rod-Like Growth with Sporadic Nucleation

The treatment starts with equation 92, shown here again for the sake of clarity,

$$\frac{\partial m_s}{(m_{\max} - m_s)} = 2\pi r^2 k_g \rho_c \partial t \tag{92}$$

For sporadic nucleation, the change in the number of nuclei as a function of time is given by equation 70, shown here again for the sake of clarity,

$$\rho_c = \frac{N_c}{V_T} = jt \tag{70}$$

Introducing equation 70 into equation 92 results in

$$\frac{\partial m_s}{(m_{\max} - m_s)} = 2\pi r^2 k_g jt \partial t \tag{98}$$

Integration of the above expression for the boundary conditions $m_s = 0$ at $t = 0$, and m_s at t,

$$\int_0^{m_s} \frac{\partial m_s}{(m_{\max} - m_s)} = 2\pi r^2 k_g j \int_0^t t \partial t \tag{99}$$

results in the equation

$$\ln\left(\frac{m_{\max}}{m_{\max} - m_s}\right) = \pi r^2 k_g j t^2 \tag{100}$$

which can be transformed and rearranged to

$$\frac{m_s}{m_{\max}} = 1 - e^{-\pi r^2 k_g j t^2} \tag{101}$$

Thus, the Avrami equation describing the growth of a rod-like crystal in one dimension under conditions of sporadic nucleation can be expressed as

$$\frac{SFC}{SFC_{\max}} = 1 - e^{-k_A t^2} \tag{102}$$

where

$$k_A = \pi r^2 k_g j \tag{103}$$

2.2.2 Use of the Model

The Avrami model has the general form

$$\frac{SFC}{SFC_{\max}} = 1 - e^{-k_A t^n} \tag{50}$$

This model can be linearized by a double logarithmic transformation after rearrangement to yield

$$\ln\left(1-\frac{SFC}{SFC_{\max}}\right)=-k_A t^n \tag{104}$$

and

$$\ln\left(-\ln\left(1-\frac{SFC}{SFC_{\max}}\right)\right)=\ln(k_A)+n\ln(t) \tag{105}$$

Thus, a plot of $ln(-ln(1\text{-}SFC/SFC_{max}))$ vs. $ln(t)$ should yield a straight line with slope = n and y-intercept = $\ln(k_A)$. Figure 7A shows the evolution of SFC as a function of time for the isothermal crystallization of cocoa butter at 32°C. Transformation of the SFC-t data according to equation 105 should yield a straight line when plotted. However, a straight line is not obtained, as usually is the case (Figure 7B). Thus, only the linear region of the transformed data is used to calculate the slope and y-intercept (Figure 7C).

Alternatively, SFC vs. time data can be fitted to the Avrami model in its nonlinear form, using standard curve-fitting (nonlinear regression) routines available in most modern graphical programs, and estimates of k_A and n obtained. Model fits to the data and estimates of the kinetic parameters are shown in Figure 7A. As can be appreciated, results obtained by these two methods are usually comparable.

Sometimes, multiple-step growth curves are observed in crystallization experiments. Multiple steps may be due to fractionation or polymorphic transformations taking place during crystallization. As an example we have milk fat crystallized at 10°C (Figure 8). The entire process could be modeled using a multi-component Avrami model of the form

$$SFC = SFC_0 + \sum_{i=1}^{n} SFC_{\max,\,i}\,(1 - e^{-k_i t^{ni}}) \tag{106}$$

where SFC_o is the initial, SFC, usually zero.

Fitting a single-component Avarmi model to the data results in a completely different set of kinetic parameters (Figure 9). In this case, the single-component analysis represents an average of the two events.

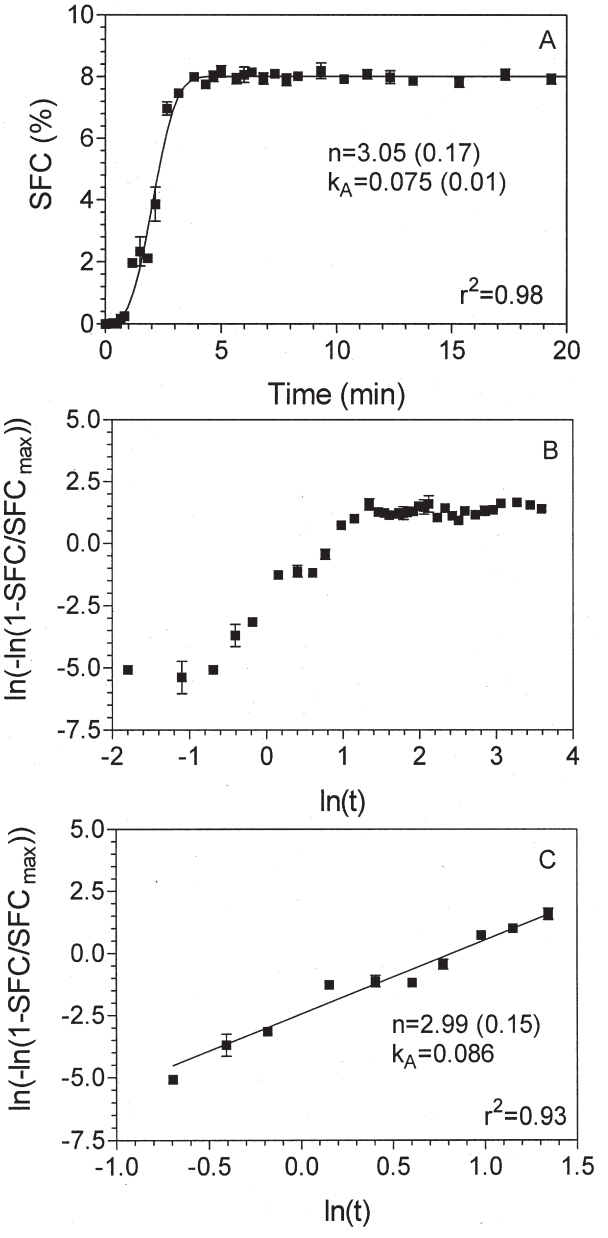

Figure 7 Isothermal crystallization of cocoa butter at 32°C.

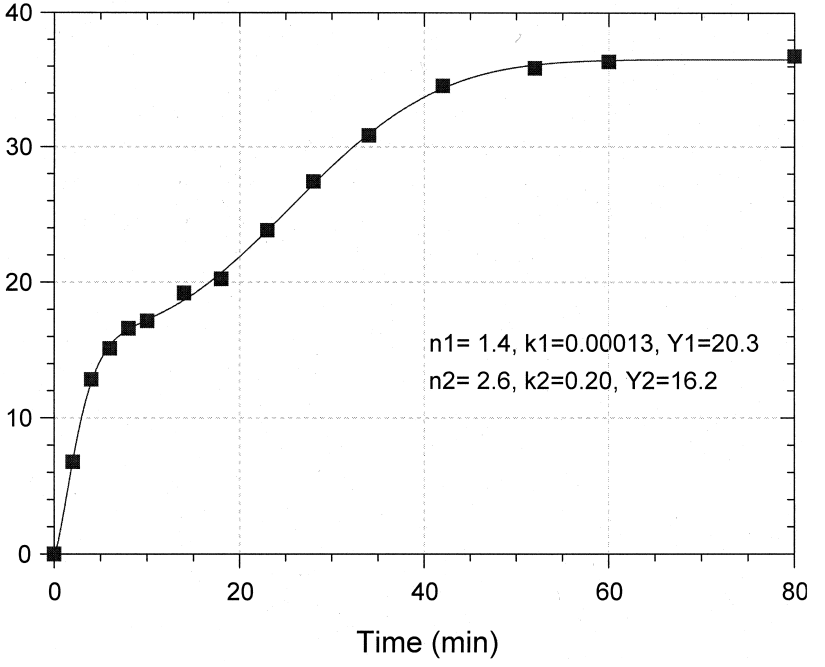

Figure 8 Solid fat content evolution in time during the isothermal crystallization of milk fat at 10°C. Shown here is a double-Avrami fit to the experimental data.

The Avrami model does not implicity take induction times into consideration. If induction times (τ_o) are known, these can be incorporated into the Avrami model as

$$\frac{SFC}{SFC_{\max}} = 1 - e^{-k_A(t-\tau_o)^n} \tag{107}$$

This is particularly important point since a process with a long induction time could be mistakenly interpreted as a crystallization process with an unusually high induction time. In my experience, Avrami exponents higher than about 5 are most probably artifactual. Artifacts will be introduced, for example, when sample cooling is inefficient. This is usually not a problem with small samples (i.e., less than 200 mg). However, a "dry bath" cooling system, where heat is exchanged from metal

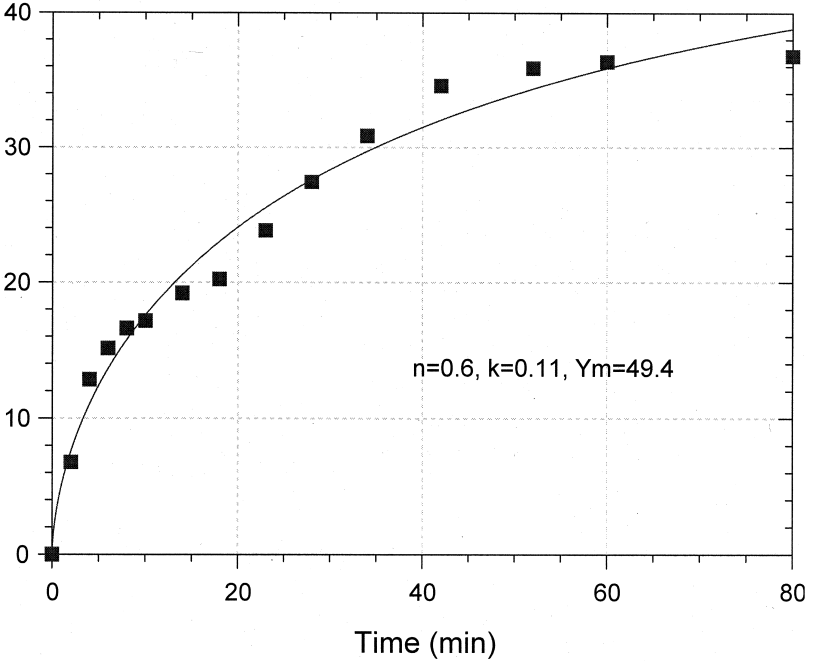

Figure 9 Solid fat content in time during the isothermal crystallization of milk fat at 10°C. Shown here is a single-Avrami fit to the experimental data.

through air to a sample in a plastic or glass containers, is not appropriate for fat crystallization studies. Even 2–4 g samples of fat will not be cooled fast enough for proper kinetic studies to be carried out (please refer to experimental methods section for further examples).

As a final note, I would like to comment on the determination of the energy of activation from the temperature dependence of the Avrami constant using the Arrenhius model

$$\ln k_A = \ln A + \frac{E_a}{RT} \tag{108}$$

A plot of $ln(k_A)$ vs. $1/T$ should yield (and does yield) a straight line with positive slope = E_a/R. This, however, is only correct if all the k_A's have the same units, that is, if the Avrami expo-

nent (n) is the same at all temperatures (not likely). Remember that the Avrami constant has units of $(\text{time})^{-n}$, thus unless the Avrami exponent remains constant for all temperatures used, an Arrenhius analysis using Avrami constants is not valid.

3. RELATIONSHIP BETWEEN CRYSTALLIZATION KINETICS AND MICROSTRUCTURE

In a study of the relationship between crystallization behavior and microstructure in cocoa butter [30], we discovered a strong effect of temperature on both crystallization kinetics and microstructure, as characterized by the box-counting fractal dimension. We, thus, plotted the values of the box-counting dimension as a function of the inverse of the induction time, in logarithmic coordinates (Figure 10A), and as a function of the Avrami exponent (Figure 10B). Some very interesting relationships became apparent. The inverse of the induction time of a process is proportional to the rate of that process. For nucleation, the inverse of the induction time (τ) is proportional to the nucleation rate (J), namely $J \sim 1/\tau$. Moreover, as shown previously, the Fisher-Turnbull model predicts that the natural logarithm of the nucleation rate is proportional to the free energy of nucleation (ΔG_n), as shown in equation 40. Taking the natural logarithm to both sides of equation 40, we obtain

$$\ln J = \alpha - \frac{\Delta G_n}{kT} \tag{109}$$

where k is Boltzman' constant, and T the absolute temperature. The parameter α corresponds to:

$$\alpha = \ln\left(\frac{NkT}{h}\right) - \frac{\Delta G_d}{kT} \tag{110}$$

where h is Planck's constant, N is the number of molecules participating in the crystallization process, and ΔG_d is the free energy of diffusion, assumed to remain constant during the crystallization process.

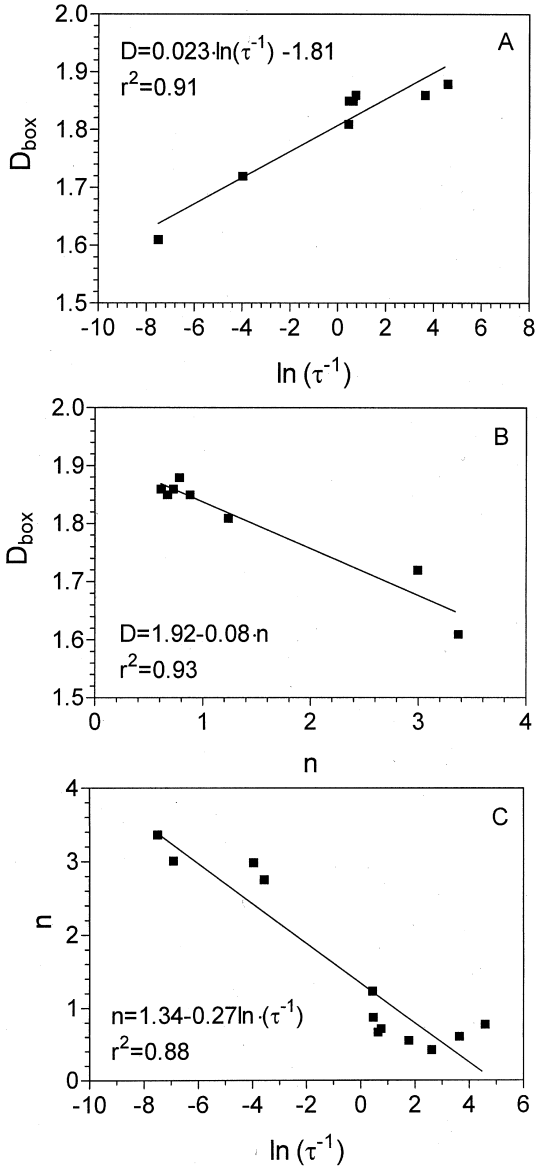

Figure 10 Relationship between the box-counting dimension, D_{box}, of the fat crystal network microstructure and natural logarithm of the inverse of the induction time (**A**). Relationship between the fractal dimension and the Avrami exponent (**B**). Relationship between the Avrami exponent and the natural logarithm of the inverse of the induction time (**C**).

Thus, our results suggested that there is a direct relationship between the nucleation rate and the resulting microstructure of the fat crystal network of the form:

$$D - D^* = \beta \ln J \tag{111}$$

where β is a constant characteristic of a particular system, and D* is the fractal dimension of a microstructure arising from a crystallization process with a nucleation rate of unity (J = 1).

This equation could also be expressed as a function of the free energy of nucleation, namely:

$$D - D^* = \kappa - \beta \frac{\Delta G_n}{kT} \tag{112}$$

where κ = αβ.

These results suggest that the microstructure is partly a consequence of the energetics of nucleation. These results agree in principle with the work of Rousset et al.[31] on the modeling of microstructural growth in POP, one of the main triacylglyerols in cocoa butter. On Figure 8 of his work, Rousset demonstrates how different nucleation regimes and rates lead to the development of different microstructures. The microstructures shown would have different box-counting fractal dimensions.

A statistically significant relationship ($P < 0.001$) also existed between the fractal dimension and the Avrami exponent (Figure 10B). The fractal dimension was inversely related to the Avrami exponent. The Avrami exponent is a function of the type of nucleation (instantaneous or sporadic) and the dimensionality of growth, and thus it is not surprising that it is strongly correlated to the final microstructure of the system. We also found a correlation between the nucleation rate and the Avrami exponent (Figure 10C). This is not surprising since the Avrami exponent contains information about the type of nucleation process. Interestingly, it is possible to define an Avrami exponent at a nucleation rate of unity (J = 1).

In what follows, we will derive the relationship in equation 111 from first principles.

The mass of an object created in a sequence of random steps will grow in time in a linear fashion,

$$M \sim t \tag{113}$$

since the amount of mass accrued during time t is proportional to the number of random steps, j(t), performed by the diffusing triaclyglycerol molecule, $j(t) \sim t$.

For a fractal object,

$$M \sim \xi^D \tag{114}$$

where ξ is the diameter of the cluster and D is the fractal dimension. Equating equation 113 to equation 114, we obtain:

$$\xi \sim t^{1/D} \tag{115}$$

or

$$\xi = kt^{\frac{1}{D}} \tag{116}$$

where k is a rate constant for growth. Thus, if an object obeys the linear mass deposition behavior (equation 113), and its growth is fractal in nature, a log-log plot of ξ vs. t will be linear with a slope (s) equal to 1/D. For the case where the growth of the cluster is Euclidean, the fractal dimension would equal the Euclidean dimension (d), and its value would be 2 or 3 depending on the type of crystal growth mechanism. The slope of the log-log plot of ξ vs. t would then the 1/2 or 1/3.

For a fractal object structured as a particle cluster, number of particles in the cluster scale as a function of cluster diameter as

$$N = a\xi^D \tag{117}$$

where N is the number of particles within a fractal cluster, a is the diameter of a particle, and ξ is the diameter of the fractal cluster. Combining equations 116 and 117, we obtain

$$N = ak^D t \tag{118}$$

The differential of N with time ($J = \frac{\partial M}{\partial t}$) has the form

$$J = ak^D \tag{119}$$

Taking the natural log of the above expression yields

$$\ln J = \ln a + D \ln k \tag{120}$$

Upon rearrangement, equation 120 can be expressed as equation 111, where

$$\beta = \frac{1}{\ln k} \tag{121}$$

and

$$D^* = \frac{\ln a}{\ln k} \tag{122}$$

This treatment was derived and is based on experiments carried out on a microscope slide (microscopy) and for small amounts of crystallizing fat. These systems are not heat-transfer limited, and thus represent an idealized situation, and will be useful in comparative studies between fats in the laboratory

CASE STUDY: COMPARISON OF EXPERIMENTAL TECHNIQUES IN LIPID CRYSTALLIZATION STUDIES

The first step in determining the free energy of nucleation is to determine the induction time of nucleation (τ). In order to determine the free energy of nucleation using standard models, the fat melt has to be cooled instantaneously to the specified crystallization temperature. If the fat starts crystallizing while still cooling, we are under dynamic crystallization condition (in contrast to static, isothermal conditions) and the standard Fisher-Turnbull treatment is not applicable. An important point to be made is whichever technique is used for the determination of the induction time (light scattering, NMR, turbidimetry, microscopy), it must be sensitive to the early stages of the crystallization process, and hopefully as close as possible to the nucleation event. What follows is a short study aimed at addressing the appropriateness of commonly used analytical techniques in the determination of the induction time of nucleation.

Introduction

Crystallization of fats is considered to encompass two distinct events, nucleation and crystal growth. While a stable nucleus

must be formed before crystal growth can occur, these events are not mutually exclusive. Nucleation may take place while crystals grow on existing nuclei [5]. In our investigations into the effects of minor components on milk fat crystallization, it became clear that minor components delayed crystallization of the milk fat triacylglycerols [32]. However, it was difficult to discern whether the effects were at the nucleation or crystal growth level. Distinguishing between nucleation and crystal growth constitutes a major challenge in lipid crystallization studies.

The shape of a crystallization curve can provide some insight into the mode of crystal growth [7]. However, the nucleation step is more elusive because the methods typically used in these studies are relatively insensitive. Pulsed nuclear magnetic resonance (pNMR), which measures solid fat content (SFC), and light scattering techniques, which measure absorbance or transmittance of light, are commonly used to monitor lipid crystallization. Anyone familiar with the pNMR method knows that, at times, small amounts of crystals are visible in the melt before any solids are detected. Clearly, at this stage, well beyond the induction time for nucleation, the pNMR signal is measuring crystal growth. Turbidimetry, while more sensitive than pNMR, *e.g.* shorter induction times are obtained, also has its limitations. Crystallization times determined by turbidimetry correlated well with the mass deposition of fat [33]. A very strong correlation was also found between induction times by pNMR and turbidimetry for the three fat systems used in the minor components study [32], suggesting that increases in turbidity are also due to mass deposition of crystals and not only nucleation (Figure 11). However, here we can also appreciate how the slope of this relationship varies from system to system, thus suggesting that although proportional to each other, induction times of crystallization are not measuring exactly the same event.

It would be beneficial to have a convenient way of unambiguously determining nucleation induction times when seeking to understand the effects of varying composition and processing conditions on nucleation, and it is essential if the induction times are used in mathematical models such the

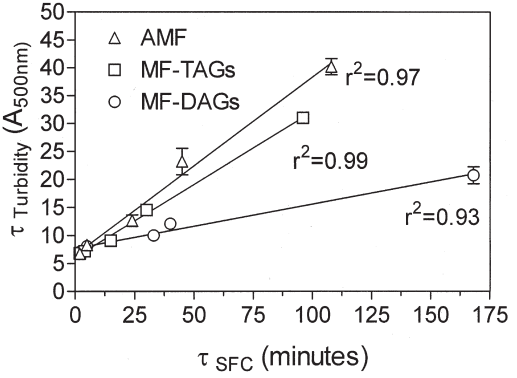

Figure 11 Induction time by turbidity ($\tau_{turbidity}$) vs. induction time by solid fat content (SFC) (τ_{SFC}) for anhydrous milk fat (AMF); milk fat triacylglycerols (MF-TAGs); and milk fat with 0.1% diacylglycerols added back (MF-DAGs), crystallized at 5.0, 10.0, 15.0, 20.0, 22.0, 25.0, and 27.5°C.

Fisher-Turnbull equation [17]. In the Fisher-Turnbull model, activation energies of nucleation are calculated from nucleation induction times. The usual assumption is that the experimental technique used to determine the induction time, provides an accurate measure of the nucleation rate.

In the Fisher-Turnbull model, free energies of nucleation can be calculated from induction times. The usual assumption is that the experimental technique used to determine the induction time provides an accurate measure of the nucleation rate. Induction times for this purpose have been determined using light scattering techniques [34]. Herrera et al. [35] used a modified laser-polarized light turbidimetric approach to obtain induction times, the details of which were described by Herrera [36]. Polarized light microscopy (PLM) has also been used to visually observe the onset of nucleation [35,37]. Similarily, nucleation and growth rates in palm oil were determined microscopically using polarized light in conjunction with a counting cell and graduated occular [11]. A similar method was automated using PLM in conjunction with a CdS photo sensor. Instead of observing the sample visually, the

sensor monitored the transmission of light through the crystallizing sample on a microscope slide [38]. This is a very sensitive approach; however, the specialized equipment required is not commonly available. Differential scanning calorimetry (DSC) has also been used to monitor isothermal crystallization of lipids [39–41].

Induction times determined by pNMR, turbidity, and light scattering measurements are compared to those determined using PLM in conjunction with image analysis. Isothermal DSC was attempted as a fifth method for comparison. However, because of the inherent lack of sensitivity at the high cooling rates required to obtain isothermal crystallization conditions, it was abandoned. This research was carried out in the context of our milk fat minor components study [32].

Experimental

Minor components (nontriacylglycerol species) were removed from anhydrous milk fat (AMF) to obtain purified milk fat triacylglycerols (MF-TAGs) by column chromatography using Florisil as the stationary phase [32]. As previously described, the crystallization behaviour of the original, A. M. F., the MF-TAGs, and MF-TAGs to which 0.1% milk fat diacylglycerol was added (MF-DAGs) was studied by pNMR and turbidimetry [32]. Although crystallization was studied between 5.0 and 27.5°C, we will concentrate only on data collected at 22.5°C.

In addition, crystallization was followed using polarized light microscopy at 22.5°C. AMF, MF-TAGs, and MF-DAGs were preheated to 80°C for 10 minutes before a drop of each was placed on a preheated (80°C) glass microscope slide and covered with a preheated (80°C) glass coverslip. The samples were imaged with a Zeiss polarized light microscope using a $10\times$ objective and equipped with a CCD Video Camera. Temperature of the slide was maintained at 22.5°C. Crystallization was followed by capturing an image every 15 seconds for 30 minutes. The images were processed using Image Tool (The University of Texas Health Science Center, San Antonio, Texas). A background subtraction was performed initially by subtracting the initial image (time = 0 seconds) for each of,

AMF, MF-TAGs, and MF-DAGs from every other image in the respective crystallization run. The images were manually thresholded, using the same value for every image in each of, AMF, MF-TAGs, and MF-DAGs. The threshold level was that which was found to most accurately reflect the original greyscale images. Once the images were thresholded, the relative amounts of black and white pixels in each image were determined. The amount of black (representing crystal mass) was plotted as a function of crystallization time.

For the light scattering studies, a phase transition analyzer (Phase Technology, Richmond, B.C., Canada) was used. 150 μL of sample, preheated to 80°C for 30 min (minutes) was pipetted into the sample container of the analyzer, which was preheated and maintained at 75°C using a thermoelectric cooler. Thereafter, the sample was rapidly cooled from 75°C to 22.5°C at a controlled rate of 50°C/min. When the sample reached 22.5°C, it was held at this temperature and crystallization was continuously monitored using an optical scattering approach. In this setup, a beam of light impinges on the sample from above. A matrix of optical sensors, in tandem with a lens system, is also placed perpendicularly above the sample. When crystals start to appear in the sample, the incident beam is scattered by the solid-liquid phase boundaries and scattered light impinges via the lens onto the detectors. As more and more crystal mass develops, the signal output increases and is automatically recorded.

Crystallization curves for pNMR, turbidity, light scattering and image analysis were normalized by dividing each value by the maximum crystallization value. The resulting fractional crystallization values compared. Induction times were determined by extrapolating the linear portion of the crystallization curves to the time axis and by baseline deviation as shown in Figure 12.

Induction times were taken as the time from when the samples were placed at 22.5°C until crystallization began. Strictly speaking, however, induction times should be taken from the point at which the sample reaches the crystallization temperature until crystallization is detected. In all experi-

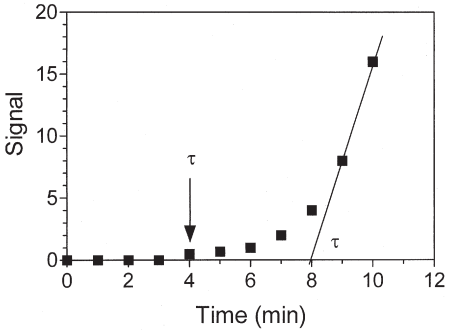

Figure 12 Determination of crystallization induction times by baseline deviation and linear extrapolation to the time axis.

ments, however, it takes some time for isothermal conditions to be established. It is possible that differences in the cooling rates between the four methods could influence crystallization. This will be true regardless of how induction time is defined. Considering time zero as the point at which 22.5°C is reached ignores the fact that crystallization will occur between the melting temperature and 22.5°C. AMF, MF-TAG and MF-DAG have Mettler dropping points of approximately 34°C [32]. Therefore, during cooling below 34°C and at 22.5°C the fats experience the same degree of supercooling. This eliminates concerns of having different thermodynamic factors at work in the three fats and makes the comparison of their crystallization behaviours much easier to define. However, there are very real concerns regarding differences in cooling rates between the different experimental methods. The cooling curves for the pNMR, turbidity and light scattering are shown in Figure 13. A cooling curve was not determined for the microscopy experiment, although the temperature was found to equilibrate at 22.5°C within approximately 30 seconds. The rate constants of cooling for the initial decrease in temperature to the dropping point (34°C) are shown in Table 2.

Figure 12 and Table 2 show that the cooling for the pNMR and light scattering are reasonably rapid and linear to 22.5°C.

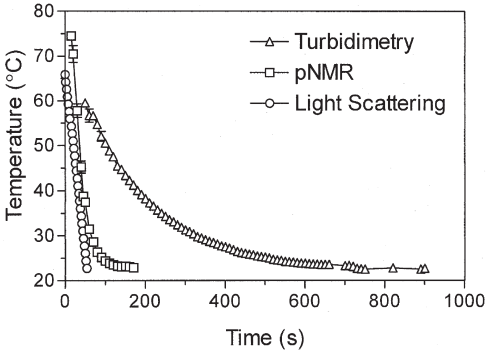

Figure 13 Cooling curves for samples in pulsed nuclear magnetic resonance (pNMR), turbidimetric, light scattering experiments.

Similarly, the microscope slides reached the crystallization temperature very rapidly. This makes it easier to assign any differences observed between these experimental methods to the sensitivity of the methods, and not specifically to different cooling rates. Newtonian type cooling was observed for the turbidity experiments. This meant that 22.5°C was not reached for nearly 15 minutes. This is longer than most of the induction times determined for turbidimetry (Table 3). Therefore, these induction times actually correspond to crystallization at temperatures higher than 22.5°C and we must be careful in drawing information from the results. In the cases where the crystallization temperature was attained very quickly and

Table 2 Rate Constants of Cooling Determined from the Initial Linear Decrease in Temperature to 34°C for pNMR, Turbidimetry, and Light Scattering Spectroscopy

Experimental Method	Cooling Rate Constant (°C/second)
pNMR	-1.060 ± 0.119
turbidimetry	-0.156 ± 0.008
light scattering	-0.774 ± 0.000

within approximately the same time frame (pNMR, light scattering and microscopy) the comparison between the methods is more appropriate. Every effort should be made to achieve rapid and linear cooling during crystallization experiments to avoid such complications. In the case of turbidimetry this resulted because of the poor heat transfer between the sample and the surrounding metal cell holder through which cooling water was circulated. More efficient heat transfer was achieved when the glass pNMR tubes were plunged into a water bath at the crystallization temperature, in the chamber of the phase transition analyzer, and when the glass microscope slides were placed on a metal platform.

Results and Discussion

Figure 14 shows thresholded polarized light micrographs of MF-TAGs at various crystallization times at 22.5°C. Crystallization curves for, AMF, MF-TAGs, and MF-DAGs by pNMR, turbidity, and PLM-image analysis are shown in Figure 15.

MF-TAGs crystallized first, followed by AMF and MF-DAGs. MF-DAGs had the longest induction times determined by pNMR, while by turbidimetry and microscopy, AMF had the longest induction times. Crystallization curves for, AMF, MF-TAGs and MF-DAGs obtained from measurements of light scattering intensities are shown in Figure 16. In this case, MF-TAGs crystallized first and AMF had the longest induction times. The induction times for the crystallization curves are reported in Table 3.

Induction times determined as the time of deviation from the baseline were shorter than those calculated by extrapolation of the linearly increasing curves, although the same trends were observed. Also, Table 3 shows that while the relative trends were similar, there were large differences in the absolute value of onset times of crystallization between the four methods. Despite the fact that the absolute values for the induction times differed, removal of the minor components consistently decreased the induction times of the triacylglycerols. We can thus be certain that milk fat minor components exhibit an inhibitory effect on triacylglycerol crystallization.

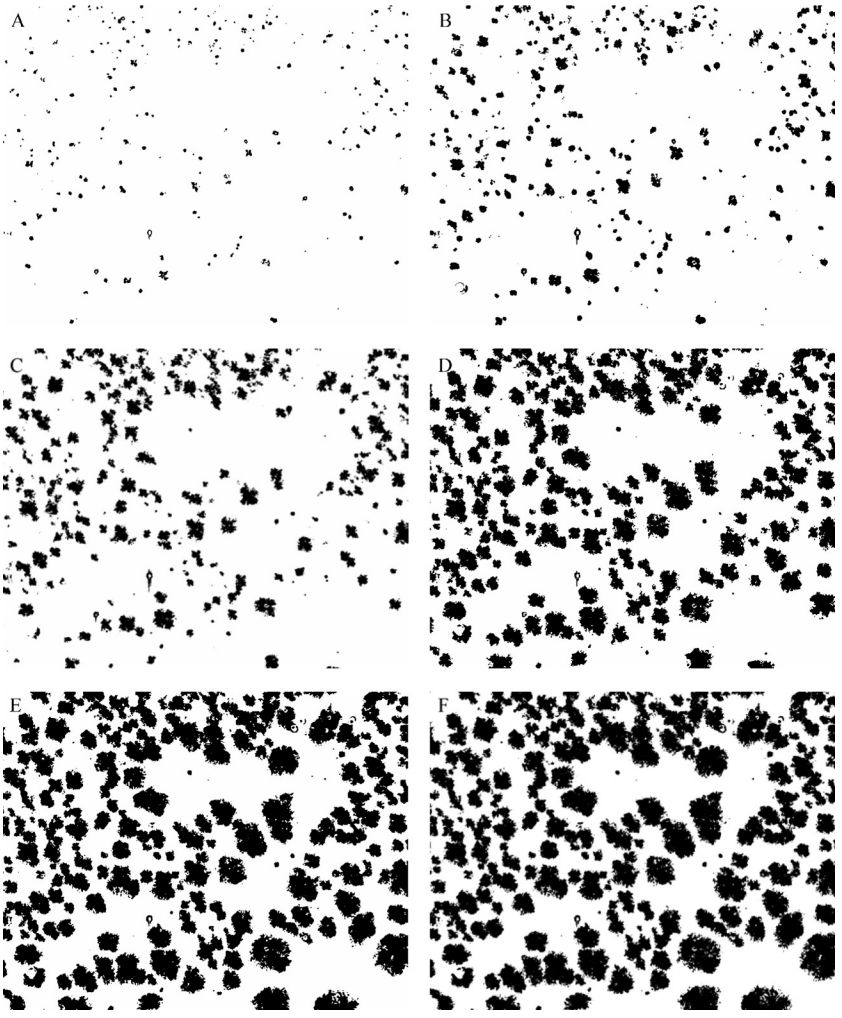

Figure 14 Thresholded polarized light microscope images of milk fat triacylglycerols (MF-TAGs) at various crystallization times at 22°C: (**A**) 1 min, (**B**) 3 min, (**C**) 5 min, (**D**) 10 min, (**E**) 20 min, (**F**) 28 min.

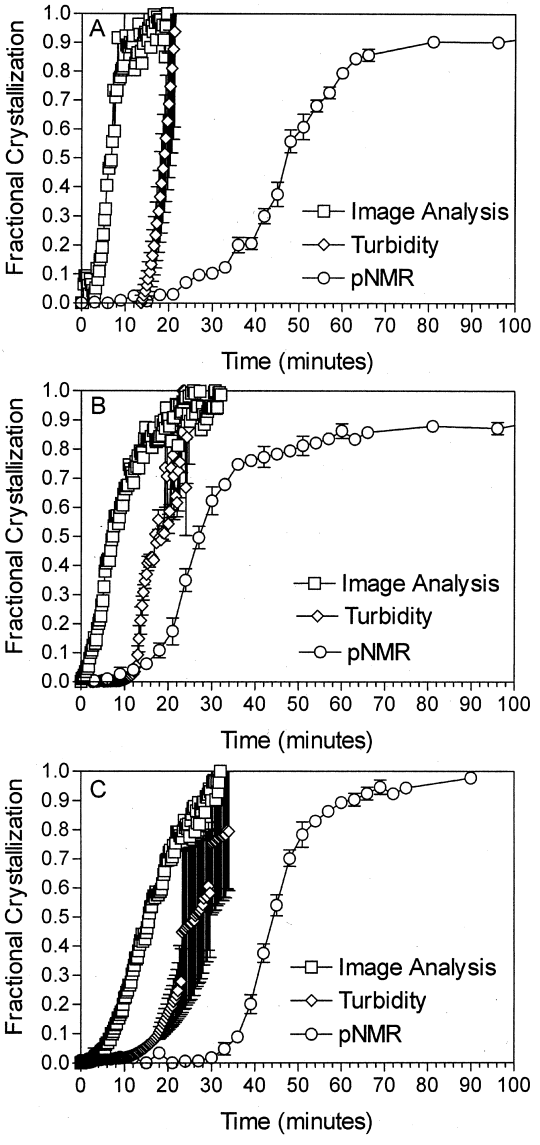

Figure 15 Fractional crystallization of anhydrous milk fat (AMF) (**A**), milk fat triacylglycerols (MF-TAGs) (**B**), and milk fat with 0.1% diacylglycerols added back (MF-DAGs) (**C**) determined by pulsed nuclear magnetic resonance (pNMR) measurements of solid fat content (SFC), turbidity measurements, and polarized light microscopy coupled to image analysis at 22.5°C. Symbols in (**A**) and (**B**) represent average and standardized errors of three replicates.

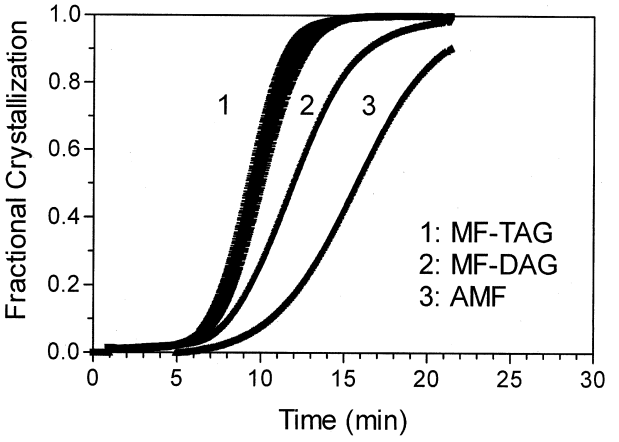

Figure 16 Fractional crystallization of anhydrous milk fat (AMF), milk fat triacylglycerols (MF-TAGs), and milk fat with 0.1% diacylglycerols added back (MF-DAGs) determined by light scattering spectroscopy.

Table 3 Induction Times (minutes) Determined by Linear Extrapolation and Baseline Deviation for AMF, MF-TAGs, and MF-DAGs Monitored by pNMR, Turbidimetry, Light Scattering Spectroscopy, and by Polarized Light Microscopy Coupled to Image Analysis. Average and Percent Error Reported.

	pNMR	Turbidimetry	Light Scattering	Microscopy
By Extrapolation				
AMF	28.2 (4.2%)	14.9 (8.4%)	9.9 (0.5%)	3.0 (3.8%)
MF-TAGs	14.7 (6.2%)	12.3 (11.8%)	6.7 (1.1%)	1.5 (3.0%)
MF-DAGs	33.3 (4.9%)	12.9 (11.0%)	7.1 (0.7%)	5.3 (1.8%)
By Baseline Deviation				
AMF	21.7 (4.1%)	16.3 (8.1%)	7.5	3.0
MF-TAGs	11.0 (9.1%)	11.8 (3.7%)	5.0 (10.0%)	1.5
MF-DAGs	34.0 (5.9%)	12.7 (9.5%)	6.5	3.5

Table 3 shows that the induction times determined by pNMR were the longest, while those determined by the image analysis technique were the shortest. Therefore, with the image analysis approach we were able to detect some early crystallization events beyond the sensitivity of the other methods. The higher sensitivity demonstrated allowed for the detection of early crystallization events, possibly in the vicinity of the true nucleation events.

If cooling rates could be controlled in a better fashion, turbidimetry could be a more sensitive technique for the study of the early stages of a crystallization process than pNMR. Poor heat transfer was the major disadvantage with the turbidimetric experiments, although there are other inherent limitations. Light scattering spectroscopy proved to be a more sensitive method than turbidimetry and pNMR. In this method, the intensity of scattered light, rather than the attenuation of the signal intensity (I/I_o) is measured. The particular geometry of the sample cell and positioning of the detectors also maximizes the collection of the scattered light. This technique proved to be very convenient, user-friendly and reproducible.

Polarized light microscopy (PLM) has inherent advantages over turbidimetry. The PLM technique exploits the difference in refractive index of a beam of incident light polarized in two perpendicular directions. This phenomenon is known as birefringence. Anisotropic materials, such as a fat crystal will display birefringence. Because fat crystals are birefringent, they will appear as sharp bright objects in a non-birefringent, and therefore dark, background. The use of polarizers set at 90° removes most of the non-birefringent background signal (colored melt and scattering impurities), thereby considerably increasing the signal-to-noise ratio. As well, since the entire transmitted light beam in the field of view is collected by the lenses and focused on the camera, signal intensity and, therefore, sensitivity are increased.

Ultimately, the experimental technique of choice will depend on the application. pNMR provides the best method to characterize the overall crystallization process. For this reason it is suitable for use in the Avrami analysis. The water

bath based cooling used in the pNMR experiments also offered rapid cooling and accurate temperature control. Both turbidity and scattering intensity signals tend to become saturated prior to the completion of the crystallization process. Thus, it is not possible to obtain reliable data on the latter stages of crystallization. Although turbidity seems to offer the advantage of improved sensitivity, in our experience there can be large errors associated with its measurement, concerns with poor reproducibility, and major challenges with temperature control. Light scattering improves on this because it measures reflectance of light as opposed to transmittance. It offers extreme sensitivity to early crystallization events, is easy to use and requires only a small volume of sample. Cooling rates and temperature can also be accurately controlled in the instrument. Microscopy coupled with image analysis also proved to be sensitive and had good temperature control, although it was the most cumbersome technique. It does have the advantage that morphological information can be acquired simultaneously as the kinetics are quantified.

CASE STUDY: ON THE USE AND MISUSE OF THE AVRAMI EQUATION IN CHARACTERIZATION OF THE KINETICS OF FAT CRYSTALLIZATION

In the late 1930s and early 1940s, Michael Avrami developed a theory of the kinetics of phase change [26–28]. The well known Avrami equation [27] describes changes in the volume of the crystals as a function of time during crystallization, and has the general form

$$F = \frac{V}{V_m} = 1 - e^{(-Bt^k)} \tag{123}$$

where V is the volume of the crystals, V_m is the maximum crystal volume attained after crystallization is complete, F is the volume fraction of crystals, B is the Avrami constant (dimensionless), and k is the Avrami exponent (t^{-B}). From a to-

pological perspective, this function can fit patterns from hyperbolic to sigmoidal, depending on the numerical values of the adjustable parameters B and k. The maximum plateau value is given by the parameter V_m. Low B and high k values will result in a hyperbolic curve while high B and low K values will result in a sigmoidal curve. For sigmoidal patterns, a period of limited crystal growth is followed by a region of rapid increase in crystal mass. As the amount of supersaturated material is depleted, crystal growth slows down until the equilibrium concentration of crystal mass is attained.

As stated above, in the absence of curve fitting programs, crystallization data can be fitted to the linearized form of this equation by simple linear regression as

$$\ln\left(-\ln\left(1-\frac{SFC}{SFC_{\max}}\right)\right)=\ln\left(k_A\right)+n\ln(t) \tag{124}$$

Hence, a plot of $ln(-ln(1-(SFC/SFC_{max})))$ vs. $ln(t)$ has a slope of n and a y-intercept of $ln(k_A)$. When using this linearization procedure, as opposed to nonlinear regression, SFC_{max} cannot be adjusted and must be fixed as a constant.

In the literature, some researchers have suggested fixing the Avrami exponent to a set integer value (usually n = 3), leaving k_A as the only adjustable parameter. This would solve many problems, including being able to use k_A's in an Arrhenius-type analysis since all constants would have the same units of t^{-1}. The form of this modified equation is

$$\frac{SFC}{SFC_{\max}}=1-e^{-(k_A^* t)^n} \tag{125}$$

And, in linear form,

$$\left(-\ln\left(1-\frac{SFC}{SFC_{\max}}\right)\right)^{\left(\frac{1}{n}\right)}=-k_A^* t \tag{126}$$

Thus, for the modified Avrami equation, a plot of $(-ln(1-(SFC/SFC_{max})))^{1/n}$ vs. t should yield a straight line with slope $-k_A^*$.

However, this modification does not have any theoretical justification, and this function has very little to do with the Avrami model. The only conjecture sometimes presented is

that this modification would remove the correlation between estimates of n and k_A, and make the estimate of k_A more reliable, since it would be independent of the value of n.

The units of the Avrami constant n are t^{-n}, since the exponential factor must be dimensionless. This modification transforms the Avrami constant from a complex constant of an nth order process to a first order rate constant with units of t^{-1}. Crystallization is not a first order process. Even though it might be nicer to report a first order rate constant, this does not justify the use of the modified model.

The difference between the two functions lies in the exponential term

$$e-(k_A^* t)^n = e-k_A t^n \tag{127}$$

Taking the natural logarithm on both sides and multiplying by -1, one obtains

$$(k_A^* t)^n = k_A t^n \tag{128}$$

which is equivalent to

$$(k_A^*)^n t^n = k_A t^m \tag{129}$$

Dividing by t^n results in

$$(k_A^*)^n = k_A \tag{130}$$

Hence, the modified Avrami equation constant k_A^* is the nth root of the Avrami model constant k_A,

$$k_A^* = (k_A)^{\frac{1}{n}} \tag{131}$$

Hence, this modification of the Avrami model explicitly *creates* a fixed dependence of k_A on n.

The Avrami and modified Avrami equations were fitted to literature-derived palm oil crystallization data (SFC *vs.* time at 5°C) [41] by nonlinear regression using the software package Scientist 2.0 for Windows (Micromath Scientific Software, Salt Lake City, Utah). In both cases convergence was achieved once suitable initial estimates for k_A and n had been found (Figures 17 and 18), and no sensitivity to initial conditions was detected.

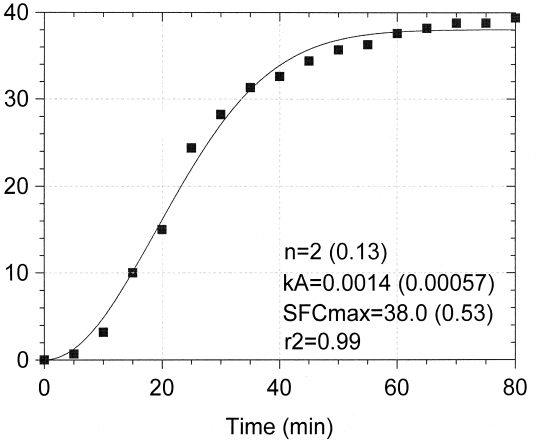

Figure 17 Nonlinear least squares fit of the Avrami equation to palm oil crystallization data. Values in parenthesis represent the standard deviations of the estimates.

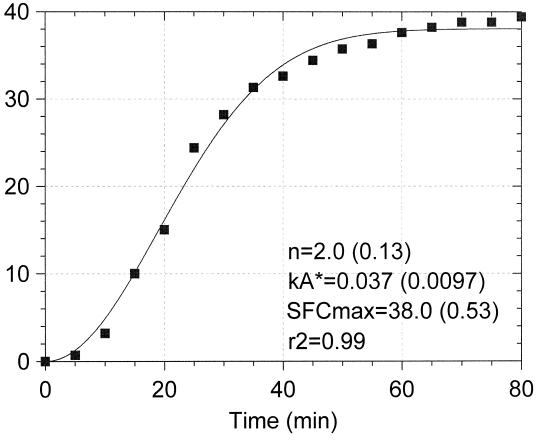

Figure 18 Nonlinear least squares fit of the modified Avrami equation to palm oil crystallization data. Values in parenthesis represent the standard deviations of the estimates.

From a curve-fitting perspective, there are no differences between these two functions. Nonlinear least-squares fits of the Avrami and modified Avrami equations to crystallization data worked very well—convergence was readily achieved with no parameter value sensitivity to initial conditions. The standard deviation of the estimates was similar and the r^2 of the fits was greater than 0.99. However, the modified Avrami equation has no theoretical foundation; therefore, the Avrami equation should be used in its original form since it is based on a sound theoretical development.

Empirical Fits of Crystallization Data to Polynomial Functions and Their Relationship to the Avrami Equation

Some researchers equate the order of a polynomial fit to crystallization data to the Avrami exponent n. This is not correct. An exponential function can be expanded into a power series. Expanding the Avrami equation into a power series, we obtain

$$SFC = SFC_{\max}(1 - e^{-k_A t^n})$$
$$SFC = SFC_{\max} - SFC_{\max} k_A \left(t^n + \frac{t^{2n}}{2!} + \frac{t^{3n}}{3!} + \frac{t^{4n}}{4!} + L\right) \quad (132)$$

We can compare this expression to a polynomial function,

$$SFC = SFC_{\max}(a + bt + ct^2 + dt^3 + et^4 + L) \quad (133)$$

One can immediately notice that the Avrami equation series contains an extra term in the exponent of each expansion term. Therefore, the dependent variable (SFC) in the Avrami equation increases more steeply as a function of time than the dependent variable for a n-equivalent polynomial function (e.g., n = 2 and a second order polynomial function).

We fitted polynomial functions to the crystallization data of Ng and Oh [41] using Graphpad Prism 3.0 (San Diego, CA, USA) and found that a fifth order polynomial fitted the data significantly better than a second or third order polynomial ($P < 0.05$) (Figure 19). No significant differences ($P > 0.05$) in the goodness-of-fit were observed using higher order poly-

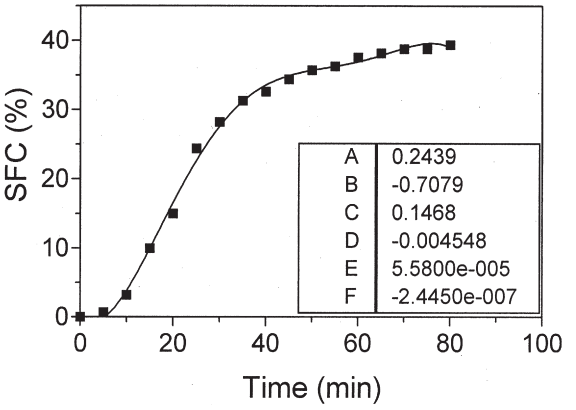

Figure 19 Fifth-order polynomial fit to palm oil crystallization data.

nomials using an F-test criterion. This is a standard analytical option of this graphical package.

Therefore, an Avrami equation with an exponent of 2.0 (Figure 17) is equivalent to a fifth-order polynomial equation (Figure 19). When using polynomial functions to fit crystallization data, it is imperative to remember that the order of the polynomial function obtained from nonlinear fits to the data is not equivalent to the Avrami exponent— the order of the polynomial equation has no mechanistic meaning.

The Misuse of Turbidity Measurements to Monitor Fat Crystallization

In many studies of fat crystallization, researchers have equated increases in the volume of crystallized material (V) to increases in absorbance (A) due to scattering at a particular wavelength, and thus

$$\frac{V - V_o}{V_m - V_o} = \frac{A - A_o}{A_m - A_o} \tag{134}$$

The first problem with this assumption is that A_m is usually taken as the off-scale turbidity value. This maximum absorbance does not correspond to the end of crystallization, or the

maximum volume or mass of crystallized material achieved. It simply represents the point at which the crystallizing material becomes too opaque, and the amount of transmitted light becomes negligible. However, the crystallization process continues well after the turbidity values have gone off scale. Without a true maximum absorbance value which corresponds to the end of the crystallization process, the Avrami equation cannot be used.

Secondly, the relationship between the amount of absorbed light due to scattering (A_s) and particle concentration is very complex. Consider the relationship between A_s and concentration,

$$A_s = -\ln \frac{I}{I_o} = \tau c l \tag{135}$$

In the Raleigh regime, no multiple scattering (from the same particle) occurs, that is, particles in a dilute medium are smaller than $\lambda/20$ and are considered isotropic point scatterers. As well, as for all scattering experiments, it is assumed that no absorption takes place. For this case

$$\tau = \frac{16\pi}{3} R_{90^o} \tag{136}$$

where τ is a turbidity parameter analogous to an exctinction coefficient, and R_{90° is the Raleigh ratio at 90° and refers to primary scattering from unit volume of solution. For Raleigh scattering,

$$R_{90^\circ} = KCM \tag{137}$$

where K is a constant, C is concentration (grams per unit volume) and M is the molecular weight of the particle (grams per mole) [42]. Substituting equations 122 and 123 into equation 121 yields the expression

$$A_s = \frac{16\pi}{3} KMC^2 \tag{138}$$

Thus, A_s is not only a function of the amount of material present in the suspension, but also of its size. During crystallization, the number and size of particles increases in time, making the equivalence of A_s with concentration somewhat

dubious. Moreover, the absorbance due to turbidity increases as the square of the concentration of scattering material.

As particles become larger than $\lambda/20$, these assumptions do not apply. For example, if we use 600 nm light, the limit of applicability of turbidity measurements would be for particles 30 nm or smaller [42].

Thirdly, an observed decrease in transmitted light could be due to light refraction— an apparent change in velocity of the transmitted light beam as it travels through the sample. Fat crystals are extremely birefringent, and light is transmitted through them. This could cause significant refraction of the incident light, and lead to a drop in the intensity of the transmitted light. This increase in turbidity would then have nothing to do with the volume or mass of crystals present in the sample.

For these reasons, turbidity measurements should not be used in the quantitative kinetic characterization of crystallization processes, other than for the detection of induction times.

REFERENCES

1. Guy AG. Introduction to materials science. New York: McGraw-Hill, 1972:310–315.
2. Garside J. General principles of crystallization. In: Food structure and behavior; food and technology: a series of monographs. Blanshard JMW, Lillford P, Eds. London: Academic Press, 1978:35–49.
3. Larsson K. The crystal structure of β-form of trilaurin Arkiv Kemi 1964; 23:1–15.
4. Boistelle R. Fundamentals of nucleation and crystal growth. In: Crystallization and polymorphism of fats and fatty acids. Garti N, Sato K, Eds. New York: Marcel Dekker, 1988:133–178.
5. Sato K, Yoshimoto N, Arishima T. Crystallization phenomena in fats and lipids J Dispersion Science and Technology 1989; 10:363–392.
6. Frank FC. The influence of dislocations on crystal growth Disc Far Soc 1949; 5:48–54.

7. Sharples A. Introduction to polymer crystallization. London: Edward Arnold, Ltd., 1966:44–59.

8. Sato K, Okada M. Growth mechanism of stearic acid single crystals J Crystal Growth 1977; 42:264–271.

9. Sato K, Okada M. Step morphology of giant growth spirals of long-chain stearic acid crystals frown from solution J Crystal Growth 1983; 64:177–184.

10. Aquilano D. Complex growth polytypism and periodic polysynthetic twinson octacosane crystals J Crystal Growth 1977; 37: 215–228.

11. van Putte KPAM, Bakker BH. Crystallization kinetics of palm oil J Am Oil Chem Soc 1987; 64:1138–1143.

12. burton WK, Cabrera N, Frank FC. Dislocations in crystal growth Nature 1949; 163:398–399.

13. Skoda W, van den Tempel M. Growth kinetics of triglyceride crystals J Crystal Growth 1967; 1:207–217.

14. Skoda W, Hoekstra LL, van Soest TC, Bennema P, van den Tempel M. Structure and morphology of β-crystals of glyceryl tristearate Kolloid-Z 1967; 219:149–156.

15. van den Tempel M. Surface-active lipids in foods. SCI Monograph No. 32. London: Society of Chemical Industry, 1968: 22–36.

16. Walstra P. Secondary nucleation in triglyceride crystallization Prog Colloid Polym Sci 1998; 108:4–8.

17. Strickland-Constable RF. Kinetics and mechanism of crystallization. London: Academic Press, 1968:74–129.

18. Gilmer GH. Growth on imperfect crystal faces J Crystal Growth 1976; 35:15–28.

19. Simon B, Grassi A, Boistelle R. Cinétique de croissance de la face [110] de la paraffine en solution. II. Croissance en presence d'un inhibiteur, la dioctadécylamine J Crystal Growth 1974; 26:90–96.

20. Aronhime J, Sarig S, Garti N. Emulsifiers as additives in fats: effect on polymorphic transformations and crystal properties of fatty acids and triglycerides Food Struct 1990:337–352.

21. Sarig S, Kahana F. On the association between sparingly soluble carbonates and polyelectrolytes J Crystal Growth 1976; 35: 145–152.

22. Sarig S, Kahana F. Thermal decomposition of basic lead carbonate Thermochim Acta 1976; 14:263–268.

23. Addadi L, Weiner S. Interactions between acidic proteins and crystals: stereochemical requirements in biomineralization Proc Nat Acad Sci USA 1985; 82:4110–4114.

24. Eidelman N, Azoury R, Sarig S. Reversal of trend in impurity effects on crystallization parameters J Crystal Growth 1986; 74:1–9.

25. Small D. Glycerides. In: The physical chemistry of lipids: from alkanes to phospholipids, 2nd edition. Small D, Ed. New Yok: Plenum Press, 1986:345–392.

26. Avrami M. Kinetics of phase change I. General Theory J Chem Phys 1939; 7:1103–1112.

27. Avrami M. Kinetics of phase change I. I. Transformation-time relations for random distribution of nuclei J Chem Phys 1940; 8:212–224.

28. Avrami M. Kinetics of phase change I. I. I. Granulation, phase change, and microstructure J Chem Phys 1941; 9:177–184.

29. Christian JW. The theory of transformations in metals and alloys: an advanced textbook in physical metallurgy. London: Permagon Press, 1965:471–495.

30. Marangoni AG, McGauley SE. Relationship between crystallization behaviour and structure in cocoa butter Crystal Growth and Design 2003; 3:95–108.

31. Rousset P. Modeling crystallization kinetics of triacylglycerols. In: Physical properties of lipids. Marangoni AG, Narine SS, Eds. New York: Marcel Dekker, 2002:1–36.

32. Wright AJ, Hartel RW, Narine SS, Marangoni AG. The effect of minor components on milk fat crystallization J Am Oil Chem Soc 2000; 77:463–475.

33. Wang FS, Lin CW. Turbidimetry for crystalline fractionation of lard J Am Oil Chem Soc 1995; 72:585–589.

34. Herrera ML, Gatti M, Hartel RW. A kinetic analysis of cryustallization of a milk fat model system Food Res Int 1999; 32: 289–298.

35. Herrera ML, Falabella C, Melgarejo M, Añon MC. Isothermal crystallization of hydrogenated sunflower oil: I-nucleation J Am Oil Chem Soc 1998; 75:1273–1280.

36. Herrera ML. Crystallization behaviour of hydrogenated sunflower seed oil: kinetics and polymorphism J Amer Oil Chem Soc 1994; 71:1255–1260.

37. Ng Wl. A study of the kinetics of nucleation in a palm oil melt J Am Oil Chem Soc 1990; 67:879–881.

38. Koyano T, Hachiya I, Arishima T, Sato K, Sagi N. Polymorphism of POP and S. O. S. II. Kintetics of melt crystallization J Amer Oil Chem Soc 1989; 66:675–679.

39. Dibildox-Alvarado E-, Vazquez J. Isothermal crystallization of tripalmitin in sesame oil J Am Oil Chem Soc 1997; 74:69–76.

40. Metin S, Hartel RW. Thermal analysis of isothermal crystallization kinetics in blends of cocoa butter with milk fat or milk fat fractions J Am Oil Chem Soc 1998; 75:1617–1624.

41. Ng WL, Oh CH. A kinetic study on isothermal crystallization of palm oil by solid fat content measurements J Am Oil Chem Soc 1994; 71:1135–1139.

42. Shaw DJ. Introduction to colloid and surface chemistry, 3rd edition. Boston: Butterworths, 1983:44–52.

3

Lipid Phase Behavior

K. L. HUMPHREY and SURESH S. NARINE

Agri-Food Materials Science Centre, Department of Agricultural, Food and Nutritional Science, University of Alberta
Edmonton, Alberta, Canada

1. INTRODUCTION

A phase is a domain, homogenous with respect to chemical composition and physical state [1,2]. Some natural fats are examples of systems of coexisting homogeneous domains that are not necessarily in equilibrium. The phases within a fat system may be categorized in terms of liquid/solid, polymorphic forms, and volume expansion upon crystallization of the fat. Because many physical definitions of a phase exist, it is important to define very carefully what is used as a phase in any particular study of lipids. For example, within the solid phase of a fat there can exist many different polymorphs, and

within each polymorphic type there can exist many different microstructures. Therefore, clear definitions of what constitutes a phase are important in any particular study. The relationship and occurrence of phase change in a fat system is referred to as the phase behavior of the lipid. Phase behavior, such as that obtained through the study of the solid fat content (SFC), dilatometry, melting behavior, and/or polymorphism of a lipid sample, is important in optimizing production processes and maintaining production quality, and has been used in the past to predict important attributes such as mouth-feel and hardness in fat-containing food products. Studies of phase behavior also help to provide a better understanding of the ways in which fat blends interact; an important aspect since the large-scale industrial production of shortenings and other fat-containing products often require blending of lipids from many different sources.

Phase behavior is commonly connected with the equilibrium mixture of liquid, vapor, and solid phases of a mixture of substances, as a function of temperature, pressure and composition, and is therefore well represented by phase diagrams. Liquid-vapor pressure composition diagrams, as shown in Figure 1, describe the liquid-vapor equilibria of a binary mixture of substances, in this case, benzene and toluene at 20°C [3]. The benzene-toluene system is commonly used to illustrate

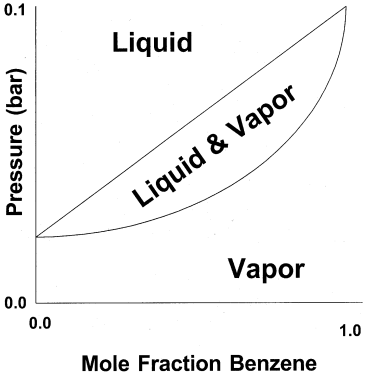

Figure 1 Ideal phase behavior of the benzene/toluene system [3].

phase behavior because the system approximates an ideal system due to the molecular complementarities of the component substances. One can determine the composition of the liquid (a) that gives rise to a given vapor pressure, as well as the composition of the vapor (b) at the given pressure and temperature. The inverse is also true when one knows the composition of the solution; one can find the vapor pressure of the solution and the composition of said vapor at a particular temperature. Thus, the phase behavior diagram imparts information about the properties and states of the system composed of the two substances.

Also associated with the phase behavior is a phase rule that states the relation between the number of phases (P), components (C), and degrees of freedom (Φ) [3]. The number of components is defined as "the least number of independently variable chemical species necessary to describe the composition of each and every phase of the system." [3] The degree of freedom is described as "the least number of intensive variables that must be specified to fix the values of all the remaining intensive variables." [3] The phase rule for a multicomponent system is given as:

$$\Phi = C - P + 2 \tag{1}$$

For a one-component system, the phase rule can be simplified to:

$$\Phi = 3 - P \tag{2}$$

2. TYPES OF PHASE BEHAVIOR

Many different types of phase behavior exist. The main classes are monotectics, eutectics, and peritectics. Binary systems for which the melting points or boiling points of the solutions of differing compositions are not lower than the melting points or boiling points of either of the components are called monotectic systems (note that "solutions" are used here in both the solid and liquid sense). "Eutectic," in Greek, means "easily melted" [3] and indicates a melting point or boiling point lower for the solution than that of the individual pure products in solution.

Peritectics or "incongruent melting points" are seen in compounds that decompose upon melting into another solid instead of taking on a liquid form [4]. Given these definitions and the plurality of definitions of lipid phase behavior mentioned before, it is obvious that when one discusses a particular type (monotectic, eutectic, peritectic) of behavior for lipids, one must do so within the particular confines of the physical state being investigated. That is, solid-liquid phase behavior and polymorphic-type phase behavior will mean different things in terms of a monotectic, eutectic, or peritectic.

Monotectic systems are those in which the components have similar melting points, molecular volumes, and polymorphic forms [5]. An example of a monotectic binary lipid system is 1-palmitoyl, 2-olyoyl, 3-stearoyl-sn-glycerol (POSt) and 1,3-stearoyl, 2-olyoyl-sn-glycerol (StOSt) [5]. Figures 2*A* and 2*B* illustrate monotectic binary systems. Figure 2*A* shows a monotectic continuous solid-state phase diagram of a binary mixture of theoretical triacylglycerides (TAGS) X and Y. The monotectic partial-solid-solution phase diagram of the binary mixture of TAGs X and Y is shown in Figure 2*B*. Figures 2*A* and 2*B* differ in that the solid phase in Figure 2*A* is continuous

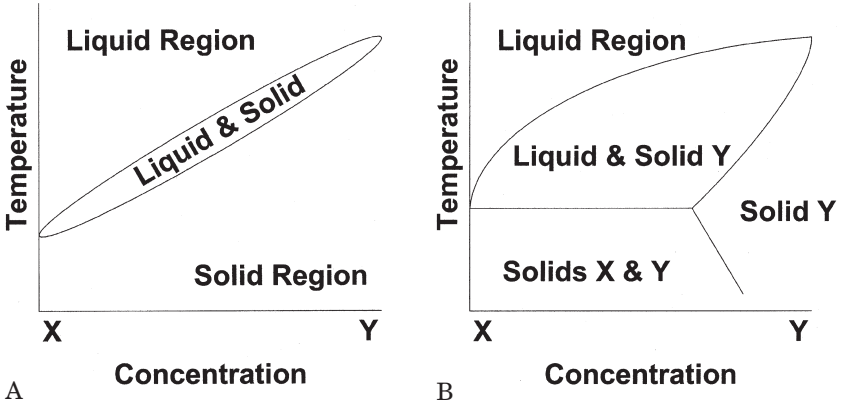

Figure 2 **A** Phase behavior of a theoretical monotectic system. **B**. Phase behavior of a theoretical monotectic system with solid solution changing.

and not differentiated while, in Figure 2*B*, both the solid and liquid phases are differentiated, in that one can define a partial solid-liquid phase as well as differentiate the type of solid that exists at various compositions (e.g., solid XY or solid Y). A solid solution exists for all compositions of X and Y in the lower-most region of Figure 2*A*. A true solid solution does not exist in Figure 2*B*, as the lower left-hand side region consists of a solid component Y dispersed in liquid X and the lower right-hand side region consists of purely solid Y. The midsection in Figure *2A* defines the temperature and composition constraints wherein both components, X and Y, exist in a mixture of liquid and solid forms. A similar region exists in Figure 2*B*; however, the solid portion is composed only of component Y. In both figures, the uppermost region illustrates a region, defined by temperature and composition, where a solution of X and Y exist in liquid form.

The most common binary mixtures of TAGs that form eutectics are those with components that differ with respect to molecular volume, shape, and polymorph, and do not vary drastically with respect to melting point [5]. Some examples of such systems are tri-palmitoyl-sn-glycerol (PPP) and tri-stearoyl-sn-glycerol (StStSt), POSt and 1,3-palmitoyl, 2-olyoyl-sn-glycerol (POP), and StOSt and 1,2-stearoyl, 3-oyloyl-sn-glycerol (StStO) [5]. Figure 3 shows an example of a binary

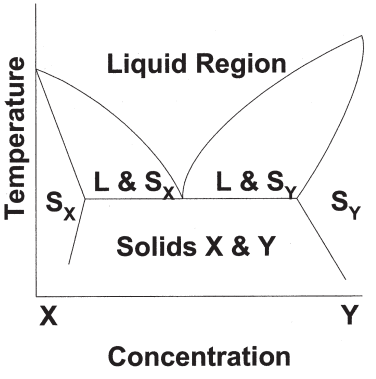

Figure 3 Phase behavior of a theoretical eutectic system.

eutectic system for a mixture of TAGs X and Y. A liquid mixture of components X and Y exists in the uppermost region of Figure 3. The existence of a minimum point of the lower boundary line for this region indicates that the system represented is a eutectic. In the area to the left of this minimum point, toward a greater concentration of component X, there exists solid X within a binary liquid. To the right of the minimum point, component Y exists in a solid form within a binary liquid. TAG X can be found in solid form when the temperature and concentration conditions are within the range as indicated by the lower left hand portion of Figure 3. For a range of temperatures, as the sample approaches 100% Y, as illustrated by the lower right region of Figure 3, Y is present in pure solid form. Components X and Y coexist in solid form for lower temperatures as indicated by the bottom-most and central region of Figure 3. The eutectic behavior results in the liquification of the mixture at specific compositions. This can be a catastrophic situation in lipid applications where hardness, texture, and SFC are important. However, it is also beneficial when one wants to avoid crystallization.

Peritectics normally occur in mixed saturated—unsaturated systems with at least one TAG which has two unsaturated fatty acids [5]. Figure 4 shows an idealized binary peritectic system of the theoretical TAGs X and Y. These TAGs,

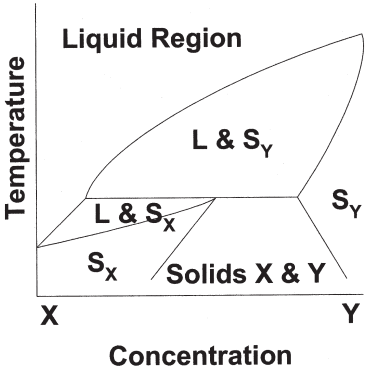

Figure 4 Phase behavior of a theoretical peritectic system.

X and Y, exist in solid form in the lower left and right sides of the graph, respectively. In the lower midregion of Figure 4, components X and Y exist in solid form without exclusion. Component X also exists in solid form, but within the binary liquid in the region to the left of the graphs at temperatures above the region where solid X exists exclusively. For temperatures higher than those in which component X exists as a solid, X exists as a liquid, either concurrently with solid Y or with liquid Y.

3. IDEAL SOLUBILITY BEHAVIOR

Since the phase behavior of any particular mixture of substances is related integrally to the degree of intersolubility of the components in the mixture, ideal solution behavior is briefly discussed here. The melting temperature of blends of solid TAGs have been found to be independent of the nature of any liquid oils present in the blend if the liquid oils do not participate in crystallization [6]. The solubility effects of a lipid mixture are important as they affect the crystallization behavior of TAGs, and hence the phase behavior of the TAGs in the mixture. The ideal solubility behavior of a binary lipid mixture can be predicted by the Hildebrand equation [6,7]:

$$\log_{10} X = \frac{\Delta H_f}{R}\left(\frac{1}{T_m} - \frac{1}{T_b}\right) \tag{3}$$

where X represents the mole fraction of the higher melting component, ΔH_f the enthalpy of melt for the higher melting component (in J/mol), R is the universal gas constant (8.314 J/mol K), and T_m and T_b are the melting temperatures of the higher melting component and the blend (in K), respectively. For those binary mixtures that demonstrate ideal solubility behavior, it is clear that the solid-liquid boundary at various compositions can be established by application of the Hildebrand equation. Furthermore, it is clear that binary mixtures which demonstrate ideal solubility behavior would produce a straight line plot if $\log_{10}X$ is plotted against $1/T_b$. This, therefore, can become a predictive equation for phase behavior if it

is known *a priori* that a binary mixture forms an ideal solution. Furthermore, for binary lipid mixtures that demonstrate a straight line plot of $\log_{10}X$ versus $1/T_b$ for only a limited range of X, over that range, the Hildebrand equation becomes predictive of the phase behavior of the sample. In practice, the higher melting component may actually be an ensemble of TAGs, rather than a single molecular species. In this case, many researchers tend to use the onset of melt of the ensemble, or the melting maximum of the ensemble as determined by differential scanning calorimetry (DSC) as T_m and utilize a weighted mean molecular mass of the ensemble to determine, X. ΔH_f is also an experimentally determined value based usually on DSC data. In this manner, the practicability of the Hildebrand equation can be extended to those blends which are primarily of a high melting ensemble of molecules and a low melting ensemble of molecules, such as the blending of a hydrogenated fraction with a base oil, as is done in the manufacturing of many shortenings and margarines.

TAGs found in North American vegetable oils are typically those containing C16 and C18 fatty acids. These TAGs are claimed to obey the Hildebrand solubility equation which is also known as the ideal solubility law [7]. However, work by Humphrey et al. [8] has pointed to the formation of mixed crystals with C16:0 and C18:0 mixed TAGS. Deviations from ideality can occur at high solvent to solute ratios as the change in volume increases the entropy of mixing during melting [7]. As well, solid solutions or the formation of imperfect crystals can also cause deviations from ideality as imperfect crystals have greater solubility than perfect crystals.

4. LIPID PHASE BEHAVIOR DETERMINATION

The phase behavior of lipid systems has been researched by many [5–22]). The methods used by researchers to produce phase diagrams include: SFC to produce iso-solid lines, liquid-solid phase diagrams, polymorphism phase diagrams and iso-dilatation lines.

4.1. Solid Content

The SFC of a fat system is the amount of solid fat as a percentage of the total fat present. Pulsed-nuclear magnetic resonance (NMR) is one popular method used to determine the SFC of a fat system at a series of temperatures after a given tempering scheme and is used often in the creation of iso-solid phase diagrams. NMR provides an accurate measure of SFC ($\pm 0.5\%$ generally) given the time and temperature resolution of the instrument [5]. The generally accepted procedure for SFC measurements [5] to create iso-solid phase diagrams is to cool the fat sample at a desired rate to 0°C and hold at 0°C for 90 minutes prior to sampling the SFC. The sample is then heated at a constant rate to 5°C, and this temperature is held for 30 minutes prior to sampling the SFC. The temperature of the sample is continually increased in this manner by 5°C increments, holding for 30 minutes at each temperature. One problem with this series of measurements is that each change in temperature and each waiting time will affect the SFC of subsequent measurements. Thus, one must be precise in the temperature scheme used to heat the sample. Alternatively, one may choose to perform the measurements in parallel rather than series, which eliminates the changes occurring within the fat as the temperature is stabilized at each measurement temperature. That is, samples would be cooled to 0 °C, held for 90 minutes and then heated to the required temperature directly. The SFC of a lipid sample can also be established via the use of DSC or dilatometry, however, SFC determination via NMR is an American Oil Chemists' Society (AOCS) recommended practice [5].

It is important to note here that SFC and solid fat index (SFI) are not interchangeable terms. The SFI of a lipid is obtained by dividing the dilatation by 25 [5]. This method assumes that all fats have the same total melt dilatation of a factor of 2500 and that the variation of dilatation with temperature is negligible. In fact, at 0°C, the total melt dilatation average factor is 2000 for a variety of fats, and the total melt dilatation depends on the particular fat sample as well as the cooling scheme [5].

4.2. Melting Point

Data for liquid-solid phase diagrams can be obtained via the use of DSC, slip melting points, Mettler dropping points, and Wiley melting points. Currently, the most widely accepted and reliable method of obtaining the melting point of a fat is through the use of DSC. Differential scanning calorimetry measurements are taken by heating the fat sample at a constant rate (e.g., 2°C per minute [16], or 0.2°C per minute [9], and determining the temperatures at which peaks occur. Decisions on appropriate heating rates relate to the resolution of the particular instrument as well as to the melting range of the lipid sample. Researchers have used both the onset of melt as well as the peak maximum as the melting point. Figure 5 shows a typical DSC melting curve, with the onset of melt and peak maximum indicated. These melting temperatures, which

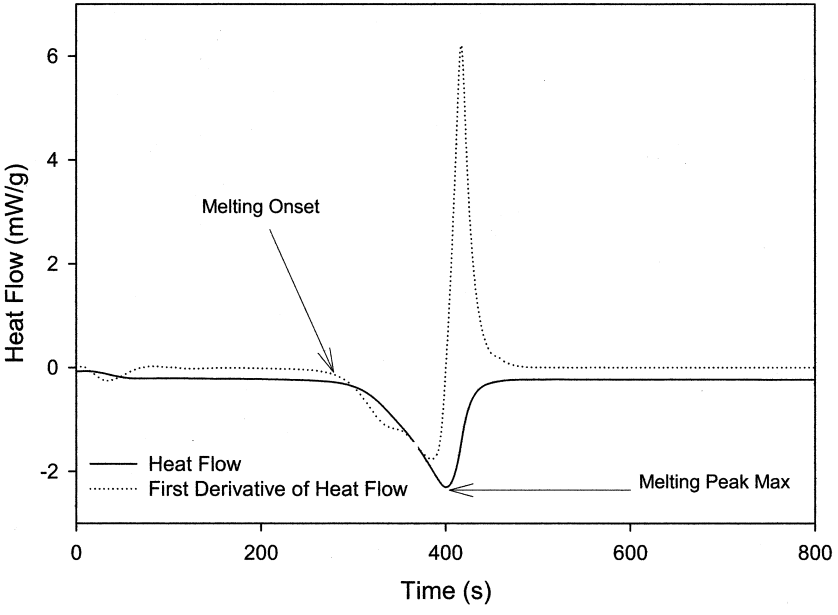

Figure 5 Enthalpy of melt curve and first derivative curve from DSC. The onset of melt and peak maximum is indicated by the arrows.

indicate the boundaries between phases, are then plotted against the composition of the fat sample (i.e., percent concentration in a binary lipid sample) [5,16]. One of the disadvantages of using DSC measurements to construct phase diagrams is the assumption that there is a definite temperature at which the phase transition occurs [9]. In pure substances, it would be ideal if transitions occurred at one temperature rather than a temperature span but this is seldom the case. Finite sample size and instrumental effects contribute to the widening of the window within which the phase transition can occur [9]. Furthermore, and as is usually the case, the crystallized portion of the sample is composed of an ensemble of different molecules and a continuous variation of molecular compounds of differing crystallization and melting temperatures, so that the "window" of crystallization temperatures in "real" systems can be widened significantly. Another complication is the possibility of formation of different polymers upon crystallization of the same ensemble of molecules with different polymorphs having variable crystallization and melting temperatures. Therefore the liquid-solid transition can be complicated significantly by these effects.

4.3. Polymorphic Type

The phase changes caused by a change in the polymorphism of a lipid sample are usually measured with x-ray diffraction (XRD), although infrared vibrational spectroscopy [23–30], atomic force microscopy [31], and nuclear magnetic resonance spectroscopy [32–39] have also been used. A change in the peak shape or position (of a diffraction profile) is indicative of a change in the polymorphism. Elsewhere in this book is described the theory and practice of XRD determination of the various polymorphs of a lipid network. Reference is made here only to the short spacing, or "d," value of the diffraction patterns. The alpha polymorphic form has a d value of 0.42 nanometers, the beta-prime d value is within the range of 0.42–0.43 nanometers and 0.37–0.40 nanometers, and the beta form has a d value of 0.46 nanometers [8]. In order to find the polymorphic form of a sample for the purposes of creating a phase

behavior diagram, where in this case, a phase is defined as the polymorphic type of crystal, the sample is tempered to 0°C or lower, and then heated in 5°C intervals at a constant rate [14]. The polymorphic form is determined and then plotted against the composition of the lipid blend. Polymorphism phase data are often included in liquid-solid phase diagrams along with the melting point data, such as in the case of Figure 2*B*.

4.4. Volume Expansion

Dilatometry is used to determine the iso-dilatation lines of a fat sample, which imparts information on the rate of expansion vs. temperature [11]. The dilatation tube is constructed and filled as described by Jasperson and McKerrigan [11]. The tube itself is a U-shaped volumetric type tube with a 6–7 mL bulb which is sealed with a ground glass stopper with a convex bottom. The other arm of the U-tube is a graduated ($\pm$ 0.005 mL) capillary tube with a 2-mm interior diameter. The bulb is filled with 1.5 mL of water, which is carefully drawn up the capillary tube. When the fat is added to the bulb portion and stoppered, the lipid sample pushes the water up the tube. The filled tube is heated to above the melting point of the fat, and then allowed to cool to 4°C overnight. To obtain the measurements for the dilatation curve, the dilatometer is immersed in temperature controlled water baths at intervals of 5°C for 15–30 minutes beginning at 10°C, and the height of the water in the stem of the tube is recorded at each temperature. One disadvantage of this process is that if the water bath warms up above the temperature at which the measurement is to be recorded, the entire stepwise process has to be redone as the tempering procedure has changed [11]. As well, volume expansion of lipid samples, in addition to the error-inducing effects mentioned before, can be dependent on the rate of increase so that this rate must be kept carefully controlled to ensure that the crystal polymorphism and microstructure is grown along similar templates. For example, a faster rate of cooling may lead to a denser microstructure [40] thus resulting in a smaller volume expansion.

Much investigation of the physical properties of lipids has been perfected using phase behavior studies. Many such studies on cocoa butter have been completed [5,14,18]. One reason for the attention that cocoa butter receives is due to its industrial importance as a confectionery fat. Cocoa butter requires careful tempering to achieve desired results, so there are many efforts focused on finding suitable replacements for cocoa butter which do not require such careful treatment. Loisel [14] and Minato et al. [16] have investigated the polymorphic phase transitions of cocoa butter and PPP-POP mixtures respectively. Knoester et al. [7] studied the solid-liquid phase behavior of TAGs containing palmitic and stearic acids, and Timms [22] used both solid-liquid behavior as well as iso-solid lines to study Palm kernel oil, a lipid used as a cocoa butter replacement. Iso-solid diagrams were also used by Lambelet and Raemy [12] in their study of coca butter and milk fat fractions and by Rousseau et al. [19] in their study of the interesterification of butterfat. Marangoni and Lencki [15] extended the concept of iso-solid binary phase behavior to ternary phase behavior for milk fat fractions. Dilatation was used by Jasperson and McKerrigan [11] on the "natural fats"; cocoa butter, palm kernel oil, palm oil, lard, and tallow, and by Rossell [18] on the study of cocoa butter alternatives and mixtures of pure TAGs. Inoue et al. [9,10] used both DSC and XRD data to create liquid-solid phase diagrams in the study of binary mixtures of palmitoleic, ascelepic, and cis-monounsaturated acids of varying omega chain length.

4.5. Constructing Lipid Phase Diagrams

In order to effectively study lipids using phase behavior techniques, one must be able to construct and correctly interpret a phase diagram. Liquid-solid phase diagrams and polymorphism phase diagrams are relatively easily constructed. The melting point and/or polymorphic form are plotted against the composition of the sample. If the DSC thermogram has more than one melting peak, the temperature of each peak maxima or onset is plotted. For each composition point, the highest melting temperature forms the liquidus line. At temperatures

above the liquidus line, the entire sample is in liquid form. The lower melting temperatures form the solidus line, below which the entire sample is solid. Between the liquidus and solidus lines, the sample is a solution of liquid and solid phases. XRD adds another dimension of information to the liquid-solid diagram. At any point on the phase diagram where a solid exists, the solid can be classified with respect to polymorphic form. Therefore, the region below the solidus line may be further subdivided, using polymorphic data from XRD, into its composite polymorphic forms if there is indeed a phase transition between forms occurring in the sample. The liquid may also exhibit some structural organization observable by XRD, and the liquid section may also be divided according to the organization that takes place at different concentrations and dilutions.

Phase diagrams containing iso-solid or iso-dilatation lines are not as easily created as the liquidus-solidus phase diagrams. There are three ways to construct iso-solid or iso-dilatation graphs. The first method consists in plotting the average of the actual results using a method for iso-dilatation lines outlined by Rossell [18]. A series of dilatation curves are drawn for measurements made at regular composition intervals. The number and size of intervals will affect the quality of the final iso-dilatation curve as too few measurements will cause the curves to be discontinuous, and potentially inaccurate. If one chooses too small an interval the measurements become very time consuming. A series of dilatation values are then chosen and the temperatures which give these dilatations are read off the dilatation curves. A plot is then made of these temperatures with respect to the composition, with each line representing a dilatation value.

A second, less time consuming and more easily reproducible method consists of using a quadratic interpolation, as previously described by Timms [21], to build iso-solid lines at specific percent SFC. The SFC is again plotted against temperature as shown in Figure 6 (in this case for different fractions of milk fat). An equation to describe the SFC versus temperature curve is obtained using computer-assisted quadratic or parabolic interpolation methods. A table of iso-solid tempera-

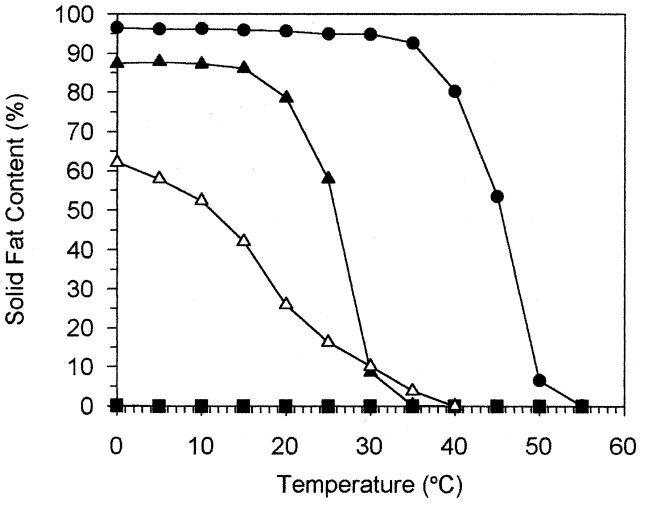

Figure 6 SFC vs temperature for varying fractions of milk fat. (■ represents LMF, △ represents another LMF, ▲ represents MMF, ● represents HMF.)

tures for each sample is constructed and this data is interpolated in the same manner to find the temperature data at 1% composition intervals. The interpolated temperatures are then plotted against composition, with a line for each SFC value. Timms [41] has created a commercial program, IsoSol, that calculates the appropriate tables and interpolations in a seamless manner.

The third method also requires that the SFC be plotted versus temperature for each dilution, as in Figure 6. This graph can then be interpolated to obtain the necessary temperature to achieve a given SFC using appropriate graphing software (i.e., GraphPad Prism, San Diego, California, U.S.A.). A multiple line graph of temperature versus composition can be made, as in the method above with each line representing one SFC value [8].

6. INTERPRETATION OF PHASE DIAGRAMS

The phase behavior of a lipid sample can be illustrated by phase diagrams, be it liquid-solid, polymorphism, iso-dilata-

tion, or iso-solid phase diagrams or a combination of these different forms. Phase diagrams impart a great deal of information about the lipid sample if they are correctly interpreted.

Figure 7*A* shows a monotectic system of fully hydrogenated canola in soybean oil. This monotectic is illustrated via a SFC versus composition graph. As the composition tends to 25% fully hydrogenated canola in soybean oil, the SFC of the sample increases without any local maxima or minima. Thus, the samples exhibit ideal solubility behavior.

Solubility behavior can also be deduced from phase diagrams. The iso-solid phase diagram, Figure 7*B*, shows a ternary monotectic of the High Melting Fraction of Milkfat (HMF) (5S), the Middle Melting Fraction of Milkfat (HMF) (−28S), and the Low Melting Fraction of Milkfat (HMF) (−28L) at 30°C. The nearly straight line of 10% SFC, parallel to the bottom axis, indicates ideal mixing behavior as predicted by the Hildebrand solubility equation [15]. Ternary phase diagrams are a relatively new addition to the study of lipid phase behavior; Timms stated: "No complete and reliable phase diagram for mixtures of more than two TAGs has been reported" [5]. However, ternary phase diagrams have been used extensively in the engineering sciences [42–44].

Figure 7*C* is an iso-solid diagram of HMF in MMF, with the bottom line representing 5% SFC, and the uppermost representing 90% SFC. As one moves up the graph the SFC value of the lines increases in 5% increments. There is an increasing trend as the composition of the sample tends to 100% HMF, with the minimum occurring at 0% HMF. There is no composition for which a given SFC occurs at a lower temperature than at 0% HMF, thus the system illustrated is a monotectic system.

Figure 8*A* is an iso-solid phase diagram showing the ternary phase behavior of HMF, MMF, and LMF at 0°C. The eutectic in Figure 8*A* is distinguished by the lines which deviate from linearity (i.e., the 40% SFC line) which indicate a formation of solution intermediates between the three components [15].

Figures 8*B* and 8*C* are iso-solid diagrams. Figure 8*B* illustrates the phase behavior of the HMF in cocoa butter system.

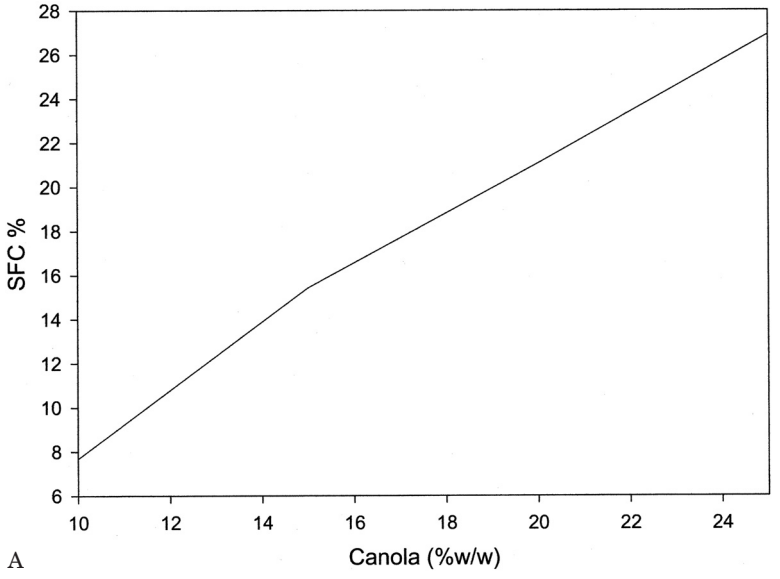

A

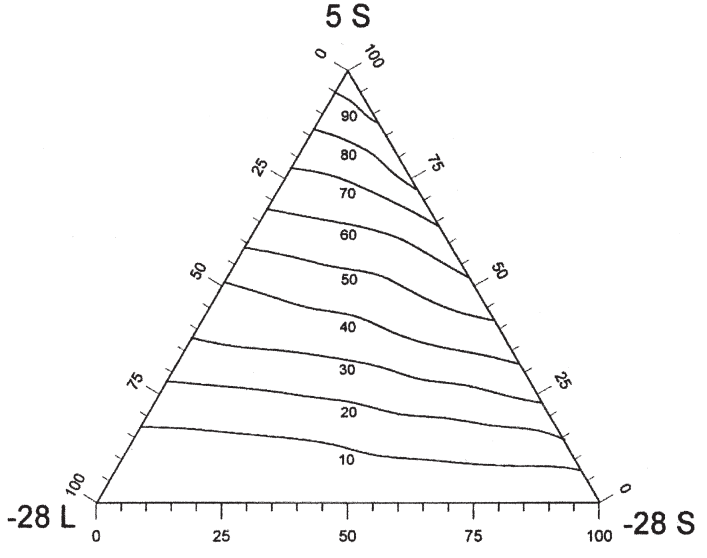

B

Figure 7 **A.** Experimental binary montoectic of fully hydrogenated canola in soybean oil via SFC. **B.** Experimental ternary monotectic of HMF (5S), LMF (−28L), and MMF (−28S) at 30°C via iso-solid lines.

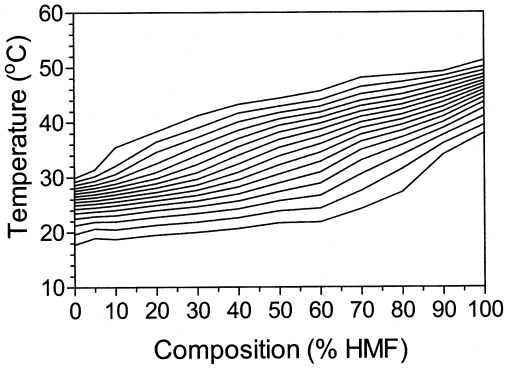

C

Figure 7 C. Experimental binary monotectic of MMF and HMF via iso-solid lines. The bottom-most line represents 5% SFC, and subsequent lines increase in increments of 5% to a maximum of 90% SFC as the uppermost line.

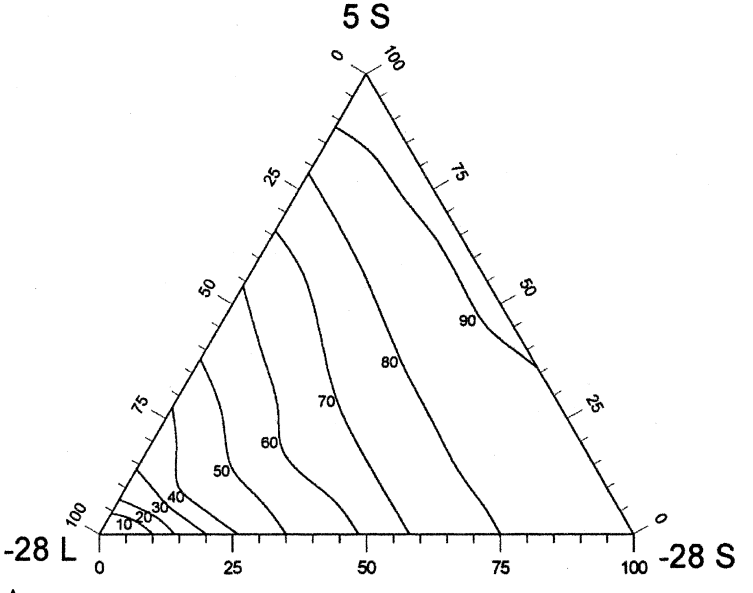

A

Figure 8 A. Experimental ternary eutectic of HMF (5S), LMF (−28L), and MMF (−28S) at 0°C via iso-solid lines.

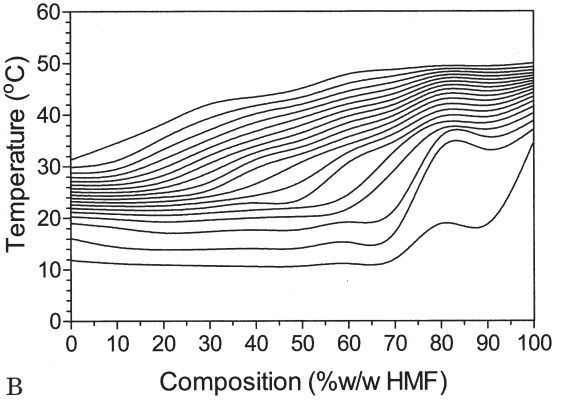

B

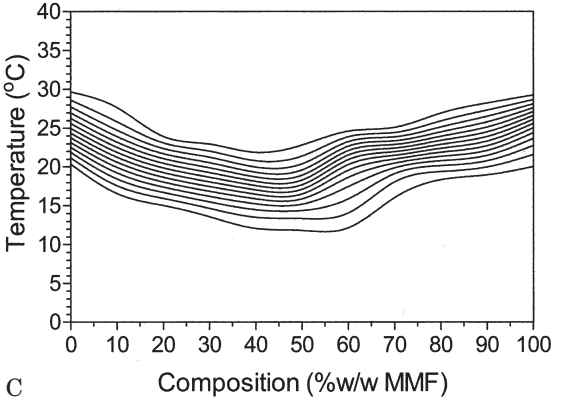

C

Figure 8 **B.** Experimental binary eutectic of cocoa butter–HMF via iso-solid lines. The bottommost line represents 5% SFC, and subsequent lines increase in increments of 5% to a maximum of 90% SFC. **C.** Experimental binary eutectic of cocoa butter–MMF via iso-solid lines, an exaggerated case. The bottom-most line represents 10% SFC, and subsequent lines increase in increments of 5% to a maximum of 75% SFC.

The bottom line represents 5% SFC, while the subsequent lines increase in 5% increments to 90% SFC. As the composition of the binary system approaches 100% HMF, the SFC lines increase in temperature. This trend is true for all but the six lowest iso-solid lines on the figure. These lines demonstrate no increase with %HMF until approximately 50% HMF. There is a noticeable decrease in temperature in the curves of iso-solid lines at approximately 70% HMF. This indicates that at these compositions, at an SFC range of 5–10% there exists a eutectic. Furthermore, a second eutectic is presented at approximately 90% HMF by the lowermost five iso-solid lines in the figure. These curves indicate that the sample is slightly eutectic, more so than Figure 7*C*. Figure 8*C* illustrates the phase behavior of the MMF/cocoa butter system. The bottom line represents 10% SFC, while the subsequent lines increase to 90% SFC in 5% increments. Unlike, Figure 8*B*, Figure 8*C* has a minimum point for all SFC lines occurring between 40 and 60% MMF. This minimum point indicates a very strong eutectic.

Due to the trend established in each of Figures 7*C*, 8*B*, and 8*C*, one might be tempted to conclude, as Timms did, that "no significant improvement in hardness of milk chocolate with hydrogenation and fractionation of milk fat was observed" [5]. In fact, while this statement is true in the specific case that Timms refers, it is not generally true that eutectics as demonstrated by iso-solid phase diagrams impart information on hardness of the solutions at the eutectic compositions. In many instances, iso-solid line behavior may not indicate changes in polymorphism of the samples and certainly does not impart information beyond the prediction of hardness by SFC, a method that has been shown to be imperfect [45–47]. As well, the solution behavior demonstrated by iso-solid line diagrams does not always account for all observed trends in the melting behavior, as both intersolubility and polymorphic changes may occur simultaneously. Phase behavior as observed from iso-solid lines are important in elucidating some aspects of inter-solubility behavior, but is ultimately limited in scope, as are most physical techniques applied in isolation to the study of structure-composition-functionality studies. On

the other hand, DSC phase measurements can reflect changes in polymorphism as well as intersolubility. However, such changes are not attributable to either polymorphic or intersolubility effects in isolation utilizing just DSC data. Therefore, it is important to study phase behavior using a number of different techniques.

7. THE USE OF PHASE BEHAVIOR IN CONJUNCTION WITH OTHER TECHNIQUES: A CASE STUDY

As the study of phase behavior is just one additional tool in a repertoire of many such to effect an elucidation of the physical properties of mixtures of lipid species, one study which utilizes a number of different analytical techniques in unison is explained here. The intent is that the reader gain an appreciation of both the power and limitations of using phase studies in the study of lipid mixtures

We present therefore a study of a binary mixture of fully hydrogenated canola in soybean oil [8]. The iso-solid line phase diagram constructed from the SFC of a binary lipid sample of canola in soybean oil is shown in Figure 9*A*. The iso-solid line at the very top of the figure is the zero SFC line. From the zero SFC line, the percent solid increases from left to right in 5% increments. It is evident that as the temperature and percentage of hydrogenated canola increases, the iso-solid lines converge to the right. The shape of each iso-solid line is similar to that of the neighboring lines with the slope of the iso-solid lines appearing to be similar. The iso-solid diagram also shows that a shortening made using fully hydrogenated canola and soybean oil can have a 20% solid fat content at temperatures between 30 and 60°C when the percentage hydrogenated canola is between 20 and 50%. It also shows that at temperatures above 55°C, temperature variation must be carefully controlled as SFC varies greatly with temperature above this point. This figure does not impart information as to the melting point, polymorphism, or hardness of each sample as illustrated in Figures 9*B*, 9*C*, and 9*D*, respectively.

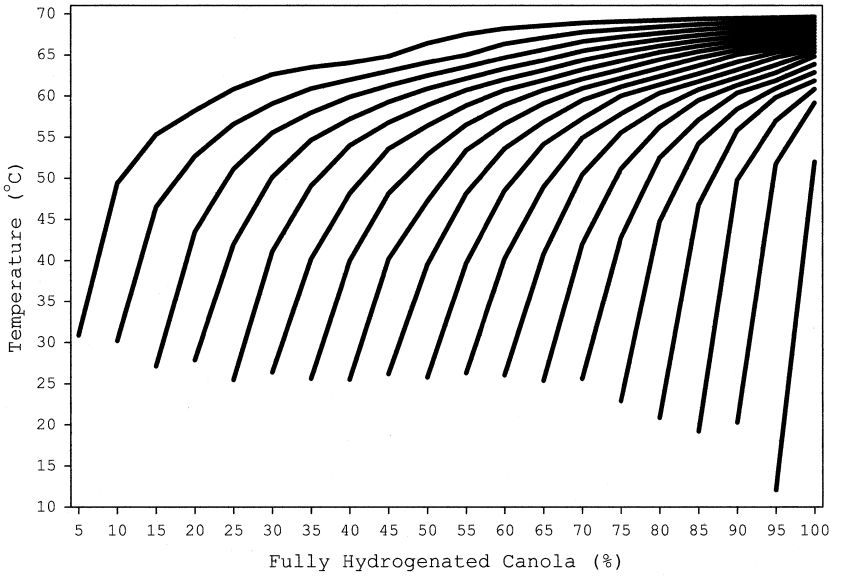

A

Figure 9 **A.** Iso-solid lines created using the interpolation method. Each curve connects points with a common SFC value. The leftmost curve is the 5% SFC line with the percent SFC increasing in 5% increments as one moves right on the graph.

Obtained through the use of DSC, the enthalpy of melt curves for the same fat samples as in Figure 9*A* are shown in Figure 9*B*. Changes in the shape of the enthalpy curves are due to the variances in polymorphic structure assumed by the sample. There is a steady increase in the location of the melting peak maximum for the 5–65% canola solutions. One would expect these samples to be of similar polymorphic form. A new trend in peak maxima occurs for the 70–95% samples as the peaks become narrower with the maxima starting a new increasing trend beginning lower than the peak max of the 65% canola blend. Clearly, for these samples, the polymorphic form is different than for the 5–65% samples. As well, the 95% canola blend has a unique type of melting behavior as the curve has a shoulder occurring at a lower temperature than the main

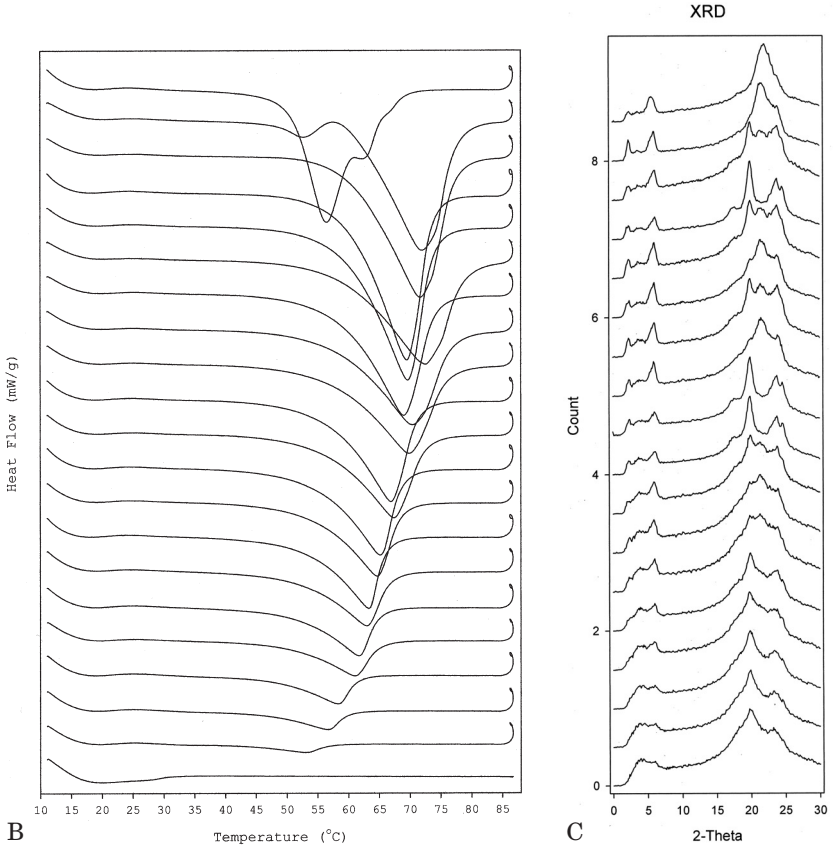

Figure 9 **B.** Melting heat flow versus temperature Curves after 48 hours with inset enthalpy of melting vs. composition curve. Each curve represents the heat flow during the melting process for a sample. The 0% canola sample is the bottom-most curve on the graph and the percent canola composition of the samples increases by 5% for each subsequent curve to the 100% canola sample at the top of the graph. **C.** X-ray diffraction curves versus d. Each curve is a diffraction spectrum for a specific sample composition. The bottom-most curve is the 15% canola blend, and the percent canola increases by 5% for each curve above. The uppermost curve is the spectrum obtained for the 100% canola sample.

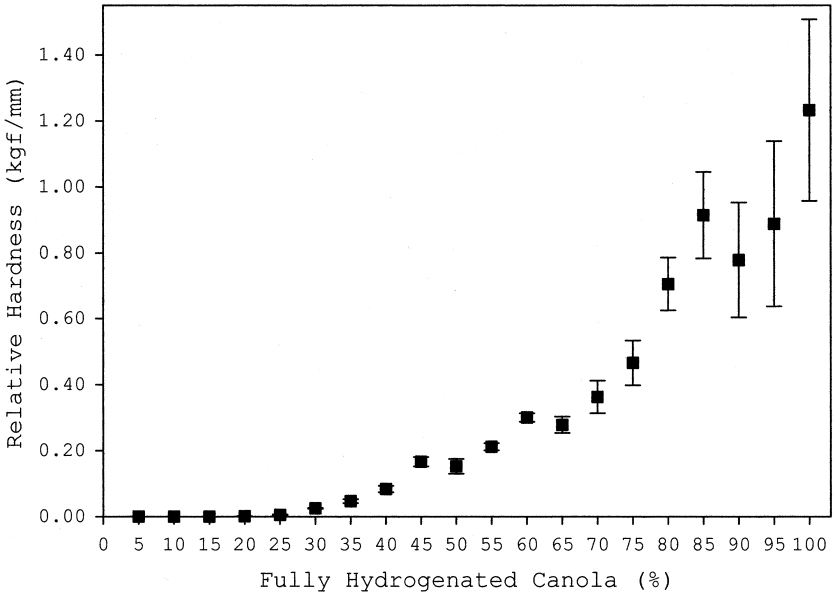

D

Figure 9 D. Variation of hardness with composition.

peak. The melting behavior exhibited by the 100% canola sample is unique as the enthalpy curve is characterized by a shoulder peak at a higher temperature than the main peak, with the maximum value at a lower temperature (57 °C) than all but the 5 and 10% samples. Therefore, unique polymorphic forms are to be associated with the 95 and 100% canola samples. The changes in polymorphic form suggested by DSC data are not seen in Figure 9*A*, thus melting behavior data sheds new light on the same sample set.

Figure 9*C* shows the XRD spectra for the same sample set, for all samples with 15% or more canola. Those samples with less than 15% were not measured due to difficulties in creating the requisite sample tubes. The lowest curve shown is the spectrum for the 15% canola blend with subsequent lines representing samples with increasing canola content until the 100% canola blend spectra at the top of the figure. Two peak

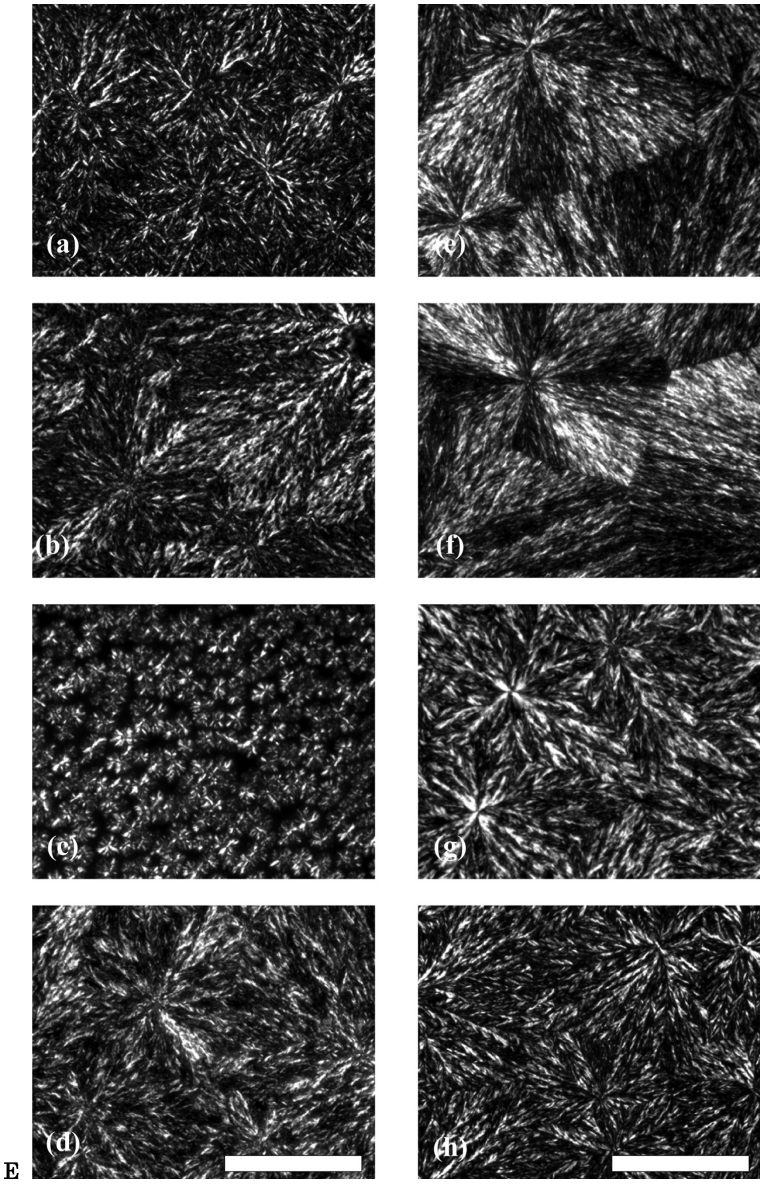

E

Figure 9 E. Composite diagram of the microstructure of selected samples after 48 hours. The given samples vary with respect to percent canola: (*a*) 40%, (*b*) 45%, (*c*) 50%, (*d*) 55%, (*e*) 80%, (*f*) 85%, (*g*) 90%, and (*h*) 95%. (bar = 500 μm)

regions exist on each curve. The rightmost imparts information as to the polymorphic form of the crystals within the sample (the so-called short spacing), and the peaks on the left hand side of the curve which may be due to secondary reflections or the polytype of the fat. The 100% canola peak is a well-defined single peak, and as one decreases the canola content to 95% a shoulder appears on the main peak. Further decreases in the percent canola in the sample leads to the appearance of 2 to 3 peaks on the right hand side of the XRD curve. For the lowest (15–35%) percentages of canola, the peak shape assumed is a large well-defined peak with a smaller shoulder peak on the right hand side. The left hand side peak on the curve is not well defined at lower concentrations of canola. At 40% canola a peak is defined and this becomes more apparent with increasing canola. At 65% canola, a second, smaller peak further left on the curve becomes clear, and at 95% canola these two peaks are of the same size distinction, with the rightmost peak disappearing in the spectra for the 100% canola sample.

A second peak on the left hand side of the XRD curves in Figure 9*C* for the 70–95% canola blends corresponds to the new trend in peak maxima in Figure 9*B* where the peaks become narrower with the maxima starting a new increasing trend beginning lower than the peak max of the 65% canola blend. Also in Figure 9*B*, the 95% canola blend's unique melting curve is possibly due to a polymorphic change as seen by the presence of a distinct second peak on the left hand side of the curve in Figure 9*C*. Again, the unique behavior of the 100% canola sample may be due to the polymorphism of the sample as the second peak on the left hand side of the curve in Figure 9*C* is not present.

Figure 9*D* shows an increasing hardness trend as the percent canola increases. The first three values, corresponding to the 5, 10, and 15% canola blends, are not zero but have very small values ($3.3 \times 10^{-5} \pm 4 \times 10^{-6}$ kgf/mm, $3.6 \times 10^{-5} \pm 2 \times 10^{-5}$kgf/mm, $6.4 \times 10^{-5} \pm 2 \times 10^{-5}$ kgf/mm). The 0% canola sample was not tested for hardness as it was entirely soybean oil. Fluctuations, where the fat sample with a higher percentage of canola exhibited a smaller slope during the hard-

ness measurement, occur in three areas of this graph; at the 50%, 65%, and 90% canola mixtures.

The deviation in Figure 9*D* at 50% canola is mirrored by inconsistencies in Figure 9*B*. In Figure 9*B*, there is a deviation in the trend of increase in location of melting peak max for 5–65 % blends at the 50% canola sample, indicating a change in melting behavior between the 45 and 50% blends (i.e., a polymorphic change).

Unlike the deviation in the hardness trend at 50% canola, the deviations in Figure 9d at the 65 and 90% canola blend are not due to melting behavior of the samples as the corresponding enthalpy of melt curves in Figure 9*B* are similar. The polymorphisms of the 60 and 65% samples differ as shown by the XRD curves in Figure 9*C*. Thus, the hardness variations are due to the differences in the packing of molecules between the 60 and 65% canola samples. For the third deviation at the 90% blend, the polymorphisms of the samples differ as shown by Figure 9*C*.

Figure 9*C* illustrates the microstructure of selected mixtures of fully hydrogenated canola oil and soybean oil. Except for minor deviations such as the placement of structures, the microstructures of the samples are alike with two exceptions. In the 50% canola blend, the structures appear smaller ($\approx$100 μm) than that for the other solutions shown (average $\approx$500 μm). Note that these structures are clearly aggregates of micro-structural elements, which are themselves aggregates of crystals. In the 50% canola sample, the structures are not closely packed and have spaces between them ($\approx$10 μm). The other samples exhibit the close packed arrangement as seen in the 45% canola sample. The 80 and 85% canola samples, though having the same crystal size as the 90 and 95% samples, are also more densely packed than those in the 90 and 95% samples as seen by the appearance of well-defined Maltese crosses. The distinct Maltese crosses indicate that these samples contain well-defined spherulites.

The deviation in increasing hardness from Figure 9*D* at the 50% canola solution is due to the microstructure assumed as well as polymorphism and intersolubility. In Figure 9*E*, one can see that the sample with 50% canola is characterized by

structures which are approximately 100μm in diameter with large (~10 μm) spaces in between the structures. The other samples shown have large, closely packed structures approximately 500 μm in diameter. Thus, one can expect that under pressure from an Instron cone the 50% sample will simply compress, with structures filling the spaces, whereas there is no room for similar compression in the 45% sample.

The deviation from the trend in the hardness curve at the 65% canola solution is not due to the microstructure assumed. All of the samples have a close-packed network of structures approximately 500 μm in diameter. Thus the variation in the hardness graph is not due to the microstructure of the samples.

The deviation from the trend in the hardness curve at the solution of 90% canola is partially due to changes in microstructure as well as polymorphism (as seen in Figure 9*C*). The changes in microstructure can been seen in Figure 9*E* as the 85 and 90% blends have the same crystal size but the 85% canola sample is more densely packed and demonstrates greater spherulitic behavior as suggested by the well-defined Maltese crosses indicating the presence of well-defined spherulites.

Therefore, the use of iso-solid lines as the sole method to study the phase behavior of the lipid mixture of fully hydrogenated canola in soybean oil was an insufficient method as not all of the deviations in melting behavior, polymorphism, microstructure, and hardness were elucidated by the iso-solid lines.

8. SUMMARY

The study of phase behavior is a powerful technique for studying the physical properties of lipids and has been used often by researchers in the field. However, phase behavior studies must also be complemented by a variety of other measurement techniques as one cannot completely describe the structure and physical properties of a fat system simply by studying phase behavior alone.

REFERENCES

1. Atkins PW. Phase diagrams. In: Physical Chemistry Atkins PW, Ed. Oxford: Oxford University Press, 1998:191–214.
2. Moore W. States of matter. Basic Physical Chemistry Moore W, Ed. Englewood Cliffs. NJ: Prentice-Hall, 1983:27.
3. Barrow G. Phase equilibria. Physical Chemistry Barrow G, Ed. New York: McGraw-Hill, 1988:381–431.
4. Noggle JH. Equilibrium in pure substances. In: Physical Chemistry Noggle JH, Ed. Glenview. Ill: Scott, Foresman and Co., 1989:171–209.
5. Timms R. Phase behavior of fats and their mixtures Prog Lipid Res 1984; 23:1–38.
6. Wright A, McGauley S, Warine S, Willis W, Lencki R, Marangoni A. Solvent effects on the crystallization behavior of milk fat fractions J Agric Food Chem 2000; 48:1033–1040.
7. Knoester M, De Bruijne P, van den Tempel M. The solid-liquid equilibrium of binary mixtures of triglycerides with palmitic and stearic chains Chem Phys Lipids 1972; 9:309–319.
8. Humphrey KL, Moquin PHL, Narine S. Phase behavior of a binary lipid shortening system: from molecules to rheology J Am Oil Chem Soc 2003; 80(2):1175–1182.
9. Inoue T, Motoda I, Hiramatsu N, Suzuki M, Sato K. Phase behavior of binary mixtures of cis-monounsaturated fatty acids with different omega-chain length Chem Phys Lipids 1992; 63: 243–250.
10. Inoue T, Motoda I, Hiramatsu N, Suzuki M, Sato K. Phase behavior of binary mixture of palmitoleic acid (cis-9-hexadecenoic acid) and asclepic acid (cis-11-octadecenoic acid) Chem Phys Lipids 1993; 66:209–214.
11. Jasperson H, McKerrigan A. The use of differential curves in the dilatometry of fats J Sci Food Agric 1957; 8:46–54.
12. Lambelet P, Raemy A. Iso-solid diagrams of fat blends from thermal analysis data J Am Oil Chem Soc 1983; 60(4):845–847.
13. Liang B, Shi Y, Hartel R. Phase equilibrium and crystallization behavior of mixed lipid systems J Am Oil Chem Soc 2003; 80(4): 301–306.

14. Loisel C, Keller G, Lecq G, Bourgaux C, Ollivon M. Phase transitions and polymorphism of cocoa butter J Am il Chem Soc 1988; 75(4):425–439.

15. Marangoni A, Lencki R. Ternary phase behavior of milk fat fractions J Agric Food Chem 1998; 46:3879–3884.

16. Minato A, Ueno S, Yano J, Wang, ZH, Seto H, Amemiya Y, Sato K. Synchrotron radiation x-ray diffraction study on phase behavior of PPP-POP binary mixtures J Am Oil Chem Soc 1996; 73(11):1567–1572.

17. Rossell J. Phase diagrams of triglyceride systems Adv Lipid Res 1967; 5:353–408.

18. Rossell J. Interactions of triglycerides and of fats containing them. Chem Ind 1973:832–835.

19. Rousseau D, Forestiere K, Hill A, Marangoni A. Restructuring butterfat through blending and chemical interesterification. 1. Melting behavior and triacylglycerol modifications J Am Oil Chem Soc 1996; 73(8):963–972.

20. Sato K. Solidification and phase transformation behavior of food fats—a review Fett/Lipid 1999; 101(12):467–474.

21. Timms R. Computer program to construct isosolid diagrams for fat blends Chem Ind 1979:257–258.

22. Timms R. Physical properties of oils and mixtures of oils J Am Oil Chem Soc 1985; 62(2):241–248.

23. Amey R, Chapman D. Infrared spectroscopic studies of model and natural biomembranes. In: Biomembrane Structure and Function, Topics in Molecular and Structural Biology Chapman D, Ed. Deerfield Beach. Fla: Weinheim, 1984:4.

24. Chapman D. Infrared spectroscopic characterization of glycerides J Am Oil Chem Soc 1960; 37:73–77.

25. Chapman D. Infrared spectroscopy of lipids J Am Oil Chem Soc 1964; 42:353–371.

26. Freeman N. Applications of infrared absorption spectroscopy in the analysis of lipids J Am Oil Chem Soc 1968; 45:798–809.

27. O'Connor R, DuPre E, Feuge R. The infrared spectra of mono-, di-, and triglycerides J Am Oil Chem Soc 1955; 33:88–93.

28. Yano J. Vibrational spectroscopic study on structures and polymorphic transformations of triacylglycerols. Ph.D. dissertation, Osaka University, 1988.

29. Yano J, Kaneko F, Kobayashi M, Kodali D, Small D, Sato K. Structural analysis of triacylglycerol polymorphs with FT-IR techniques. 2. b'1-form and 1,2-dipalmitoyl-3-myristoly-sn-glycerol J Phys Chem B 1987; 101:8120–8128.

30. Yano J, Kaneko F, Kobayashi M, Sato K. Structural analysis of triacylglycerol polymorphs with FT-IR techniques. 1. Assignments of CH2 progression bands of saturated monoacid triacylglycerols J Phys Chem B 1997; 101:8112–8119.

31. Birker P, Blonk J. Alkyl chain packing in a b' triacylglycerol measured by atomic force microscopy J. Am. Oil Chem. Soc. 1993; 70:319–321.

32. Arishima T, Sugimoto K, Kiwata R, Mori H, Sato K. C-13 cross-polarization and magic-angle spinning nuclear magnetic resonance of polymorphic forms of three triacylglycerols J Am Oil Chem Soc 1996; 73:1231–1236.

33. Boceik S, Ablett S, Norton I. C-13 NMR study of the crystal polymorphism and internal mobility's of the triglycerides tripalmitin and tristearin J. Am. Oil Chem. Soc. 1985; 62: 1261–1266.

34. Calaghan P, Jolly K. The use of C-13 spin relaxation to investigate molecular motion in liquid tristearin J Chem Phys Lipids 1977; 19:56–73.

35. Chapman D. Nuclear resonance spectra of the polymorphic forms of glycerides J Chem Soc 1960:436–444.

36. Eads T, Blaurock A, Bryant R, Roy D, Croasman W. Molecular motion and transitions in solid tripalmitin measured by deuterium nuclear magnetic resonance J Am Oil Chem Soc 1992; 74: 1213–1220.

37. Gibon V, Durant F, Deroanne C. Polymorphism and intersolubility of some palmitic, stearic and oleic triglycerides: PPP, PSP, and P. O. P. J Am Oil Chem Soc 1986; 63:1047–1055.

38. Hagemann J, Rothfus J. Polymorphism and transformation energetics of standard monoacid triglycerides from differential scanning calorimetry and theoretical modeling J Am Oil Chem Soc 1983; 60:1123–1131.

39. Norton I, Lee-Tuffnel C, Ablett S, Bociek S. A calorimetric, NMR and X-ray diffraction study of the melting behavior of tripalmitin and tristearin and their mixing behavior with triolein J Am Oil Chem Soc 1985; 62:1237–1244.

40. Campos R, Narine S, Marangoni A. Effect of cooling rate on the structure and mechanical properties of milk fat and lard Food Res Int 2002; 35:971–981.

41. Timms R. Consultant—Oil and Fats. http://:www.timms/.demon.co.uk/ 2003:2004.

42. Ahm T, Smf A. Solvent flooding displacement efficiency in relation to ternary phase behavior Soc Petroleum Engineers J 1972; 12(2):89.

43. Lv P, Smf A. Ternary phase behavior at high temperatures Society of Petroleum Engineers Journal 1968; 8(7):381.

44. Mam C, Has M, Mn D, Ejsg D. Binary and ternary phase behavior of alpha-pinene, beta-pinene, and supercritical ethene J Chem Eng Data 1996; 41(5):1104–1110.

45. Narine SS, Marangoni AG. Relating structure of fat crystal networks to mechanical properties: a review Food Res Int 1999; 32(4):227–248.

46. Narine SS, Marangoni AG. Factors influencing the texture of plastic fats Inform 1999; 10(6):565–570.

47. Narine SS, Marangoni AG. Microscopic and rheological studies of fat crystal networks J Cryst Growth 1999; 198/199: 1315–1319.

4

Rheology Fundamentals and Structural Theory of Elasticity

ALEJANDRO G. MARANGONI
Department of Food Science
University of Guelph
Guelph, Ontario, Canada

SURESH S. NARINE
Agri-Food Materials Science Centre, Department of Agricultural, Food and Nutritional Science,
University of Alberta
Edmonton, Alberta, Canada

1. RHEOLOGY OF SOLIDS

1.1 Hooke's Law

The theoretical foundations for the characterization of the properties of solids were devised by Robert Hooke (1635–1703). Hooke observed that, for small elongations, the amount of elongation of a spring, ΔL, was directly proportional

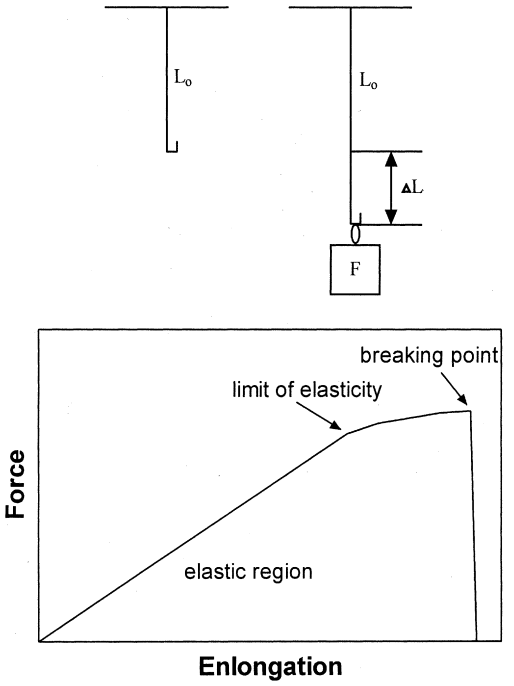

Figure 1 Idealized force-deformation curve for a Hookean spring.

to the applied force. This observation is expressed mathematically as Hooke's law:

$$F = k\Delta L \quad (1)$$

The range of elongation where Hooke's law is obeyed is called the *elastic region* of the spring (Figure 1). Within this elastic region, spring deformations are *reversible*, that is, once the force is removed, the spring returns to its original length (L_o). At elongations above the *elastic limit* of the spring, irreversible deformations take place, and Hooke's law is no longer applicable—no linear relationship between the applied force and the amount of spring elongation is observed. Beyond the *limit of elasticity*, the spring eventually reaches its *breaking point* (Figure 1).

Materials are usually analyzed rheologically, assuming they behave as springs. Most materials display an elastic re-

gion at small deformations, usually in a range not exceeding 1–3%. When these materials are taken above their *limit of elasticity*, they will be permanently deformed and will not recover to their original dimensions once the stress is removed. Substances that deform considerably beyond their *limit of elasticity* without breaking are termed plastic. For plastic deformations, a small increment in the applied force leads to a large deformation. These materials are termed ductile, e.g., lead, copper. Materials that break shortly after the limit of elasticity is reached are termed brittle, e.g., glass, steel. The *yield stress* corresponds to the value of the stress at the limit of elasticity.

Hooke's law can be used for the characterization of any solid material, as long as a linear relationship exists between the applied force and the amount of deformation of the material. Most solid materials obey Hooke's law for deformations up to 1–3%. When referring to small deformations in this chapter, we will be referring to any deformation below a 1% change in dimension in the direction of the applied force.

1.2 Stress-Strain Relationships and Elastic, Shear, and Bulk Moduli

The amount of deformation of a material will depend not only on the applied force and the nature of the material, but also on sample dimensions. Hooke's law is therefore of limited practical utility, since the constant k will be a function of the nature of the material being studied and its dimensions. One way of solving this problem is to modify Eqn. 1 to take into account the amount of force per cross-sectional area, rather than force, being applied, and the resulting relative, rather than absolute, change in dimension of the material:

$$\frac{F}{A} = M\frac{\Delta L}{L_o} \tag{2}$$

We define the applied *stress* (σ) as:

$$\sigma = \frac{\mathrm{F}}{\mathrm{A}} \tag{3}$$

where F is the applied force [N] and A is the cross-sectional area [m^2]. We define the resulting *strain*(s) as:

$$s = \frac{\Delta L}{L_o} \tag{4}$$

where ΔL is the change in length, and L_o is the original length of the sample. *Stress* (σ) has units of [N/m^2], or Pascals, *strain* (s), a dimensionless quantity, is usually expressed as a fraction or percentage, and the *modulus of elasticity* (M) has units of [N/m^2], or Pascals. Equation 2 can therefore be rewritten as:

$$\sigma = M \cdot s \tag{5}$$

The *strain* is directly proportional to the applied *stress*, and the *elastic modulus* is a constant that characterizes the elastic properties of the material. This constant is independent of sample dimensions, and dependent strictly on the nature of the material being studied.

1.3 Types of Stresses and Corresponding Definitions of Moduli

Tensile stress arises when a material is stretched in one dimension, compressive stress arises when a material is compressed in one dimension, and shear stress arises when opposite forces are applied on a material across its opposite faces (Figure 2), in one or two dimensions. A material can also be hydrostatically compressed in three dimensions. This last situation causes a change in volume.

For tensile and compressive stresses, the *Young's modulus of elasticity* is defined as:

$$E = \frac{\sigma}{\varepsilon} \tag{6}$$

where ε is the compressive strain, $\Delta L/L_o$, as shown in Figure 2. For shear stresses, the *shear modulus* is defined as:

$$G = \frac{\sigma}{\gamma} \tag{7}$$

where γ is the shear strain, $\Delta L/L_o$ or tan$a$, as shown in Figure 2. For small deformations, tan$a \approx a$ [radians].

For three-dimensional compression, the *bulk modulus* is defined as:

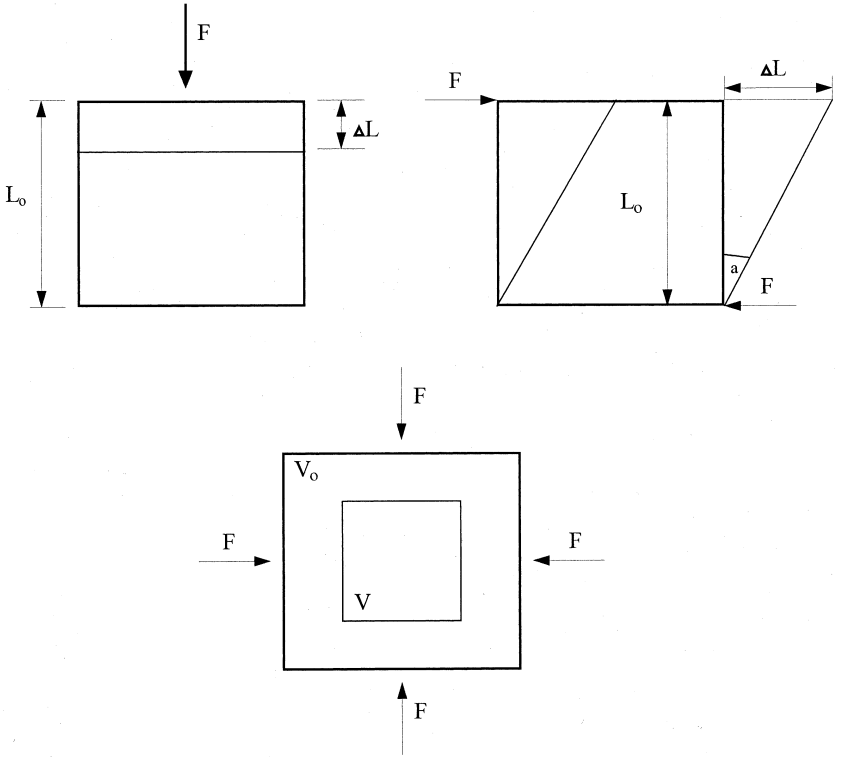

Figure 2 Effect of different types of stresses on a material's deformation.

$$K = \frac{\Delta P}{\left(\frac{\Delta V}{V_o}\right)} \tag{8}$$

where P is the change in pressure, i.e., hydrostatic stress, and $\Delta V/V_o$ is the relative change in volume of the solid, i.e., volumetric strain, as shown in Figure 2.

The reciprocal of the Young's, shear and bulk moduli describes the strain per unit stress, and is referred to as the *compliance* (J) of a material:

$$\mathrm{J} = \frac{1}{\text{modulus}} \tag{9}$$

Another fundamental quantity in the study of the rheology of solids is the Poisson's ratio, a dimensionless quantity defined as the change in diameter per unit original sample diameter $\Delta D/D_o$) over the change in length per unit original sample length ($\Delta L/L_o$) under the influence of an external applied stress. In other words, the Poisson's ratio is the ratio of the lateral expansion or contraction, as a fraction of the diameter of the sample, over the longitudinal strain:

$$\mu = \frac{(\Delta D / D_o)}{(\Delta L / L_o)} \tag{10}$$

When the volume of a material does not change upon stretching or contraction, $\mu = 0.5$. If the volume decreases, then $\mu < 0.5$. For materials which can be compressed with no change in diameter, $\mu = 0$. These fundamental moduli are interrelated, namely:

$$G = \frac{9EK}{(9K - E)} \tag{11}$$

$$K = \frac{E}{3(1-2\mu)} = \frac{EG}{(9G-3E)} = \frac{2}{3}G\frac{(1+\mu)}{(1-2\mu)} \tag{12}$$

$$E = \frac{9GK}{(3K+G)} = 2G(1+\mu) = 3K(1-2\mu) \tag{13}$$

$$\mu = \frac{(E-2G)}{2G} = \frac{1}{2}\frac{(1-E)}{3K} \tag{14}$$

These fundamental quantities which characterize the rheological behavior of a material have meaning only when derived using rheological tests within the elastic range of the material, when the material being tested is continuous, homogenous, and isotropic, and when the test piece is of uniform and regular shape.

1.4 Elastic behavior

Elastic behavior can be explained in terms of intermolecular bonding mechanisms that provide coherence to the sample. An applied external force will cause spatial displacements, or compressions and tensions, of the structural elements within the solid. The nature of intermolecular, internanostructural or intermicrostructural interactions, and the geometry of the

network can influence the mechanical properties of materials. The displacement, or deformation, of the microstructures results in an increase in the free energy of the system, as inter-or intramicrostructural bond tensions and compressions balance the applied external force. When the applied force is removed, the internal energy stored in compressed and extended inter- or intramicrostructural bonds is dissipated by restoring the microstructures to their original positions, or shape and dimension. For a reversible deformation process, the sample will return to its original state and dimensions upon removal of the applied stress. For an irreversible deformation process, the sample's original structure will have been changed, e.g., compression could have occurred, and therefore it will not return to its original state and dimensions upon removal of the applied stress.

1.4.1. Structural Theory of Elasticity

In most solids, atoms and molecules are arranged in some order. How rigidly these atoms and molecules are held about their equilibrium positions depends on the relative strength of the short-range forces between them. In the classical picture of a regular material such as a metal, the extension of say a metal wire is due to a displacement of the molecules within the wire from their mean positions. If the displacement is small enough, the restoring force towards the mean positions of the molecules is proportional to the displacement. To understand this statement, one may consider the variation of potential energy, U, between two molecules at a distance r apart. Depending on the separation distance, the potential energy is either negative or positive. The general form of the potential energy function, therefore, is given by

$$U(r) = \frac{a}{r^p} - \frac{b}{r^q} \tag{15}$$

where p and q are powers of r and a and b are constants. Since the force F between the two molecules is given by

$$F = -\frac{dU}{dr} \tag{16}$$

The positive term with the constant a in Eqn. 15 indicates a repulsive force and the negative term with the constant b represents an attractive force. It is difficult to formulate the exact mathematical form of the potential energy curve that describes the interaction of molecules, partly because there are different types of bonds or forces between atoms and molecules in solids, depending on the nature of the solid. A much-used general expression for the potential energy relationship for nonpolar molecules is given by the expression attributable to the English chemist J. E. Lennard-Jones:

$$U(r) = \left(\frac{\mu}{r}\right)^{12} - \left(\frac{\lambda}{r}\right)^{6} \tag{17}$$

where λ and μ are adjustable parameters. In an ionic solid, for example sodium chloride, the potential energy relationship is given by

$$U(r) = \frac{a}{r^9} - \frac{b}{r} \tag{18}$$

If one considers the Lennard-Jones form of the potential energy function, as is depicted in Figure 3, it can be seen that there is a value of r which corresponds to a potential energy minimum; this value of r, r_o, is the equilibrium spacing between the molecules. Figure 3 also shows the force as a function of r, given by Eqn. 16. At a distance r_o, the repulsive and attractive forces balance, i.e., $F = 0$. If the separation r between the molecules is slightly increased from r_o, the attractive force between them will restore the molecules to their equilibrium position after the external force is removed. If the separation is decreased from r_o, the repulsive force will restore the molecules to their equilibrium position after the external force is removed. Therefore, the molecules of a solid oscillate about their equilibrium or mean position. If one examines Figure 3 closely, the graph of F vs. r is approximately linear at small distances from the equilibrium position r_o. This means that the extension of the bond is proportional to the applied force, when the displacement is small distances away from the equilibrium position of the molecules. The force constant, k between the molecules is given by:

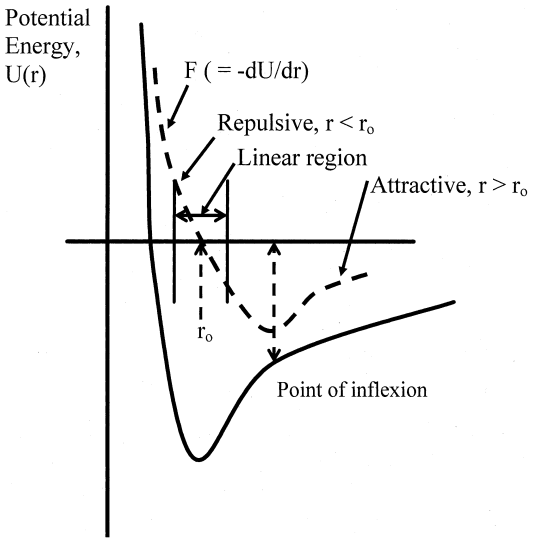

Figure 3 Schematic Lennard-Jones potential energy curve.

$$F = -k(r - r_0) \tag{19}$$

where r is slightly greater than r_o. Therefore,

$$k = -\frac{dF}{dr} \tag{20}$$

or the force constant is given by the negative of the gradient of the tangent to the force-distance curve at $r = r_o$. In a macroscopic sense, this behavior of the molecules leads to Hooke's law, which states: "the extension is proportional to the force or tension in a material if the proportional limit is not reached." So the extension of the wire is due to the displacement of its molecules from their equilibrium positions. The molecules are therefore undergoing simple harmonic motion, vibrating about their equilibrium position, and up to the proportional limit, the energy gained or stored by the stretched wire is molecular potential energy, which is recovered when the external force is removed. Therefore, for systems such as a wire or a large sodium chloride crystal, where the arrangement of the molecules are such that the macroscopic structure is built up by the constant repetition of the molecular lattice,

or unit cell, the elastic properties, characterized by an elastic constant k, may be inferred from a molecular argument.

Hooke's law behavior is, however, also observed for materials where one cannot easily explain the elasticity from molecular considerations. Such materials include colloidal gels, fat crystal networks, composite materials such as concrete, and ceramics, etc. In such materials, there are distinct hierarchies of structure, and the stressing or elongation of the microstructure does not necessarily relate to a stressing of the molecular level. In such materials, the limit of elasticity is encountered at levels of structure that are supermolecular. Therefore, the structural entities that are stressed when the macrostructure is stressed may be aggregates of molecules, aggregates of crystals, single crystal entities, polymer strands, etc. However, the molecular picture does provide an important analogy in the pursuit of an understanding of the elasticity of such materials. It is not an unreasonable assumption that at some level of structure that is being stressed, the applied force varies with the change in distance between the structural entities of importance in a linear manner, which translates to the macroscale. It is never a trivial matter to attribute responsibility for the elasticity of a material to a particular structural level. Therefore, although it is implicitly understood that the material is composed of a large number of discrete structural entities that are responsible for its elasticity, it is advantageous to regard the system as a continuous distribution of matter.

To therefore develop an understanding of physical quantities of a material such as its elastic modulus, we consider the material as a deformable continuum. When external forces are applied to such a system, a distortion results because of the displacement of the "relevant structural entities" from their equilibrium positions, and the body is said to be in a state of stress. After the external force is removed, the body returns to the equilibrium position, providing the applied force was not too great. Therefore, the elasticity of a material is defined as the ability of a body of this material to return to its equilibrium shape after the application of an applied force. To reach a quantitative definition of elasticity, one must first understand the concepts of stress and strain.

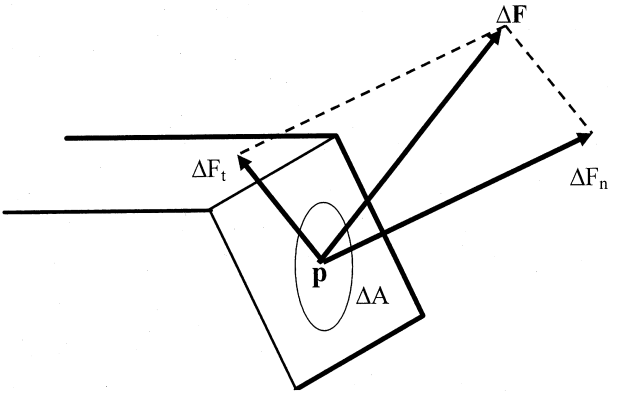

Figure 4 Schematic of a body being acted upon by an external force.

If we consider that a body is acted upon by an external force, $\Delta\overline{F}$ which is neither tangential, nor normal to the surface upon which it acts, as is depicted in Figure 4, then the average stress on the surface with area ΔA is defined as the force per unit area:

$$\overline{S} = \frac{\Delta\overline{F}}{\Delta A} \tag{21}$$

Therefore at some infinitesimal point p on the surface, the stress is given by:

$$\overline{S} = \underset{\Delta A \to 0}{Lim} \frac{\Delta\overline{F}}{\Delta A} = \frac{d\overline{F}}{dA} \tag{22}$$

If we consider that the external force $\Delta\overline{F}$ acting may be resolved in two components—one that is tangential to the surface, and one that is normal to the surface at the point p, then the stress $\overline{S}$ may also be resolved into tangential and normal stress. The tangential component of the stress is referred to as the shear stress, and the normal component is referred to simply as normal stress. The normal stress may either be in compression or tension, depending on whether the applied force is a push or pull, respectively. Referring to Figure 4, the normal stress, s, at point p is given by:

$$s = \frac{dF_n}{dA} \tag{23}$$

and the shear stress, τ, at the point p is given by:

$$\tau = \frac{dF_t}{dA} \tag{24}$$

Now, the effect of an applied stress on a body is to cause a change in size and shape of the body. Strain is the quantity that measures the relative change in size or shape of the body when under the applied stress.

If one considers a rectangular rod, with a cross-sectional area A, which is subject to a normal force, F, then the application of the force will induce a change in length of the rod. If the initial length of the rod is L_o and the increased length of the rod is L, then the change in length is given by $\Delta L = L - L_o$. Recall that the normal stress is given by:

$$s = \frac{F_n}{A} \tag{25}$$

and the strain ε induced by this stress, called the longitudinal or tensile strain, is given by:

$$\varepsilon = \frac{L - L_o}{L_o} = \frac{\Delta L}{L_o} \tag{26}$$

Within the elastic region of the material, the ratio of stress to strain is called the elastic modulus and is constant, and in the case of a normal stress and a tensile strain, the ratio of stress to strain is called the Young's modulus or tensile modulus. The Young's modulus, E, is given by:

$$E = \frac{s}{\varepsilon} = \frac{F_n / A}{\Delta L / L_o} \tag{27}$$

The dimensions of the Young's modulus are the same as those of stress, since strain is a dimensionless quantity. These dimensions are N/m^2 or Pa. Now, within the region where stress/strain is constant, the material is obeying Hooke's law:

$$F_n = k\Delta L \tag{28}$$

where k is the stiffness of the material, sometimes referred to as the spring constant of the material. One may then relate the

stiffness of the material to its Young's modulus by considering Eqns. 27 and 28:

$$k = \frac{EA}{L_o} \tag{29}$$

Therefore, for a given material, within the elastic region, the Young's modulus and stiffness constant are important parameters that yield information about the deformability of the material, and therefore about the sensory impact of the material when one deforms it in the mouth.

The proportionality relationship between s and ε holds only if stress is less than a certain maximum value. This point at which maximum value is reached is referred to as the proportional limit or yield point or yield value. Beyond the yield point, the material begins to undergo a plastic deformation and a small increase of stress causes the material not regain its original shape and length upon removal of the applied force, but rather, induces the material to begin flowing.

The shear elastic modulus, which is the ratio of the shear stress to the shear strain, may be derived in like manner to the Young's modulus as above. Figure 5 shows a schematic of a material deformed under the action of a pair of equal and opposite forces not acting along the same line of action. The resulting shear stress produces a change in the shape of the body (but no change in length) and therefore induces a strain, called the shear strain. The points ABCD under the action of the shear stress have moved to the points abcd, while the points EFGH are not displaced. The shear stress is therefore given by

$$\tau = \frac{F_t}{A} \tag{30}$$

and the shear strain, v, is defined as the ratio of the displacement, Δx and the length l as shown in Figure 5. Therefore, the shear elastic modulus G (also called the modulus of rigidity or torsion modulus) is given by:

$$G = \frac{\tau}{v} = \frac{F_t / A}{\Delta x / l} \tag{31}$$

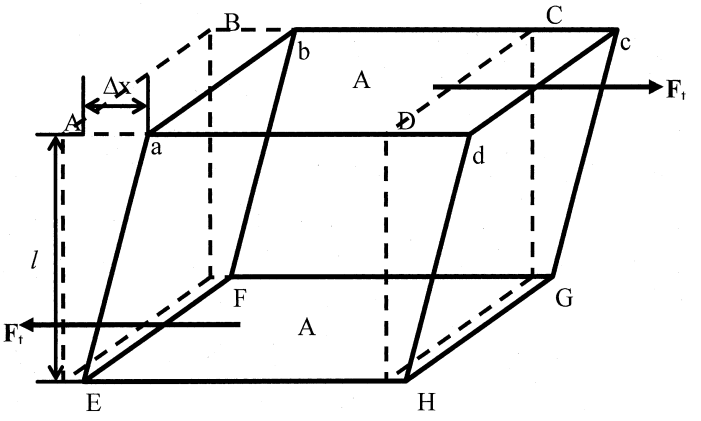

Figure 5 Schematic of a material deformed under the action of a pair of equal and opposite forces.

The shear elastic modulus therefore also has units of N/m^2 or Pa. In general, the tensile modulus or Young's modulus, E, is related to the shear elastic modulus or rigidity modulus by:

$$G = \frac{E}{3} \tag{32}$$

Fat crystal networks demonstrate a tensile modulus as well as a shear elastic modulus. Figure 6 shows an example of the shear elastic modulus of cocoa butter. For viscoelastic materials like fat crystal networks, both the loss modulus, G'' (related to the liquid portion of the network) and a storage elastic modulus, G' (related to the solid network) can be measured. The range of stress/strain within which the elastic modulus is constant is called the linear viscoelastic range (LVR). As is demonstrated by Figure 6, this range for fat crystal networks is very small. Therefore, the system is elastic only for very small stress values. Figure 7 shows the behavior of a typical elastic system: up to point A, the system is perfectly elastic, then between point A and point B, stress is not proportional to strain, but if the stress is removed, the body should return to its original shape. If the applied stress is beyond point C, then permanent deformation occurs in the body and leads to breakage of different levels of structure. Point A is usually taken as the yield point. Since the

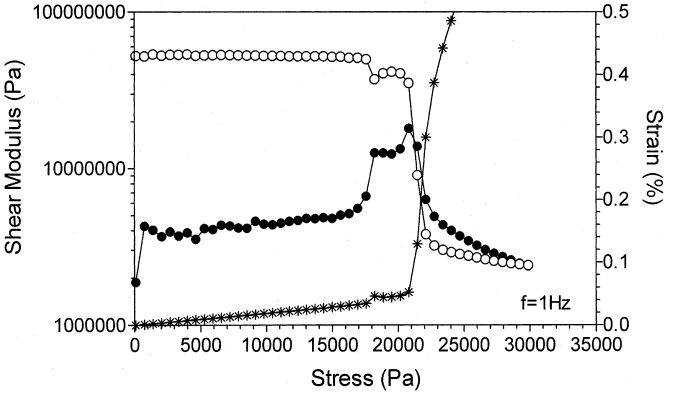

Figure 6 Effect of applied stress on the storage (*open circles*) and loss (*closed circles*) moduli, as well the strain (*stars*), of cocoa butter at 22°C.

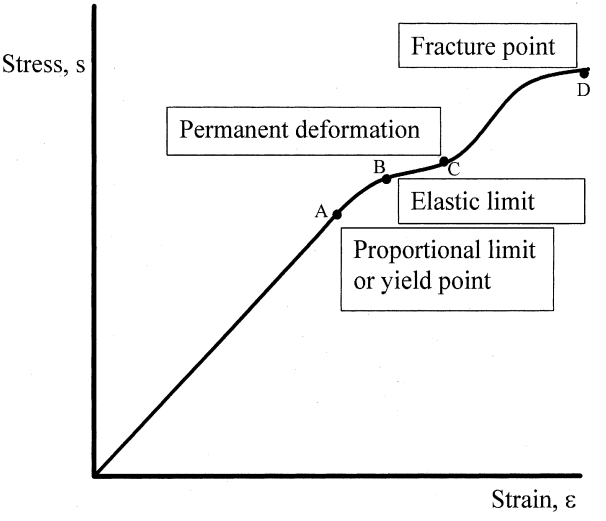

Figure 7 Stress-strain behavior of a typical elastic system.

shear elastic modulus is the slope of the plot of stress vs. strain, it is obvious that changes in elastic modulus will be produced by changes in the yield point. Thus, a relationship between these two parameters is self-evident.

The relationship of elastic modulus to yield value depends on the levels of structure that are affected in the network during elastic measurements and measurements of the yield value, and the relative strength of these levels of structure. In a classical material such as a metal wire, at stresses beyond the yield point, the elongation of the material is caused by the movement of crystal planes, called slip, and the origin of slip lies in crystal dislocations, which correspond to a lack of symmetry in the crystalline nature of the material. In a way, these dislocations may be thought of as fault lines or planes, along which the material flows under external forces large enough to stress the material beyond its elastic point. However, since the yield point is influenced by the ability of the material to flow beyond its elastic limit, it is not immediately evident that the magnitude of changes in the yield point of a material will be related in a straightforward manner to magnitudes of changes in elastic modulus for materials such as fat crystal networks. Even in classical materials such as a crystal of so-

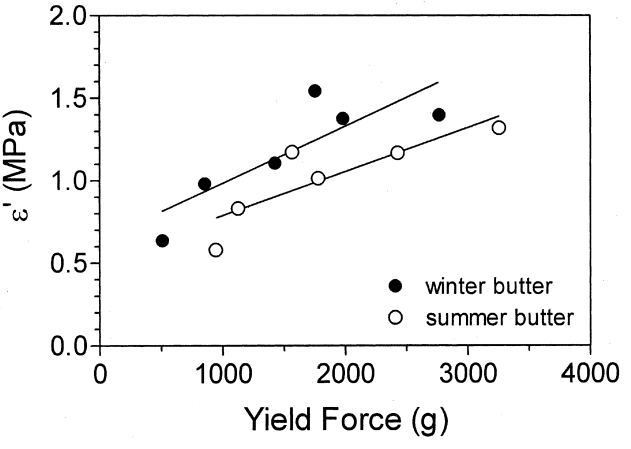

Figure 8 Relationship between the compression storage modulus and the yield force in two different types of milkfat at 5°C.

dium chloride, the yield point would be affected by the amount of dislocations in the crystal, which is a function of the purity of the material and of the environmental conditions under which the crystal was formed. The relationship of elastic modulus to yield value would therefore depend on the levels of structure that are affected in the network during elastic measurements and measurements of the yield value, and the relative strength of these levels of structure.

In most of our studies we have found that the shear storage modulus (G′) and the Yield Force (F_y), or Hardness Index (HI) are directly proportional to each other (Figures 8–10). However, the proportionality constant between these two parameters is system specific (slopes are not the same). This becomes particularly evident when considering the relation-

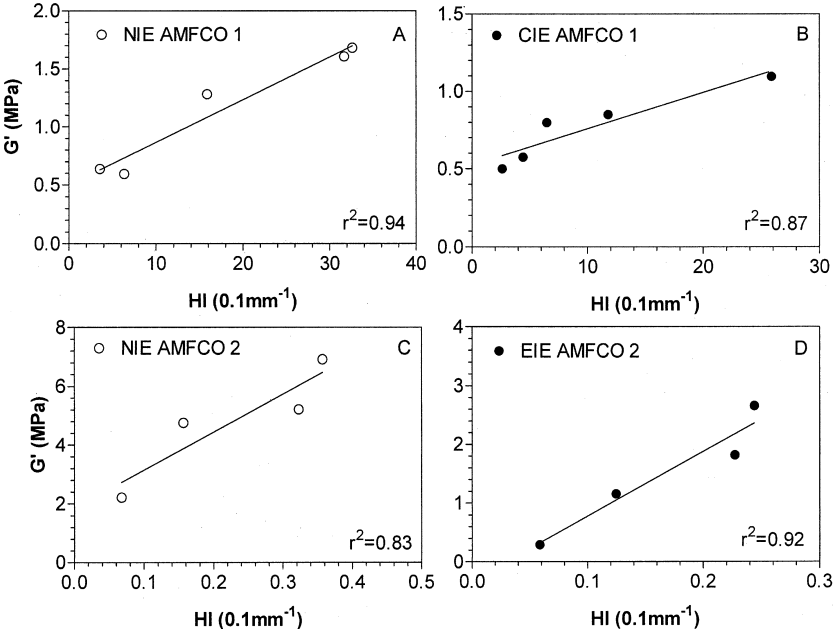

Figure 9 Relationship between the shear storage modulus (G′) and the hardness index in anhydrous milkfat-canola oil (AMFCO) blends at 5°C. NIE = non-interesterified, CIE = chemically interesterified. EIE = enzymatically interesterified.

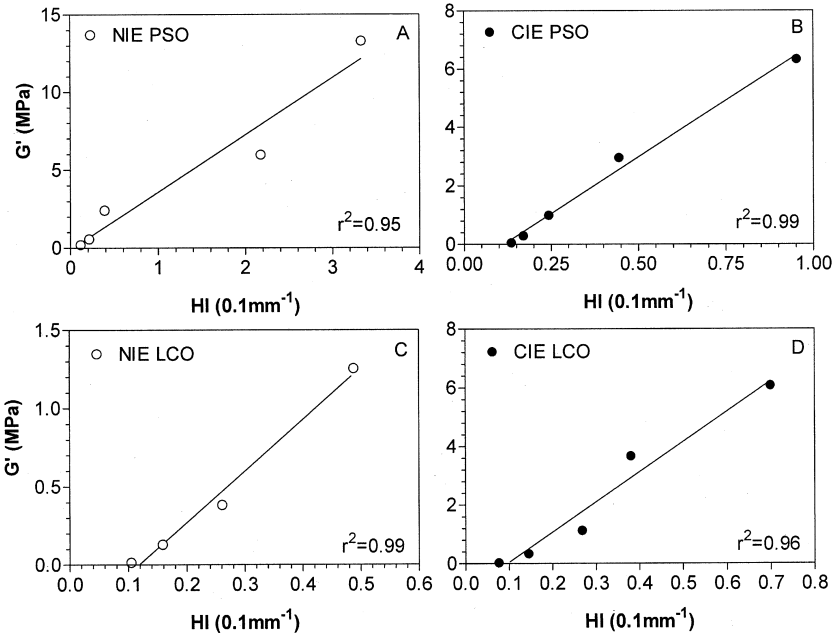

Figure 10 Relationship between the shear storage modulus (G′) and the hardness index in Palm-soybean oil (PSO) and lard-canola oil (LCO) blends at 5°C. NIE = non-interesterified, CIE = chemically interesterified.

ship between G′ and the F_y in milkfat crystallized at different cooling rates (Figure 11). In all cases, G′ is directly proportional to F_y, however, the proportionality constant for the covariation of these two parameters is a function of the cooling rate of the material! The microstructure of milkfat is a strong function of the cooling rate experienced upon crystallization [1,2]. Thus, different microstructures will influence the relative relationship between small and large deformation rheological parameters.

1.5 Yield Value from Constant Force Cone Penetrometry Measurements

The cone penetrometer is widely used in the fats and oils industry for the measurement of the consistency of plastic fats

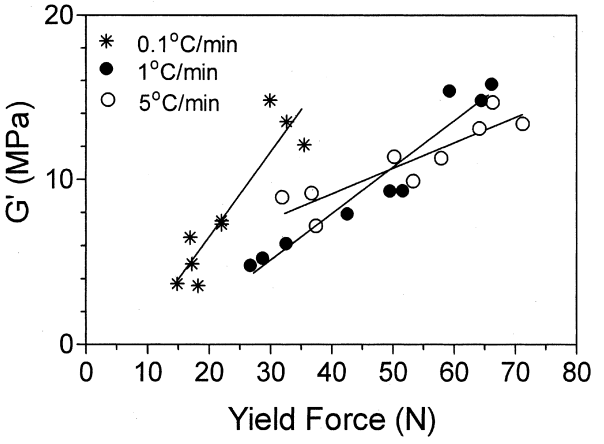

Figure 11 Relationship between the shear storage modulus (G′)and the yield force in milkfat crystallized at three different cooling rates from the melt to 5°C.

(American Oil Chemists Society, AOCS method Cc 16–60). This method involves the penetration of the fat network by a metal cone of known mass and geometry. By monitoring the depth reached by the cone and the time it takes to achieve that depth, a parameter referred to as the yield value of the network may be calculated. As explained above, yield values are determined to be the point at which the stress on the network is such that the network is just at its elastic limit. If one considers a typical plastic material, at stresses below the yield point, the material will behave as a perfectly elastic solid, i.e., the strains are proportional to the applied stress. However, from the yield point onward, this proportional relationship is lost, and the material begins to flow, i.e., some level of structure has been broken. The relation of cone penetrometer measurements to the yield value of the network has been formulated by a series of investigators in the fats and oils field, but unfortunately, many of these formulations did not totally agree. However, it is important to provide a brief review of these developments, as is done in the following.

Rebinder and Semenko [3] formulated the yield value as calculated from cone penetrometry measurements to be given by:

$$Y = \frac{Mg\cos^2(\alpha)}{p^2\tan(\alpha)} \tag{33}$$

where M is the mass of the penetrating cone, α is the half-angle of the cone, p is the penetration depth of the cone in a prescribed amount of time (5 seconds), and g is the acceleration due to gravity. Later, Haighton [4] proposed the following formulation:

$$Y = \frac{KMg}{p^{1.6}} \tag{34}$$

where K is a constant depending on the cone angle, and the other parameters are as defined earlier. Following the work of Haighton, Mottram [5] proposed the following formula:

$$Y = \frac{KMg^2}{p^n} \tag{35}$$

where K is a constant, n and is an exponent which is close to 2, but allowed to vary with the nature of the network. Following this work, Vasic and deMan [6] proposed to define hardness as force divided by area of penetration (so, essentially defining hardness as a pressure, which has been done before). They related this hardness to penetration values by the following equation:

$$H = \frac{Mg \cdot 10^{-3}}{\left[p\pi\frac{\tan(\alpha)}{\cos(\alpha)}\left(p + \frac{2r}{\tan(\alpha)}\right) + r^2\pi\right] \cdot 10^{-4}} \tag{36}$$

where H is the hardness and r is the radius of the flat tip of the cone, and all other symbols are as defined earlier. Dixon and Parekh [7] related hardness of butter from sensory investigations with a measure of hardness from cone penetrometer measurements, which they called the cone stress index (C_v), and found that C_v correlated very well with sensory impressions of hardness. They formulated the cone stress index as:

$$C_v = \frac{MA^{-1.65}}{p^2} \tag{37}$$

where A is the angle of the cone, and all other symbols are as defined earlier.

As noted by Hayakawa and deMan [8], most of the aforementioned equations suggest that the yield value used as a measure of hardness, or hardness expressed as some relationship to the yield value, follows a general form of dependence on the mass of the cone, the geometry of the cone, and the penetration depth, given by:

$$H = C\frac{M}{p^n} \tag{38}$$

where H is hardness or yield value, C is a constant depending on the geometry of the cone, and other symbols are as defined earlier. Hayakawa and deMan [8] also noted that if a cone of 20° angle is used as is specified in the AOCS method, then Eqn. 38 may be reduced to:

$$HI = \frac{M}{p^n} \tag{39}$$

where HI is the hardness index of the material.

Hayakawa and deMan [8] presented experimental proof from their own experiments, and summarized the experiments of others to support that the hardness index of a plastic fat is best represented by Eqn. 39 when n is equal to 1. However, this relationship does not hold unless the penetration depth between 15 and 150 units. Penetration depth is measured in units of 0.1 mm, therefore the actual range for the penetration depth for Eqn. 39 to be valid when $n = 1$, is 1.5–15 mm.

2. RHEOLOGY OF LIQUIDS

2.1 Viscosity

Fluid flow takes place as a fluid deforms when acted upon by an external force. This flow can be visualized as the movement of thin layers of fluid molecules. *Viscosity* is the frictional force between the different layers of the fluid as they move past one another. This frictional force arises due to cohesive forces between liquid molecules, or in gases, due to collisions between molecules in different layers.

The dynamic viscosity of a fluid is characterized quantitatively by the coefficient of viscosity (η), which is defined in the

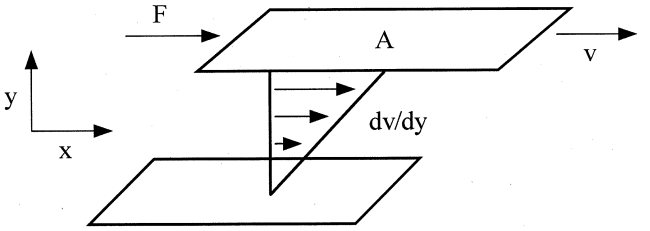

Figure 12 Idealized flow of two contiguous fluid layers depicting the gradient in fluid velocity as a function of distance from the walls.

following way. Envision a thin layer of fluid contained between two flat plates (Figure 12). While the bottom plate is held stationary, a force is applied to the upper plate to make it move. Due to the frictional force between molecules in the different fluid layers, a fluid layer velocity gradient ($\partial v/\partial y$) is established between the stationary plate and the moving plate. This fluid drag arises due to attractive forces between fluid molecules. The fluid molecules in direct contact with upper plate move at the same speed as the plate, while the fluid molecules in direct contact with the bottom plate remain stationary. This stationary fluid layer retards the flow of an adjacent fluid layer. This slower moving fluid layer then itself retards the flow of an adjacent fluid layer, and so forth. This process gives rise to the fluid layer velocity gradient mentioned earlier. Hence, viscosity is usually defined as *the resistance to flow,* and is a direct consequence of the strength of interaction, or force of adhesion, between fluid molecules.

For a particular fluid, the magnitude of the established velocity gradient dv/dy (Figure 12) is directly proportional to the force applied on the upper plate, and inversely proportional to the area of the plate:

$$\frac{\partial v}{\partial y} \alpha \frac{F}{A} \tag{40}$$

The proportionality constant for this equation is defined as the coefficient of viscosity (η),

$$\frac{\partial v}{\partial y} = \eta \frac{F}{A} \tag{41}$$

In a similar fashion as for the rheological analysis of solids, the quantity F/A is defined as the applied stress (σ), with units of N/m^2 or Pa. The shear strain (γ) for this system is defined as the change in position of a layer of fluid in the x axis (∂x) as a function of a change in position in the axis (∂y) in the region between the stationary and moving plates:

$$\gamma = \frac{\partial x}{\partial y} \tag{42}$$

The rate at which the shear strain varies in time is defined as the shear strain rate (γ), with units of $[s^{-1}]$. Considering that velocity is the change in displacement as a function of time, the velocity gradient established between the two parallel plates is the shear strain rate, namely:

$$\dot{\gamma} = \frac{\partial \gamma}{\partial t} = \frac{\partial x}{\partial y \partial t} = \frac{\partial v}{\partial t} \tag{43}$$

Equation 41 then becomes:

$$\sigma = \eta \dot{\gamma} \tag{44}$$

The viscosity η [Pa·s] characterizes the dynamic viscosity of a fluid. The still widely used CGS unit for dynamic viscosity is the Poise [dyn/cm^2·s]. For comparative purposes, 1cP is equivalent to 1mPa≅s. Water has a dynamic viscosity of 1mPa·s at 20.2°C.

2.2 Types of Fluid Flow

2.2.1 Ideal, Newtonian Behavior

Flow curves are linear and pass through the origin for ideal, Newtonian fluids (Figure 13*A*). The slope of the line is the coefficient of viscosity, which has a time-independent, constant value at all shear strain rates.

2.2.2 Nonideal, Non-Newtonian Behavior

The different types of non-Newtonian fluids are summarized in Figure 14 and hypothetical flow curves shown in Figure 13. Each type will be discussed in turn.

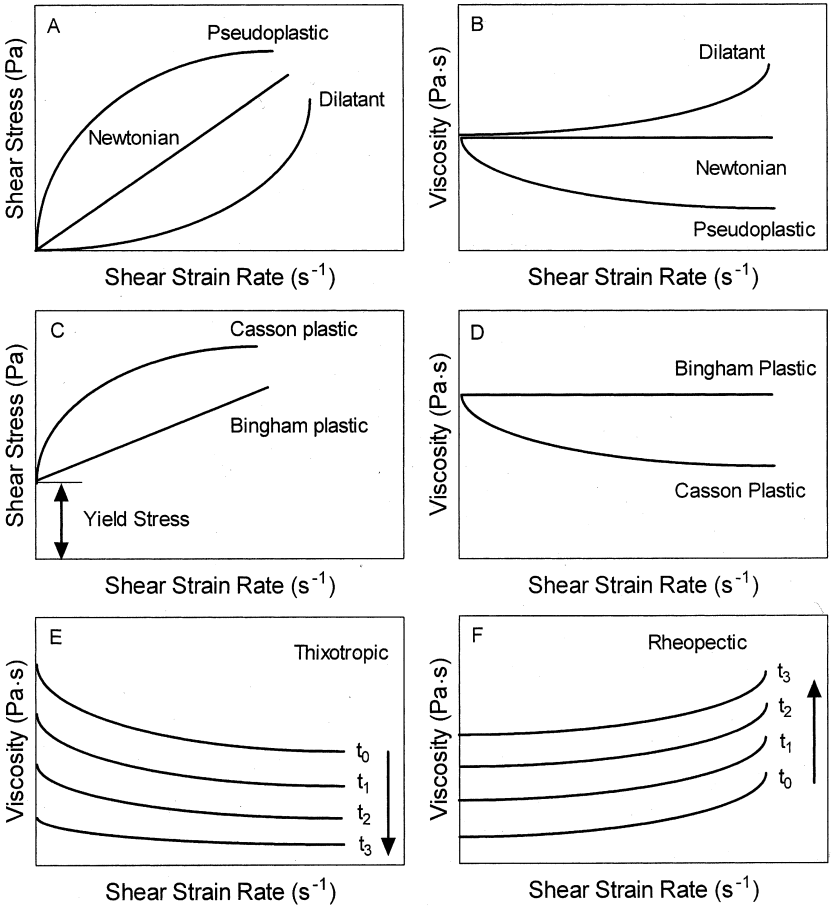

Figure 13 Idealized flow curves for Newtonian and non-Newtonian fluids.

2.2.2.1 Time-independent fluids

Flow curves for these fluids are nonlinear—the coefficient of viscosity is a function of the shear strain rate. The coefficient of viscosity, however, does not change with time. Two major types of flow behavior are observed within time-independent nonideal fluids, namely, shear-thinning or pseudoplastic, and shear-thickening or dilatant. For pseudoplastic fluids, viscos-

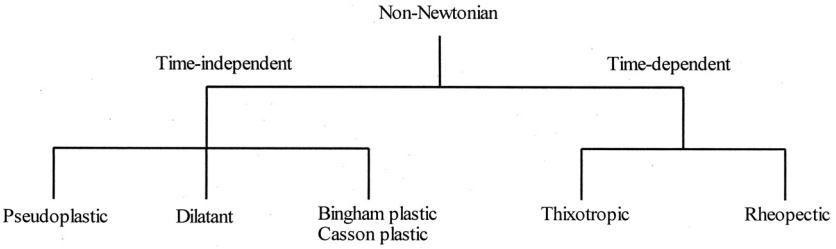

Figure 14 Types of non-Newtonian flow behavior.

ity decreases as a function of increasing shear strain rate, while for dilatant fluids, viscosity increases as a function of increasing shear strain rates (Figures 13*A* and 13*B*). A special case of these time-independent fluids are those materials that display a yield stress before starting to flow (Figure 13*C*). The same Newtonian and shear thinning behavior is observed once the material starts to flow (Figure 13*D*), however, the common names of these fluids is, however, different.

2.2.2.1 Time-dependent fluids

Flow curves for these fluids are nonlinear—the coefficient of viscosity is a function of the shear strain rate. In this case, the coefficient of viscosity does change with time. Two major types of flow behavior are observed within time-dependent nonideal fluids, namely, thixotropic and rheopectic. At a fixed shear strain rate, the coefficient of viscosity for thixotropic fluids *decreases* as a function of time (Figure 13*E*), suggesting fluid structural breakdown, while it *increases* for rheopectic fluids (Figure 13*F*), suggesting enhancement of fluid structure.

2.3 Modeling Flow Behavior

The flow of most materials can be modeled using:

$$(\sigma - \sigma_o)^m = \eta_{app} (\dot{\gamma})^n \tag{45}$$

or

$$m \log(\sigma - \sigma_o) = \log\eta_{app} + n \log\dot{\gamma} \tag{46}$$

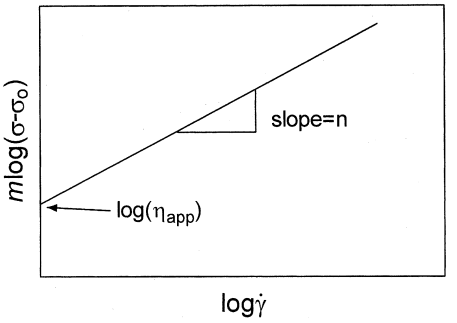

Figure 15 Linearized graphical representation of the viscosity model.

where σ is the applied stress [Pa], σ_o is the yield stress [Pa], η_{app} is the apparent viscosity [$Pa^m \cdot s^n$)], $\dot{\gamma}$ is the shear strain rate, *n* is the flow index. For a Newtonian fluid, n 1, for a shear-thinning fluid, $n < 1$, while for a shear-thickening fluid, $n > 1$. An empirical parameter *m* can also be included in the model to improve fits, usually in the form of a fraction. For an ideal, Newtonian fluid, $n = 1$, $m = 1$, $\sigma_o = 0$, and thus Eqn. 45 reduces to Eqn. 44. An example of a plot of Eqn. 46 is shown in Figure 15.

REFERENCES

1. Wright AJ, Marangoni AG. The effect of minor components on milk fat microstructure and mechanical properties J Food Science 2003; 68:182–186.

2. Rye GG, Litwinenko JW, Marangoni AG. Structure and mechanical properties of fats. In: Bailey's Industrial Oils and Fats Products. 6th ed. Shaihidi F, Ed: John Wiley and Sons, Inc., 2004.

3. Rebinder PA, Semenko NA. Use of the penetrating cone method for the characterization of structural-mechanical properties of visco-plastic material Proc Acad Sci (USSR) 1949; 64:835–838.

4. Haighton AJ. The measurement of the hardness of margarine and fats with cone penetrometers J Am Oil Chem Soc 1959; 36: 345–348.

5. Mottram FJ. Evaluation of pseudo-plastic materials by cone penetrometers Lab Pract 1961; 10:767–770.

6. Vasic I, deMan JM. Effect of mechanical treatment on some rheological properties of butter. In: Rheology and Texture of Foodstuffs Soc Chem Ind 1968; 27:251–264.

7. Dixon BD, Parekh JV. Use of the cone penetrometer for testing firmness of butter J Am Oil Chem Soc 1979; 10:421–434.

8. Hayakawa M, deMan J. Interpretation of cone penetrometer consistency measurements of fats J Texture Studies 1982; 36: 345–348.

5

Viscoelasticity

ALEJANDRO G. MARANGONI
Department of Food Science
University of Guelph
Guelph, Ontario, Canada

1. INTRODUCTION

Elasticity and viscosity are just two ways in which materials can respond to externally applied stress. Materials can display solid or liquid behavior depending on their characteristic time and the time required for the process to occur, hereby referred to as process time. Whether a material exhibits elastic or viscous behavior depends on our frame of reference. We will clarify this point later.

The characteristic time of a material, t_c, is the time that it takes for stress, or strain, to be relaxed by 1/e of its original value, approximately a 37% drop. The *Deborah number* is the ratio between the characteristic time and the process time,

$$D = \frac{t_c}{t} \tag{1}$$

High Deborah numbers are associated with materials displaying solid-like behavior, while low Deborah numbers are associated with materials displaying liquid-like behavior. Take, for example, the case of glass. Glass has a long characteristic time, making its Deborah number relatively high for short process times. However, given a process time of hundreds of years, the Deborah number of glass becomes quite small, characteristic of liquids. Another example of the relativistic nature of the elasticity and viscosity of materials is that of water. Water has a very short characteristic time, making its Deborah number relatively low for a short process time. However, if the process time is shortened drastically, the Deborah number increases, making water feel as a solid. Having a bucket of water gently poured over one's head as opposed to being sprayed with water using a high-pressure nozzle should illustrate this point quite clearly. Another interesting consideration is that of the rate of deformation. If a material is deformed very rapidly, it will respond predominantly as a solid, where most of the energy will be stored in the bonds between the structural elements responsible for the observed macroscopic rheological behavior. On the other hand, if the deformation takes place slowly, the structural elements will have sufficient time to rearrange, align themselves in the direction of the applied force, and flow.

Another peculiar property of viscoelastic materials is the existence of a normal force perpendicular to the plane of the applied shear deformation. The so-called Weissenberg effect is a manifestation of this normal force. The Weissenberg effect is evident when mixing flour and water in a home mixer. As the dough forms (a viscoelastic material), it will start climbing up the mixer's shaft. Mixing a Newtonian liquid, on the other hand, will merely result in the formation of a meniscus. The Weissenberg effect is consequence of a stress gradient in the viscoelastic fluid radially outwards from axis of rotation (wall, tip of impeller, etc.). The fluid layers that are furthest way from the axis of rotation will experience a greater torque, namely torque = rF, where F is tangential force experienced

at the particular fluid layer, and r is the distance between the axis of rotation and the layer of rotating fluid. Thus, fluid layers furthest away form the axis of rotation will experience a greater force, or stress, and will therefore deformed to a greater extent. In order to dissipate this stress gradient, the material pushes inward toward regions of lower stress, which results in fluid being pushed upward (there is nowhere for the material to go but up!).

Fat is a good example of a viscoelastic material. Fats have an underlying fat crystal network composed of polycrystalline particles arranged into larger clusters. A deformation will stretch intercluster, and/or interparticle bonds, raising the energy of the system. If the strain is within the elastic region, below the limit of elasticity, the material will respond as a solid. Upon removal of the applied stress, stretched bonds will return to their equilibrium, i.e., lower energy, state. On the other hand, if the stress is such that the strain at the limit of elasticity is exceeded, bonds will break, the material will undergo plastic deformation and flow. Therefore, at strains beyond the limit of elasticity, the material will behave as a fluid. Depending on the extent and rate of bond breakage, the material will display viscoelastic behavior, where the material's response will be both elastic as well as viscous. Bonds can also reform once the stress is removed, contributing to the elastic character of the material. Fats can therefore behave both as solids and liquids.

1.1 Creep and Recovery/Stress Relaxation

In a creep and recovery test for viscoelasticity, the response time of the strain dependence of both the elastic and viscous components of a material is determined. A creep and recovery test is carried out under constant stress conditions. On the other hand, a stress relaxation test is carried out under constant strain conditions. The response time of the stress dependence of both the elastic and viscous components of a material is determined. In this chapter we will restrict our discussion to the case of creep and recovery.

A solid will deform when subjected to an applied stress, and the energy of deformation elastically stored in the material's structure. This deformation will be fully recovered upon removal of the stress (Figure 1). For the case of an ideal Newtonian solid, both stress and strain are time independent ($\tau = G\gamma$). On the other hand, an ideal Newtonian liquid will deform at a particular rate (i.e., it will flow) when subjected to an external stress ($\tau = \eta\partial\gamma/\partial t$), but this deformation will be fully maintained once the stress is removed (Figure 1). The deformation of a liquid will never be recovered, since the energy that made the material flow is fully transformed into shear heat, and lost to the system surroundings. A viscoelastic material behaves rheologically as a combination of a solid and a liquid. Such material will initially deform elastically when subjected to an external stress, and given sufficient time, it will start flowing. Upon removal of the stress, the elastic component will recover, while the viscous component will not, and a permanent deformation will be observed.

What follows is a brief discussion of the different models developed in an attempt to understand and model the behavior of viscoelastic materials. Our discussion is strictly limited to

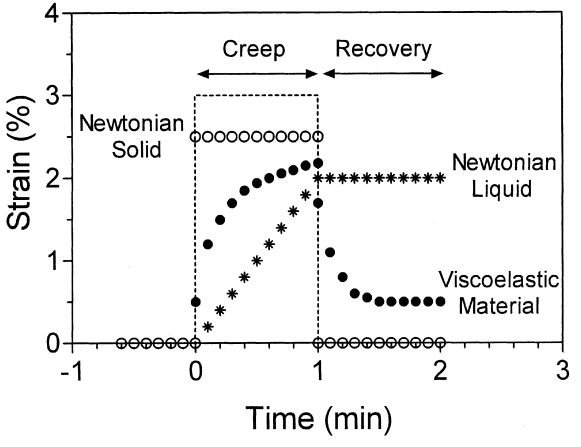

Figure 1 Creep-recovery curves for an idealized Newtonian solid, Newtonian liquid, and a viscoelastic material.

materials within their linear viscoelastic region (LVR), where stress is linearly related to strain. This is usually the case at deformation of 1% or less. In the LVR, rheological parameters are a function the material's structure and not as much of instrumentation and test conditions.

1.1.1 Kelvin-Voigt Solid

A Kelvin-Voigt solid combines a spring and a dashpot in parallel (Figure 2). When stress is applied to such a system, the force is equally distributed between the spring and the dashpot. For this case, the total strain (γ) is equal to the strain in the spring (γ_e), which also equals the strain in the dashpot (γ_v), namely:

$$\gamma = \gamma_e = \gamma_v \tag{2}$$

The total stress applied on the system (τ), on the other hand, is equal to the sum of the stresses on the spring and the dashpot:

$$\tau = \tau_e + \tau_v \tag{3}$$

Since $\tau_e = G/\gamma_e$ and $\tau_v = \eta\partial\gamma_v/\partial t$, in light of Eqn. 3, the total stress on the system can be expressed as

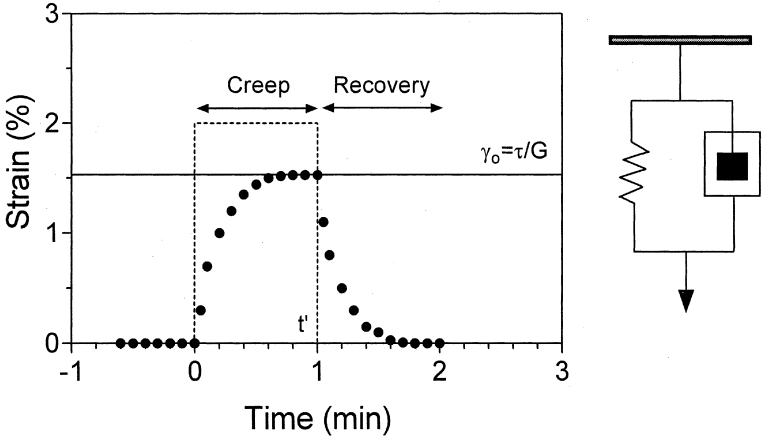

Figure 2 Creep-recovery pattern for a Kelvin-Voigt element.

$$\tau = \frac{G}{\gamma} + \eta \frac{\partial \gamma}{\partial t} \tag{4}$$

This equation can be rearranged to

$$\frac{\partial \gamma}{\partial t} + \frac{1}{\lambda \gamma} = \frac{\tau}{G} \tag{5}$$

where λ corresponds to the relaxation time, and is defined as $\lambda = \eta/G$. The solution to the above first order ordinary differential equation is:

$$\gamma = \frac{\tau}{G}(1 - e^{-\frac{t}{\lambda}}) \tag{6}$$

Notice that when the time tends to infinity, the strain will approach a limiting maximum value γ_o, where $\gamma_o = \tau/G$, the final maximum response of the spring. The viscous component thus merely retards the response of the spring. Knowledge of this limiting maximum strain value and the applied stress would allow for the determination of the modulus of the spring component of a Kelvin-Voigt solid ($G = \tau/\gamma_o$).

Upon removal of the stress, the Kelvin-Voigt solid will recover to its initial state (Figure 2). The strain will decay in a simple exponential fashion from the limiting maximum value (γ_o) to zero:

$$\gamma = \gamma_o e^{-\left(\frac{t-t'}{\lambda}\right)} \tag{7}$$

The relaxation times are the same for the creep and recovery phases when conditions of linear viscoelasticity prevail. Being an idealized viscoelastic solid, irreversible structural change does not take place, i.e., the material does not flow.

1.1.2 The Maxwell Fluid

In this model, a spring and a dashpot are arranged in series rather than in parallel as for the case of the Kelvin-Voigt solid (Figure 3). For a Maxwell fluid, the total stress on the system (τ) is equal to the stress on the spring (τ_e), which also equals the stress on the dashpot (τ_v), namely:

$$\tau = \tau_e = \tau_v \tag{8}$$

The resulting strain on the system (γ), on the other hand is equal to the sum of the strains on the spring and the dashpot:

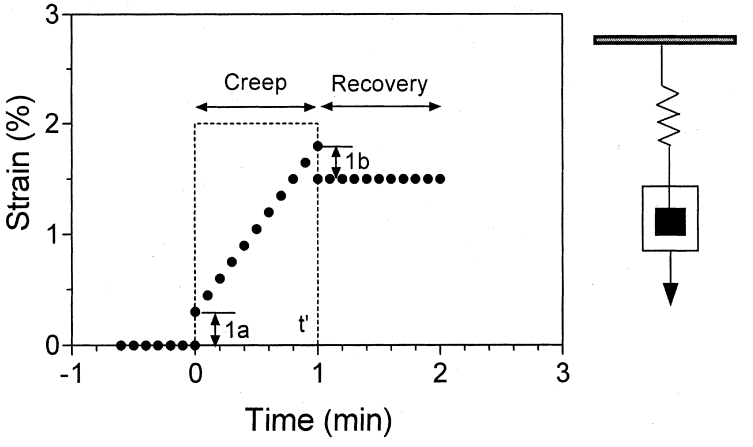

Figure 3 Creep-recovery pattern for a Maxwell element.

$$\gamma = \gamma_e + \gamma_v \tag{9}$$

The change in strain as a function of time thus equals:

$$\frac{\partial \gamma}{\partial t} = \frac{\partial \gamma_e}{\partial t} + \frac{\partial \gamma_v}{\partial t} \tag{10}$$

Since

$$\frac{\partial \gamma_v}{\partial t} = \frac{\tau}{\eta} \tag{11}$$

and

$$\frac{\partial \gamma_e}{\partial t} = \frac{1}{G}\frac{\partial \tau}{\partial t} \tag{12}$$

Equation 10 can be expressed as:

$$\frac{\partial \gamma}{\partial t} = \frac{1}{G}\frac{\partial \tau}{\partial t} + \frac{\tau}{\eta} \tag{13}$$

Integration of the above equation after variable separation for the boundary conditions $\gamma = 0$, $\tau = 0$ at $t = 0$,

$$\int_0^{\gamma} \partial \gamma = \frac{1}{G}\int_0^{\tau} \partial \tau + \frac{\tau}{\eta}\int_0^{t} \partial t \tag{14}$$

Results in the expression:

$$\gamma = \frac{\tau}{G} + \frac{\tau}{\eta} t \tag{15}$$

When subjected to a stress, this viscoelastic liquid initially responds with an instantaneous strain (Figure 3*1a*), corresponding to the deformation of the elastic component of the material, i.e., the spring ($\gamma_i = \tau/G$). This is immediately followed by a constant increase in strain, determined by the viscosity of the material, i.e., the dashpot. Knowledge of this instantaneous strain and the applied stress would allow for the determination of the elastic modulus of the spring component of a Maxwell fluid ($G = \tau/\gamma_i$).

When the applied stress is removed, the strain drops immediately to a new constant level (Figure 3*1b*). This instantaneous drop is due to the recovery of the elastic component, i.e., the spring, of the Maxwell fluid. Notice, however, how the strain levels never return to their original value. This is because the material has flowed, and obviously this irreversible deformation cannot be recovered.

2.1.3 The Burger Model

Neither the Kelvin-Voigt, nor the Maxwell fluid models can describe the rheological behavior of real viscoelastic materials. The Burger model comes a step closer to the description of a real viscoelastic material. The Burger model is mainly a Kelvin-Voigt element placed in series with a Maxwell element (Figure 4).

Since these elements are placed in series, the total stress on the system is the same for the Kelvin-Voigt and Maxwell elements, namely:

$$\tau = \tau_{KV} = \tau_M \tag{16}$$

The total strain on the system, on the other hand, is an additive function of the strains on the Kelvin-Voigt and Maxwell elements, namely:

$$\gamma = \gamma_{KV} + \gamma_M \tag{17}$$

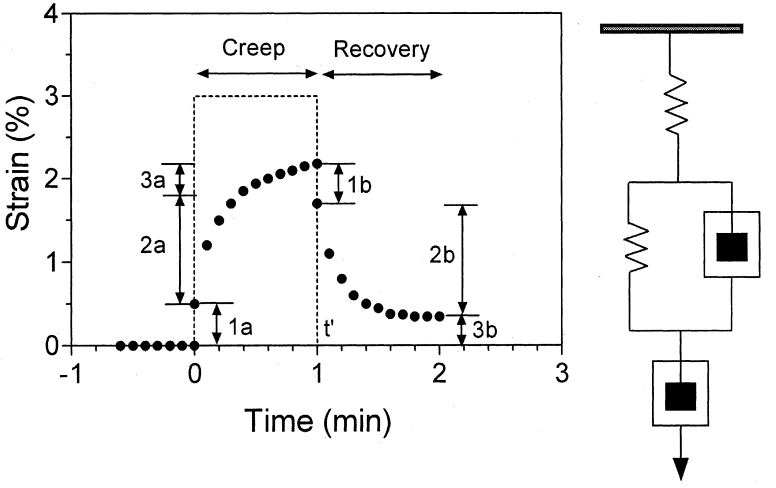

Figure 4 Creep-recovery pattern for a Burger element.

Substituting equations 6 and 15 into the above equation, and rearrangement results in:

$$\gamma = \frac{\tau}{G_M} + \frac{\tau}{G_{KV}}(1 - e^{-\frac{t}{\lambda}}) + \frac{\tau}{\eta_M} t \tag{18}$$

This equation describes the time-dependent change in strain during the creep phase. The initial increase in strain observed in Figure 4*1a* is due to the instantaneous deformation of the spring component of the Maxwell element. This is followed by an exponential increase in strain attributed to the Kelvin-Voigt element (Figure 4*2a*). The purely viscous response that follows is related to the Maxwell dashpot (Figure 4*3a*), after the Kelvin-Voigt element has reached its maximum strain value.

Thus, since the value of the stress is known, measurement of the instantaneous strain (γ_i) would allow for the determination of the spring modulus of the Maxwell element ($G_M = \tau/\gamma_i$). Equally straightforward is the determination of the viscosity attributed to the Maxwell dashpot. Knowledge of the slope of the linearly increasing strain region in the creep phase would

yield an estimate of η_M ($\eta_M = \tau$/slope). Finally, an exponential curve-fit of Eqn. 6 to experimental γ *versus* time data would yield estimates of G_{KV} and the relaxation time λ, where $\lambda = \eta_{KV}/G_{KV}$. This exercise could be followed by a global curve-fit of equation 18 to experimental data in order to improve the estimates of the rheological parameters.

Similar information can also be derived from the recovery phase of the experiment. Upon removal of the applied stress at time t′, a certain proportion of the total strain will be immediately recovered (Figure 4*1b*). This instantaneous recovery is due to the Maxwell spring. Thus, as before, the modulus of the Maxwell spring can be determined from knowledge of theinstantaneous strain recovered (γ_i) and the applied stress ($G_M = \tau/\gamma_i$). The strain will then gradually decrease in an exponential fashion governed by the Kelvin-Voigt element (Figure 4*2b*) to a limiting value dictated by the irreversible flow from the Maxwell dashpot (Figure 4*3b*). Thus, the strain decay function for $t > t'$ will have the form:

$$\gamma = \frac{\tau}{\eta_M} + \frac{\tau}{G_{KV}} e^{-\left(\frac{t-t'}{\lambda}\right)} \tag{19}$$

As time approaches infinity, the value of the strain will approach the τ/η_M limit. Thus, knowledge of this limiting minimum strain value (γ_L) would allow for the determination of η_M ($\eta_M = \tau/\gamma_L$). A nonlinear exponential curve-fit of equation 19 to experimental data would allow for the determination of G_{KV} and λ.

If during the rheological tests, conditions were restricted to the linear viscoelastic range of the material, then the elements that give rise to the elastic response will give similar results in the creep and recovery phases. The relaxation times in the creep and recovery phases are identical in this model.

2.1.4. Real Viscoelastic Materials

The rheological behavior of real viscoelastic materials is too complex to be modeled by the Kelvin-Voigt, Maxwell, and Burger models. Very popular is the construction of extended Maxwell and Kelvin-Voigt models where elements can be

placed in an infinite number of arrangements. The problem with this approach is that, very quickly, the entire model building process turns into a curve-fitting exercise. This is not necessarily a bad thing, but one should exercise extreme care in describing the structure of a material as a combination of springs and dashpots since it is difficult to assign real physical meaning to these abstract structural elements.

Thus, for the creep phase of a creep-recovery experiment, a general function that describes the observed increase in strain upon loading has the form:

$$\gamma = \frac{\tau}{G_{i,c}} + \frac{\tau}{G_{d,c}} \sum_{i=1}^{n} (1 - e^{-\frac{t}{\lambda_i}}) + \frac{\tau}{\eta} t \tag{20}$$

where $G_{i,c}$ corresponds to the apparent elastic modulus of structural elements responsible for the instantaneous elastic response of the material upon loading in the creep phase of the rheological test ($G_{i,c} = \tau/\gamma_{i,c}$), $G_{d,c}$ corresponds to the apparent modulus of structural elements responsible for the time-dependant, delayed, elastic response of the material, while η corresponds to the apparent viscosity of structural elements that flow during the creep phase of the rheological test. Notice how instead of a single relaxation time we now have a spectrum of relaxation times λ_i. All these elements need not be present in a particular material.

The situation is similar for the recovery stage of the rheological test. An equation that describes the decay in strain after removal of the externally applied stress at $t = t'$, i.e., upon unloading, is:

$$\gamma = \frac{\tau}{\eta} + \frac{\tau}{G_{d,r}} \sum_{i=1}^{n} e^{-\left(\frac{t-t'}{\lambda_i}\right)} \tag{21}$$

After an instantaneous strain recovery upon unloading ($\gamma_{i,r} = \tau/G_{i,r}$) at $t = t'$, the remaining strain will decay in a time-dependent, delayed, fashion to a limiting permanent value γ_p, where $\gamma_p = \tau/\eta$. As stated before, structural elements within the material have deformed irreversibly, i.e., they have flowed, during the creep phase of the test. These elements have an apparent viscosity η. Notice how instead of a single relaxation time we now have a spectrum of relaxation times λ_i.

It is important to keep in mind that fats are extremely complex systems. As will be described later, the rheological response of fat crystal networks is quite time-dependent and is also a function of the applied stress. To make matters worse, fats also tend to flow during creep tests, and therefore $\gamma_{i,c} \neq \gamma_{i,r}$. It is for these reasons that I have explicitly defined parameters for the loading (creep) and unloading (recovery) phases of the rheological test.

2.1.5 Creep-Recovery Studies of Fats

Creep-recovery studies on fats are very rare. Of note are the study of deMan et al. [1] and Shellhammer et al. [2]. Fats are very difficult to study because the underlying fat crystal network is easily destroyed. deMan et al. [1] could measure creep-recovery curves in butter and margarine using a home-made rheometer (Figure 5). In these curves, he identified an instantaneous deformation at loading (A), an instantaneous deformation recovery upon unloading (B), a time-dependent deformation recovery after unloading (C), as well as a permanent deformation (D). All deformations (B, C, D) are expressed as strains, relative to the total deformation (B + C + D).

He also calculated viscoelastic parameters such as the instantaneously recovered elasticity (IRE),

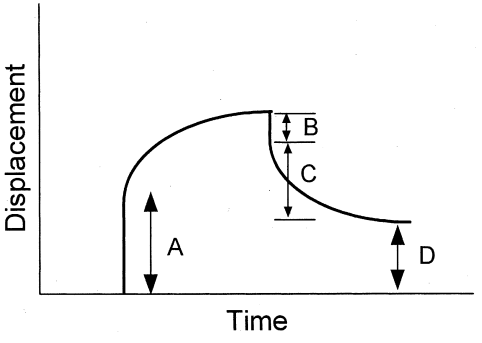

Figure 5 Idealized creep-recovery curve for milkfat.

$$IRE = \frac{loading\ stress\,(Pa)}{B} \tag{22}$$

the time-dependent recovered elasticity (TDRE),

$$TDRE = \frac{loading\ stress}{C} \tag{23}$$

and the viscous flow (VF),

$$VF = \frac{loading\ stress\,(Pa)}{D} \times (time\ of\ flow, s) \tag{24}$$

In this study, deMan and coworkers reported the viscoelastic response in terms of strains as well as the viscoelasticity parameters defined above.

This study demonstrated the experimental difficulties associated with these materials. For example, fats do not behave as typical viscoelastic materials since the instantaneous strain upon loading (A) is much greater than the strain instantaneously recovered after unloading (B). Thus, structural rearrangement takes place during the rheological test. Recovered strains, as well as permanent strains, were also a strong function of the loading time (Figure 6). As expected, as the loading time increased, so did the permanent strain (PS), while the instantaneously recovered strain after unloading (IRS) decreased. The time-dependent recovered strain after unloading (TDRS), on the other hand, remained relatively constant. Thus, it is advisable that the loading time be as short as possible, while still retaining sensitivity. The effect of loading force on viscoelasticity parameters was quite pronounced as well (Figure 7). As the loading force increased (5°C, 10 minute loading time), both the IRE and TDRE decreased. Surprisingly, the viscous flow decreased as well.

Even if plagued with uncertainties, the creep-recovery technique proved useful in detecting differences between butter and margarine samples. Surprisingly, the differences even between different butter types were quite dramatic (Table 1).

The viscoelastic properties of both butter and margarine were strongly dependent on temperature (Figure 8). The IRE, TDRE, and VF decreased as a function of increasing temperature — the materials became less elastic at higher tempera-

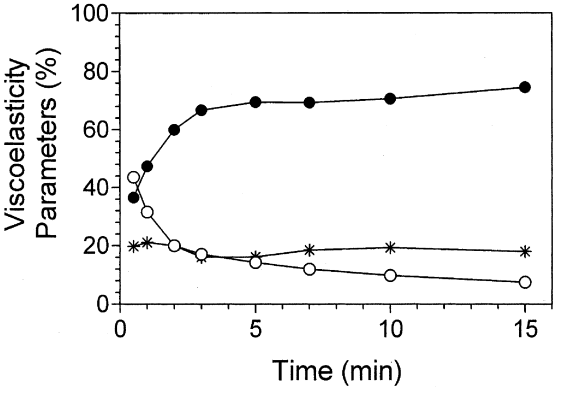

Figure 6 Effect of loading time at 5°C on viscoelasticity parameters. Open circles correspond to the instantaneously recovered strain, closed circles correspond to the permanent strain, while stars correspond to the time-dependent recovered strain.

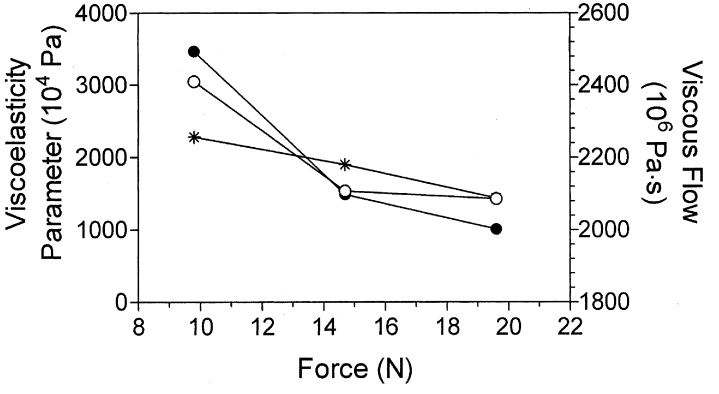

Figure 7 Effect of loading force at 5°C, 10 min loading time, on viscoelasticity parameters. Open circles correspond to the instantaneously recovered elasticity, closed circles correspond to the viscous flow, while stars correspond to the time-dependent recovered elasticity.

Table 1 Viscoelastic Parameters of Butter and Margarine at 5°C (10 min loading)

Sample	IRE 10^4Pa	TDRE 10^4Pa	VF 10^6Pa·s
Butter A	1540	1903	2098
Butter B	928	837	1854
Margarine A	622	593	1774
Margarine B	994	767	2074

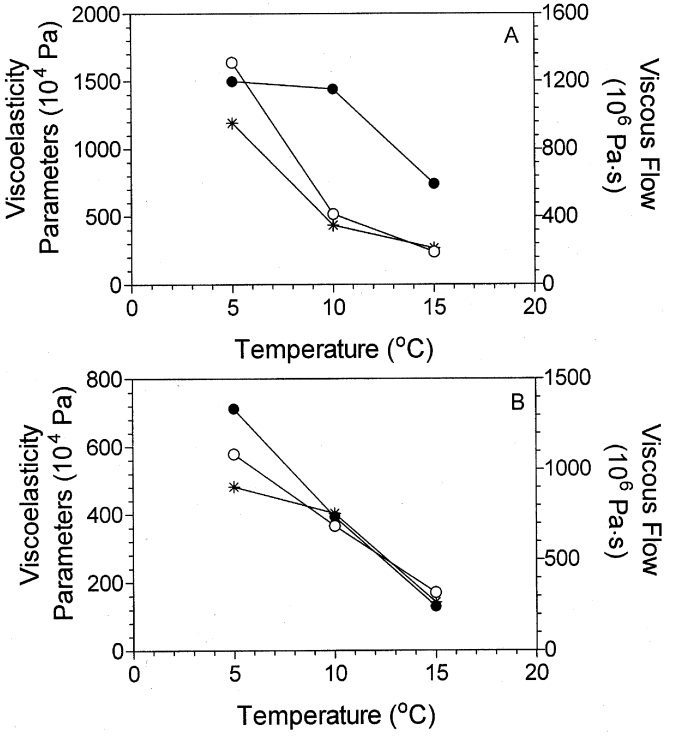

Figure 8 Effect of temperature, 10 min loading time, on viscoelasticity parameters for (**A**) butter and (**B**) margarine. Open circles correspond to the instantaneously recovered elasticity, closed circles correspond to the viscous flow, while stars correspond to the time-dependent recovered elasticity.

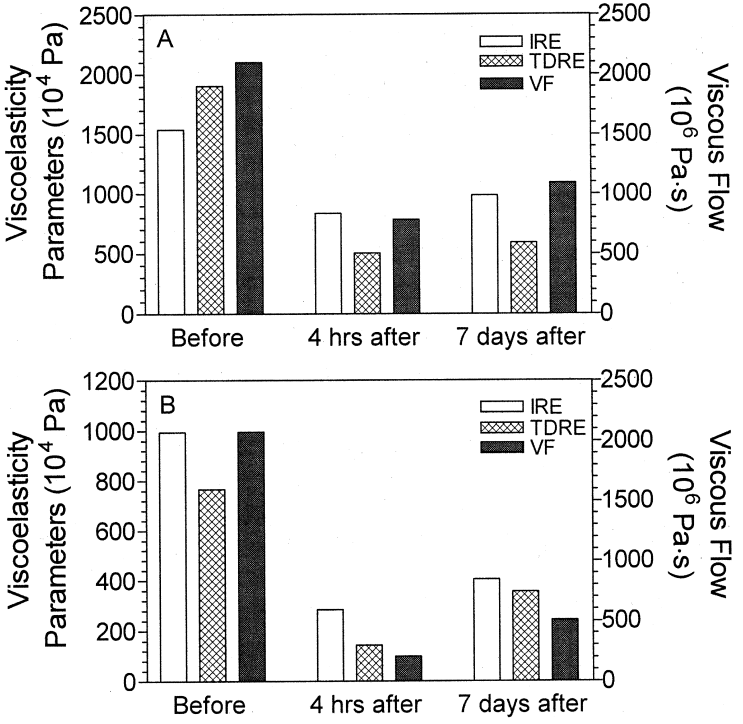

Figure 9 Effect of shear working at 5°C, 10 min loading time, on viscoelasticity parameters.

tures. Another interesting effect is that of shear working on the viscoelasticity of butter and margarine (Figure 9). The elasticity of the material was decreased 4 hours after shear working relative to the non-shear worked material, but was partially regained 7 days after shear working. Thus, this method was quite sensitive to changes in the structure of the underlying fat crystal network.

In all these experiments, one would have expected the viscous flow to increase as the elasticity parameters decreased (and vice versa), however this was not the case. This effect was probably due to the resetting of the material during the rheological test, which would affect the determination of the time of flow (Equation 24).

REFERENCES

1. deMan JM, Gupta S, Kloek M, Timbers GE. Viscoelastic properties of plastic food products J Am Oil Chem Soc 1985; 62: 1672–1675.
2. Shellhammer TH, Rumsey TR, Krochta JM. Viscoelastic properties of edible lipids J Food Engineering 1985; 33:305–320.

6

Dynamic Methods

ALEJANDRO G. MARANGONI

Department of Food Science
University of Guelph
Guelph, Ontario, Canada

1. INTRODUCTION

Instead of applying a constant stress, leading to steady-state flow, it is possible to subject viscoelastic materials to oscillating stresses or strains. These dynamic tests offer an alternative to creep-recovery and stress-relaxation methods in the study of viscoelastic materials.

In a controlled-stress rheometer, stress is applied as a sinusoidal time function, with maximum amplitude τ^* and angular velocity ω [rad/s],

$$\tau = \tau^* \sin(\omega t) \tag{1}$$

The rheometer will record the time-dependent strain function with maximum amplitude γ^*, and phase angle δ (relative to

the input stress wave). The angular velocity ω is related to the frequency f [Hz] by

$$\omega = 2\pi f \tag{2}$$

Alternatively, in a controlled-strain rheometer, strain is applied as a sinusoidal time function, with maximum amplitude γ^* and angular velocity ω [rad/s],

$$\gamma = \gamma^* \sin(\omega t) \tag{3}$$

The rheometer will, in this case, record a time-dependent stress function with maximum amplitude τ^*, and phase angle δ (relative to the input strain wave).

An in-phase response ($\delta = 0°$ or 0 radians) is considered an elastic response, while a 90° ($\delta = \pi/2$ radians) out-of-phase response is considered a viscous response, while a response with a phase angle between 0 and 90° ($0 < \delta < \pi/2$ radians) is characteristic of viscoelastic materials (Figure 1).

When working within the linear viscoelastic region (LVR) of a material, controlled-stress and controlled-strain experiments yield similar results.

It is possible to carry out dynamic tests in shear or compression mode. In controlled-stress/strain rotational rheometers, the bottom plate is stationary while the upper plate, or cone, is made to deflect alternatively for a small angle to the left and to the right in a sinusoidal, time-dependent fashion. In controlled-stress/strain dynamic mechanical analyzers, the bottom plate is stationary while the upper plate is made to deflect alternatively for a small angle upward and downward in a sinusoidal, time-dependent fashion.

A sample placed into that shearing or compression gap will be deformed in the same sinusoidal fashion causing stresses within the sample. These stresses will be sinusoidal, with their amplitude dependent on the nature of the material. In order to remain within the linear LVR of the material, deformation angles should not exceed 1°. At these small deformations, the structure of viscoelastic materials will not be irreversibly affected; hence, it is possible to probe their "at-rest" structure in this fashion.

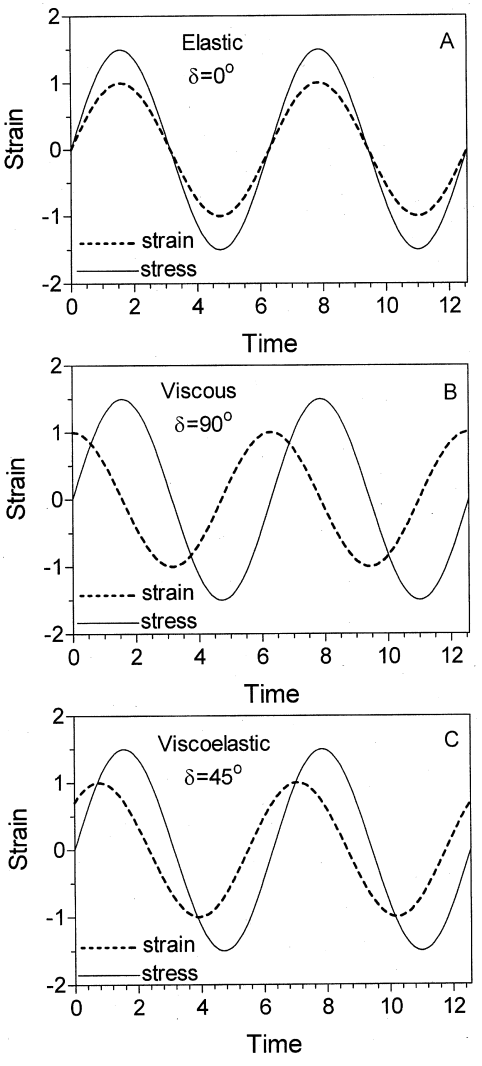

Figure 1 Stress- and strain-wave functions for a hypothetical dynamic rheologic test. Shown here are typical patterns for an idealized elastic response (**A**), viscous response (**B**), and viscoelastic response (**C**)

1.1 Theoretical Considerations

The basic stress-strain relationships for a Hookean solid (elastic response) and a Newtonian fluid (viscous response) have been established before. For a Hookean solid (spring) within its elastic region, stress is directly proportional to strain:

$$\tau = G\gamma \tag{4}$$

where τ is the elastic stress [Pa], G is the shear elastic modulus [Pa], and γ is the shear strain [dimensionless]. For a Newtonian fluid, stress is directly proportional to shear strain rate:

$$\tau = \eta \frac{\partial \gamma}{\partial t} \tag{5}$$

where τ is the viscous stress [Pa], η is the coefficient of viscosity [Pa≅s], and $\partial\gamma/\partial t$ is the shear strain rate [s^{-1}]. The relaxation time [s^{-1}] of a material is defined as the ratio of the coefficient of viscosity over the shear elastic modulus:

$$\lambda = \frac{\eta}{G} \tag{6}$$

A high value for the relaxation time is characteristic of fluids, while a low value for the relaxation time is characteristic of solids.

In this section, we will establish a general stress-strain relationship for viscoelastic materials. However, before we do this, it is useful to establish such relationships for Hookean solids, Newtonian fluids, Kelvin-Voigt and Maxwell viscoelastic materials.

1.1.1. Hookean Solids (Springs)

When a Hookean solid (spring) is subjected to a sinusoidal stress wave, τ, with maximum amplitude τ^*, and angular velocity ω [rad/s],

$$\tau = \tau^* \sin(\omega t) \tag{7}$$

it will give rise to an in-phase strain wave, γ, with maximum amplitude, or strain, γ^*, and angular velocity ω [rad/s]:

$$\gamma = \gamma^* \sin(\omega t) \tag{8}$$

Substituting equation 8 into equation 4 leads to the dynamic-stress function

$$\tau = G\gamma^*\sin(\omega t) \tag{9}$$

An important property of Hookean solids is that their elastic modulus is frequency independent, namely:

$$G = \frac{\tau}{\gamma} = \frac{\tau^*\sin(\omega t)}{\gamma^* \sin(\omega t)} \tag{10}$$

which simplifies to:

$$G = \frac{\tau^*}{\gamma^*} \tag{11}$$

The elastic modulus determined using a dynamic test has the same form as the elastic modulus determined using a static test, and its value is independent of frequency.

For a dynamic test, the shear elastic modulus, G, is referred to as the storage modulus, G′. The term storage modulus refers to the fact that the stress energy is temporarily stored during the test, but is fully recovered after the stress is removed.

1.1.2. Newtonian Fluids (Dashpots)

When a Newtonian fluid (dashpot) is subjected to a stress wave (τ), with maximum amplitude, or stress, τ^* [Pa], and angular velocity ω [rad/s],

$$\tau = \tau^* \sin(\omega t) \tag{12}$$

it will deform, or strain, at a particular rate, i.e., it will flow. As stated earlier, the shear stress wave will give rise to a shear-strain wave:

$$\gamma = \gamma^*\sin(\omega t) \tag{13}$$

The shear-strain rate $\partial\gamma/\partial t$ is simply the time-derivative of the shear-strain function,

$$\frac{\partial\gamma}{\partial t} = \omega\gamma^* \cos(\omega t). \tag{14}$$

For a Newtonian fluid, stress (τ) is linearly proportional to the shear strain rate $\partial\gamma/\partial t$, and, thus, substituting equation 14 into equation 5 leads to the dynamic stress function

$$\tau = \eta\omega\gamma^*\cos(\omega t). \quad (15)$$

Therefore, for Newtonian fluids (dashpots), the stress and strain waves are 90° out of phase. For a dynamic test, equation 15 can be written as:

$$\tau = G''\gamma^*\cos(\omega t), \quad (16)$$

where G'' is referred to as the loss modulus [Pa], where:

$$G'' = \eta\omega \quad (17)$$

The term *loss modulus* refers to the fact that the stress energy which has been used to initiate the flow of the material has been irreversibly transformed into heat, and therefore cannot be recovered after the strain is removed. An important property of Newtonian fluids (dashpots) is that the loss modulus (G'') is linearly proportional to frequency (see equation 17 and Figure 2), in contrast to the case of Hookean solids (springs), where the storage modulus (G') is frequency independent (see equation 11).

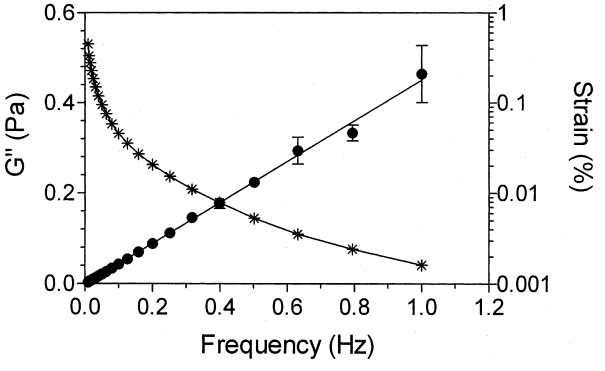

Figure 2 Dynamic frequency sweep of canola oil at 22°C using an oscillatory stress of 0.002 Pa. The geometry used was the DIN conical concentric cylinder.

1.1.3. Kelvin-Voigt Viscoelastic Solid

The simplest model for a viscoelastic material is the Kelvin-Voigt model. In a Kelvin-Voigt element, a spring (elastic component) and a dashpot (viscous component) are arranged in parallel. For such an arrangement, the strain is equal for both the spring and the dashpot, while the stress is the sum of the individual stresses, the elastic stress (τ_e) and the viscous stress (τ_v),

$$\tau = \tau_e + \tau_v \tag{18}$$

Substituting equations 4 and 5 into equation 18 yields

$$\tau = G\gamma + \eta\frac{\partial y}{\partial t}. \tag{19}$$

Substituting the respective expressions for the dynamic-strain (equation 13) and strain-rate (equation 14) functions into equation 19, we obtain

$$\tau = G\gamma^*\sin(\omega t) + \eta\omega\gamma^*\cos(\omega t), \tag{20}$$

or

$$\tau = G'\gamma^*\sin(\omega t) + G''\gamma^*\cos(\omega t), \tag{21}$$

where G' and G'' are, respectively, the storage and loss shear moduli [Pa].

The dynamic-stress function (τ) in this model is given by a linear combination of an in-phase stress response and a 90° out-of-phase stress response. As for the case of Hookean solids (springs) and Newtonian fluids (dashpots), an important characteristic of a Kelvin-Voigt material is the frequency independence of the storage modulus (G'), and the linear dependence of the loss modulus (G'') on frequency ($G'' = \eta\omega$).

Substituting the relaxation time (λ) for the coefficient of viscosity into equation 17, we obtain

$$G'' = G'\omega\lambda \tag{22}$$

This equation implies that for a Kelvin-Voigt solid at low frequencies, the material's rheologic properties are defined by its elastic component, while at high frequencies its rheologic properties are defined by its viscous component. At intermedi-

ate frequency, values the rheologic properties of a Kelvin-Voigt material are defined equally by its viscous and elastic components.

1.1.4. Maxwell Viscoelastic Fluid

In the Maxwell model, a spring (elastic component) and a dashpot (viscous component) are arranged in series. For such an arrangement, the stress is equal for both the spring and the dashpot, while the strain is the sum of the individual strains, the elastic strain (γ_e), and the viscous strain (γ_v):

$$\gamma = \gamma_e + \gamma_v \tag{23}$$

By differentiation of the above expression, we obtain

$$\frac{\partial \gamma}{\partial t} = \frac{\partial \gamma_e}{\partial t} + \frac{\partial \gamma_v}{\partial t}. \tag{24}$$

Substituting the strain time derivatives from equations 4 and 5 into equation 24, results in

$$\frac{\partial \gamma}{\partial t} = \frac{1}{G}\left(\frac{\partial \tau}{\partial t}\right) + \frac{\tau}{\eta}. \tag{25}$$

Finally, substituting equation 14 into the left side of equation 25 yields

$$\omega \gamma^* \cos(\omega t) = \frac{1}{G}\left(\frac{\partial \tau}{\partial t}\right) + \frac{\tau}{\eta} \tag{26}$$

The analytical solution of this familiar first-order ordinary linear differential equation has the following form:

$$\tau = \left[\frac{G\lambda^2\omega^2}{(1+\lambda^2\omega^2)}\right]\sin(\omega t) + \left[\frac{G\lambda\omega}{(1+\lambda^2\omega^2)}\right]\cos(\omega t) \tag{27}$$

where λ is the relaxation time, has been defined previously ($\lambda = \eta/G$). This equation can be rewritten as

$$\tau = G'\sin(\omega t) + G''\cos(\omega t), \tag{28}$$

where G' represents the storage modulus [Pa] while G'' represents the loss modulus [Pa],

$$G' = \frac{G\lambda^2\omega^2}{(1+\lambda^2\omega^2)} \tag{29}$$

and

$$G'' = \frac{G\lambda\omega}{(1+\lambda^2\omega^2)} \tag{30}$$

As in the case for the Kelvin-Voigt model, the dynamic-stress function for a Maxwell viscoelastic fluid is a linear combination of an in-phase elastic stress function and a viscous, 90° out-of-phase stress function. For a Maxwell fluid, however, both storage and loss moduli are frequency dependent. We can, however, define two different frequency regimes.

At low frequencies, $\lambda^2\omega^2$ becomes very small and $(1+\lambda^2\omega^2) \sim 1$. The expressions for the moduli then become:

$$G' = G\lambda^2\omega^2 \tag{31}$$

and

$$G'' = G\omega\lambda \tag{32}$$

Therefore, in the low-frequency range, the storage modulus (G′) increases as a function of frequency in a quadratic fashion, while the loss modulus (G″) increases linearly as a function of frequency. The slopes of the log-log plot of G′ vs. frequency and G″ vs. frequency are therefore 2 and 1, respectively. These effects are clearly appreciated in a simulation of the behavior of the dynamic moduli vs, the frequency (Figure 3).

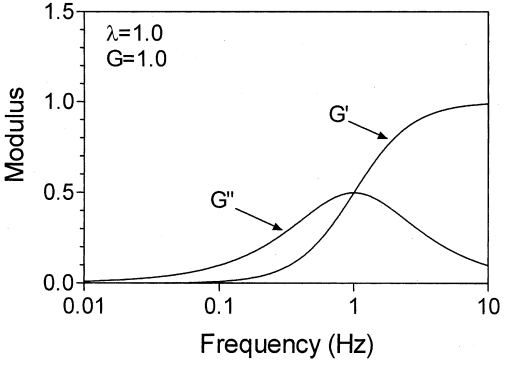

Figure 3 Simulations of the frequency-dependence of the storage (G′) and loss (G″) moduli of a Maxwell fluid

At high frequencies, $\lambda^2\omega^2$ becomes very high and $(1+\lambda^2\omega^2)\sim\lambda^2\omega^2$. The expressions for the moduli then become:

$$G' = G \tag{33}$$

And

$$G'' = \frac{G}{\lambda\omega} \tag{34}$$

At high frequencies, the slopes of the log-log plot of G′ vs. frequency and G″ vs. frequency are therefore 0 and -1, respectively. For a Maxwell material, therefore, the storage modulus (G′) becomes independent of frequency, while the loss modulus (G″) decreases as a function of increasing frequency. These effects are clearly shown in Figure 3.

Closer examination of equations 29 and 30 suggests that, at low frequencies, the loss modulus G″ is larger than the storage modulus G′. A Maxwell material will behave like a Newtonian fluid (viscous fluid) at low frequencies, since the viscous component has enough time to react to a given stress or strain. At high frequencies, however, this relationship is reversed–the material will behave like a Hookean solid (elastic spring) since the viscous component will not have enough time to react to the applied stress or strain.

1.1.5. Real Viscoelastic Materials–Generalization of the Model

Real viscoelastic materials are more complex than Maxwell and Kelvin-Voigt materials. It is possible to have different configurations of springs and dashpots, such as in the case of the Burger model.

1.2. The Complex Modulus

The complex modulus (G*) is the ratio of the maximum resulting stress amplitude to the maximum applied strain amplitude, as per our definition of a shear modulus (equation 11),

$$G^* = \frac{\tau^*}{\gamma^*} \tag{35}$$

and represents the total resistance of the material to the applied strain. For real viscoelastic materials, the complex modulus and phase angle are both dependent on frequency. The phase angle increases as a function of increasing frequency while the complex modulus decreases.

The challenge then remains how to derive values for the storage (G′) and loss (G″) moduli in the absence of a rheologic model, i.e., Kelvin-Voigt, Maxwell, Burger.

We know from our treatment that a phase angle of 0° corresponds to a Hookean solid, a phase angle of 90° to a Newtonian fluid, while a phase angle between 0° and 90° corresponds to a viscoelastic material. It would stand to reason that if the complex modulus is a combination of the storage (G′) and loss moduli (G″), then the following relationships would apply:

$$G' = G^*\cos\delta \tag{36}$$

and

$$G'' = G^*\sin\delta \tag{37}$$

If the phase angle (δ) is zero, as is the case for a Hookean solid, i.e., the material is purely elastic, then $G' = G^*$ and $G'' = 0$. If the phase angle is 90°, as is the case for a Newtonian fluid, i.e., the material is purely viscous, then $G' = 0$ and $G'' = G^*$. For phase angle values $0° < \delta < 90°$, storage and loss moduli correspond to proportions of G* between 0 and 100%.

The most convenient way of establishing a quantitative relationship between complex modulus and the storage and loss moduli is by the use of complex numbers. A complex number is composed of a real and an imaginary part:

$$z = a + bi \tag{38}$$

where $i = (-1)^{1/2}$

Therefore, as shown in Figure 4, the complex modulus G* can be defined as a vector composed of a real part corresponding to the storage modulus (G′), and an imaginary part corresponding to the loss modulus (G″), namely,

$$G^* = G' + iG'' \tag{39}$$

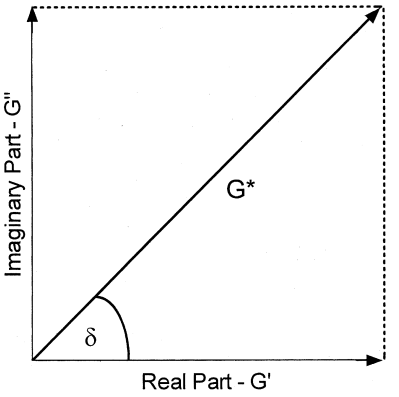

Figure 4 Argand diagram depicting the complex modulus as having a real part (G′), and an imaginary part (G″), weighted by the phase angle (δ).

The phase angle δ defines the relative weighting of G′ and G″ in G*. This definition of complex modulus is universal and a mechanical model is not required to derive values of G′and G″.

It is also possible to define a complex compliance, J*,

$$J^* = \frac{1}{G^*} \tag{40}$$

and therefore,

$$J^* = J' + iJ'' \tag{41}$$

1.3 Complex Viscosity

We can equally easily define a complex viscosity (η*). The complex viscosity is defined as the ratio of the maximum resulting stress amplitude over the maximum applied strain amplitude times the angular velocity, as defined in equation 15:

$$\eta^* = \frac{\tau^*}{\omega\gamma_o} \tag{42}$$

The complex viscosity η* represents the total resistance of the material to flow. The complex viscosity and phase angle are both dependent on frequency. The phase angle decreases as a

function of increasing frequency while the complex viscosity increases.

In the same fashion as for the complex modulus, the complex viscosity is a combination of a storage viscosity, η', the elastic component, and a dynamic viscosity, η'', the viscous component. The storage and dynamic viscosities are functions of the complex viscosity and the phase angle, and are related to the storage and loss moduli:

$$\eta'' = \eta^* \cos\delta = \frac{G'}{\omega} \tag{43}$$

and

$$\eta' = \eta^* \sin\delta = \frac{G''}{\omega} \tag{44}$$

The complex viscosity η^* can also be defined as a vector composed of a real part corresponding to the storage viscosity ($\eta\delta''$), and an imaginary part corresponding to the dynamic viscosity (η'), namely,

$$\eta^* = \eta'' + z\,\eta' \tag{45}$$

The stress response in dynamic testing can now therefore be written in terms of moduli or of viscosities:

$$\tau = G'\gamma^*\sin(\omega t + \delta) + G''\gamma^*\cos(\omega t + \delta) \tag{46}$$

or:

$$\tau = \eta''\omega\gamma^*\sin(\omega t + \delta) + \eta'\,\omega\gamma^*\cos(\omega t + \delta) \tag{47}$$

1.4. Some Basic Considerations for Rheologic Studies of Fats Under Dynamic Conditions

Under small deformation dynamic rheologic testing (stresses below 5000 Pa and strain below 0.01%), fats behave very much like elastic solids. Storage (G') and loss (G'') moduli are frequency-independent and the tanδ (G''/G') is usually below 0.1 (Figure 5).

Having said this, G' does exhibit a slight frequency dependence as shown in Figure 6 (when using a linear, rather than logarithmic, scale for the y-axis). Most practitioners of rheol-

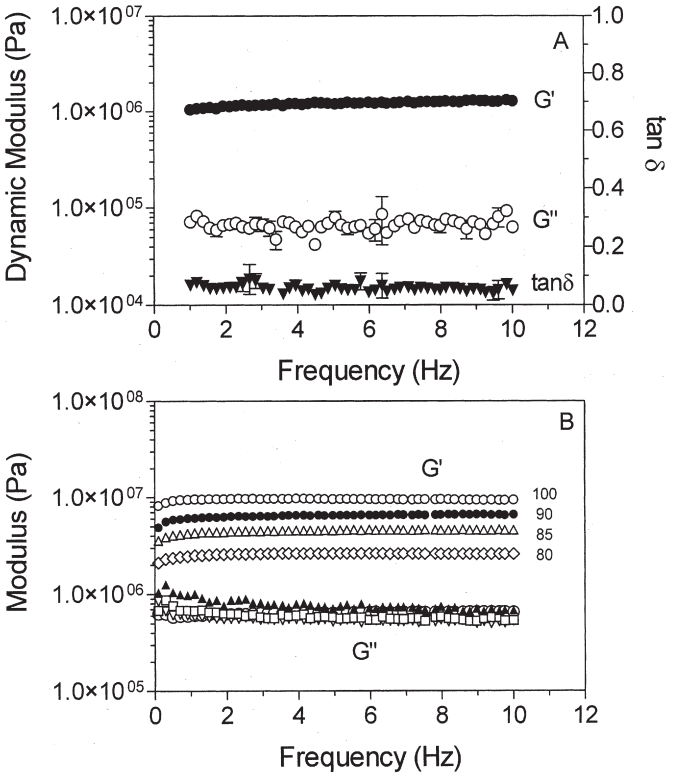

Figure 5 (*A*) Frequency dependence of the storage (G′) modulus, loss (G″) modulus and the tangent of the phase angle (tanδ) for a commercial shortening at 5°C. (*B*) Frequency dependence of the G′ and G″ for milk fat and milk fat-canola oil (100– 80% milk fat) blends at 5°C.

ogy would not consider this a significant effect. However, the slight dependence is evident. We usually fix the frequency at 1Hz, where the material maintains its integrity during the lifetime of the rheologic test.

In our experience, it is best to always carry out a stress sweep, at a fixed frequency for every sample measured (Figure 7). This ensures that the rheologic parameters obtained are derived from within the LVR of the material, where stress and

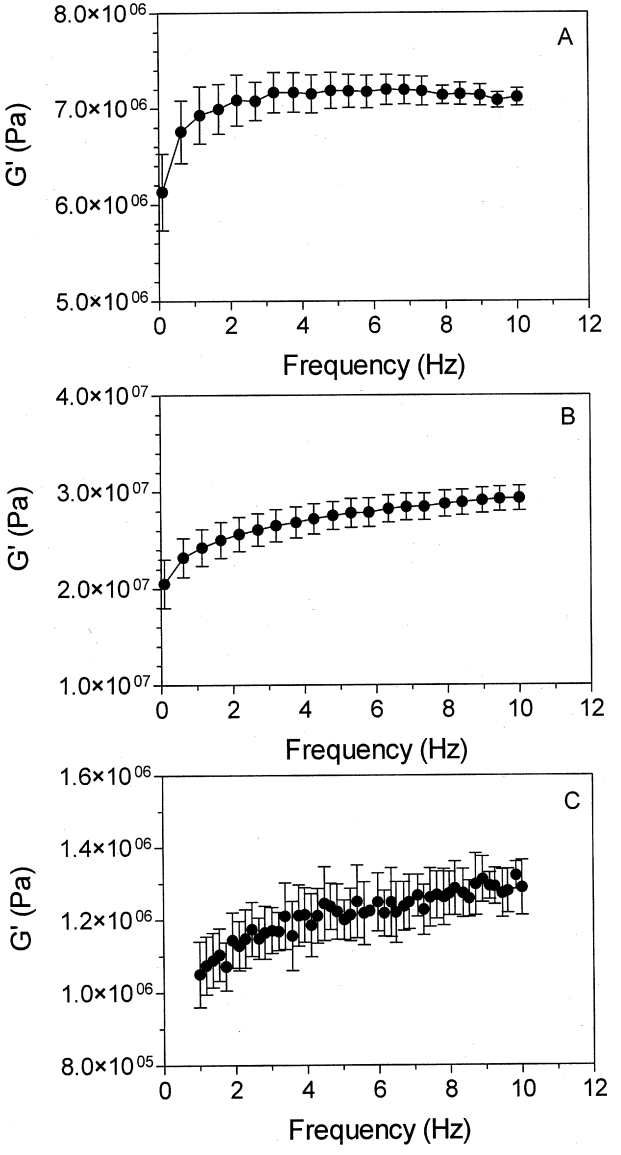

Figure 6 Frequency dependence of the storage modulus (G′) for milkfat (*A*) at 5°C, cocoa butter at 20°C, and a commercial shortening at 5°C.

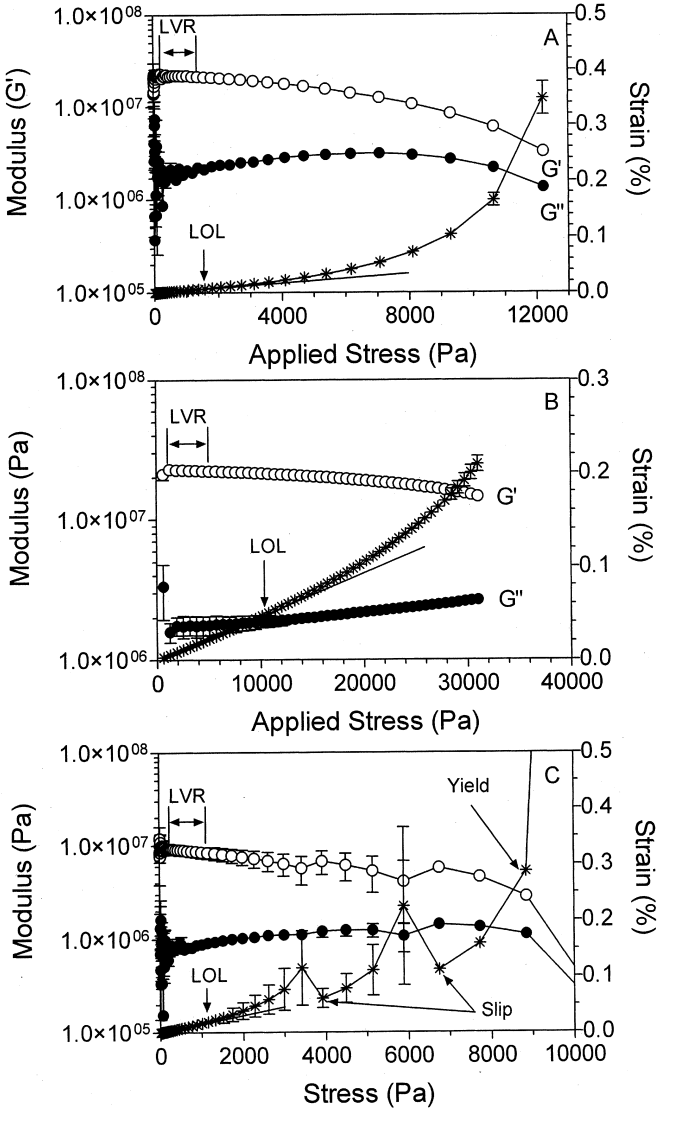

Figure 7 Stress sweeps for cocoa butter at 22°C (*A*), tallow at 5°C (*B*) and milkfat at 5°C. All stress sweeps were carried out at a frequency of 1Hz. Evident in the graphs are the linear viscoelastic regions (LVR) as well as the limit of linearity (LOL) for ideal behavior. Evidence of slip and plastic yielding can be found in the strain data for milk fat (*C*)

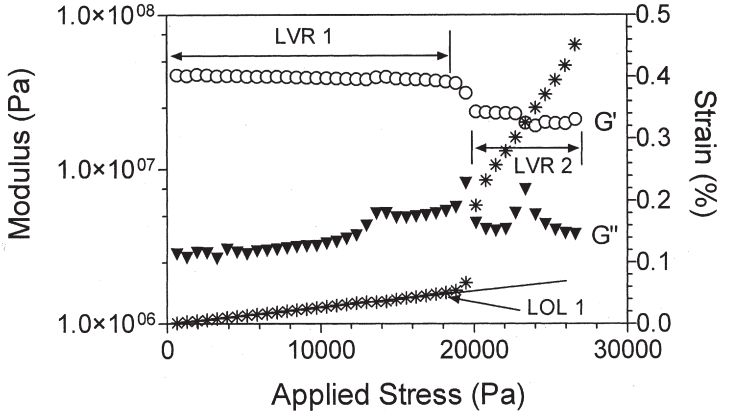

Figure 8 Stress sweep for cocoa butter at 22°C (f = 1Hz) demonstrating the existence of multiple linear viscoelastic regions (LVR). Also depicted is the limit of linearity (LOL 1) of the first LVR.

strain are linearly proportional to each other. We have found large variabilities in the range of stresses corresponding to the LVR, and thus carry out a stress sweep every time. Some interesting features can be appreciated in Figure 7, such as the limit of linearity (LOL), where the stress-strain relationship departs from linearity. This stress usually corresponds to the upper limit of the LVR, but not always. We can also find evidence of slippage of the plates used in this rheologic test (Figure 7*C*). The sudden drop in strain corresponds to slippage. As well, drastic increases in the strain are indicative of plastic yielding of the material and the beginning of flow (Figure 7*C*).

An interesting aspect to keep in mind is that multiple LVRs can be present in the material at different stress levels (Figure 8) Different levels of structure within the material are being probed in this fashion.

7

Microstructure

SURESH S. NARINE

Agri-Food Materials Science Centre,
Department of Agricultural, Food and
Nutritional Science,
University of Alberta
Edmonton, Alberta, Canada

ALEJANDRO G. MARANGONI

Department of Food Science
University of Guelph
Guelph, Ontario, Canada

1. INTRODUCTION

The macroscopic rheologic properties of networks formed by lipids are of extreme importance in food products that contain significant amounts of fats. Such products include butter, margarine, chocolate, peanut butter, ice cream, and many spreads such as cream cheese. Many of the sensory attributes such as

spreadability, mouthfeel, snap, and texture are dependent on the mechanical strength of the underlying fat crystal network. However, it must not be inferred from this that knowledge of the mechanical properties of the fat network provides complete knowledge of the food product within which it is formed. In addition to this obvious industrial importance, fat crystal networks form a particular class of soft materials, which demonstrate a yield stress and viscoelastic properties, rendering these materials plastic. From a materials sciences point of view, the rheologic behavior of these materials is also extremely important.

This section provides a review of the development of techniques and models which attempt to relate the microstructure structural organization of fat crystal networks to their mechanical properties. In addition, the work provides a chronicle of the authors' own attempts at the problem, focusing mainly on the effects of the microstructure level on the macroscopic elastic moduli of fat crystal networks and the quantification of this level of structure utilizing fractal geometrical analysis techniques.

Fat crystal networks, like many other materials, demonstrate distinct hierarchies of structural organization, the identification and quantification of which provides insight into the relationship of composition, processing, structure, and mechanical properties of the networks formed by these materials. As such, the macroscopic properties of the network are influenced by the different levels of structure as well as the processing conditions under which the network is formed. Figure 1 depicts the structural hierarchy defined during the crystallization of a typical fat crystal network, the factors which affect it, as well as some indicators commonly used in the quantification of the relationship between structure and macroscopic properties.

Efforts to model the mechanical strength [1–8] of these networks have met with more failure than success over the past 50 years, mainly due to the lack of a comprehensive model to relate *all* structural network characteristics and solid/liquid ratios of lipid networks to their mechanical strength. This lack stemmed partly from the fact that many scientists in this area

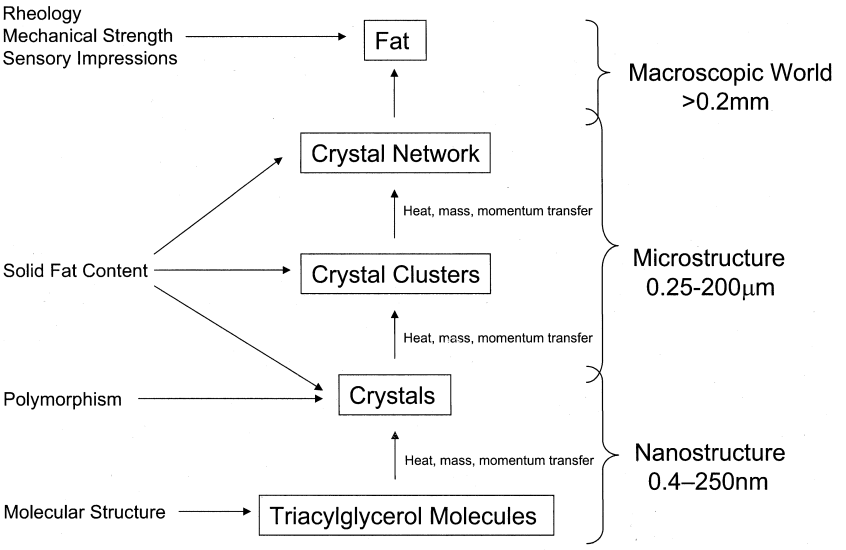

Figure 1 Schematic showing the structural hierarchy defined during the formation of a fat crystal network

concentrated only on the lipid composition, polymorphism, and solid fat content (SFC) of the networks, in large part ignoring the in situ microstructure of the network. Lately, much work has been done in analysis of the microstructure of the network, leading to encouraging results, which suggests that consideration of this level of structure (together with the other levels previously studied) is absolutely essential in assessing the mechanical strength of the fat network.

2. THE MESOSCALE IN A FAT CRYSTAL NETWORK

The microstructural level, or mesoscale, of a fat crystal network may be defined as those structures in the length range between approximately 0.5 μm and 200 μm. This level of structure has an enormous influence on the macroscopic rheological properties of the network, noted as early as 1987 by deMan and Beers [9]. Other researchers have also noted the importance of the mesoscale on the rheologic properties of the network, and

the fact that the microstructure is easily changed with crystallization conditions [10–12], as well as with interesterification [13].

With the advent of confocal laser scanning fluorescence microscopy (CLSFM) [14] and multiple photon microscopy (MPM) [15,16], two new tools have been added to the standard tools of light microscopy (LM) [17–20] and electron microscopy (EM) [10,21–25], which, in the past, were the most widely used to study the microstructure of fats and foods in general. Heertje's work [10,11,14,26] on the visualization of the microstructure in fats remains one of the most important contributions to the field. In his method, a cold solvent mixture was used to remove the liquid oil from the solid fat in a sample mounted on a special holder. After removing the liquid oil, the structure of the solid fat network could be visualized.

Interest in the microstructure of fat crystal networks in our laboratory arose during studies of factors affecting the hardness and spreadability of chemically interesterified (CIE) and enzymatically interesterified (EIE) milk fat and milk fat-canola oil blends, CIE palm oil and palm oil-soybean oil blends, and CIE lard-canola oil blends [13,27–34]. The hardness index and storage moduli (G′, dynamic shear elastic modulus) of CIE milk fat at equivalent SFCs was lower than their noninteresterified (NIE) counterparts. The traditional indicators of macroscopic hardness, such as dropping points, SFC, and polymorphism of the CIE and NIE milk fat samples, were investigated in an attempt to explain the observed changes in G′ and the hardness index. Much to the authors' surprise, upon chemical interesterification, there was little or negligible change in dropping points of NIE and CIE milk fat and milk fat-canola oil blends between 60% and 90% (w/w) milk fat-canola oil. There was little or negligible change in the SFC of NIE and CIE milk fat and milk fat-canola oil blends between 25% and 50% SFC, and crystalline packing of the CIE milk fat was similar to that observed for NIE milk fat (the polymorphism was the same).

Therefore, it was obvious that the traditional indicators of macroscopic hardness were insensitive to the changes in the structure of the milk fat on CIE, which caused the resulting

changes in elastic moduli and hardness index. It must be mentioned here, in order to avoid misinterpretation, that the above phenomena was observed for CIE and NIE milk fat, but that this does not imply that traditional indicators such as dropping points, polymorphism, and SFC are *always* insensitive to changes in macroscopic mechanical properties. What this case study proved was that is was possible for these indicators to prove insensitive in some cases, therefore suggesting that perhaps there existed other structural indicators that must also be taken into consideration. It was interesting, however, that polarized light microscopy (PLM) and CLSFM demonstrated that the structure of the fat network at the mesoscale (i.e., at the level of structure that is visible by light microscopy) upon CIE was significantly altered [28].

This provided motivation to search for new "structural indicators" of the mechanical strength of fat crystal networks that were somehow related to the next logical structural level; the microstructure of the network. A rheologic approach was adopted by Rousseau and Marangoni [13,31,34], the motivation for which stemmed from work done on the fractal nature of colloidal gels and adapted to fat crystal networks [35]. In order to introduce the reader to the developments made in the rheologic analysis of fat crystal networks utilizing the progress in the colloidal field, we provide an introduction first to fractal theory, and then to the application of fractal theory to colloidal gels.

2.1 Fractals

Classical or Euclidean geometry is based on the use of regular shapes to describe objects. The reader will be familiar with the use of straight lines, circles, conic sections, polygons, spheres, quadratic surfaces, etc., and combinations of these elements to describe objects around us. However, many patterns in nature defy description by these regular shapes. The geometry of coastlines, mountains, trees, and vegetables, for instance, cannot always be defined adequately by spheres, cubes, or cones. Fractal geometry was born out of this lack of geometrical tools. Benoit Mandelbrot is credited with having developed the field of fractal geometry to describe many of these natural shapes [36]. According to Mandelbrot [36], "I conceived and developed

a new geometry of nature and implemented its use in a number of diverse fields. It describes many of the irregular and fragmented patterns around us, and leads to full-fledged theories, by identifying a family of shapes I call fractals."

The unifying concept underlying fractals is the concept of self-similarity. Self-similarity essentially means invariance against changes in scale or size, and is demonstrated in many of the laws of nature. Self-similarity is one of a vast number of symmetries that exist in nature. Symmetry is usually taken to mean invariance against some change—i.e., some aspect of an object stays the same regardless of changes in the state of the observer. For example, there is symmetry in regular bodies such that they may be operated on by a number of operations, and, yet, after the operation is carried out, every point of the body in its original state is coincident with an equivalent point in its altered state. We have been able to take advantage of underlying symmetries in nature—most notably in the previous example of the application of group theory to the symmetry operations which render groups of molecules invariant against sets of operations consisting of reflections, rotations, translations, inversions, and combinations of these operations [37]. Equally useful, and more popular, are symmetries in nature, including the exploitation of invariance against uniform motion, which has spawned the theory of special relativity and the equivalence of acceleration and gravity, which is the basis of Einstein's general theory of relativity. Even classical physics is built along the lines of symmetry in nature—the electrostatic or gravitational attraction or repulsion between two bodies demonstrates mirror symmetry—there is no partiality shown to left or right. Suffice it to say, therefore, that symmetry in nature has aided us tremendously in understanding and quantifying our world. As will be demonstrated, the symmetry of self-similarity at different length scales is equally as useful as those symmetries mentioned earlier. To quote Schroeder [38], "Yet, among all these symmetries flowering in the Garden of Invariance, there sprouts one that, until recently, has not been sufficiently cherished: the ubiquitous invariance against changes in size, called self-similarity."

The word *fractal* stems from the fact that fractal objects demonstrate fractional dimensions rather than the integer dimensions for objects encountered in Euclidean geometry. The connection between fractional dimension and self-similarity is that the easiest way to construct a set that has fractional dimension is through self-similarity [39]. In classical Euclidean geometry, objects have integer dimensions: the reader would be familiar with the reasoning that a line is a 1-dimensional object, a plane a 2-dimensional object,t and a volume a 3-dimensional object. In this way, Euclidean geometry is suited for quantifying objects that are ideal, man-made, or regular.

One may imagine that if enough kinks are placed in a line or a plane, the result is to have an object that may be classified as being an intermediate between a line and a plane or a plane and a cube. The dimension of such an object is fractional (i.e., between 1 and 2 or between 2 and 3) and the object may be classified as a fractal object—from the fact that instead of having a Euclidean dimension (integer) it has a fractional dimension. One of the most important features of fractal objects is that they are self-similar; i.e., there is a repetition of patterns in the object at many different scales. For natural objects, such as trees, clouds, coastlines, etc., Euclidean geometry fails to provide an adequate quantification, yet many of these natural objects are self-similar at different scales. For example a tree has branches, these branches have smaller branches and so on, and if one changes the scale of observation of the tree, the same pattern is observed, at least in a statistical sense if not in a deterministic sense. Therefore, fractal geometry provides a good measure of such objects with nonintegral dimensions.

The concept of fractional dimension was introduced by Hausdorf [40]. As early as 300 years ago, Leibniz [41] used the scaling invariance of the infinitely long straight line for its definition. However, as self-similar entities with fractional dimensions started appearing in the mathematical literature, they were met with distaste. Charles Hermite, the famous mathematician, for example, labeled such entities monsters. However, largely due to the efforts of Mandelbrot [36], fractal

geometry is now an accepted and extremely useful method of describing and quantifying entities that demonstrate scale invariance and fractional dimensions.

The reviews by Jullien and Botet [42], Meakin [43], and Lin et al. [44], as well as the books by Julien and Botet [42], Russ [45], and Viczek [46] on the subject of fractals and fractal aggregation are recommended for further review.

For a disordered distribution of mass, such as in a clustering of stars in the Milky Way or the clustering of particles in a colloid, fractal geometry is also useful. A short example is useful. For a solid 1-dimensional line, a 2-dimensional plane, or disc (Figure 2), or a 3-dimensional cube (Figure 3), the relationship of mass (M) to the length (L) of the object is given by:

$$M(r) \sim L^d \tag{1}$$

where d is the Euclidean dimension of the object. In this case, the dimension is an integer, and the object is therefore a Euclidean object. However, for a disordered distribution of mass (Figure 4), if, at different scales of observation, the patterns are statistically self-similar, then the relationship of radius to mass may be given by [35,36,42,47]:

$$M(r) \sim L^D \tag{2}$$

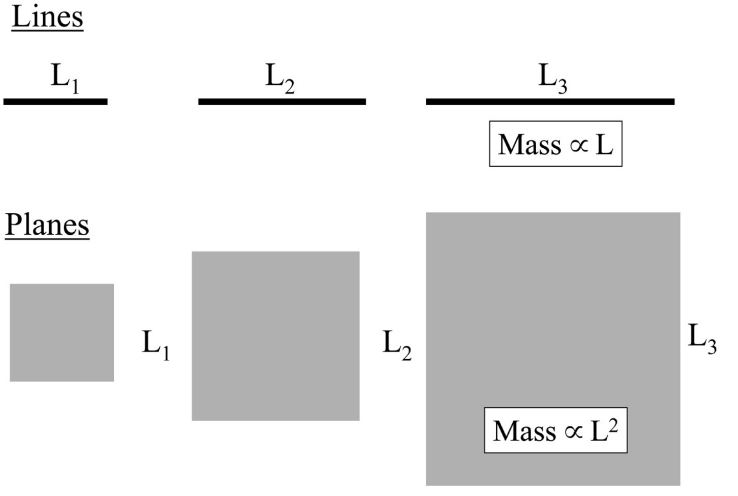

Figure 2 Mass-length scaling for lines and planes

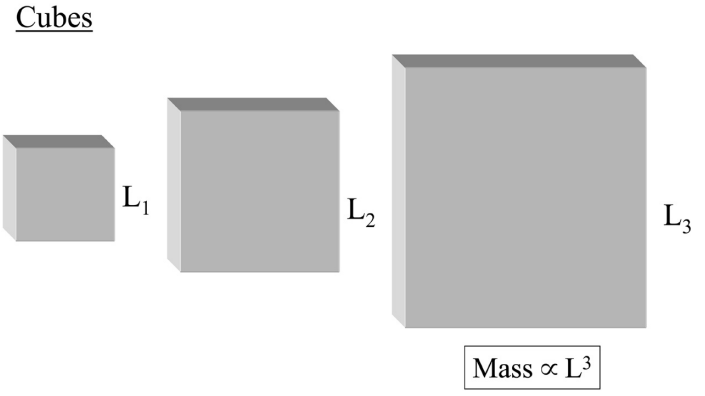

Figure 3 Mass-length scaling for cubes.

where D is a fractional or *fractal dimension,* known as the mass fractal dimension. Here, the symbol ~ is taken to mean "approximately proportional to."

2.2 Scaling Theory as Applied to Colloidal Gels

The irreversible aggregation of small particles to form clusters is a common natural phenomenon; for example, this is seen

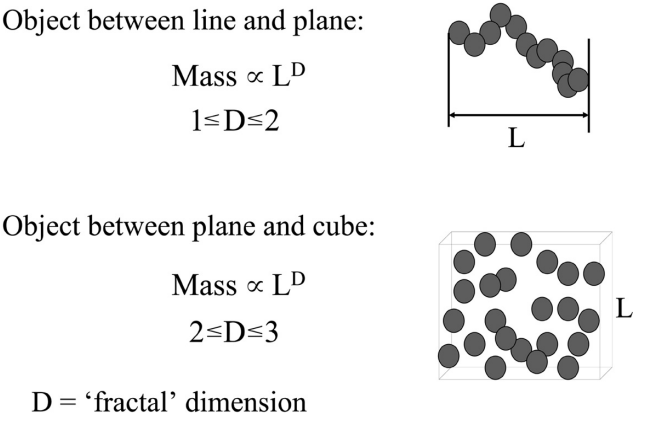

Figure 4 Mass-length scaling for non-Euclidean objects with non-integrer dimensionality.

in colloids [48], coagulated aerosols [49], chemical species precipitating from a supersaturated matrix, and crystals growing from a supercooled melt [50]. The final structure of such aggregates is important not only because it can potentially yield information about the mechanical strength of the resulting structures but also because it can suggest methods to alter the structure kinetically. In many cases, the rate limiting step of the formation of these aggregates is the diffusion of species towards a growing surface (mass-limited transfer), or the transfer of heat away from the growing surface, or a combination of these factors, depending on the stage of growth.

As early as 1979, Forrest and Witten [51] demonstrated a class of aggregates that were shown to have density correlations of a power–law form. These aggregates were formed when a metal vapor produced by heating a plated filament was quench condensed, causing metal particles of the order of 40Å radius to drift down onto a microscope slide. The particles were found to arrange in aggregates of the order of 10^5 particles per aggregate. In 1981, Witten and Sander [52] constructed a computer simulated model for random aggregation that is diffusion limited and demonstrated that the density correlations within the model aggregates fall off with distance in a fractional power–law, like that of the metal aggregates. Following their earlier work, Witten and Sander [53] showed that by constructing diffusion-limited aggregation models, the objects so formed are scale-invariant whose fractional dimensionality (Hausdorf dimension) is independent of short-range details. Additionally, they showed that diffusion-limited aggregation has no upper critical dimension. This study made the point that the properties associated with scale invariance are long-range and universal, and that such long-range properties do not arise from long-range forces—rather, these long-range correlations are built up by short-range forces. In 1983, diffusion-limited cluster–cluster aggregation models were introduced by Meakin [54] and Kolb et al. [55], serving to fuel the flurry of interest in analyzing the structural properties of aggregated colloids using fractal theories generated by the work of Witten and Sanders. Meakin's and Kolb et al.'s simulation studies suggested that the colloidal aggregates behave as

stochastic mass-fractals on a scale that is large compared to the primary particle size. Subsequent experimentation by Weitz et al. [56,57] on aqueous gold colloids and Schaefer et al. [58] on colloidal aggregates of small silica particles confirmed the behavior suggested by the simulations. Following this, Brown and Ball in 1985 produced a computer model that simulated chemically limited aggregation and suggested that the structures so formed should also behave as mass fractals. Much experimental work in this area ensued in the following years, with Aubert and Cannell performing further work on colloidal silica aggregates [59], Schaefer and Keefer [60], Courtens et al. [61], and Vacher et al. [62] on silica aerogels, Rojanski et al. [63] on mesoporous silica gels, Dimon et al. [64] on gold colloids, Bolle et al. [65] on polystyrene lattices, and, in a *Nature* paper, Lin et al. [44] investigated three different colloids—colloidal gold, colloidal silica, and polystyrene latex. In all the experimental work detailed previously, the fractal nature of the colloidal aggregates was well demonstrated. Additionaly, colloidal-like gels, such as casein gels [66], have been shown to be composed of homogenous clusters of particles, with the structure within the clusters being fractal in nature.

For a particulate system that is composed of a number of aggregate clusters that are fractal, the number of particles, which are assumed identical, making up the fractal aggregate may then be given by (following equation 2):

$$N_a(\xi) \sim \left(\frac{\xi}{a}\right)^D \tag{3}$$

where $N_a(\xi)$ is the number of particles in a fractal aggregate of size ξ, containing particles of size a, and the system is assumed to be fractal within the range bounded by the size of one primary particle and the size of the entire structure. The particle volume fraction of the object may be expressed in terms of the size of the aggregate and the fractal dimensionality, if one assumes a model such as is described next, originally developed by de Gennes [67] for polymer gels, independently by Brown [68] for a network of fractal clusters, and shown experimentally to be applicable to colloidal gels by Dietler *et al.* [69] and others. The treatment below is loosely adapted

from Bremer *et al*. [66], since these researchers provide an elegant development of the model originally developed by de Gennes and Brown.

One may imagine that a regular square lattice is laid over the fractal object, where each lattice site is occupied by a primary particle, or by a volume element of solution (Figure 5). If the particles are arranged in a fractal manner, the number of occupied lattice (or aggregate) sites is given by equation (3). It is important to note that each particle does not completely fill each lattice site; we do not often encounter square particles in nature. The total number of available, unoccupied lattice sites in the 2-dimensional lattice shown in Figure 5 (N) is given by:

$$N = \left(\frac{\xi}{a}\right)^2 \tag{4a}$$

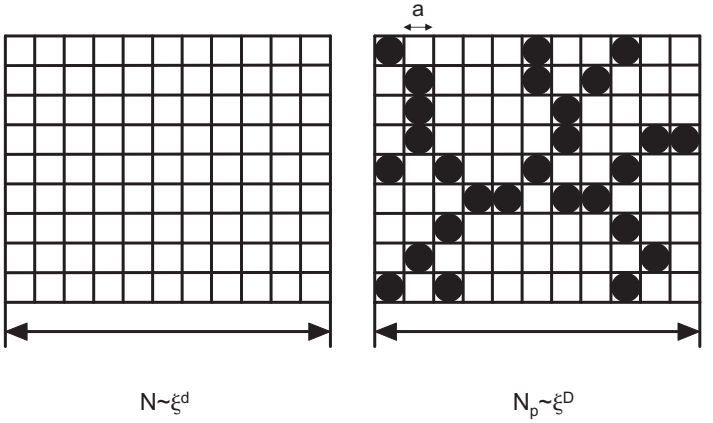

$$\Phi = N_p V_p / NV \sim (\xi/a)^D/(\xi/a)^d$$
$$\Phi \sim (\xi/a)^D/(\xi/a)^d = (\xi/a)^{(D-d)}$$
$$\Rightarrow \xi \sim a\Phi^{1/(D-d)}$$

Figure 5 Square two-dimensional microstructural lattice representing a putative aggregate in which particles are embedded.

The model assumes a square lattice, with square lattice elements, which is not usually the case, so that equation 4a is more correctly written as:

$$N \sim \left(\frac{\xi}{a}\right)^2 \tag{4b}$$

Therefore, the volume fraction of particles within this two-dimensional lattice (Φ) is given by the ratio of occupied lattice sites (N_p) to the total number of available, unoccupied lattice sites (N):

$$\Phi = \frac{N_p}{N} \sim \frac{(\xi/a)^D}{(\xi/a)^2} = \left(\frac{\xi}{a}\right)^{D-2} \tag{5}$$

According to the models for cluster–cluster diffusion-limited aggregation, which were verified experimentally as discussed earlier, the aggregates grow until they become space filling, thus forming a gel. Therefore, the fractal dimensionality within each gel is maintained, while, at length, scales above the characteristic length of one aggregate, i.e., the colloid scales in a Euclidean manner. The sum of all available lattice sites in the gel (N_t), which is a space-filling collection of aggregates, occupied by both solution and particles is given by:

$$N_t = \sum_{i=1}^{n} N_i \sim \sum_{i=1}^{n} \left(\frac{\xi}{a}\right)_i^2 \tag{6}$$

where n is the total number of aggregates in the gel. Therefore, the overall volume fraction of particles, Φ_t, is given by the total number of sites filled by particles divided by the total number of sites in the gel:

$$\Phi_t = \frac{\Phi \sum_{i=1}^{n} N_i}{N_t} \sim \frac{\Phi N_t}{N_t} = \left(\frac{\xi}{a}\right)^{D-2} \tag{7}$$

This model assumes that the gel is a space-filling collection of aggregates, each having the same volume fraction of particles within the aggregates (Φ).

From equation 7:

$$\xi \sim (\Phi_t)^{\frac{1}{D-2}} \tag{8}$$

Therefore, the characteristic diameter of an aggregate is related to the overall volume fraction of particles via the mass fractal dimension of the aggregates. As will be discussed in the next section, this relationship suggests that the two factors influencing this relationship are the degree of occupancy of the regular lattice by particles and the degree of the packing order of the lattice sites by particles.

2.3. Elastic Properties of Colloidal Gels: Exploiting theFractal Nature of the Aggregates

Colloidal gels respond to small amplitude deformations as elastic solids. In 1986, Sonntag and Russel [70] showed that the storage modulus of a volume-filling network formed by Brownian flocculation of aqueous polystyrene lattices scaled with the volume fraction of particles in a power–law manner, given by:

$$G' \sim \Phi^{\mu} \tag{9}$$

Sonntag and Russel were not the first to experimentally demonstrate this behavior for aggregated systems. For example, other researchers, such as Nederveen [3] and van den Tempel [8] showed that storage modulus of dispersed systems of microcrystals formed from oils vary with the particle concentration in a power–law manner, and Payne [6] showed that the storage modulus of systems formed from aggregates of carbon-black particles in mineral oil demonstrated a power–law relationship with particle concentration. Buscall [71] demonstrated a similar relationship with systems of polystyrene lattices in water. However, Sonntag and Russel were among the first researchers to suggest that scaling arguments put forward by other researchers, such as Kantor and Webman [72], on the elastic properties of random percolating systems and computer simulations of random lattices by Feng et al. [73,74] may support the relationship that they observed experimentally. At this point, however, the scaling theory had not been developed sufficiently to totally explain the experimental behavior observed by Sonntag and Russel.

Brown [68], soon after, addressed the elasticity of a network of clusters. His method consisted of calculating the elas-

ticity of an individual fractal cluster and then supposing that in an overcrowded system, fractal behavior survived on a scale related to the overall volume fraction by:

$$\xi \sim \Phi^{\frac{1}{D-3}} \tag{10}$$

which is the same relationship arrived at in the treatment above (equation 8). Brown predicted that the storage modulus should scale in the following manner:

$$G \sim \Phi^{\mu} \tag{11}$$

which is consistent with that seen by Sonntag and Russel and a number of other researchers, cited earlier. Additionally, Brown suggested that the exponent u is given by:

$$\mu = \frac{3 + d_{chem}}{3 - D} \tag{12}$$

where d_{chem} is the so-called chemical length exponent introduced earlier in simulation studies by Brown and Ball [75]. Soon after the model of Brown, Buscal et al. [71] published experimental evidence supporting this model for a system of silica particles. Later work by Ball [76] on the elasticity of aggregates explains higher fractal dimensions than were originally suggested by Kolb et al. [55] and Meakin [54] and had been reported by Courtens et al. [61] and Vacher et al. [62], by considering that there may be consolidation beyond a critical size of the clusters. Soon after, Edwards and Oakeshott [77] outlined broad guidelines for the treatment of the transmission of stress in an aggregate without really achieving more than stating the complexity involved. However, this work is worth mentioning here because it does point out that the model by Brown [68] assumes that stress is transmitted in one-dimensional paths that are branched and are characterized by a fractal dimension, while, in some cases, the situation is more complicated, because the stress has to be spread among several neighbors in order to maintain stability of the aggregate.

Following Brown and Ball, Bremer et al. [66,78,79] suggested elastic models for colloidal protein networks. These researchers envisioned the networks to be composed of strands of elastic material, where deformation causes a stretching of

the strands of the network. The storage modulus is then a function of the number of stress-carrying strands per unit area, the geometry of the network, and the character of the bonds within the strands. Bremer et al. formulated two different scaling relationships for the storage modulus to the particle volume fraction that depend on the geometry of the strands. For straight stress-carrying strands, the relationship is:

$$G' \sim \Phi^{\frac{2}{3-D}} \tag{13}$$

while for curved stress-carrying strands the relationship is:

$$G' \sim \Phi^{\frac{3}{3-D}} \tag{14}$$

In 1990, Shih et al. [80] developed a scaling theory to explain the elastic properties of colloidal gels well above the gelation threshold. The model of a colloidal gel visualized by Shih et al. corresponds well with the model of a colloidal gel described earlier: i.e., they define a colloidal gel above the gelation threshold to be a collection of flocs or clusters, which are fractal in nature. These researchers defined two regimes based on the relative value of the elastic constant of the interfloc links to that of the flocs themselves, and claim that the scaling in these types of gels is affected mainly by the structure of the individual flocs, as opposed to percolation-type scaling.

An in-depth development of the model created by Shih et al. [80] is provided next, since this model is used extensively in other parts of this section. In large part ignoring the progress made in describing the scaling relationship of the characteristic length of the cluster/floc size with particle volume fraction for colloidal gels described earlier, Shih et al. uses this identical relationship (given by equations 8 and 10), but justifies its use because of the fact that it was found to be true for polymeric gels by de Gennes [67]. They defend the use of this relationship for colloidal gels because colloidal gels are similar to polymeric gels by the fact that both are viscoelastic materials, and that both are formed by aggregation processes; polymeric gels by polymerization and/or crosslinking, and colloidal gels by particle aggregation. However, Shih et al. does quote the experimental evidence of Dietler et al. [69] for the

validity of this relationship for colloidal gels. It is important to mention that there is indeed sound theoretical reason why this relationship may be used for colloidal gels as well, as was developed and discussed earlier (after Brown [68], and Bremer [66]).

According to Shih et al., the elastic properties of a floc/cluster is dominated by its effective backbone (connected path of particles responsible for transmission of stress), the size of which is ξ, same as the size of the floc/cluster. This backbone may be assumed to be a linear chain of springs, with each spring representing the bond between particles forming the backbone; a justifiable assumption, since the formation of aggregates via cluster-cluster aggregation which is either reaction limited or diffusion limited have very few loops. The point made by Edwards and Oakeshott [77], as discussed above, concerning the limitations of an effective backbone argument must also be reiterated at this point—it is not entirely clear to the author whether this is a valid assumption, for the reasons given by Edwards and Oakeshott. An earlier publication by Kantor and Webman [72] formulated the elastic constant of a linear chain of springs as:

$$K_s = \frac{G}{N_{bb} S_{\perp}^2} \tag{15}$$

where G is the bending elastic energy, N_{bb} is the number of springs in the chain and $S_{\perp}$ is the radius of gyration of the projection of the nodes of the chain in the **F** x **Z** direction, **F** being the applied force and **Z** being the displacement normal to the plane within which the chain lies. Equation 15 ignores the stretching elastic energy of the chain, since it has been shown by Kantor and Webman [72] to be negligible for long chains, and is only important for comparatively straight chains stretched along their long dimension. Therefore, when the chain in question is the effective backbone of a floc/cluster, the elastic constant of the floc is given by:

$$K_{\xi} = \frac{G}{N_{bb} \xi^2} \tag{16}$$

where the radius of gyration has now been replaced by the size of the effective backbone (or the size for the floc), since

these two quantities would be the same. Now, the backbone of the flocs themselves are fractal objects, for which a fractal dimension between 1 and 2 can be defined, since instead of a straight chain, the backbone would have a certain tortuosity. In keeping with the fractal concept, where a line is kinked enough so that its dimension is raised to a fractional index between 1 and 2, the number of particles, and therefore the number of springs, in the backbone is given by:

$$N_{bb} \sim \xi^x \tag{17}$$

where x is the fractal dimension of the effective backbone, or the tortuosity of the effective backbone, and $x \geq$ in order to provide a connected path through the floc/cluster. Now, combining equations 16 and 17, one may represent the elastic constant of the floc by:

$$K_\xi \sim \frac{G}{\xi^x \xi^2} = \frac{G}{\xi^{2+x}} \tag{18}$$

Now, if the elastic energy G is not a function of concentration, then the elastic constant of the flocs should decrease rapidly with increasing floc size. This point strikes the author as being suspect, because it is inconceivable that the elastic energy of a bent chain is not dependent on the density of the springs which comprises the chain. It is conceivable that the density of the particles (density of springs) never really changes with concentration because the length of the effective backbone (length of the chain) also changes with concentration (via equation 8). If the change in particle volume concentration of the entire system is compensated for in terms of an increased effective backbone length, resulting in no change of the density of particles in the effective backbone, then the bending elastic energy, G, may be considered independent of particle volume concentration. Therefore, if the flocs are allowed to grow larger, they behave as weaker springs. Now, the macroscopic elastic constant of the system of flocs may be expressed either as a function of the elastic constant of the flocs, K_ξ, or the elastic constant of the links between flocs, K_l, depending on the relative strength of K_ξ and K_l because, from equations 8 and 10, the characteristic length of the flocs/clusters, ξ, is re-

lated to the particle volume concentration, and because the elastic constant of the flocs will decrease with increasing ξ to a power of 2 + x(>3), the relative strengths of K_ξ and K_l will be affected by the particle concentration of the system. To illustrate this, one may express the elastic constant of the flocs in terms of the particle volume concentration, by substituting for ξ in equation 18:

$$K_\xi \sim \frac{G}{\xi^{2+x}} \sim \frac{G}{\left(\Phi^{\frac{1}{D-3}}\right)^{2+x}} = \frac{G}{\Phi^{\frac{2+x}{D-3}}} = G\Phi^{\frac{2+x}{D-3}} \tag{19}$$

Therefore, the elastic constant of the flocs will get larger with increasing particle volume concentration. Obviously, as the particle volume concentration increases, there will be a cross-over point at which the elastic constant of the flocs is greater than the elastic links between the flocs, resulting in the elastic constant of the entire system being determined by the nature of the links between clusters (this is called the weak-link regime). The converse, where the particle volume fraction decreases beyond the cross-over point, is also true, and in this case the elastic constant of the flocs grow weaker than the elastic constant of the links between flocs, leading to the elastic constant of the system being determined by the nature of the elastic constant of the flocs (this is called the strong-link regime).

Therefore, for the strong-link regime, the macroscopic elastic constant of the system is given by:

$$K \sim \left[\frac{L}{\xi}\right] K_\xi \tag{20}$$

where L is the macroscopic size of the system. Therefore, for a constant macroscopic size of the system, combining equation 20 with equation 19, and again substituting for ξ from equation (8):

$$K \sim \xi^{-1} G\Phi^{\frac{2+x}{3-D}} \sim \Phi^{\frac{1}{3-D}}\Phi^{\frac{2+x}{3-D}} = \Phi^{\frac{3+x}{3-D}} \tag{21}$$

assuming that the elastic energy of the effective backbone does not change with concentration. Therefore, the macroscopic elastic constant of a colloidal gel at comparatively low concentrations is given by (the strong-link relationship):

$$K \sim \Phi^{\frac{3+x}{3-D}} \tag{22}$$

As is evident from equations (22) and (12), the strong-link formulation of Shih et al. is consistent with that developed by Brown [68], if one assumes that the tortuosity, x, is the same as the chemical length exponent, a concept which is does not deviate from the explanation offered by Brown. Shih et al. [80] also studied two types of boehmite alumina gels, Catapal and Dispal powders, rheologically. The elastic behavior of both gels confirmed the strong-link relationship given by equation (22). Fractal dimensions calculated from the rheologic measurements agreed well with those calculated from static light-scattering measurements.

For the weak link regime, the macroscopic elastic constant of the system is given by:

$$K \sim \left[\frac{L}{\xi}\right] K_l \tag{23}$$

Substituting for ξ from equation (8):

$$K \sim \Phi^{\frac{1}{3-D}} \sim G' \tag{24}$$

where G' is the shear storage modulus of the system. Here, equation (24) assumes that the links between flocs/clusters are of constant strength. It is important to note that the elastic constant of the links between flocs is not expressed in terms of the geometry of the network. However, equation (24) does provide a scaling relationship of the elastic constant of colloidal gels at high concentrations, with the particle volume fraction.

After the development by Shih et al. [80], Chen and Russel [81] studied the elastic behavior of a synthesized model system consisting of submicrometer silica spheres coated with octadecyl chains suspended in hexadecane. This study demonstrated that the storage modulus of the colloidal system increased with particle volume concentration in a power–law manner, and that the power–law exponent increased with increasing temperature, indicating a structural change in the network. It was obvious that the power–law exponent was sensitive to the packing of the particles (disturbed when the temperature is increased)—suggesting that the power was

dependent on the fractal dimension. This work further served to lend credibility to the scaling models outlined by Brown [68], Bremer [66,78] and Shih et al. [80].

Vreeker et al.[82] showed that colloidal-like aggregates of whey protein gels are fractal in nature, utilizing dynamic light scattering measurements. Additionally, they analyzed the protein gels rheologically, showing that the elastic moduli and yield stresses varied with protein concentration according to a power–law. They related the power–law exponent to the equivalent models by Brown [68] and (strong-link model) by Shih et al. [80], and to the models by Bremer [66,78]. By the value of the exponent measured experimentally, they were able to calculate fractal dimensions according to the various models. The fractal dimensions so calculated were all in reasonable agreement with those measured by the dynamic light scattering experiments. Therefore, based on their experiments, these researchers concluded that there was no basis for the validity of one model versus another, which partly stemmed from their inability to measure the chemical length exponent or tortuosity. In this work, they assumed x had a value which varied between 1.0 and 1.3 (suggested by Shih et al. [80] based on conductivity measurements).

Hagiwara et al. [83,84] have analyzed a number of different types of protein gels using both rheologic measurements to study the elasticity of the gels, and analysis of confocal laser scanning microscopy images of the gels, to study the structure of the gels. These researchers found that for the gels they studied, the weak-link regime of Shih et al. [80] was valid. The gels demonstrated a power–law dependence on particle volume concentration, and the fractal dimensions calculated from the power–law exponent, using the weak-link formulation, agreed very well with fractal dimensions calculated from image-analysis of the confocal laser scanning micrographs of the gels. Therefore, both the strong-link formulation and the weak-link formulation of Shih et al. [80] have been demonstrated experimentally. The weak link has been demonstrated more convincingly, because, with the strong-link regime, experimentalists have had to assume a value for the tortuosity

of the backbone, and, therefore, the theory could not be tested well against Bremer's theories [66,78].

2.4 Application of Scaling Theory Developed for Colloidal Gels to Fat Crystal Networks

In 1992, Vreeker et al. [35] presented an interpretation of rheologic data for aggregate fat networks in the framework of scaling theories developed for colloidal gels. These authors showed that the storage modulus of the network (G') varied with the volume fraction of solids (Φ_{SFC} = SFC/100), according to a power–law, similar to that predicted by models for the elasticity of colloidal gels. It is important to remember that Φ_{SFC} is not equivalent to the particle volume fraction Φ. However, in the Vreeker et al. [35] paper, and in many similar publications after, these two parameters have been used as being equivalent. As will be demonstrated below, Φ_{SFC} and Φ are directly proportional to each other. For the sake of simplicity in the treatment that follows, these two parameters will be considered equivalent. The article by Vreeker et al. provides an interpretation of rheologic data for low Φ fats in terms of the strong-link model of Shih et al. [80], developed, as detailed earlier, for colloidal gels at low particle concentrations. From this rheologic investigation of the fat network, a fractal dimension could be calculated using the strong-link formulation given by equation (22) and assuming that the tortuosity of the system, x, had a value between 1 and 1.3. This article also details the measurement of a fractal dimension of the network via light scattering methods, which agreed well with that calculated from the strong-link formulation. However, no attempt was made in this article to show that the structure of a fat crystal network at such low SFCs (low Φ) is organized in a similar manner to the way a colloidal gel is organized in order to warrant the use of the strong-link formulation. It was unclear as well, in this article, what the primary particles of the gel constituted and at what length scales the network was fractal (although the fact that light scattering methods were used to calculate the fractal dimension suggests that perhaps the length scales of importance lay in the microstructure region, i.e., at a length scale greater than the crystalline level of structure). Therefore, this article served solely to demonstrate

that the elastic constant of the network varied in a power–law manner, reminiscent of that demonstrated by colloidal gels. No justification for using the strong-link model was made from a structural perspective, mainly because these authors did not adequately define the structure of the network. However, this article remains one of the most important developments in the field, for it demonstrated conclusively that the storage modulus of low Φ fat crystal networks scale in a power–law fashion with the solid fat content. The physical and structural implications of the calculated fractal dimension using the strong-link formulation of Shih et al. [80] was, at this point, unclear.

Work by Johansson [85] provided strong experimental evidence for the fractal nature of fat crystal networks, as well as showed for the first time that the relationship $\xi \sim \Phi^{1/(D-3)}$ held for fat crystal netwoks, which could then be considered as weak gels of crystals dispersed in oil.

The analyses of Vreeker et al. and Johansson were interesting enough for Marangoni and Rousseau [13] to apply the model developed by Shih et al. [80] for high-concentration colloidal gels (weak-link theory described earlier) to fat crystal networks of high solid fat concentration. As explained previously, the weak-link model offers the ability to relate small deformation rheologic measurements (shear storage modulus) to the fractal dimension of the network. As was the case with the work by Vreeker et al. [35], Marangoni and Rousseau had no structural basis on which to justify the application of the weak-link theory, developed for a particular geometry of colloidal aggregates, to fat crystal networks. The main reason for applying this type of analysis was the fact that the analysis by Vreeker et al. [35] produced a power–law relationship for low SFC fats. Additionally, as described before, the only variation of structure that accompanied the decrease in hardness index and elastic moduli of milk fat upon chemical interesterification was a change in the microscopically observed microstructure. Marangoni and Rousseau [13] attributed the weak-link model with a quantification of the microstructure of the network, but offered no explanation as to why the fractal dimension calculated from the application of the weak-link theory was a quantification of microstructure. However, the rheo-

logic application of the weak-link theory of Shih et al. [80] to NIE and CIE milk fat blends demonstrated a power–law relationship between the shear elastic moduli of the networks and the SFC of the networks, given by $G' \sim \Phi^{\mu}$. Fractal dimensions calculated using the weak link theory produced fractal dimensions of 2.46 and 2.15 for the NIE milk fat and CIE milk fat, respectively. Given that there was a qualitative change in microstructure on chemical interesterification and that there was a large change in the fractal dimension of these gels on application of the weak-link theory, it did indeed seem possible that the fractal dimension was a measure of microstructure, albeit in some undefined manner. At any rate, Marangoni and Rouseau [13] attributed the change in structure indicated by a change in fractal dimension to the change in hardness of the milk fat on chemical interesterification, a reasonable conclusion. In defense of the claim by Marangoni and Rousseau [13] that the fractal dimension was in some manner a quantification of microstructure, it must be recalled that Vreeker et al. [85] utilized dynamic light scattering measurements to calculate a fractal dimension that agreed well with their rheologic analysis, therefore suggesting that the structures that were indeed fractal are in the microstructure.

Following their 1996 work, Rousseau and Marangoni [31] utilized the weak-link model to analyze the rheologic behavior of NIE milk fat and enzymatically interesterified milk fat (EIE). The fractal dimension of milk fat changed from 2.59 to 2.50 on interesterification. However, there was also a large decrease in SFC on enzymatic interesterification, so that the drop in hardness index and shear elastic moduli observed by these authors was mainly due to the decrease in SFC. However, here again, the rheologic scaling behavior was observed, and fractal dimensions could be calculated from the weak-link formulation. One is reminded by the results of this study that indicators of macroscopic mechanical properties such as SFC are indeed valid and necessary for a comprehensive description of the mechanical properties of the network, although, as with the case of the CIE and NIE milk fat samples detailed earlier, such variables are not always direct indicators of changes in mechanical properties.

Marangoni and Rousseau [31] also studied the rheological scaling behavior of NIE and CIE lard-canola oil blends and palm oil-soybean oil blends. The power–law relationship of storage modulus to SFC was again observed, and fractal dimensions could be calculated for all the systems by using the weak-link formulation. No change was observed in hardness index or storage modulus of the palm oil-soybean oil blends on CIE, nor were there any changes in the fractal dimension after CIE. Solid fat content did not change, either. Therefore, it seems that the fractal dimension was, indeed, an indicator of macroscopic hardness: whether this was true because it was an indicator of the microstructure could not reasonably be extrapolated from the evidence presented by Marangoni and Rousseau [31]. The hardness index and elastic moduli of lard increased with CIE, but the fractal dimension did not change, and neither did the SFC. It therefore appears, at first glance, that not only is the SFC an insensitive indicator of macroscopic hardness but so is the fractal dimension. Here, again, one is reminded that there are many structural indicators of macroscopic mechanical properties, and one must consider them all in concert. However, are there other indicators of hardness that can be accessed through the rheological analysis? At this point, it is perhaps important to briefly examine the method of rheologic analysis used by these authors. The weak-link theory of Shih et al. was tested by plotting ln G′ as a function of ln Φ for various fat systems. According to the weak-link theory of Shih et al. (equation 24) the slope of such a plot should yield $1/(3-\mathrm{D})$. What about the intercept of the graph? Marangoni and Rousseau [31] wrote equation 24 as:

$$G' = \gamma \Phi^{\frac{1}{3-D}} \tag{25}$$

and defined γ a constant that is related to the particles that make up the network. In this, Marangoni and Rousseau were influenced by Bremer et al. [78], who, in their publication, formulated a similar law in which the pre-exponential factor was a constant depending on the nature of the particles and the links between them. Equation (25) bears further scrutiny at this point—it should be evident that equation (24) may be written as:

$$G' \sim \Phi^{\frac{1}{3-D}} K_l \tag{26}$$

where, as the reader would recall, K_l is the elastic constant of the links between aggregates. Certainly, therefore, K_l would depend on the nature of the particles and the links between them, and would contribute to the value of γ. Although Marangoni and Rousseau (131) did not offer this justification for their description of the constant γ, it seems to be appropriate. At any rate, the intercept of the $\ln(G')$ vs. $\ln \Phi$ graph should yield $\ln(\gamma)$ as the intercept, allowing a value of γ to be calculated. Therefore, if the fractal dimension offered a quantification of the spatial distribution of the microstructure (as yet undefined now), then the constant γ contained information on the influence of the particles and the links between them on the elastic constant of the network. Now, on CIE, there was a four-fold increase in the value of the constant γ for the lard-canola oil system, which, according to equation (25), should have been accompanied by an increase in the storage modulus, as was observed experimentally by Marangoni and Rousseau. As for the palm oil-soybean oil system, there was comparatively no change in the value of γ.

As a matter of fact, the decrease in G′ and hardness index originally observed by Marangoni and Rousseau in 1996 was due to a decrease in γ rather than a decrease in the fractal dimension. A decrease in fractal dimension would have resulted in an increase in the elastic moduli and hardness! Thus, the parameter γ, at a constant SFC, was the true culprit in the observed decrease in mechanical strength on CIE of milk fat.

Therefore, the scaling behavior of the fat crystal network, if the weak-link is utilized, seems to suggest that there are three important indicators of macroscopic hardness: SFC, the fractal dimension, and the constant γ. It must be stated at this point that this does not mean that other indicators, such as the crystalline nature of the network and the molecular ensemble of the network, are being ignored by identifying D, Φ, and γ as the three important indicators. Since γ has been suggested to depend on the nature of the particles and the links between them, it almost certainly is dependent on the

polymorphism of the network, which in turn is dependent on the molecular composition of the network.

2.5 Network Models

As presented previously, phenomenologic investigations have been made on the rheology of fat crystal networks, the results of which have been interpreted by models developed for colloidal gels. Not only has this not been structurally justified but this analysis has excluded any structural and mechanical model of the fat network. In large part, the authors working in the field (mainly Marangoni and Rousseau et al. and Vreeker et al.) could not include a structural and mechanical model of the network, because, at the time, there existed no mechanical and structural model that predicted that the structure of the fat crystal network at any length scale was fractal in nature. It must also be mentioned that the scaling behavior demonstrated experimentally by these authors was not adequately explained by the existing network models. Presented in the following is a brief introduction to the network models that existed in the literature before the work being detailed in this publication.

Early work on a network model was performed by van den Tempel [7]. In his 1961 publication, he suggested modeling the network as a collection of particles held together by van der Waals-London forces. The structural model that was assumed by van den Tempel was that the network is made up of straight chains oriented in three mutually perpendicular directions, with each chain consisting of a linear array of particles. The bonds between particles were formed from van der Waals-London forces. The relationship of the storage modulus to the solid fat content of the network arrived at by van den Tempel is:

$$G' = \frac{5AD^{0.5}}{24\pi H_o^{3.5}}\Phi \tag{27}$$

where A is the Hamaker's constant, D is the diameter of the particles, H_0 is the equilibrium distance between particles, and Φ is the volume fraction of solids.

However, the relationship of G' to Φ in most fats, has been experimentally determined to be a nonlinear, power–law type

of relationship, as shown for palm oil diluted with soybean oil in Figure 6. The work by van den Tempel failed to correctly predict this experimentally observed power–law relationship of G' to Φ because, according to Vreeker et al. [35], it did not take into consideration the fractal arrangement of the network at certain length scales. Furthermore, van den Tempel only considered the attractive forces in his treatment, choosing to ignore whatever repulsive forces were present.

In 1963, Nederveen [3] used the same structural model as van den Tempel, but incorporated the repulsive forces acting between particles (he considered the Lennard-Jones potential

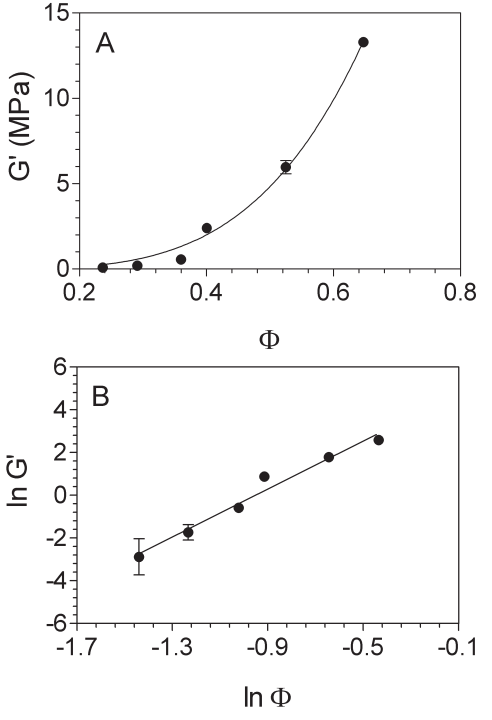

Figure 6 Power—law scaling behavior of the storage modulus (G') with solid fat content (Φ) for palm oil (**A**) and the corresponding linear log-log plot (**B**).

between two particles). Nederveen found the following formula for the modulus of elasticity:

$$E = \left(\frac{A\Phi}{2\pi d_o}\right)\left(1 - \frac{11R\varepsilon}{d_o^2}\right) \tag{28}$$

where R is the particle radius, ε is the strain of the deformation, d_o is the equilibrium distance between two particles, and A and Φ are as defined earlier. Again, Nederveen's formulation failed to show the nonlinear dependence on Φ, due, perhaps, to an unrealistic structural model of the network that did not involve the fractal geometry detailed in the previous section.

In 1964, Payne [6] tried to apply the linear chain concept of van den Tempel to carbon black networks in oil, but found that the shear modulus was inversely proportional to some power of the particle diameter, which was not in agreement with van den Tempel's or Nederveen's equation. This study may, however, be inconclusive about the validity of these equations because the discrepancy may have been due to the nonhomogenous distribution of the carbon black spheres.

In 1968, Sherman [86] proposed a different model for flocculated o/w emulsions involving chainlike configurations that form coils with cross-linkages, resulting in interlinked spherical structures. In his model, localized regions of densely packed particles are joined to less densely packed regions, so, consequently, the degree of interlinking is not the same throughout the entire flocculate. The formulation of G' for this model is:

$$G' = \Phi(1 + 1.828v)\frac{A}{36\pi D^3 H_o^3} \tag{29}$$

where v is the total volume of the continuous phase held in voids between the particles, D is the diameter of the particles, H_o is the minimum equilibrium distance between particle surfaces and A is called the interaction constant (Hamaker's constant) and Φ is as defined earlier. While Sherman's equation agreed with Payne's observations in terms of particle diameter, it also shows a linear relationship with Φ that is contrary to what has been demonstrated experimentally.

In 1979, van den Tempel [8] revised his structural model of fat crystal networks; he suggested that clusters (microstruc-

tures) of particles make up the chains rather than particles. Additionally, he suggested that the forces holding the clusters together were due to common "chains" of particles between clusters. He used this argument to modify his original equation, but again did not take into consideration any fractal arrangement of the network. He suggested, here, that the relationship between the shear elastic modulus and the volume fraction of solids was a nonlinear, power–law type of relationship ($G \sim \Phi^{\mu}$). Moreover, he observed that the scaling factor μ was proportional to the number of particles within the clusters and that several parameters that determine the state of aggregation of the system could be lumped into this scaling factor, μ. He also estimated that about 10^6 crystal particles made up the clusters and that increasing agitation lead to less aggregation. Various other researchers have tried to modify van den Tempel's work in varying degrees of complexity [1,2,4,5]. However, none of these models took into consideration a fractal arrangement of the network, and none demonstrated a power–law dependence of G' on Φ, which is observed experimentally.

3. WHERE LIES THE FRACTALITY IN FAT CRYSTAL NETWORKS?

In this section, the structure of fat crystal networks at the microstructure level will be investigated and discussed. It has been detailed in section 2 that other authors have attributed some amount of importance to the microstructure of fats. Particularly, the microstructure will be investigated so as to determine whether there is a structural organization present which warrants the application of the weak-link theory developed for colloidal gels to fat crystal networks. Furthermore, because the microstructure of fat networks have been rather loosely characterized before this work, effort will be made to utilize a number of different imaging techniques to provide a description of the network at the microstructure level that is supported by various types of microscopic evidence.

3.1 Characterizing Microstructure

Figures 7*A* and *B* show SEM micrographs of anhydrous milk fat with the liquid oil not removed. The entire network, how-

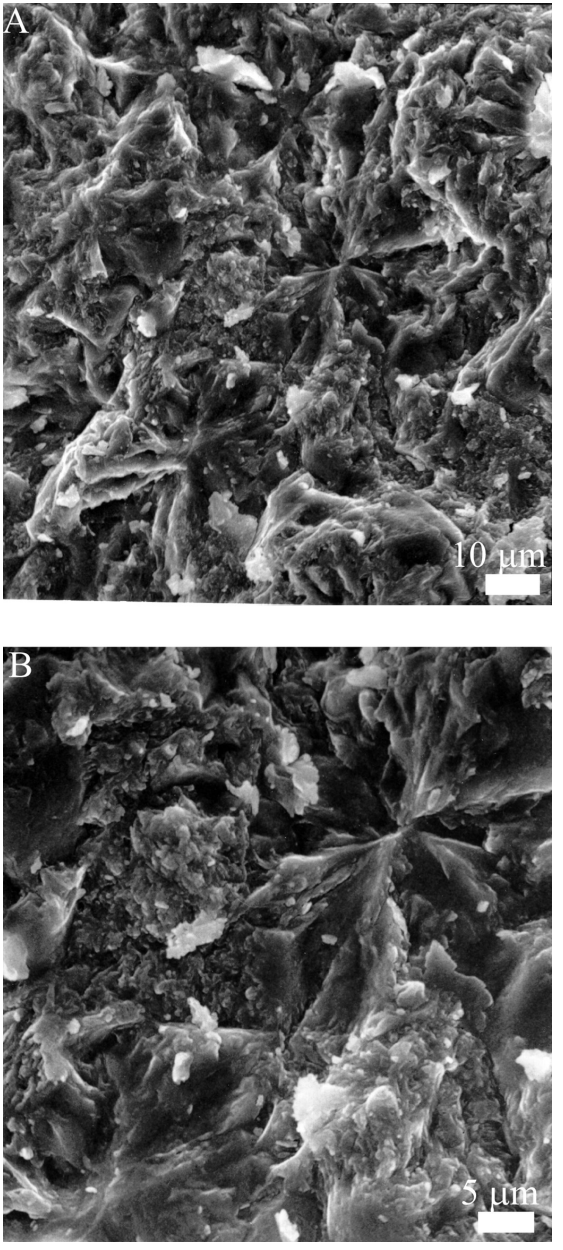

Figure 7 Freeze-fracture scanning electron microscope images of anhydrous milkfat, with the liquid oil in the samples not removed.

ever, has been frozen and then sputter-coated. As shown by Figure 7, it is difficult to tell which part of the structure is due to liquid oil and which to solid crystals. However, there does seem to be evidence of some type of repeating structure at the 30 μm range. Figure 8 shows a sample of CIE milk fat from which the liquid oil was not removed. Two structures are shown in this figure, which seem to be in the range of 50–60 μm, and, because this surface image is a fracture surface, these structures seem to belong to spherical structural entities in the fat. However, it cannot be ascertained whether the area around the two entities is frozen oil or of crystalline nature. The fracture plane being imaged here also does not necessarily pass through the equator of these entities. Therefore, these entities may actually be larger than represented. Figure 9

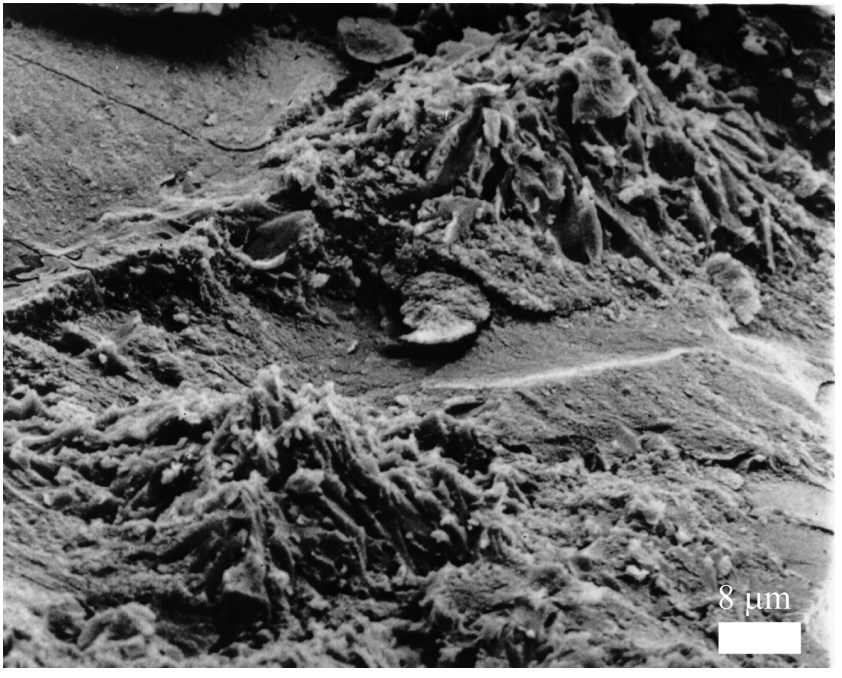

Figure 8 Freeze-fracture scanning electron microscope image of chemically interesterified milk fat, with the liquid oil in the sample not removed.

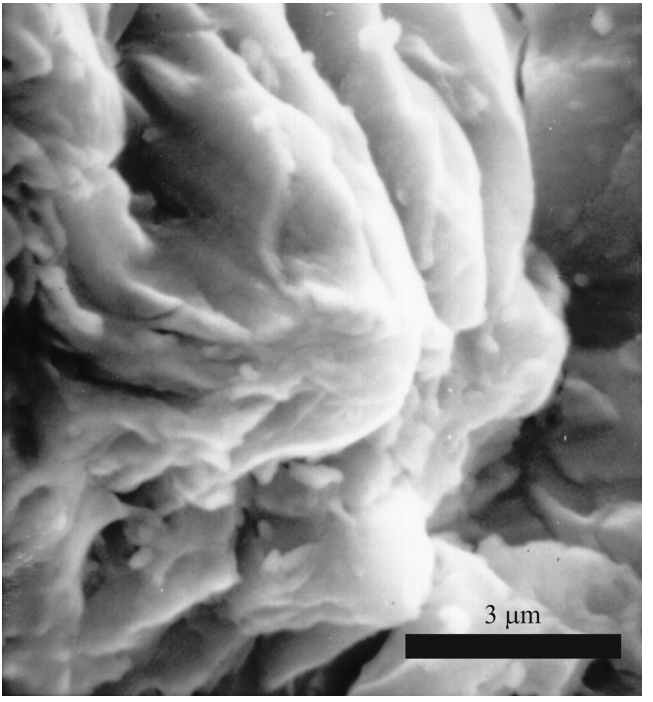

Figure 9 Freeze-fracture scanning electron microscope image of chemically interesterified milkfat, with the liquid oil in the sample not removed.

shows a micrograph from a sample of CIE milk fat, from which the liquid oil has not been removed. This micrograph shows a structural entity that is approximately 6 μm across, and which may be spherelike. Not much else can be determined from this micrograph. Micrographs of SEM images of fat are very typical of the images shown here. In other words, nothing definitive can be said about the structure of the fat network from such images in most cases due to the destructive sample-preparation methods necessary for SEM imaging.

Figure 10 shows polarized light micrographs of cocoa butter crystallized at 22°C for one day. The figure demonstrates dense "clusters" (which seem to be composed of smaller crystallites. The "particles" seem to be in the low micron range, but it

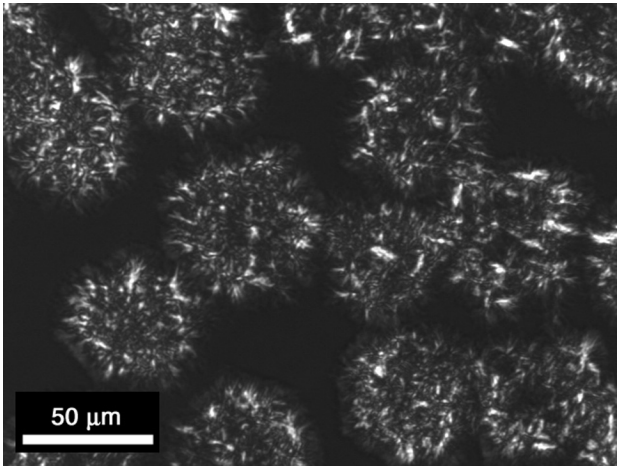

Figure 10 Polarized light micrograph of cocoa butter crystallized at 22°C for 1 day on a microscope slide under a coverslip.

is difficult to determine with certainty. Figure 11*A* shows a crystal cluster of anhydrous milk fat crystallized at 25°C for 24 hours, while Figure 11*B* shows the details of the interior of one of these clusters. The "particles" in this cluster are in the low micron range. In conjunction with evidence provided by Heertje and coworkers [10,26,87], which demonstrated that clusters as large as 100–200 μm are possible, this emerging picture of the network—clusters of small crystallites—is at least plausible.

Figure 12 shows confocal laser scanning micrographs of the crystal network of milk fat crystallized at 18°C in a 1-mm-thick film without a cover slip. The samples were negatively stained with Nile Blue, causing the solid crystals to appear as darker entities in the micrographs. It must be mentioned here that it is uncertain how the presence of Nile Blue affects the formation of the network itself. Figure 12 suggests that there are clusters present of the order of 30 μm. One must bear in mind that the individual "particles" are not present in this figure, because, here, the network is being observed at a lower magnification. Furthermore, there seem to be subclusters within the larger clusters, of the order of 70 μm. The evidence proposed by Figure 12 also is in agreement with the observa-

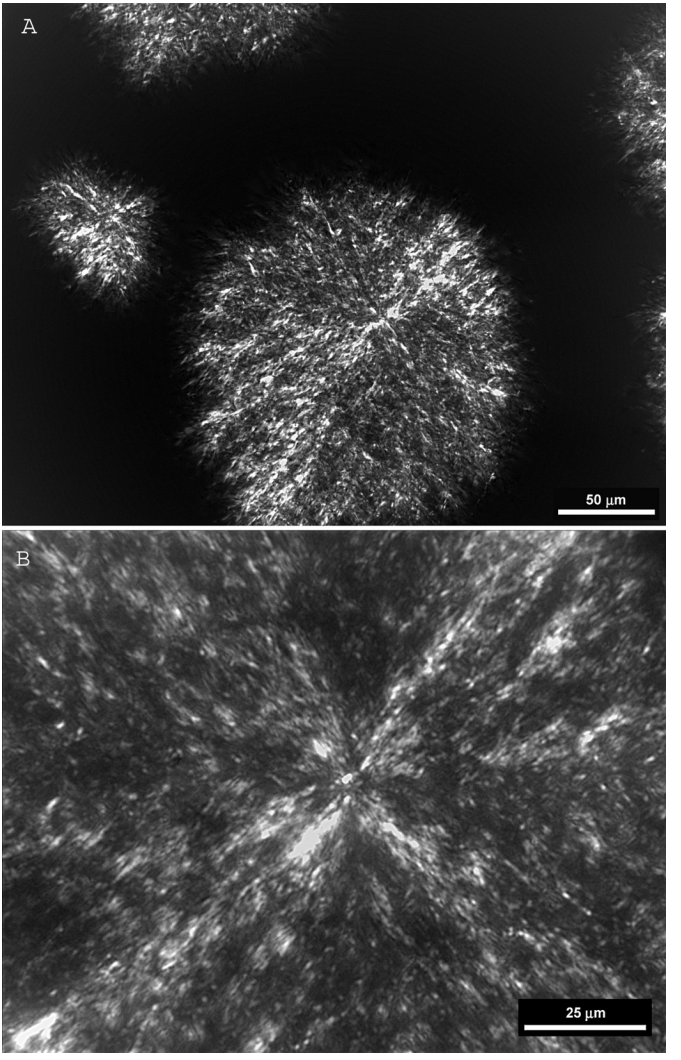

Figure 11 Polarized light micrograph of milkfat crystallized at 25°C for 1 day on a microscope slide under a coverslip at two different magnifications.

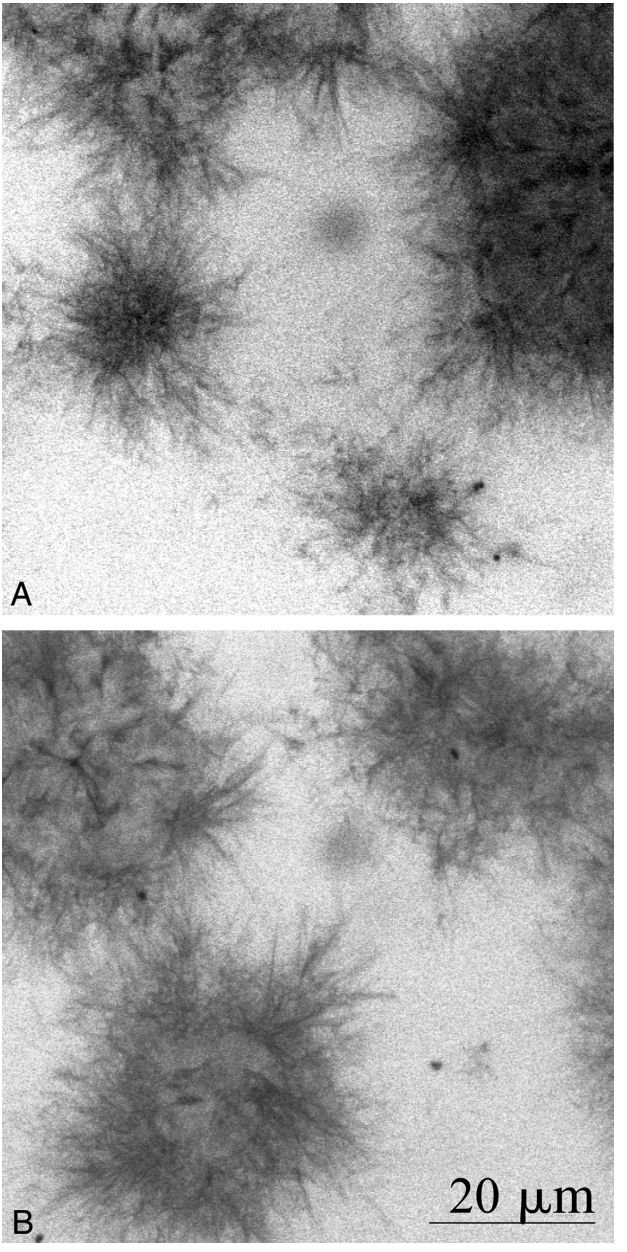

Figure 12 Confocal laser scanning microscopy images of milkfat crystallized at 22°C for 1 day and stained with Nile Blue.

tions of Heertje and coworkers, as they have reported cluster sizes of 100 μm in milk fat. Interestingly, the observations outline earlier are also supported by the SEM images shown in Figures 7–9. The structural entities shown in Figure 7 are almost certainly clusters of intermediate size (recall they were of the order of 30–40 microns in size) and the larger structures shown in Figure 8 are almost certainly the large clusters, i.e., clusters of clusters. The "particle" shown in Figure 9 is also of a similar size to the particles seen in both the polarized light micrographs shown in Figures 10 and 11. Therefore, the emerging picture of the structural arrangement of the fat crystal network at the microstructure scale has been consistent in the three different methods of imaging discussed thus far.

Figure 13 shows a composite of atomic-force microscopy images of a sample of the high-melting fraction of milk fat that was spin coated onto a silicon substrate. Figure 13*A* shows what appears to be a "particle" of the order of 4–5μm. The edges of this particle are not well defined, probably due to the nature of the atomic-force microscope's method of imaging. It is difficult to effectively define the boundaries between closely spaced particles because the vertical range of the atomic force microscope is limited; therefore, rather than define a definite boundary, the tip of the microscope will instead indicate a low point in the image, which may appear as an intermediate depth. Total darkness in these images represents the limit of the tip's vertical displacement, while the whitest color in the image represents the highest point in the image. Figure 13*B* identifies at least three neighboring "particles" of the same average size. Figure 13*C* and 13*D* show intermediately sized clusters of particles, while Figure 13*E* shows what appears to be a section of a large cluster of the order of 90μm–100μm. Figure 13*F* shows what appears to be the boundary between two or three large clusters. All of these images were imaged on the same sample, with Figure 13*E* located over a spot adjacent to the spot over which Figure 13*F* was located. Figures *13A–D* are all within the area shown in Figure 13*E*. Figure 14 shows a composite of images taken from the same sample as Figure 13, except that these images were taken over a different location on the surface of the sample. As can be seen, similar

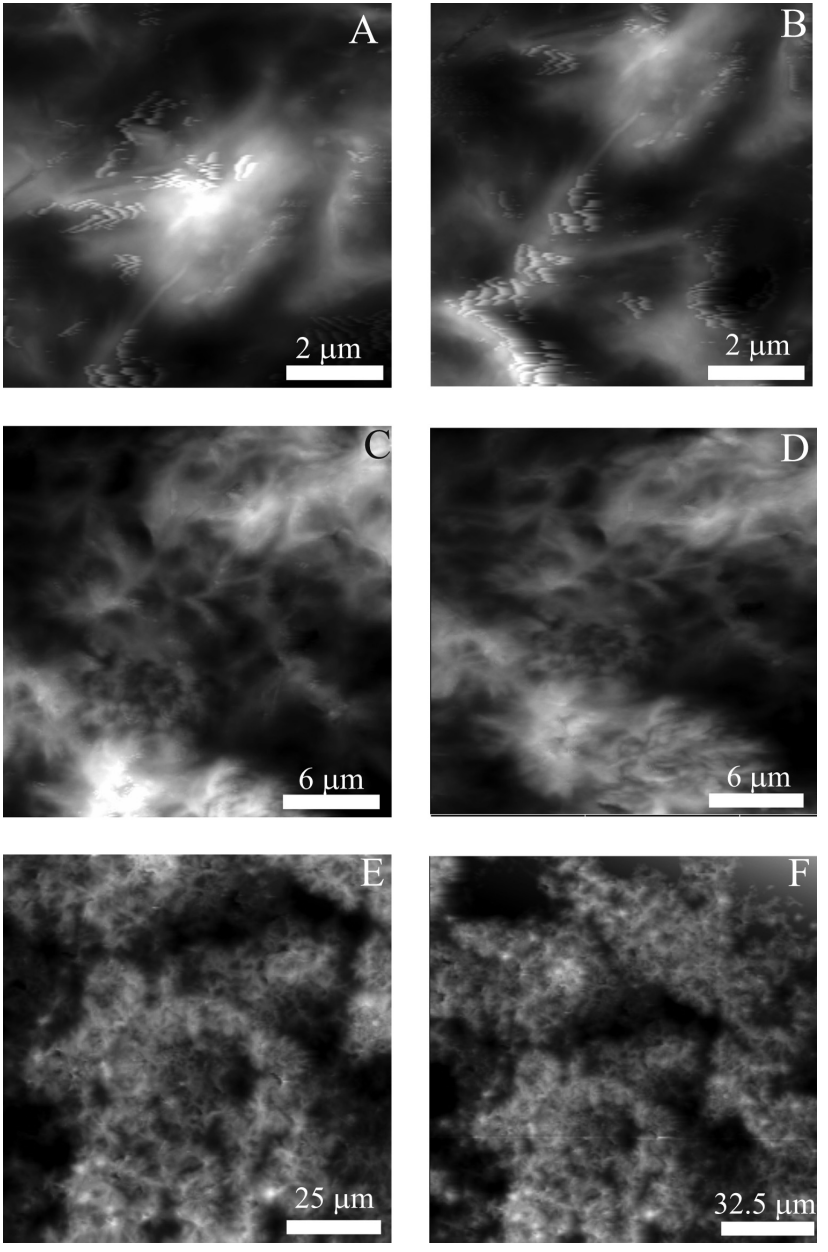

Figure 13 Atomic Force microscopy images of the high melting fraction of milkfat. Sample was spin-coated onto a silicon substrate.

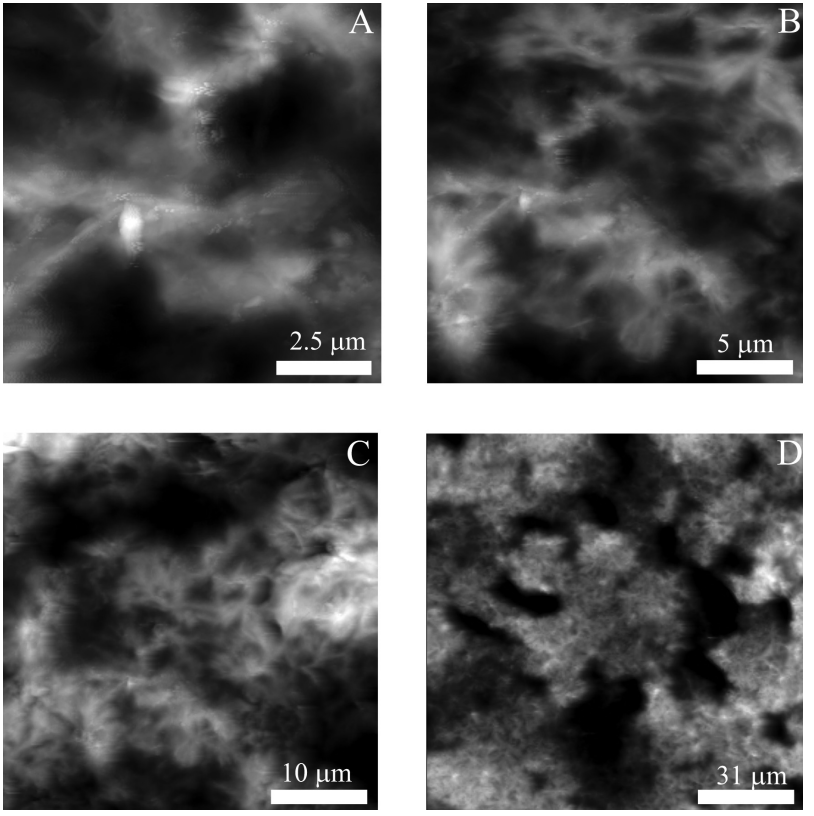

Figure 14 Atomic Force microscopy images of the high melting fraction of milk fat. Sample was spin-coated onto a silicon substrate.

types of structure as described previously are observed. Figure 15 is of the high-melting fraction of milk fat as well, only this sample was prepared in a rheologic mold rather than spin-coated onto a silicon substrate, as were the samples shown in Figures 13 and 14. As can be seen, this image is in agreement with Figures 13 and 14, except that, at the low magnifications (i.e., for Figures 15*D–F*), there are a series of very high, round spots. It is believed that these spots are due to wax particles found on the samples that were prepared in the rheologic molds (part of the process requires the sandwiching of the fat samples by Parafilm, which may have been contaminated with

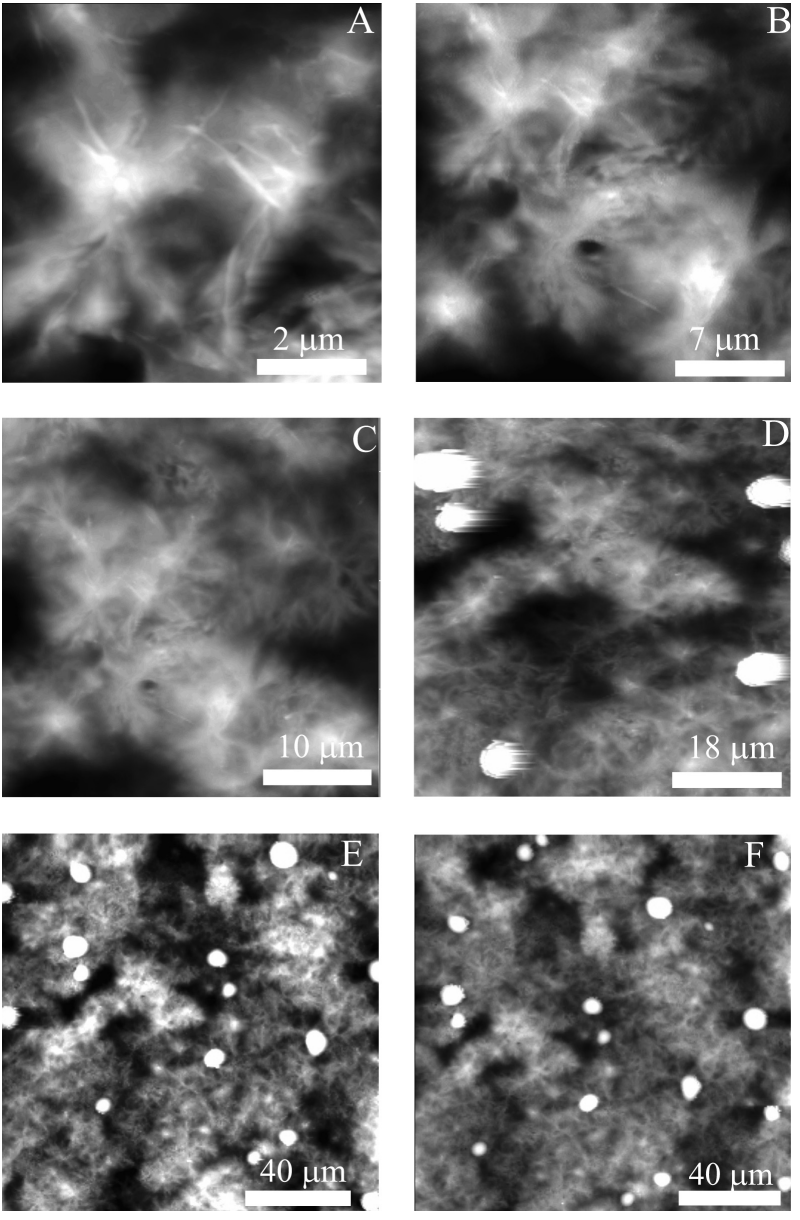

Figure 15 Atomic Force microscopy images of the high melting fraction of milk fat. Sample was prepared in a mold used in rheology studies.

dust or wax crystals) because these types of spots were observed with all the samples prepared in the molds. What is also important to note in Figures 13–15 is that the structures at different magnifications, i.e., at different length scales, look quite similar. These structures seem to demonstrate some sort of statistical self-similarity at different length scales, bounded by the size of one "particle" and the size of one large cluster (because, as we shall see from other images presented in this chapter and from Heertje and coworkers' publications, the large clusters pack in a regular space filling manner to form the network). Identification of self-similarity in natural structures is usually a rather qualitative process (due to the inexact nature of the self-similarity), such as the realization that clouds and trees are self-similar. However, this process is usually the first physical clue that the object under scrutiny may

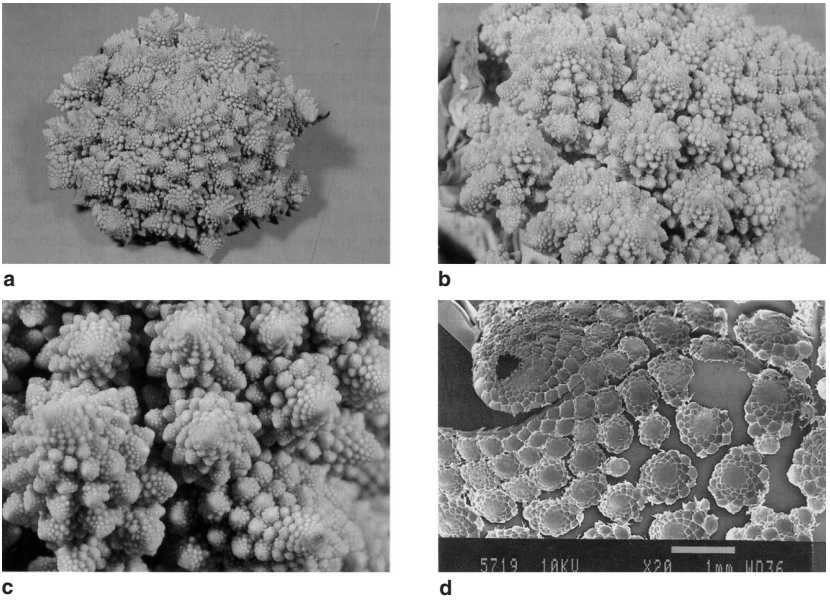

Figure 16 (**A–C**) Photographs of a Minaret cauliflower showing self-similarity at different length scales. (**D**) Electron micrograph (SEM) of Alverda cauliflower on submillimeter scale. (Adapted from Grey and Kjems, 1989).

be fractal in nature—for example, Figure 16 shows the qualitative self-similarity of a cauliflower, which is a typical natural fractal. Figure 17 show AFM images of a sample containing a 50:50 mixture of the high-melting fraction of milk fat (HMF) and the medium-melting fraction (MMF) of milk fat, spin coated onto a silicon substrate. Again, these structures are very similar to those of the high-melting fraction—individual particles (not very defined, for reasons mentioned earlier) seem to be arranged in clusters, which are further arranged

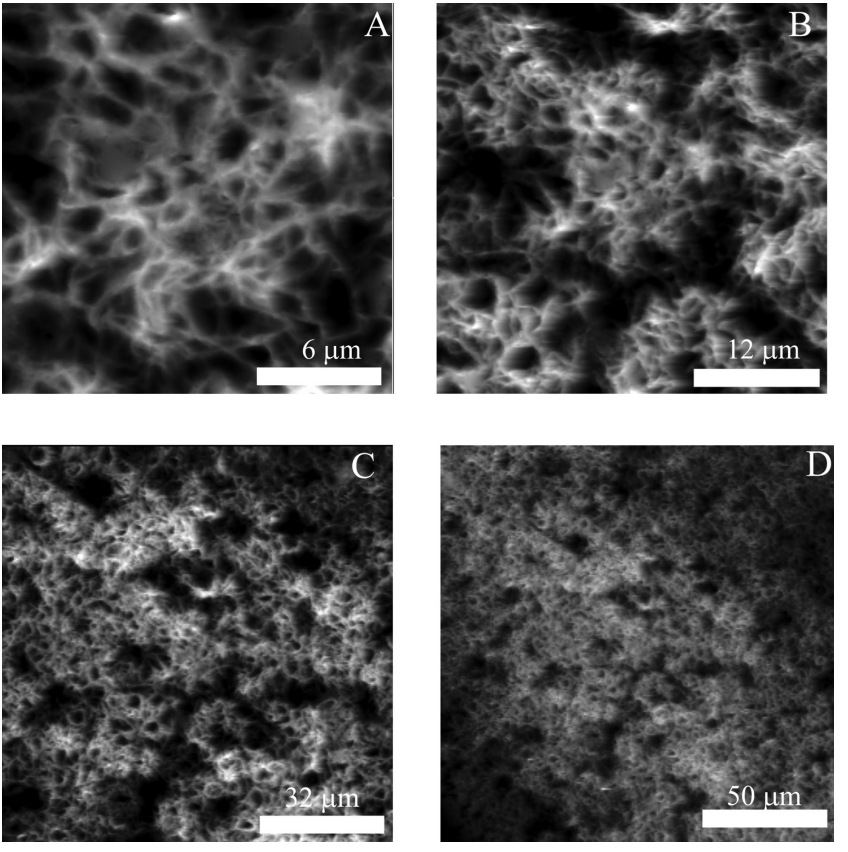

Figure 17 Atomic force microscopy images of a 50:50 w/w mixture of the high melting fraction of milkfat and the medium melting fraction of milkfat. Sample was spin-coated into a silicon substrate.

into one large cluster (of approximately 100–125 μm), shown in Figure 17*D*. As well, the self-similarity of the structure at the different magnifications shown is readily apparent. Figure 18 shows composites of a 50:50 mixture of HMF and MMF, but in this case the samples were prepared in rheologic molds. As is evident, the structures shown in Figures 17 and 18 are quite similar, except for the appearance, again, of the suspected wax particles. As well, the self-similar nature of the structure at different magnifications is evident. Figure 19 shows AFM images of a sample containing a 70:30 mixture of the HMF and the MMF of milk fat, spin-coated onto a silicon substrate. The structures shown demonstrate the same general organization as the other AFM images, and again the self-similar nature of the structures at all length scales within a large cluster (the smallest magnification, Figure 19*C*, is still within an entire large cluster) is evident. Figure 20 shows AFM images of cocoa butter. Figure 20A is interesting in that it represents a level of magnification not shown previously in any of the AFM images. This level of magnification is showing structures that are within the "particles." The image suggests that the "particles" are composed of intertwined crystalline material, a picture which is reinforced by the polarized light micrographs shown in Figure 10.

Figure 20B shows the familiar "particles" packed fairly close together, and, again, in this image, the appearance of the "particles" as being composed of intertwined crystallites is reinforced. Figure 20C is a rather poor image at a lower magnification, which is, however, suggestive of the clustering of intermediately sized clusters. It is unfortunate that current atomic-force microscopes are not capable of a lateral range of scan much greater than 150μm. As a result, using this method, it is very difficult to image two or more of the large clusters reported by Heertje and coworkers and seen in the confocal images. However, some of the images do indicate the presence of these large clusters, although it is obviously not possible to assign a finite size, shape and packing regularity to these structures. It is conceivable that one may be able to perform adjacent scans of a surface and then reconstruct these images to represent the packing of a large area on the sample, but this

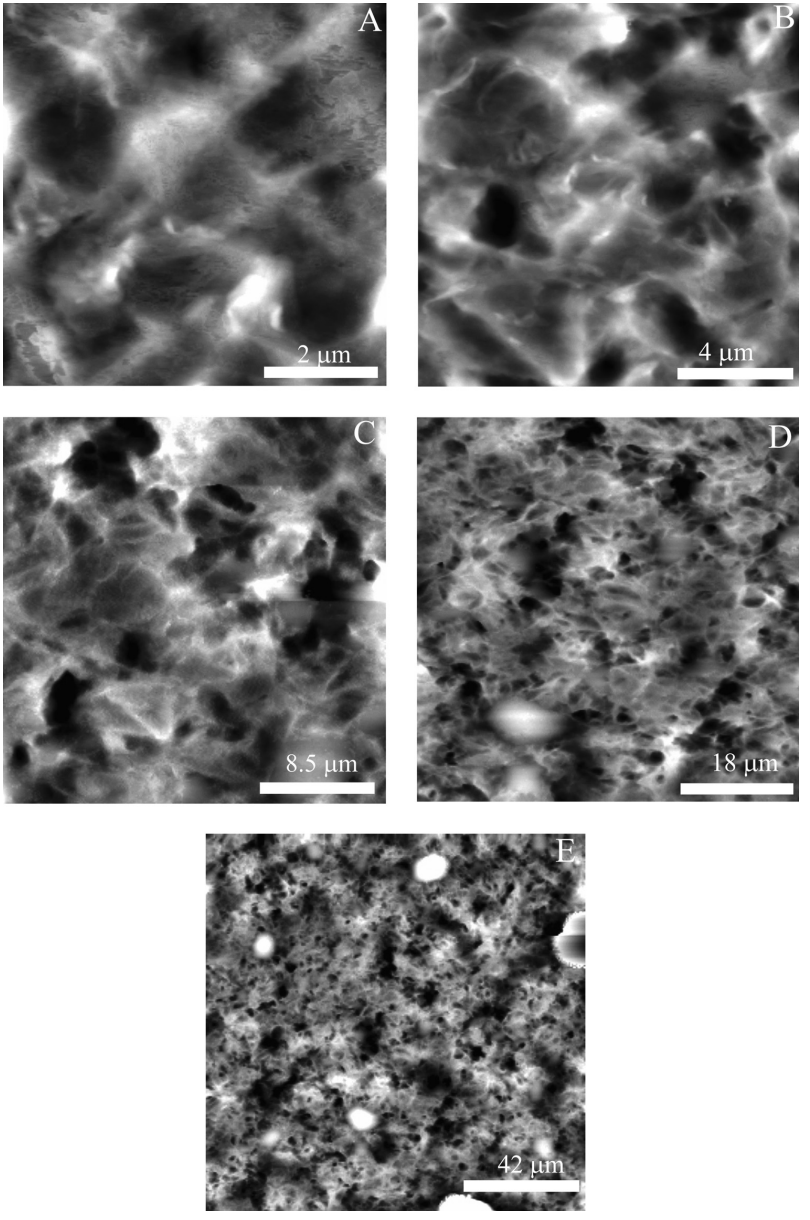

Figure 18 Atomic force microscopy images of a 50:50 w/w mixture of the high melting fraction of milkfat and the medium melting fraction of milkfat. Sample was prepared in a rheological mould.

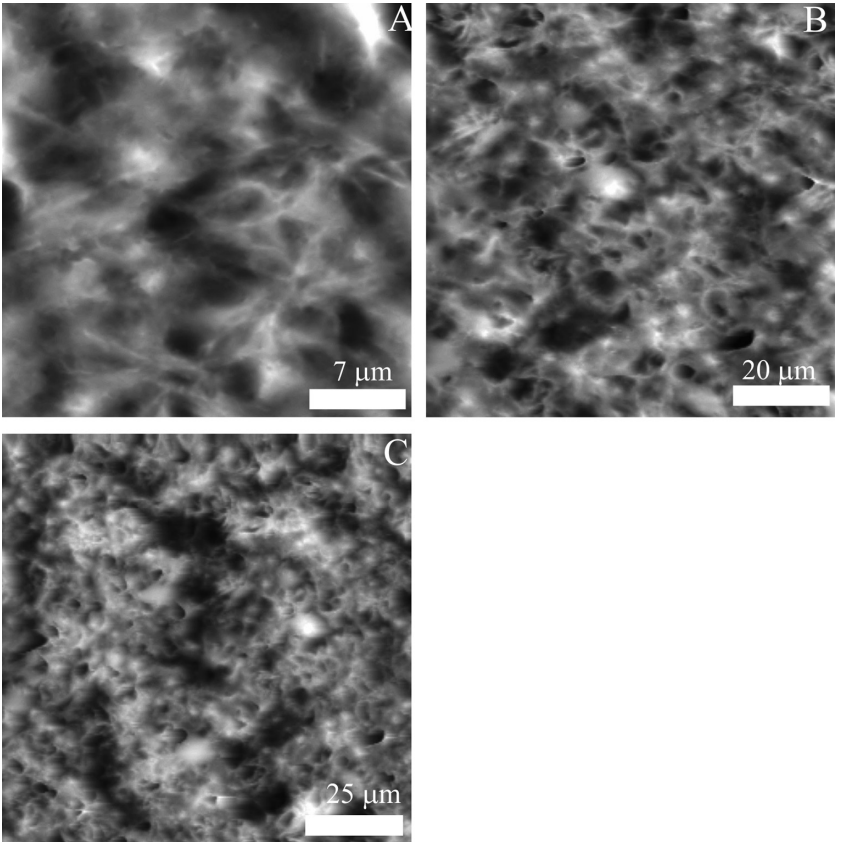

Figure 19 Atomic force microscopy images of a 70:30 w/w mixture of the high melting fraction of milkfat and the medium melting fraction of milk fat. Sample was spin-coated into a silicon substrate.

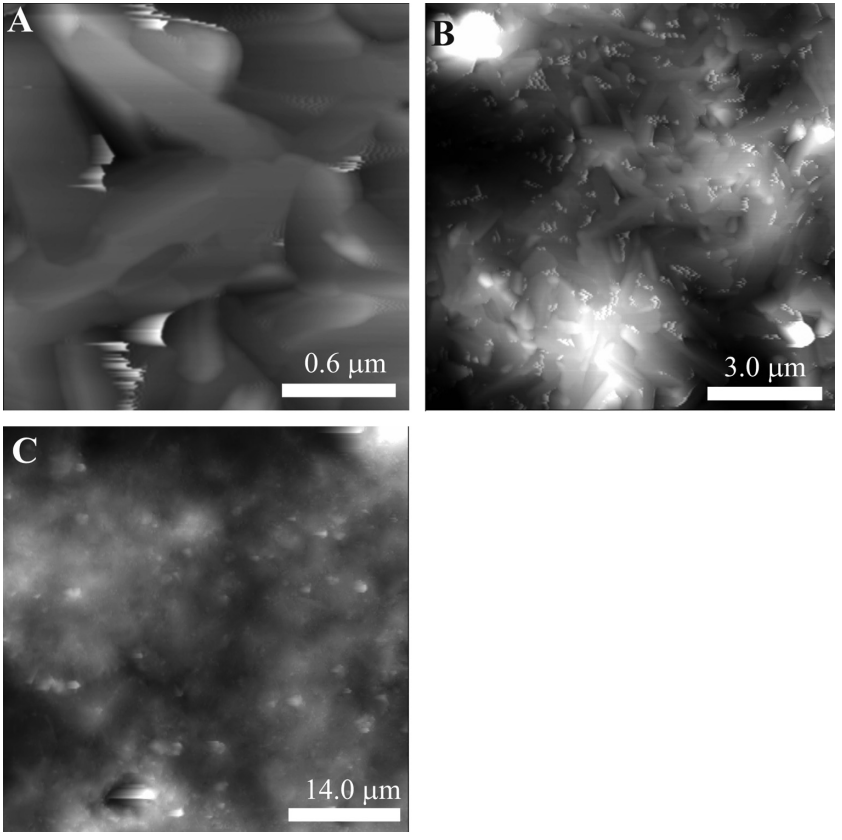

Figure 20 Atomic force microscope images of cocoa butter. A thick sample was crystallized on a glass microscope slide without a coverslip.

procedure is not straightforward due to the severe hysteresis found in the piezoelectric crystal drives of the atomic-force microscope. However, the atomic-force images presented here lend support to the structural organization suggested by the other forms of microscopy outlined so far.

Figures 21 shows *in situ* light micrographs of milk fat clusters using phase contrast (Figure 21*A* and *C*) and polarized light (Figure 21*B* and *D*). Figure 22 shows light micrographs of a 30% (w/v) mixture of the high-melting fraction of milk fat

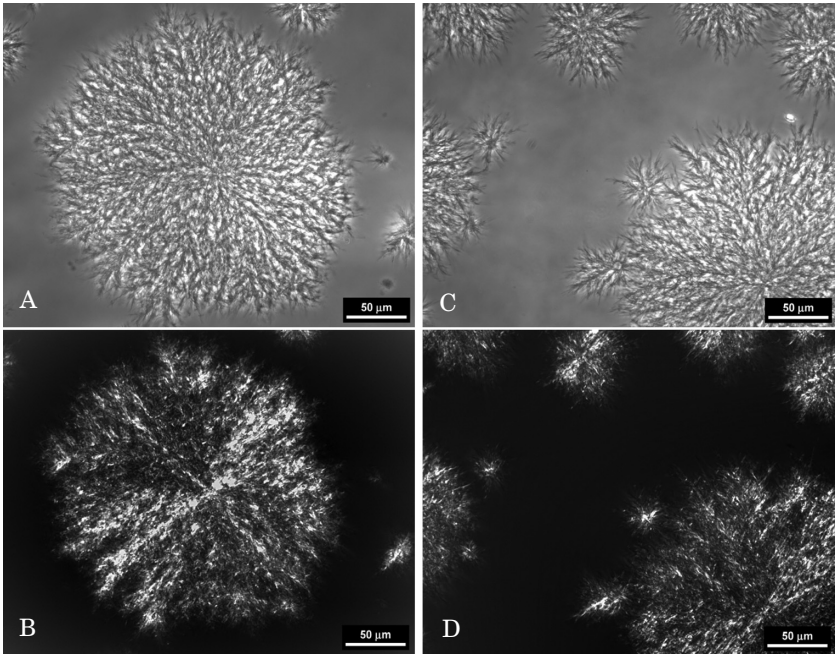

Figure 21 *In-situ* light microscope images of milkfat at 22°C viewed under phase contrast (**A** and **C**) and polarized light (**B** and **D**)

and triolein with 0.5% Tween 60 added under phase contrast (Figure 22A) and polarized light (Figure 22B). It is important to discuss what these figures represent before we begin a discussion of the structures that are represented in them. First of all, it is obvious that the views offered by polarized light and phase contrast microscopies are different. The polarized light image has been transformed relative to the more representative phase contrast image— the cluster appears particulate and less dense. Thus, the PLM technique selects lightfor a subset of crystallite orientations which are visible under full extinction. This, as will be discussed later, allows for the fractal analysis to be carried out on these birefringent fat crystal networks. Second, these images are of the *in situ* network, and have a definite depth. Since the images have been deliberately

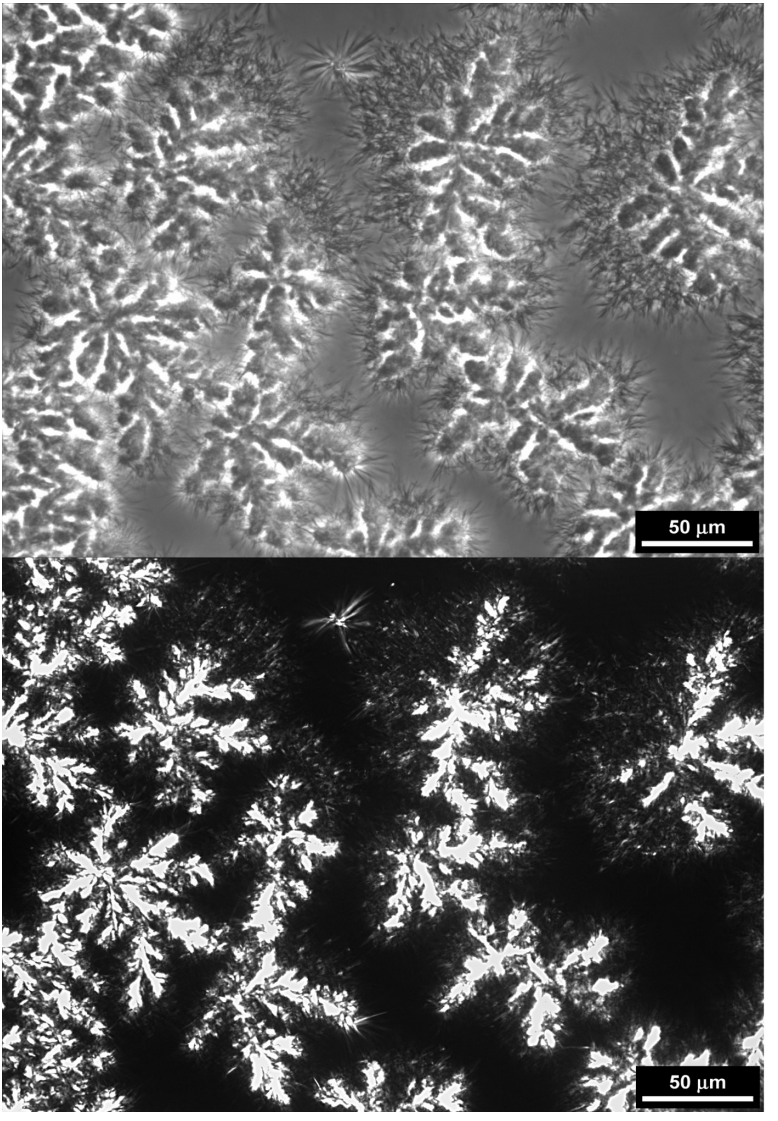

Figure 22 *In-situ* light microscope images of a mixture of the high melting fraction of milkfat and triolein with 0.5% Tween 60 at 22°C viewed under phase contrast (**A**) and polarized light (**B**).

made very thin, this depth is not significant enough to attenuate appreciable amounts of the light passing through, and, therefore, the image presented is not totally opaque, but gives a good representation of all the "particles" (reflections from a subset of crystallites oriented in a particular orientation)—both in the depth of the sample as well as in the focal plane of the microscope. Care was taken to focus on those "particles" at the top of the sample, and those particles in the depth of the sample are, therefore, represented as out-of-focus entities that appear smaller than their actual size and as higher levels of gray than the in-focus particles, which appear as higher levels of white. Since the depth of the samples are represented here, it is not possible to identify the boundaries of intermediate clusters that may be present because, if those were present, the boundaries would most likely be rendered indistinct due to the presence of particles belonging to other clusters in the depth of the sample, which are not at the same x-y coordinates of the clusters in focus. Therefore, the field of view is representative of *all* "particles" in the thin three-dimensional sample, except for those in direct geometrical shadow of "particles" in focus. Now, since the images are created due to the refraction of polarized light through the anisotropic crystalline nature of the "particles," only part of a typical particle will be visible; however, by rotating the polarizer 45 degrees, it is possible to render those parts of the "particles" that were not visible, visible. This process, of course, renders the previously visible parts invisible; however, it serves to ensure that one can discern between neighboring particles. The so-called Maltese Cross pattern is, for instance, due to a spherelike "particle," but, because of the orientation of the crystallites in the "particle," not all of them are visible when one looks at the particle under polarized light. Therefore, while it is possible to represent all of the "particles" present in the thin three-dimensional sample in the PLM image, each particle will be missing mass, some particles will appear larger than others, and some particles will appear more in-focus than others. However, the presence of all particles except those in direct geometrical shadow (negligible if the sample is suffi-

ciently thin) may be noted if the image is taken with some care. One can identify and measure "particles" of the order of 1–5μm, in agreement with the AFM technique, which is a more direct probe of the nature of the particles within the fat crystal network than PLM.

The evidence presented by the different types of microscopy are all in agreement —the microstructure of fat crystal networks seems to be organized in hierarchical levels of structure: "particles" composed of intertwined crystallites, of the order of 1–5 μm are organized in intermediately sized clusters, which are packed into large clusters of the order of 100–150 μm, similar to the way the "particles" pack. Not much evidence has been presented yet of the large clusters themselves, although the work of Heertje and coworkers has been quoted, which demonstrates that the large clusters in a fat network pack in an orthodox space-filling manner to form the network.

In an effort to observe the formation of the fat crystal network from the melt, the kinetics of formation of the network was monitored by PLM. Figure 23 shows images of the network formed by milk fat triacylglycerols at 5.5 min. (*A*), 7 min. (*B*), 8.5 min (*C*), 10 min (*D*), 11.5 min. (*E*), 13 min (*F*), 25 min (*G*), and 32.5 min. (*H*) after appearance of the first visible signs of crystallization in the field of view. As is demonstrated by Figure 22, growth, in the early stages of crystallization, is concentrated around a few centers of nucleation. However, as the growth process continues, there is an aggregation process that takes place because of the appearance of many more centers of growth (with advanced growth having already taken place, therefore suggesting that these "new" centers of growth were not new nucleation events) than there were nuclei in the field of view. The centers' crystallization growth process continues until they reach a certain maximum size, whereupon the aggregation process continues slowly. After approximately one-half hour, the aggregation process is no longer visibly evident, although quite often there is massive rearrangement of the structure over 24, and sometimes even 48 and 72, hours. It is unfortunate that this type of microscopy does not allow the definition of intermediately sized cluster

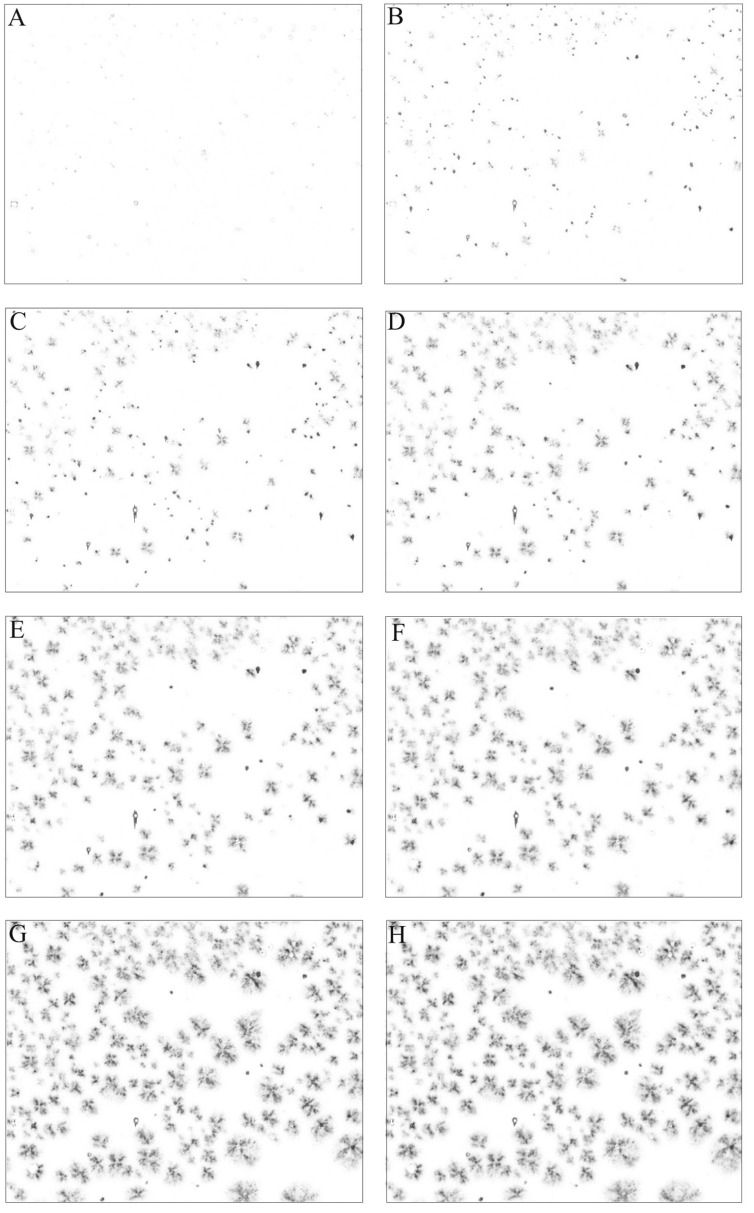

Figure 23 Polarised light microscope images of milkfat triacylglycerides at various times after appearance of first visible signs of crystallization: (**A** 5.5 mins, (**B**) 7 mins, (**C**) 10 mins, (**D**) 11.5 mins, (**E**) 13 mins, (**F**) 25 mins, and (**G**) 32.5 mins.

boundaries, because it would also be interesting to observe the process of aggregation of these clusters themselves. One can begin to see cluster formation during the crystallization/aggregation process. For example, in Figure 23C, one can begin to see the formation of the intermediately sized clusters, the process of which can be easily followed through Figures 23*E* and 23*F*; however, by 23*G* and 23*H*, the field of view is so filled with "particles" that the cluster boundaries become indistinct. One of the reasons the cluster boundaries are no longer visible, of course, is due to the aggregation of the clusters, which is blurring the boundaries. This type of growth/aggregation behavior is demonstrated by all of the fats studied in this work—cocoa butter, tallow, lard, palm oil and milk fat all demonstrate these growth modes. It seems reasonable to assume that "particles" aggregate into intermediately sized clusters (while also growing to some optimum size) and then the intermediately sized clusters themselves aggregate into the large clusters. The aggregation processes for particles and intermediately sized clusters must be similar, given the similar manner in which they have been observed to pack, in the AFM and CLSM images presented before. This is also true because the aggregation process continues after the clusters have been formed.

3.2 Structural Model of the Fat Crystal Network

The microscopic evidence presented previously forms a composite picture of the structure of fat crystal networks. No one method of microscopy on its own reflects the composite picture; however, by considering the various images from the different types of microscopy, one can build a structural model of fat crystal networks which is supported by all the forms of microscopy. One of the needs in the fats and oils industry is the establishment of nomenclature that will unambiguously identify different levels of microstructure. Perhaps the best way to establish such nomenclature is to trace the development of the fat network as it forms from the melt. At the start of crystallization, there is a process of nucleation followed by

growth of these nuclei into crystallites. Molecular thermodynamics and kinetics most probably control this process. As we have seen, these crystallites associate in dense packets, with several intertwined crystallites tending to form "particles" of the order of 1–5 μm. It is proposed that these "particles" be called *microstructural elements* because they form the smallest repeating structure at a length scale visible under a light microscope. These microstructural elements then continue to grow larger through further crystallization, although there is an aggregation process that takes place as well, leading to the formation of intermediately sized clusters, which further aggregate to form large clusters. This aggregation process is most probably controlled by mass and heat transfer limitations. The large clusters, which, it is proposed, should be called *microstructures*, pack in an orthodox, space-filling manner to form the network, as has been shown by Heertje and coworkers. Additionally, evidence of the microstructures has been presented here, in CLSM, AFM, and PLM images, and, to a less certain extent, in SEM images. Figure 24 is a schematic, two-dimensional representation of the structural hierarchy of the microstructure of fat crystal networks. The microstructural elements, the intermediately sized clusters, and the microstructures have all been represented by circles, indicating that they are spherical. There is evidence from all of the methods of microscopy that these structures are spherelike (which may be taken to mean stretched and distorted spheres as well). However, whether they are smooth spheres is something that cannot be determined, and this factor will most probably differ with the type of fat. Certainly, SEM and AFM micrographs of the microstructural elements suggest that these are not smooth spheres, and that the sphericity is not perfect. However, representing these structural entities as spheres is probably fairly representative, providing one keeps in mind that this is an imperfect approximation. The packing of the microstructural elements within the microstructures is quite disordered, as has been seen in the images presented earlier. However, it is important to recall that, at length scales ranging from the diameter of the microstructural elements to the dia-

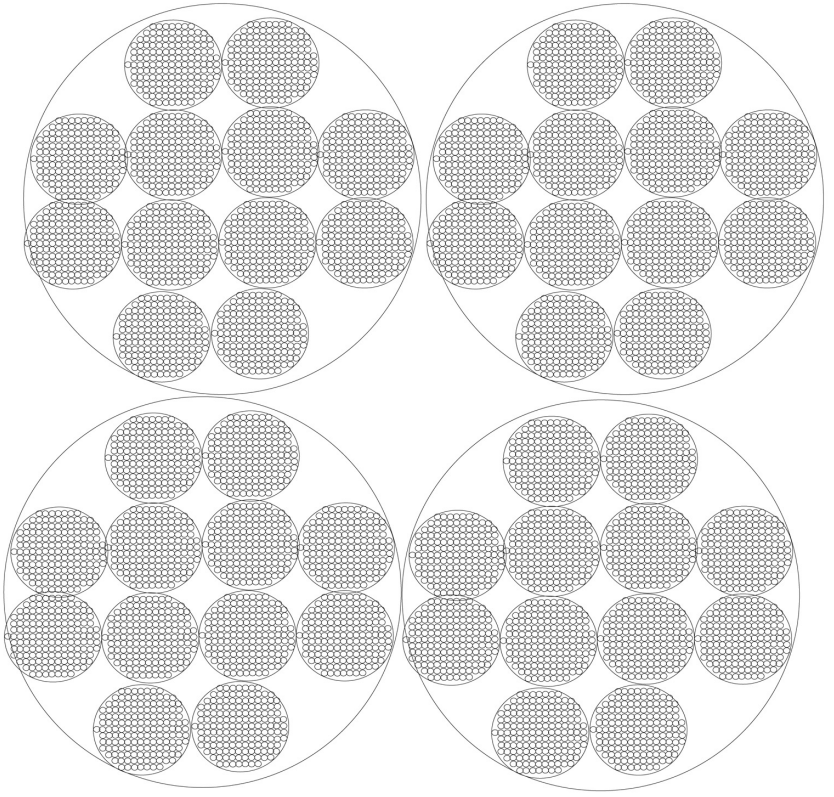

Figure 24 Idealized two-dimensional schematic representation of the self-similar structural hierarchy of the microstructure of fat crystal networks.

meter of the microstructures, these structures appear to be statistically self-similar, i.e., the structure within this range of length scales, at different magnifications, appears to be similar. This, of course, is most strikingly obvious in the atomic-force micrographs. Therefore, in an idealized attempt to demonstrate this self-similarity, Figure 24 shows that the packing of the microstructural elements within clusters is similar to the packing of the clusters themselves into the microstructures. In order to easily achieve this effect, the microstructural

elements and the clusters are arranged in an ordered manner; however, in reality, these arrangements are quite disordered, as is evidenced by the microscopy images shown earlier. The fact that there appears to be statistical self-similarity in the length ranges between the size of the microstructural elements and the microstructures is not surprising, since the method of growth/aggregation between these two length ranges is limited by the same physical constraints.

3.3 Fractality

Now that the structural organization of the microstructural level of a typical fat crystal network has been established, the next logical step is an attempt to quantify this level of structure. Apart from monitoring microstructural element size, cluster size, and microstructure size (not an easy task due to the nature of the methods of microscopy), it seems important as well to ask the question: what is the spatial arrangement of the mass of the network at the microstructural level? Certainly, the size of the various hierarchical levels of structure will determine the way in which forces holding the network together will be affected. Equally as certain, however, is how the spatial arrangement of the various levels of structural entities will also affect the forces that hold the network together. Of course, additional factors such as the nature of the crystalline material (polymorphism) and the nature of the constituent molecules themselves are also important factors; but, from a microstructural perspective, the parameters that can be determined are concerned with the size, shape, and spatial arrangement of the structural entities. Certainly the density of this level of structure will yield some information about the spatial arrangement of the mass of the network, but density alone does not give information about the actual packing—i.e., it is a rather macroscopic measurement, which does not yield structural information about the actual order of packing of the structural units of interest. Due to the extremely disordered nature of the packing of levels of structure below the size of the microstructures, it is difficult to assign lattice parameters to the positioning of the microstructural elements. Fractal

analysis has, in the past, been used to characterize the spatial arrangement of such disordered structures that demonstrate self-similarity at different length scales. Additionally, based on the calculation of a fractal dimension from rheologic measurements on fats which were fitted to a fractal model developed for colloidal gels (section 2), it seems fitting that one tries to apply fractal principles to the study of the microstructural level of structure in fats. Certainly, the self-similarity of the structure suggested by the AFM, CLSM, SEM, and PLM images of the network encourages this endeavor. The challenge, here, is that each of the methods of microscopy that have been presented previously demonstrate inherent artifacts, and none of them presents an unbiased, complete view of the network. What seems plausible is that the structure is self-similar at length ranges bounded by the size of the microstructural elements and the size of the microstructures. We have successfully applied a particle-counting method, as well as a box-counting method, to the analysis of *in situ* polarized light micrographs of crystallized fats. These methods are described in the Analytical Methods section of the book.

Before ending this section, we would like to leave the reader with the image in Figure 25. This micrograph shows a fat crystal network of the high-melting fraction of milk fat at different magnifications, in the range usually used in fractal analysis. The box-counting dimension of all these images is identical, providing further evidence that, for certain systems, fat crystal networks display self-similarity in the range of magnification that includes structural elements from 1 to 100 μm in size.

3.4 The Weak Link Revisited

Now that the general structural arrangement of the microstructure of fat crystal networks has been established, it is relevant to examine how this structural organization relates to the weak-link theory. The model of the structure of fat crystal networks developed above identifies the microstructures as the largest structural building block of the network. It seems reasonable that any stress that is put on the network will first

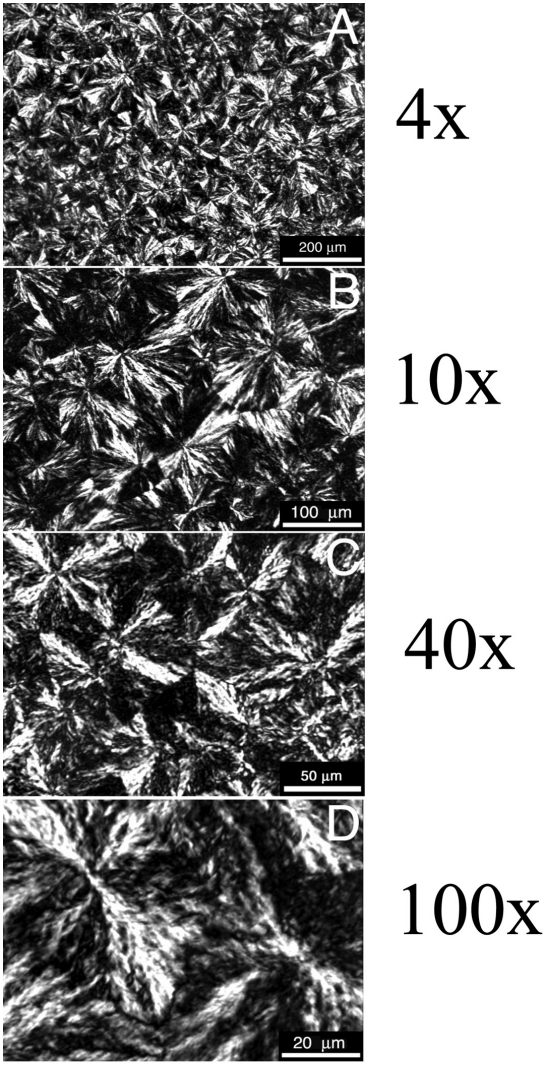

Figure 25 Polarized light image of a fat crystal network of the high-melting fraction of milk fat at different magnifications. All images yield the same box-counting dimension, thus providing evidence for self-similarity in this range of magnifications.

be felt by the microstructures. The question is, how do the microstructures behave under this stress? Heertje and coworkers [10,26,87] have demonstrated that the microstructures are separated when the network is stressed, yet they remain intact (maintaining their shape and size). Therefore, it seems reasonable to expect that, when the network is stressed, the links between the microstructures are the first level of the structure that is stressed. Figure 26 shows a theoretical schematic of the network under stress. It seems reasonable to expect that the stressing of the network within the elastic limit results in a stressing of the links between microstructures, which are a repeating, regularly packed structural unit. Referring to Figure 25, if one were to express the force-constant of the links between microstructures as K_L, then the macroscopic elastic constant, K, (in 1 dimension) of the network could be written as:

$$K = \left[\frac{L}{\xi}\right]^{d-2} K_L \tag{30}$$

where ξ is the diameter of one microstructure, L is the macroscopic size of the system, and d is the Euclidean dimension of

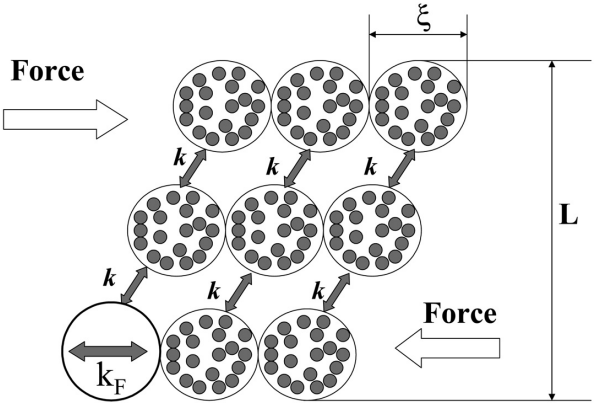

Figure 26 Theoretical schematic of the fat crystal network under a small stress which is insufficient to exceed the elastic limit of the network.

the sample (=3). However, as has been shown earlier, the structure within the microstructures is fractal in nature. We can therefore relate the diameter of the microstructure (or aggregate) to the particle volume fraction of the entire network. Therefore, using equation (31):

$$\xi \sim (\Phi_t)^{\frac{1}{D-3}} \tag{31}$$

and substituting this expression into equation 30 yields:

$$K \sim \left[\frac{L}{(\Phi)^{\frac{1}{D-3}}}\right] K_L \tag{32}$$

Now, if the links between microstructures are identical, and the size of the system is a constant, we can write equation 8 as:

$$K \sim (\Phi)^{\frac{1}{3-D}} \tag{33}$$

Recognizing that the shear storage modulus of the network is related in a proportional manner to the tensile elastic constant, we can write equation 33 as:

$$G' \sim \Phi^{\frac{1}{3-D}} \tag{34}$$

The theory espoused by equation 34 relates the shear storage modulus to the particle volume fraction via the fractal dimension of the network. The particle volume fraction of the network is not easily measured (in fact, the author knows of no experimental method that yields this value). It must be stated clearly, here, that particle volume fraction is used to mean microstructural element volume fraction—it is obvious from the development above that the "particles" refer to the microstructural elements. It will be shown below that the Φ_{SFC}, determined as SFC/100, is proportional to the particle volume fraction, Φ. Therefore, one may use Φ_{SFC} in the stead of Φ in equation 34, bearing in mind that the nature of the proportionality constant is now changed. One can now replace the proportionality sign by the constant λ (γ in our previous nomenclature), bearing in mind that this constant would be dependent on the links between microstructures and the relationship between ξ, Φ, and D, as well as the nature of the proportionality

between Φ_{SFC} and Φ, given the origin of the proportionality constant, as developed above:

$$G' = \lambda \Phi^{\frac{1}{3-D}} \tag{35}$$

Equation 35 is of course equivalent to the expression arrived at by Shih et al. [80] for the weak-link theory for colloidal gels. Therefore, from a structural perspective, it seems that use of this formulation for fat crystal networks is warranted. Not surprisingly, therefore, the work by Rousseau and Marangoni showed that the weak link theory when applied to fats yielded plausible results. Additionally, these authors were not incorrect in assuming that the fractal dimensions that they calculated from this rheologic treatment were related to the microstructure—as was previously shown, such a fractal dimension is related to the way in which the microstructural elements are distributed in the microstructures of the fat network. The obvious challenge, therefore, is to compare the fractal dimensions calculated by rheologic methods to those calculated by image analysis methods. The most important issue here, of course, is the need to emulate the same processing conditions for the rheologically prepared samples and the samples prepared for microscopy on a glass slide.

3.5 Relating the Particle Volume fraction to the Solid Fat Content

The solid fat content, Φ_{SFC}, of a fat network may be defined as:

$$\Phi_{SFC} = \frac{n_{ME} V_{ME} \rho_{ME}}{M_T} \tag{36}$$

where n_{ME} is the number of microstructural elements, V_{ME} is the volume of one microstructural element, ρ_{ME} is the solids density of a microstructural element, and M_T is the total mass of the network (solid mass + liquid mass). Equation 36 can be rewritten as:

$$n_{ME} = \frac{\Phi_{SFC} M_T}{V_{ME} \rho_{ME}} \tag{37}$$

Now, the total particle volume concentration, Φ_t of the network is given by:

$$\Phi_t = \frac{n_{ME} V_{ME}}{V_T} \tag{38}$$

where V_T is the total volume of the network. Substituting for n_{ME} in equation 37:

$$\Phi_t = \frac{\frac{\Phi_{SFC} M_T}{V_{ME} \rho_{ME}} V_{ME}}{V_T} \tag{39}$$

yields:

$$\Phi_t = \frac{\rho_t}{\rho_{ME}} \Phi_{SFC} \tag{40}$$

where $\rho_t = \frac{M_T}{V_T}$, and is the density of the network itself. The solids density of the microstructural elements, ρ_{ME}, is higher than the density of the network, ρ_t, because the microstructural elements are very densely packed (recall the AFM image shown in Figure 20A, which showed that the microstructural elements are made up of intertwined crystallites), while the network itself contains a lot of liquid oil and dispersed microstructural elements. However, as established by equation 40, the particle volume fraction of the network is proportional to the SFC of the network. Therefore, although it is difficult to measure the particle volume fraction of the network, the SFC may be used in its stead, bearing in mind that these two entities are not equal but are proportional.

3.6 Rheology

Plots of G' vs. Φ shown in Figure 27 support the power–law dependence of G' on Φ suggested by equation 34. Figure 27A shows data for milk fat at 5°C. This is in the form of a straight line, which implies, from equation 34, that the fractal dimension must be equal to 2. Figure 27B shows data for tallow at 5°C, Figure 27C shows data for palm oil at 5°C, and Figure 27D shows data for lard at 5°C. Figures 27*B–D* show a nonlinear, power–-law dependence of G' on Φ. As has been explained, a

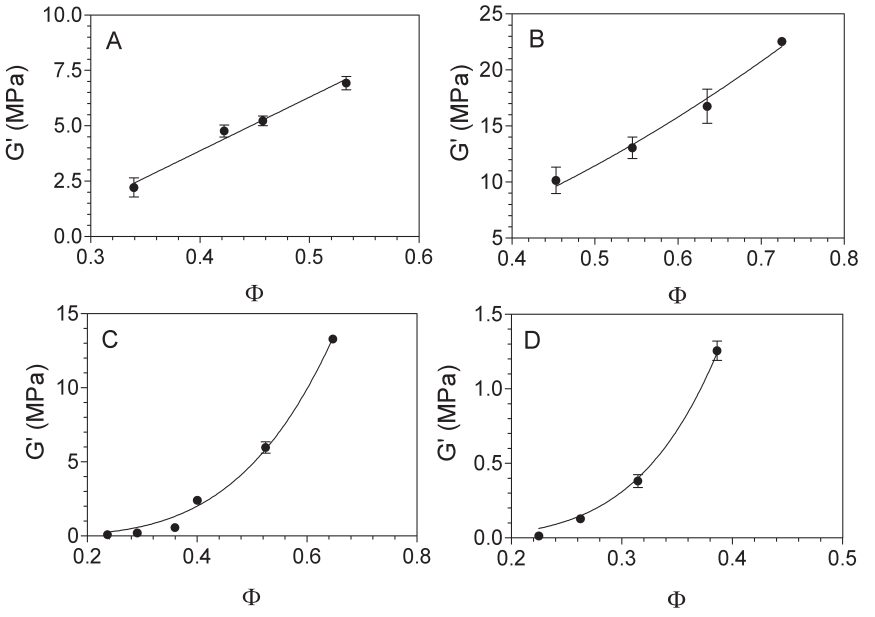

Figure 27 Plots of $\log_{10} G'$ vs. Φ for: (**A**) milkfat, (**B**) tallow, (**C**) palm oil, and (**D**) lard.

plot of ln G′ vs. ln Φ yields a straight line with slope equal to $1/(3 - D)$; such plots are shown in Figure 28 for milk fat (28*A*), tallow (28*B*), palm oil (28*C*), and lard (28*D*). All the systems we have studied to date display the power–law scaling behavior characteristic of fractal networks. Figures 29–31 are a few examples of this power–law scaling behavior.

Table 1 summarizes the values of D and (obtained for a variety of systems crystallized isothermally at 5°C using the double logarithmic plots described previously.

3.7 Physical Significance of Fractal Dimension

The previous discussion of experimental data shows that fat crystal networks are fractal within certain length ranges and

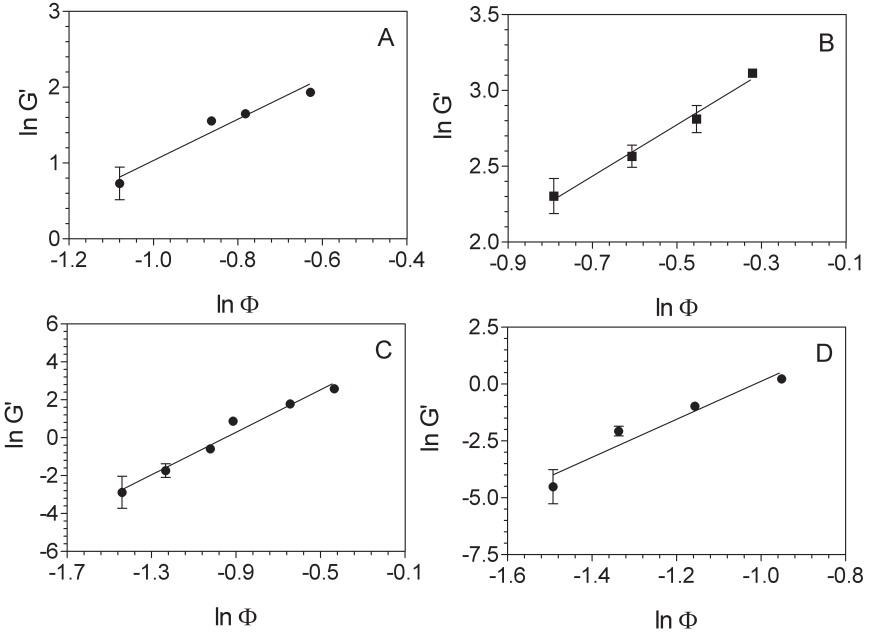

Figure 28 Plots of G' vs. ln Φ for: (**A**) milkfat, (**B**) tallow, (**C**) palm oil, and (**D**) lard.

that the structural arrangement of the microstructure of fat crystal networks makes it possible to apply the weak-link theory to analyze the mechanical properties of the networks. Central to this finding is the calculation of a fractal dimension. Therefore it is relevant that we attach some physical significance to this quantity if it is to be a useful parameter.

Note that for a higher fractal dimension, the density of the packing of the microstructural elements must be higher because, according to equation 3, the number of microstructural elements is proportional to the characteristic length raised to a power equal to the fractal dimension. Density of packing of the microstructural elements does not refer to the traditional definition of density of the network (total mass/

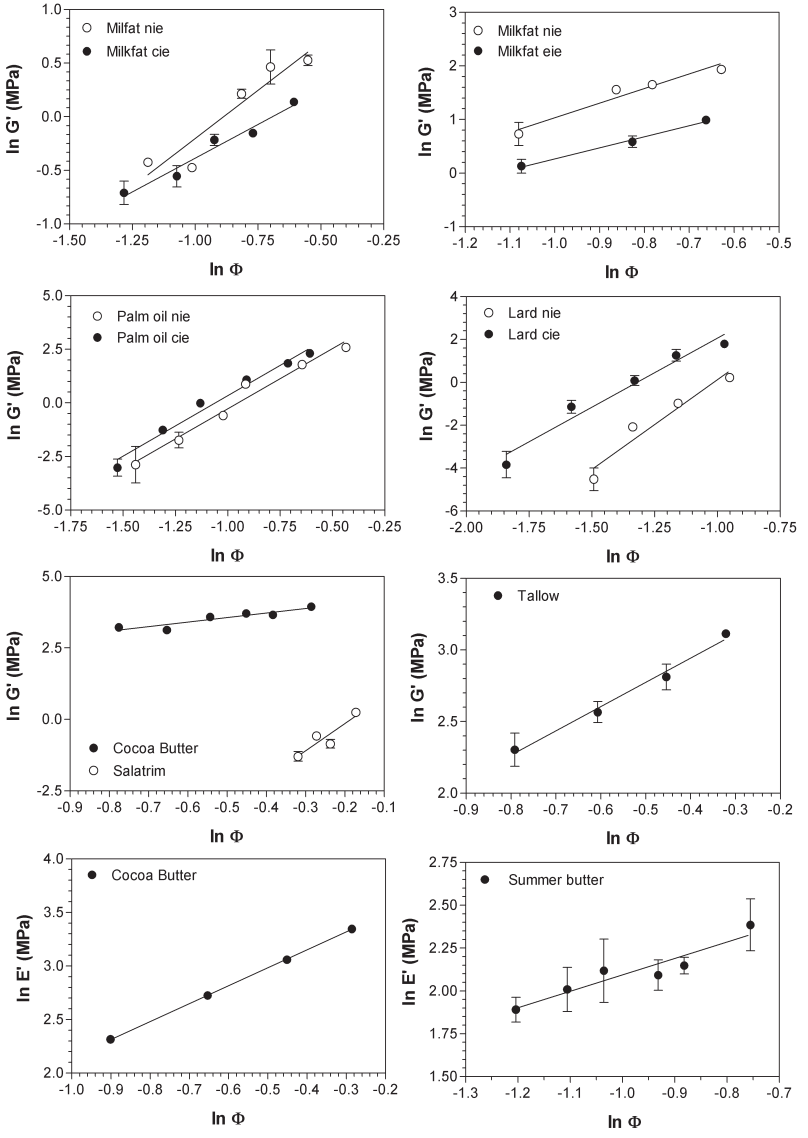

Figure 29 Plots of the ln G' vs. ln Φ for a series of fats. The acronyms NIE = noninterested, CIE = chemically interesterfied, and EIE = enzymatically interesterified.

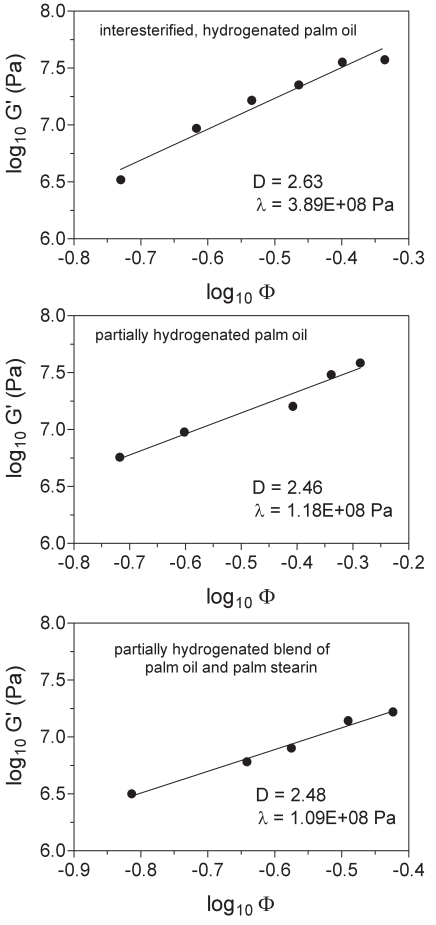

Figure 30 Plots of the lnG' vs. ln Φ for a series of palm oil-based fats.

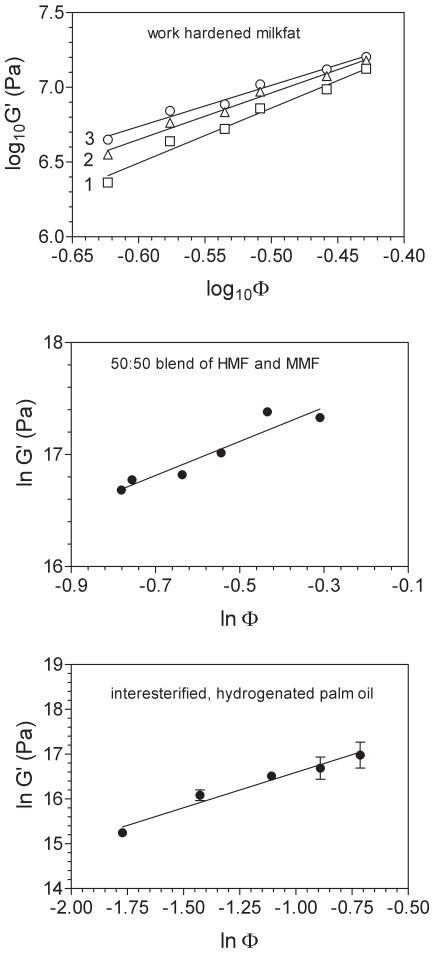

Figure 31 Plots of the lnG' vs. ln Φ for a series of fat systems. Work hardening increases from 1 to 3. The acronyms HMF and MMF refer to, respectively, to the high-melting and medium-melting fractions of milkfat.

Table 1 Fractal Dimensions (D) and Parameter λ Determined Rheologically for a Series of Fat Systems Crystallized Isothermically at 5°C

System	D	λ(MPa)
Milkfat-canola oil (MF-CO) 1 shear	2.63	43.1
Milkfat-canola oil (MF-CO) 2 shear	2.44	4.93
Milkfat-canola oil (MF-CO) 3 shear	2.73	37.0
Milkfat-canola oil (MF-CO) 4 shear	2.62	95.1
Milkfat-canola oil (MF-CO) 1 compression	1.96	21.2
Milkfat-canola oil (MF-CO) 2 compression	2.01	23.6
MF-CO enzymatically interesterified shear	2.52	10.4
MF-CO chemically interesterified shear	2.20	2.40
Milkfat TAGs-canola oil shear	2.71	135
Cocoa butter-canola oil shear	2.37	77.8
Cocoa butter-canola oil compression	2.40	45.6
Salatrim-canola oil shear	2.89	5.85
Tallow-canola oil shear	2.41	37.4
Palm oil-soybean oil (PO-SBO) shear	2.82	210
PO-SBO chemically interesterified shear	2.82	398
Lard-canola oil (LCO) shear	2.88	4870
LCO chemically interesterified shear	2.84	4890
Interesterified, hydrogenated palm oil-canola oil shear	2.63	389
Partially hydrogenated palm oil-canola oil shear	2.46	118
Partially hydrogenated palm stearin/palm oil blend-canola oil shear	2.48	109
Interesterified, hydrogenated palm oil-peanut oil shear	2.36	77.8

total volume), nor does it refer to the density *within* a typical microstructural element (which has been used in equation 40 as the symbol ρ_{ME}). The density of packing of the microstructural elements refers to the density of the microstructural elements *within* one microstructure. Therefore, if one is observing a particular fat after it has been processed differently, then the increase or decrease of the amount of microstructural elements within a certain characteristic length will signal the increase or decrease of the fractal dimension. However, given the nature of the PLM images, this is not a parameter that is easily

ascertained without image analysis. Additionally, as is discussed later, the fractal dimension is not only dependent on the density of the packing of the microstructural elements, it is also dependent on the *order* in which they pack. Certainly, these two parameters are interrelated, since the order in which the elements pack also influences the density of the packing and is itself influenced both by the nature of the inter-microstructural element forces and the mass and heat transfer limitations during the formation of the network.

If one considers a line, with microstructural elements placed at some equilibrium nearest-neighbor distance apart, then one has a picture represented by figure 32*A*. The projection of the positions of the microstructural elements onto a line represents an ordered array. Now, the line containing the microstructural elements represents a 1-dimensional object.

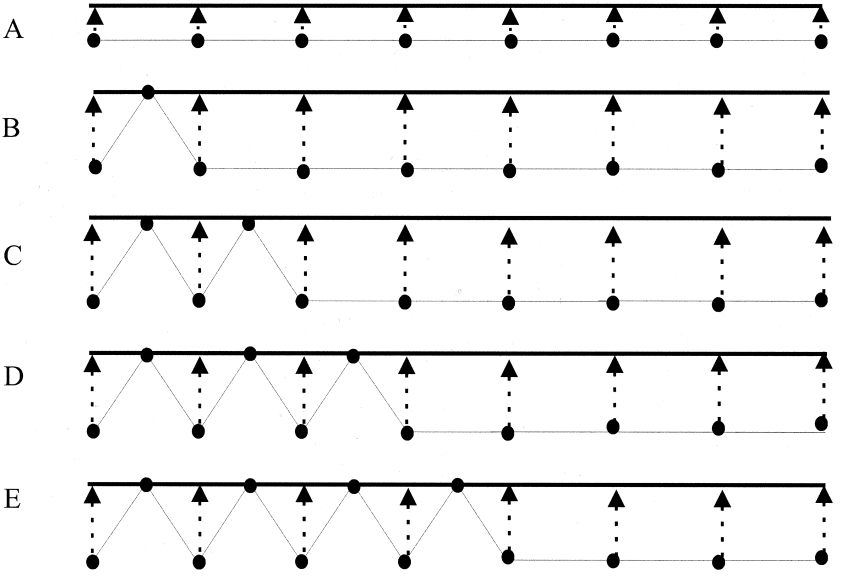

Figure 32 Schematic of microstructural elements placed on a line at equal distances apart. The dimensionality of the line increases from (**A**) to (**E**). Microstructural elements on the thin line are projected onto the thick line.

If one starts to put kinks in this line, one starts to raise the dimension of the line to a value just above 1, and less than 2. This scenario is represented in Figure 32B. Now, the microstructural elements must still be placed at a nearest-neighbor equilibrium distance from each other on this new "space," so, therefore, the projection of the positions of the microstructural elements onto a line begins to look disordered, as shown in the figure. It is useful to have a working quantitative definition of order in this analogy. When one looks at the projection of positions, one may define high order as the positions all being a common average distance apart from each other. Therefore, the standard deviation of the various distances apart of nearest-neighbour projection positions is a good representation of the deviation from order (lower standard deviation implies higher order). Figure 32C–*E* demonstrates situations in which more and more kinks are placed in the line containing the microstructural elements—therefore, the fractal dimension is increasing from (Fig. 32*A*–*E*. Table 1 shows the distance apart of nearest-neighbor projections of each situation (and lists an additional two situations following the same trend of kinks, not shown in figure 32) and the standard deviation in these values for each situation. As can be seen, as the fractal dimension increases, the order initially (for a small amount of kinks in the line) decreases before it begins to increase as the fractal dimension gets larger and larger (i.e., closer and closer to 2). Of course, the fractal dimension referred to here is qualitatively getting larger (the actual dimension has not been computed), but it is generally accepted that more and more kinks in a line represent higher and higher fractal dimensions, because the line is closer approximating a plane. This situation is exactly what happens in the case where dimension is between 2 and 3. An interesting effect to note is that, as the fractal dimension and order increases, so does the packing density of microstructural elements in the observed region. This is, of course, in agreement with the foregoing discussion on density and order.

3.8 Conclusions

It has been shown in this chapter, from a structural basis established by a multitude of microscopy techniques, that fat

crystal networks crystallized statically are fractal within certain length ranges. Furthermore, it was shown that the weak-link theory is applicable to fat crystal networks. The next stage in this developmental process is to begin establishing links between heat and mass transfer conditions and the resulting microstructure of the fat from knowledge of the crystallization kinetics and phase behavior of the individual triacylglycerols present in the sample. This work is ongoing.

REFERENCES

1. Kamphuis H, Jongschaap RJJ. The rheological behaviour of suspensions of fat particles in oil interpreted in terms of a transient-network model Colloid Polym Sci 1985; 263:1008–1024.
2. Kamphuis H, Jongschaap RJJ, and Mijnlieff P.F. A transient-network model describing the rheological behaviour of concentrated dispersions Rheol Acta 1984; 23:329–344.
3. Nederveen CJ. Dynamic mechanical behavior of suspensions of sat particles in oil J Colloid and Interface Sci 1963; 18:276–291.
4. Papenhuijzen JMP. Superimposed steady and oscillatory shear in dispersed systems Rheol Acta 1971; 10:493–502.
5. Papenhuijzen JMP. The role of particle interactions in the rheology of dispersed systems Rheol. Acta 1972; 11:73–88.
6. Payne AR. The elasticity of carbon black networks J Colloid Sci 1964; 19:744–754.
7. van den Tempel M. Mechanical properties of plastic-disperse systems at very small deformations J Colloid and Interface Sc 1961; 16:284–296.
8. van den Tempel M. Rheology of concentrated suspensions J Colloid and Interface Sci 1979; 71(1):1820.
9. de Man JM, Beers AM. Fat crystal networks: structure and rheological properties J Text Stud 1987; 18:303–318.
10. Heertje I, Leunis M, et al. Product microscopy of fatty products Food Microstructure 1987; 6:1–8.

11. Heertje I, van Eendenburg J, et al. The effect of processing on some microstructural characteristics of fat spreads Food Microstructure 1988; 7:189–193.

12. Shukla A, Rizvi SSH. Relationship among chemical composition, microstructure and rheological properties of butter Milchwissenschaft 1996; 51(3):144–148.

13. Marangoni AG, Rousseau D. Is plastic fat rheology governed by the fractal nature of the fat crystal network J Amer Oil Chem Soc 1996; 73:991–993.

14. Heertje I, van der Vlist P, et al. Confocal laser scanning microscopy in food research: some observations Food Microstruct 1987; 6:115–120.

15. Marangoni AG, Hartel RW. Visualization and structural analysis of fat crystal networks Food Technol 1998; 52(9):46–52.

16. Xu C, Zipfel W, et al. Multiphoton fluorescence excitation: new spectral windows for biological nonlinear microscopy Proc Natl Acad Sci USA 1996.

17. Flint O. Applications of light microscopy in food analysis Microscope 1984; 32:133–140.

18. Flint O. Microscopy in the development of new food products Eur Microsc Anal 1991; 10:21–23.

19. Inoe S. Video Microscopy. New York: Plenum Press, 1987.

20. Yiu SH. A fluorescence microscopic study of cheese Food Microstruct 1985; 4:99–106.

21. Brooker BE. Low temperature microscopy and x-ray analysis of food systems Trends in Food Sci and Tech 1990; 1:100–103.

22. Buchheim W. Aspects of samples preparation for freeze-fracture/freeze-etch studies of proteins and lipids in food systems. A review Food Microstruct 1982; 1:189–208.

23. de Man JM. Microscopy in the study of fats and emulsions Food Microstruct 1982; 1:209–222.

24. Kalab M. Electron microscopy of foods. In: Physical properties of foods Peleg M, Bagley EB, Eds. Westport. CT: AVI Publishing Co., 1983:43–104.

25. Sargeant JA. The application of cold stage scanning electron microscopy to food research Food Microstruct 1988; 7:123–135.

26. Heertje I. Microstructural studies in fat research Food Structure 1993; 12:77–94.

27. Rousseau D, Forestiere K, et al. Restructuring butterfat through blending and chemical interesterification. 1. Melting behavior and triacylglycerol modifications J Am Oil Chem Soc 1996; 73:963–972.

28. Rousseau D, Hill AR, et al. Restructuring butterfat through blending and chemical interesterification. 2. Microstructure and polymorphism J Am Oil Chem Soc 1996; 73:973–981.

29. Rousseau D, Hill AR, et al. Restructuring butterfat through blending and chemical interesterification. 3. Rheology J Am Oil Chem Soc 1996; 73:983–989.

30. Rousseau D, Marangoni AG. Tailoring the textural attributes of butterfat/canola oil blends via *Rhizopus arrhizus* Lipase-catalyzed interesterification. 1. Compositional modifications J Agric Food Chem 1998; 46:2368–2374.

31. Rousseau D, Marangoni AG. Tailoring the textural attributes of butterfat/canola oil blends via *Rhizopus arrhizus* Lipase-catalyzed interesterification. 2. Modifications of physical properties J Agric Food Chem 1998; 46:2375–2381.

32. Rousseau D, Marangoni AG, et al. The influence of chemical interesterification on the physicochemical properties of complex fat systems. 2. Morphology and polymorphism J Am Oil Chem Soc 1998; 75:1833–1839.

33. Marangoni AG, Rousseau D. The influence of chemical interesterification on physicochemical properties of complex fat systems 1. Melting and crystallization J Am Oil Chem Soc 1998; 75:1265–1271.

34. Marangoni AG, Rousseau D. The influence of chemical interesterification on the physicochemical properties of complex fat systems. 3. Rheology and fractality of the crystal network J Am Oil Chem Soc 1998; 75:1633–1636.

35. Vreeker R, Hoekstra LL, et al. The fractal nature of fat crystal networks Colloids and Surfaces 1992; 65:185–189.

36. Mandelbrot BB. Is Nature fractal Nature 1998; 279:783–784.

37. Cotton FA. Chemical applications of group theory. New York: Wiley Interscience, 1971.

38. Schroeder M. Fractals, chaos, power laws. New York. W.H.: Freeman and Company, 1991.

39. Crownover RM. Introduction to fractals and chaos. Boston: Jones and Bartlett, 1995.

40. Hausdorf F. Dimension und ausseres mass Mathematische Annalen 1919; 79:157–179.

41. Leibniz GW. Principia philosophiae, more geometrico demonstrata, 1721.

42. Jullien R, Botet R. Aggregation and fractal aggregates. Singapore: World Scientific Publishing Co., 1987.

43. Meakin P. Fractal aggregates Adv Colloid Interface Sci 1988; 28:249–331.

44. Lin MY, Lindsay HM, et al. Universality in colloid aggregation Nature 1989; 339:360–362.

45. Russ JC. Fractal surfaces. New York: Plenum Press, 1984.

46. Viczek T. Fractal growth phenomena. 2nd edition. Singapore: World Scientific Publishing Co., 1992.

47. Uriev NB, Ladyzhinsky IY. Fractal models in the rheology of colloidal gels Colloids and Surfaces A 1996; 108:1–11.

48. Medalia AI Surf Colloid Sci 1971; 4:1.

49. Friedlander SK. Smoke, dust and haze. New York: Wiley, 1977.

50. Mullins WW, Sekerka RF. Morphological stability of a particle growing by diffusion or heat flow J Appl Phys 1963; 34:323.

51. Forrest SR, Witten JTA. Long range correlations in smoke-particle aggregates J Phys A 1979; 12:L109.

52. Witten TA, Sander LM. Diffusion-limited aggregation, a kinetic critical phenomenon Phys Rev Lett 1981; 47(19):1400–1403.

53. Witten TA, Sander LM. Diffusion-limited aggregation Physical Review B 1983; 27(9):5686–5697.

54. Meakin P. Formation of fractal clusters and networks by irreversible diffusion-limited aggregation Phys Rev Lett 1983; 51: 1119.

55. Kolb M, Botet R, et al. Scaling of kinetically growing clusters Phys Rev Lett 1983; 51:1123.

56. Weitz DA, Oliveria M. Fractal tructures formed by kinetic aggregation of aqueous gold colloids Phys Rev Lett 1984; 52:1433.

57. Weitz DA, Huang JS, et al. Limits of the fractal dimension for irreversible kinetic aggregation of gold colloids Phys Rev Lett 1985; 54:1416.

58. Schaefer DA, Martin JE, et al. Fractal geometry of colloidal aggregates Phys Rev Lett 1984; 52:2371.

59. Aubert C, Cannell DS. Restructuring of colloidal silica aggregates Phys Rev Lett 1986; 56:738.

60. Schaefer DW, Keefer KD. Structure of random porous materials: silica Aerogel Phys Rev Lett 1986; 56(20):2199–2202.

61. Courtens E, Pelous J, et al. Brillouin-scattering measurements of phonon-fracton crossover in silica aerogels Phys Rev Lett 1987; 58(2):128–131.

62. Vacher R, Woignier T, et al. Structure and self-similarity of silica aerogels Phys Rev B 1988; 37(11):6500–6503.

63. Rojanski D, Huppert D, et al. Integrated fractal analysis of silica: adsorption, electronic energy transfer, and small-angle X-ray scattering Phys Rev Lett 1986; 56(23):2505–2508.

64. Dimon P, Sinha SK, et al. Structure of aggregated gold colloids Phys Rev Lett 1986; 57:595.

65. Bolle C, Cametti C, et al. Kinetics of salt-induced aggregation in polystyrene lattices studied by quasielastic light scattering Phys Rev A 1987; 35:837.

66. Bremer LGB, van Vliet T, et al. Theoretical and experimental study of the fractal nature of the structure of casien gels J Chem Soc, Faraday Trans 1989; 85:3359–3372.

67. de Gennes PG. Scaling concepts in polymer physics. Ithaca. NY: Cornell University Press, 1979.

68. Brown WD. The structure and physical properties of flocculating colloids. Cambridge, Engl.: University of Cambridge, 1987.

69. Dietler G, Aubert C, et al. Gelation of colloidal silica Phys Rev Lett 1986; 57:3117.

70. Sonntag RC, Russel WB. Elastic properties of flocculated networks JColloid Interface Sci 1987; 116:485–489.

71. Buscall R, Mills PDA, et al. Scaling behaviour of the rheology of aggregate networks formed from colloidal particles J Chem Soc, Faraday Trans 1988; 84:4249–4260.

72. Kantor Y, Webman I. Elastic properties of random percolating systems Phys Rev Lett 1984; 52(21):1891–1894.

73. Feng S, Sen P. Percolation on elastic networks: new exponent and threshold Phys Rev Lett 1984; 52:216.

74. Feng S, Sen P, et al. Percolation on two-dimensional elastic networks with rotationally invariant bond bending forces Phys Rev B 1984; 30:5386.

75. Brown WD, Ball RC. Computer simulation of chemically limited aggregation J Phys A 1985; 18:L517..

76. Ball RC. Fractal colloidal aggregates: consolidation and elasticity Physica D 1989; 38:13–15.

77. Edwards SF, Oakeshott RBS. The transmission of stress in an aggregate Physica D 1989; 38:88–92.

78. Bremer LGB, Bijsterbosch BH, et al. On the fractal nature of the structure of acid casien gels Colloid Surf 1990; 51:159–170.

79. Bremer LGB, Bijsterbosch BH, et al. Formation, properties and fractal structure of particle gels Advances in Colloid and Interface Sci 1993; 46:117–128.

80. Shih WH, Shih WY, et al. Scaling behavior of the elastic properties of colloidal gels Phys Rev A 1990; 42:4772–4779.

81. Chen M, Russel B. Characteristics of flocculated silica dispersions J Colloid and Interface Sci 1991; 141(2):565–577.

82. Vreeker R, Hoekstra LL, et al. Fractal aggregation of whey proteins Food Hydrocolloids 1992; 6:423–435.

83. Hagiwara T, Kumagai H, et al. Analysis of aggregate structure in food protein gels with the concept of fractal Biosci Biotech Biochem 1997; 61:1663–1667.

84. Hagiwara T, Kumagai H, et al. Fractal analysis of aggregates in heat-induced BSA gels Food Hydrocolloids 1998; 12:29–36.

85. Johansson D. Weak gels of fat crystals in oils at low temperatures and their fractal nature J Amer Oil Chem Soc. 1995; 72: 1235–1240.

86. Sherman P. The influence of particle size on the viscoelastic properties of flocculated emulsions, 5th International Congress on Rheology, Kyoto, Japan, 1968.

87. Juriaanse AC, Heertje I. Microstructure of shortenings, margarine and butter—a review Food Microstructure 1988; 7: 181–188.

8

The Yield Stress and Elastic Modulus of a Fat Crystal Network

ALEJANDRO G. MARANGONI

Department of Food Science
University of Guelph
Guelph, Ontario, Canada

1. INTRODUCTION

The yield stress is one of the most important macroscopic properties of fats and fat-containing products because it is strongly correlated to sensory perception of hardness and spreadability, as well as to material stability. The apparent yield stress of a plastic solid is usually defined as the point at which, when the stress is increased, the deforming solid first begins to show liquidlike behavior [1]. Even though the concept of a yield stress has been incorporated into phenomenological rheologic models, the relationship between a material's structure and its yield stress has not been established. In this chapter, we

develop a general model relating the structure of a fat crystal network to its yield stress and elastic modulus.

MODEL

The change in free energy (∂G) of a system at constant pressure, volume, and temperature equals the change in internal energy (∂U) minus the product of the change in entropy (∂S) times temperature (T):

$$\partial G = \partial U - T\partial S. \tag{1}$$

The change in free energy of a flocculated colloidal network as a function of changes in extensional strain (∂ε) at constant temperature, pressure (P), volume (V), and composition (μ), where deformation takes place without any rupture of bonds, equals the product of stress (σ) times volume [2]:

$$\left(\frac{\partial G}{\partial \varepsilon}\right)_{T,P,V,\mu} = \left(\frac{\partial U}{\partial \varepsilon}\right)_{T,P,V,\mu} - T\left(\frac{\partial S}{\partial \varepsilon}\right)_{T,P,V,\mu} = \sigma \cdot V. \tag{2}$$

The main assumption in this model is that the change in free energy of the network upon deformation arises due to changes in elastic energy ($\partial E_{elastic}$), namely:

$$\frac{\partial G}{\partial \gamma} = \frac{\partial E_{elastic}}{\partial \gamma}. \tag{3}$$

The elastic energy of the network can be expressed in terms of deformation (ΔL), or strain ($\varepsilon = \Delta L/L$),

$$E_{elastic} = \frac{1}{2}k(\Delta L)^2 = \frac{1}{2}L^2 k\varepsilon^2, \tag{4}$$

where k is the elastic constant of the network. The elastic constant k can be substituted by A·E/L, where E corresponds to the Young's modulus, A is the area over which the force is applied, and L is the size of the system. The product of the area times the length corresponds to the volume of the network, while the product of the Young's modulus times the strain corresponds to stress. Thus, the change in elastic energy as a function of strain can be expressed as

$$\frac{\partial E_{elastic}}{\partial \varepsilon} = \frac{\partial}{\partial \gamma}\left(\frac{1}{2}LAE\varepsilon^2\right) = VE\varepsilon = V\sigma. \tag{5}$$

Sonntag and Strenge [2] have shown that the entropic contribution to the change in free energy of a flocculated colloidal network on a small elastic deformation is much smaller than the contribution from changes in the internal energy of that network. Thus, for the case where $\partial U > T\partial S$,

$$\frac{\partial G}{\partial \varepsilon} \approx \frac{\partial U}{\partial \varepsilon} = VE\varepsilon. \tag{6}$$

On integration and rearrangement, an expression for the Young's modulus of the network can be obtained,

$$E = \frac{2\Delta U}{V\varepsilon^2}, \tag{7}$$

where ΔU corresponds to the change in the internal energy of the network upon deformation, which equals the total interaction energy per floc.

The volume of the system can be expressed as a function of the particle volume fraction (Φ) and the total volume occupied by the flocs,

$$V = \frac{V_a N_a N_\xi}{\Phi}, \tag{8}$$

where V_a is the volume of an individual particle, N_a is the number of particles in a floc, and N_ξ is the total number of flocs in the system. Flocs are assumed to occupy space in a close-packed fashion and are thus completely space-filling. The number of particles in a floc is given by

$$N_a \sim \left(\frac{\xi}{a}\right)^D, \tag{9}$$

where ξ is the diameter of the flocs, a is the diameter of the particles within the floc, and D is the fractal dimension for the arrangement of particles within the floc. The volume fraction of particles within the floc (Φ_ξ) is therefore given by

$$\Phi_\xi \sim \frac{N_a V_a}{N_s V_s} \sim \left(\frac{\xi}{a}\right)^{D-d}, \tag{10}$$

where N_s is the number of available embedding space elements within the floc ($N_s \sim (\xi/a)^d$), V_s is the volume of an element of embedding space, and d is the Euclidean dimension of the

embedding space. At this point we will assume that a particle volume is equal to the volume of an element of embedding space, namely $V_a = V_s$. Thus, the diameter of the flocs varies with the volume fraction of particles within the floc as

$$\xi \sim a\Phi_{\xi}^{\frac{1}{D-d}}. \tag{11}$$

Flocs pack in a regular, close-packed, Euclidean fashion; hence, at the floc level of structure, the material can be considered as an orthodox amorphous substance. Within the flocs, however, particles pack in a non-Euclidean, fractal fashion. For such a structural arrangement, the volume fraction of particles in a floc (Φ_ξ) is equivalent to the volume fraction of particles in the entire system (Φ), namely $\Phi_\xi = \Phi$. This well-known relation of polymer physics [3] has been experimentally shown to also apply to colloidal aggregates above their gelation threshold [4].

Thus, considering all of the aforementioned, for spherical particles packed in a fractal fashion within a floc, the Young's modulus of the network can be expressed as

$$E = \frac{12\Delta U}{\pi a^3 N_\xi \varepsilon^2}\Phi^{d/(d-D)}. \tag{12}$$

In the weak-link rheologic regime described by Shih et al. [5], the links between flocs of colloidal particles yield under an external stress, i.e., the flocs are mechanically stronger than the links between them. Thus, in this regime, the macroscopic deformation of the network (ΔL) can be related to the interfloc deformation, $\Delta L = (n-1)(l-l_o)$, where l_o is the equilibrium distance between flocs, l corresponds to the distance between flocs under an applied stress, and (n-1) corresponds to the number of links between flocs in the direction of the applied stress (Figure 1).

The number of flocs in the direction of the applied stress roughly equals the number of links between flocs for the case where $L > \xi$. The macroscopic strain terms can be expressed as $n(l-l_o)/L$, or $(l-l_o)/\xi$, since the term L/n corresponds to the size of the flocs, ξ, for the case where $\xi >> l_o$. Substituting the strain terms with $(l-l_o)/\xi$, and ξ with $a\Phi^{-1/(d-D)}$, results in the expression

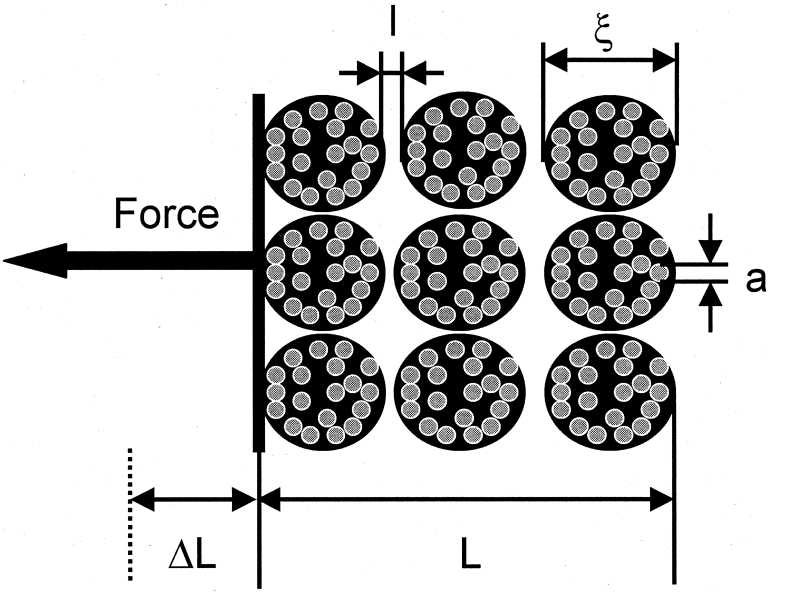

Figure 1 Idealized flocculated colloidal network under extension. Particles (a) are packed in a fractal fashion within flocs (ξ). A force (F) acting upon the network causes the links between flocs to yield, and the original length of the system in the direction of the applied force (L) to increase (ΔL). Thus, the interfloc separation distance (l), also increases.

$$E = \frac{12\left(\frac{\Delta U_\xi}{(l-l_o)^2}\right)}{\pi a}\Phi^{\frac{1}{(d-D)}}, \tag{13}$$

where ΔU_ξ ($\Delta U_\xi = \Delta U/N_\xi$) is the effective change in internal energy per floc.

Let us consider the case where a network is stretched to its elastic limit. Beyond this critical strain (ε*), this material begins to flow. The critical strain can be defined as

$$\varepsilon^* = \frac{l^* - l_o}{\xi}, \tag{14}$$

where l* is the critical deformation at the elastic limit, l_o is the equilibrium separation distance between flocs, while ξ is

the diameter of the flocs. The product of the Young's modulus (E) and ε* equals the yield stress (σ*), which can be obtained by multiplying both sides of equation 13 by ε*,

$$E\varepsilon^* = \frac{12\left(\frac{\Delta U_\xi}{(l^*-l_o)^2}\right)}{\pi a}\frac{(l^*-l_o)}{\xi}\Phi^{\frac{1}{(d-D)}}, \tag{15}$$

yielding

$$\sigma^* = \frac{12\left(\frac{\Delta U_\xi}{(l-l_o)}\right)}{\pi a \xi}\Phi^{\frac{1}{(d-D)}}. \tag{16}$$

The term $\Delta U_\xi/(l\text{-}l_o)$ can be substituted with the expression of a force ($\Delta E/\Delta x = 1/2$ F). The force required to pull two flocs apart corresponds to the force of adhesion (F_{ad}), which for two rigid, incompressible spheres of equal diameter can be estimated for the case where $\xi > l_o$ using the Derjaguin approximation [6],

$$F_{ad} = \pi\delta\xi, \tag{17}$$

where ξ corresponds to the diameter of the spheres, and δ to the surface free energy per unit area ($J\ m^{-2}$). This surface free energy is equivalent, in our case, to the crystal-melt interfacial tension ($N\ m^{-1}$).

Substituting equation 17 into equation 16 results in an expression for the yield stress of a solid material structured as a space-filling collection of fractal flocs of particles,

$$\sigma^* = \frac{6\delta}{a}\Phi^{\frac{1}{d-D}}. \tag{18}$$

Moreover, the Young's modulus of the material can then be estimated from

$$E = \frac{\sigma^*}{\varepsilon^*} = \frac{6\delta}{a\varepsilon^*}\Phi^{\frac{1}{d-D}}. \tag{19}$$

Equation 19 is basically equivalent to the model of Marangoni [7], which is based on van der Waal's arguments,

$$E \sim \frac{A}{2\pi a \varepsilon^* d_o^2}\Phi^{\frac{1}{d-D}}, \tag{20}$$

where A is Hamacker's constant, and d_o is the interfloc separation distance. The current model is a variation of this model using a semiclassical approach based on bulk properties. The purpose of developing an alternative form of the pre-exponential factor λ was to make it more accessible from computational, as well as experimental, points of view. Equation 20 can be easily obtained from equation 19 by substituting δ with $F_{ad}/\pi\xi$, and F_{ad} with the attractive van der Waals' force between two spheres of equal diameter, $F_{vw} = A\xi/12d_o^2$. Keep in mind that $F = 2\partial E/\partial x$ when checking the derivation.

Values for the shear modulus (G) could be obtained from knowledge of the Poisson ratio (μ) of the material since $E = 2(1+\mu)G$. For a material where no volume change takes place when it is stretched or compressed, the Poisson's ratio is 0.5, and thus $E = 3G$ and:

$$G \sim \frac{A}{6\pi a \varepsilon^* d_o^2} \Phi^{\frac{1}{d-D}} \tag{21}$$

Thus, the yield stress of such a material is determined by the amount of network material present (volume fraction of solids), the structure of the network (primary particle size, fractal dimension) and intermolecular forces (solid-liquid interfacial tension). This universal expression can be applied to any flocculated particulate system, including colloidal gels and crystals, as well as pastes and other types of soft, condensed matter.

Figure 2 shows simulations of the effects of δ, D, and a on the yield stress. Of particular interest is the large effect of D on the calculated yield stress–a lower fractal dimension results in a higher yield stress. The δ for triacylglycerols has been determined experimentally to be about 0.01 mJ m^{-2} [7].

In this work, we consider the stress at the limit of linearity as the yield stress. Small deformation mechanical testing is much more sensitive than large deformation techniques. In a large deformation mechanical test, the apparent yield stress is a strong function of the loading rate and loading history. Usually, high loading rates are used for the determination of the yield stress of soft, plastic solids due to sensitivity issues–the higher the loading rates used, the higher the appa-

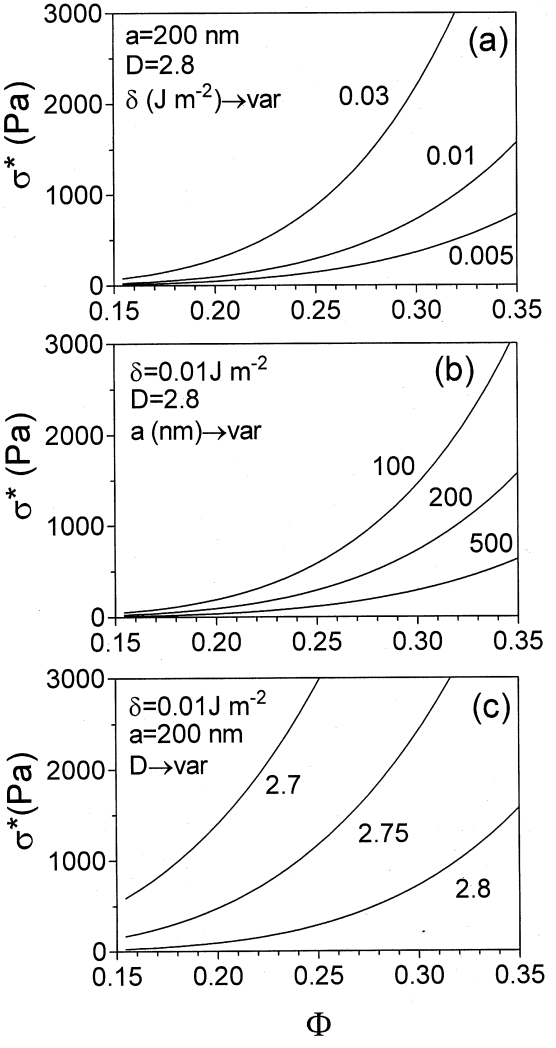

Figure 2 Simulations of the effects of (*A*) surface free energy, (*B*) primary crystal size, and (*C*) fractal dimension on the yield stress of a plastic disperse system at different solids' volume fractions (Φ).

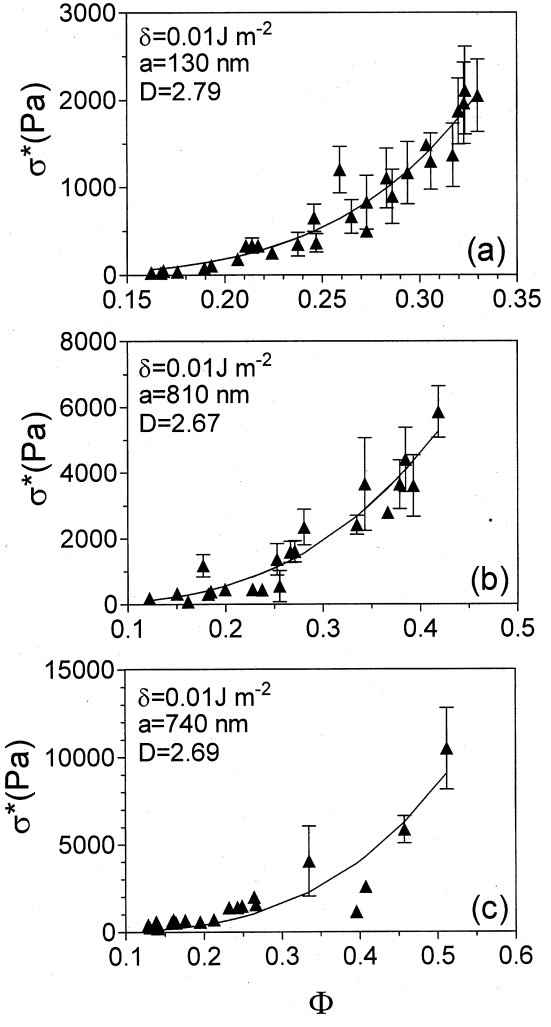

Figure 3 Experimentally determined changes in σ* as a function of Φ for blends of (A) milk fat, (*B*) cocoa butter, and (*C*) modified palm oil with canola oil. Samples were crystallized statically from 40°C to 5°C at a cooling rate of 1°C/min, and annealed at 5°C for 24hr. Symbols represent the average and standard deviation of 2–6 samples. The line through the data was generated by nonlinear least-squares minimization of the model to the experimental data. Indicated are the estimates of the model parameters. The surface free energy term (δ) was fixed as a constant.

rent yield stress of the material. When the loading rate is higher than the rate of deformation of the material, a higher apparent yield force will be determined. For this reason, it is sometimes not possible to determine the yield stress of a soft, plastic material at low loading rates. This, however, does not mean that the material does not have a yield stress. The more sensitive, small deformation techniques should be used instead.

Figure 3 shows changes in the yield stress (σ^*) as a function of solids' volume fraction (Φ) for blends of milk fat (Figure 3*A*), cocoa butter (Figure 3*B*) and modified palm oil (Figure 3*C*) with canola oil crystallized for 24hr at 5°C. The yield stress was determined using a small-deformation, controlled stress shear rheometer (TA Instruments AR2000, Mississauga, ON, Canada) as described in the methods section. The fractal dimensions of the three fat crystal networks were determined from the slope of the log-log plot of σ^* vs. Φ (not shown), assuming a weak-link rheologic regime [$D = 3\text{-(slope)}^{-1}$]. The σ^*–Φ scaling relationships for milk fat, cocoa butter, and modified palm oil were, respectively, $\sigma^* \sim \Phi^{5.8}$, $\sigma^* \sim \Phi^{3.0}$, and $\sigma^* \sim \Phi^{2.1}$, yielding fractal dimensions of 2.82, 2.66 and 2.52. respectively. Our model was then fitted to σ^*–Φ data by nonlinear regression using Scientist 2.0 (Micromath Scientific Software, Salt Lake City, Utah, USA), and parameter estimates were obtained. As can be seen, the model fit the data quite well for the three different systems, and the values obtained for D and a were reasonable. In our experience it was necessary to either fix δ or a as a constant in order to obtain reliable parameter estimates–in our case, δ was fixed.

Thus, based on this work, we propose a structural definition for the yield stress of a particle network: the yield stress corresponds to the force required to move an ensemble of network structural elements from their equilibrium separation distance, l_o, characterized by an interaction energy, U_{eq}, to a critical separation distance, l^*, where the interaction energy equals zero.

REFERENCES

1. Barnes HA. The yield stress–a review of "παντα"–everything flows J Non-Newtonian Fluid Mech 1999; 81:133–178.

2. Sonntag H, Stremge K. Coagulation kinetics and structure formation. New York: Plenum Press, 1987:345–392.

3. de Gennes PG. Scaling concepts of polymer physics. Ithaca. NY: Cornell University Press, 1979.

4. Dietler G, Aubert C, et al. Gelation of colloidal silica Phys Rev Lett 1986; 57:3117–3120.

5. Shih WH, Shih WY, Kim SI, Lin J, Aksay IA. Scaling behavior of the elastic properties of colloidal gels Phys Rev A 1990; 42: 4772–4779.

6. Israelachvili J. Intermolecular and surface forces. 2nd ed., Academic Press. 1992:163.

7. Marangoni AG. Elasticity of high-volume fraction fractal aggregate networks: a thermodynamic approach Phys Rev B 2000; 62: 13951–13955.

8. Phipps LW. Heterogeneous and homogeneous nucleation in supercooled triglycerides and n-paraffins Trans Faraday Soc 1964; 60:1873–1883.

9

Experimental Methodology

RODRIGO CAMPOS
Department of Food Science
University of Guelph
Guelph, Ontario, Canada

1. INTRODUCTION

This chapter is a step-by-step description of the most common analytical methods used in the study of physico–chemical properties of fat crystal networks. The methodologies covered include those used in the investigation of nucleation and crystallization kinetics, thermal properties and polymorphism, microstructure (both by microscopic and rheologic approaches), and mechanical properties of fat crystal networks. With the aim of providing the reader with a complete panorama of the presented experimental methodologies, a brief theoretical background is included that covers the fundamental concepts related to the phenomena and instrumentation used. This is

followed by a comprehensive description of experimental procedures, from sample preparation to data analysis, including some illustrative examples. This is not an exhaustive review of all of the analytic methods available in the area of fat material science research, but, rather, of the most commonly used methods in our laboratory.

2. CRYSTALLIZATION

By studying the development of solid crystalline material as a function of time, different kinetic and thermodynamic parameters can be obtained, which provide insight into the nature of the crystallization process. Three different analytical techniques can be used to investigate crystallization: pulsed nuclear magnetic resonance (pNMR), cloud point analysis, and microscopy.

2.1. Crystallization Kinetics by Pulsed Nuclear Magnetic Resonance

The solid fat content (SFC) of a fat sample can be measured by pNMR (Fig. 1). This technique measures the response of

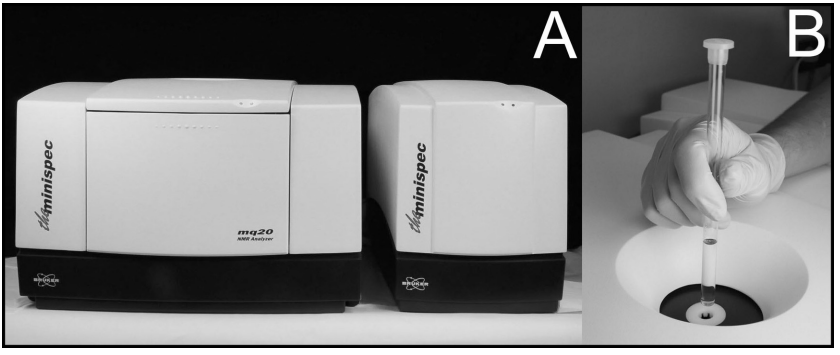

Figure 1 Pulsed Nuclear Magnetic Resonance (pNMR) instrument (Bruker PC/20 series NMR Analyzer, Bruker, Milton, ON, Canada) (**A**), and sample tube which is to be analyzed for solid fat content percentage by pNMR (**B**).

hydrogen nuclei (protons) to a short intense pulse of radio frequency energy in a magnetic field. When a radio frequency pulse is applied to a sample (such as fat), a magnetization signal is induced. The initial amplitude of this signal is proportional to the number of protons present in the sample. When more than one proton-containing component (i.e., liquid and solid fat) is present, the signal decay corresponding to each component is different. As observed in Figure 2, there is an initial decay in the magnetization signal intensity, which is characteristic of the solid component. The remaining magnetization displays a slower decay, which arises from the liquid component. The distinct decay times represent the solid and

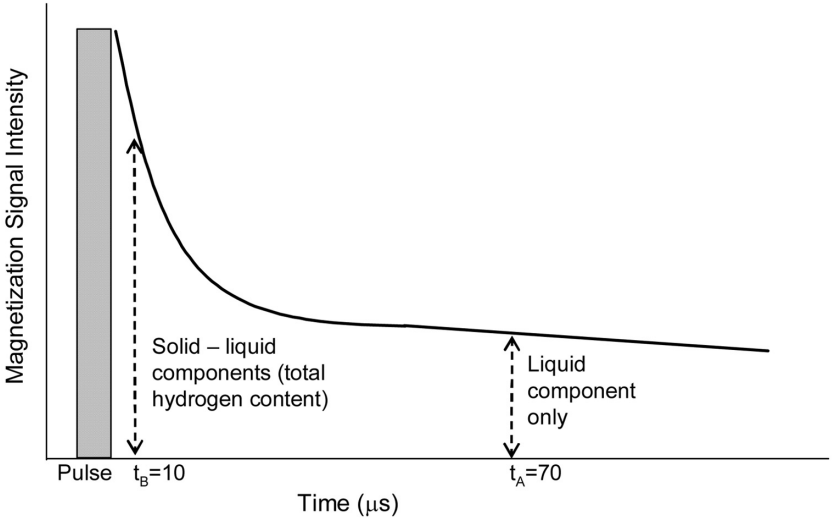

Figure 2 Magnetization decay of a fat sample used in the determination of the solid fat content (SFC) by pulsed Nuclear Magnetic Resonance (pNMR). The initial amplitude is proportional to the response of the total number of protons present in the sample after application of a radio frequency pulse. The protons in the solid phase exhibit a faster signal decay relative to the protons in the liquid phase. The difference between the signal resulting from both the solid and liquid phases and the liquid phase only is proportional to the amount of protons present in the solid phase, from which the solid fraction is calculated.

liquid components of the fat sample. By sampling the decaying signal at two suitable time points, the percent solid or liquid fat is obtained [1].

2.1.1. Procedure

2.1.1.1. Sample Preparation

Melt the sample in an oven at a temperature that ensures that all crystal memory is erased. For most edible fats, 80°C for 30 minutes, after the sample has melted, is sufficient. Yet, some high-melting-point fats require a higher temperature to erase all crystal memory; for example palm oil needs to be heated at 120°C for 10 minutes. Transfer approximately 3 g of the molten fat to glass pNMR tubes (10 mm diameter, 1 mm thickness, and 180 mm height) preheated at 80°C. Wipe the outside of the tube with tissue paper, making sure that the exterior is clean and dry. To prevent the entry of dust, solvent vapors, or moisture, close the tubes with a cap or rubber stopper.

2.1.1.2. Experimental Procedure

Once the sample is prepared, immediately transfer the tubes to a water bath, which has been preset to the desired temperature of study. It is important to make sure that the sample is completely molten before readings are taken. If the sample is cooled during preparation, heat again to melt the sample and ensure that all crystal memory is erased. Take SFC readings at appropriate time intervals with a pNMR analyzer. The time intervals chosen and duration of the experiment will depend on the fat and temperature of crystallization. For samples exhibiting rapid crystallization (such as in situations with high degrees of undercooling), measurements may be taken every 30 seconds, whereas for slower crystallization processes (low degrees of undercooling), measurements taken every 5 minutes may suffice. Continue to take measurements until the SFC readings reach a plateau and the system stabilizes, reaching an equilibrium SFC reading.

2.1.1.3. Data Analysis

Construct crystallization curves with the obtained data by plotting the SFC(%) as a function of time, as shown in Fig-

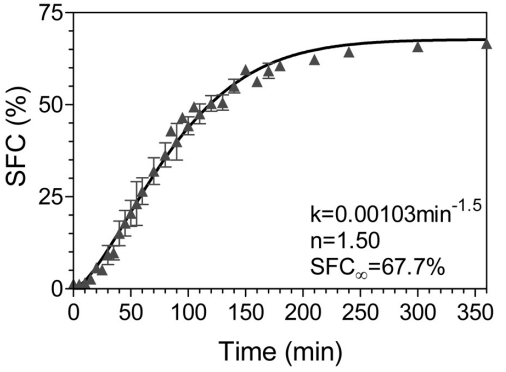

Figure 3 Crystallization curve of cocoa butter cooled at 1°C/min and stored at 24°C. Data is collected using pulsed nuclear magnetic resonance (pNMR) spectrometry. The crystallization curve is fitted to the Avrami equation. The Avrami parameters describe the crystallization kinetics of cocoa butter under these crystallization conditions.

ure 3. Fit the crystallization curves to the Avrami equation using nonlinear regression with the assistance of data fitting software. Figure 3 shows an example of crystallization data fitted to the Avrami equation. The Avrami [2] model, as applied to fats, has the following form:

$$\frac{SFC(t)}{SFC_{\infty}} = 1 - e^{-kt^n} \tag{1}$$

where SFC(t) is the SFC(%) as a function of time, SFC_{∞} is the limiting SFC as time approaches infinity, the Avrami constant (k) represents the crystallization rate constant, and the Avrami exponent or index of crystallization (n) indicates the crystal growth mechanism. The Avrami index is a combined function of the time dependence of nucleation and the number of dimensions in which growth takes place. Nucleation can be either instantaneous, with nuclei appearing all at once early on in the process, or sporadic, with the number of nuclei increasing with time. [2,3]. Possible values for the Avrami exponent for different types of nucleation are shown in Table 1.

Table 1 Avrami Exponent (n) Values for Different Types of Nucleation and Dimensionality of Growth

Avrami exponent (n)	Various types of growth and nucleation
1 + 0 = 1	Rodlike growth from instantaneous nuclei
1 + 1 = 2	Rodlike growth from sporadic nuclei
2 + 0 = 2	Disclike growth from instantaneous nuclei
2 + 1 = 3	Disclike growth from sporadic nuclei
3 + 0 = 3	Spherulitic growth from instantaneous nuclei
3 + 1 + 4	Spherulitic growth from sporadic nuclei

Half-times of crystallization, which reflect the magnitudes of the rate constants, are calculated using the following relationship, which is derived from the Avrami model:

$$t_{1/2} = \left(\frac{0.693}{k}\right)^{1/n} \tag{2}$$

2.2 Nucleation Events

Crystallization begins with the supercooling ($\Delta T = T_f - T_m$) of the molten fat (equivalent to the supersaturation of the solution). This is when liquid fat is taken to a temperature (T_f) below its melting temperature (T_m). In the melt, fat molecules are in random thermal motion; upon supercooling, solid nuclei embryos form. The newly formed embryos will continue to form and dissolve until they reach a critical size. The Gibbs free energy of the embryos will reach a maximum at this critical size. In order to maintain a minimum amount of free energy, these embryos will either redissolve or continue to grow, forming stable nuclei. Nuclei will grow continuously as other lipid species in the melt diffuse onto its growing surface. Crystal growth continues followed by aggregation into clusters and formation of bridges with each other, eventually resulting in the creation of a crystal network.

The time required for stable nuclei to form is the induction time of crystallization ($\tau_{crystallization}$), and is influenced by the

degree of supercooling (ΔT) and the activation free energy of nucleation (ΔG_c). When a fat system is highly supercooled, the energy barrier for nucleation is lower; this translates into a lower $\tau_{crystallization}$, which in turn is inversely proportional to the nucleation rate (J), namely:

$$J \approx \frac{1}{\tau_{crystalization}} \tag{3}$$

Although pNMR is widely used to measure the SFC of fats, it is incapable of accurately measuring less than 1% of crystalline material; it is, thus, insensitive to the initial nucleation events that take place in the melt. Crystals can be observed before the pNMR detects a signal. Hence, other analytical techniques are used to study the early stages of crystallization (i.e., the determination of $\tau_{crystallization}$ and ΔG_c). Such techniques include monitoring the changes in turbidity of a crystallizing sample through measurements of absorbance or by light scattering intensity.

2.2.1. Measurement of Inductions Times by Spectrophotometry

Changes in the turbidity of a fat sample as a function of time can be measured using a spectrophotometer equipped with a temperature-controlled sample holder, reading absorbance (A) at 500 nm. The drawback of this technique is usually poor sample temperature control. This is due to the relatively large sample volumes used (3 mL) and the poor heat transfer rates. The glass or plastic material of which cuvettes are made acts as an insulation barrier toward temperature changes. This results in uncontrolled, slow cooling rates of the fat samples.

2.2.1.1. Procedure

2.2.1.1.1. Sample Preparation: Melt the sample in an oven at a temperature that ensures that all crystal memory is erased. For most edible fats, 80°C for 30 minutes, after the sample has melted, is sufficient. Yet, some high melting point fats require a higher temperature to erase all crystal memory; for example palm oil needs to be heated at 120°C for 10 min-

utes. Transfer 3 mL of molten fat to a preheated spectrophotometer cuvette. Special care should be taken so that the cuvette is clean and free from scratches. Foreign particles or abrasions in the cuvette will scatter light leading to inaccurate results. Maintain the cuvette above 40°C to prevent any crystallization from taking place. Care should be taken when using plastic cuvettes as they may melt or deform when exposed to high temperatures.

2.2.1.1.2. Experimental Procedure: Set the wavelength on the spectrophotometer to 500 nm and zero the instrument against a sample of totally molten fat. Set the sample holder to the temperature of study. Make sure that the temperature of the sample holder has stabilized before performing any measurements. Transfer the sample cuvette to the sample holder of the spectrophotometer and take absorbance readings at appropriate time intervals until the absorbance reaches a plateau.

2.2.1.1.3 Data Analysis: Construct a curve by plotting the obtained absorbance readings as function of time as shown in Figure 4. The value of $\tau_{crystallization}$ for each sample can be obtained from the plot as the time when there is an absorbance

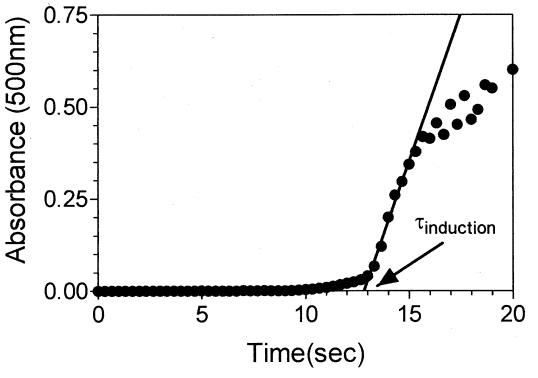

Figure 4 Increase in absorbency measured at 500 nm as a function of time of milk fat triacylglycerols crystallized at 22.5°C, from which the induction time ($\tau_{induction}$) is calculated.

reading different from zero. This corresponds to the time at which crystalline material appears in the sample, which will absorb light. Another way of calculating $\tau_{crystallization}$ is by extrapolating it from the linearly increasing portion of the curve to the time axis, as shown in Figure 4.

A key factor in the study of nucleation under isothermal conditions is that crystallization should not take place during cooling. If crystallization initiates during the cooling of the sample, then the crystallization process is dependent on time and temperature variables, making it a dynamic crystallization process. In order to achieve isothermal crystallization, with no nucleation taking place above the temperature of study, cooling rates higher than 20°C/min are required. The poor heat transfer in most spectrophotometer cell holders makes it difficult to achieve fast and controlled cooling of the sample. For this reason, other techniques are recommended.

2.2.2. Measurement of Inductions Times by Light Scattering

An alternative approach to measuring nucleation induction times is light scattering. A cloud point analyzer such as the Phase Transition Analyzer (Phase Technology, Richmond, BC, Canada) shown in Figure 5*A*, is used to quantify the light scattered by the growing crystalline mass in a sample of cooled molten fat. A relatively small sample is placed in a sample chamber (Fig. 5*B*) and a beam of light is impinged on it. When crystals start to appear in the sample, the incident beam is scattered by the solid-liquid phase boundaries onto detectors in the chamber. As more and more crystal mass develops, the signal output increases and is automatically recorded. The sample chamber is maintained under dry conditions to prevent vapor condensation and the temperature of the fat is precisely controlled using a Peltier element. This technique is reliable, reproducible, and allows for the accurate monitoring of the early stages of nucleation.

2.2.2.1. Procedure

2.2.2.1.1. Sample Preparation: Melt the sample in an oven at a temperature that ensures that all crystal memory

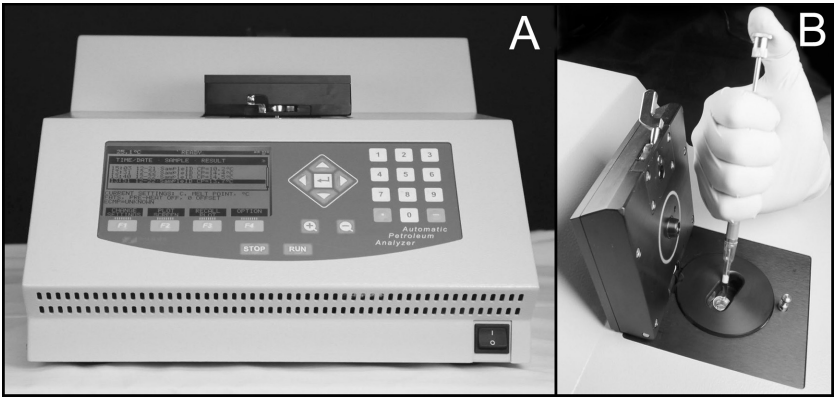

Figure 5 Phase Transition Analyzer (**A**) (Phase Technology, Richmond, BC, Canada) used in nucleation studies of fats. The fat sample is placed in the sample chamber (**B**) and a beam of light is impinged on it. When the nucleation and early crystallization events take place, the incident beam is scattered by the solid–liquid phase boundaries onto detectors in the chamber, and the detected signal is automatically recorded.

is erased. Pipette 150μL of melted sample into the sample chamber of the Phase Transition Analyzer (Fig. 5*B*).

2.2.2.1.2 Experimental Procedure: Turn on the instrument and allow it to warm up. Make sure that the coolant supply (tap water that is clean and free of deposits) is on and that desiccant materials are in good condition. Initiate the software that controls the instrument (LBT-466, Phase Technology Richmond, BC, Canada). To set up a program, open the TCS control widow (as shown in Fig. 6).

Press the "Edit" button to make a new program or edit an existing program. The program should begin by melting the sample at a temperature and time combination that erases the crystal memory of the sample (80°C for 30 minutes for most edible fats). In the case of nucleation studies, the sample is cooled at a controlled rate and allowed to crystallize isothermally at a given temperature. Once the program is established and the sample is loaded into the sample chamber, press

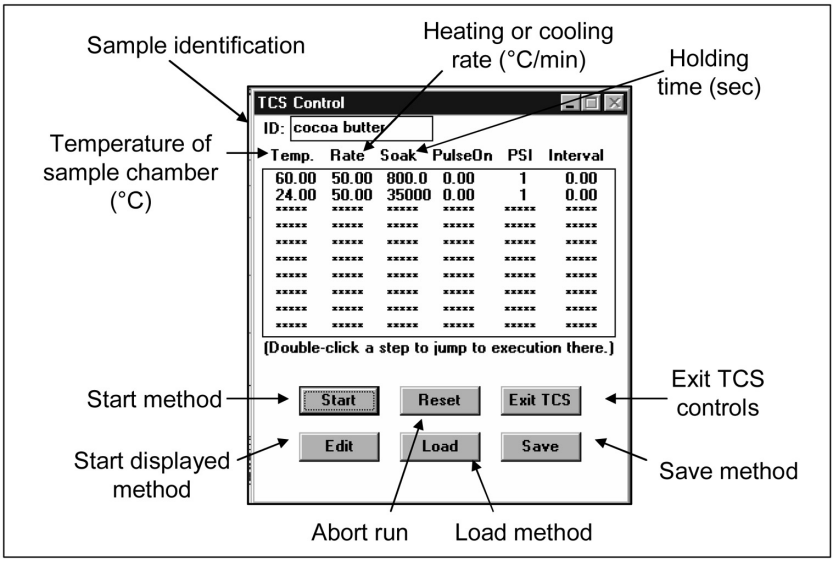

Figure 6 TCS[??] controls used as experimental parameter in the Phase Transition Analyzer (Phase Technology, Richmond, BC, Canada).

"Start" in the TCS control window. The experiment will now run. Through the course of the experiment, data is gathered and plotted in real time by the software. The user has the option of changing the variable of the x-axis of the real time plot to be either time (sec) (Fig. 7*A*) or Temperature (°C) (Fig. 7*B*). At the end of the experimental run, the collected data may be saved with a ".dat" extension and subsequently imported into Microsoft Excel or any other spreadsheet program for data analysis purposes.

2.2.2.1.3. Data analysis: Throughout the entire experimental run, data will be saved, including the melting, holding, and cooling of the sample. Import the saved file into a spreadsheet program. It is important to select only the data that corresponds to the isothermal crystallization of the sample for the analysis. As mentioned previously, it is of utmost importance that no crystallization takes place during cooling in the

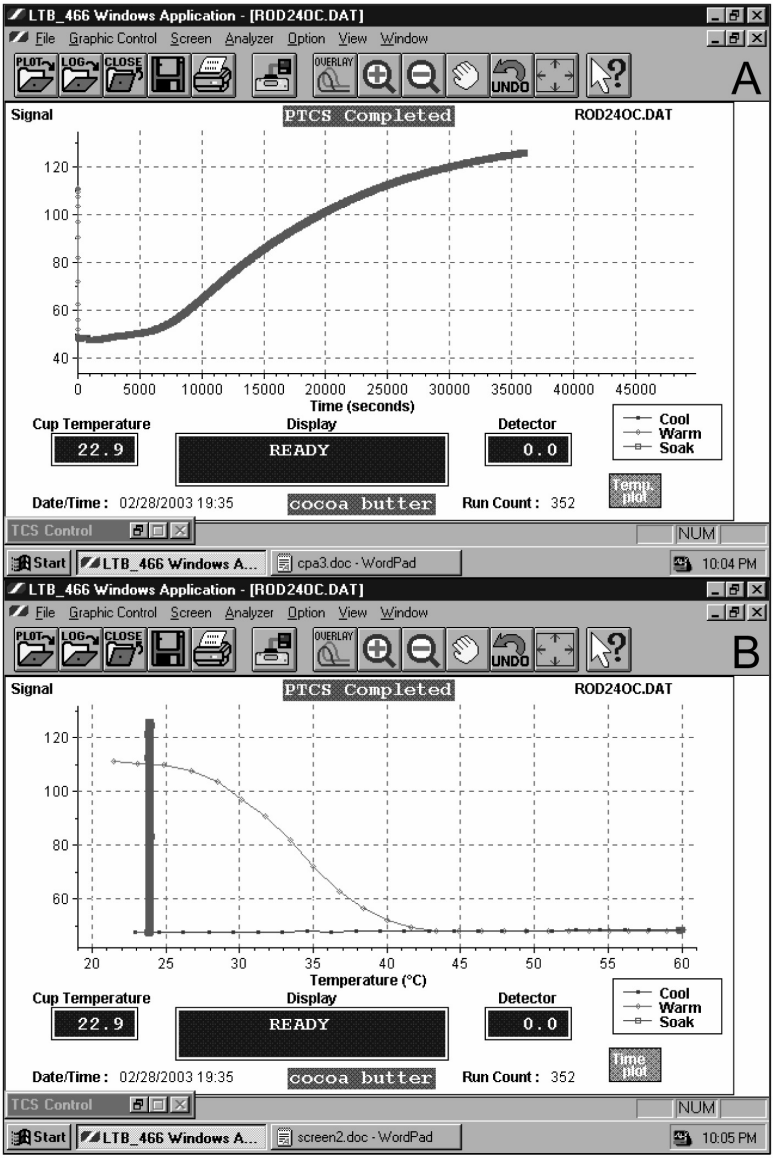

Figure 7 Graphic plot of the signal as a function of time (**A**) or temperature (**B**) obtained in real time from the Phase Transition Analyzer (Phase Technology, Richmond, BC, Canada).

study of isothermal crystallizations. Plot the signal obtained during the crystallization of the sample as a function of time as observed in Figure 8. Consider the initial time as the point when the sample has reached the temperature of crystallization; $\tau_{crystallization}$ can be defined either as the point in time when the signal deviates from the baseline or as the onset time of linear turbidity development. In either case, the induction time is the point at which initial nuclei are present and scatter light. An example of $\tau_{crystallization}$ determination is shown on Figure 8.

From the determination of various $\tau_{crystallization}$, the free energy of nucleation (ΔG_c) may be evaluated using a Fisher-Turnbull plot of $\ln\tau T$ vs. $1/(T\Delta T^2)$. Obtain the resulting slope (m) from the plot, and then use the slope to determine the ΔG_c using the following equation:

$$\Delta G_c = \frac{mk_B}{(T_m - T_f)^2} \tag{4}$$

where k_B is the Boltzman's constant (1.38×10^{-23} J/K), T_m is the melting temperature of the sample and T_f is the crystallization temperature.

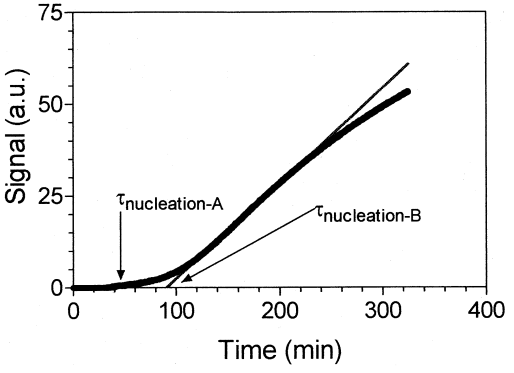

Figure 8 Phase Transition Analyzer singnal as a function of time plot from which the induction time is obtained when the signal deviates from the baseline ($\tau_{induction\text{-}A}$) or as the onset time of linear turbidity development ($\tau_{induction\text{-}B}$).

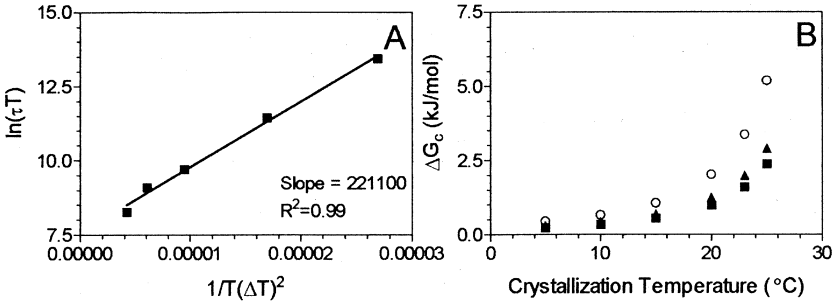

Figure 9 Fitting of induction times for nucleation data to the Fisher-Turnbull equation used in the calculation of ΔG_c of the retentate obtained from the fractionation of milk fat by short path distillation at 175°C (**A**), and the effect of degree of ΔT in ΔG_c of native milk fat (○) and the retentate obtained from the fractionation of milk fat by short path distillation at 175°C (■), and 200°C (▲) (**B**).

For the calculation of ΔG_c, obtain the $\tau_{crystallization}$ at different crystallization temperatures. Using the $\tau_{crystallization}$, crystallization temperatures and melting point of the samples, construct a plot of $\ln(\tau T)$ vs. $1/T(\Delta T)^2$, as observed in Figure 9*A*. Calculate the slope of the resulting line. Substitute the slope (m), Boltzman constant (k), melting temperature of the sample (T_m), and each crystallization temperatures (T_f) in equation 3 to obtain the ΔG_c of the sample for each crystallization condition. Figure 9*B* illustrates the effect of ΔT on the ΔG_c of native milk fat and the retentates obtained at different fractionation temperatures by short path distillation.

2.3. Estimations of Inductions Times and Nucleation Rates by Polarized Light Microscopy

Polarized light microscopy (PLM) allows the birefringent solid microstructural elements of the fat crystal network to be directly observed as sharp bright features against a dark background. Polarized light microscopy, aside from being useful in the quantification of the microstructural elements of a crystal network, is also useful in imaging the early nucleation events.

Consequently, PLM can be used as an analytical technique to obtain indicators of induction times and nucleation rates in the study of fat crystallization. The topic of microscopy is comprehensively covered in the microscopy methods section of this chapter. This section will only briefly describe the experimental procedure to be followed in the estimation of induction times and nucleation rates using PLM and will focus on the analysis of data. For more detailed information regarding calibration of the microscope, image acquisition, image processing, and basic concepts of microscopy, refer to the microscopy section of this chapter.

2.3.1. Procedure

2.3.1.1. Sample Preparation

Melt the sample in an oven at a temperature that ensures that all crystal memory is erased. Using a preheated capillary tube, place a small droplet (about 10 μL) of melted fat on a preheated (80°C) glass slide. Carefully place a preheated glass cover slip over the sample to produce a film of uniform thickness.

2.3.1.2. Experimental Procedure

Immediately transfer the cover slide to a temperature-controlled stage set at the temperature of study. Capture digital grayscale images under polarized light using a 90° crossed-polarizer every 15 seconds for 30 minutes to monitor the crystallization process. Polarization at 90° allows the removal of most of the nonbirefringent background signal. The time intervals given here are a mere suggestion. When performing the experiment, the user will have to determine the length of the experiment as well as appropriate time intervals. Longer time intervals for an extended period of time may be used for slower crystallization processes or low degrees of undercooling.

2.3.1.3. Data Analysis

The first step in the calculation of induction time and nucleation rate is to threshold the acquired series of images using image-analysis software (e.g., Photoshop [Adobe Sys-

tems Incorporated, San Jose, CA, USA]). It is important to ensure that the threshold value used accurately represents the microstructure imaged in the original grayscale images and that the same threshold value is applied to all the micrographs in the series. The resulting images will have white features representing a crystalline mass surrounded by black liquid oil. Invert the images, so that the crystalline matter is represented as black features on a white background. Figure 10*A*–*F* shows a series of images acquired at different time intervals during the crystallization of a mixture of high- and low-melting milk fat fractions at 5°C. The result of processing these images (i.e., threshold and inversion) is shown in Figure 10*G*–*L*. Quantify the amount of black in each inverted thresholded image using image-analysis software (e.g., Photoshop). Plot the percent of black, which is proportional to the solid fraction of the network, as a function of crystallization time. Obtain the induction time of crystallization ($\tau_{crystallization}$) by extrapolating from the linearly increasing portion of the crystallization curve to the time axis as shown in Figure 11*A*.

Another parameter used in the study of the nucleation events is the nucleation rate (J), which can be calculated from the obtained images using the following relationship:

$$J \approx \frac{dN_p}{dt} \tag{5}$$

where N_p is the number of particles at a time, t, in the region of linear increase of crystalline material. For this, compute the number of particles or black features of the thresholded inverted images with a suitable image analysis software package (i.e., Photoshop). Plot the number of particles (N_p) as a function of time. Calculate the slope of the first derivative of the curve as shown in Figure 11*B*. This value is an estimate of J, which is inversely proportional to τ crystallization.

3. THERMAL BEHAVIOR AND POLYMORPHISM

3.1. Melting Profiles by Solid Fat Content

Melting profiles can be constructed by measuring the SFC as a function of temperature. SFC is defined as the quantity of

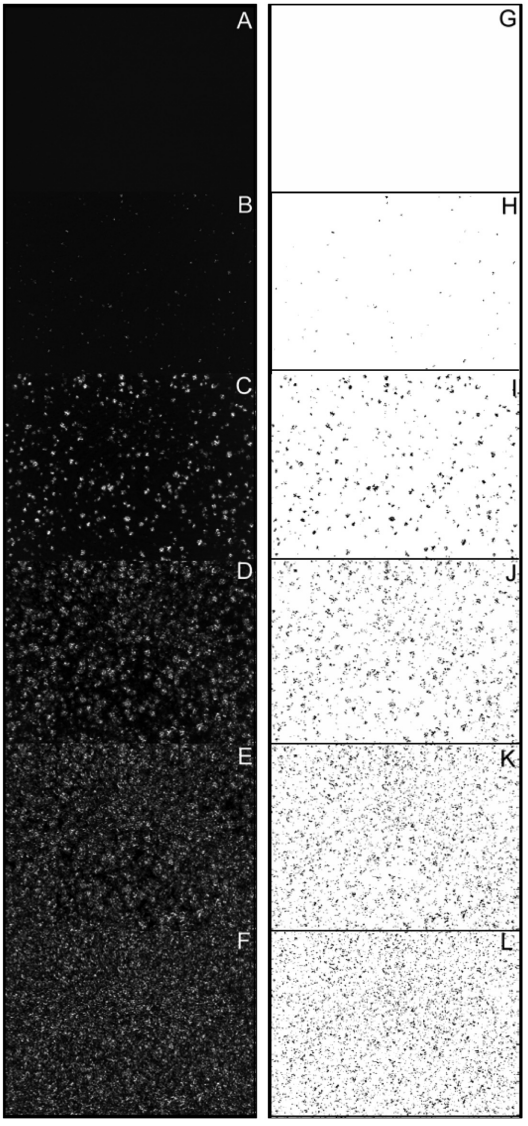

Figure 10 Polarized light micrographs taken at time 0 (**A**), 12.5 (**B**), 13 (**C**), 13.5 (**D**), 14 (**E**), and 15 (**F**) seconds of static isothermal crystallization at 5°C of a mixture of high- and low-melting milk fat fractions (30:70) used in the analysis of nucleation events. Images **G–L** correspond to thresholded and inverted images at the same time points.

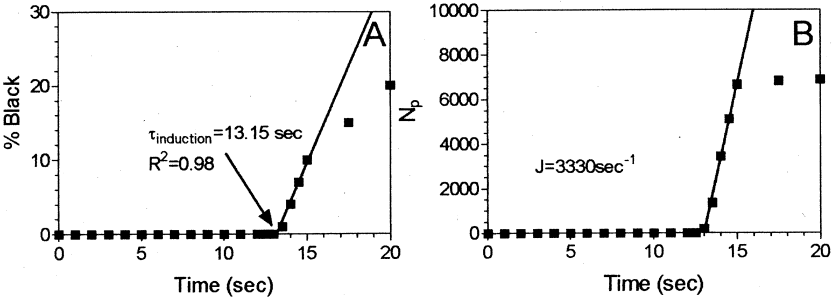

Figure 11 Determination of the induction time (**A**) and the nucleation rate (**B**) from polarized light micrographs of a mixture of 30% high-melting fraction and 70% low-melting fraction of milk fat crystallized at 5°C.

solid glycerides in an oil or fat, determined as the percentage of hydrogen nuclei (protons) in the sample that are in the solid phase, measured by pNMR [5]. For a brief description regarding pNMR refer to the crystallization kinetics section of this chapter.

SFC values at a determined temperature depend on the thermal history of the crystallized fat. In some cases there is the need for polymorphic stabilization of the sample. For this, the construction of melting profiles by SFC makes a distinction between stabilizing and nonstabilizing fats. While for stabilizing fats there is the need for a polymorphic transformation through tempering, for nonstabilizing fats this is not an issue. Examples of nonstabilizing fats are margarine, conventional oils and fats, cocoa butter substitutes, and replacers. On the other hand, cocoa butter and certain specialty fats that contain appreciable amounts of 2-oleo-disaturated glycerides are examples of stabilizing fats.

When performing a melting profile experiment, samples may be subjected to the different temperatures of interest in either a parallel or a serial fashion. When done in parallel, one sample tube is prepared for each temperature to be measured; hence, there will be as many tubes as temperatures at which SFC levels are determined. Alternatively, in the serial proce-

dure, only one sample tube is prepared, which is measured sequentially at all measuring temperatures beginning with the lowest. Both methods yield good results. However, in the case of some fats, important differences will be observed between the two procedures. As such, these differences should be noted and quantified, especially when the analysis affects the commercial value of the analyzed sample [1]. One advantage of the parallel method over the serial method is the considerably shorter period of time required to carry out the experiment. Following are descriptions of the two approaches (both serial and parallel) for the analysis of stabilizing and nonstabilizing fat samples, along with the data analysis performed.

3.1.1. Procedure

3.1.1.1. Sample Preparation

Melt the sample in an oven at a temperature that ensures that all crystal memory is erased. For most edible fats, 80°C for 30 minutes, after the sample has melted, is sufficient. Yet, some high melting point fats require a higher temperature to erase all crystal memory; for example, palm oil needs to be heated at 120°C for 10 minutes. If the sample is not clear, filter it with paper at a temperature above its melting point. Homogenize the sample and transfer 3 g of the molten fat to glass nuclear magnetic resonance (NMR) tubes (10-mm diameter, 1-mm thickness, and 180-mm height). Wipe the outside of the tube with a tissue, making sure that the exterior is clean and dry. To prevent the entry of dust, solvent vapors, or moisture, close the tubes with a cap or rubber stopper.

Depending on the type of fat (i.e., stabilizing or nonstabilizing), the samples are then subjected to a tempering procedures as per the prescribed cooling regimes outlined in Figure 12.

3.1.1.2. Experimental Procedure

After the samples are prepared and tempered, they are placed in water baths set at the different measuring temperatures. The measuring temperatures will depend upon the

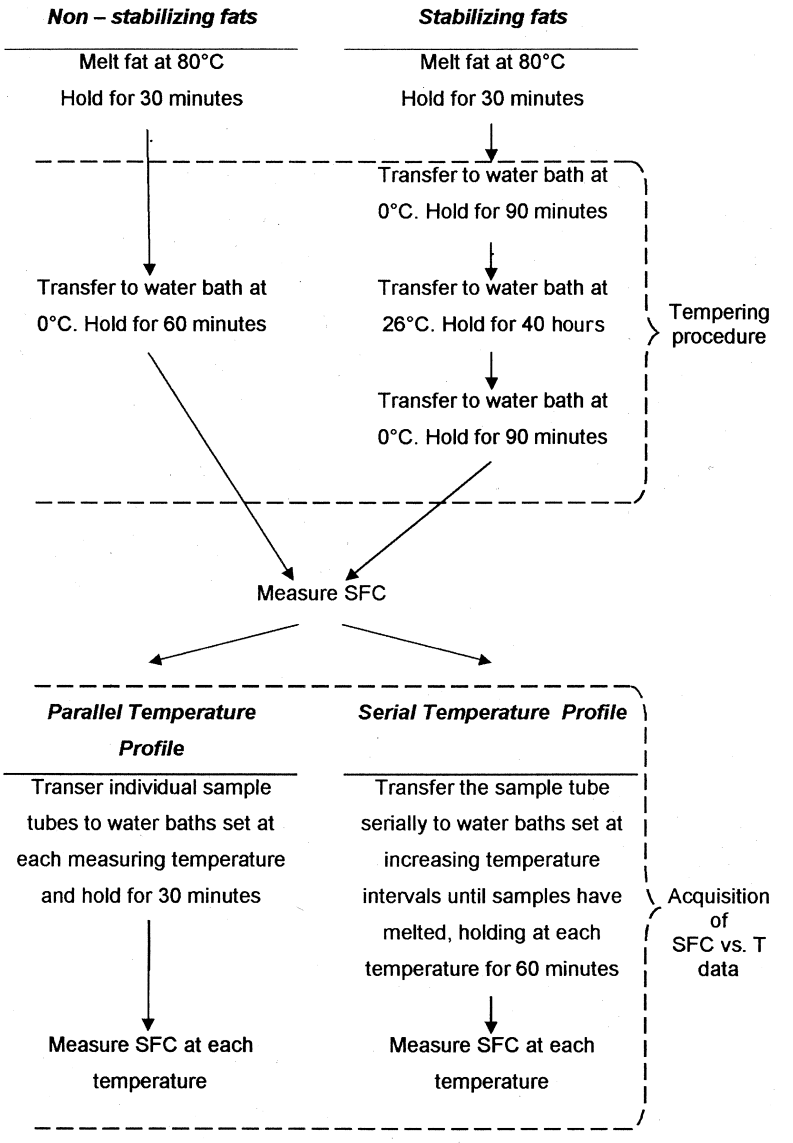

Figure 12 Experimental temperature profiles used in determining melting profiles of stabilizing and nonstabilizing fats by serial and parallel methods.

method being used. Temperatures of 10, 21.1, 26.7, 33.3, and 37.8°C are used in the AOCS Official Method [5], while the IUPAC Standard Method [6] indicates measurements at 10, 20, 25, 30, 35, and 40°C. A systematic description of this methodology can be found in both the AOCS Official Method Cd 16b-93 and the IUPAC Standard Method 2.150 [5,6].

If a serial method is to be used, measure the SFC after the sample has been cooled to 0°C, then transfer to a water bath set at the lowest measuring temperature. Hold for 30 minutes for nonstabilizing fats and 60 minutes for stabilizing fats. Measure the SFC and transfer to a water bath set at the next lowest measuring temperature, hold tubes for the appropriate time, then measure the SFC. Repeat this procedure until a measurement at the highest temperature is performed. At this temperature, the fat should be completely melted. In the case of a parallel method, measure the SFC after the sample has been cooled at 0°C. Transfer each sample tube to a water bath set at each measuring temperature, hold for 30 minutes in the case of nonstabilizing fats and 60 minutes in case of stabilizing fats, then measure the SFC.

3.1.1.3. Data Analysis

3.1.1.3.1. Melting Profiles Determination: Construct the melting profile of each sample by plotting the SFC as a function of temperature and join the points with a line. An example of this analysis for mixtures of high melting milk fat fraction (HMF) and cocoa butter is shown in Figure 13. From the melting profiles, it is observed that HMF melts over a narrower temperature range than cocoa butter, melting completely at 35°C, while cocoa butter begins to melt at around 20°C. As the proportion of HMF is increased, the sample melts at a higher temperature; that is, at any give temperature, the SFC increases as the fraction of HMF is increased.

3.2. Iso-Solid Phase Diagram Determination

When two fats with different chemical composition are combined, the physico-chemical properties of the mixture are not necessarily the same as those of the original components. To

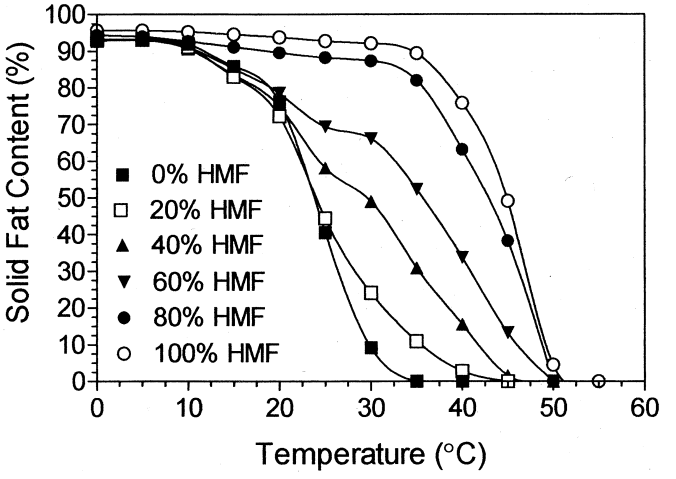

Figure 13 Melting profiles of (○) 100% high-melting milk fat fraction (HMF), (●) 80% HMF, and 20% cocoa butter, (▼) 60% HMF and 40% cocoa butter, (▲) 40% HMF and 60% cocoa butter, (□) 20% HMF and 80% cocoa butter, and (■) 100% cocoa butter.

better understand and predict the physico-chemical properties of a mixture of two independent fat systems, it is necessary to study their phase behavior through the construction of phase diagrams. In this context, iso-solid phase diagrams are used to study the solution behavior of a binary system. Iso-solid diagrams have been thoroughly used in the study of phase behavior of mixtures of confectionery fats with milk fat and milk fat fractions [7–10].

3.2.1. Procedure

3.2.1.1. Sample Preparation

Melt and homogenize the two components whose phase behavior will be studied. Prepare mixtures (w/w) of the two components in 10% increments from 0 to 100%. Transfer 3 g of each mixture to glass NMR tubes (10-mm diameter, 1-mm thickness, and 180-mm height). Melt the mixtures in an oven at a temperature that ensures that all crystal memory is

erased. For most edible fats, 80°C for 30 minutes, after the sample has melted, is sufficient. However, when one of the components is a high melting fat (i.e., palm oil), melt at 120°C for 10 minutes. Make sure that the exterior of each tube is clean and dry. Temper the sample tubes as described in the sample preparation in section of this chapter entitled "Melting Profiles by Solid Fat Content."

3.2.1.2. Experimental Procedure

After the mixtures are tempered, measure the SFC at determined temperature intervals. For more information regarding the generation of SFC data points, refer to the experimental procedure section of this chapter entitled "Melting Profiles by Solid Fat Content."

3.2.1.3. Data Analysis

Construct a melting profile of each mixture by plotting the SFC as a function of temperature as shown in Figure 13. Fit the points to a cubic spline curve with the assistance of curve fitting software. A cubic spline fitting produces a curve that passes through every data point, bending and twisting as needed. Based on the fitting results, obtain temperatures corresponding to SFC values in the range of interest in 2–5% SFC increments. Construct a plot of temperature as a function of composition (percent of component A) for each SFC value for all blends. Perform an additional cubic spline curve fit to smooth the final iso-solid data lines. Figure 14 illustrates examples of iso–solid diagrams for mixtures of HMF with the middle melting milk fat fraction (MMF) (14*A*), HMF with cocoa butter (14*B*), and MMF with cocoa butter (14*C*). In the construction of the diagram, temperature data were generated for SFC levels in 5% increments from 0 to 100%. Each line observed corresponds to the same SFC level.

As shown in the Figure 14, different phenomena are observed in terms of the compatibility between the components of different fat binary mixtures. As previously mentioned, iso-solid diagrams are functional in the study of compatibility between different fats. Based on this, the following can occur

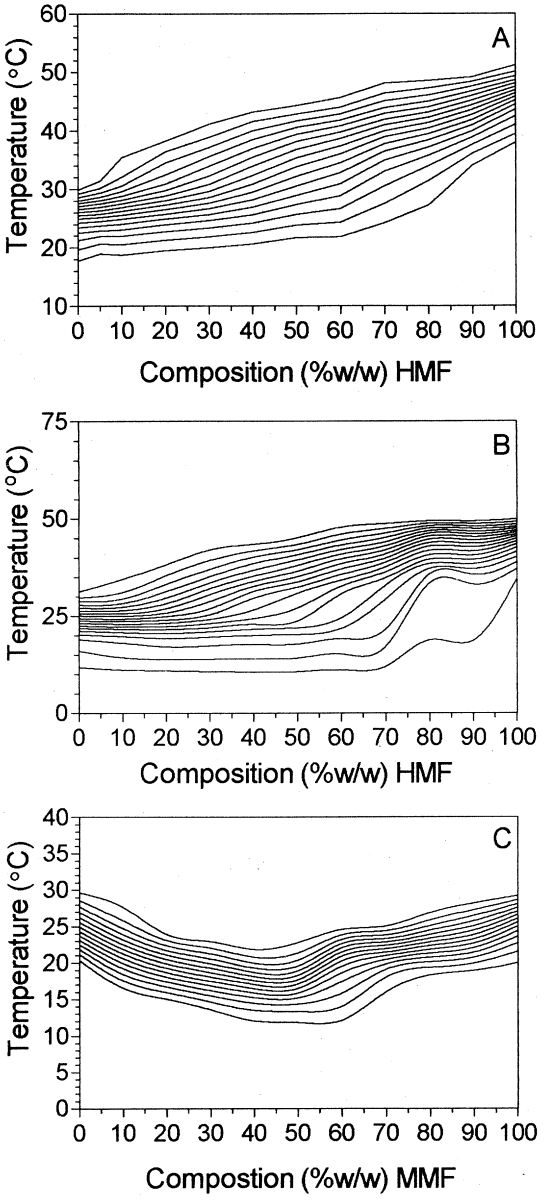

Figure 14 Iso-solid phase diagram for MMF–HMF (**A**), HMF–cocoa butter (**B**), and MMF–cocoa butter (**C**) mixtures.

upon the combination of two fats: compatibility (monotectic), partial compatibility, and incompatibility (eutectic). Figure 14*A* illustrates the compatibility between the triacylglycerol (TAG) molecules of MMF and HMF resulting in the formation of mixed crystals (solid solution) due to the dissolution of one component in to the other. When HMF is mixed with cocoa butter, partial compatibility is observed (Fig. 14*B*). There is partial solid solution formation, both a monotectic and a slight amount of thermodynamic incompatibility between two components is observed. Incompatibility between the two fat components can be observed in Figure 14*C*. When cocoa butter and MMF are mixed, a eutectic is observed due to the incompatibility between the two fats. In this case, a mixture of solid MMF and solid cocoa butter (CB) crystals are formed upon solidification.

3.3. Thermal behavior via Differential Scanning Calorimetry

The thermal behavior of fat samples can be studied using differential scanning calorimetry (DSC) (Fig. 15). The basis of this technique is the measurement of the temperature or heat input between a sample pan and a reference pan. This differential is used to characterize changes associated with phase transitions (i.e., crystal formation or melting). Thermograms associated with phase changes of the samples are constructed as the temperature is increased or decreased at a controlled rate.

3.3.1. Procedure

3.3.1.1. Sample Preparation

Melt the sample in an oven at a temperature that ensures that all crystal memory is erased. For most edible fats, 80°C for 30 minutes, after the sample has melted, is sufficient. Yet, some high melting point fats require a higher temperature to erase all crystal memory; for example palm oil needs to be heated at 120°C for 10 minutes. The sample preparation involves the encapsulation of the fat in pans designed for calorimetric analysis as shown in Figure 16. At all times, use clean tweezers to handle the sample pans. Touching them, as well

Figure 15 Differential Scanning Calorimeter (DSC) Q 1000 (TA Instruments, Mississauga, ON, Canada) used in the thermal analysis of edible fats and oils.

as using dirty tweezers and placing sample pans on dirty surfaces, could leave a residue that may affect the results. Weigh the empty sample pan and lid (Fig. 16*A*). Weigh 5–10 mg of the fat sample into the sample pan being careful not to spill any fat onto the lip of the pan (Fig. 16*B*). Place the lid on the sample pan as illustrated in Figure 16*C* and proceed to seal the pan with the sample encapsulation press shown in Figure 17. Always inspect the pan, making sure that the bottom and the seal are smooth. Additionally, prepare two empty sealed pans of known weight in the same way as the sample pans. These will be used as reference pans.

3.3.1.2. Calibration of the Differential Scanning Calorimetry

When operating a DSC, an inert purge gas flow must be used at all times. The purpose of the purge gas is to provide an

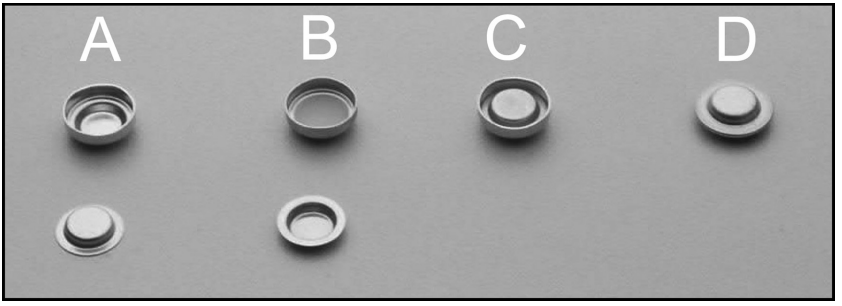

Figure 16 Illustration of the encapsulation process of a differential scanning calorimetry (DSC) pan: initially sample pan and lid are weighted (**A**), 5–10 mg of molted fat are place on the sample pan (**B**), the pan lid is placed over the sample pan being careful not to spill any fat onto the lip of the pan (**C**), and, finally, the pan is sealed with an encapsulation press (**D**).

efficient heat transfer in the cell, supplying a smooth thermal "blanket" in the cell, eliminating hot spots and allowing a better cooling of the cell. Additionally, it removes any moisture and oxygen from the cell that may have accumulated over time. Nitrogen is most commonly used as a purge gas as it is inexpensive, inert, and easily available; additionally, it does not interfere with heat measurements due to its low thermal conductivity. Helium may also be used as a purge gas if faster cooling rates are required. Also make sure that the mechanical cooling system is turned on, which provides the necessary controlled cooling rates during the experimental run.

A series of calibrations have to be performed prior to any experimental run to obtain adequate experimental results. After the calibrations are carried out, the results are saved and reused each time the instrument is used. Each set of calibrations is specific to the experimental conditions used. For this reason, the instrument should be calibrated each time any of the following experimental conditions are changed: temperature range, cooling or heating rates, and type of purge gas. Recalibration is also required when the cooling accessory is changed or when a cell is used for the first time.

Figure 17 Sample encapsulating press used to hermetically seal sample pans used in differential scanning calorimetry (DSC) (TA Instruments, Mississauga, ON, Canada).

Three different calibrations of the DSC are performed. They are (1) baseline calibration; (2) cell constant calibration; and (3) temperature calibration (TA Instruments User Manual). Following are generalities pertaining to each of these calibrations. Specifics on how to perform them may vary between instruments. Refer to the instrument's manual for further detailed information. When performing calibrations, the instrument has to be used in calibration mode.

3.3.1.2.1. Baseline Calibration: The baseline calibration compensates for subtle differences between the reference and sample thermocouples. During this calibration, the empty cell is heated through the temperature range used for the experimental runs under the same experimental conditions (i.e., ramp rates and purge gas). With an empty cell, the heat flow signal should be zero and the baseline should have a minimum slope. In reality, this does not happen. The output of this calibration is the calculation of a baseline slope and offset values, which are used to flatten the baseline and zero the heat-flow signal. Both of these parameters are to be recorded and used during each DSC experiment. A baseline calibration is illustrated in Figure 18, and an example of a method to be used for this calibration is shown in Table 1.

3.3.1.2.2. Cell-Constant Calibration: The cell-constant calibration is a calibration factor used to correct for subtle differences in the calorimetric response of the DSC cell. During this calibration, a high-purity metal standard of known weight (e.g. indium) is heated through its melting peak

Table 2 Example of Method Log to be Used for a Baseline Calibration

Method name: Baseline calibration
Method segments:
1. Equilibrate at −20°C
2. Isothermal for 2 minutes
3. Ramp 5°C/min to 90°C
4. Isothermal for 2 minutes
5. End of method

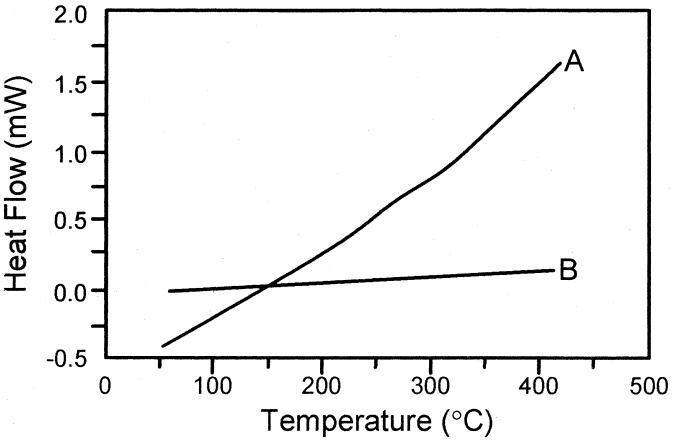

Figure 18 Baseline calibration of the differential scanning calorimetry (DSC) baseline (**A**) has a slope and is offset from the zero heat flow signal. The baseline calibration is used to flatten the baseline and zero the heat flow signal (**B**) (adapted from TA Instruments Q1000 user manual).

using the same experimental conditions (i.e., heating ramp and purge gas) that will be used in subsequent experiments. When any of these conditions are changed, a new calibration has to be performed. The output of this calibration is the cell constant and onset slope, which are then used during each DSC experiment. The cell constant is the ratio between the theoretical heat of fusion and the measured experimental heat of fusion of the high purity standard used. As the metal standard sample melts, it draws heat, creating a temperature difference between the sample and the sample thermocouple. The onset slope is the calculation of the thermal resistance between the sample and the sample thermocouple. A cell-constant calibration is illustrated in Figure 19, and an example of a method to be used for this calibration is shown in Table 3.

3.3.1.2.3. Temperature Calibration: The temperature calibration ensures that the sample thermocouple reading is correct under the experimental conditions chosen. During this calibration, high-purity standard metals of known weight

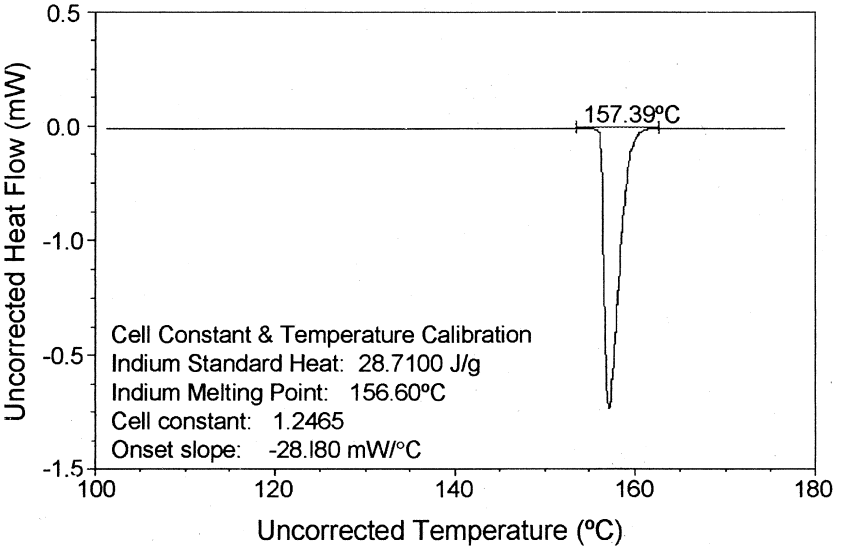

Figure 19 Cell constant and temperature calibration of the differential scanning calorimet (DSC) cell using and Indium high-purity standard.

Table 3 Example of Method Log to be Used for a Cell Calibration

Method name: Cell constant
Method :
Equilibrate at 130°C
Isothermal for 2 minutes
Ramp 5°C/min to 180°
Isothermal for 2 minutes
End of method

(e.g., indium and gallium) are heated through their melting point using the same ramp rate, purge gas, and pan type that will be used in subsequent experiments. The observed melting point is compared with the theoretical melting point; the calculated difference is used for temperature calibration, the same method as in the cell-constant calibration. Calibration of temperature can be performed using one of, and up to, four standards. When only one high-purity metal is used, the entire curve is shifted to the melting point of the standard used. When more than one sample is used, the temperature is corrected by a cubic spline fit. For this reason, more accurate results are obtained when the temperature is corrected using more than one standard sample. A temperature calibration using two high-purity standards is recommended. An example of a temperature calibration performed with a high purity standard of indium is shown in Figure 19, where the true melting point of indium (156.60°C) is compared with the observed peak melting temperature (157.39°C).

All the calibration parameters obtained are entered in the DSC calibration table and are used during each experimental run. Figure 20 shows an example of a calibration table.

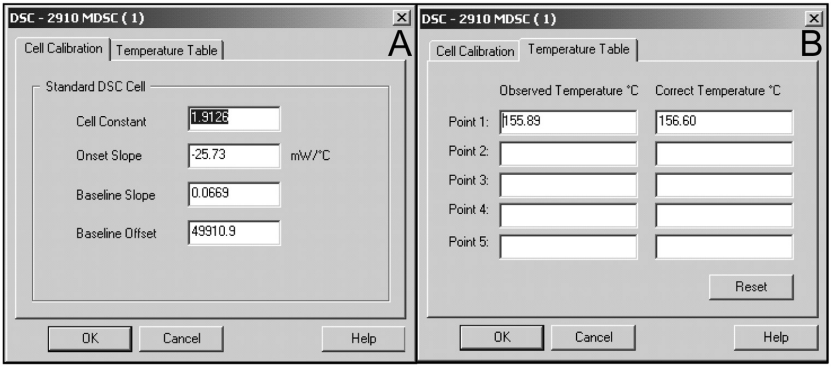

Figure 20 Example of the calibration table (from instrument control software, Thermal Advantage 1.1A, TA Instruments, Inc., Mississauga, ON, Canada, 1999), in which the cell calibration (**A**) and temperature calibration (**B**) results are input.

3.3.1.3. Experimental Procedure

When performing calorimetric analyses, the DSC should be in experimental mode. Elaborate a method that describes the thermal chronicle to which the sample will be subjected. The method segments will depend on the type of experiment that is to be performed. As previously stated, two different types of experiments can be executed. These include exothermic phase changes from liquid to solid (crystallization) or endothermic phase changes from solid to liquid (melting of the crystalline material). Input the sample information once the method is recorded and saved into the software controlling the instrument. This information includes sample name, file in which the run is to be saved, size (weight) of sample, operator, method name, run date, and any additional comments. Make sure the refrigerating cooling system and purge gas are turned on. Load the sample and reference pan in the sample cell; to do so, remove the cell cover and the metal lids from the cell. Carefully place the pans inside the cell. The reference pan goes on the rear position of the cell as illustrated in Figure 21. Care should be taken to center the pans on the platforms inside the cell. Replace the metal lids and cell cover. Start the run with the start function of the software. During the experiment, heat flow data will be collected as a function of time and tempera-

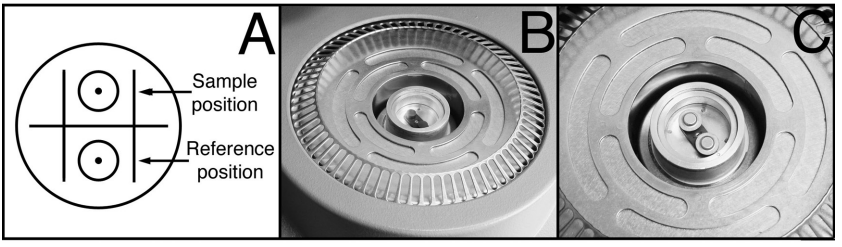

Figure 21 Positioning of reference and sample pans in a differential scanning calorimet (DSC) standard cell (**A**) (adapted from TA Instruments Advantage Manuals, TA Instruments, Mississauga, ON, Canada), view of an empty DSC cell (**B**), and view of a DSC with the sample and reference pans in position (**C**).

ture. If there is the need to stop the run, press the stop or reject functions of the software. The stop function will save any collected data obtained until the point at which the experiment was stopped. The reject function will discard all experimental data obtained. Following are descriptions of crystallization and melting experiments for fats and oils.

3.3.1.3.1. Crystallization: For this type of determination, the sample is melted to erase all crystal memory, cooled at a controlled rate to the desired temperature of crystallization, and maintained isothermally at the temperature of study to allow its crystallization. The cooling rate used is very important for two reasons. Firstl, if low cooling rates (typically, below 20°C) are used, nucleation will commence during the cooling of the sample. For isothermal crystallizations, no crystallization should take place during cooling. When performing crystallization experiments, the sample should be cooled at high rates (above 20°C/min) or at the instrument's maximum cooling velocity. In this case, nucleation will take place at the desired crystallization temperature and not at higher temperatures. Second, the cooling rate used will directly affect the resulting crystalline form of the fat. Under rapid cooling conditions, TAG molecules usually crystallize in metastable polymorphic forms, which subsequently transform into polymorphs of higher stability. On the other hand, at slow cooling rates, TAG molecules of similar chain lengths have time to associate with each other in more stable geometrical arrangements, resulting in the formation of a more stable polymorphic form. Due to the dependence of fat crystallization on the degree of undercooling and the cooling rate used, different results will be observed when using different cooling rates.

3.3.1.3.2. Melting: The melting properties of a crystallized fat can be investigated by heating the sample at a controlled rate until the fat is totally melted while measuring the heat flow as a function of temperature and time. Care should be taken with regard to the heating rate, as different rates will yield slightly different information. At very low melting rates (1°C/min or lower), the heat transfer is going to be slow allowing molecular rearrangements to occur. Some thermal events, such as melting of existing polymorphic forms, poly-

morphic transformations, and remelting of the newly formed polymorphic forms, may be observed when a sample is melted slowly, but will be unnoticeable when melting at high heating rates (10°C/min or higher). This results from the sample melting before any structural changes can take place. It is recommended, from experience in our laboratory, that fat samples be melted at a rate of 5°C/min.

Results obtained when a crystallized fat is melted are also dependent on the time of crystallization. Different thermal melting behavior will be observed in fat samples that have been crystallized under identical conditions, but stored for different periods of time. As such, there are two different approaches that may be taken in the analysis of the melting characteristics of a fat by DSC. A fat can be melted either immediately after crystallization has taken place or after it has been crystallized and stored for a pre-determined period of time. Melting a sample shortly after solidification allows for examination of the initial metastable crystalline structures and the polymorphic transformations that the fat underwent during the crystallization process. On the other hand, when a sample is crystallized and stored for a specific period of time, it is possible to characterize the stable crystalline structures present in the sample, and any polymorphic transformations that may have taken place during storage.

An example of a procedure used to characterize the thermal behavior of a fat sample is shown in Table 4. In this method, the sample is initially melted at 60°C to ensure that all crystal memory is erased, after which it is cooled at the highest rate attainable by the instrument. The purpose of this method is to examine the initial metastable crystalline structure. To do this, the fat is melted in the DSC cell after only 5 minutes of crystallization at a rate of 5°C/min, up to a final temperature of 60°C, at which point all the fat will be molten. To analyze the thermal behavior of the sample after an extended period of storage, crystallize the sample in the DSC following the same method as shown in Table 4, then transfer the sample pan to a temperature–controlled incubator set at the temperature of study. After the storage period, transfer the sample pan to the DSC for melting, taking care that the

Table 4 Method Log for the Thermal Analysis of Cocoa Butter by Differential Scanning Calorimetry (DSC). In this Method, the Sample is Initially Crystallized at 25°C for 5 Minutes, Followed by Melting at a Heating Rate of 5°C/min

Method log:	
1. Equilibrate at 60.0°C	Melting to erase all crystal memory
2. Isothermal for 30.0 min	
3. Data storage: on	Crystallization
4. Jump to 25.0°C	
5. Equilibrate at 25°C	
6. Isothermal for 5.0 min	
7. Ramp 5°C/min to 60°C	Melting
8. Equilibrate at 60°C	
9. Isothermal for 2 min	
10. Data storage: off	
11. End of method	

temperature of the cell is equal to the incubation temperature when placing sample pans in the DSC cell.

3.3.1.4. Data Analysis

Results from an experimental DSC run are graphically represented as a thermogram wherein heat flow is plotted as a function of time or temperature. A spreadsheet containing the data acquired during the experiment may also be created by exporting the numerical data points from the instrument's software. Further analysis of the data may then be performed using suitable software applications (eg., Microsoft Excel, Graph Pad, etc.). Figure 22 shows an example of the thermogram resulting from the method described in Table 4. In the thermogram, both phase transition phenomena (i.e., crystallization and melting) are observed. Crystallization is an exothermic event, as energy is released during the process, which is observed in the thermogram as an exothermic peak (↑). On the other hand, melting is an endothermic event in which energy is absorbed, resulting in a decrease of the energy flow of the system, and is observed in the thermogram as an endothermic peak (↓).

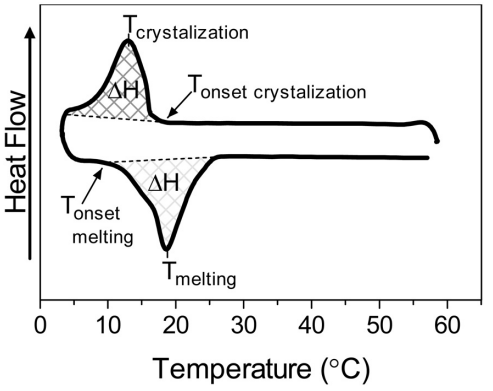

Figure 22 Differential scanning calorimetric analysis of cocoa butter crystallized at 5°C followed by melting at 5°C/min. The parameters used to thermally characterize the sample are indicated.

Several parameters can be calculated to describe the thermal behavior of the sample. These include the peak temperature of crystallization (T_c) and melting (T_m), onset temperature of crystallization (T_{oc}) and melting (T_{om}), and the peak area which corresponds to the enthalpy of crystallization (ΔH_c) and fusion (ΔH_m). When analyzing pure samples, the peak is very narrow, as all species crystallize within a narrow temperature range. When working with complex systems, such as edible oils, which form mixed crystals, the peak is broader, as different lipid species have different crystallization and melting temperatures. The peak temperature is calculated as the peak's point of maximum deviation from a linear baseline drawn between two points on the curve and corresponds to the temperature at which the sample has the highest heat flow. This temperature is related to the temperature at which the largest proportion of lipid species crystallize or melt, depending on the phase transition that is being analyzed and is considered an average of the melting or crystallizing point of the sample. T_{oc} is the temperature at which the first crystallites are formed, while T_{om} is the temperature at which the fat sample begins to melt. Both parameters are defined as the temperature at which the heat flow begins to deviate from the base-

line. The peak area corresponds to the enthalpy of the phase transition (ΔH), which is calculated as the area under the thermogram curve. When integrating the area under the peak, two limit points are established that correspond to the start and end temperatures observed during thermal event. In the analysis, a baseline is drawn between these upper and lower limits. This baseline can be linear, sigmoidal, or extrapolated (TA Instruments Universal Analysis Software). A linear baseline is a straight line drawn between the upper and lower limits and is used when the baseline changes linearly with time. A sigmoidal baseline is an S-shaped line that changes in level or slope that compensates for changes in baseline that take place during the transition. To calculate a sigmoidal baseline, two horizontal lines (in case of sigmoidal horizontal) or two tangent lines (in case of sigmoidal tangent) are drawn between the lower and upper limits of the observed transition, and a sigmoidal curve which joins both lines is drawn. It is also possible to extrapolate the baseline. To do this, four points are selected and tangent lines drawn between pairs of consecutive points, so that the extrapolated baseline intersects the range of data bracketed by the other two points. This is carried out by the software as it evaluates potential tangent lines between consecutive points, and uses the tangent line that will intersect the data between the remaining points. The area under the peak is proportional to the total amount of crystalline material formed during crystallization or the amount of solid phase converted to liquid phase during melting.

The effect of storage on the thermal properties of a crystallized sample is observed in the thermograms shown in Figure 23. Anhydrous milk fat was cooled at 5°C/min and allowed to crystallize at 5°C for different periods of time. A first sample is molten after only15 minutes and a second one after 7 days of crystallization. When melting after only 15 minutes, the peak melting temperature is around 13°C. In this case, most lipid species melt below 20°C, which correspond to the metastable α polymorphic form. When the samples are allowed to crystallize for 7 days, the peak melting temperature is above 20°C, indicating the occurrence of a polymorphic transformation from the α form to the more stable β′ form.

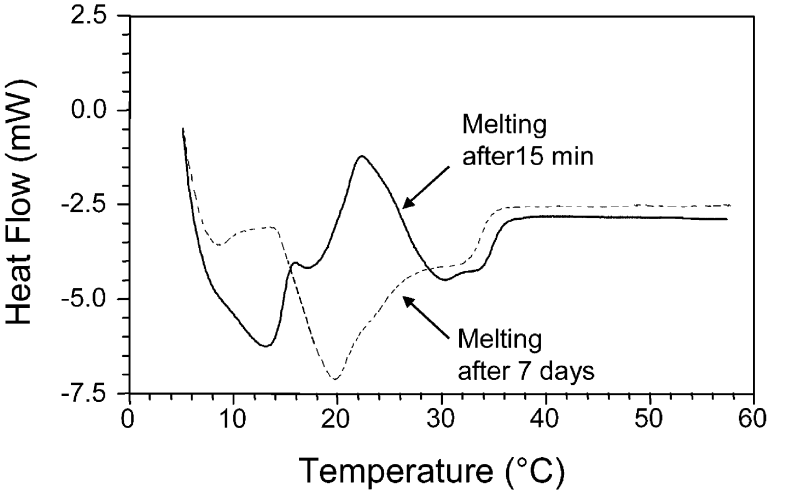

Figure 23 Differential scanning calorimetric melting curves of anhydrous milk fat after 15 minutes (*solid line*) and 7 days (*dotted line*) of crystallization at 5°C.

3.4. Polymorphism

Triacylglycerol molecules have the ability to pack in different geometric conformations during crystallization. Various polymorphs exhibit different crystalline structures with identical chemical composition but with dissimilar physical properties (i.e., density, stability, and melting point). The characteristics of the different polymorphic forms in TAGs are summarized in Table 5. During crystallization, the initial polymorphic form found is that of least stability; as the TAG molecules do not have time to become ordered into lower energy states. With time, molecules rearrange into more stable forms possessing lower energy states. The latter phenomenon is defined as polymorphic transformation.

Due to the different geometric configurations, different polymorphic forms deflect X-rays at different angles; hence, X-ray diffraction analysis is used in the study of fat polymorphism. A MultiFlex X-ray diffraction instrument is shown in Figure 24 (Rigaku/MSC, The Woodlands, TX, USA). X-rays

Table 5 Characteristics of the Ddifferent Polymorphic Forms in Triacyleglycerols (TAGs)

Characteristic	α Form	β′ Form	β Form
Chain packing	Hexagonal	Orthorombic	Triclinic
Short spacing(s)	0.415 nm	0.38 and 0.42 nm	0.46 nm
IR Spectrum (-CH_2-) rocking vibration	Singlet at 720 cm^{-1}	Doublet at 727 and 719 cm^{-1}	Singlet at 717 cm^{-1}
Density	Least dense	Intermediate	Most dense
Melting point	Lowest	Medium	Highest
Stability	Least stable	Intermediate	Most stable

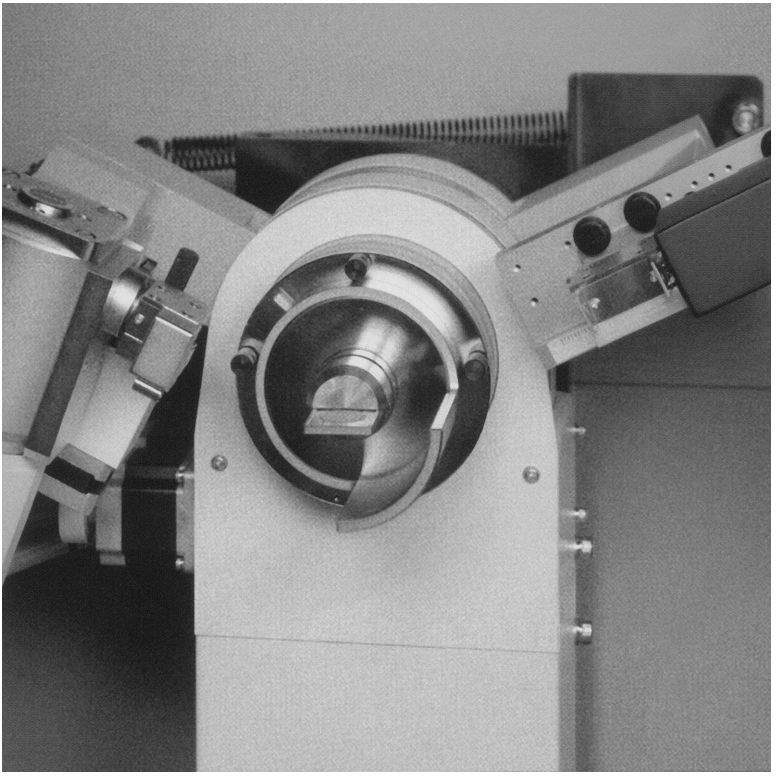

Figure 24 MultiFlex X-ray diffraction sample holder (photography courtey of Rigaku/MSC, The Woodlands, TX, USA).

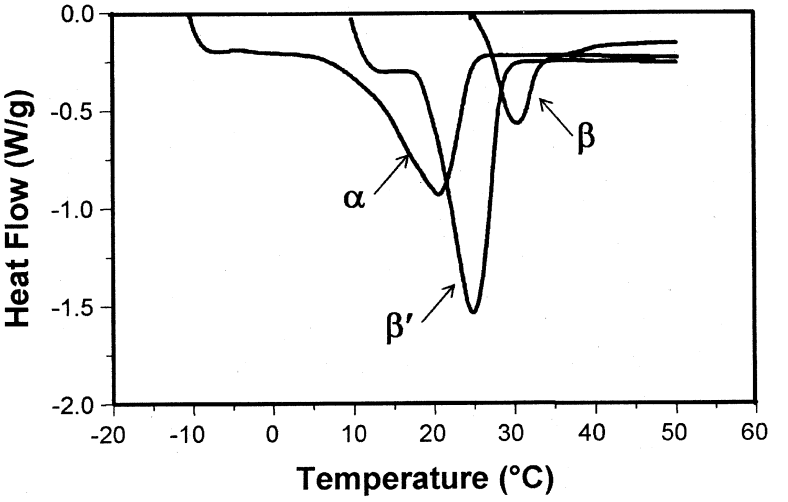

Figure 25 Differential scanning calorimetric curves of the different polymorphic forms present in cocoa butter.

incident on crystalline fats can be deflected in wide and small angles. Wide diffraction angles correspond to the characteristic small spacing of the subcells within the crystal lattice, while the small diffraction angles correspond to the long spacing of the unit cell. This allows X-ray diffraction to be used as a precise analytical technique to determine the polymorphic forms present in a fat sample [11].

As lipid polymorphs have different melting points, they can also be differentiated by their thermal properties using DSC. Figure 25 shows typical melting peaks for different polymorphs found in cocoa butter. However, this method of characterization must always be confirmed by X-Ray diffraction patterns, as the melting points of various polymorphs are different for each fat system.

4. MICROSTRUCTURE

4.1. Polarized Light Microscopy

Polarized light microscopy is a well-established analytical technique used to image the microstructure of fat crystal net-

works and study the relationship between this level of structure and other physical properties. Polarized light microscopy exploits the high contrast between the birefringent solid microstructural elements and the nonbirefringent liquid fraction. The latter can either surround the crystalline material in a low solid fraction system or be entrapped within the solid fraction forming a structured fat crystal network. This contrast is possible as PLM allows the distinction between isotropic and anisotropic materials. Isotropic materials, such as the liquid phase of a fat crystal network, have a single refractive index; hence, the same optical properties in all directions. On the other hand, anisotropic materials, such as the solid phase of a fat crystal network, have optical properties that vary with the orientation of incident light [12].

In light, electromagnetic waves vibrate in all planes perpendicular to the direction of propagation. Polarizers are filters of polymer molecules oriented in a single direction, which restrict the propagation of light waves to a single plane, producing what is referred to as plane polarized light. The light waves that vibrate in the same plane as the polymer oriented molecules are absorbed, while light waves vibrating at perpendicular angles to the direction of the polymer molecules pass through the polarizer [13,14]. This phenomenon is represented in Figure 26.

A polarized light microscope is equipped with two polarizers. A first polarizer is positioned in the light path before the

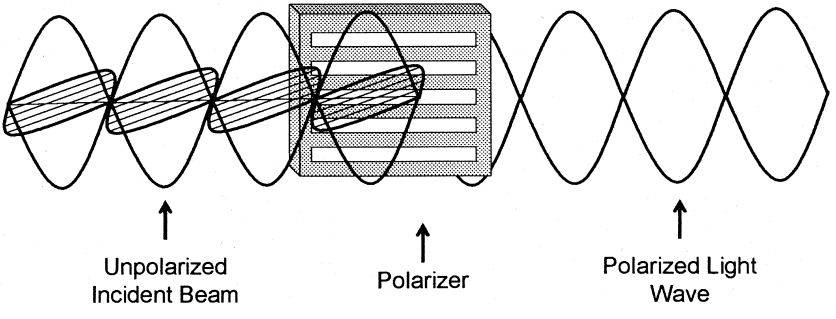

Figure 26 Schematic diagram of a light polarizer (adapted from Ref. 14.)

specimen to be imaged, and a second polarizer, called the analyzer, is placed in the optical pathway between the objective and the observation tube. Anisotropic materials act as beam splitters, such that when light passes through an anisotropic crystal, it is refracted into two rays, each polarized and refracted at right angles to each other and traveling at different speeds. This phenomenon of double refraction is called birefringence. The analyzer recombines the two beams traveling in the same direction and vibrating in the same plane. The polarizer ensures that the two beams have the same amplitude at the time of recombination for maximum contrast [15]. Polarized light microscopy exploits the interaction between the two light rays produced by the birefringent specimen, as they are reunited along the same optical path to produce image contrast, which yield qualitative and quantitative information about the observed materials.

4.1.1. Procedure

4.1.1.1. Microscope Alignment

Prior to any imaging or recording performed with the polarized light microscope (Fig. 27), all its optical components must be aligned. For optimum performance of the microscope, and, hence, good quality imaging, the light source has to be centered, and the condenser and field diaphragm should be properly adjusted. The following is a general procedure for the alignment of the optical components of the microscope.

To begin, switch the light source on and adjust the illumination intensity. Care should be taken not to switch on the light source at a high intensity, as this reduces the life of the light bulb. A microscope with direct observation and recording capabilities (i.e, with a camera) will be equipped with a light path selector knob. The knob position determines the amount of light that will be directed to the observation tube or the phototube. For direct observation, the knob is positioned so that all of the light is directed to the binocular tube. To record images with a camera, the knob should be set at the position that directs light to the phototube, and, hence, the camera. For the calibration and alignment of the microscope, the knob

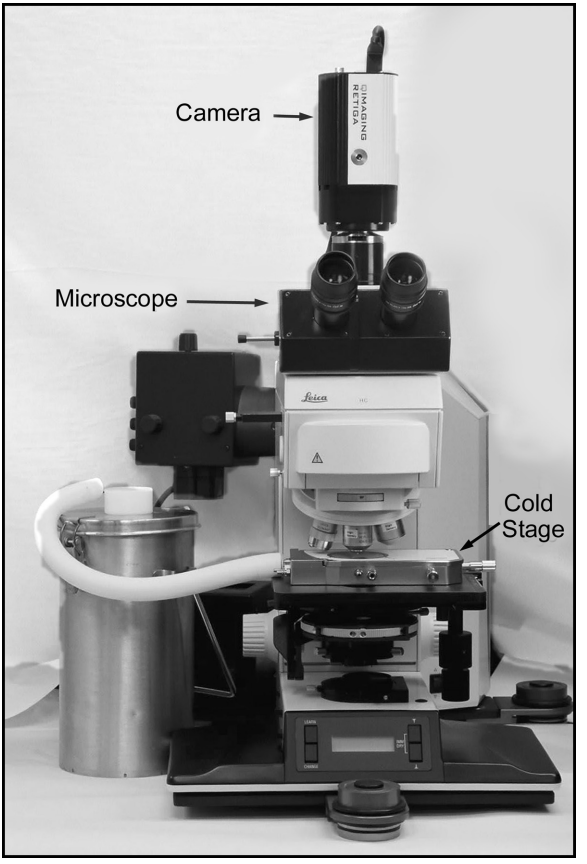

Figure 27 Polarized light microscope (DMR XA2 Microscope, Leica Microsystems, Wetzlar, Germany) equipped with a camera for image acquisition (Q-imaging Retiga, Burnaby, BC, Canada) and a heating–freezing stage (Linkam Scientific Instruments, Surrey, UK) to keep samples at a specific temperature.

should allow all light to go to the binocular tube. Place a sample similar to that which will be imaged on the microscope stage and bring it into focus with the 10x objective. Close the iris diaphragm completely with the field iris diaphragm ring. A blurred image will be seen through the eyepiece. This is the image of the field, which is observed as a blurred polygon, as

depicted in Figure 28*A*. Move the condenser up or down with the condenser height adjustment knob to focus the image of the field diaphragm as observed in Figure 28*B*. The field iris diaphragm controls the diameter of the ray bundle impinging on the specimen surface increasing the image definition. Open the field iris diaphragm to increase the diameter of the field progressively until it is outside the field of view, as observed in Figure 28*C–E*. Center the condenser while opening the diaphragm using the condenser centering screws to bring the diaphragm image into the center of view, as observed in Figure 28*D*. Adjust the aperture of the iris diaphragm based on the imaging conditions, such as numerical aperture of the objective, image contrast, depth of focus, and flatness of field. It is suggested to adjust the aperture iris diaphragm to 70% or 90% of the numerical aperture of the objective. Remove the eyepiece from the observation tube and look through the observation tube. Open the aperture iris diaphragm ring until 70 % or 90% of the field is covered.

Remove the sample from the light path so that a transparent field of view is observed. Set the polarizer and analyzer at position "0," which is the crossed-filter position. Rotate the polarizer ring until the desired extinction is obtained. Figure 29 demonstrates the difference between an image acquired with no polarization and an image under total polarization of

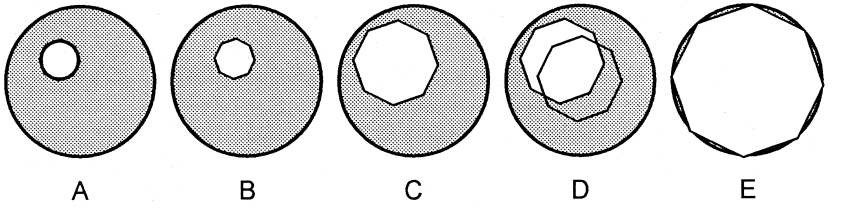

Figure 28 Schematic representation of the view field in a microscope during illumination alignment. Initially the iris diaphragm is closed completely, a blurry polygon indicating that the condenser has to be adjusted (**A**), while a focused polygon indicates that the condenser is properly set (**B**). The diaphragm is progressively centered and opened until it covers the entire field of view (**C–E**).

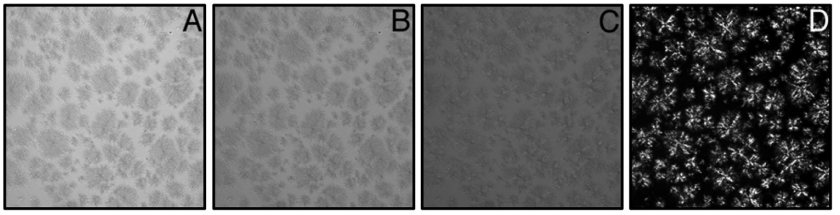

Figure 29 Unpolarized (**A**), partially polarized (**B** and **C**), and fully polarized (**D**) micrographs of fat crystal network images

light so that the microstructural features of the network appear clear and distinct from the liquid phase. Position the light path knob so that light is directed to the photometric tube, allowing the acquisition of images. Cover the eyepieces so that no light will go through the binocular tube, as this will adversely affect the illumination conditions. Finally, fine focus the sample. The above procedure is to be performed each time the microscope is turned on and for each objective used. Refer to the microscope manual of operation for further information.

When imaging is done at temperatures different from room temperature, when there is the need for minimum fluctuations in temperature or when a thermal treatment is to be applied on the sample, a heating/freezing stage, as the one observed in Figure 30, can be used. The temperature-controlled stage is placed over the microscope stage and should be secured with the use of clamps to prevent movement during image acquisition. This should be done prior to the calibration of the microscope so that calibration is performed with the stage in place.

4.1.1.2. Sample Preparation

Melt the sample in an oven at a temperature that ensures that all crystal memory is erased. For most edible fats, 80°C for 30 minutes, after the sample has melted, is sufficient. Yet, some high melting point fats require a higher temperature to erase all crystal memory; for example palm oil needs to be heated at 120°C for 10 minutes. Place a small droplet (about 10μL) of melted fat on a clean preheated glass slide, using a

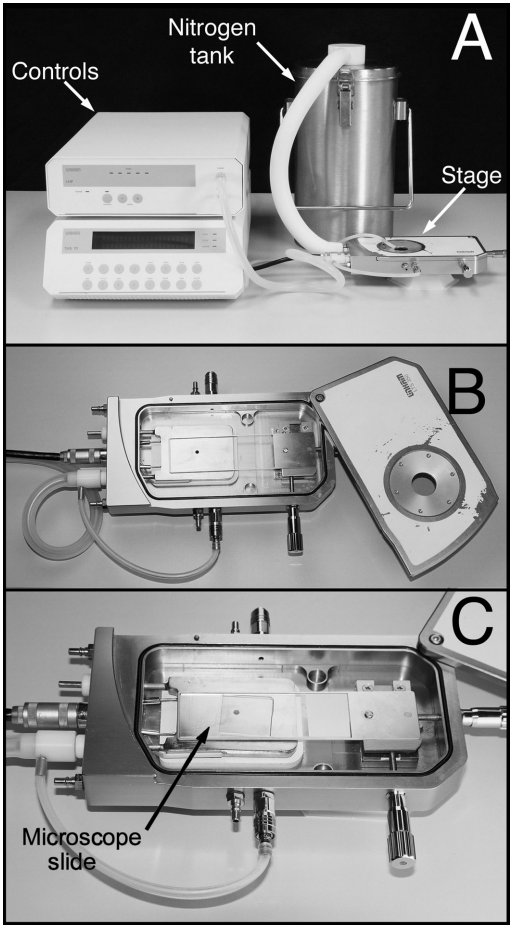

Figure 30 Heating–Freezing temperature-controlled microscope stage (Linkam Scientific Instruments, Surrey, UK).

preheated capillary tube. Special care should be taken to avoid any dust or debris on the microscope slide, as this may induce secondary nucleation. Place a preheated glass cover slip over the sample to produce a film of uniform thickness, avoiding the introduction of air bubbles into the sample. The previously described procedure is illustrated in Figure 31.

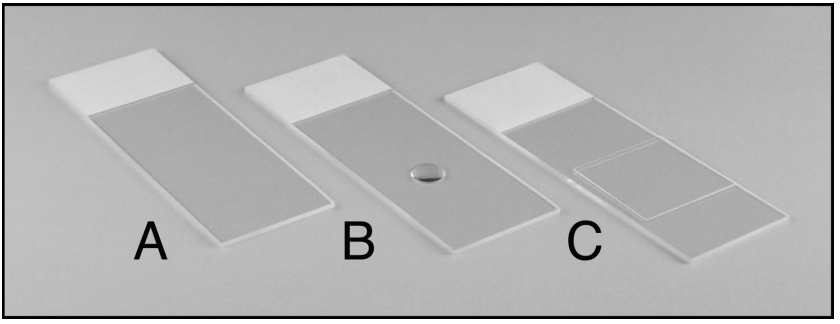

Figure 31 Illustration of the sample preparation for the imaging of fat crystal networks by polarized light microscopy. A clean microscope slide is preheated (**A**), a small droplet (about 10μL) of fat is place over the microscope slide (**B**), and a preheated glass cover slip is place over the fat to produce a film of uniform thickness (**C**)

4.1.1.3. Experimental Procedure

Immediately transfer slides containing the samples to be imaged to incubators set at the desired crystallization temperature and store them for the desired length of time. Prior to imaging, visually inspect the slides, as only those which appear to have a uniform thickness of sample (i.e., no obvious directionality of the crystallized fat exists) should be analyzed. Transfer the prepared slide to a programmed heating freezing temperature control stage positioned on the microscope stage (Fig. 27), which has been equilibrated to the temperature of study. Fine focus the sample and acquire the desired images according to the camera and software setup available. From this setup, grayscale images of the microstructure of the network will be obtained.

Care should be taken with regard to the gain of the camera. The gain of the camera can be automatic or manual. In automatic gain, the camera will automatically amplify the image signal to an appropriate level, whereas in the manual gain, no such adjustments are made. For further information regarding the operation of the camera and software, refer to the appropriate operation manuals.

4.1.1.4. Data Analysis

Imaging is only the first step in the study of the microstructure of fat crystal networks. The acquired micrographs are nothing but raw data from which qualitative and quantitative information can be obtained through image analysis. When attempting to analyze the microstructure, the first thing to do is to define what information is of interest. Image processing is then used to improve the visual appearance of images and to prepare them for quantitative measurements [16], depending on the features of interest. The correction of any defects in the images during acquisition and the enhancement of visibility of structures are performed on the acquired images. Qualitative analysis can be made when there are obvious and dramatic differences between the micrographs, such as the presence or absence of certain features, as well as large differences in morphology and size. For quantitative analysis, descriptive numeric parameters are obtained that concisely characterize the information of interest in the image. In this section, basic image processing tools such as correction for nonuniform illumination and thresholding will be described, as well as quantitative image-analysis techniques, such as those used to determine the size and number of features, percent black related to the solid fraction of the network, and the calculation of the fractal dimension (D_f). For both image processing and analysis, several software packages are available. Unless otherwise noted, this text will describe treatment and analysis performed with Adobe Photoshop 6.0 (Adobe System Incorporated, San Jose, CA, USA) and the Image Processing Tool Kit 4.0 plug-ins (Reindeer Games, Inc, Asheville, NC, USA).

4.1.1.4.1. Automatic Background Leveling: When the background of a micrograph, which is either darker or lighter than the microstructural features, varies gradually due to nonuniform illumination at the time of image acquisition, it can be corrected by automatic background leveling. Using the function Autolevel Bright in the Filter>IP●Adjust menu, the background is modeled by a polynomial function. The image is divided up into a 9×9 grid of rectangles; the histogram of each region is examined to find the brightest or dar-

kest values present, and uses the 81 values and their locations to construct a polynomial for brightness as a function of position, which is subtracted from the original image. When the background is the darkest phase present in the image, the function Autolevel Dark is used. In cases when the image contrast varies across the image, as well as the background brightness, the function Auto Contrast is used which fits functions to both the brightest and darkest pixels in each region of the image, maximizing the contrast range in all areas of the image [16]. In Figure 32, we observe an example of an image acquired under uneven illumination conditions (Fig. 32*A*) and the result of image processing using the automatic background leveling tool in the defective image (Fig. 32*B*). Regardless of this function, extreme care should be taken in the calibration of the instrument to avoid an uneven illumination when imaging. It is suggested that the image be taken after the microscope illumination has been aligned to verify that there is no problem with uneven backgrounds.

4.1.1.4.2. Thresholding: The purpose of thresholding is to convert the acquired grayscale images (i.e., images that contain a wide array of gray tones that go from pure white to pure black) to binary images (i.e., images in black and white

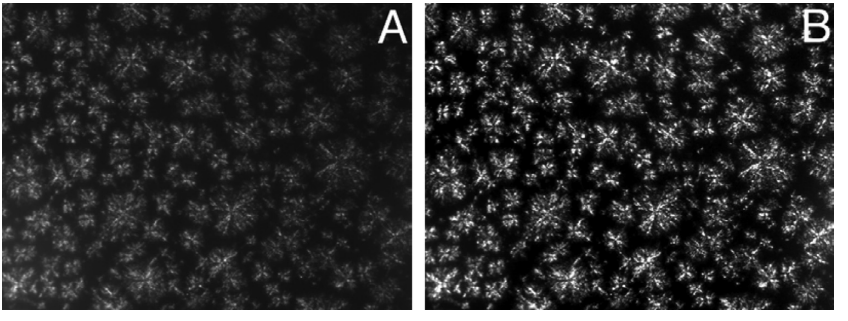

Figure 32 Micrograph of a fat crystal network with uneven illumination (**A**), which is processed using Photoshop (Adobe Systems Incorporated, San Jose, CA, USA), with the automatic background level function used to obtain an image with a uniform background (**B**).

only). Thresholding is necessary for further image analysis, as the algorithms used rely on the discrimination between features and background. In the case of polarized light micrographs of fat crystal networks, the background is set to black and the fat crystals are set to white. The resulting binary image is used for subsequent image analysis.

The function BiLevel in the menu Filter>IP●Adjust is used to threshold grayscale images. When used, a dialog box like the one shown in Figure 33 appears. In the center of the dialog box, the image histogram is presented, which is the number of pixels at each brightness level, along with an accumulative plot. Brightness values of the histogram range from 0, representing pure white, to 255, representing pure black. The cursor beneath the histogram can be moved to manually select a particular brightness value within the range of 0–255. On the left side of the dialog box there is a preview window in which any part of the corresponding binary image can be

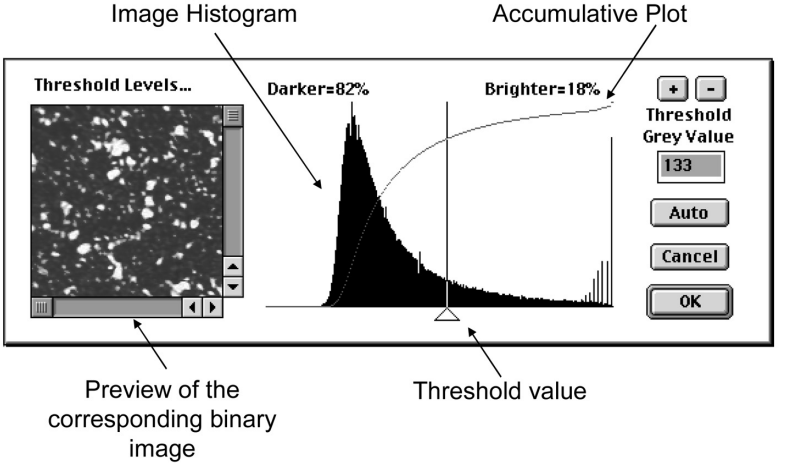

Figure 33 Dialogue box used to threshold a grayscale image. It contains an image histogram of the number of pixels at each brightness level, a preview of what will result in a binary image, and controls used in the determination of threshold values (adapted from Photoshop 6.0, Adobe System Incorporated, San Jose, CA, USA).

screened using the scroll bars. This is used to ensure that the chosen thresholded value represents the original image. The dialog window also displays the area fraction of each phase and the threshold value. An image can be thresholded manually by moving the cursor in the histogram or by entering a threshold value. It is important to ensure that all the solid mass present in the grayscale image is represented in its corresponding thresholded image. This process relies on the human eye to decide what features should be included and measured and, thus, is inherently subjective and inconsistent. To overcome this problem, a threshold value can be set automatically by the software by choosing an "Auto" threshold in the dialog box. On each portion of the histogram, the significant differences are evaluated statistically (t- test) by the software. The automatic threshold value is the point of brightness that has the highest probability of significant difference. This automatic threshold value is different for each image and independent of the user. In this way, the subjectivity from the user's input is decreased.

Typically, measurement routines will count or identify black features on a white background. This binary color scheme is the opposite to that obtained when thresholding a fat crystal network imaged by PLM. For this reason, the image has to be inverted by using the invert function in the Image>Adjust menu. It is a straightforward function, which interchanges black and white. Figure 34 shows an example of a grayscale image (Fig. 34*A*), which is thresholded to produce a

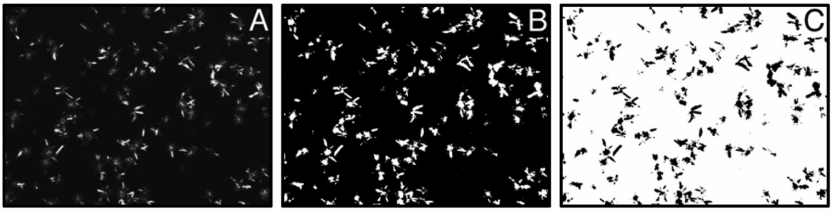

Figure 34 Grayscale (**A**), thresholded (**B**) and inverted (**C**) images of the microstructure of a fat crystal network

binary image (Fig. 34*B*), and inverted (Fig. 34*C*) to obtain a black image on a white background.

4.1.1.4.3. Numeric Parameters of the Microsctructure: As previously mentioned, information regarding the size and number of crystallites, as well as total crystalline mass, can be obtained with the aid of an image analysis software package (e.g. Adobe Photoshop, Image J, Object Image, etc.).

4.1.1.4.3.1 Quantification of Crystalline Mass: The quantity of solid phase present in the network can be measured in different ways, i.e., number of particles and pecentage of black that is related to the amount of crystalline mass. To obtain the number of crystals present, threshold the raw, grayscale image making sure that all solid mater is represented in the binary image. Any reflection of a crystal that is eliminated in the thresholding process will not be counted and, hence, will contribute to inaccuracy in the results. Invert the image, as most algorithms will count the number of black features over a white background. Finally, count the number of features, which is proportional to the number of crystals or number of particles (N_p) imaged.

The solid fraction of the network is proportional to the reflections produced by the birefringent crystalline material in the sample. To measure this, calculate the percentage of black and/or white. A simple way to do it is by recording the percentage of black that results when each image is thresholded.

The mean crystal area can provide important information regarding the crystallization process of the network. Its calculation relies on dividing the total-imaged crystal area by the N_p. To do so, record the percent black from the inverted binary image. Calculate the area in squared pixels that represents crystal mass by multiplying the percent black by the total number of pixels in the acquired image. Using the micrograph of a stage micrometer, calibrate the pixel to μm ratio and convert the total pixel^2 to μm^2. This will correspond to the area in the micrograph that represents solid mass. Calculate the N_p of the image and divide the total mass area by this value.

This will yield the mean particle area, or mean crystal size of the image's microstructures.

4.1.1.4.4. Fractal Dimension: Fat crystal networks are complex structures composed of a particulate and a non-particulate mass, distributed in space in a seemingly random fashion. At the mesoscale level (1–200μm) these structures cannot be described by traditional Euclidean geometry; hence fractal geometry is used instead. The mass fractal dimension can be thought of in terms of the scaling relationship between the mass (M) and the radius of a microstructural feature (r):

$$M \sim r^{D_f} \tag{6}$$

where D_f is the fractal dimension. If this equation were used to define a two-dimensional object, the value of D_f would have an integer value of 2. In the case of fat crystal networks, were the distribution of mass is fractal in nature, the dimensionality is fractional.

Two different approaches have been thoroughly used in our laboratory to quantify D_f from PLM images. These are the particle-counting method and the box-dimension method. The particle-counting method is more sensitive to the degree of order and packing of mass distributed in a fat crystal network, while the box-counting method is more sensitive to the degree of fill. In the following, the reader will find sections dedicated to the concise explanation on the principle on which both techniques are based, as well as their experimental protocols.

4.1.1.4.4.1. Particle Counting: The determination of the fractal dimension by PLM using the particle-counting method is based on the relationship:

$$N_p = cR^{D_f} \tag{7}$$

where $N_p$is the number of reflections or "particles" in a region of interest (ROI)of R size, and c is a proportionality constant. D_f is calculated by counting the number of crystal reflections or "particles" (N_p) observed within boxes of increasing length size (R) placed over a properly thresholded and inverted image. The value of D_f is obtained from plotting the logarithm of N_p as a function of the logarithm of R, where the slope gives the fractal dimension and the intercept corresponds to c [9,17]

The first step in the calculation of D_f by particle counting is to convert the grayscale images to binary images through proper thresholding, ensuring that all of the solid features are represented. An inversion of the thresholded images is necessary, as black features will be counted. Hence, the particles need to be black on a white background. An algorithm in Object Image 2.01 software (http://simon.bio.uva.nl/object-image.html) is used to calculate the number of individual features (N_p) that correspond to crystal reflections in a defined ROI. Initially, the particles in the entire image are counted. Sequentially, the ROI is reduced by 5% from all the edges resulting in a smaller ROI from which N_p values are obtained. It is important to note that the ROI corresponds to an area value. The square root of the area values (which correspond to R) are to be used in the calculations of D_f. Once the numbers of particles in each box are obtained, a log–log plot of N_P vs. R is constructed using a standard software package (e.g. Excel, Graph Pad, Sigma Plot, etc.). Care should be taken in using the square root of the ROIs, as they correspond to an area, not to the length of the box. The slope of the resulting line corresponds to the fractal dimension of the network. Figure 35 illustrates the particle-counting procedure used to determine D_f.

When calculating the fractal dimension with the particle-counting method, there are two important things to consider: the range of sizes of the ROI and the inclusion or exclusion of the particles that are touching the edges of each ROI. When using small-sized boxes, the numbers of particles present drops dramatically, leading to changes in the estimation of the fractal dimension. It is recommended that boxes representing 30% of the original image size and below should not be used, thus avoiding any errors in the fractal analysis. There is experimental evidence that the value of D_f changes significantly when the particles that touch the edges of the ROIs are included or excluded from the calculation. It is then advised that, in the fractal analysis, an average be made between the value of D_f obtained both including and excluding all particles that touch the perimeter of the ROI [9]. The algorithms used for the calculation of N_p with Object Image can be seen in the

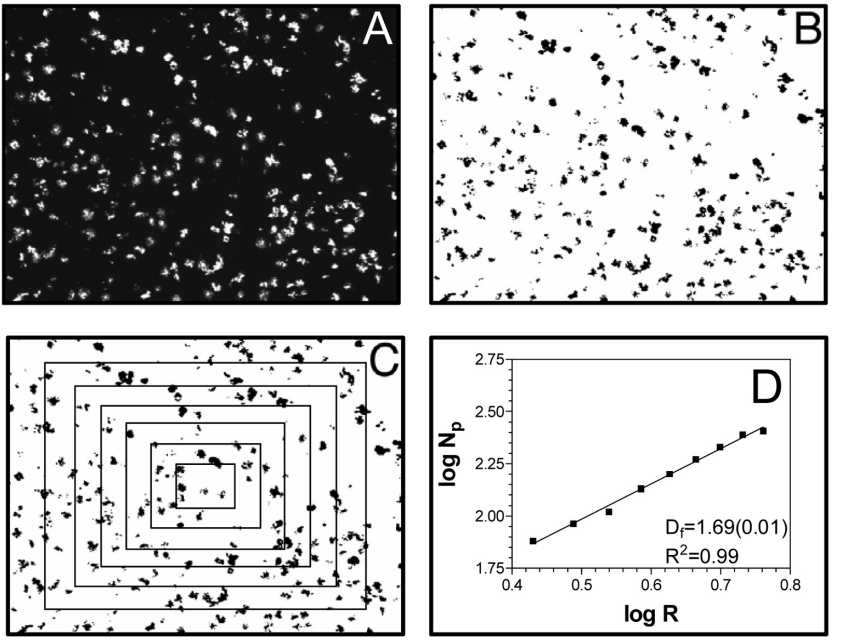

Figure 35 Determination of the fractal dimension by polarized light microscopy using the particle-counting method. A grayscale image (**A**) of the fat crystal network is thresholded and inverted (**B**). The number of crystal particles within boxes of increasing size placed over the thresholded image are counted (**C**). The fractal dimension is the slope of the log-log plot (**D**) of the number of particles (N_p) as a function of the box size (R).

DVD, "Fat Crystal Networks," which is included with this book.

4.1.1.4.4.2. Box Counting: The calculation of the fractal dimension with the box-dimension method is based on the relationship:

$$N \sim D^{-D_b} \tag{8}$$

were N is the number of boxes of a linear size d that covers the reflections in a two-dimentional plane. D_b is calculated by placing a grid formed by boxes of decreasing size d over a prop-

erly thresholded image; followed by the quantification of the number of boxes (N) necessary to cover the observed crystal reflection. At a given size of boxes d, the number of boxes needed to cover an array of reflections should be minimized; hence, the grid is progressively rotated 90° at set angular increments. The number of occupied boxes is counted and only the minimum value of N is used to calculate D_b. The logarithm of N is plotted as a function of the logarithm of d. If the microstructure is of a fractal nature, the plot will follow a straight line, where the slope corresponds to D_b. The box sizes used follow a geometric progression (i.e., 1,2,4,8, etc.) in order to obtain an evenly spaced plot [18].

Benoit 1.3 software package (TrueSoft Int'l, Inc, St. Petersburg, FL, USA) is recommended for this calculation. To perform the analysis, properly threshold the acquired micrographs. Although the software includes an automatic thresholding function, it is recommended that the threshold be performed using Adobe Photoshop (San Jose, CA, USA), to ensure that all solid mass depicted in the original grayscale images is represented in the processed image. For the box-counting method, the microstructural features have to be white; hence, no inversion of the image is necessary. Benoit 1.3 software package analyzes bitmap format images; thus, all image files have to be converted to BMP files.

The Benoit software contains several methods for fractal analysis on diverse systems. When initiating the software, a list of these methods will appear (Fig. 36). In the case of fat crystal networks, select the "box dimension" method and click the OK button. A dialogue window will appear that allows the user to browse through the computer directories and open the image to be analyzed (Fig. 37). Select and open the thresholded image to be quantified.

When the image is selected, the software will open it immediately and begin the analysis. The screen capture observed in Figure 38 presents the analysis parameters, as well as the results. When the analysis is being performed, grids formed by different-sized boxes are laid over the binary image at different orientations. This, along with the analysis considerations, is observed on the right side of the screen. On the left side of the

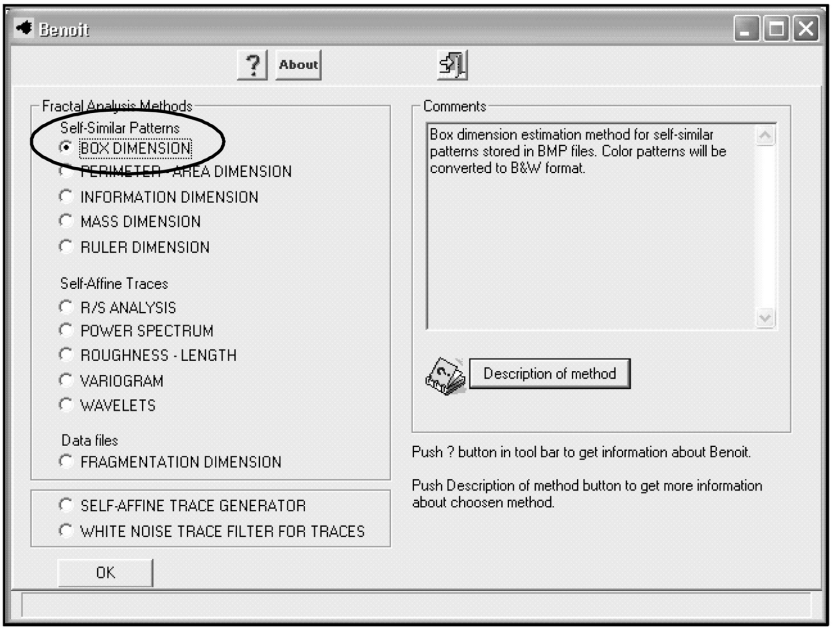

Figure 36 Screen capture of Benoit 1.3 software (TrueSoft Int'l Inc., St. Peterburg, FL, USA, 1999). On the left half of the screen the different fractal analysis methods are listed. On the right half of the screen a brief comment of each method is displayed, as well as the button entitled "Description of method," which displays a complete description of each method.

screen, the resulting log-log plot is progressively constructed while the analysis is taking place. In the plot, the equation of the line obtained from the log–log plot is shown.

Once the analysis has finished, a results window appears (Figure 39) that includes the resulting D_b and the standard deviation (SD) of the plot, as well as the used method, name, path, and size of the analyzed image. Inconsistent results can be observed for very small or very large d values, which may be eliminated from the analysis by selecting them manually. Figure 40 illustrates an example in which the slope of the line changes significantly (from 1.8 to 1.35) when the d values of 10 pixels or lower are eliminated. When a manual selection of

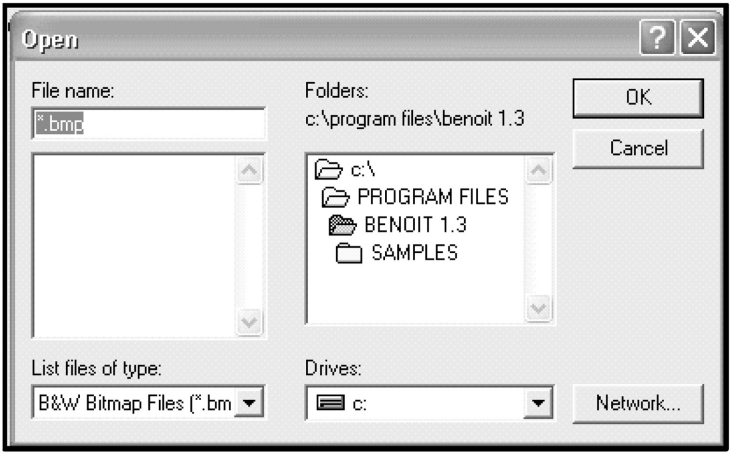

Figure 37 Screen capture of Benoit 1.3 software (TrueSoft Int'l Inc., St. Peterburg, FL, USA, 1999) with the dialogue window in which the image files to be analyzed are opened.

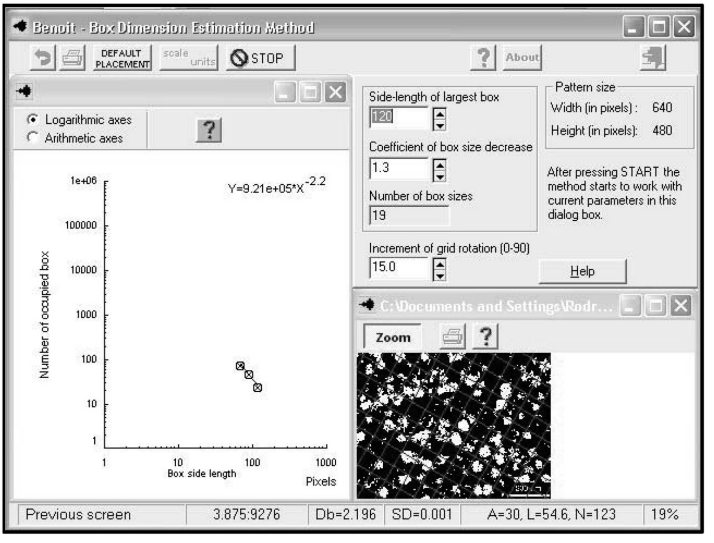

Figure 38 Screen capture of Benoit 1.3 software (TrueSoft Int'l Inc., St. Peterburg, FL, USA, 1999) of the analysis of the fractal dimension being performed.

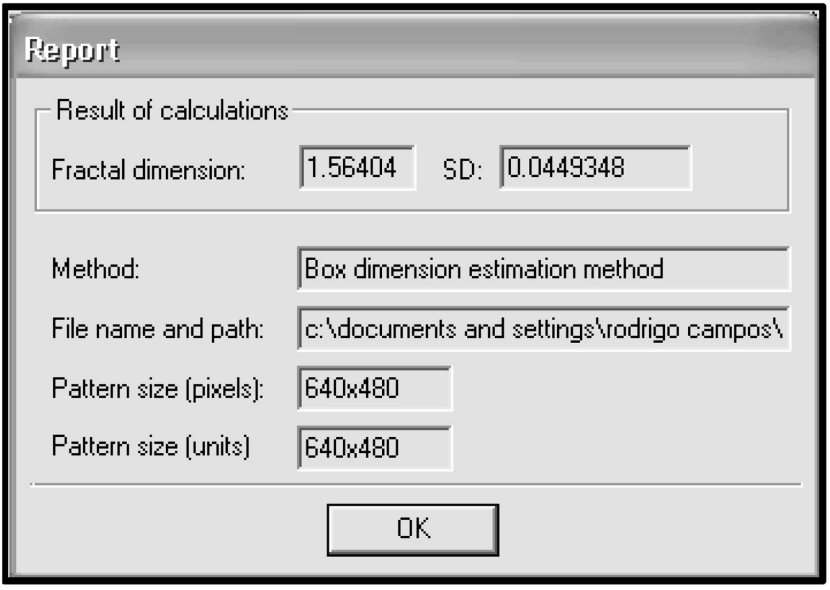

Figure 39 Screen capture of Benoit 1.3 software (TrueSoft Int'l Inc., St. Peterburg, FL, USA, 1999) of the dialogue window that displays the results for the analysis.

the range of d values to be used in the fractal analysis is made, the new resulting value of D_b can be obtained either from the equation of the plot, or from the information bar located at the bottom of the software window.

5. MECHANICAL PROPERTIES

Early nucleation and crystal growth events lead to the formation of submicron primary crystallites from the melt. These crystallites associate into micron-range particles, which further aggregate into clusters, until a continuous three-dimensional network with voids filled with liquid fat is formed [9]. It is during crystallization that the template for the final physical properties of the resulting fat crystal network is created. Hence, the mechanical properties of a fat crystal network are

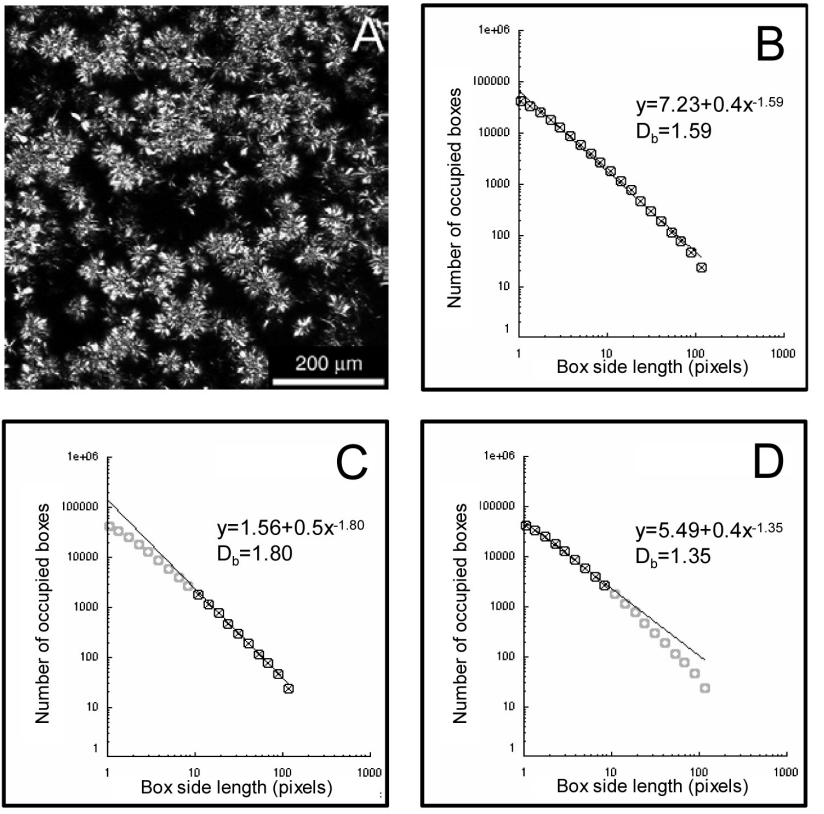

Figure 40 Fractal analysis of cocoa butter crystallized at 24°C by imaging its microstructure (**A**) followed by its analysis with Benoit 1.3 software (TrueSoft Int'l Inc., St. Peterburg, FL, USA, 1999) (**B**). In the figure, we observe that the value of D_b changes from 1.59 when using all *d* values, to 1.8 when manually selecting *d* values of 10–100 pixels (**C**) or 1.35 when manually selecting *d* values of 1–10 pixels (**D**).

determined by the different levels of structure, such as chemical composition, solid fat content (SFC), and crystal habit (polymorphism and microstructure). To study the mechanical properties of fat crystal networks, rheologic tests are used, which measure how the crystallized material responds to applied forces (stress) and deformations (strain) [19].

5.1. Small Deformation Rheology and Calculation of the Fractal Dimension

5.1.1. Small Deformation Rheology

Small deformation rheology refers to testing procedures that do not cause structural damage to the sample. At low levels of applied stress, fat crystal networks behave like Hookean solids, in which the stress (σ) is directly proportional to the strain (γ), (i.e., $\sigma \propto \gamma$), as observed in Figure 41. It is in the LVR that the stress increases linearly with strain until a critical strain is reached. Beyond this critical strain (strain at the limit of linearity), deformation of the network occurs; this is known as the yield point. The elastic limit quickly follows, where permanent deformation and sample facture occurs [20]. Thus, it is important that small deformation rheology tests be carried out within the LVR of the fat crystal networks.

Small deformation oscillatory methods collect strain information by applying a controlled stress via the application of a sinusoidal stress wave. The variation of strain is measured

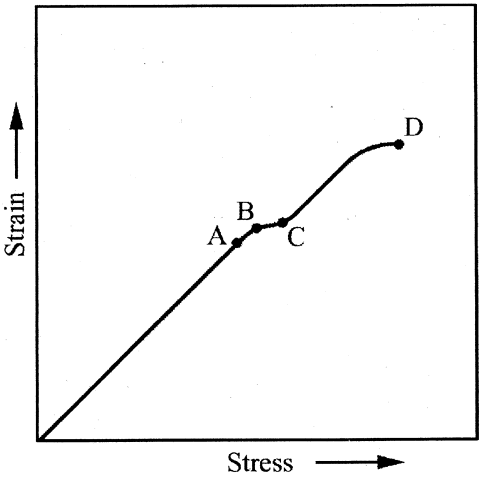

Figure 41 Stress-strain behavior of a typical elastic system. Indicated are the yield point (**A**), elastic limit (**B**), irreversible deformation (**C**), and fracture (**D**).

as a function of applied stress by the rheometer in terms of the strain magnitude and phase angle (δ) between applied stress and resulting strain wave. Figure 42 shows typical stress-strain sinusoidal relationships, in which the resulting strain can be in phase or out of phase of the applied stress. The parameters obtained from small deformation oscillatory rheology describe the material's mechanical properties. These include the complex modulus (G^*), the shear storage modulus (G'), the shear loss modulus (G'') and the tangent of the phase shift or phase angle ($\tan\delta$). The amount of deformation is measured and the strain is released from the sample, the amount of recovery, G', is the shear modulus; alternatively, the amount of energy lost is the G'', or the loss modulus. The strain response can be broken down into its elemental components of stress, which are in phase or out of phase, to derive the values for G' and G''. Both G' and G'' are dependent on the phase angle of the system and are derived from the vectorial components of G^*. This may also be characterized by the sine and cosine of δ multiplied by the modulus of the system. The vectorial resolution shown in Figure 43 of the stress-strain ratio can be used to calculate G^*, which is the ratio of stress to strain; G', which is $G^*\cos\delta$; and G'', which is $G^*\sin\delta$.

The storage modulus, G', is the ratio of the applied stress that is in phase with the strain ($\delta = 0°$), consequently it is an

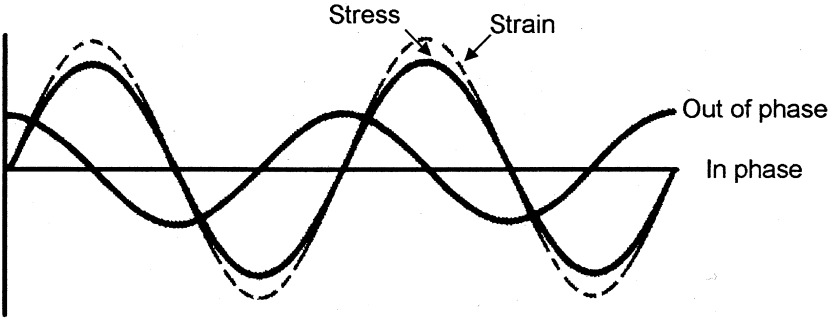

Figure 42 Time profile of an applied sinusoidal stress wave and the corresponding resulting sinusoidal strain wave as they apply to small deformation rheological testing.

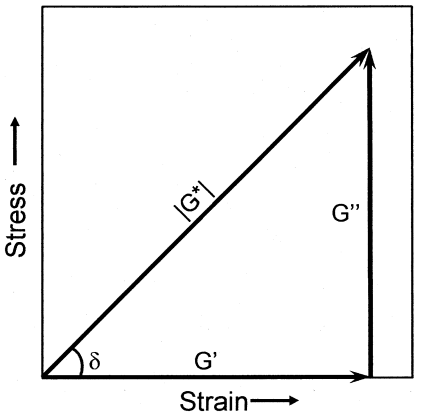

Figure 43 Vectorial resolution of the complex modulus components. Indicated are the complex modulus (G*), storage modulus (G′), loss modulus (G″), and phase angle (δ).

expression of the magnitude of the energy stored in the material recoverable per deformation cycle [21]. G′ is useful to asses the solidlike structure of a material [22] and is related to the hardness and strength of the network. The loss modulus, G″, is the ratio of the applied stress that is out of phase with the strain ($\delta = 90°$); thus, it is a measurement of the energy lost as viscous dissipation per deformation cycle [21]. G″ is an indicator of the fluidlike behavior of the material [22], and it is related to the spreadability of the system. The balance of both the elastic components to the viscous components of the material is represented by tanδ, which is the ratio of the loss moduli to the storage moduli.

5.1.2. Fractal Dimension

The concept of fractal geometry has been used to characterize systems with a disordered distribution of mass and statistical self-similar patterns, such as colloids [23] and fat crystal networks [9]. A statistical system self-displays, on average, similar appearance, distribution, and structure within a limited range of magnifications. Fractal theory predicts that the mass

of a fractal aggregate (or distribution of mass within the system), M, is related to the size of the object (or ROI), R, in the following power–law fashion:

$$M \sim R^{D_r} \tag{9}$$

were D_r is the fractal dimension of the object or the distribution of mass within a region of the network.

The elasticity of fat crystal networks is dependent on its microstructure, including the spatial distribution of mass. The shear modulus (G) scales with the volume fraction of solids in a power–law fashion, from which the following relationship is obtained:

$$G \sim \lambda \Phi^{\frac{1}{3-D_r}} \tag{10}$$

where λ is a constant independent of the volume fraction, but dependent on several primary particle structural parameters as well as intermolecular forces, and Φ is the solid volume fraction or SFC/100 [9,19,24]. Based on this relationship, an estimate of D_r of a fat system can be obtained using rheologic data by constructing a logarithmic plot of G′ at different Φ of network material. Dilution of a fat allows for a controlled variation of the SFC. Work in our laboratory has shown that canola oil is a good diluent for D_r determinations, as it does not crystallize above 0°C, nor does it appear to solubilize or cocrystallize significantly with the fat studied. The slope of a plot of log G′ vs. logΦ is used to determine D_r.

5.1.3. Procedure

5.1.3.1. Sample Preparation

5.1.3.1.1. Dilution Preparation: A series of dilutions are prepared with the sample fat to be analyzed and a vegetable oil (i.e., canola oil). The latter will be used as a diluent to control the solid fraction of the system. Care should be taken when choosing the oil that will be used as a diluent as it should neither crystallize at the temperature of study nor should it solubilize the crystal network formed by the hard stock fat. The oil to be used has to dilute the solid fraction without alter-

ing its crystal network structure. Our experience suggests that canola oil is a good oil to use when preparing dilutions because it does not affect the crystallization of the hard stock fats at low crystallization temperatures and high cooling rates.

Melt and mix the fat to ensure that it is homogenized. Prepare a series of dilutions in 2–5% increments using the fat and the oil. The dilution concentration range is a function of the SFC range of interest for the study. The percent increment in concentration of the prepared dilutions depends on how thorough the study is planned. A volume of 20 g of each dilution is recommended, as it is enough for small and large deformation rheology studies. Once prepared, keep dilutions in screw-cap glass containers, which are advantageous for heating and cooling.

Melt the sample dilutions in an oven at a temperature that ensures that all crystal memory is erased. For most edible fats, 80°C for 30 minutes after the sample has melted is sufficient; although, some high-melting-point fats require a higher temperature to erase all crystal memory (i.e., palm oil needs to be heated at 120°C for 10 minutes). Transfer the sample to either rheology molds or to NMR tubes as directed in the next sections.

5.1.3.1.2. Sample Disk Preparation: Plastic PVC molds are used to prepare discs of crystallized sample of uniform dimensions. The molds, shown in Figure 44, are comprised of three sections. The upper plate contains 6 holes for the screws and fasteners to seal the three sections together. The lower plate contains 6 screws, which connect the other two sections, forming a tight seal. The intermediate plate contains six screw holes as well as six perforations to be filled with the molten sample. For small deformation rheology, the perforations have a diameter of 20 mm and a height of 3 mm. Between each of the PVC sections, a layer of Parafilm "M" is used to ensure a tight seal and to prevent the molten sample from leaking. Wingnuts hold the three sections of the mold together.

Prior to sample disk preparation, equilibrate the three parts of the mold and strips of Parafilm to the temperature of

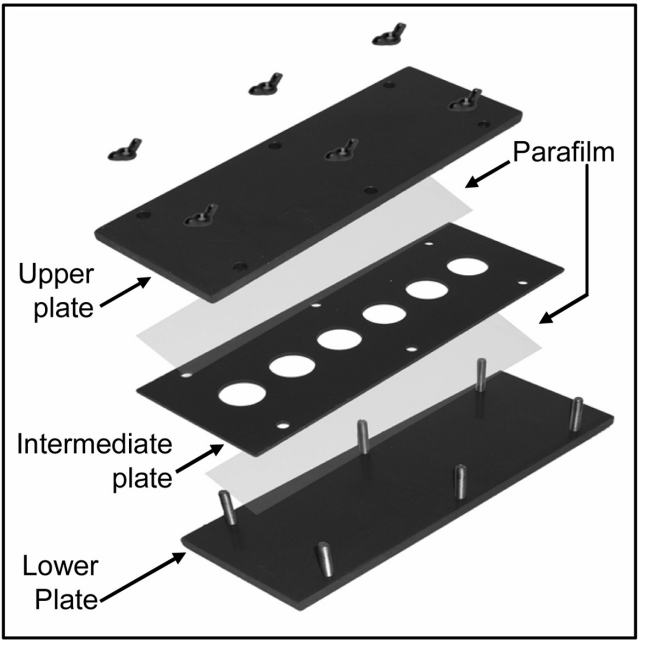

Figure 44 PVC molds used to prepare fat sample discs of uniform dimensions used in rheologic studies.

study to avoid any temperature variations. Assemble molds in preparation to fill them with liquid fat. Do this by placing a strip of Parafilm over the lower plate and fitting the intermediate plate on top by inserting the screws of the lower plate into the holes of the intermediate plate. Melt the prepared dilution samples as previously indicated. Allow the samples to cool to approximately 60°C. This prevents the Parafilm from melting while not allowing crystallization to take place. Transfer the sample into the molds by filling the wells until the fat forms a convex surface above the level of the spacer (the middle plate) with the aid of a pipette. Use a different pipette for each dilution. Avoid contaminating the different dilutions. Place a second strip of Parafilm over the convex layer of fat; this will displace the excess sample, forming an even layer of fat. Placing the long side of the strip of Parafilm against the length side of the mold and slowly folding it over the openings of the

mold accomplishes this most easily. Care should be taken in preventing the formation of air bubbles within the fat when plating the strip of Parafilm on top of the liquid samples. If bubbles rise, remove the Parafilm, add sufficient fat to avoid the generation of air pockets between the sample and the strip of Parafilm, and cover with a new Parafilm strip. Measuring sample discs with air bubbles present on the surface will lead to inaccurate results. Place the upper plate on top of the Parafilm and use wing nuts to hold the three section of the mold together. Immediately transfer the molds to a temperature-controlled incubator set at the temperature of study for 24 hours before measurements are taken. Most fractal work entails a temperature regime of 5°C for 24 hours; however, the user may decide the time-temperature profile to be used.

5.1.3.1.3. Nuclear Magnetic Resonance Sample Preparation: Temper the pNMR tubes (10-mm diameter, 1-mm thickness, and 180-mm height) to the temperature of study to ensure similar cooling regimes for the pNMR and rheology work. Melt the prepared dilution samples as previously indicated. Transfer 3 g of the molten fat samples to the glass pNMR tubes. Wipe the outside of the tube with tissue making sure that the exterior is clean. Cap the tubes and transfer to a temperature control incubator set at the temperature of study for the duration of the experiment. For more details on the determination of SFC by pNMR, refer to the crystallization section of this chapter.

5.1.3.2. Preparation of the Instrument

In our laboratory, dynamic oscillatory rheology is performed using an AR 2000 Shear Dynamic Rheometer (TA Instruments, Mississagua, ON, Canada), shown in Figure 45. Ensure that the instrument, airflow, and water circulation bath are all turned on before starting. The TA Instruments Smart Swap Peltier Plate (Mississagua, ON, Canada) removes heat to ensure the sample does not fluctuate from the temperature of study; therefore, ice must be added to the water recirculation bath to ensure that heat is removed from the Peltier Plate. Load the program, Rheological Advantage Instrument Control, and then create an oscillation procedure. Select the

Figure 45 AR 2000 Dynamic Shear Dynamic Rheometer (TA Instruments, Mississauga, ON, Canada).

procedure in the menu and go to the new oscillation option. Three options should appear. First, the conditioning step, under settings, should include the start temperature; set this to the temperature of study. This window also includes the equilibration time; set it to 10 seconds. Ensure that the "wait for temperature" icon is selected, it is important to ensure that the temperature tab is at the temperature of study before commencing the experiment. This prevents the experiment from proceeding at a higher temperature than recommended. Select the frequency sweep option from the toolbar. Under test type, select stress sweep; at this point, the name should change from second stage to stress sweep step.

Under test settings, then sweep and oscillation stress, the value entered depends on the SFC of the sample. If the sample has an SFC less than 30%, a stress set between 0.06 and 1000 Pa should suffice. However, if the sample possesses a higher SFC, the stress should increase to approximately 15,000 Pa. The stress sweep should encompass both the liner viscoelastic region and the point of linearity. As well, set the frequency at 1Hz. The final check box for postexperiment step is left unchecked.

Select "new geometry" under "description." This allows for the selection of parallel plate geometry. Uncheck "solvent trap" because evaporation of sample is not an issue. The dimensions of the plate, as well as the gap, are required. Select a 20-mm steel plate. The magnitude of the gap should be checked and defined by the user for each system. To define the gap, it is suggested that the geometry slightly touches the sample. Excessive compression of the sample as well as slipping should be avoided. Again it is important to save the session. As well, in this window, set the backoff distance to 10,000 μm, this will allow the sample disk to be placed under the geometry. The final window is "notes"; this window records information deemed important by the user.

From this point, the saved procedure can be loaded by selecting session under "file" on the toolbar menu.

5.1.3.2.1. Spindle and Peltier Plate Preparation: Cover the metal spindle with sand paper, which is cut to the exact shape and size of the spindle. The sand paper, 60-grit

aluminum oxide, is glued using an epoxy resin (i.e., Instant Krazy Glue), onto the peltier plate. Sand paper is placed onto the peltier plate and onto the spindle to ensure the fat pellet sample will not slip during oscillation. The sandpaper is epoxied to ensure that the deformation in the displacement of the fat disk and not a rotation of the paper. The sand paper on peltier plate does not have be the exact shape; however, it is important that it is larger then the sample.

5.1.4. Experimental Procedure

5.1.4.1. Storage Modulus Determination

Load the program to be used by loading the session created earlier, under file menu. At this point, the directions given must be followed each time prior to using the Rheometer. Calibration of the inertia and bearing friction must be accomplished prior to each use; it is important that this is done prior to each run. Each calibration is measured in the absence of the geometry. The final calibration, or mapping, must have the number of iterations set at 3, and select "precision" under bearing mapping. Once again, it is important to do this in the absence of the geometry (spindle).

At this point, two different methods may be used to measure with the shear modulus. Standardizing the normal force or by standardizing the gap width may determine the shear modulus. Recent work by our group suggests that the normalized force provides more accurate results, due to the fact that there will be surface imperfections when creating the mold. Thus, when deformation occurs via gap width, different percentages of deformations will occur. Normalized force is independent of the surface and does not require an exact height. To accomplish the normal force measurements, it is important, prior to use, that the normal force generated by the sandpaper and peltier plate be removed. As well, at this point, the normal force and the gap should be zeroed. Standardize the normal force to 10N for hard (high SFC) samples and contact with the soft (low SFC) samples. A general rule is, if 10N of force is enough to visually compress the sample, contact will suffice. This will prevent the sample from slipping. If the normalized

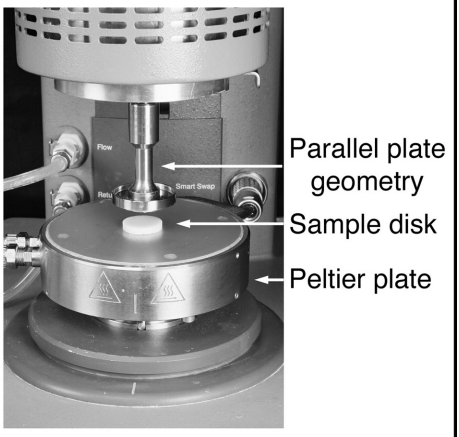

Figure 46 AR 2000 Shear Dynamic Rheometer (TA Instruments, Mississauga, ON, Canada).

gap method is chosen, a gap width of 2700 μm is recommended. Figure 46 illustrates the sample loaded on the peltier plate over sand paper and the parallel plate geometry which is used in these experiments, Generally, six repetitions are carried out for each dilution to ensure the most accurate results possible. However, it is advised to not go below three repetitions due to the high variation of results within each dilution.

5.1.4.2. Solid Fat Content Determination

After crystallization at the temperature of study and appropriate has elapsed, proceed to measure the SFC of each dilution by pNMR. For more details on SFC determination by pNMR, refer to the crystallization section in this chapter. The SFC readings will be used to determine the volume fraction (ϕ).

5.1.5. Data Analysis

Both G′ and Φ determine the fractal dimension, however, useful information about the sample is obtained from the G″ and

tanδ. During the analysis, each of these values should be taken from the LVR.

For the fractal analysis, plot the logarithm of G′ as a function of the logarithm of Φ as shown in Figure 47. If the microstructure is of fractal nature, the plot will follow a straight line. Fit the data to a linear regression and obtain the slope and the x-intercept. The slope (m) is used to determine D_r based on the following equation:

$$m = \frac{1}{3 - D_r} \therefore D_r = 3 - \frac{1}{m} \tag{11}$$

Based on work by Narine and Marangoni [25], Marangoni [9], and Marangoni and Rogers [24], it is understood that λ yields important information regarding particle properties independently of Φ. Derived from Equation 9, the following is proposed:

$$G \approx \frac{2\delta}{a}\Phi^{\frac{1}{3-D_r}} \approx \frac{A}{6\pi a d_o^2 \varepsilon^*}\Phi^{\frac{1}{3-D_r}} \tag{12}$$

where δ is the crystal-melt interfacial tension, a is the diameter of primary particles (assuming that microstructures are spherical structures), A is the Hamacker's constant, and d_o is

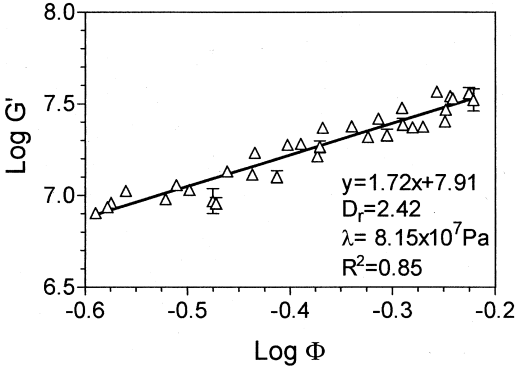

Figure 47 Log-Log plot of the storage modulus (G′) as a function of the solid volume fraction (Φ) used in the determination of the fractal dimension (D_r) of a fat crystal network.

the intercluster separation distance, and εε* is the compressional strain at the limit of linearity. Hence, λ, which is the inverse logarithm of y-intercept from the log-log plot of G′ as a function of Φ, is defined as:

$$\lambda = \frac{2\delta}{a} \tag{13}$$

The factor λ is mainly influenced by particle properties yet independent of Φ [9]. Obtain the values of D_r and λ as described previously.

5.2 Large Deformation Rheology

Large deformation rheology is based on the deformation of a sample at a constant rate to the point were the force exceeds the structural capacity of the sample, causing it to permanently deform and break [26]. By measuring the amount of applied force required to induce a change in the sample, a representative measurement of hardness, spreadability, cutting force, or yield force is obtained [26]. One such method involves the compression, by the application of uniaxial paralle force, of a sample between two parallel plates to determine relative hardness values via the measurement of yield force. It is important to note that there are several parameters that will influence the yield force, such as the rate of the applied stress and the load. Figure 48 shows a typical load-deformation curve, which can be used to derive values for yield stress, yield strain, compressive yield work, and, depending on the linearity of the onset of compression, a compressive modulus [26]. These measurements can be used to provide an index of hardness for fats, which have been successfully correlated to the textural attributes of hardness and spreadability obtained through sensory evaluation [26]. Unfortunately, these tests are destructive in nature and yield little information about the native microstructure of the system.

5.2.1. Sample Preparation

Prepare sample disks by crystallizing the fat sample in PVC molds to ensure uniform dimensions, similar to preparation for

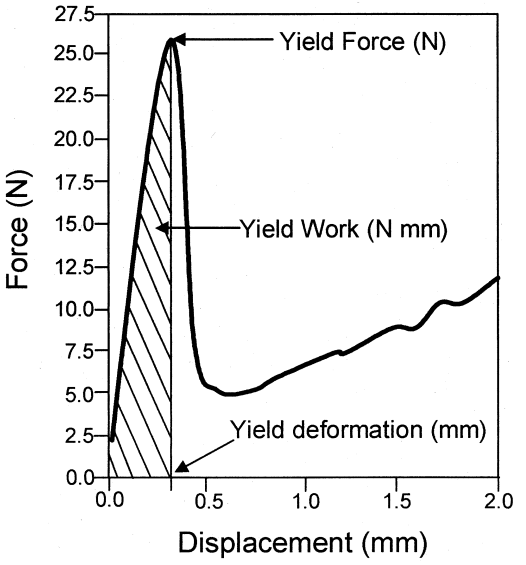

Figure 48 Typical load-deformation curve obtained from the compression of a sample between two parallel plates used to characterize its mechanical properties through the following parameters: yield force, displacement at yield force, compressive yield work, and compression modulus.

small deformation rheology. In the case of large deformation studies, the dimensions of the disks are of 10-mm diameter and 6-mm height. As with small deformation rheology testing, samples are transferred to temperature-controlled incubators set at the desired temperature of study for the period of time on interest for the analysis. Storage of the crystallized samples at 5°C for 24 hours is recommended; however, the time-temperature profile may be changed by the user according to the objectives of each study.

5.2.2. Instrument Calibration

In our laboratory, a Stable Micro System Materials Tester Model MT-LQ (Stable Micro Systems, Surrey, England), with a 50-kg load cell calibrated using a 10-kg standard weight and

34-mm flat plate geometry, as shown in Figure 49, is used to measure the apparent yield force. The fixed plate is attached to a recirculation water bath in order to maintain a constant temperature at the surface of the plate. The instrument is controlled, and data is compiled by the appropriate software package.

Two calibrations are performed by the instrument: force calibration and probe position calibration [27]. For force calibration, the weight hanger is connected to the load cell, and the instrument will analyze the signal that is present for zero force. Care should be taken so that the hanger is not touching the base, nor any weight is applied to the hanger. Consecutively, a 10-kg standard weight is placed on to the hanger con-

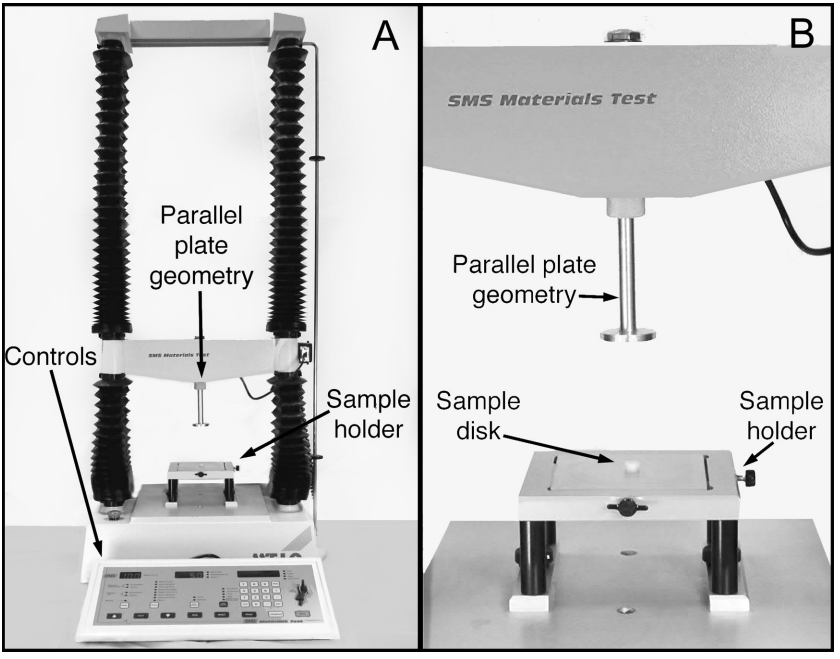

Figure 49 Stable Micro System Materials Tester Model MT-LQ (Stable Micro Systems, Surrey, England), with a 34-mm flat plate geometry used for large deformation rheologic analyses (two plate compression).

nected to the load cell, and the instrument will analyze the signal resulting from the weight, as observed in Figure 50.

The probe calibration procedure is used to calibrate the probe position that will enable the measurement of product height to make strain (displacement) calculations. To perform the probe calibration, attach the selected probe geometry (i.e., 34-mm flat plate geometry) and make sure that the probe is clear of any obstruction. Bring the probe close (roughly 10 mm) to the lower plate. Set a value for probe return displacement and run the calibration. The instrument will calibrate the probe position by making the tip of the probe touch the lower plate so it can reset the travel displacement to zero, followed by the probe returning to the previously established distance. All movement of the probe is tracked.

5.2.3. Experimental Procedure

Make sure that both the lower plate and the flat plate geometry are clean prior to use. It is recommended that ethanol is used for cleaning so that all fat residues are eliminated. Set the recirculation water bath at the temperature of study and allow it to equilibrate. Establish the test parameters that will determine the experimental conditions. The list of parameters, as well as recommendations based on experimental work performed in our laboratory, are shown in Table 6.

Transfer a sample disk to the lower plate of the rheometer and begin the run. The instrument will perform the experiment based on the preestablished parameters and will collect data accordingly.

5.2.4. Data Analysis

During the experiment, the instrument compiles the data and makes them available in the form of a rheogram (a load-deformation curve). Analysis functions are included in the instrument's software. Yet, if the user wants to perform further analysis using a plotting software, the data is also available in a spreadsheet form.

Figure 50 Force calibration of the Stable Micro System Materials Tester Model MT-LQ (Stable Micro Systems, Surrey, UK) using a 10-kg standard weight. During the force calibration, the instrument will analyze the signal resulting from the weight.

Table 6 Test Parameters Used in Large Deformation Rheologic Testing. Included are Recommendations of the Experimental Conditions Based on Experimental Work Done in our Laboratory; However, Experimental Conditions have to be Determined by the User Based on the Analysis Objectives and Sample Characteristics

Parameters (units)	Units	Recommendations
Pretest speed	mm/s	5 mm/s
Test speed	mm/s	10 mm/s
Post-test speed	mm/s	5 mm/s
Displacement	mm	5 mm
Force	g	1000 g
Time	s	5

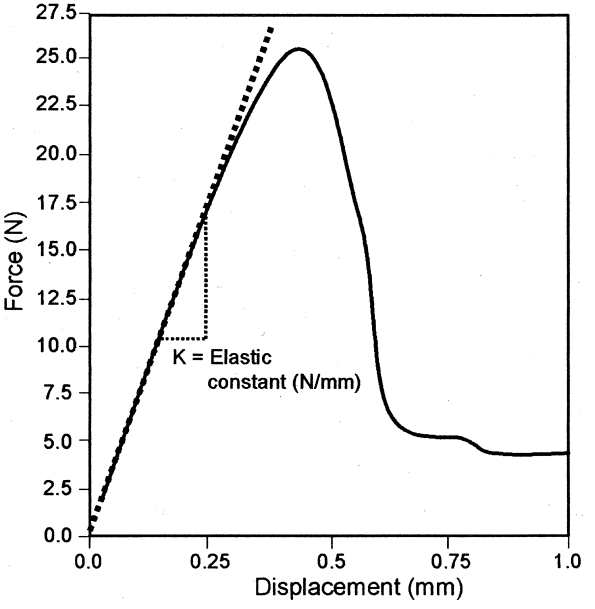

Figure 51 Load-deformation curve obtained from the compression of a disk sample from which the elastic constant is calculated as the slope of the displacement observed by the application of force prior to the rupture of the sample.

Several measurements characterize large deformation rheology and are obtained from the load-deformation curve (Fig. 48 and Fig. 51). The yield force or yield stress is measured as the force measurement at the apparent breaking point or yield point of the sample discs. Furthermore, the yield work corresponds to the area under the curve to the yield point, and the yield strain corresponds to the ratio of geometry displacement at the yield point to sample height.

REFERENCES

1. Bruker. Bruker PC/20 Series Nuclear Magnetic Resonance Analyzer, Instrument's Manual. Milton. ON. Canada: Bruker, 1989.
2. Avrami M. Kinetics of phase change I General theory J Chem Phys 1939; 7(12):1103–1112.
3. Sharples A. Overall kinetics of crystallization. In: Sharples A, Ed Introduction to polymer crystallization. London: Edward Arnold Publishers, Ltd., 1996:44–59.
4. Wright AJ, Hartel RW, Narine SS, Marangoni AG. The effect of minor components on milk fat crystallization J Amer Oil Chem Soc 2000; 77:463–475.
5. American Oil Chemists' Society (AOCS). Official methods and recommended practices of the American Oil Chemists' Society. American Oil Chemists' Society, Champaign, IL. USA. Solid fat content (SFC) by low-resolution nuclear magnetic resonance, official method Cb-16b-93.
6. International Union of Pure and Applied Chemistry (IUPAC). Standard Methods for the Analysis of Oils, Fats & Derivatives, International Union of Pure and Applied chemistry. Oxford, UK: Blackwell Scientific Publications. Solid content determination in fats by NMR, standard method 2.150.
7. Hartel RW. Applications of milk-fat fractions in confectionery products J Am Oil Chem Soc 1996; 73(8):945–953.
8. Marangoni AG, Lenki RW. Ternary phase behavior of milk fat fractions J Ag Food Chem 1998; 46:3879–3884.

9. Marangoni AG. The nature of fractality in fat crystal networks Trends in Food Science and Technology 2002; 13:37–47.

10. Timms RE. Confectionery Fats Handbook: Properties, Production and Application. Bridgewater. UK: The Oily Press, 2003: 25–36.

11. de Mann JM. X-ray diffraction spectroscopy in the study of fat polymorphism Food Res Inter 1992; 25:471–476.

12. Robinson P, Davidson MW. Introduction to polarized light microscopy. www.microscopyu.com/articles/polarizedintro.html.

13. Dutch S. Light and polarization. www.uwgb.edu/dutchs/petrolgy/genlight.htm.

14. Murphy D, Spring KR, Davidson MW. Polarization of light. www.microscopy.fsu.edu/primer/lightandcolor/polarizedlightintro.html.

15. Abramowitz M, Bradbury S, Robinson PC, Spring KR, Flynn BO, Long JC, Parry-Hill MJ, Tchourioukanov KI, Davidson MW. Polarized light microscopy. www.microscopy.fsu.edu/primer/techniques/polarized/polarizedhome.html.

16. Russ J. The image Processing and Analysis Cookbook. Ashville. NC: Reinder Graphics, Inc., 1999.

17. Narine SS, Marangoni AG. Fractal Nature of fat crystal networks Phys Rev E 1999; 59(2):1908–1920.

18. Daubert CR, Foegeding EA. Rheological principles for food analysis in food analysis. 2nd editionNielsen SS, Ed. Gaithersburg. MD: Aspen Publishers, Inc., 1998:551–569.

19. Marangoni AG. Elasticity of high volume fraction fractal aggregate networks: a thermodynamic approach Phys Rev B 2000; 62(21):13951–13955.

20. TruSoft International, 1999. Beneit 1.3 fractal analysis system.

21. Rao MA. Measurement of flow and viscoelastic properties. In: Rheology of fluid and semisolid foods: principles and applications Rao MA, Ed. Gaithersburg. MD: Chapman & Hall, 1999: 59–152.

22. Steffe JF. Viscoelasticity. In: Rheological methods in food process engineering. 2nd edition. East Lansing. MI: Freeman Press, 1996:294–349.

23. Shih WH, Shih WY, Kim SI, Lin J, Aksay IA. Scaling behavior of the elastic properties of colloidal gels Phys Rev A 1990; 42: 4772–4779.

24. Marangoni AG, Rogers MA. Structural basis for the yield stress in plastic disperse systems Appl Phys Lett 2003; 82(19): 3239–3241.

25. Narine SS, Marangoni AG. Mechanical and structural model of fractal networks of fat crystals at low deformations Phys Rev E 1999; 60(6):6991–7000.

26. Wright AJ, Scanlon MG, Hartel RW, Marangoni AG. Rheological properties of milk fat and butter J Food Science 2001; 66(8): 1056–1071.

27. Stable Micro Systems, 1997. User Manual. Surrey, England.

10

Scaling Behavior of the Elastic Modulus in Colloidal Networks of Fat Crystals

TAREK S. AWAD, MICHAEL A. ROGERS, and ALEJANDRO G. MARANGONI

Department of Food Science
University of Guelph
Guelph, Ontario, Canada

INTRODUCTION

Fats are the main structural components in many food products, including margarine, chocolate, butter, and spreads. The sensory characteristics of fat-structured materials such as spreadability, hardness, and mouth-feel are highly dependent on the structure of the underlying fat crystal network, which controls its macroscopic rheologic properties [1–5]. This fat crystal network is built by the interaction of polycrystalline fat particles, which provides firmness or solidlike behavior to

the plastic fats [1–5]. The amount, geometry, and spatial distribution of solid fat crystals, as well as their interactions at different levels within the network all affect the rheological properties of fats and fat-structured food products.

Structural analogies between fat crystal networks and colloidal gels have been drawn since 1961 [6,7]. Vreeker et al. [8] first proposed that a network of tristearin crystals in paraffin oil resembled a colloidal gel that could be analyzed using fractal scaling theories. Our group has developed this concept further by relating the different structural levels in a fat crystal network to macroscopic elastic properties [9–11]. Further studies [12–14] have shown that consideration of the mesoscale level of structure is important in modeling the mechanical properties of fat crystal networks.

The scaling behavior of the elastic modulus with solids' volume fraction in flocculated colloidal aggregates has been studied extensively [15–22], and a theory was developed to relate the elastic properties of colloidal gels to their structure [16]. Subsequently, Shih et al., in 1990 [18] proposed the existence of two rheological regimes, namely, the strong-link regime at low solids' volume fractions and the weak-link regime at high solids' volume fractions. Recently, a transition regime was proposed by Wu and Morbidelli in 2001 [22]. In these studies, the fractal concept was used to characterize the spatial distribution of the gel network mass. The fractal dimension (D), which defines the cluster size, has been evaluated by light scattering and rheology techniques [8,17–23] and, more recently, by microscopy [24–26]. Rheology is the most common technique for the quantification of microstructure in fat crystal networks and by utilizes the relationship of the shear storage modulus (G′) to the volume fraction of network solid mass (Φ) via the mass fractal dimension (D) of the network. In previous work from our group, we considered that fat crystal networks, at relatively high SFCs, were in the weak-link rheological regime [9,10]; this is based on the fact that crystal clusters are relatively hard structures, not likely to yield at small deformations, and, instead, the links between these hard spheres would yield. However, conclusive evidence for the existence of

these rheological regimes in fat systems has not been provided yet.

In this work we demonstrate the scaling behavior of the elastic modulus with (SFC) in fats and examine the occurrence of the two common regimes (i.e., weak and strong link). For this purpose, the rheological properties of three common fats were determined at different SFCs. For each fat, the existence of a particular regime was confirmed, as in colloidal gels, by studying the behavior of the stress at the limit of linearity at different SFCs. In addition, the feasibility of using the stress at the limit of linearity to obtain structural information about the fat crystal network and to determine the mass fractal dimension was also investigated. We also monitored changes in the microstructure of the fats upon variation of SFC to determine whether there is a relationship between mechanical properties, crystallization behavior, and network structure.

Theory

Vreeker et al. [8] showed that the storage modulus (G') of an aggregated fat crystal network scaled with particle concentration (Φ) according to a power–law, similar to flocculated colloidal gels. Subsequently, Marangoni and Rousseau [9] applied the theory of Shih et al. [18] to fats at high SFC, assuming the weak-link regime. According to the scaling theory of Shih et al., the scaling behavior of the elastic properties of colloidal gels can belong to either of two regimes. These regimes are dependent on the strength of the links between the clusters (microstructures in the fat crystal network) of a colloidal gel relative to the strength of the clusters themselves.

Strong-Link Regime

In the strong-link regime, the individual flocs or clusters of colloidal gels grow large so that each cluster acts as a weak spring. As a result, the elastic constant of the system as a function of particle concentration is dominated by the elastic constant of the flocs and not by the elastic constant between the flocs (interfloc links). The expression for the strong-link regime, as proposed by Shih et al. [18] is

$$K \sim \Phi^{[(d\ +\ x)/(d\ -\ D)]} \tag{1}$$

where K [N/m] is the macroscopic elastic constant, d is the Euclidean dimension, x is the chemical length exponent, or backbone fractal dimension, usually assumed to have a value between 1 and 1.3, and D is the fractal dimension of the flocs. Therefore, the elastic modulus increases with the particle volume fraction in a power–law manner with an exponent $[(d + x)/(d - D)]$.

Weak-Link Regime

In the weak-link regime, the interfloc links are weak compared to the flocs, and can be considered small rigid springs. The elastic constant of the system, then, is dominated by the elastic constant of interfloc links, which is weaker than that of the flocs. This behavior is observed at high particle concentrations. The elastic constant (K) of a system in the weak-link regime can be expressed as

$$K \sim \Phi^{(d-2)/(d-D)} \tag{2}$$

Therefore, the elastic modulus increases with the particle volume fraction in a power law manner with an exponent $[(d - 2)/(d - D)]$.

Thus, the relationship between the elastic constant K and solids' volume fraction Φ yields a straight line with slope equal to $(3 + x)/(3 - D)$ in the strong-link regime, or $1/(3 - D)$ in the weak-link regime for $d = 3$.

Strain at the Limit of Linearity (γ_o)

The strain at the limit of linearity is the point at which the weakest bond in a floc breaks after applying force beyond a critical value. Above the limit of linearity, the network is broken and the linear elastic behavior does not exist anymore. According to the model of Shih et al. [18], the relationship between the strain at the limit of linearity (γ_o) and solids' volume fraction for the strong link regime is

$$\gamma_o \sim \Phi^{[-(1+x)/(d-D)]} \tag{3}$$

From Equation 3, we can deduce that the strain at the limit of linearity γ_o should decrease with increasing the solids' volume

fraction Φ. In contrast, γ_o increases with increasing Φ for the weak-link regime (d = 3) as

$$\gamma_o \sim \Phi^{1/(d\ -\ D)} \tag{4}$$

A practical way to pinpoint whether a system is in the strong-link or weak-link regimes is by determining the dependence of the strain at the limit of linearity on the solids' volume fraction.

In our work, we determined the stress at the limit of linearity (σ_o) [Pa] that was then used instead of γ_o since $\sigma_o \sim \gamma_o$ in the linear viscoelastic region (LVR). Therefore, σ_o-Φ scaling could be used to determine the fractal dimension, assuming a weak-link regime using

$$\sigma_o \sim \Phi^{1/(d\ -\ D)} \tag{5}$$

EXPERIMENTAL

Samples

Samples of anhydrous milk fat (AMF), palm oil (PO), and cocoa butter (CB) were used in this study. Samples were melted at a high temperature (80°C) for 30 minutes before dilution with canola oil to erase any crystal history. A higher temperature (120°C) was used in the case of PO because of its high maximum melting temperature. Different amounts of commercial-grade canola oil were mixed with fats to achieve different SFC values. Dilutions were prepared for each fat in 2% increments. Samples were stored in a refrigerator (2°C).

Solid Fat Content

Samples were first melted at 80°C for 30 minutes (120°C for PO) to erase the crystal history and mixed thoroughly to ensure homogeneity. Glass NMR tubes (10-mm diameter) were filled with approximately 3 g of sample and were then kept in a refrigerator at 5°C for 24 hours. SFC (%) measurements were then taken using pNMR with a Bruker PC/20 series NMR Analyzer (Bruker, Milton, ON, Canada). Three tubes were prepared for each mixture and one measurement was carried out

on each mixture. The average value of these three replicates was used in further analysis.

Rheology

Rheological measurements at small deformations were performed using a controlled stress AR2000 Shear Dynamic Rheometer (TA Instruments, Mississauga, ON, Canada). Sandpaper (Grade-60 for wood) was glued to the upper and lower 2 cm plates using Krazy Glue to prevent slippage. The sample platform temperature was controlled using a Peltier element, allowing samples to be analyzed at the specified temperature (i.e., 5°C). Melted samples were poured into precooled cylindrical plastic molds of uniform diameter (20 mm) and thickness (3.2 mm), and were crystallized and stored at 5 °C for 24 hours. Compression was set to a standardized normal force of 10N for samples with an SFC greater than 30%, and contact for samples with an SFC smaller than 30%. This ensures good contact between the parallel plate attachment and the fat sample. The LVR for each sample was first determined by performing oscillatory stress sweeps from 0.65 to 1000 Pa for samples having low SFCs (less than 30%) and from 0.60 to 15,000 Pa for samples having high SFCs (more than 30%), at a constant frequency of 1 Hz. A total of 480 samples (80 dilutions $\times$ 6 replicates) were measured for each fat. The average value of these six replicates was used in further analysis.

Crystallization and Melting

The crystallization and melting behaviors of the three fats at different SFCs were studied by differential scanning calorimetry (DSC). Completely melted (120°C for 30 minutes) and well-mixed fat samples (8–12 mg) were pipetted into aluminum pans and hermetically sealed. An empty pan of known weight was used as the reference pan. Pans were then transferred to a Dupont Model 2910 DSC (TA Instruments, Mississauga, ON, Canada). Samples were heated to 80°C and equilibrated for 30 minutes to erase crystal memory, and then cooled to 5°C at 1°C/min and kept for 10 minutes (crystallization). Samples were then heated to 80 °C at 5 °C/min (melting). Fresh samples of the three diluted fat systems were measured using the same

temperature program. The onset of crystallization was estimated from the temperature value at which the exothermic peaks started to rise (i.e., deviate from the baseline), whereas melting temperatures were estimated from the endothermic peak maxima.

Polarized Light Microscopy

Fats were heated at 120°C for 30 minutes to erase crystal memory. All glassware was preheated to 80°C to avoid crystallization of the melted fats during sampling. A small droplet (approximately 10 μL) of the melted fat was placed on a microscope glass slide (25 mm × 75 mm × 1 mm). A coverslip (22 mm × 22 mm) was then placed parallel to the plane of the slide and centered on the drop of sample to ensure that the sample thickness was uniform (approximately 20 μm). The microscope slides and covers were purchased from Fisher Scientific (Fisher Finest, Pittsburgh, PA, USA.). Four slides of each sample were stored at 5°C in a refrigerator for 24 hours or less depending on the experiment. Samples were then observed under polarized light using an Olympus BH polarized light microscope (Olympus, Tokyo, Japan). A Linkam LTS 350 large heating and freezing stage operated by a Linkam TP93 temperature programmer (Linkam Scientific instruments, Ltd., Surrey, England) was used to maintain the temperature of the slides at 5°C during imaging. A continuous flow of liquid nitrogen (BOC gases, Guelph, Ontario) was used to cool the stage. Images were acquired with a Sony XC-75 CCD video camera (Sony Corporation, Japan) with the gain switch in the auto position. The images were digitized using a Scion LG-2 PCI frame grabber board and using Scion Image software (Scion Corporation, Fredrick, MD, USA). Image quality was enhanced by taking the average of 16 frames and by applying a background correction using the Scion software. Three images were captured from each of four slides at the same time-temperature combination.

Image Processing and Fractal Dimension Determination

Images were processed using Adobe Photoshop 6.0 (Adobe Systems Inc., San Jose, CA, USA). Original images (640 × 480

pixels) were first converted to 8-bit mode, with their contrast adjusted to the level at which the actual microstructures, seen under polarized light, were all represented. Images were then inverted and thresholded using the bilevel auto threshold command.

The mass fractal dimension (D) was estimated by two image analysis methods: box-counting and particle-counting. The box-counting method requires that the features to be analyzed appear white, hence the images were not inverted before thresholding. The box-counting analysis was performed using Benoit 1.3 (Truesoft International, St. Petersburg, FL, www.trusoft-international.com). The slope of the log-log plot of the number of filled boxes vs. the box side length corresponds to D_b. The D_b value was estimated using box side lengths in the range of 10–100 pixels. In the particle-counting method, the thresholded and inverted images were analyzed using a particle counting algorithm in which the number of reflections, or particles, within boxes of decreasing size (5% increments), are counted. The slope of the log-log plot of the number of particles vs. the box size is equal to D_f. The D_f was determined by averaging counts including and excluding particles that touch the perimeter of the region of interest (ROI) box.

Thick Sample Preparation

About 4–5 drops of the heated and well-mixed melt were transferred into a metal ring (height, 300 μm) placed on a glass slide and was then covered with a cover slip. Care was taken to avoid tilting the slide, and contact between the sample and the coverslip was minimized to allow the spatial distribution of microstructures in three dimensions without confinement effects. The sample was then kept in a refrigerator for 24 hours at 5°C, or directly monitored during crystallization inside the thermostatically controlled platform mentioned earlier. Images were acquired with a Retiga 1300 Cooled Mono 12-bit CCD video camera (Q-imaging, Corporation, Burnaby, BC, Canada) mounted on a motorized tube with two camera exits in a fully automated Leica DM RXA2 microscope (Leica

Microsystems Wetzlar GmbH, Germany) equipped with a motorized focus drive that travels 25 mm at 0.015-μm increments. It also has a motorized and interchangeable X–Y stage z-control and additional control for separate z-movement. The Leica CTR MIC electronics box contains the external power unit for the lamp and the motorized microscope units as well as the electronic cards for driving the motorized functions on the microscope. Image enhancement and acquisition were performed using Openlab 3.1 software (Quorum Technologies Inc., Guelph, ON, Canada, www.improvision.com) run on a Machintosh G4 computer.

Pattern Analysis

Break points in graphs were determined both visually and mechanically, using an iterative Pearson correlation coefficient maximization criterion. Linear regressions of putative linear regions within graphs were generated initially based on visual assessment (initial conditions). Points were then added to the extremes of the initially chosen linear regions. Improvements, or no change, in the correlation coefficient lead to the incorporation of those points into that linear region. A greater than 5% decrease in the correlation coefficient due to inclusion of adjacent points lead to the exclusion of those points from the linear region. This is how the different linear regions were identified.

RESULTS AND DISCUSSION

Figure 1 shows the SFC values as a function of dilution for the three fats. For all fats, increasing the amount of canola oil decreased the SFC in a linear fashion. In addition, the linear trend and the absolute SFC values were different between fats, mainly due to the large differences in composition. Worthy of notice is that the linear regression line for the different fats will not intercept the x-axis at a value of 1.0 (100% canola oil) when the SFC is zero. The x-intercepts for AMF, CB, and PO were 13.6, 8.2, and 4.3, respectively. This effect is probably due to the solubility of a certain amount of the fats into the

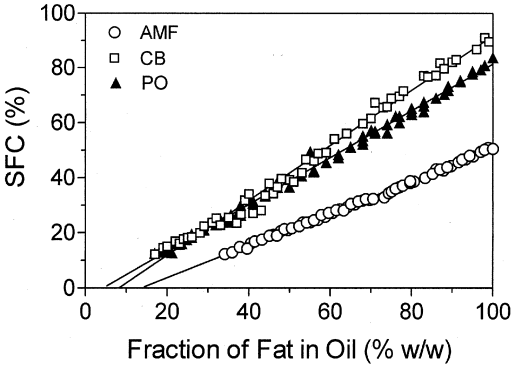

Figure 1 Relationship between the dilution of the fraction of fat diluted in canola oil and solid fat content (SFC) for anhydrous milk fat (AMF), palm oil (PO), and cocoa butter (CB). The crystallization was performed at 5°C for 24 hours.

canola oil, even under conditions of rapid cooling at high degrees of undercooling. This is an important point, since the rheological technique for fractal dimension determination requires that the diluent used (i.e., the canola oil at 5°C in our case) only dilute, and not dissolve, solid network material. This solubility could have an effect on the rheological determination of the fractal dimension of a fat crystal network, and constitutes a limitation of this method. This effect is, however, system-dependent.

Fat Crystal Network as a Particle Gel?

Figure 2 shows plots of the shear storage modulus (G′) vs. SFC for AMF. The relationship of G′ to SFC is a nonlinear, power–law type relationship, similar to that of a colloidal gel. This power–law relationship can be exploited to obtain structural information of the fat crystal networks, such as the spatial distribution of mass (mass fractal dimension). Moreover, Figure 3 shows the fat crystal network in cocoa butter as clusters of crystallites, quite similar in nature to fractal colloidal aggregates described in the literature [17–22]. These samples were allowed to crystallize freely on a glass slide without a

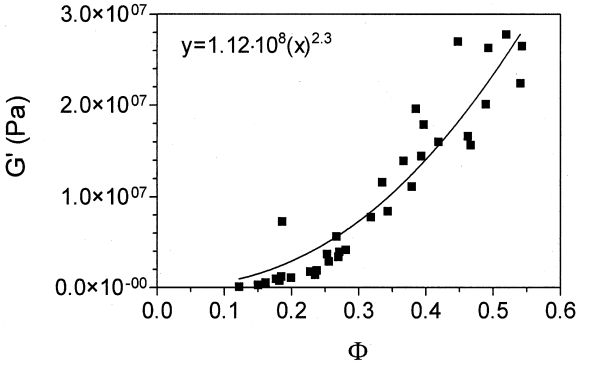

Figure 2 Power–law relationship between the storage modulus (G′) and the solids' volume fraction (Φ = SFC/100) for cocoa butter in the SFC range (12,40%).

coverslip so that the structure of the fat crystal network could be observed without confinement effects. The micrographs show that CB formed clusters of crystallites, which increased in size and number as a function of time, to the point where the clusters touch their nearest neighbors. Further deposition of solids will only coarsen the network without affecting cluster size. Our observations suggested that, on crystallization, these fats formed a network of polycrystalline crystal clusters, similar in nature to that of colloidal gels.

Rheology

To estimate the mass fractal dimension (D) of fat crystal networks, it was necessary to determine the storage modulus at varying SFCs. Small deformation rheological tests were performed to obtain the shear storage modulus (G′) of the blends in the LVR. The log-log plot of G′ versus Φ (SFC/100) yielded a straight line with slope (μ). This slope was used to estimate D. This mass fractal dimension is for an object embedded in 3-dimensional Euclidean space. The rheological results of AMF, PO, and CB at different SFC values are shown in Figures 4–6, respectively. Anhydrous milk fat and PO displayed three different linear regions, yet only two regions were identi-

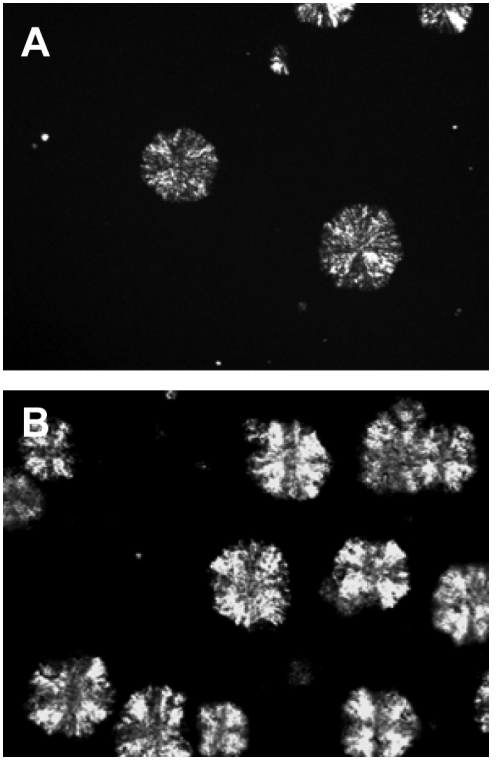

Figure 3 Polarized light micrographs of CB thick samples (20% SFC) crystallized at 5°C for (*A*) 1 hour, (*B*) 3 hours.

fied in CB. These regions indicated different mechanical responses in the same material depending on the solids' concentration. The existence of these regions could be interpreted as the fat crystal network in the weak-, intermediate-, and strong-link regimes, in order of decreasing SFC. To test the above hypothesis, the dependence of the stress at the limit of linearity on Φ was studied. The stress at the limit of linearity (σ_o) was estimated from plots of the storage modulus (G′) to the applied oscillatory stress. σ_o was estimated as the stress at which the storage modulus (G′), as well as the loss modulus (G″), started to deviate from a constant value. The σ_o determined in our studies always increased with increases in Φ for

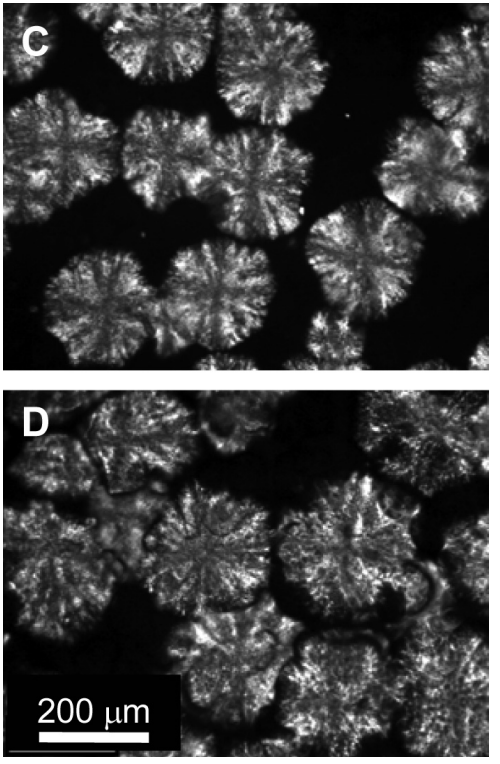

Figure 3 (Continued) (*C*) 8 hours, and (*D*) 20 hours.

the three fats (Figure 7). This suggested that the three fat systems were in the weak-link regime in the entire SFC range studied. Accordingly, the fractal dimensions assuming the weak-link regime were calculated for each fat, as shown in Table 1. The values obtained assuming the weak-link regime were quite reasonable and comparable to previously reported values in our laboratory [10]. In contrast, calculation of D assuming a strong-link behavior yielded unreasonable estimates (Table 1).

Determinations of the stress at the limit of linearity indicated that all fats were in the weak-link regime. Shih et al. [18] defined the strong-link regime at particle concentrations below 10%, where the strain at the limit of linearity (γ_o) in-

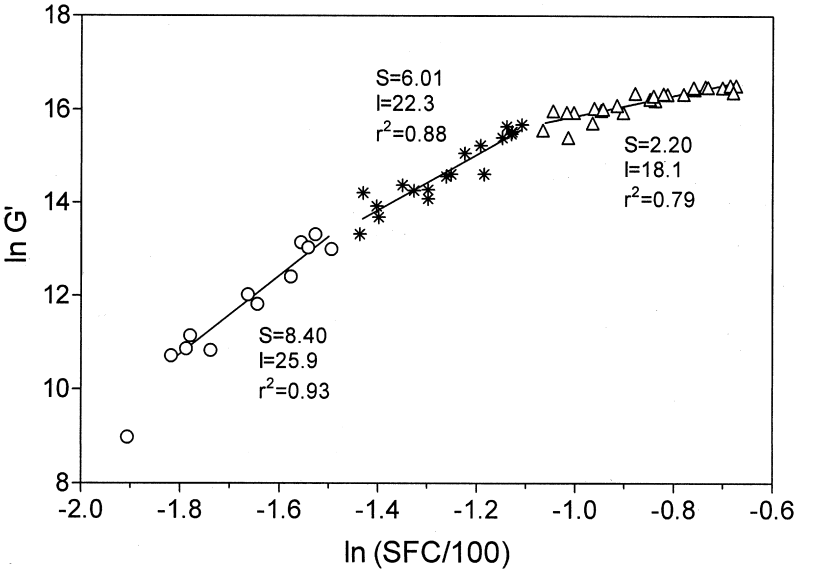

Figure 4 Relationship between the storage modulus (G′) of and the solids' volume fraction (Φ = SFC/100) for anhydrous milk fat. S = slope, I = y-intercept, r^2 = Pearson correlation coefficient of the linear regression lines.

creased as a function of Φ. In our study, rheological tests were difficult to perform at these low SFC levels because the fats became too soft to be analyzed. The lowest SFC that could be studied was 12%.

Scaling Behavior of σ_o with Solid Fat Content

Figure 7 shows changes in σ_o as a function of Φ for blends of milk fat (Figure 7*A*), palm oil (Figure 7*B*), and cocoa butter (Figure 7*C*). The fractal dimensions of the three fat crystal networks were determined from the slope of the log-log plot of σ_o vs. Φ, assuming a weak-link rheological regime [D = 3-(slope)$^{-1}$], and are reported in Table 1. The fractal dimensions calculated from the storage modulus (i.e., G′ vs. Φ) and the stress at the limit of linearity data (i.e., σ_o vs. Φ) were comparable (Table 1). Three different regions were identified for AMF

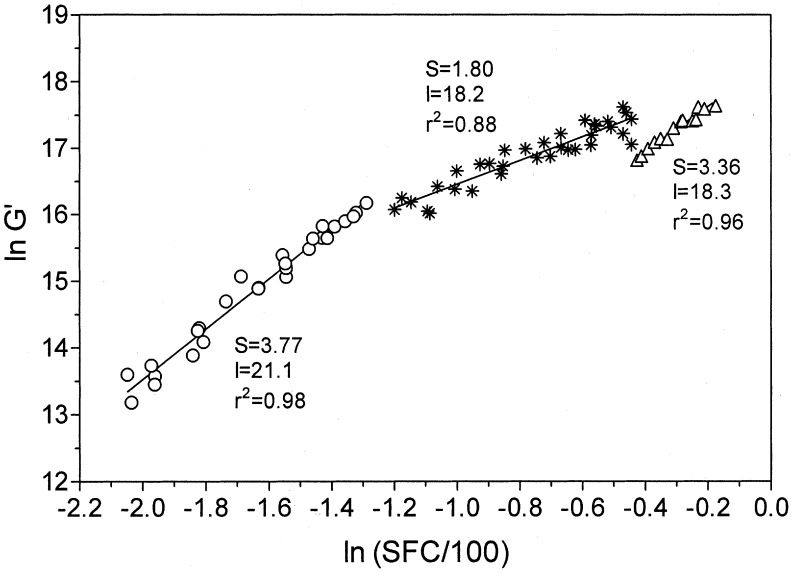

Figure 5 Relationship between the storage modulus (G′) of and the solids' volume fraction (Φ = SFC/100) for palm oil. S = slope, I = y-intercept, r^2 = Pearson correlation coefficient of the linear regression lines.

(Figure 7*A*) and two regions in CB (Figure 7*C*), in agreement with the G′–Φ results. For PO, however, no breaks in the log-log plot were observed. This points out to system-specific effects on G′ and σ_o.

Crystallization and Melting Behavior

Figure 8 shows plots at the onset of crystallization (T_c) as a function of SFC for AMF, PO, and CB. Increasing the canola oil mass fraction, or decreasing the SFC, caused a gradual decrease in T_c as expected from colligative property arguments (freezing point depression). For example, the T_c of AMF at high SFC (52%) decreased from 17.5 °C to 16.0 °C (35% SFC) and to 9.0 °C (16% SFC), as shown in Figure 8*A*. As can be appreciated, the crystallization behavior of PO (Figure 8*B*) and CB (Figure 8*C*) were also similar. The break points, identified by

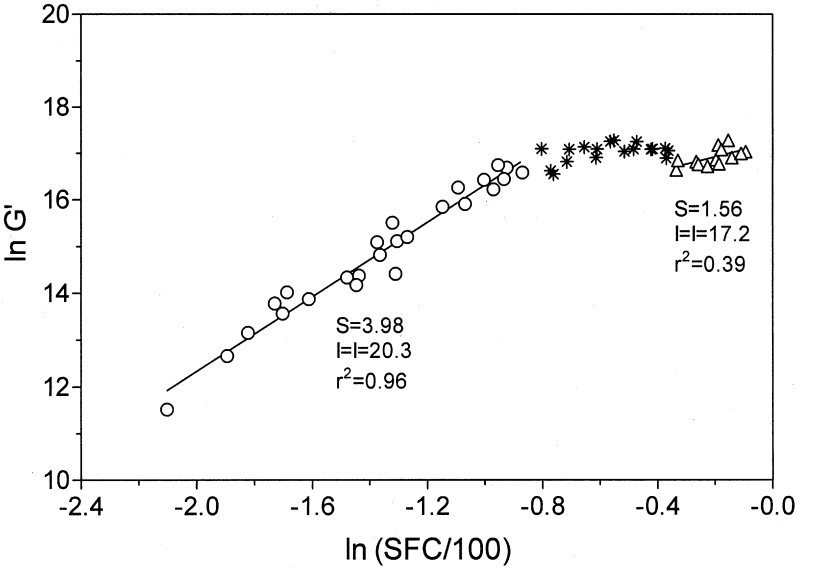

Figure 6 Relationship between the storage modulus (G′) of and the solids' volume fraction (Φ = SFC/100) for cocoa butter. S = slope, I = y-intercept, r^2 = Pearson correlation coefficient of the linear regression lines.

arrows in Figure 8, as well as the span of the linear regions were very similar (not identical) to those identified in G′ vs. SFC plots. This indicated a possible relationship between the mechanical properties of the material and the kinetics of crystallization.

Peak melting temperatures also decreased with decreasing SFC for the three fats (Figure 9). Using this data, the solubility of fat crystals in canola oil was studied using the Hildebrand model [27,28]:

$$\log_{10} x = \frac{\Delta H}{R}\left(\frac{1}{T_m^{HMF}} - \frac{1}{T_m}\right) \quad (6)$$

where x is the mole fraction of solid fat (x = SFC/100 in our case) and T_m is the peak melting temperature of the mixture, and T_m^{HMF} corresponds to the melting temperature of the

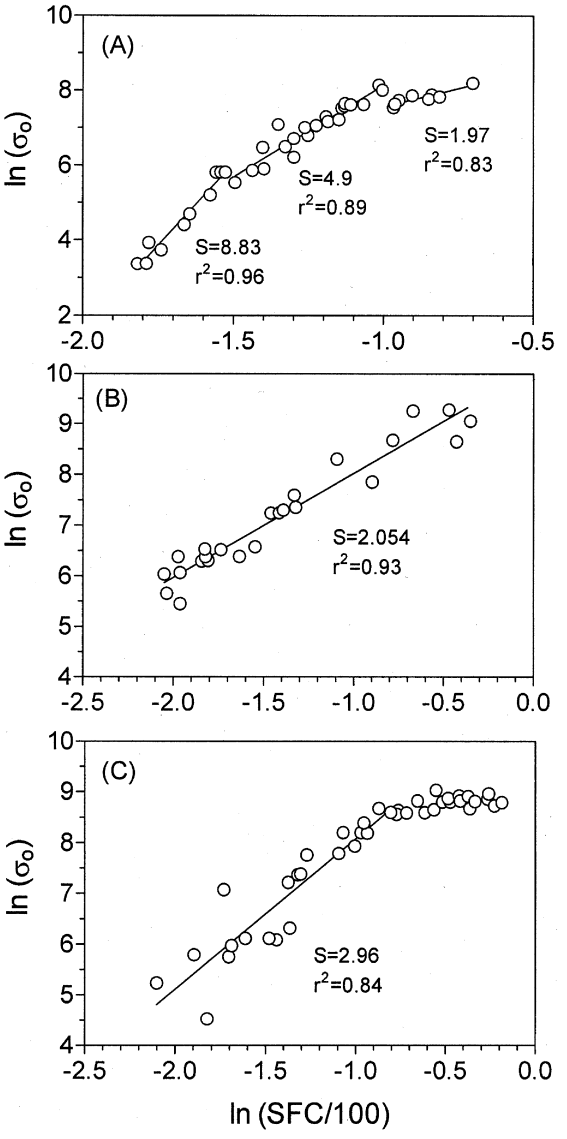

Figure 7 Relationship between the stress at the limit of linearity (σ_o) and the solids' volume fraction (Φ = SFC/100) for blends of (*A*) anhydrous milk fat, (*B*) palm oil, and (*C*) cocoa butter.

Table 1 Fractal Dimension (D) for Anhydrous Milk Fat (AMF), Palm Oil (PO), and Cocoa Butter (CB) at Low, Intermediate, and High Solid Fat Contents (SFCs) Determined from Rheologic Measurements

	SFC (%)	D_{WLR}	D_{SLR}	$D\sigma_o$
AMF	37–51	2.54	1.18	2.49
	21–35	2.83	2.33	2.79
	12–20	2.88	2.52	2.89
PO	64–78	2.70	1.81	
	31–59	2.44	0.77	2.51
	16–26	2.73	1.94	2.51
CB	72–90	2.36	0.43	
	12–47	2.75	1.99	2.66

D_{WLR}, Fractal dimension determined assuming the weak-link regime.
D_{SLR}, Fractal dimension determined assuming the strong-link regime.
$D\sigma_O$, Fractal dimension determined from the stress at the limit of linearity.

highest-melting fraction (HMF) in the mixture. A straight line in a $\log_{10}$x vs $1/T_m$ plot is suggestive of ideal solubility of the fat crystals in canola oil. Figures 9D–F show plots of $\log_{10}$ x vs. $1/T_m$ for AMF, PO, and CB, respectively. Three linear regions were identified for AMF (Figure 9*D*) and PO (Figure 9*E*), whereas only two regions were identified for CB (Figure 9*F*). This was in agreement with the patterns observed in the T_c-SFC plots (Figure 8). The heats of fusion (ΔH) determined from the slopes were found to increase as a function of increasing dilution. ΔH increased from 31.2, 64.8, and 38.7 kJ/mol to 51.8, 158 and 66.3 kJ/mol for AMF, PO, and CB, respectively. The increase in ΔH as a function of increasing dilution is indicative of the formation of less mixed (more pure or homogeneous) crystals. The formation of more pure crystals at higher dilutions is mainly due to decreases in diffusional limitations (due to a lower melt viscosity), as well as decreases in the rates of nucleation and growth (due to decreases in the supersaturation of the melt). These two factors—greater molecular mobility and a slower crystallization process—allow for the forma-

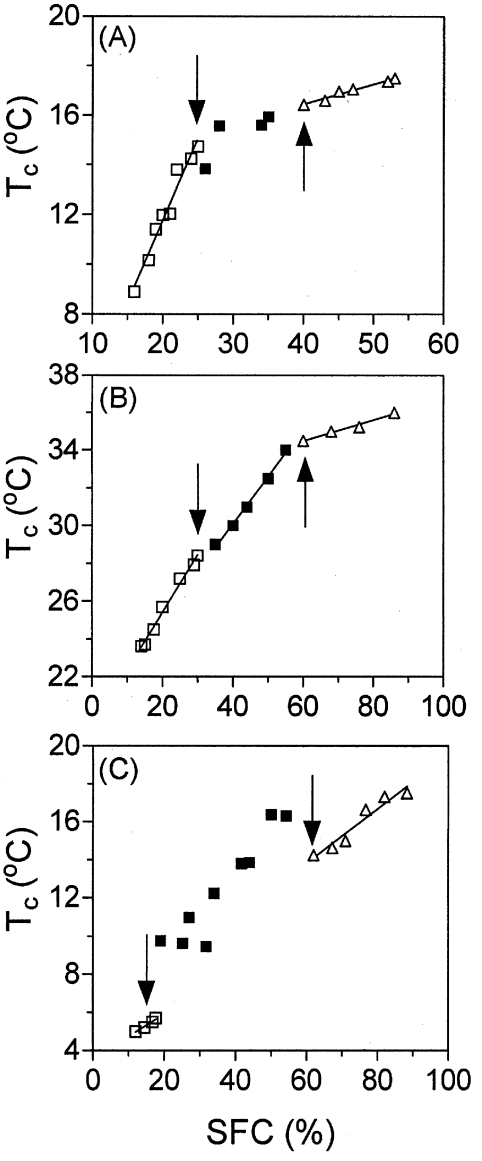

Figure 8 Changes in the crystallization onset temperature (T_c) as a function of solid fat content (SFC) for (*A*) anhydrous milk fat (AMF), (*B*) palm oil (PO), and (*C*) cocoa butter (CB). The *arrows* indicate the breakpoints.

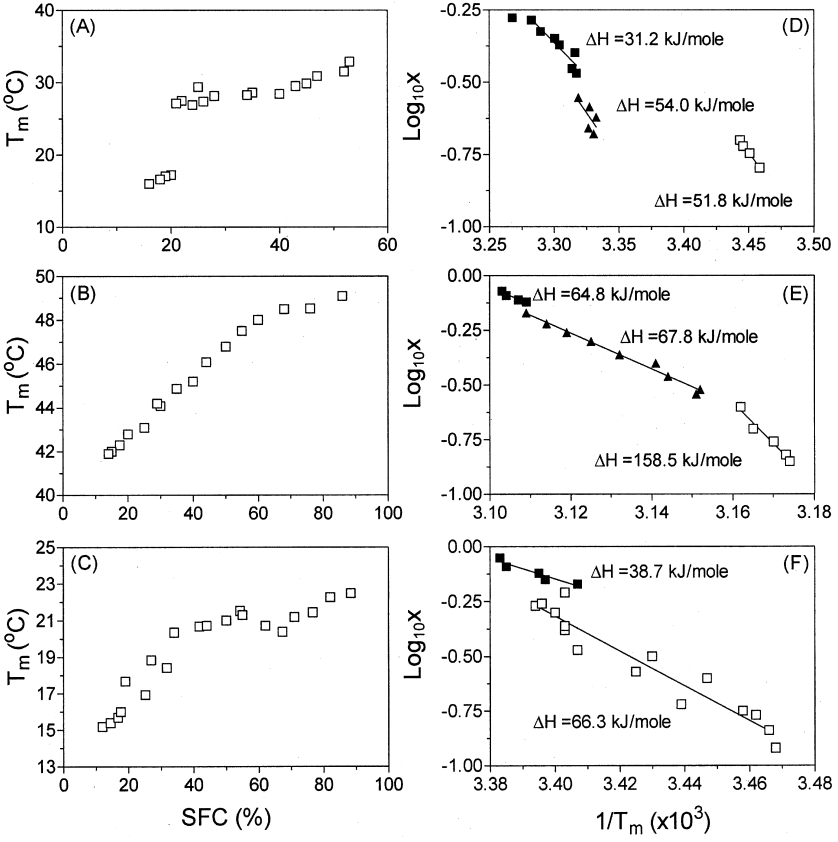

Figure 9 Changes in the peak melting temperature (T_m) as a function of solid fat content (SFC) for (*A*) anhydrous milk fat (AMF), (*B*) palm oil (PO), and (*C*) cocoa butter (CB), and Hildebrand plots for (*D*) anhydrous milk fat (AMF), (*E*) palm oil (PO), and (*F*) cocoa butter (CB).

tion of more pure crystals at higher dilutions. The different linear regions observed in Figure 9 are indicative of the formation of different polymorphic forms, different solid solutions [29], imperfect crystals [30], and/or combinations [31] thereof, depending on the concentration of crystallizing material.

Based on these results, we postulate that different crystal types (polymorphs and/or solid phases) are formed depending

on solids' content. These changes in solution behavior were probably responsible for the changes observed in the crystallization behavior of the material, which eventually translated into different mechanical properties. It would stand to reason, therefore, that the microstructure of the material would also be affected by changes in solution behavior and crystallization kinetics.

Polarized Light Microscopy

The microstructure of the fats was observed using polarized light microscopy. Figure 10 shows polarized light micrographs of AMF taken at different magnifications. As can be appreciated, relatively large clusters were observed at 12% SFC (Figure 10*A,B*) and by increasing the SFC to 19%, the clusters decreased in size and increased in number (Figure 10*C,D*). The SFC of the samples in Figures 10*A–D* corresponds to the low SFC region (12–20%). In the intermediate SFC (21–35%) and high SFC ranges (above 37%), only small crystallites were evident (Figure 10*E–H*). Figure 11 shows micrographs of the PO samples. Large clusters were observed in the low SFC range (16–26%) (Figure 11*A,B*), while combinations of small and a few large clusters were observed in the intermediate SFC region (31–59%) (Figure 11*C,D*). In the highest SFC range (64–78%), samples showed combinations of large clusters and smaller crystallites filling the spaces between clusters (Figure 11*E,F*). Although the large clusters grown at low SFCs (Figure 11*A,B*) were similar in morphology to those at higher SFCs (Figure 11*C–F*), small crystallites were not observed at low SFCs.

For CB at low SFCs (19%), large and irregular-shaped spherulites were observed (Figure 12*A*). By increasing the SFC to 25%, spherulites increased in size, maintaining the same shape (Figure 12*B*). Between 34 and 42% SFC, however, spherulites were much more regular (Figure 12*C,D*). By increasing the SFC to 54%, the clusters became more spherical and displayed a fine, granular texture (Figures 12*E*), quite different from the spherulites observed at low SFCs (Figures 12*A–D*). Above 54%, only a fine mass of crystallites was observed (Figure 12*F–F*).

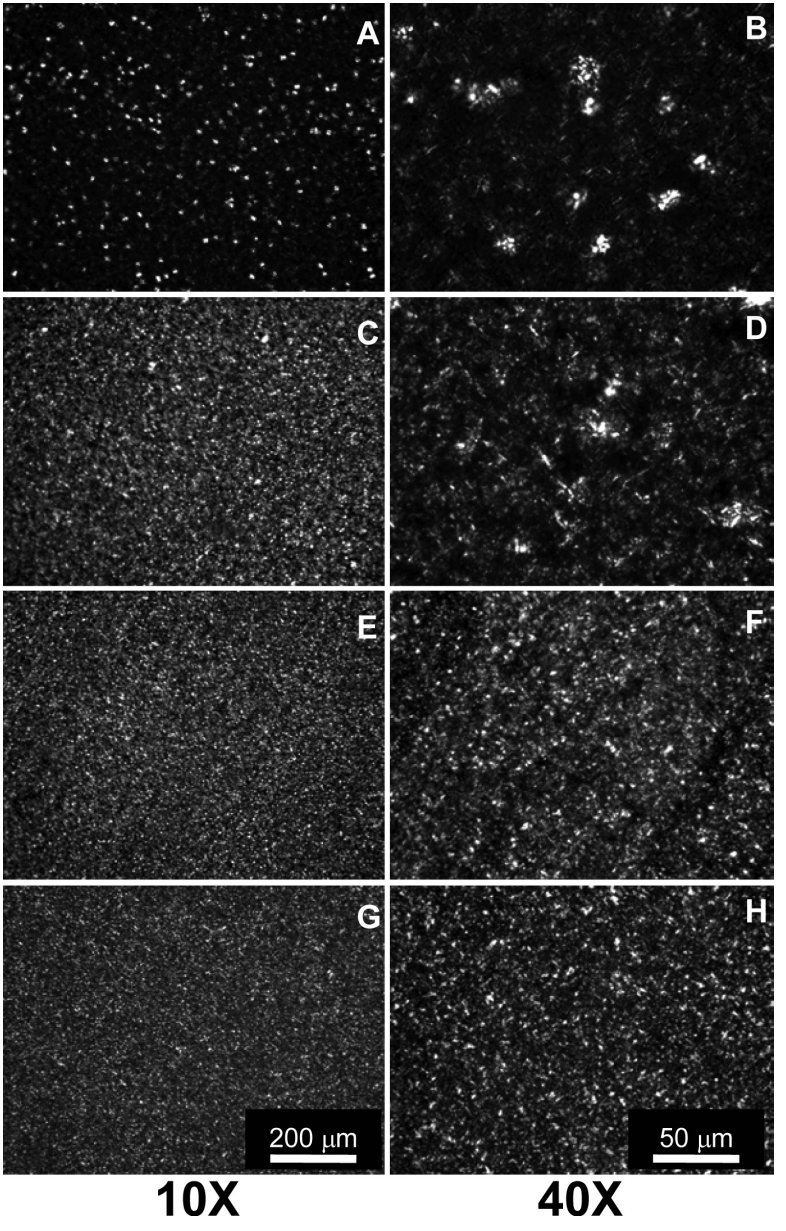

Figure 10 Polarized light micrographs of anhydrous milk fat (AMF) crystallized in 20 μm films at 5°C for 24 hours. The SFC values are (*A,B*) 12%, (*C,D*) 19%, (*E,F*) 35%, and (*G,H*) 51%.

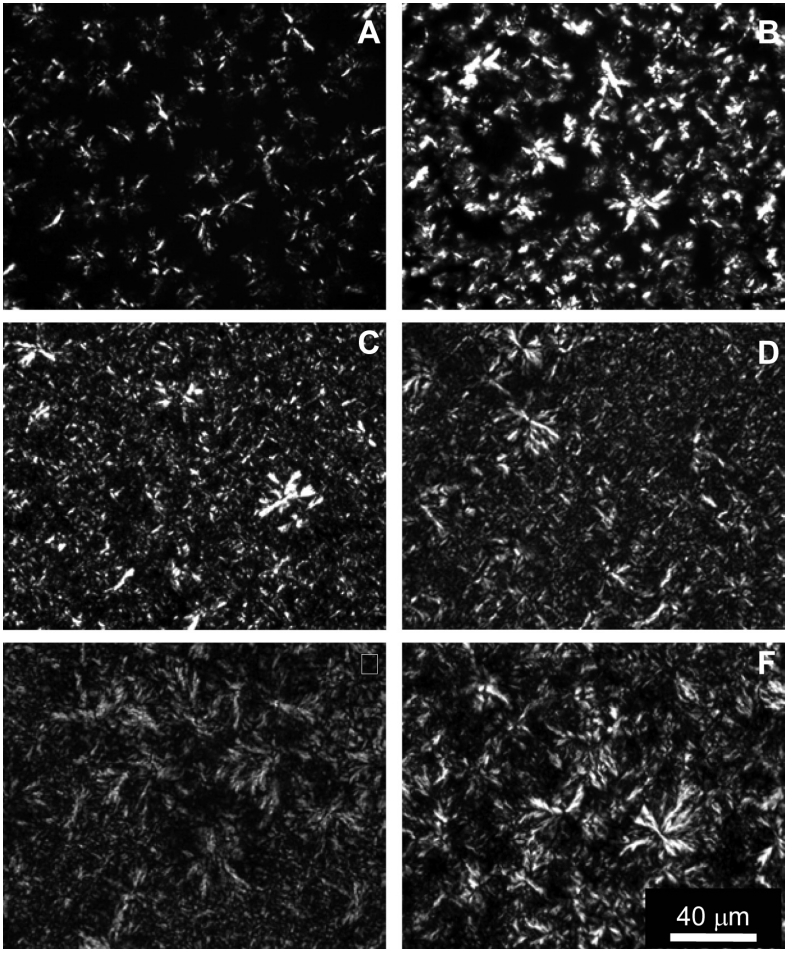

Figure 11 Polarized light micrographs of palm oil (PO) crystallized in 20 μm films at 5°C for 24 hours. The SFC values are (*A*) 16%, (*B*) 17.5%, (*C*) 42.5%, (*D*) 55%, (*E*) 70%, and (*F*) 75%.

The effects of varying SFC on cluster size were also monitored in freely crystallized (nonconfined) CB samples at low and high SFCs. At low SFC (20%), a few large clusters (200 μm) were observed (Figure 13*A*) while more numerous small clusters (50–60 μm) were observed at high SFC values (70%), as shown in Figure 13*B*.

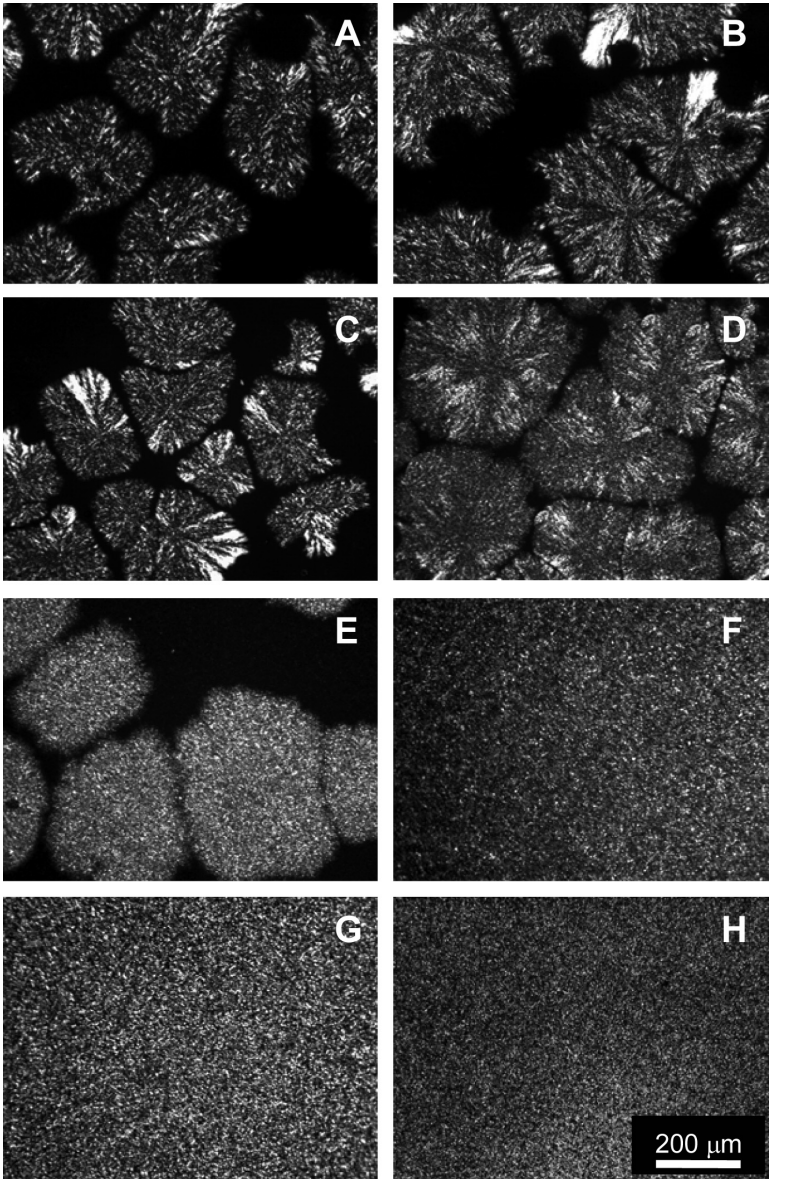

Figure 12 Polarized light micrographs of cocoa butter (CB) crystallized in 20 μm films at 5°C for 24 hours. The SFC values are (*A*) 19%, (*B*) 25%, (*C*) 34%, (*D*) 42%, (*E*) 54%, (*F*) 60%, (*G*) 65%, and (*H*) 85%.

In general, at higher dilutions (lower SFCs), larger clusters were observed. This effect is in agreement with the observed increases in the fractal dimension of the fat crystal networks at lower SFCs (Table 1). Fractal cluster size (ξ) scales with the solids' volume fraction (Φ) as:

$$\xi \sim \Phi^{\frac{1}{D-d}} \tag{7}$$

where D is the mass fractal dimension and d is the Euclidean dimensionality of the embedding space. Thus, a decrease in SFC and an increase in the fractal dimension would lead to an increase in cluster size. The change in cluster size occurs in a narrow range of SFCs, thus pointing to the fractal dimension as being an important factor in determining cluster size. In the weak-link regime, the fractal dimension simply defines the cluster size, and cluster size is the only factor influencing the mechanical response of the material because the cluster itself does not deform.

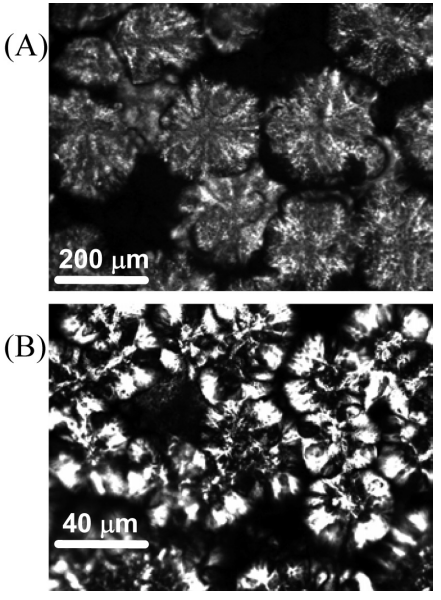

Figure 13 Polarized light micrographs of cocoa butter (CB) thick samples (*A*) low solid fat content (SFC) (20%) and (*B*) high SFC (70%).

Image Analysis

Figure 14 shows changes in the box-counting fractal dimension (D_b) for the spatial distribution of mass within the fat crystal networks as a function of SFC using images acquired at low (10× objective) and high magnifications (40× objective). The overall results indicated that D_b increased with increasing SFC, reaching a plateau at high SFC values. Analysis of the images of AMF taken at both magnifications (Figure 14*A*) indicated no significant increase in D_b with increasing SFC from the intermediate SFC region (21–35%) to the high SFC region of (73–51%). In addition, the SFC value at which the D_b became constant was similar to the break point at 22% SFC observed in the T_c-SFC curve (Figure 8*A*). Similar behavior was also shown for PO (Figure 14*B*), with a breakpoint occurring at 62% SFC, similar to the high SFC breakpoint shown in Figure 8*B*. In the case of CB (Figure 14*C*), D_b increased gradually as a function of SFC similarly at both magnifications. Above 67% SFC, the curve became flat, in agreement with the high SFC breakpoint shown in Figure 8*C*. These results agreed well with the CB images (Figure 12), which showed diversity in microstructures at different SFC. Accordingly, the lower D_b values corresponded to larger microstructures at low SFC, whereas samples having a large number of smaller clusters at higher SFC characterized by higher D_b. It is worth mentioning that fractal dimensions did not vary above a critical SFCs because fat crystals filled space homogeneously on the microscope slide. Nevertheless, the similarity between the breakpoints in Figure 14 (D_b) and those in Figure 8 (T_c) indicates sensitivity of the box-counting fractal dimension to changes in crystallization kinetics and polymorphism. Previous work from our group [11,24] has shown that D_b is strongly correlated to crystallization kinetics and polymorphism in CB and in mixture of milk fat fractions and CB.

In the particle-counting method, D_f increased as a function of SFC for PO, yet no clear trends were observed for AMF and CB and, thus, an average D_f value was determined for AMF (1.93 ± 0.02) and CB (1.90 ± 0.08). This points to a limitation of this method when the material in question fills

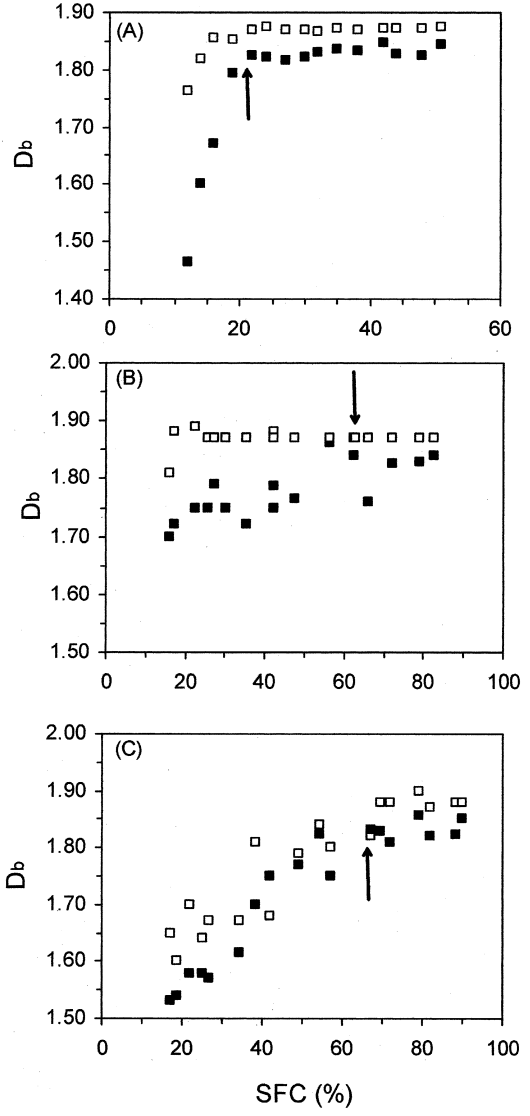

Figure 14 Changes in the box-counting fractal dimension (D_b) as a function of SFC for (*A*) anhydrous milk fat (AMF), (*B*) palm oil (PO), and (*C*) cocoa butter (CB). The *arrows* indicate the breakpoints. The *open squares*indicate the analysis of images acquired using the 10× objective, while the *filled squares* indicate the analysis of images acquired using the 40× objective.

space homogeneously and fully, particularly at high solids' contents. Figure 15 shows the plot of SFC vs. D_f for PO. As can be seen in Figure 15, a significant linear trend extended up to 45% SFC then there is a plateau, after which D_f increased again.

The usefulness of the fractal dimension in explaining differences in elasticity between fats can be easily demonstrated. Work from our group [14] has shown that the elastic modulus of a fat is related to the solids' content (Φ) and the structure of its fat crystal network by:

$$G' = \lambda \Phi^{\mu} \tag{8}$$

where λ and μ are constants related to structural characteristics of the network. The usefulness of this model becomes obvious when trying to model changes in mechanical properties between fats at the same SFC. For example, the G′ at an SFC of 27.2% ($\ln(SFC/100) = -1.3$) differs between fats (Figs. 4–6). The lnG′ for AMF, PO, and CB are, respectively, 14.4, 16.2, and 15.3, while the rheologically determined fractal dimensions are 2.83, 2.73, and 2.75, respectively (Table 1). Thus, a

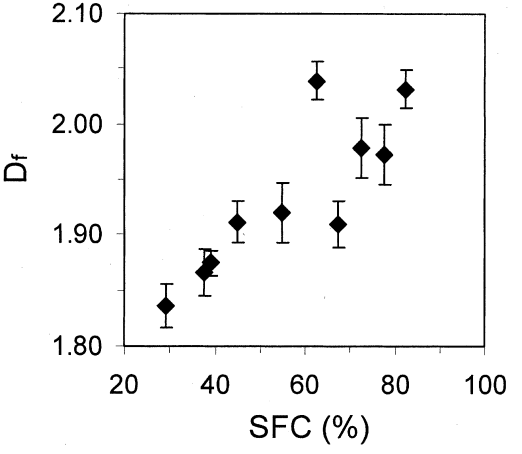

Figure 15 Changes in the fractal dimension determined by the particle-counting method (D_f) as a function of solid fat content (SFC) for palm oil.

decrease in the fractal dimension of a system, at equal SFC leads to an increase in the G′ of the system. Changes in the G′ across systems can be quantified by:

$$\ln G'_1 - \ln G'_2 = \ln \lambda_1 - \ln \lambda_2 + (\mu_1 - \mu_2) \ln (SFC/100) \quad (9)$$

A quick calculation using the parameters listed in Figures 4–6 (μ = S and $\ln\lambda$ = I) will quickly demonstrate how changes in G′ can be explained in part by changes in the fractal dimension of the fat crystal network. Certainly, changes in crystallite size and morphology will also strongly influence mechanical properties.

We have shown that changing blend composition, or the SFC of three fats, affected the mechanical properties in terms of the elastic modulus and the stress at the limit of linearity, and this change is due, in part, to changes in the fractal dimension of the network. Although fats showed different mechanical responses as a function of SFC, they all were in the weak-link rheologic regime. The relationship between SFC and either the G′ or σ_o offered two ways of determining the mass fractal dimension of a fat crystal network. These results lend strong support to the application of fractal scaling theories to colloidal networks of fat crystals. Network structure was strongly affected by varying the SFC, which was accompanied by alterations in solution behavior and crystallization kinetics of the material. Therefore, changes in microstructure, induced by changes in crystal-melt solution behavior and crystallization kinetics, resulted in different mechanical properties of the fats.

As a final remark on the results of the current work, it is noteworthy that, considering the different levels of structures, starting from the early stages of crystallization (nanometer/molecular scale) to macromolecular network formation (micrometer/mesoscale) provides considerable information, which may help link fat crystal network microstructure to mechanical properties. Crystallization conditions and chemical composition can then be manipulated to control final network structure and, consequently, the macroscopic rheologic properties of fats.

REFERENCES

1. Heertje I. 1993. Microstructural studies in fat research. *Food Struct* 12:77–94.
2. Juriaanse AC, Heertje I. 1988. Microstructure of shortenings, margarine and butter- A review. *Food Microstruct* 7:181–188.
3. Narine SS, Marangoni AG. Relating structure of fat crystal networks to mechanical properties: A review. *Food Res. Int. 32: 227–248.*
4. Wright AJ, Scanlon MG, Hartel RW, Marangoni AG. 2001. Rheological properties of milkfat and butter. *J Food Sci* 66: 1056–1071.
5. Marangoni AG. 2002. The nature of fractality in fat crystal networks. *Trends in Food Science and Technology* 13:37–47.
6. Van den Tempel M. 1961. Mechanical properties of plastic disperse systems at very small deformations. *J Colloid Sci* 16: 284–296.
7. Van den Tempel M. "Rheology of Concentrated Suspensions." Journal of Colloid and Interface Sci 71:18–20.
8. Vreeker R, Hoekstra LL, den Boer DC, Agterof WGM. 1992b. The fractal nature of fat crystal networks. *Colloids and Surfaces* 65:185–189.
9. Marangoni AG, Rousseau D. 1996. Is plastic fat rheology governed by the fractal nature of the fat crystal network? *J Am Oil Chem Soc* 73:991–994.
10. Narine SS, Marangoni AG. 1999a. Fractal nature of fat crystal networks. *Phys Rev E* 59:1908–1920.
11. Narine SS, Marangoni AG. 2002. Structure and mechanical properties of fat crystal networks. *Advances in Food and Nutrition Research* 44:33–145.
12. Marangoni AG. 2000. Elasticity of high-volume fraction fractal aggregate networks: A thermodynamic approach. *Phys Rev B* 62:13951–13955.
13. Narine SS, Marangoni AG. 1999. Mechanical and structural model of fractal networks of fat crystals at low deformations. *Phys Rev E* 60:6991–7000.

14. Marangoni AG, Rogers MA. Structural basis for the yield stress in plastic disperse systems. Applied Physics Letters 2003; 82: 3239–3241.

15. Kantor Y, Webman I. (1984). "Elastic Properties of Random Percolating Systems." *Phys Rev Lett* 52(21):1891–1894.

16. Brown WD. The Structure and Physical Properties of Flocculating Colloids, University of Cambridge.

17. Bremer LGB, van Vliet et al. (1989). "Theoretical and experimental study of the fractal nature of the structure of casien gels." *J Chem Soc Faraday Trans* 85:3359–3372.

18. Shih WH, Shih WY, et al. (1990). "Scaling behavior of the elastic properties of colloidal gels." *Phys Rev A* 42:4772–4779.

19. Sonntag RC, Russel WB. (1987). "Elastic properties of flocculated networks." *J Colloid Interface Sci* 116:485–489.

20. Buscall R, Mills PDA et al. (1988). "Scaling behaviour of the rheology of aggregate networks formed from colloidal particles." *J Chem Soc Faraday Trans* 84:4249–4260.

21. Hagiwara T, Kumagai H, et al. (1997). "Analysis of aggregate structure in food protein gels with the concept of fractal." *Biosci Biotech and Biochem* 61:1663–1667.

22. Wu H, Morbidelli M. (2001). 'A model relating structure of colloidal gels to their elastic properties.' in *Langmuir* 17: 1030–1036.

23. Wright AJ, Marangoni AG. The Effect of Minor Components on Milk Fat Microstructure and Mechanical Properties. J of Food Science 2003; 68:182–186.

24. Marangoni AG, McGauley SE. 2003. Relationship between crystallization behaviour and structure in cocoa butter. Crystal Growth & Design 3:95–108.

25. Marangoni AG, Narine SS. Identifying key structural indicators of mechanical strength in fractal networks of fat crystals. Food Res Int 2002; 35:957–969.

26. Litwinenko JW, Rojas AM, Greschenson LN, Marangoni AG. Relationship between crystallization behavior, microstructure and rheological properties in a palm oil-based shortening. J Am Oil Chem Soc 2002; 79:647–654.

27. Hildebrand JH, Scott RL. Regular solutions In: The solubility of nonelectrolytes. Prentice Hall. NJ: Englewood Cliffs, 1962: 1–40.

28. Timms RE. The solubility of milkfat, fully hardened milkfat and milk fat hard fractions in liquid oils. Australian J Dairy Technology 1978; 33:130–135.

29. Mulder H. 1953a. Melting and solidification of milk fat. *Neth Milk Dairy J* 7:149–174.

30. Sherbon JW. 1974. Crystallization and fractionation of milk fat. *Am Oil Chem Soc* 51:22–25.

31. Knoester M, de Bruijne P, and van den Tempel M. The solid-liquid equilibrium of binary mixtures of triglycerides with palmitic and stearic chains Chem Phys Lipids 9:309–319.

11

Comparison Between Image Analyses Methods for the Determination of the Fractal Dimension of Fat Crystal Networks

TAREK S. AWAD and ALEJANDRO G. MARANGONI

Department of Food Science
University of Guelph
Guelph, Ontario, Canada

INTRODUCTION

Fractal structures are created by agglomeration, or clustering, of small particles to form a larger object in a random, iterative fashion under some constraint [1–4]. In a similar fashion, fat crystal networks are built from clusters of polycrystalline particles (crystallites) that aggregate in a diffusionally limited,

fractal fashion [5,6]. With time, clusters continue to increase in size and number to the point where clusters touch their nearest neighbors. Eventually, the network develops into an amorphous three-dimensional space-filling structure. Fat crystal networks are statically self-similar, which means that the microstructure in a fat crystal network looks similar at different magnifications. All of these criteria indicate the fractal nature of fat crystal networks, which would thus have fractional dimensions.

Fractal geometry has recently been utilized for characterizing the structure of materials such as whey protein gels [7–10], for predicting optical responses of colloid-adsorbate films [11], for measuring the degree of dispersion in composite two-dimensional arrays [12], for depicting the irregular nature of solid absorbents like zeolites [13,14], and for describing food surfaces [15]. In fat systems, fractal mathematics have been used to relate the elastic properties of fat crystal networks to the spatial distribution of the network mass [16–19] and to link crystallization kinetics and phase behavior to microstructure [20,21].

Polarized light microscopy (PLM) is the most commonly used technique for the study of fat-structured materials, and relies on the optical properties of materials, particularly their birefringence. Depending on the crystal system, hexagonal crystals have two indices of refraction (birefringent), while orthorhombic, triclinic, or monoclinic crystals have three indices of refraction (trirefringent) [22]. Birefringence arises due to splitting of light into two components of different refractive indices, which travel at different speeds through the material. Fats are among those biological materials whose crystals have a well-defined anisotropic molecular structure. The ability of PLM to detect changes during the formation of fat crystals is mainly due to the fact that, under polarized light, only crystallized materials will appear white. With the aid of image analysis techniques, PLM has been successfully utilized to evaluate the mass-spatial distribution (fractal dimension) of fat crystal networks grown as thin films [20,21,23,24].

Particle counting and box counting are two methods that have been used to determine the fractal dimension of fat crystal networks [6,21,23–25]. These methods require that the analyzed systems are fractal in nature and, accordingly, microstructural mass should be related, through a power–law, to a length scale.

In this work we describe and apply the methods used for evaluating the mass fractal dimension of fat crystal networks. We will briefly introduce the fundamentals of these methods below and how they can be used for the determination of the fractal dimension of fat crystal networks.

PRELIMINARY CONSIDERATIONS

Fourier Analysis and Fractality

Fourier analysis is a method that can be also be applied to the analysis of polarized light micrographs of fats. The method does not require inversion or thresholding prior to analysis, but it does require high resolution square images [26]. Figure 1 shows a power spectrum, a plot of log(magnitude^2) vs. the log (frequency), for cocoa butter (CB), palm oil (PO), and anhydrous milk fat (AMF). As can be observed, two slopes were observed for each fat. These results are consistent with our view that a fat crystal network is composed of polycrystalline particles arranged in a fractal fashion within clusters, which themselves pack in a Euclidean (homogeneous), nonfractal fashion [6]. A power-spectrum slope of -1 is indicative of a structure created by Brownian effects (fractal structure), while a slope of -2 is indicative of a regular Euclidean pattern [29]. A slope of 0 corresponds to white noise, as shown for PO (Figure 1*B*) and AMF (Figure 1*C*). The high slope obtained for AMF (-3.24) on the right side of the plot (Figure 1*C*) can be explained by the lack of resolution of 8-bit images, which reduces the amplitude of the power spectrum at the high frequency end, and increases the slope [26]. Although fractal signatures were detected for the different samples, the method

was not sensitive to differences between samples, probably due to the relatively low quality of 8-bit images in this type of analysis.

Particle-Counting Method

Based on theories developed for colloidal gels, Narine and Marangoni [5] developed a microscopy technique for the determination of the fractal dimension of a fat crystal network. The microstructural mass (M) of an object is related to its radius (R) in a power–law fashion:

$$M \sim R^D \tag{1}$$

where the term D refers to the mass fractal dimension: a number that expresses the spatial distribution of the network mass. The total mass M is equal to the number of particles (N) multiplied by the particle mass (m). Assuming that particles are of equal mass,

$$M = N \cdot m \tag{2}$$

Therefore, the number of particles scale with the radius as:

$$N \sim R^D \tag{3}$$

This relationship forms the basis of the particle-counting method. A particle-counting algorithm was designed so that the number of crystal reflections or "particles" is counted within boxes of decreasing size (5% increments) placed over a properly thresholded and inverted image. The fractal dimension (D_f) can be obtained by plotting the logarithm of the box side length (L) on the horizontal axis vs. the logarithm of N on the vertical axis. If the set is fractal, the log-log plot will follow a straight line whose slope is equal to D_f.

Box-Counting Method

The box-counting is defined as the exponent D_b in the relationship:

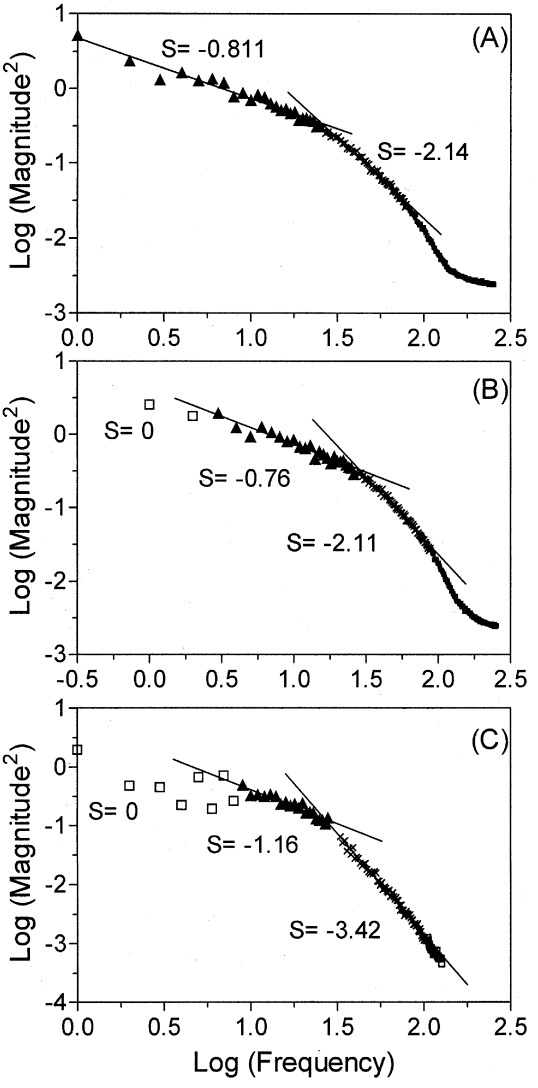

Figure 1 Power spectrum plots of log (magnitude^2) vs. log (frequency) determined by Fourier analysis for images of (**A**) cocoa butter (CB), (**B**) palm oil (PO), and (**C**) anhydrous milk fat (AMF).

$$N(d) \approx \frac{1}{d^{D_b}} \quad (4)$$

Where N(d) is the number of boxes of linear size d necessary to cover a data set of points distributed in a two-dimensional plane. The basis of this method is that, for objects that are Euclidean, Equation (4) defines their dimension.

The box-counting method requires that the features to be analyzed appear white and, hence, the images should not be inverted before thresholding. The box-counting analysis is performed using Benoit 1.3 (Truesoft International, St. Petersburg, FL, www.trusoft.netmegs.com). The routine is used to count the number of boxes of a decreasing size that are required to cover projected microstructural features. If the set is indeed fractal, a logarithmic plot of the number of occupied boxes (N) vs. the box size (d) will yield a straight line with a slope equal to $-D_b$.

MATERIALS AND METHODS

Materials

Samples of AMF, PO, and CB were diluted with canola oil to achieve different solids' volume fractions [19]. Milkfat [27] plus diacyglycerols (MF-DAG), triacyglycerols and milkfat triacyglycerols (MF-TAG) were also used in this study.

Sample Preparation

Care was taken to ensure that all microscopy slides were prepared in the same way, which is important for the purpose of this work. Briefly, samples should be completely melted (80°C, 30 min). A drop of the sample is then transferred using a preheated pipette to a preheated microscopic slide, which is then covered with a preheated glass coverslip after ensuring that the drop is homogeneously smeared under the cover. This yields a sample of uniform thickness (about 20 μm). Samples

were then kept in a refrigerator to crystallize at 5 °C for 24 hours before imaging. Other microscopy slides of AMF, MF-DAG, MF-TAG, and CB were also stored at different temperatures and times.

Polarized Light Microscopy

Samples were observed under polarized light using an Olympus BH polarized light microscope (Olympus, Tokyo, Japan). A Linkam LTS 350 large heating and freezing stage operated by a Linkam TP93 temperature programmer (Linkam Scientific instruments Ltd., Surrey, England) was used to maintain the temperature of the slides at 5°C during imaging. A continuous flow of liquid nitrogen (BOC gases, Guelph, Ontario) was used to cool the stage. Images were acquired with a Sony XC-75 CCD video camera (Sony Corporation, Japan) with the gain switch in the auto position. The images were digitized using a Scion LG-3 PCI frame grabber board and using Scion Image software (Scion Corporation, Fredrick, MD, USA). Image quality was enhanced by taking the average of 16 frames applying a background correction using the Scion software. Three images were captured from each of four slides at the same time-temperature combination.

Optimization of Image Acquisition and Processing

Before acquisition, images must be carefully adjusted so that all the network features (i.e., particles and/or clusters) that are seen under microscope are represented. Applying a background correction is also necessary and can be performed by imaging a clean, blank, and well-focused glass slide and then subtracting the background from all the acquired images using the command "save blank field," found in the special menu of Scion image software mentioned earlier. The choice of magnification will depend on the scale at which a nonhomogenous distribution of mass (fractality) is observed. This region should

theoretically correspond to the intracluster region of the fat crystal networks. One must be aware that, at scales above the size of a particle cluster, mass will be distributed in a homogenous fashion [6].

Processing the images includes two steps: (i) adjusting mode, levels, and contrast and (ii) thresholding. First, images must be converted to 8-bit mode. Adjustment of the levels and contrast can be performed using the autolevel or the "auto contrast" command in the tools menu of any image-processing program. Thresholding converts a grayscale image to a binary image, a necessary step in any image analysis, while inversion (white crystals become black) is necessary because the features to be analyzed need to be black. However, the inversion step is not required for the box-counting method, as mentioned previously. Images for the particle-counting analysis are then saved in TIFF format (Tagged Image File Format). Images for the box-counting analysis using "Benoit" software must be converted to a Windows BMP (bitmap) format.

Three slides were prepared for each sample and four images acquired at random from each slide. Analysis was performed on each acquired image and the average and standard error reported.

One should realize that misrepresentation of the features (to be analyzed) will strongly create artifacts and affect the analysis results. Therefore, we reiterate that images should be critically optimized under the microscope before acquisition, and the threshold value should also be inspected by visually comparing original images to thresholded ones.

RESULTS AND DISCUSSION

Particle-Counting Method

Including and Excluding Issue

By placing boxes of decreasing size on the region of interest (ROI), particles that touch the edge of the boxes should not be

neglected. Upon cropping the image, within each box, counts including, as well as excluding, particles that touch the ROI are averaged and used to determine the fractal dimension (D_f).

Figure 2 shows the log-log plot of the number of particles (N) vs. the box side length (L in pixels) from counts including and excluding the particles that touch the ROI boundary for AMF, PO, and CB. Similar trends were observed for analyses including and excluding particles touching the edge of the ROI, both with high correlation coefficients. However, excluding the particles touching the ROI resulted in high slopes and D_f values of 2.19, 2.02, and 2.18 for AMF, PO, and CB, respectively. Unless there is an inverse gradient or artifacts, the fractal dimensions determined from thin sections belong to a two-dimensional spatial distribution and, thus, should have values not more than 2.0 [6]. Therefore, excluding particles that touch the edge of the ROI is not advisable in the determination of the fractal dimension of a particle network. By including the particles that touch the perimeter of the ROI, D_f values dropped to 1.96, 1.85, and 1.89 for AMF, PO, and CB, respectively; a more reasonable result. However, sole consideration of the particle counts including particles that touch the edge of the ROI may skew the results toward a lower slope value. Thus, both "excluding" as well as "including" counts should be averaged instead.

Small Boxes Issue

The range of box sizes is another important issue that should be considered because the number of particles decreases dramatically below a certain box size. This effect is more pronounced in networks that contain large clusters of crystallites. At a certain point, the number of particles within the ROI (defined by the box size) becomes very small, to the point where no particles are counted ($N = 0$). Since the relative reduction in the ROI box area is much greater than that of the perimeter [$(P/A) = (4/L)$], the number of the particles counted will be a function of particle size and shape. Larger and needle-shaped

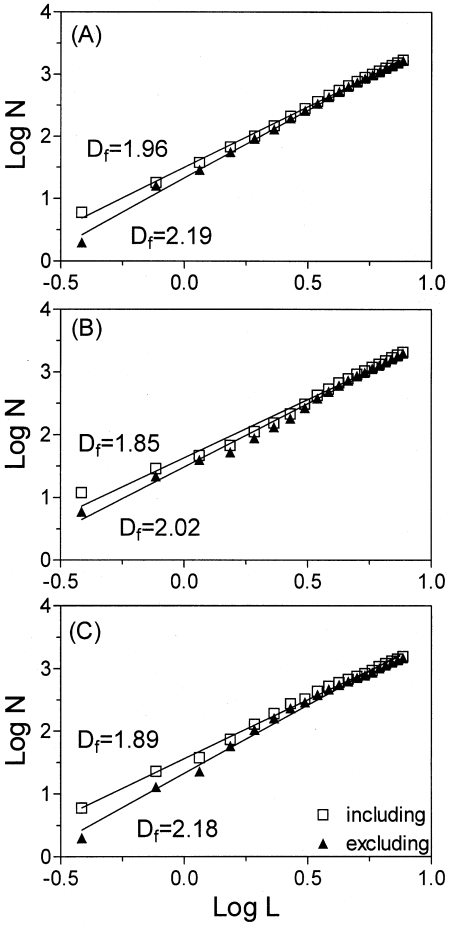

Figure 2 Particle counting results for the determination of the mass fractal dimension (D_f) with and without exclusion particles that touch the perimeter of the region of interest (ROI) for (**A**) anhydrous milk fat (AMF), (**B**) palm oil (PO), and (**C**) cocoa butter (CB).

particles maybe excluded more readily than smaller and spherical ones [6].

Figure 3 shows the particle counting analysis by including (whole range) and excluding (limited range) small boxes having side lengths less than 35% for AMF, PO, and CB at 16% SFC. In this SFC range, good linearity is always observed. The data shown was determined after averaging counts including and excluding particles touching the ROI perimeter. As shown in Figure 3, considering small boxes of less than 35% of the original image size skewed the slope, raising the D_f values to 2.03, 2.17, and 2.18 for AMF, PO, and CB, respectively. In contrast, D_f values of 1.92, 1.98, and 1.76 were determined after excluding the small boxes. As previously mentioned, the slope of the log-log linear plot of the box side length vs. the number of particles corresponds to the fractal dimension, and, thus, one must inspect the numbers used to construct this plot, as the inclusion of a single point in the small box sizes range can cause a relatively large increase in the slope of the line, even though the correlation coefficient is high (Fig. 3).

The D_f determined by including and excluding the small boxes followed the same trend as shown in Figure 2. Figure 4 shows strong correlations between D_f (including) and D_f (excluding) determined for the three fat systems at 16% SFCs by using the limited range and neglecting boxes sized less than 35% of the original image size. In contrast, poor correlations resulted when the whole range (including small boxes) was used. Table 1 lists the D_f values for AMF in different SFC ranges using the whole range as well as the limited range. Using the whole range, and excluding counts that touch the ROI, D_f values over 2 were obtained, while using the limited range gave values less than 2. One must again be aware that a high correlation coefficient does not mean the analysis is correct, and, thus, we recommend that the particle counting algorithm be carried out in the range bounded by the original image size (100%) and 35% of the original image size.

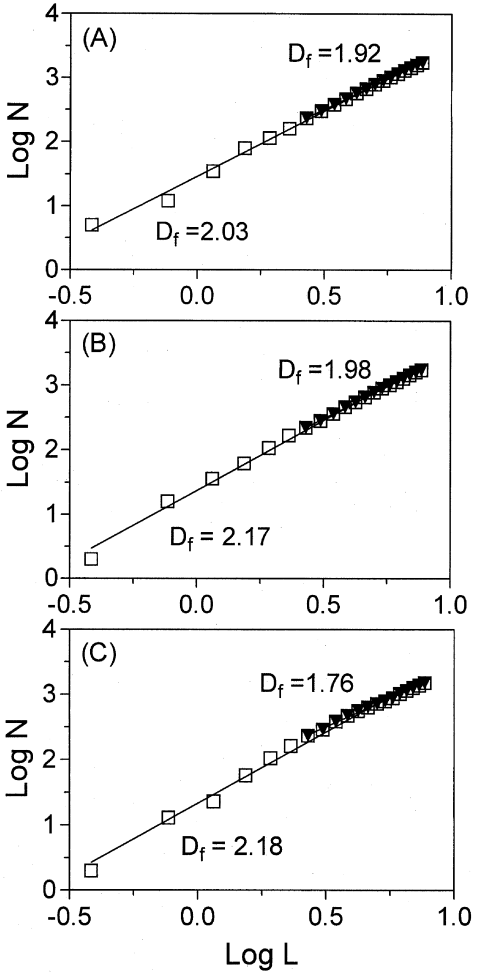

Figure 3 Particle counting results for the determination of the fractal dimension (D_f) with and without exclusion small boxes less than 35% of the original image size for (**A**) anhydrous milk fat (AMF), (**B**) palm oil (PO), and (**C**) cocoa butter (CB).

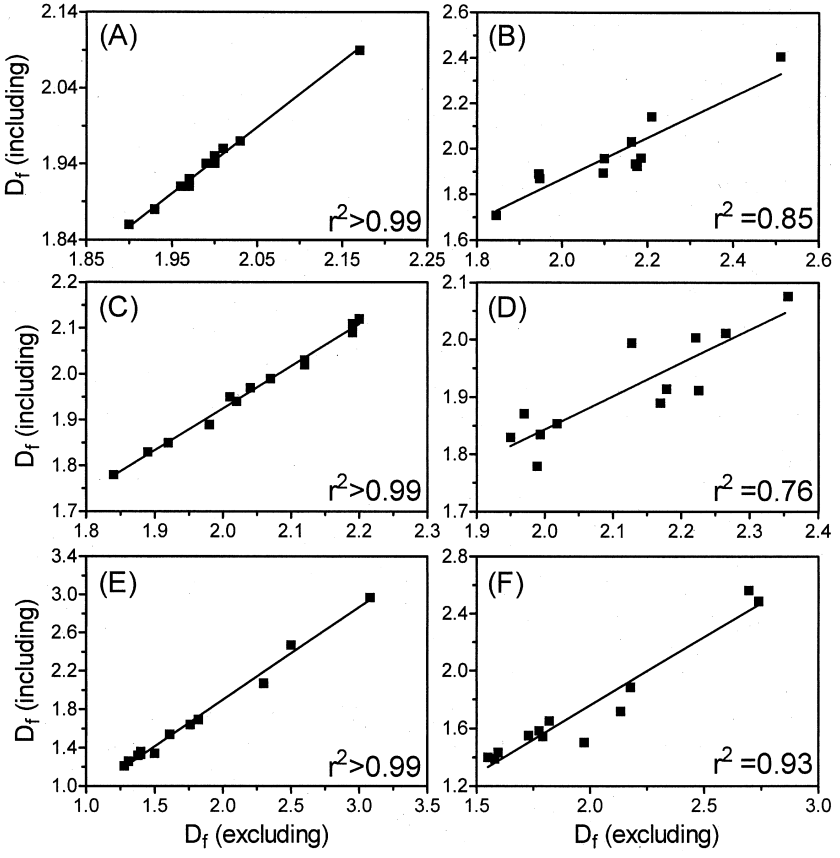

Figure 4 Correlations between the fractal dimensions (D_f) determined by the particle-counting method with and without exclusion particles that touch the perimeter of the region iof interest (ROI) for (**A,B**) anhydrous milk fat (AMF), (**C,D**) palm oil (PO), and (**E,F**) cocoa butter (CB). The small boxes less than 35% of the original image size were included (**A,C,E**) and excluded (**B,D,F**).

Table 1 Fractal Dimension (D_f) of Anhydrous Milk Fat (AMF) at Different Solid Fat Content (SFC) Ranges Estimated by Particle Counting Method Using the Whole and Limited Ranges of ROI*

SFC range (%)	Excluding[1]	Including[1]	Average[2]	Excluding	Including	Average
whole ROI**				Limited ROI***		
12–20.7	2.05	1.87	1.96	1.96	1.89	1.93
21–35	2.04	1.90	1.97	1.95	1.89	1.92
37–51	2.05	1.91	1.98	1.97	1.90	1.94

*: region of interest, **: 100–35% of box sizes, **: 100–5% of box sizes.
[1] Each value represents the average of five replicates of each sample.
[2] Each value represents the average of including and excluding ROI.

To examine applicability of the particle-counting method to different fat crystal networks, D_f was determined at different SFCs (Fig. 5). As can be seen in Figure 5, optimized D_f values (i.e., averaging counts from including and excluding particles that touch the ROI boundaries and excluding small boxes) exhibited a significant linear trend extended up to 45% SFC then there was a plateau after which D_f increased again (Fig. 5*A*). In contrast, no clear trends were observed before optimizing the method (Fig. 5*B*).

Box-Counting Method

Ranges Issue (Small, Large, and Whole Range)

In the box-counting method, grids or boxes are placed over the image of projected microstructures and the number of occupied boxes is counted. Figure 6 shows three ways of determining the fractal dimension (D_b) by box counting, using the entire range of box sizes (Fig. 6*A*), using large (10–100 pixels) box sizes (Fig. 6*B*) and using small box sizes (Fig. 6*C*). As can be seen, the slope changes in the small box range. The D_b determined using only small boxes was very low (1.22), while D_b determined using large boxes had a value of 1.85. Consider-

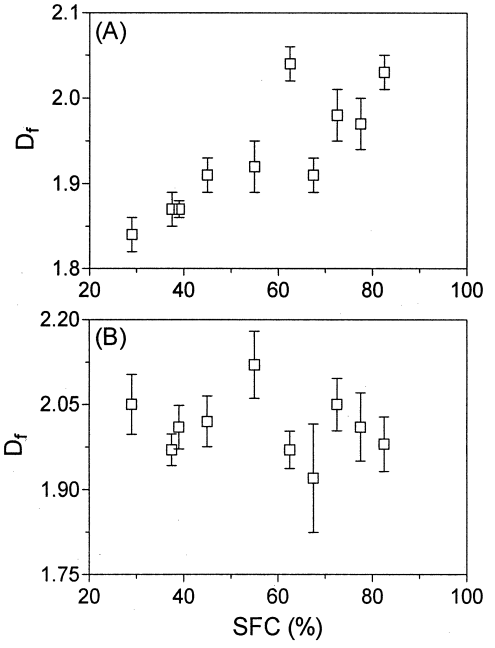

Figure 5 Plots of fractal dimension determined by the particle-counting method (D_f) vs. solid fat content (SFC) for palm oil (PO) (**A**) after and (**B**) before optimization.

ing the entire range of box sizes resulted in a value in between (1.56). In our experience, D_b should be determined from N vs. *d* plots using large box sizes. Table 2 shows an example of D_b values determined from the three regions. Therefore, we recommend the exclusion of small boxes, below 10 pixels, and large boxes, above 100 pixels, because inclusion of these ranges affects the linear trends, decreases the correlation coefficients, and skews the value of D_b.

D_f vs. D_b

Figure 7 shows changes in D_f and D_b as a function of crystallization temperature for AMF, MF-DAG, and MF-TAG. For the

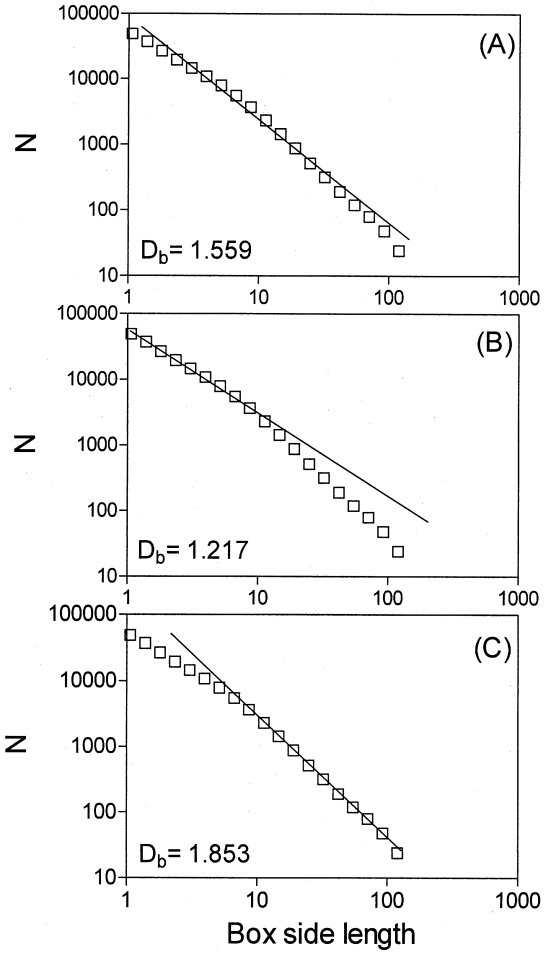

Figure 6 Box counting results for the determination of the mass fractal dimension (D_b) from (**A**) the entire range of box sizes, (**B**) the small range of box sizes, and (**C**) the large (10–100 pixels) range of box sizes. $r^2 > 0.99$.

Table 2 Fractal Dimensions (D_b) Determined by Box-Counting Method from the Entire Range, 10–100 Pixels and Small Boxes Range for Different Images of Anhydrous Milk Fat (AMF) (16% SFC)

Entire range	10–100 pixels	Small boxes range
1.28	1.67	0.96
1.26	1.76	0.97
1.25	1.67	0.96
1.29	1.72	1.01
1.32	1.72	1.04
1.34	1.76	1.05
1.33	1.74	1.04
1.35	1.78	1.00
1.34	1.77	0.99
1.35	1.79	1.00
1.35	1.78	0.99

three fats, no changes in D_f or D_b were detected after increasing temperature from 5 to 10 °C. Moreover, D_f and D_b were similar at low temperatures (i.e., 5–10 °C). Above 15°C, opposite trends of increasing D_f and decreasing D_b were evident. Above 20°C, the D_f of AMF kept increasing (Fig. 7*A*) whereas the D_f of MF-DAG decreased from 2.03 (22.5°C) to 1.84 (25 °C). As for the D_f of MF-TAG, it decreased from 1.96 at 20°C to 1.93 at 22.5°C, and then increased to 1.95 at 25°C. In contrast, the decreasing trend in D_b changed to an increasing one for the three fats, as shown in Figure 7*A*–*C*. The opposite trends in D_f and D_b are probably due to the different microstructures obtained at different temperatures. At low temperatures (i.e., 5–10°C), the networks contained more solid material and were composed of a large number of small and randomly distributed (less ordered) crystallites. At this high degree of mass fill and

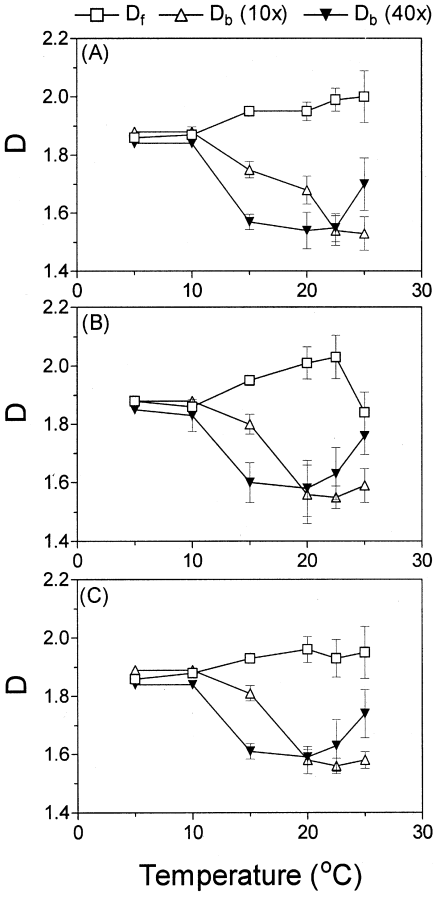

Figure 7 Plots of fractal dimensions determined by the particle-counting method (D_f) and box-counting method (D_b) vs. crystallization temperatures for (**A**) anhydrous milk fat (AMF), (**B**) milk fat-diacylglycerols (MF-DAG), and (**C**) milk fat-triacylglycerols (MF-TAG).

disorder, it was difficult to distinguish between the fractal dimensions determined by the two methods. After increasing the temperature, a lower SFC and a slower crystallization process provided more time for the development of larger crystallite clusters, causing the degree of fill (D_b) to decrease and the degree of order to increase (D_f). Upon further increases in temperature above 20°C, clusters increased further in size and became more ordered (high D_f), and more highly filled (high D_b). Figure 8 shows plots of D_f vs. D_b for AMF, MF-DAGs, and MF-TAGs. The correlation coefficients between D_f and D_b varied depending on the nature of the spatial distribution of mass in terms of cluster size, degree of fill, and degree of order at the different temperatures. The effect of temperature on the fractal dimension of CB crystal networks is shown in Figure 9. In contrast to the trend observed in the AMF systems (Fig. 8*A–C*), D_f as well as D_b of CB decreased as a function of increasing temperature (Fig. 9*A*). The correlation between D_f and D_b was strong (i.e., $r^2>0.99$), as shown in Figure 9*B*.

The aforementioned results indicated that the fractal dimensions determined by the particle-counting and box-counting methods do not describe the same characteristics of a fat crystal network in the AMF system (Fig. 8). Each method offers a unique perspective of the spatial distribution of network mass. In the CB system, however, the two methods showed a similar behavior with temperature. The opposite trends between D_f(AMF) and D_f(CB) could be due to different molecular (TAGs) interactions. Polymorphic transformations occurring at high temperatures may also increase the disordering of the CB network structure.

Fractal dimensions were determined for AMF, PO, and CB at the same SFC (16%). D_f, which expresses the degree of order, was different from one fat to the other, as shown in Table 3. D_f decreased from PO (2.01) to AMF (1.96) to CB (1.73). The same behavior was also observed with the box-counting method (D_b). The D_b values were 1.81, 1.74, and 1.68 for PO, AMF, and CB, respectively. Although fats had the same amount of the solid mass (SFC), the spatial distributions of

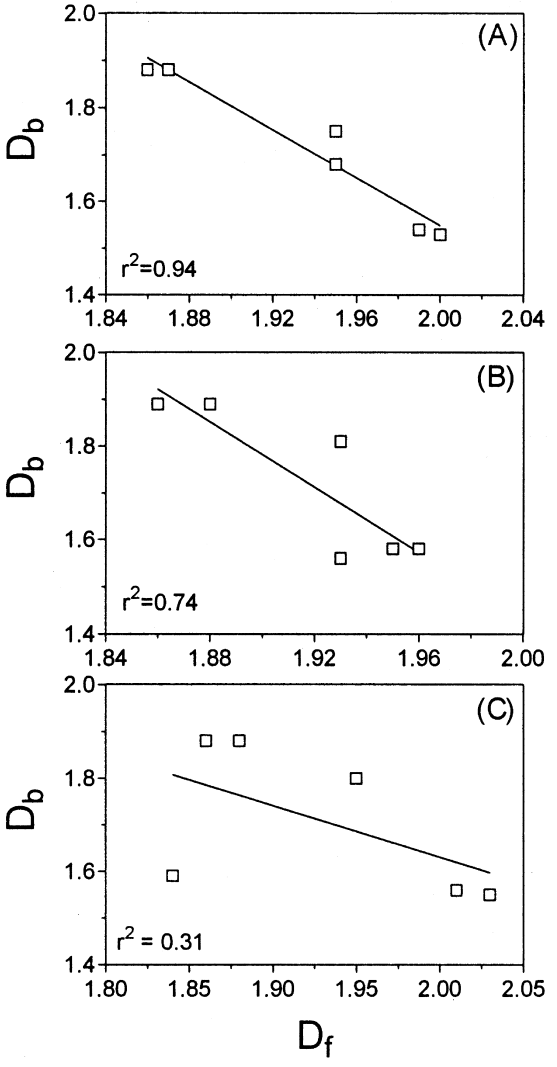

Figure 8 Correlations between the fractal dimensions determined by the particle-counting method (D_f) and box-counting method (D_b) at different temperatures for (**A**) anhydrous milk fat (AMF), (**B**) milk fat tracylglycerols (MF-TAG), and (**C**) milk fat diacylglycerols (MF-DAG).

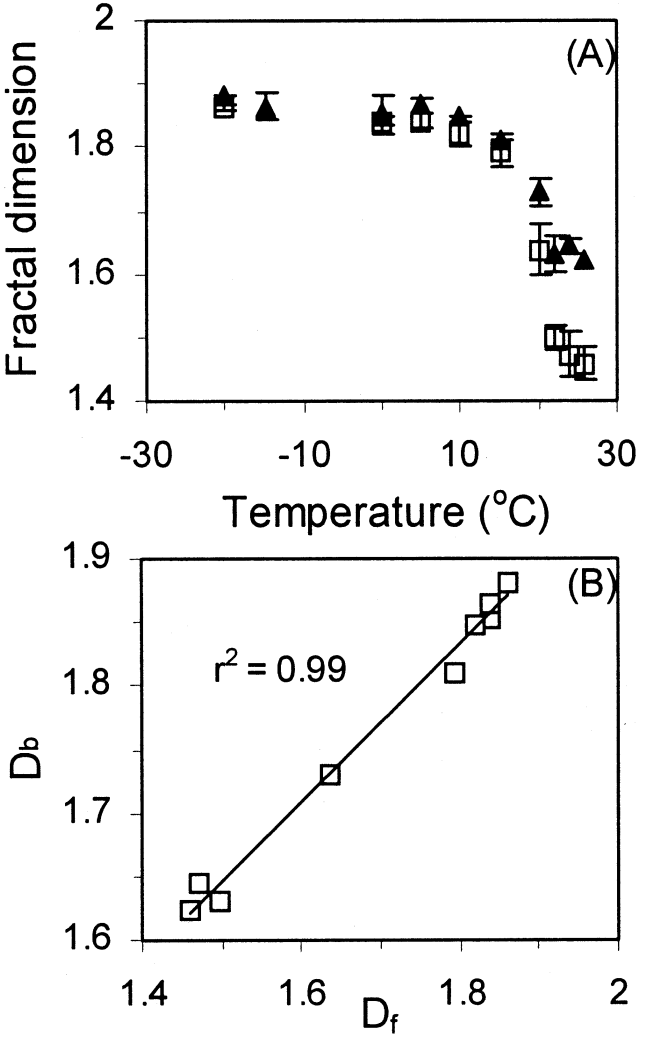

Figure 9 (**A**) Plots of fractal dimensions determined by the particle-counting method (D_f) and box-counting method (D_b) vs. crystallization temperatures for CB and (**B**) D_f vs. D_b at different temperatures. The bars in (**A**) correspond to the standard deviation values. The *open squares* and *closed triangles* correspond to D_f and D_b, respectively.

mass within the networks were different. In addition, the values of D_f, as well as D_b, (after adding "1") were relatively similar to the fractal dimensions determined by rheology in our previous work [19]. Figure 10 shows images of the networks of the three fats, which were crystallized at 5°C for 24 hours. The fat clusters were different in shape and size. Palm oil and CB displayed large clusters, while AMF displayed small clusters.

In previous work, we have shown that the mechanical properties of AMF, PO, and CB differed at low and high SFC [19]. The information obtained from the image analysis of these fats at low SFC (16%), shown in Figure 10 and Table 3, also showed differences between the fractal dimensions of their fat crystal networks. This indicated a relationship between the fractal dimensions determined for fats crystallized in thin films (2D) and those determined by rheology without confinement effects (3D). Accordingly, the two image analysis methods are sensitive to structural differences responsible for the different mechanical properties of the fats. This result lends support to the application of particle-counting and box-counting image-analysis methods for quantifying the mass

Table 3 Fractal Dimension of Palm Oil (PO), Anhydrous Milk Fat (AMF), and Cocoa Butter (CB) at Different Solid Fat Content (SFC) Ranges Estimated by Particle Counting (D_f), Box Counting (D_b), and Rheology (D_r)

Fat	D_f*	D_b*	D_r
PO	3.01	2.81	2.73
AMF	2.96	2.74	2.91
CB	2.73	2.68	2.75

*: to compare with rheology (D_r), a value of "1" was added to "D_f" as well as to "D_b", assuming a homogeneous occupacy in the Z-dimension.

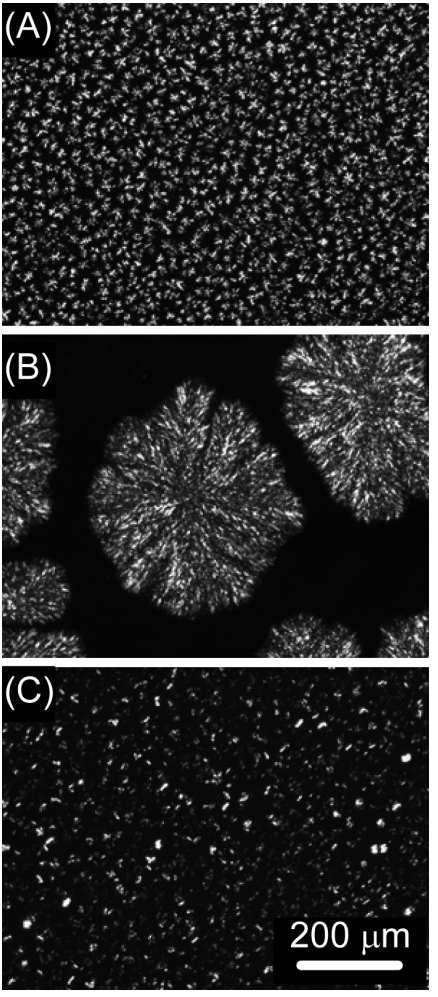

Figure 10 Polarized light micrographs of (**A**) palm oil (PO), (**B**) cocoa butter (CB), and (**C**) anhydrous milk fat (AMF) crystallized in 20 μm films at 5°C for 24 hours. The solid fat content (SFC) of each fat was 16%.

fractal dimension in fat crystal networks and its relationship to mechanical properties.

Network Structure and Fractal Dimension

The relationships between cluster size and shape and fractal dimension were studied for CB and PO. Figure 11 shows different micrographs of CB (49% SFC) that were taken at two magnifications (10× objective and 50× objective). The clusters shown in Figure 11*A–C* (10× objective) are of similar size. Significant decreases in D_b from 1.81(Figure 11*A*) to 1.76 (Figure 11*B*) and to 1.74 (Figure 11*C*) were observed with increases in the degree of fill. The same trend was also observed in micrographs taken at a higher magnification (Figure 11*D–F*). D_f, however, was not as much a function of the amount of mass present but rather a function pf the distribution and locations of the clusters. When the clusters are centered in the image (Fig. 11*C*), the decreasing boxes move from empty spaces (around the cluster) to the highly filled center of the image, which results in low degree of order and a small D_f (1.20). In contrast, starting from a full area toward an empty one will result in opposite results. As shown in Figure 11*F*, the D_f value obtained is very high (2.73, $r^2 > 0.98$) when the center of the image is "empty" (a negative density gradient). Figure 12 shows another sample of CB (58% SFC) in which D_b is also dependent on the amount of solid mass present in the micrograph. Figure 12*D*, which seems to have more solids, also has the highest D_b compared to the other micrographs. This example also demonstrates the sensitivity of the box-counting method to the degree of fill. D_f results were different and independent of the amount of network mass, but rather dependant on the distribution pattern of the mass.

Figure 13 shows the D_b values for PO samples at different SFCs. At low SFC (29–37%), D_b values of 1.76 (29%) and 1.74 (37%) were determined as shown in Figure 13*A* and 13*B*, respectively. By increasing the SFC to 63%, D_b increased to 1.85 (Fig. 13*C*). However, D_b decreased to 1.72 by further increas-

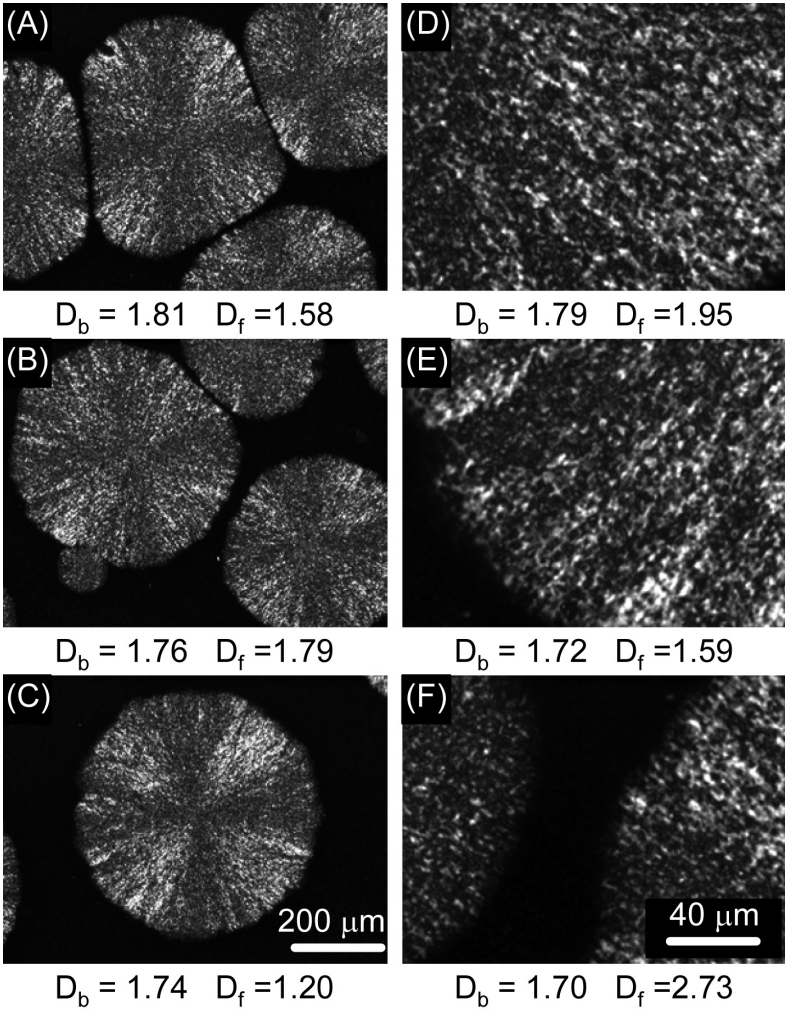

Figure 11 10× objective (**A–C**) and 50× objective (**D–F**) polarized light micrographs of cocoa butter (CB) (49% SFC) crystallized in 20-μm films at 5 °C for 24 hours. The fractal dimensions determined by the particle-counting method (D_f) and box-counting method (D_b) are shown below the images.

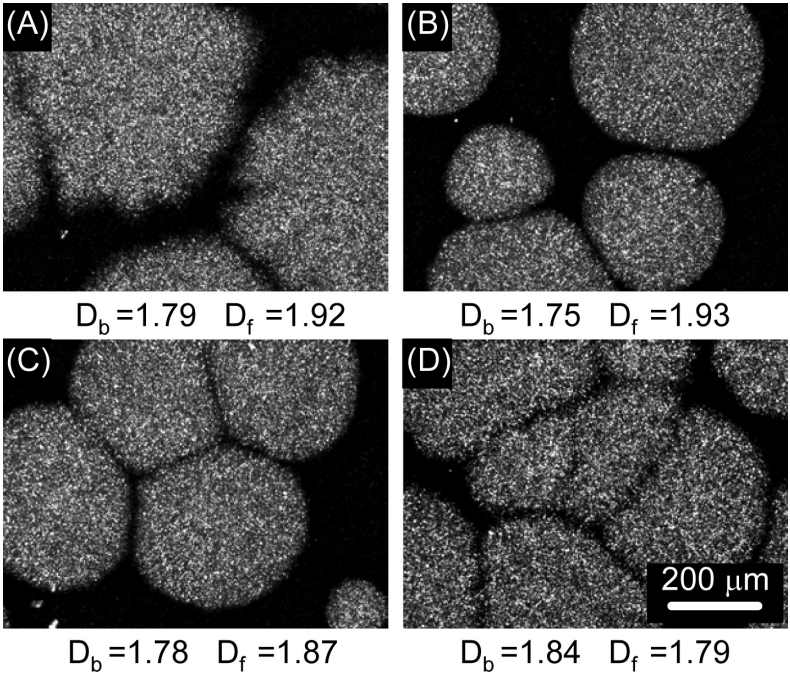

Figure 12 Polarized light micrographs of cocoa butter (CB) (58% SFC) crystallized in 20-μm films at 5 °C for 24 hours. The fractal dimensions determined by the particle-counting method (D_f) and box-counting method (D_b) are shown below the images.

ing the SFC to 68% (Fig. 13*D*), above which D_b increased again (Figs. 12*E,F*). Large clusters in Figures 12*D* and 12*E* were evident while no large clusters were observed in Figure 13*C*. Therefore, the presence of large clusters was responsible for the decrease in D_b from 1.85 (Fig. 13*C*) to 1.72 (Fig. 13*D*) and to 1.83 (Fig. 13*E*). A high D_b was obtained when the fat crystal network was homogeneously filled with particles (Fig. 13*C*). These results indicated a close relationship between network structure and the fractal dimension determined by box counting. These results, however, also suggest that, at high degrees of fill, the box-counting method loses its usefulness.

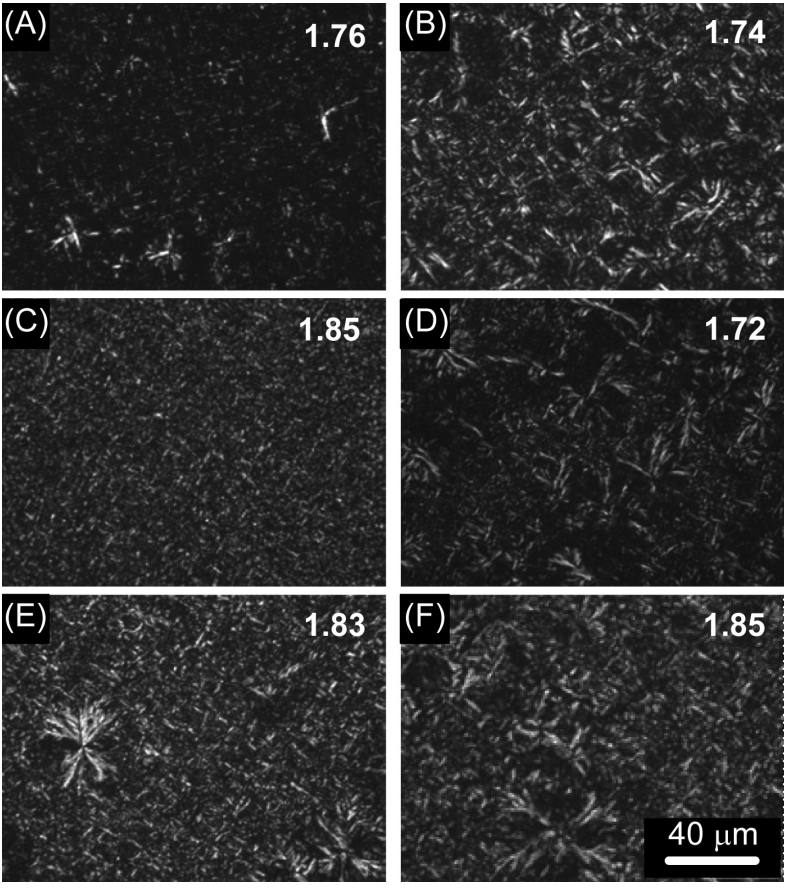

Figure 13 Polarized light micrographs of palm oil (PO) crystallized in 20-μm films at 5°C for 24 hours. The solid fat content (SFC) values are (**A**) 29%, (**B**) 39%, (**C**) 63%, (**D**) 68%, (**E**) 73%, and (**F**) 78%. The numbers on the images correspond to the fractal dimensions determined by box counting.

In networks where the distribution of particles is highly ordered, the system is more close to the Euclidean dimensionality ($D = d = 2$) and, thus, will have a high fractal dimension. Beyond that, the system is not fractal and images are similar. In this situation, the image analysis methods described here are not suitable because images are similar.

CONCLUSIONS AND RECOMMENDATIONS

Fourier analyses were consistent with our view that a fat crystal network is composed of polycrystalline particles arranged in a fractal fashion within clusters, which themselves pack in a Euclidean (homogeneous), nonfractal fashion.

The fractal dimension values determined by particle-counting and box-counting methods were different. The box-counting fractal dimension was sensitive to the degree of fill and the particle- counting fractal dimension, to the degree of order. Both methods are useful tools for quantifying the spatial distribution of mass in fat crystal networks.

In our experience, averaging the D_f values obtained from both of counts including and excluding the particles that touch the perimeter of the ROI and excluding small boxes less than 35% gave reasonable results. In the box-dimension method, our advice is to use boxes having side lengths in the range of 10–100 pixels and check the linearity of the log-log plots visually.

We also recommend that the fractal dimension, determined by any image analysis method, must be associated with a particular microstructural characteristic. This would greatly help determine links between the values obtained (i.e., D_f and D_b) and the microstructure.

REFERENCES

1. Rothschild WG. Fractal aspects of agglomeration dynamics. In: Fractals in chemistry Rothschild WG, Ed. New York: John Wiley & Sons, 1998:46–75.

2. Julien R. Aggregation phenomena and fractal aggregates Contemp Phys 1987; 28:477–493.

3. Julien R, Botet R. Aggregation and fractal aggregates. Singapore: World Scientific, 1987.

4. Meakin P. Fractal aggregation Advances in Colloids and Interface Science 1988; 28:249–331.

5. Narine SS, Marangoni AG. Fractal nature of fat crystal networks Phys Rev E 1999; 59:1908–1920.

6. Marangoni AG. The nature of fractality in fat crystal networks Trends in Food Sci & Tech 2002; 13:37–47.

7. Hagiwara T, Kumagai H, Matsunaga T. Fractal analysis of the elasticity of BSA and β-lactoglobulin gels J Agric Food Chem 1997; 45:3807–3812.

8. Hagiwara T, Kumagai H, Matsunaga T, Nakamura K. Analysis of aggregate structure in food protein gels with the concept of fractal Biosci Biotech Biochem 1997; 61:1663–1667.

9. Hagiwara T, Kumagai H, Nakamura K. Fractal analysis of aggregates in heat-induced BSA gels Food Hydrocolloids 1998; 14:29–36.

10. Marangoni AG, Barbut S, McGauly SE, Marcone M, Narine SS. On the structure of particulate gels-the case of salt induced cold gelation of heat-denatured whey protein isolate Food Hydrocolloids 2000; 14:61–74.

11. Solecka-Cermakova K, Lednicky F, Vlckova B J Phys Chem 1996; 100:4954–4960.

12. Matsushita S, Miwa T, Fujishima A. Distribution of components in composite two-dimensional arrays of latex particles and evaluation in terms of the fractal dimension Langmuir 1997; 13:258–254.

13. Kim AY, Berg JC. Fractal heteroaggregation of oppositely charged colloids J Colloid and Interface Science 2000; 229: 607–614.

14. Tather M, Erdem-Senatalar A. Method to evaluate the fractal dimensions of solid adsorbents J Phys Chem B 1999; 103: 4360–4365.

15. Quevedo R, Carlos L-G, Aguilera J, Cadoche L. Description of food surfaces and microstructural changes using fractal image texture analysis J Food Eng 2002; 53:361–371.

16. Narine SS, Marangoni AG. Mechanical and structural model of fractal networks of fat crystals at low deformations Phys Rev E 1999; 60:6991–7000.

17. Marangoni AG. Elasticity of high-volume-fraction fractal aggregate networks: a thermodynamic approach Phys Rev B 2000; 62:13951–13955.

18. Marangoni AG, Rogers MA. Structural basis for the yield stress in plastic disperse system App Phys Let 2003; 82:3239–3241.

19. Awad TS, Rogers M, Marangoni AG. Scaling behavior of the elastic modulus in colloidal networks of fat crystals. J Phys Chem B 108:171–179 (2004).

20. Marangoni AG, McGauley SE. Relationshp between crystallization behavior and structure in cocoa butter Crystal Growth & Design 2003; 3:95–108.

21. Marangoni AG, and Narine SS. Identifying key structural indicators of mechanical strength in fractal networks of fat crystals food research international 35:957–969 (2002).

22. Wolfram Research, Inc. http://scienceworld.wolfram.com/physics/Trirefringence.html (accessed June 2003).

23. Wright AJ, Marangoni AG. The effect of minor components on milk fat microstructure and mechanical properties J Food Sci 2003; 68:182–186.

24. Litwinenko JW, Rojas AM, Greschenson LN, Marangoni AG. Studies J Am Oil Chem Soc 2002; 79:647–654.

25. Dibildox-Alvarado E, Neves Rodrigues J, Gioielli LA, Toro-Vazquez JF, and Marangoni AG. Effects of crystalline microstructure on oil migration in a semisolid fat matrix. Crystal Growth & Design 2004; 4:731–736.

26. Russ JC. Hurst and Fourier analysis. In: Fractal surfaces. New York: Plenum Press, 1994:83–114.

27. Wright AJ, Hartel RW, Narine SS, Marangoni AG. The effect of minor components on milk fat crystallization J Am Oil Chem Soc 2000; 77:463–475.

12

The Nature of Fractility in Fat Crystal Networks

ALEJANDRO G. MARANGONI
Department of Food Science
University of Guelph
Guelph, Ontario, Canada

INTRODUCTION

The process of creating a supramolecular structure does not simply entail finding a thermodynamic global free energy minimum. Kinetic factors play a key role in determining which local free energy minima are chosen along the formation pathway. Environmental effects become even more important (than molecular effects) beyond the microscopic world, where heat and mass transfer effects will strongly influence the formation of nanostructures, microstructures, and eventually a network (Fig. 1) [1,2]. In order to truly understand, and even-

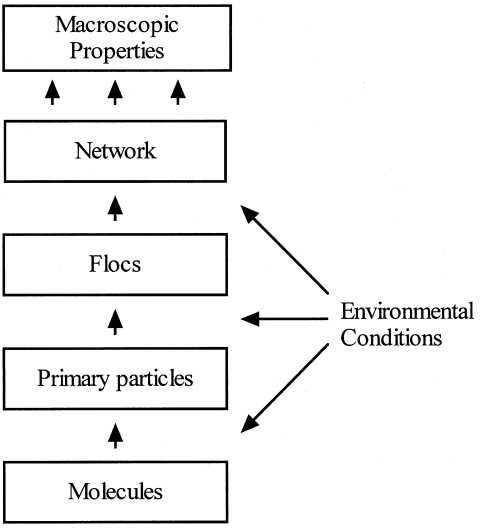

Figure 1 Structural hierarchy in many soft materials.

tually predict, the macroscopic properties of materials, it is necessary to characterize and define the different levels of structure present in the material and their respective relationship to a macroscopic property. The macroscopic properties of many soft materials cannot always be directly related to molecular structure. Rather than routinely invoking "molecular interpretations" to explain the macroscopic properties of materials, relationships between the appropriate level of structure and macroscopic properties should be sought instead. Knowledge of the relationships between molecular composition and phase behavior, solid state structure, growth mode, static structure, and macroscopic properties will eventually allow for the rational design of specific macroscopic properties in manufactured materials.

Work by Heertje and coworkers originally demonstrated that fat crystal networks can display such structural hierarchy [3,4]. When triacylglycerols (TAGs) are cooled from the melt to a temperature below their melting point, i.e., when they are supercooled, they undergo a liquid–solid transformation to form primary crystals with characteristic polymorphism.

These primary crystals aggregate, or grow into each other, to form clusters, which further interact, resulting in the formation of a continuous three-dimensional network (Fig. 2). The mechanical properties of a fat, can be influenced by all of these levels of structure; however, most directly by the level of structure closest to the macroscopic world, namely the microstructure [3,4]. For the past few decades, most of the research on the mechanical properties of fats has been directed toward establishing a link between TAG structure and phase behavior, polymorphism, and macroscopic mechanical properties. For certain important macroscopic properties, such as texture, not including all levels of structure in the analysis is undoubtedly a major reason why these attempts have only been partially successful. Notable efforts in this area include the work of van den Tempel [5,6], deMan [7], Heertje [3,4], Vreeker et al. [8], and our group [9–13].

In a cocoa butter (the fat present in chocolate), the fat crystal network crystallized statically at 22°C; for example, individual crystallites of about 1 μm in size (Fig. 3*A*) grow into each other to form particles of about 5 μm (Fig. 3*B*). These particles further aggregate to form larger clusters (Fig. 3*C*). Furthermore, the final morphology of these clusters and the mechanical properties of fats are strongly influenced by heat and mass transfer phenomena [14–17].

MECHANICAL PROPERTIES AND STRUCTURE

Originally suggested by van den Tempel [6], Vreeker and coworkers [8] proposed that the structure of a fat crystal network resembles that of a flocculated colloid, i.e., a colloidal gel. Subsequently, our group developed this concept further [12]. The solidlike macroscopic properties of materials structured as flocculated colloids, in particular elasticity, are highly dependent on their structure at the nanometer range (nanostructure), as well as micrometer range (microstructure). Early developments of a theory to explain the elastic properties of colloidal gels from their structure were carried out by W. D. Brown and R. C. Ball at Cambridge [18]. Brown and Ball pro-

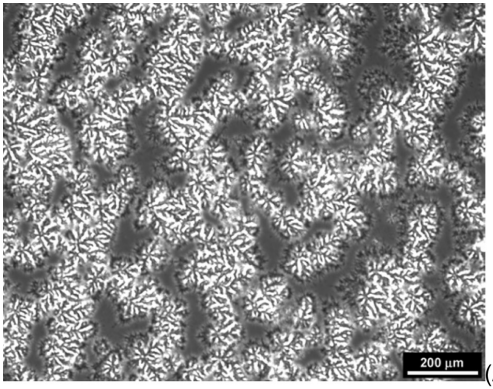

(A)

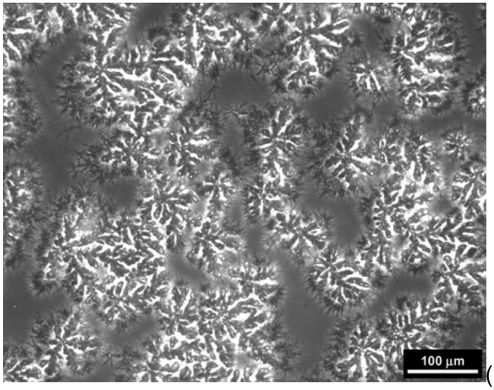

(B)

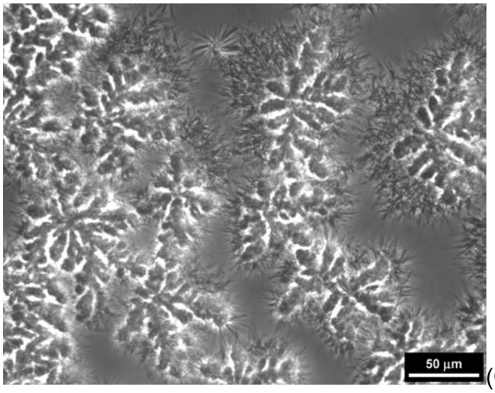

(C)

Figure 2 Phase contrast micrographs of a crystal network of the high-melting fraction of milk fat in triolein at different magnifications.

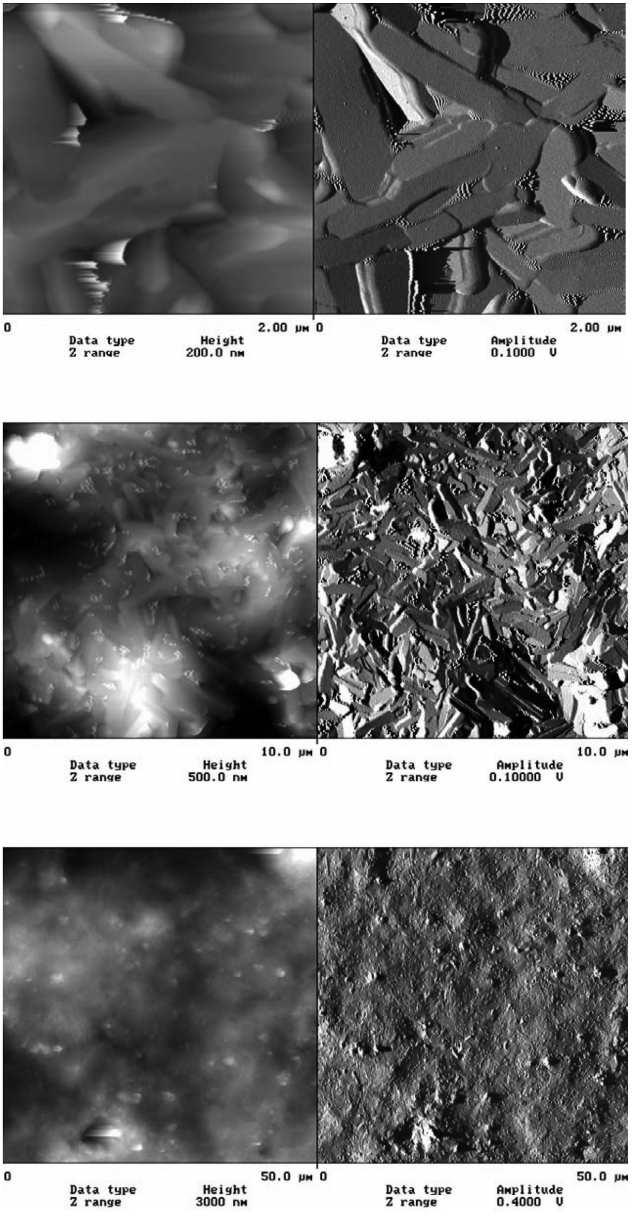

Figure 3 Tapping-mode atomic-force micrograph of cocoa butter at different magnifications. The micrographs on the left hand side correspond to height view, while the ones on the right to the phase view.

posed a power law dependence of the shear elastic modulus (G) of a colloidal network on the volume fraction Φ of network mass,

$$G \sim \Phi^{\mu} \tag{1}$$

where the exponent of the volume fraction term (μ) is related to the mechanism of particle aggregation. For example, simulations show that the exponent μ should have a value of 4.5 ± 0.2 for a reaction-limited aggregation (RLA) process and 3.5 ± 0.2 for a diffusion-limited cluster—cluster aggregation (DCA) process in three dimensions [19]. This formulation was subsequently verified experimentally, and the theory further developed by other groups [19–22]. Of great interest is the fact that this fractal scaling behavior is observed at high volume fractions ($\Phi > 0.5$), as noted by Buscall et al. [19]. In these models, clusters or flocculated particles grow until they "touch," i.e., they form a space-filling network. Beyond a certain volume fraction of aggregating material, cluster size cannot increase any further. Thus, any mass incorporated into the network beyond the point where the network becomes space-filling cannot lead to an increase in cluster size, but rather to a coarsening of the network. As suggested by the fact that "low volume fraction" fractal scaling behavior is in fact observed at high volume fractions, mass must therefore be deposited onto the fractal "scaffolding" created at the gel point, without affecting the general spatial distribution of network mass [23]. This process is affectionately referred to as "decorating the network." This is an important point since coarsening could lead to an increase in the fractal dimension of the network. If mass would randomly fill the voids in the network, this would result in a more homogenous spatial distribution of mass, with a higher fractal dimension. For these reasons, it is imperative that equation 1 remains a scaling relationship and not an exact relationship, particularly for high-volume fraction systems. It is noteworthy that most of the fats studied by our group have exponents in the vicinity of 3.5, within the expected range for a diffusionally limited aggregation process.

Based on the seminal work of Brown and Ball and Kantor and Webman [24], Shih et al. [25] outlined the development of a scaling theory to explain the elastic properties of colloidal

gels by again considering the structure of the gel network as a collection of close-packed fractal flocs of colloidal particles. However, these authors also defined two separate rheological regimes depending on the relative strength of the interfloc links vis-à-vis those within the flocs. Their formulation of the strong-link regime (applicable at low volume fractions, $\Phi<0.1$), where the flocs yield under an applied stress, was identical to that of Brown and Ball. Their formulation of the weak-link regime (applicable at high volume fractions, $\Phi>0.1$), where the interfloc links yield under an applied stress, differed from that suggested by Brown and Ball. The forms of the equations for the strong-link and weak-link regimes are, respectively:

$$G_{SLR} \sim \Phi^{\frac{d+x}{d-D}} \tag{2}$$

$$G_{WLR} \sim \Phi^{\frac{1}{d-D}} \tag{3}$$

where d is the Euclidean dimension, D the fractal dimension, and x the chemical length exponent, backbone fractal dimension, or the tortuosity of the effective chain of stress transduction within a cluster of particles yielding under an externally applied stress. The parameter x is difficult to estimate and is usually assumed to be in the range [1,1.3]. The fractal dimension is a parameter that describes the spatial distribution of mass within the network. It is possible to judge whether a system is in the weak-link or strong-link rheologic regimes by determining the dependence of the strain at the limit of linearity (γ_o) on the solids' volume fraction (Φ). According to the model of Shih et al. [25], γ_o increases as a function of Φ for the weak-link regime ($\gamma_o \sim \Phi^{1/(d-D)}$), while γ_o decreases as function of Φ for the strong-link regime ($\gamma_o \sim \Phi^{-(1+x)/(d-D)}$).

More recently, Wu and Morbidelli [26] developed an expression for the intermediate situation, where both the links and the flocs yield under an externally applied stress. These authors coined this regime the "transition" regime. The expression for the transition regime is:

$$G_{TR} \sim \Phi^{\frac{(d-2)+(2+x)(1-\alpha)}{d-D}} \tag{4}$$

where α is a constant in the range [0,1] which depends on the relative weighting of strong-link vs. weak-link behavior. A value of $\alpha = 1$ corresponds to the weak-link regime, while a value of $\alpha = 0$ corresponds to the strong-link regime. An experimental difficulty with this transition regime is the need to obtain an estimate of α. This can be done by determining the solids' volume fraction dependence of both the storage modulus (G') and the strain at the limit of linearity (γ_o).

More recently, Mellema et al. [27] developed a complete categorization scheme for rheologic scaling models of particulate gels. In this work, the authors assume protein particles form stress carrying strands, in the spirit of the treatment by Bremer et al. [21]. This is followed by a clever categorization of the rheologic behavior of gels into five classes, ranging from the weak-link regime to the strong-link regime. The general form of their model is:

$$G' \sim a_{eff}^{-\alpha} \Phi^{\frac{\alpha}{d-D}} \tag{5}$$

where a_{eff} is the effective diameter of the particles that make up the strands, $\alpha = 2\varepsilon + \delta + 1$, and ε is a scaling exponent of the contour length of a cluster spanning strand with cluster size [18], with values in the range [0,1]. The concept of a scaling exponent (δ) of the number of particles in a fractal cluster with the diameter of that cluster ($N \sim \xi$) was proposed originally in 1994 by de Rooij and coworkers [28]. The only practical problem with this scheme is the difficulty in obtaining unambiguous estimates of all parameters included in the volume fraction exponential term.

In all these treatments, the macroscopic elastic constant of the network is merely the product of the elastic constant of a basic mechanical unit (the flocs, the links between flocs, or a combination of both) and the number of these units present in the direction of an externally applied force [25]. The fractal dimension defines the size of the cluster. Thus, for example, a higher fractal dimension will result in a larger cluster size. A larger cluster size translates to less cluster–cluster interactions per unit volume, resulting in a decrease in the elastic modulus of the material. At higher volume fractions, the aver-

age cluster size decreases, thus increasing the number of cluster–cluster interactions, which leads to an increase in the value of the elastic constant.

In all of our work, we have considered fat crystal networks to be in the weak-link rheological regime. This is based on the fact that crystal clusters are relatively "hard" structures, not likely to yield at small deformations, as well as from the positive solids' volume fraction-dependence of the strain at the limit of linearity. It is more likely that the links between these clusters yield instead. As well, the value for the fractal dimension obtained assuming a weak-link regime agrees with our physical model of such networks.

In order to obtain an estimate of the fractal dimension of a colloidal gel-like material, it is necessary to determine the elastic modulus at different volume fractions of network material. This can be done by diluting the material with an appropriate solvent in a temperature range where solids are not significantly solubilized by the solvent. The slope of a log-log plot of G′ vs. Φ can then be used to determine the fractal dimension of a network assuming, a particular rheologic regime (strong-link, weak-link, or transition-regime). Figure 4 shows one such plot for lard (pig fat) crystallized at 5°C. Molten lard

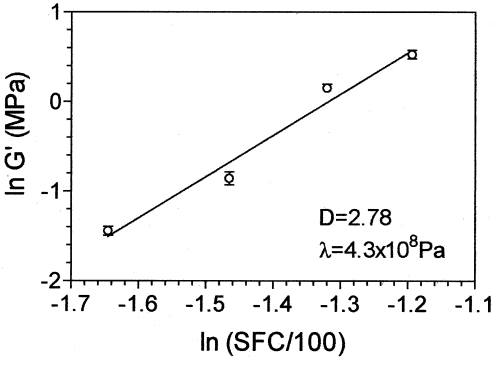

Figure 4 log-log plot of the storage modulus (G′) vs. the solids volume fraction calculated as the solid fat content divided by 100 used to determine the fractal dimension of a fat crystal network.

at 85°C was mixed with canola oil at different weight ratios, ranging from 100% lard to 70% lard, and allowed to crystallize at 5°C for 24 hours prior to measurement.

The elastic properties of fats are not solely influenced by the amount and spatial distribution of network mass, but also by particle properties, including size, shape, and particle–particle interactions. A general formulation for the relationship between the shear elastic modulus (G) of networks of particle clusters in the weak-link regime was recently derived by our group [29–31]. For spherical clusters interacting exclusively via van der Waals forces, the expression is:

$$G = \lambda \Phi^{\frac{1}{d-D}} \tag{6}$$

where

$$\lambda = \frac{A}{6\pi\gamma_o a d_o^2} = \frac{2\delta}{a} \tag{7}$$

In this expression, A corresponds to Hamacker's constant, a to the diameter of the primary particles, γ_o to the shear strain at the limit of linearity, and d_o to the intercluster separation distance. This expression was derived originally for compression and is presented here for shear stress assuming a Poisson ratio of 0.5, and, thus, $E = 3G$ (where E is the Young's modulus). The factor λ is constant within a specific range of solids' volume fractions only. Its value will differ for different solids' content regions and will be dependent on floc shape and the nature of interfloc interactions.

WHAT IS FRACTALITY?

Much controversy has recently arisen as to whether natural systems should be considered fractal [32,33]. Much of the controversy stems from a lack of understanding of the meaning of a fractal dimension. For an object, or distribution of objects, to be fractal, certain conditions should be met:

1. The object or distribution of objects should display some degree of self-similarity (exact or statistical) within a specific range of dilations (or contractions).

This means that the object looks similar at different magnifications.

2. A specific property, y (elastic modulus, number of particles, mass, etc.), should scale in a power–law fashion with length scale, x, within this specific range of magnifications ($y \sim x^{\mu}$). Thus a log-log plot of y vs. x should be linear with a slope μ.
3. The value of this "scaling factor," or "dimension" (D) should be *fractional* and be less than the dimensionality of the corresponding Euclidean embedding space (d), thus $D<d$. If these conditions are satisfied, this scaling factor could be referred as a fractal dimension.

First of all, exact self-similarity should not be considered a condition for fractality in natural systems. Randomness will always be introduced into a structure due to the inherent complexity of the processes responsible for structure formation. This will therefore negate exactness in symmetry properties, e.g., self-similarity, at the nanostructural and microstructural levels. Secondly, in my opinion, there is no reason why an object should display statistical self-similarity over countless decades in order for it to be considered fractal. In colloidal gels, for example, fractality in the spatial distribution of network mass is usually encountered between the size of a primary colloidal particle and a floc of these primary particles [33]. These limits of fractality can be justified from knowledge of the material's structure. In principle, a narrow scaling range should not, in my opinion, negate fractality. As Mandelbrot taught us [35], a fractal dimension is not a panacea, but it is a powerful means of quantifying the structure of non-Euclidean objects. The beauty of a fractal dimension is that it can capture the complexity of a structure's geometry in a single number. The challenge, however, is to give physical meaning to the number obtained. This fact, however, does not diminish its usefulness. Some amount of statistical self-similarity is evident from visual inspection of polarized light micrographs of fat crystal networks in the range 25–1000 μm (Fig. 5).

When seeking to quantify the spatial distribution of network mass, one should not consider the network to be a fractal

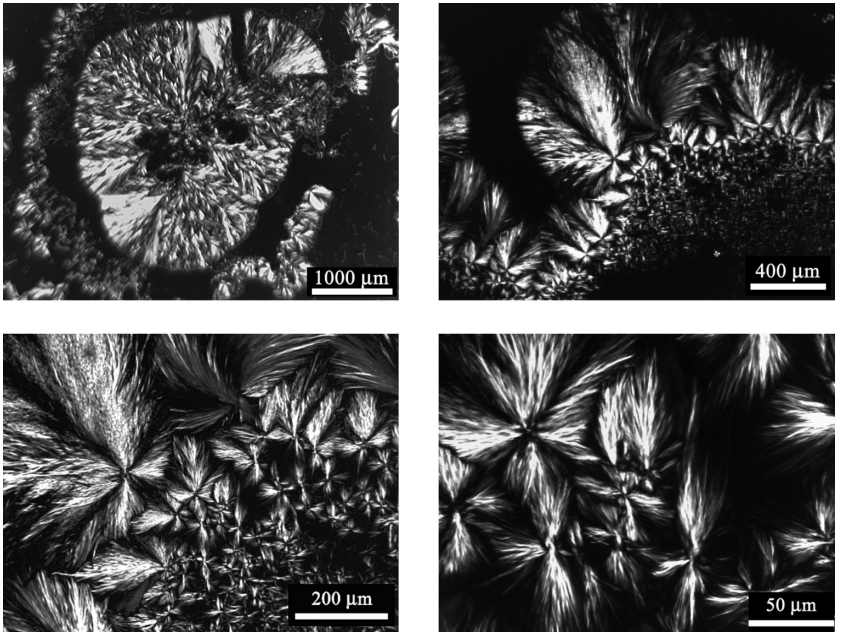

Figure 5 Polarized light images of crystalline structures of a mixture of cocoa butter and canola oil at different magnifications.

object, in the same fashion as an individual aggregate created by a diffussional process [36–38]. A seemingly disordered network of clustered polycrystalline or amorphous mass should not be considered an "object" in the traditional sense of fractal analysis. There is no appreciable "center" in this network, and there is no density gradient from the center outward. The concept of an object's perimeter has no physical meaning here either. Thus, an alternative view of fractality is required.

The treatment below was developed originally by Bremer et al. [21]. Consider a network composed of a certain amount of particulate or nonparticulate mass, distributed in a seemingly random fashion in space (Fig. 6). It is very important to remember that a "fractal" distribution of mass is usually only evident within a narrow range of magnifications. Thus, it is

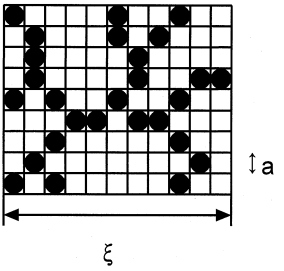

Figure 6 Spatial distribution of mass within a microstructural lattice.

imperative that any "fractal analysis" takes place within this range of fractality, where scaling behavior is observed. For colloidal aggregates, scaling behavior is usually observed between the size of a primary particle and the size of a cluster of primary particles. Above and below these limits, the system is not fractal, but homogeneous [33].

In this two-dimensional embedding space (d = 2), the maximum number of particles that can fit within this region of interest (N_{max}) is *proportional* to the ratio of the area of the region of interest (A_{ROI}) to the area of a particle (A_p), namely:

$$N_{max} \sim \frac{A_{ROI}}{A_p} \sim \frac{L^2}{a^2} = \left(\frac{L}{a}\right)^2 \tag{8}$$

where L corresponds to the diameter of the region of interest (ROI), and a to the diameter of a particle. For any d-dimensional space,

$$N_{max} \sim \left(\frac{L}{a}\right)^d, \tag{9}$$

where d is the Euclidean dimension of the space occupied by the particles. It is important to remember that this is a *proportional* rather than an exact relationship. The proportional nature of this relationship accounts for geometric and packing factors.

By analogy, the actual number of particles that occupy the ROI space (N_p) is given by:

$$N_p \sim \left(\frac{L}{a}\right)^D. \tag{10}$$

D is the mass fractal dimension, which is always smaller than the corresponding Euclidean dimension (D<d). This fractal dimension describes the order in the arrangement of mass within the ROI. A high fractal dimension is associated with a more homogeneous spatial distribution of network mass. Again, we reiterate that this is a proportional rather than exact relationship. The proportional nature of this relationship accounts for geometric and packing factors.

The volume fraction of particles within the ROI can be expressed as:

$$\Phi \sim \frac{N_p}{N_{max}} \sim \left(\frac{L}{a}\right)^{D-d} \tag{11}$$

The ROI is assumed to lie within the interior of a cluster of particles arranged in a fractal fashion. Thus, the diameter of the ROI is proportional to that of the cluster. Rearrangement of equation 12 taking this into consideration yields the familiar equation that relates the diameter of a fractal cluster (ξ), or the correlation length of the network, to the volume fraction of mass within the cluster, namely:

$$\xi \sim a\Phi^{\frac{1}{D-d}} \tag{12}$$

This is the fundamental equation used for the incorporation of fractal considerations into theoretical treatments of network structure. In all these treatments, the microstructural network is considered to be a regularly arranged, space-filling, or close-packed, agglomerate of these clusters, i.e., an orthodox amorphous substance. Thus, the volume fraction of mass for the entire network (Φ) is assumed to be equivalent to the volume fraction of mass within the cluster (Φ_ξ). It is imperative that this equation remains as a scaling relationship. This will take into account geometric, packing, and volume fraction-related factors that will strongly influence the absolute value of the cluster size.

Substituting equation 12 into equation 10, we obtain a relationship between the number of particles in a cluster as a function of volume fraction of solids and the fractal dimension,

$$N_p \sim \Phi^{\frac{D}{D-d}} \tag{13}$$

Criticisms of the use of the concept of fractal dimension in high-volume fractions systems almost always include a sample calculation of the number of particles within a fractal cluster, at high volume fractions (e.g., 0.5) and low fractal dimensions (e.g., 2.0), using equation 13. This would yield a result of four particles per cluster, which obviously does not make sense. However, consider a system such as milk fat at 5°C where $D = 2.7$ in three-dimensional space, at $\Phi = 0.5$. Using equation 13, the number of particles per cluster is calculated to be approximately 500, a reasonable result. Thus, there seems to be problem with equation 13. As stated above, the relationship expressed in equation 13 is not an exact, but rather a proportional relationship. Thus, this calculation is not correct.

The correct, and exact, expression for the relationship between the number of particles per cluster and the volume fraction of solids can be obtained from consideration of the following relationships:

$$\Phi = \frac{N_p V_p N_\xi}{V} \tag{14}$$

and

$$V = N_\xi V_\xi \tag{15}$$

where Φ is the volume fraction of solids in the system, N_p is the number of particles per cluster, V_p is the volume of a particle, N_ξ is the total number of clusters in the system, V is the volume of the system, and V_ξ is the volume of a cluster. Combining equations 14 and 15 yields:

$$N_p = \Phi\left(\frac{\xi}{a}\right)^3 \tag{16}$$

For example, for one of our high-volume fraction systems studied, $\Phi = 0.5$, $\xi = 100$ μm, and $a = 5$ μm. Thus, the number of particles per floc can be calculated to be 4000, a perfectly reasonable result. Equations 10 and 13 are not exact relationships and were never meant to be used in these types of calculations.

DETERMINATION OF THE FRACTAL DIMENSION OF FAT CRYSTAL NETWORKS BY MICROSCOPY—THE PARTICLE COUNTING METHOD

The determination of the fractal dimension of a fat crystal network can also be carried out using light scattering techniques [8], but only at very low volume fractions of solid fat. Microscopy is another technique that can be used to determine the fractal dimension of fat crystal networks. Polarized light microscopy (PLM) is by far the most popular and practical microscopy technique used in studies of fat microstructure. Thus, our efforts have centered on the use of PLM to characterize the spatial distribution of mass within a fat crystal network, and this discussion will be limited to this technique only.

Our group has developed a PLM-based technique for the determination of the fractal dimension of fat crystal networks. Lipid films of about 20-μm thickness are imaged using a standard light microscope equipped with crossed polarizers using 4x, 10x, or 40x objective lenses. The choice of magnification will depend the scale at which a nonhomogenous distribution of mass is observed. This region should theoretically correspond to the intracluster region of the fat crystal networks. As stated earlier, mass will be distributed in a homogenous fashion at scales above the size of a particle cluster. Having said this, it is my belief that the growth of fat crystals crystallized as a thin film on a microscope slide is somewhat restricted to two-dimensional growth. This being the case, the visualization of particle clusters will be difficult. Thus, we assume that the general spatial distribution of mass observed on a microscope slide under 10x–40x objective lenses corresponds to that within crystallite clusters in a fat crystallized in bulk.

The particle-counting procedure is based on counting the number of crystal reflections or "particles" within boxes of increasing size placed over a properly thresholded and inverted image (Fig. 7). Thresholding converts a grayscale image to a binary image, a necessary step in any image analysis, while inversion (white crystals become black) is necessary because some analyzed features are considered black. The slope of the

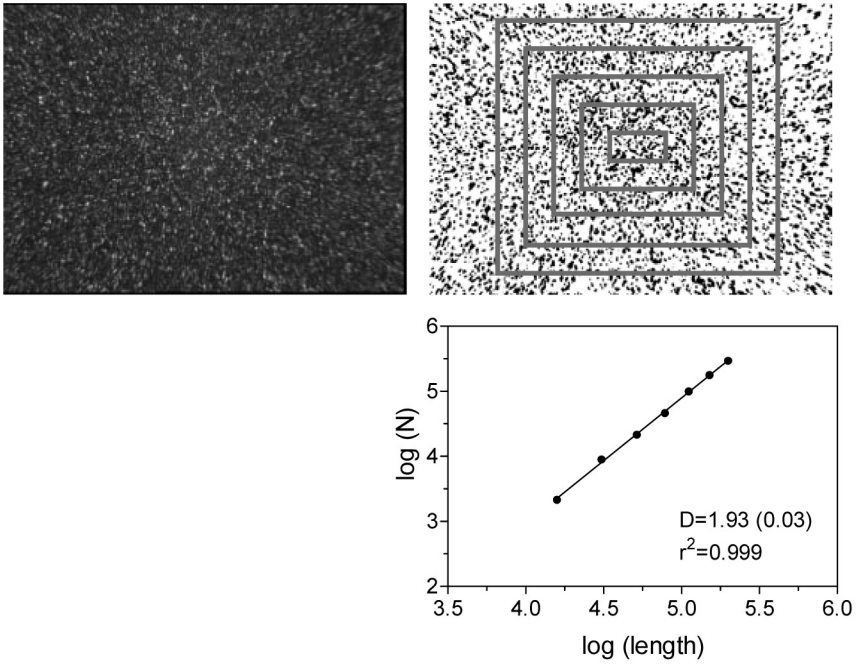

Figure 7 The particle-counting method for the determination of mass fractal dimension from polarized light micrographs of fat crystal networks. The grayscale image of milk fat crystallized at 15°C is inverted and thresholded. The slope of a log-log plot of the number of "particles" counted in the different regions corresponds to the mass fractal dimension in $d = 2$ space.

log-log plot of the number of particles vs. the box size corresponds to the fractal dimension of the network. In this procedure, it is necessary to count the number of particles within an ROI, *including* as well as *excluding* particles that touch the edge of the boxes. The estimate of the fractal dimension of a network is obtained by averaging the fractal dimensions obtained from counts including and excluding particles touching the edge of the boxes. This technique is merely an extension of mass-radius (in the case of circular ROIs), or sandbox (in the case of square ROIs) procedures for fractal dimension determination [36–38]. Instead of determining the amount of

mass contained within a radius R, or within a box centered on an arbitrarily chosen point in the micrograph, we determine the number of reflections, or particles, present in this area. One aspect to keep in mind is the issue of depth of field. Particles in the entire volume element are accounted for, and basically projected onto, a two-dimensional plane after thresholding.

Implicitly, Mass-Radius calculations may seem to require a density gradient from an object's center outward. However, this is not absolutely necessary since MR techniques are sensitive to the general spatial distribution of mass within a network—this fact can be confirmed experimentally quite readily. Density autocorrelation functions have been successfully used in this seemingly inappropriate fashion as well [39]. For Mass-Radius techniques, it is imperative to carry out many replications of analyses, starting at different "centers" within the network. The overall fractal dimension of the network corresponds to the average of the analyses from all different centers. Some algorithms carry out mass-radius analysis considering, in turn, every pixel within the micrograph as a center. The overall result corresponds to the global average of all these analyses. This, or course takes a considerable amount of computational power. Alternatively, a grid-type box-counting method could be used. We have used all of these techniques in the analysis of PLM micrographs of fat crystal networks. In the absence of artifacts, which can be numerous, agreement between Mass-Rradius, box-counting and our particle counting procedures is almost quantitative (more of this is discussed later). An excellent way to become familiar with these fractal analyses is to explore. The Benoit software package (Truesoft International, St. Petersburg, FL, USA, www.trusoft-international.com) is one of the best tools on the market available for this purpose. In this program, however, features to be analyzed have to be white, rather than the usual black. This may mean that images have to be inverted prior to analysis. I also recommend that users threshold their images prior to the analysis using Adobe Photoshop (San Jose, CA, USA) or other similar software, rather than rely on the automated thresholding that this program offers. In this way, the user can be

certain that the thresholded image actually represents what is depicted in the grayscale image.

In our experience. for our particle-counting method, it is necessary to analyze at least four images from each of five different slides in order to obtain a reasonable estimate of the fractal dimension. Care should also be exercised when using commercial image analysis programs because box counting could refer to the traditional perimeter length-based fractal analysis, which provides an estimate of the roughness of a surface or boundary. Standardized nomenclature is sorely needed in this area. Having said this, readers should have realized by now how "fluid" the concept of a fractal dimension can be.

Because Mass-Radius techniques are plagued with artifacts, a brief discussion will follow in order to define whether a fractal dimension derived using these techniques belongs to two- or three-dimensional space. Consider Figure 8; fractal analysis of the distribution of particles in $d = 3$ space ($N \sim L^D$) will yield integer dimensions for Euclidean arrangements, such as a line ($D = 1$), a plane ($D = 2$), and a cube ($D = 3$). If the distribution of mass is non-Euclidean, then fractional dimensions will be obtained. Now, consider a film of crystallized fat on a microscope slide as depicted in Figure 8. A micrograph of such film normal to the X-Y plane will yield a two-dimensional representation of the three-dimensional film. Thus, Mass-Radius analysis on such an image, where only the size of a two-dimensional box is changed, must necessarily yield a dimension smaller than 2. The volume of the film is given by $V_T = L^2 z$, where L is the length of the square ROI box and z is the depth of the film. If the volume of a particle is given by $V_p = a^3$, then the maximum number of particles that can fit within this ROI is given by:

$$N_{max} \sim \frac{V_{ROI}}{V_p} = \left(\frac{L}{a}\right)^2 \left(\frac{z}{a}\right)^1 \tag{17}$$

By analogy, the actual number of particles in the ROI (N_p) equals:

$$N_p \sim \left(\frac{L}{a}\right)^D \left(\frac{z}{a}\right)^x \tag{18}$$

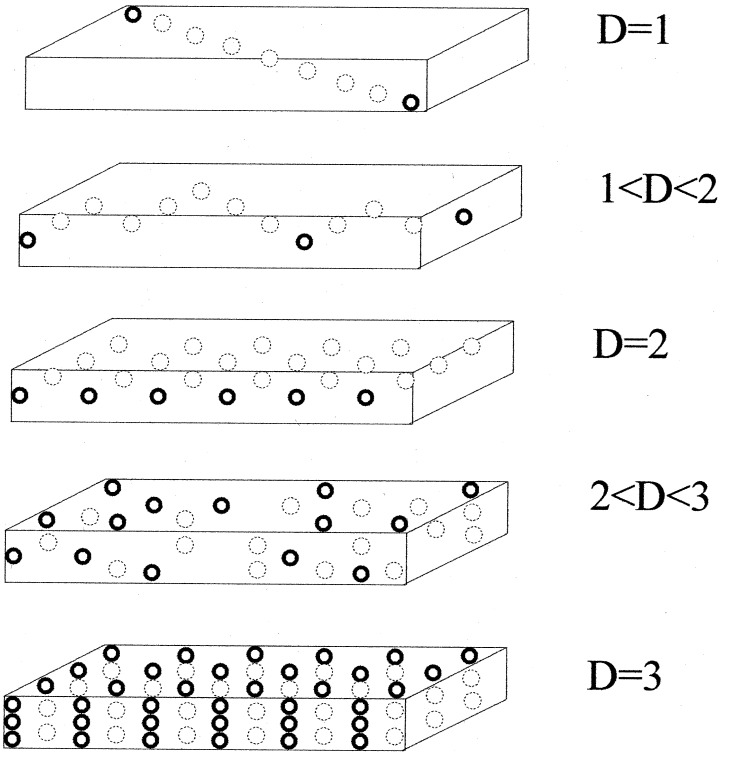

Figure 8 Spatial distribution of particulate mass and its corresponding dimensionality.

where D is the fractal dimension for the X-Y plane in $d=2$ space ($1<D<2$), while x is the fractal dimension ($0<x<1$) in the Z-dimension. The factor $(z/a)^x$ in equation 18 is constant, and can be removed from the scaling relation when performing fractal analysis. This factor will affect the absolute number of particles counted in each box, but not their relative number, i.e., their scaling behavior. The fractal dimensions obtained in this fashion will have a value smaller than 2, i.e., $D<2$. How to "map" this value of the fractal dimension back to $d=3$ space is not trivial. The usual procedure discussed by Viczek [40] is to add a "1" to the final result. This implies a homogeneous

occupancy of space in the Z-dimension, which is most probably not strictly correct, but there is no simple solution to this problem. A very thorough and informative discussion on this point can be found in the excellent book by Russ [41]. At this point, I should reiterate that particle counting has to be carried out including and excluding particles that touch the perimeter of the ROI box, and extreme care should be exercised when choosing the range of box sizes used in the analysis. As shown in Figure 9, in a certain box size (approximately 30% of original image size and lower), the value of N drops dramatically, either with or without exclusion of particles that touch the perimeter of the ROI box, effectively skewing the linear regression line to a higher slope value. This will lead to an increase in artifacts in the measured fractal dimension. My advice is to stay away from extremely small box sizes. Notice in Figure 9 how inclusion of N values for small box sizes, as well as inclusion or exclusion of particles touching the edges of the ROI box, can lead to large changes in the estimate of the fractal dimension. For example, the fractal dimension has a value of 2.49 if the entire range is analyzed and particles touching the

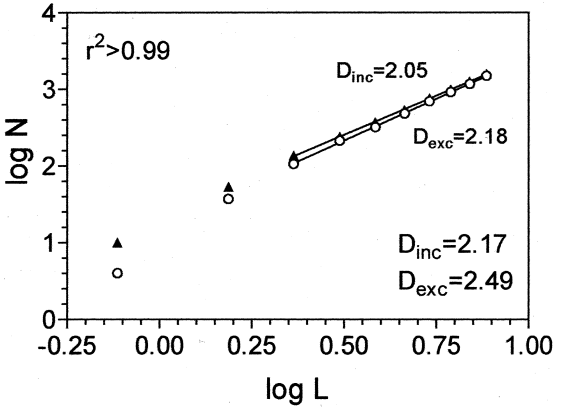

Figure 9 Particle-counting results for the determination of the fractal dimension of a fat with (○) and without (▲) exclusion of particles that touch the perimeter of the ROI box. The fractal dimensions for the entire range are also included.

perimeter are excluded, whereas the value drops to 2.17 if particles are not excluded. If the smallest two box sizes are omitted from the analysis, the fractal dimension estimate drops to 2.04 for the case where particles touching the perimeter are included, and to 2.17 when particles are excluded. What is most surprising is that the correlation coefficients for all these regressions are greater than 0.99. Thus, one cannot rely on the value of the r^2 as a diagnostic tool. The best advice is to exclude box sizes below a size that causes a significant change in the estimate of the fractal dimension and to average the fractal dimensions obtained from counts including and excluding particles that touch the perimeter of the ROI box.

The finite size problem created by the more rapid decrease in area relative to perimeter [(P/A) = (4/L)], when the size of the ROI is decreased, can have profound effects on the results obtained. One can envision how particle size and shape could influence the results obtained. For example, needle-shaped particles may be excluded more readily than spherical ones. As well, larger particles may be excluded more readily than smaller particles, effectively increasing the value of D for networks with large particles or needle-like particles. Even after taking all these factors into consideration, it is still possible to obtain values of D greater than 2.0. This will be the case when an inverse density gradient is present in the image—lower mass or particle density in the center of the image. This effect should disappear, however, given proper sampling and replication. Even though the particle counting procedure has proved to be a useful tool in our work, we are currently exploring alternative methods for the characterization of the spatial distribution of mass in fat crystal networks.

All these methods can be riddled with potential artifacts and extreme care should be exercised when applying them, and a large number of replications (upward of 20 different fields from at least three different samples) have to be used for the determination of the fractal dimension. Particularly important is to inspect log-log plots visually in order to determine whether departures from linear behavior have taken place. The value of the fractal dimension can vary enormously

if a systematic departure from linear behavior is present. Most of the time, this departure from power–law behavior is due to analytical artifacts, and extreme care should be exercised in the interpretation of the results—always inspect the data thoroughly.

RELATIONSHIP BETWEEN FRACTAL DIMENSIONS DETERMINED BY RHEOLOGY AND MICROSCOPY

For the application of fractal scaling theories to be theoretically valid, agreement between fractal dimensions determined by rheological methods and by microscopy methods must agree. We have found reasonable, but system-specific agreement between these two methods. Spatial mass fractal dimensions were determined using the box-counting algorithm in the software package Benoit 1.3, and compared to fractal dimensions determined by the small deformation rheological technique described before. Results are presented in Table 1. Mass fractal dimensions determined by standard microscopy techniques belong to two-dimensional Euclidean space. Trans-

Table 1 Comparison Between Mass Fractal Dimensions Determined Using Microscopy and Image Analysis and Small Deformation Dynamic Shear Rheology

System	D (rheology) d=3	D (microscopy) d=2
HMF[a]	2.78	1.73
50% HMF-MMF[b]	2.45	1.47
Anhydrous milk fat	2.75	1.85
Cocoa butter	2.51	1.56
Palm oil	2.72	1.87
Modified palm oil 1	2.62	1.87
Modified palm oil 2	2.66	1.88

[a]High-melting fraction of milk fat.
[b]Middle-melting fraction of milk fat.

lation to three-dimensional Euclidean space is usually carried out by adding the "1" to the value, as discussed previously. This procedure is usually satisfactory for thin samples, but can be very system specific and is sensitive to crystallization conditions. Extreme care should be exercised!

REFERENCES

1. Halsey TC. Diffusion-limited aggregation: a model for pattern formation Physics Today 2000; 53(11):36–41.
2. Yin MY, Lindsay HM, Weitz DA, Ball RC, Klein R, Meakin P. Universality in colloidal aggregation Nature 1989; 339: 360–362.
3. Heertje I. Microstructural studies in fat research Food Structure 1993; 12:77–94.
4. Juriaanse AC, Heertje I. Microstructure of shortenings, margarine and butter—a review Food Microstructure 1988; 7:181–188.
5. van den Tempel M. Mechanical properties of plastic-disperse systems at very small deformations J Colloid Science 1961; 16: 284–296.
6. van den Tempel M. Rheology of concentrated suspensions J Colloid and Interface Science 1979; 71:18–20.
7. deMan JM, Beers AM. Fat crystal networks: structure and rheological properties J Texture Studies 1987; 18:303–318.
8. Vreeker R, Hoekstra LL, den Boer DC, Agterof WGM. The fractal nature of fat crystal networks Colloids and Surfaces 1992; 65:185–189.
9. Marangoni AG, Rousseau D. Is plastic fat rheology governed by the fractal geometry of the fat crystal network J Am Oil Chem Soc 1996; 73:991–994.
10. Marangoni AG, Rousseau D. The influence of chemical interesterification on the physicochemical properties of complex fat systems. 3. Rheology and fractality of the crystal network J Am Oil Chem Soc 1998; 75:1633–1636.
11. Marangoni AG, Rousseau D. Plastic fat rheology is governed by the fractal nature of the fat crystal network and by crystal

habit. In: Physical properties of fats, oils and emulsifiers Widlak N, Ed. Champaign. IL: American Oil Chemists Society Press, 1999:96–111.

12. Narine SS, Marangoni AG. Fractal nature of fat crystal networks Phys Rev E 1999; 59:1908–1920.
13. Narine SS, Marangoni AG. Relating structure of fat crystal networks to mechanical properties: a review Food Res Inter 1999; 12:227–248.
14. Kellens M, Meeussen W, Reynaers H. Study of the polymorphism and the crystallization kinetics of tripalmitin: a microscopic approach J Am Oil Chem Soc 1992; 69:906–911.
15. Herrera ML, Hartel RW. Effect of processing conditions on crystallization kinetics of a milkfat model system J Am Oil Chem Soc 2000; 77:1177–1187.
16. Herrera ML, Hartel RW. Effect of processing conditions on crystallization kinetics of a milkfat model system: rheology J Am Oil Chem Soc 2000; 77:1189–1195.
17. Herrera ML, Hartel RW. Effect of processing conditions on crystallization kinetics of a milkfat model system: microstructure J Am Oil Chem Soc 2000; 77:1197–1204.
18. Brown WD. The structure and physical properties of flocculating colloids. Department of Physics, University of Cambridge, Cambridge, UK, 1987.
19. Buscall R, Mills PDA, Goodwin JW, Lawson DW. Scaling behavior of the rheology of aggregate networks formed from colloidal particles J Chem Soc Faraday Trans 1 1988; 84:4249–4260.
20. Sonntag RC, Russel WB. Elastic properties of flocculated networks J Colloid and Interface Science 1987; 116:485–489.
21. Bremer LGB, van Vliet T, Walstra P. Theoretical and experimental study of the fractal nature of the structure of casein gels J Chem Soc Faraday Trans 1 1989; 85:3359–3372.
22. Bremer LGB, Bijsterbosch BH, Schrijvers R, van Vliet T, Walstra P. On the fractal nature of the structure of acid casein gels Colloids and Surfaces 1990; 51:159–170.
23. Verheul M, Roefs SPFM, Mellema J, de Kruif KG. Power law behavior of structural properties of protein gels Langmuir 1988; 14:2263–2268.

24. Kantor Y, Webman I. Elastic properties of random percolating systems Phys Rev Lett 1984; 52:1891–1894.

25. Shih WH, Shih WY, Kim SI, Liu J, Aksay IA. Scaling behavior of the elastic properties of colloidal gels Phys Rev A 1990; 42: 4772–4779.

26. Wu H, Morbidelli M. A model relating structure of colloidal gels to their elastic properties Langmuir 2001; 17:1030–1036.

27. Mellema M, van Opheusden JHJ, van Vliet T. Categorization of rheological scaling models for particle gels applied to casein gels J Rheology 2002; 46:1–9.

28. de Rooij R, van den Ende MHG, Mellema J. Elasticity of weakly aggregating latex dispersions Phys Rev E 1994; 49:3038–3049.

29. Marangoni AG. Elasticity of high volume-fraction fractal aggregate networks: a thermodynamic approach Phys Rev B 2000; 62:13951–13955.

30. Narine SS, Marangoni AG. Mechanical and structural model of fat crystal networks at low deformations Phys Rev E 1990; 60:6991–7000.

31. Marangoni AG, Rogers MA. Structural basis for the yield stress in plastic disperse systems Applied Physics Letters 2003; 82: 3239–3241.

32. Avnir D, Biham O, Lidar D, Malcai O. Is the geometry of nature fractal? Science 1998; 279:39–40.

33. Mandelbrot BB. Is nature fractal Science 1998; 279:783–784.

34. Dietler G, Aubert C, Cannell DS, Wiltzius P. Gelation of colloidal silica Phys Rev Lett 1986; 57:3117–31120.

35. Mandelbrot BB. The fractal geometry of nature. New York: Freeman, 1982.

36. Julien R. Aggregation phenomena and fractal aggregates Contemp Phys 1987; 28:477–493.

37. Julien R, Botet R. Aggregation and Fractal Aggregates. Singapore: World Scientific, 1987.

38. Meakin P. Fractal aggregation Advances in Colloid and Interface Science 1988; 28:249–331.

39. Mellema M, Heesakkers JWM, van Opheusden JHJ, van Vliet T. Structure and scaling behavior of aging rennet-induced casein gels examined by confocal microscopy and permeametry Langmuir 2000; 16:6847–6854.

40. Viczek T. Fractal growth phenomena. Singapore: World Scientific, 1989.

41. Russ JC. Fractal surfaces. New York: Plenum Press, 1994.

13

Identifying Key Indicators of Mechanical Strength in Mixtures of Milk Fat Fractions and Cocoa Butter

ALEJANDRO G. MARANGONI

Department of Food Science
University of Guelph
Guelph, Ontario, Canada

SURESH S. NARINE

Agri-Food Materials Science Centre, Department of Agricultural, Food and Nutritional Science, University of Alberta
Edmonton, Alberta, Canada

INTRODUCTION

The macroscopic rheological properties of polycrystalline networks formed by lipids are of great importance in food products that contain significant amounts of fats. Such products include

butter, margarine, chocolate, peanut butter, cream cheese, and ice cream. Many of the sensory attributes such as spreadability, mouthfeel, texture, and snap are dependent on the mechanical strength of the underlying network of fat crystals [1–6]. In addition to this obvious industrial importance, fat crystal networks form a particular class of soft materials, which demonstrate a yield stress and viscoelastic properties, rendering these materials plastic. From a materials sciences point of view, therefore, these materials are also extremely important.

The mechanical properties of a fat crystal network are affected by many factors, including solid fat content (SFC), the polymorphism of the solid state, as well as the microstructure of the fat. The relative weight of each of these factors in influencing the mechanical response of the fat is, however, very system-dependent.

It is the purpose of this work to determine the effects of SFC, polymorphism, and network microstructure on the elasticity of blends of milk fat fractions and milk fat fractions with cocoa butter.

MATERIAL AND METHODS

Fats

In this study, we used binary mixtures of the high-melting fraction (HMF) of milk fat with the medium-melting fraction (MMF) of milk fat, as well as binary mixtures of HMF with commercially available cocoa butter (CB). The milk fat fractions were isolated by multiple-step solvent fractionation [7]. The chemical composition of these fractions has been reported previously [8].

Binary Phase Diagrams

Mixtures (w/w) of HMF in MMF were prepared in 10% increments from 0% to 100%. Fats were melted at 85°C for 15 minutes in order to destroy any crystal history, mixed in set proportions and mixed thoroughly by inversion and vortexing until homogeneous melt was attained. These mixtures did not phase-separate and were stable. The equilibrium SFC of the mixtures was determined from 0°C to 55°C in 5°C increments

as per the Official Method Cd16–81 of the American Oil Chemists' Society (Champlain, IL, USA). The SFC was determined by low-resolution pulsed nuclear magnetic resonance (pNMR) spectroscopy using a Bruker PC20 series NMR analyzer (Bruker, Milton, ON, Canada). In order to construct iso-solid phase diagrams, a cubic spline curve was fitted to the SFC-temperature data for interpolation purposes using the software package GraphPad Prism 3.0 (GraphPad Software, San Diego, CA, USA). Iso-solid SFC temperatures (temperature at which a specific SFC is observed) as a function of blend composition were derived from the curve fits and used in the construction of the binary phase diagrams. The method for the construction of such iso-solid phase diagrams was originally reported by Lambelet and Raemy [9]. Solid fat content determinations were carried out in duplicate and averaged.

Small Deformation Dynamic Rheology

Storage moduli (G′) were determined using a Carri-Med CSL^2 500 controlled-stress dynamic shear rheometer (TA Instruments, Mississauga, ON) at 22°C. Samples were melted at 85°C for 15 minutes in order to destroy any crystal history. Molten fat was then poured into plastic molds ($r = 10$ mm, $h = 3.2$ mm), allowed to crystallize isothermally at 22°C for 24 hours, and transferred to the rheometer prior to analysis. The bottom plate of the rheometer has a Peltier element that keeps the temperature constant to within 0.1°C of the set value. Sandpaper glued to the bottom plate and the fixture was used to minimize slippage. Storage moduli were determined from stress sweeps (20–14,000Pa) at a constant frequency of 1Hz. The value of G′ at 1043 Pa, corresponding to a shear strain of approximately 0.006%, is reported. This value is within the linear viscoelastic region of the material. Between 4 and 16 sample disks were analyzed for each mixture and the average and standard error reported.

Differential Scanning Calorimetry

Differential Scanning Calorimetry (DSC) pans with 7–10 mg of molten samples were heated for 15 minutes at 85°C and subsequently allowed to crystallize isothermally at 22°C for

24 hours in sealed aluminum pans. Pans were then placed in the calorimeter and were melted from 22°C to 70°C at a rate of 5°C/min. Differential scanning calorimetry was performed using a TA Instruments Q1000 differential scanning calorimeter (TA Instruments, Mississauga, ON, Canada).

Powder X-Ray Diffraction

Powder X-ray diffraction was carried out using a Rigaku Geigerflex D-Max II diffractometer (Rigaku, Japan) using a cobalt fine-focus source. Samples were crystallized as circular plates 25 mm in diameter, placed in the diffractometer, and scanned from 1 to 35 degrees, with 22 using a 0.004 degree step width and a 2 second time count. The power setting for the tubes were 40 kV and 25 mA. A one-sixth divergence slit was used. The receiving slit was 1 degree and the scatter slits 0.3 degree. The instrument was fitted with a graphite crystal monochromator.

Polarized Light Microscopy and Image Analysis

Crystal network microstructure was imaged by polarized light microscopy (PLM) using an Olympus BH light microscope. Samples were molten at 85°C for 15 minutes in order to destroy crystal history and 10:l of melt placed on a heated glass microscope slide. A heated glass coverslip was then carefully placed on top of the molten sample, creating a thin sample film of approximately 20-μm thickness. Samples were then allowed to crystallize for 24 hours at 22°C. Images of the crystal networks were acquired using a Sony XC-75 CCD video camera (Sony Corporation, Japan), an LG-2 PCI frame grabber and Scion Image software (Scion Corporation, Frederick, Maryland). An automatic blank field subtraction and averaging of 16 frames per image were performed using the computer software.

Mass fractal dimensions were determined from greyscale images using the box-counting algorithm available in the software package Benoit 1.3 (Truesoft International, St. Petersburg, FL, USA., www.trusoft-international.com). Values reported correspond to the means and standard errors for the analysis of three separate images from three different sample preparations.

RESULTS AND DISCUSSION

The storage modulus (G′) of HMF–MMF and HMF–CB mixtures increased as the proportion of HMF in the mixtures increased (Fig. 1). In order to explain the reason for this observed increase, several physical indicators of structure were assessed. Phase diagrams for both HMF–MMF (Fig. 2*A*) and HMF–CB (Fig. 2*B*) systems indicated montectic solution be-

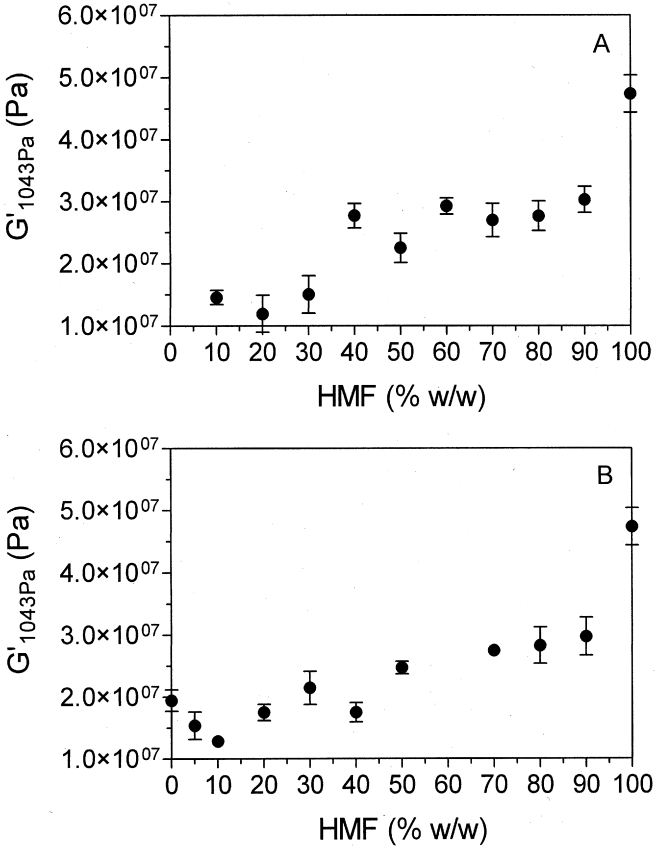

Figure 1 Changes in the shear storage modulus (G′) of (*A*) MMF–HMF and (*B*) CB–HMF systems as a function of the proportion (w/w) of HMF present in the mixture.

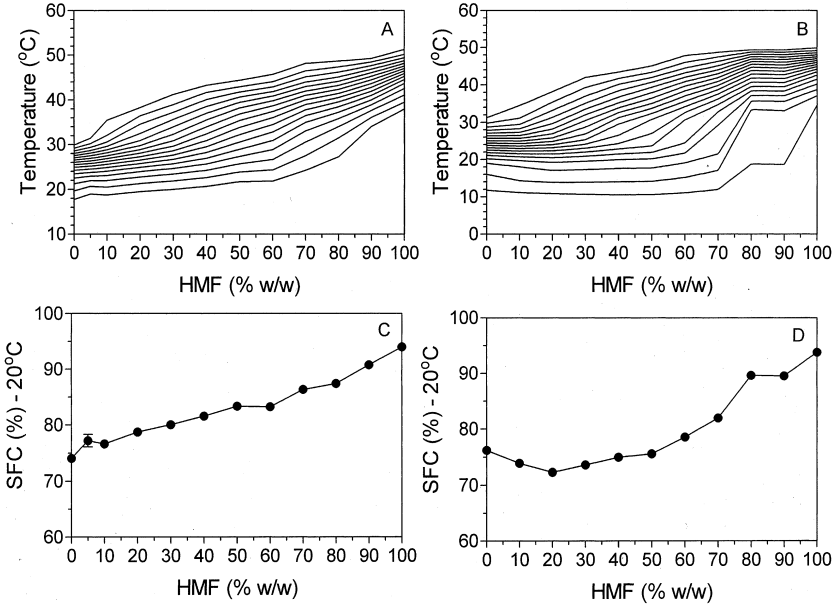

Figure 2 Iso-solid phase diagrams for (*A*) MMF–HMF and (*B*) CB–HMF binary mixtures. Changes in solid fat content (SFC) at 20°C as a function of the proportion of HMF present in the mixtures for (*C*) MMF–HMF and (*D*) CB–HMF binary mixtures.

havior for these binary mixtures. These patterns imply an apparent ideal solution behavior between the two substances and the formation of mixed crystals (solid solutions) in the solid state [10,11]. Generally, increases in G′ as a function of the proportion of HMF in both systems mirrored increases in SFC (Figs. 2*C* and 2*D*).

The structure of the solid state in both systems was characterized by powder X-ray diffraction. For the HMF–MMF mixtures, patterns were identical from 100% HMF to 70% HMF–MMF (Fig. 3*A*). The observed wide-angle reflections correspond to spacings at ~3.8Å and ~4.2Å, characteristic of a β′ polymorphic form (orthorhombic perpendicular subcell structure) [12–14]. The reflections at small angles correspond to the 001 (41Å) and 003 (14Å) planes of the triacylglycerol

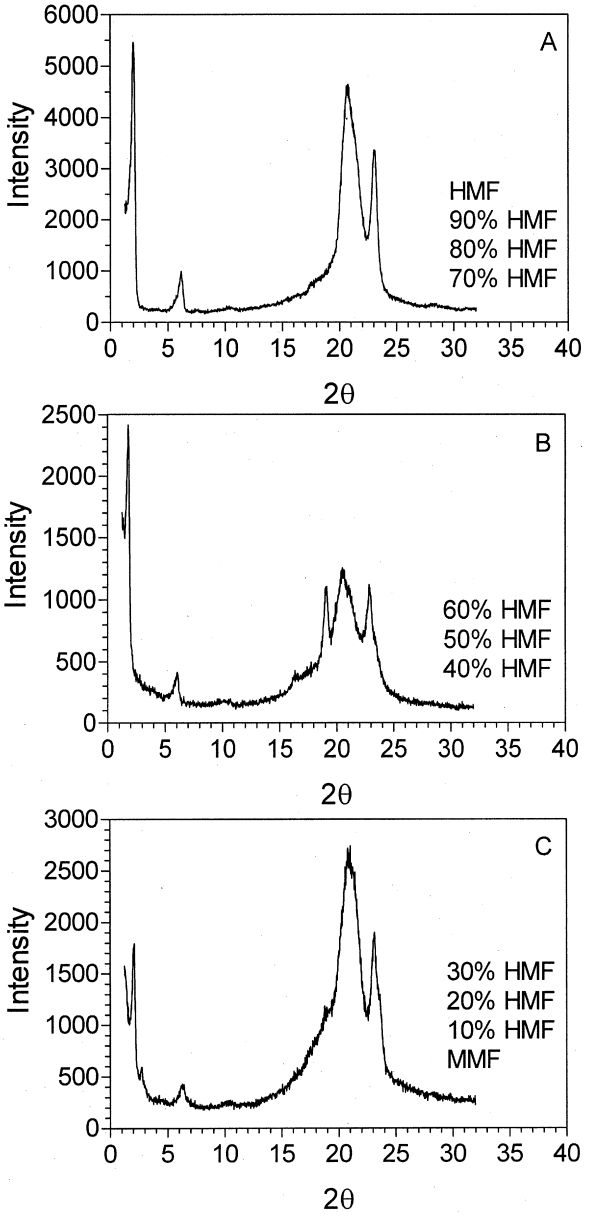

Figure 3 Powder X-ray diffraction patterns for the different MMF–HMF mixtures.

unit cell, which did not change either between 100% HMF and 70% HMF. Figures 3*B* and 3*C* show the powder XRD patterns observed for the remainder of the mixtures. Notice the appearance of a reflection corresponding to approximately 4.6Å for mixtures containing 40–60% HMF. This reflection is associated with the β polymorphic form (triclinic subcell structure [12–14]. Patterns for mixtures containing 30% HMF and less were similar to those containing high proportions of HMF, and were characteristic of the β′ polymorph.

Differential scanning calorimetry was used to monitor changes in the melting behavior of the mixtures. The melting behavior of the mixtures depends on crystal polymorphism, the chemical nature of the material, and the solution behavior between the major groups of triacylglycerols present. Figure 4 shows how melting profiles above approximately 60% HMF are dominated by HMF, while those below approximately 20% HMF are dominated by MMF. An intermediate region for mixtures ranging from approximately 30 to 50% HMF was also observed, with wide melting ranges and ill-defined melting peaks. This intermediate region corresponded well to that observed by powder XRD (Fig. 3*B*). In general, regions of characteristic melting behavior determined by DSC, corresponded to regions of characteristic polymorphism as determined by powder XRD.

Crystal polymorphic behavior is much richer in CB and its mixtures with HMF. Figure 5 shows typical powder XRD patterns for CB crystallized for 1, 7, and 20 days. Many interesting features are evident here. Cocoa butter crystallized statically at 22°C was in the β (triclinic subcell structure), as evidenced by the characteristic strong reflection at approximately 4.6Å. The minor peaks observed at wider angles help characterize specific subforms of the β polymorph [15]. In this sample we also detected two different families of unit cells with 001 reflections corresponding to about 66Å and 45Å. Empirical relationships exist between the number of carbons in triacylglycerols in the triclinic polymorphic form and the dimension of the long axis of the unit cell [13]. From this data, plus triacylglycerol single crystal studies [16–18], it is possible to approxi-

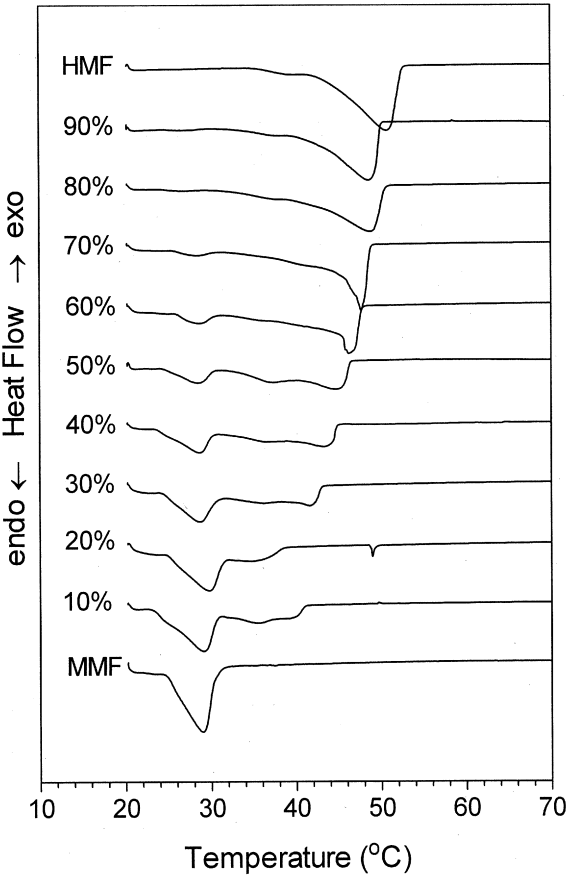

Figure 4 Differential scanning calorimetry traces for the different MMF–HMF mixtures.

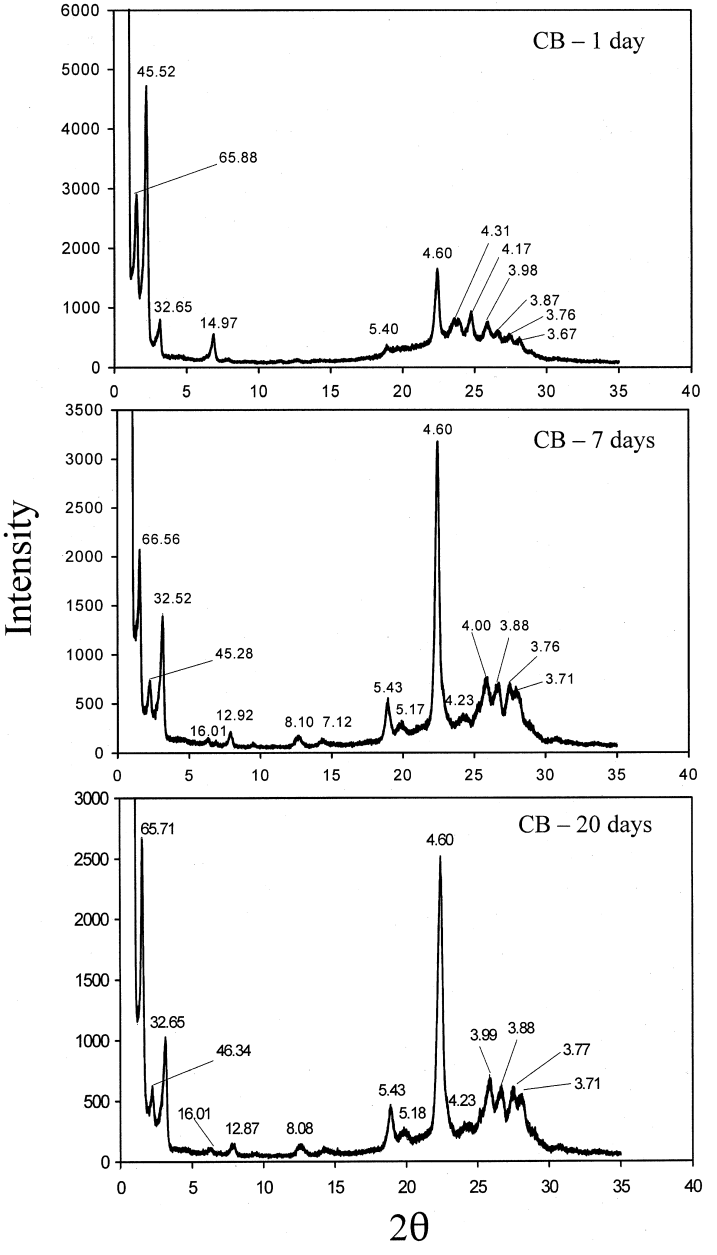

Figure 5 Powder X-ray diffraction patterns for cocoa butter (CB) crystallized at 22°C for (*A*) 1 day, (*B*) 7 days, and (*C*) 20 days.

mate the contribution of an ethylene group to the overall length of the long axis, or c axis, of the unit cells to about 2.5Å. The contribution of an ethylene group to the dimension of the long axis of long-chain normal paraffin hydrocarbons in an orthorhombic perpendicular subcell structure has been reported to be 2.5Å as well [19].

Thus, if homogeneous triacylglycerols containing predominantly 18-carbon fatty acids are stacked in a trilayer configuration, this would result in unit cells with a long axis of about 67.5Å. Bilayer stacking of triacylglycerol molecules would then result in a long axis of approximately 45Å. These fat crystal forms are therefore referred to as β-3 and β-2 forms, respectively. Both types of packing were observed in our CB samples (Fig. 5). Also evident were the 002 reflections of the β-3 polymorph and the 003 reflection of the β-2 polymorph after 1 day of crystallization. The assignment of higher-order reflections was more ambiguous, and was not attempted as it was not critical to our study. One clear effect was the growth of the β-3 polymorph characteristic patterns between 1 and 7 days of crystallization (Fig. 5). The trilayer structure (reflection at 66Å) became more prominent in this period, and so did the characteristic 4.6Å wide-angle refection of the β polymorph. Addition of HMF to CB, even at the 2% (w/w) level, profoundly affected the structure of the solid state of CB (Fig. 6). The intensities of both the 001 trilayer reflection at 66Å and the characteristic wide-angle reflection of the β polymorph (4.6Å) were drastically decreased on HMF addition. Interestingly, after 7 days, mixtures containing 2, 5, and 10% HMF reverted to the characteristic β-3 pattern of CB (Fig. 7). Mixtures containing 20%HMF crystallized in a β′-2 polymorphic form (Fig. 8). The reflection at approximately 45Å corresponds to the 001 reflection of a bilayer structure, while the reflection at approximately 15Å corresponds to the 003 reflection. The wide-angle reflections at approximately 3.8Å and approximately 4.2Å are characteristic of a β′ polymorph (orthorhombic perpendicular subcell structure). At this 20% (w/w) level of inclusion of HMF in CB, the system never managed to completely revert to the characteristic crystal form observed for CB. Between 7 and 20 days, though, the β-3 form did appear, albeit at low levels. At

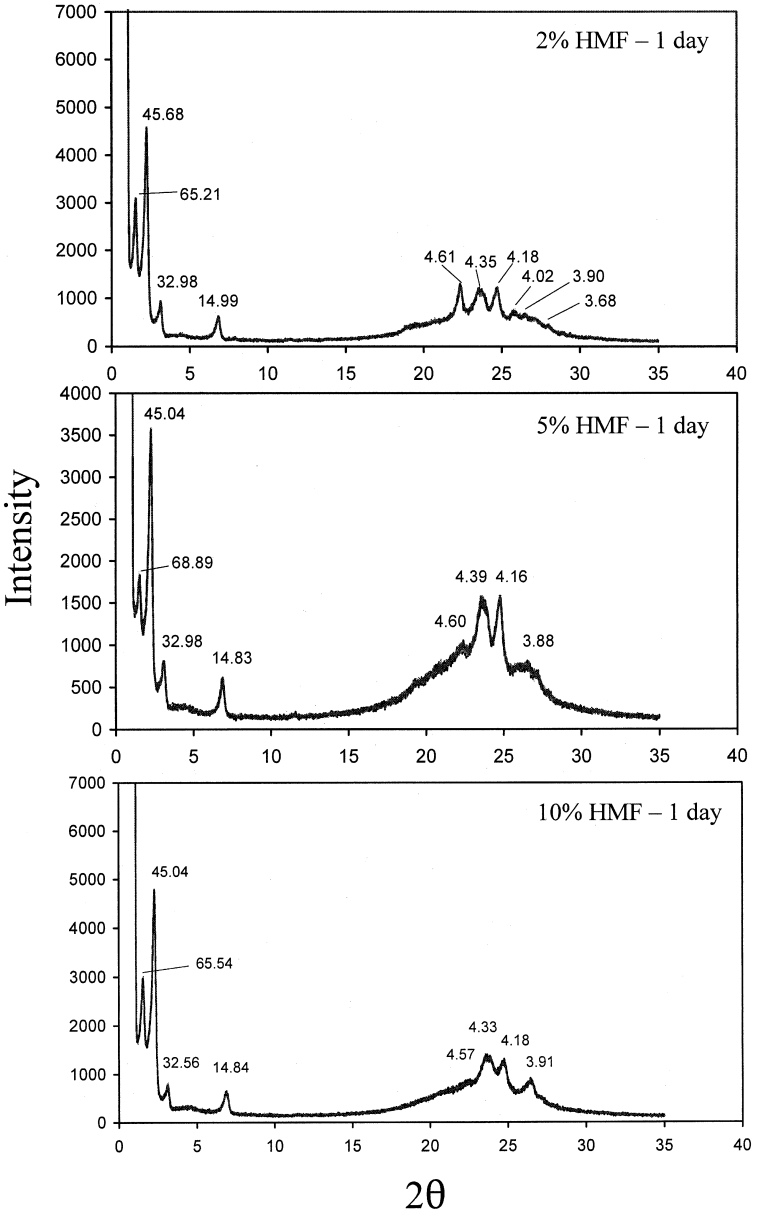

Figure 6 Powder X-ray diffraction patterns for (*A*) 2%HMF–CB, (*B*) 5% HMF–CB, and (*C*) 10% HMF–CB samples crystallized at 22°C for 1 day.

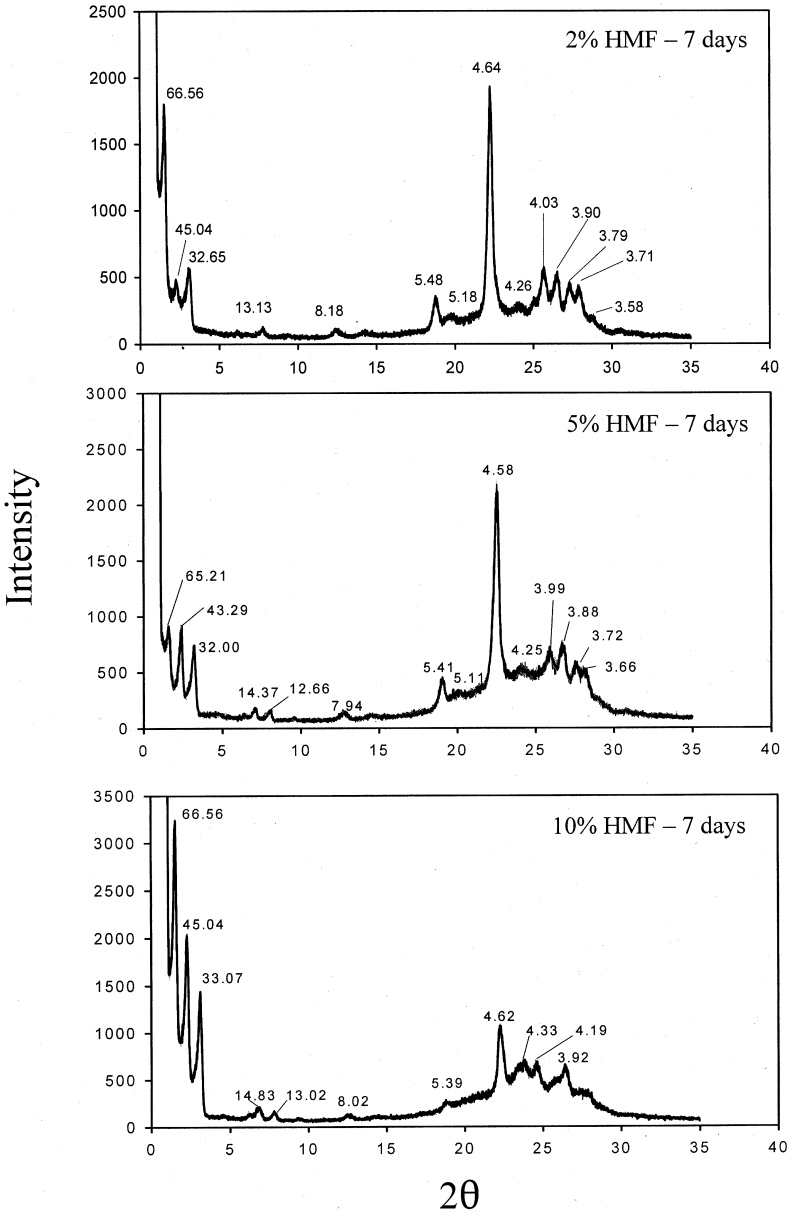

Figure 7 Powder X-ray diffraction patterns for (*A*) 2% HMF–CB, (*B*) 5% HMF–CB, and (*C*) 10% HMF–CB samples crystallized at 22°C for 7 days.

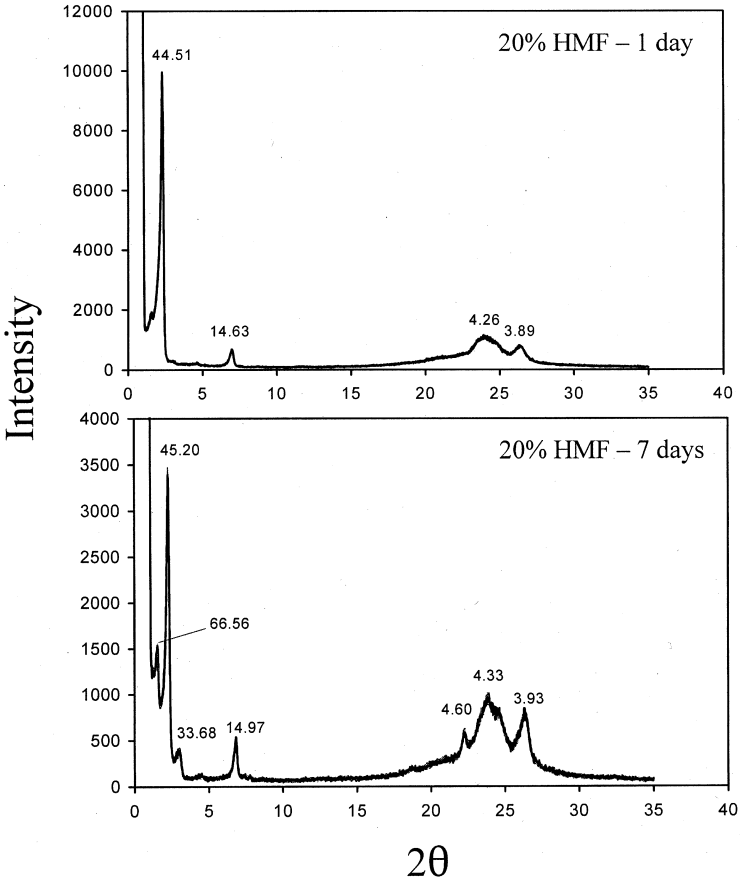

Figure 8 Powder X-ray diffraction patterns for 20% HMF–CB crystallized at 22°C for (*A*) 1 day and (*B*) 7 days.

all levels above 20% HMF, fat crystals were in a β′-2 polymorphic form (Fig. 9). Differential scanning calorimetry melting profiles (Fig. 10) basically showed regions where the melting behavior of the material was dominated by the HMF (100–60% HMF), a transitional region, where both the melting of HMF and cocoa butter were evident (50–30%HMF), and a third region, were the melting behavior was dominated by CB (10–0%HMF).

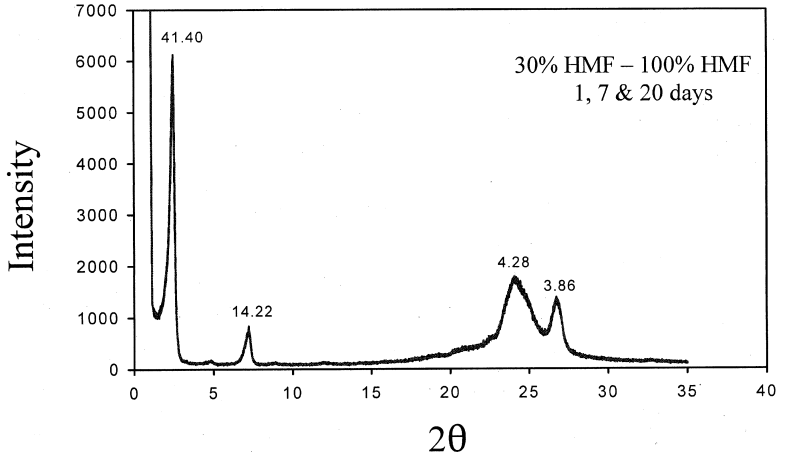

Figure 9 Powder X-ray diffraction patterns for 30–90% HMF–CB and HMF crystallized at 22°C for 1, 7, and 20 days.

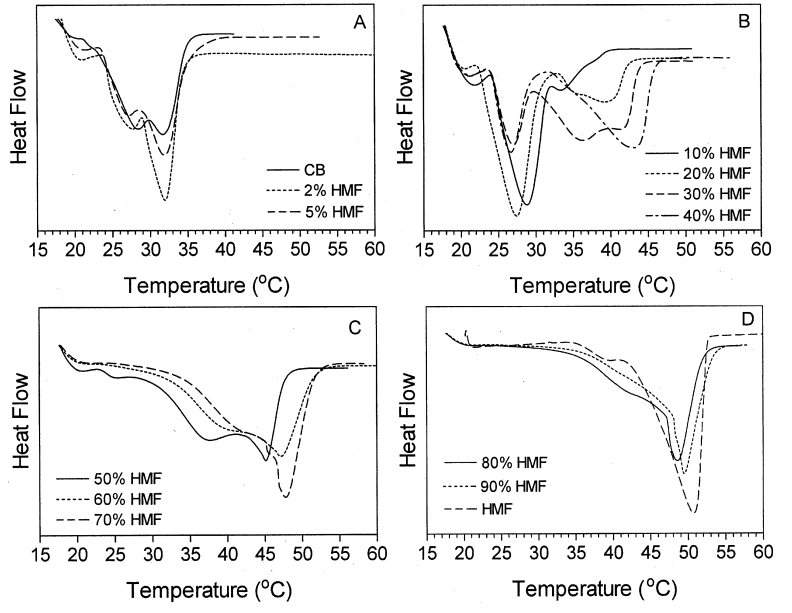

Figure 10 Differential scanning calorimetry traces for the different CB–HMF mixtures.

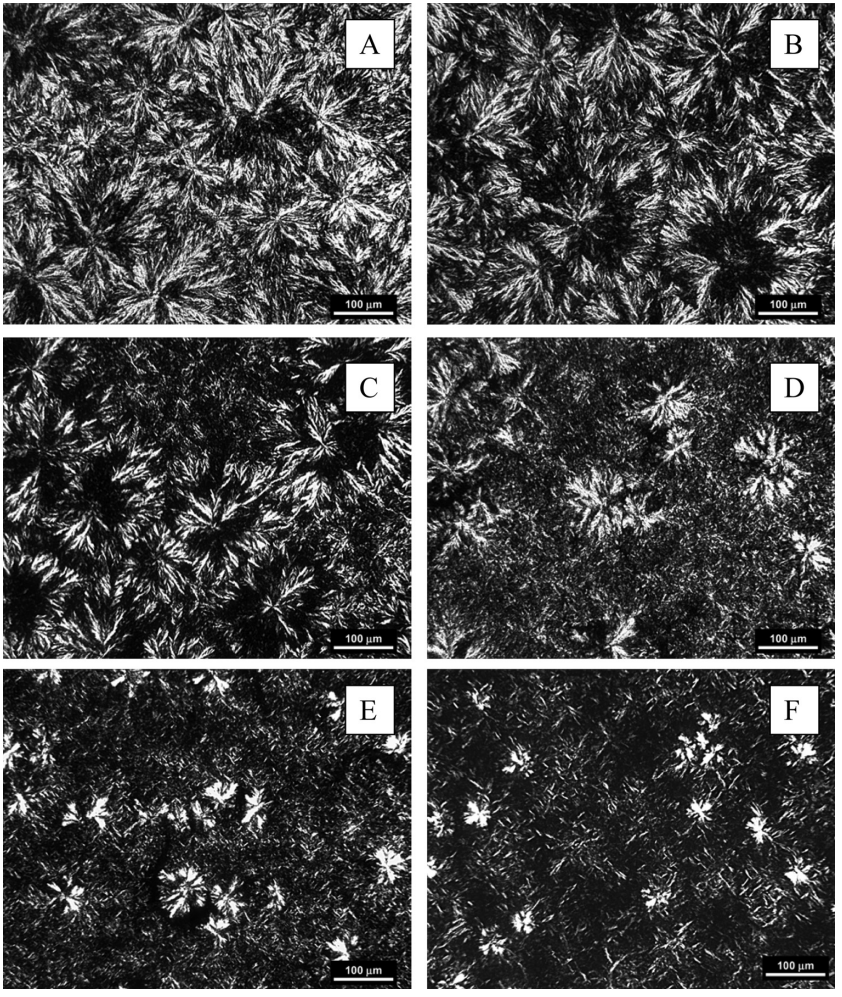

Figure 11 Polarized light micrographs of the different HMF–MMF mixtures crystallized in 20μm films under a coverslip at 22°C for 24 hours. (*A*) HMF, (*B*) 90% HMF–MMF, (*C*) 80% HMF–MMF, (*D*) 60–70% HMF–MMF, (*E*) 50% HMF–MMF, (*F*) 40% HMF–MMF, (*G*) 30% HMF–MMF, (*H*) 20% HMF–MMF, (*I*) 10% HMF–MMF, (*J*) MMF.

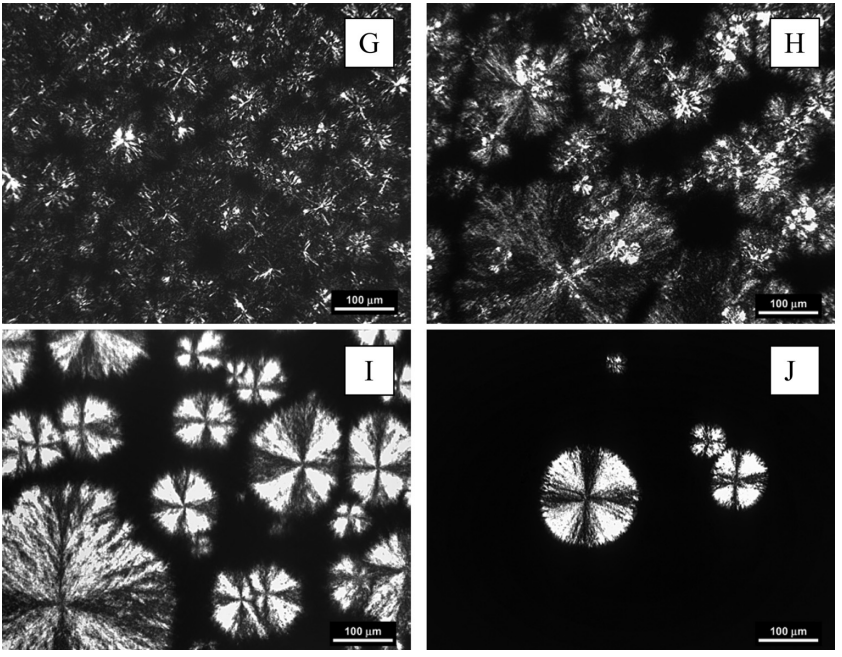

Figure 11 (Continued)

Microstructure clearly changed from 100% HMF through 100% MMF (Fig. 11), and 100% CB (Fig. 12). The spatial distribution of mass in the fat crystal networks, characterized by their mass fractal dimension, also changed for the different mixtures (Figure 13).

An interesting relationship between the mass fractal dimension and the polymorphism of the solid state become evident in this work. Changes in polymorphism, detailed earlier, were mirrored by changes in the box-counting dimension of the networks. Thus, it would seem that the initial events in the static crystallization process of these materials strongly influence heat and mass transfer events that eventually lead to the formation of a three-dimensional network of polycrystalline particles. Thus, under these conditions, the geometry of the network, i.e., the box-counting dimension, would be

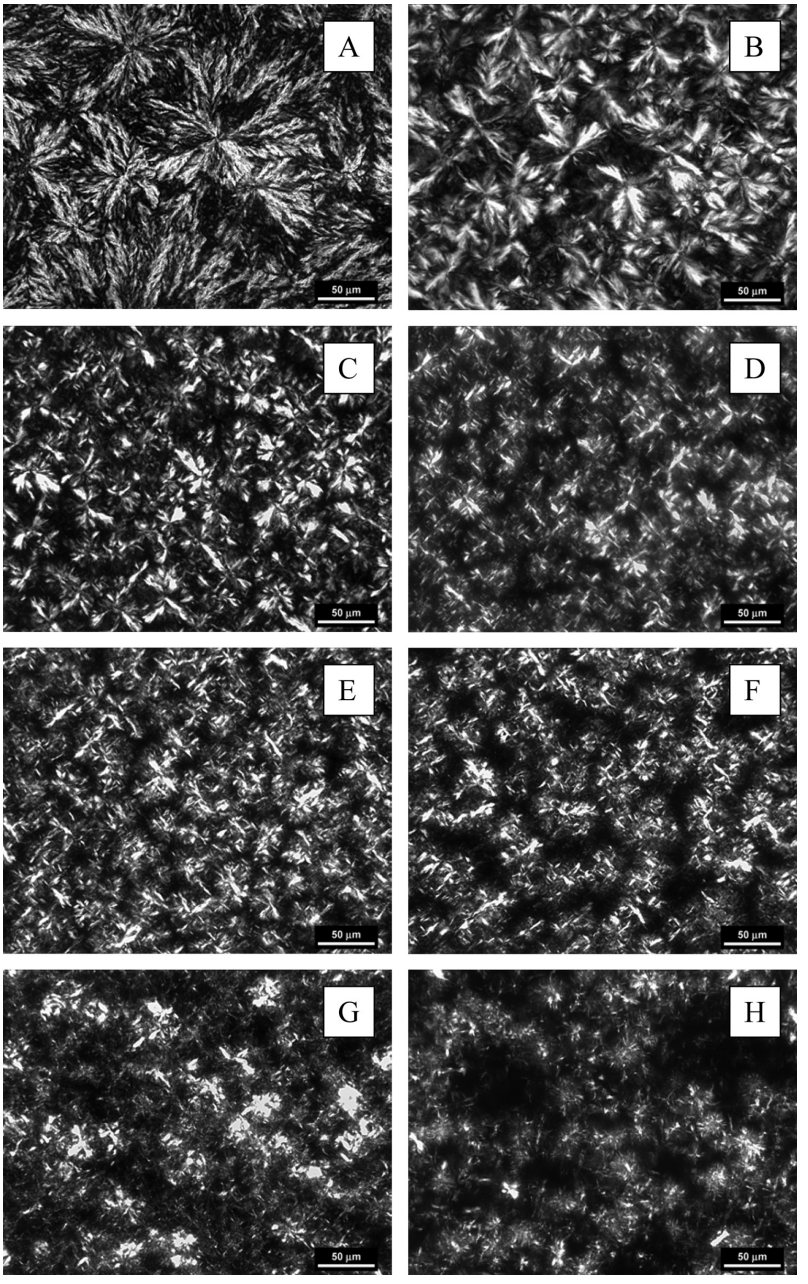

Figure 12 Polarized light micrographs of the different HMF-MMF mixtures crystallized in 20µm films under a cover-slip at 22°C for 24 hours. (*A*) HMF, (*B*) 80-90% HMF-CB, (*C*) 60-70% HMF-CB, (*D*) 50% HMF-CB, (*E*) 40% HMF-CB, (*F*) 20-30% HMF-CB, (*G*) 10% HMF-CB, (*H*) CB.

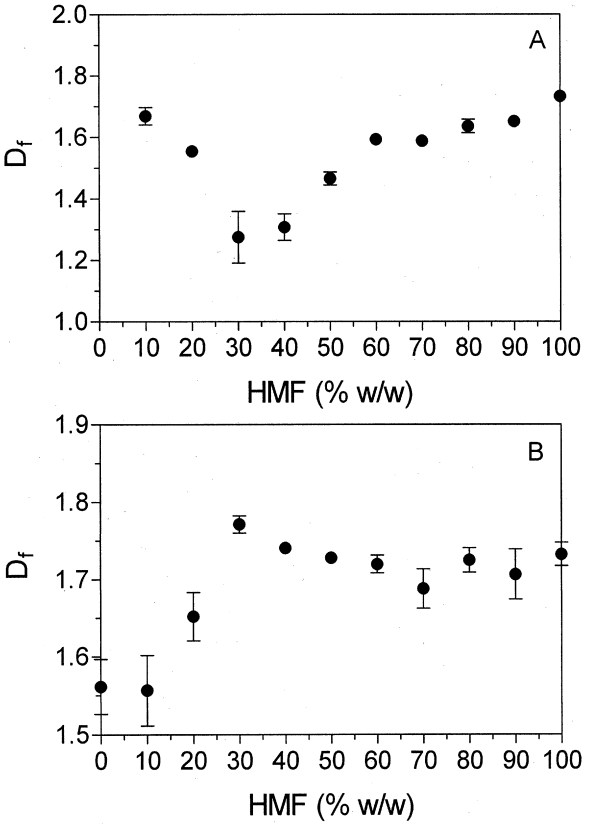

Figure 13 Changes in the box-counting mass fractal dimension as a function of the proportion of HMF present in mixtures of (*A*) MMF–HMF and (*B*) CB–HMF.

strongly influenced by the polymorphism of the solid state. However, neither of these two factors could be directly correlated to the mechanical response of the material (Fig. 1).

In this work we have shown that the mechanical properties of mixtures of milk fat fractions and cocoa butter are controlled mainly by their phase behavior, and not by the microstructure or polymorphism of the fat crystal network. The amount of solids present directly influences the elastic re-

sponse of the material, and thus knowledge of the molecular composition of the solid state is sufficient for the prediction of small deformation mechanical response in these systems.

REFERENCES

1. Heertje I. Microstructural studies in fat research Food Structure 1993; 12:77–94.

2. Juriaanse AC, Heertje I. Microstructure of shortenings, margarine and butter—a review Food Microstructure 1988; 7: 181–188.

3. Narine SS, Marangoni AG. Relating structure of fat crystal networks to mechanical properties: a review Food Res Inter 1999; 32:227–248.

4. Wright AJ, Scanlon MG, Hartel RW, Marangoni AG. Rheologic properties of milkfat and butter J Food Sci 2001; 66:1056–1071.

5. Narine SS, Marangoni AG. Structure and mechanical properties of fat crystal networks Advances in Food and Nutrition Research 2002; 44:33-145.

6. DeMan JM, Beers AM. Fat crystal networks: structure and rheological properties J Texture Studies 1987; 18:303–318.

7. Marangoni AG, Lencki RW. Ternary phase behavior of milk fat fractions J Agric Food Chem 1998; 46:3879–3884.

8. Wright AJ, McGauley SE, Narine SS, Willis WM, Lencki RW, Marangoni AG. Solvent effects on the crystallization behavior of milkfat fractions J Agric Food Chem 2000; 48:1033–1040.

9. Lambelet P, Raemy A. Iso-solid diagrams of fat blends from thermal analysis data J Amer Oil Chem Soc 1983; 60:845–847.

10. Timms RE. Phase behavior of fats and their mixtures Prog Lipid Res 1984; 23:1–38.

11. Rossel JB. Phase diagrams of triglyceride systems. In: Advances in lipid research Paoletti R, Kretchevsky D, Eds. Vol. 5. New York: Academic Press, 1967:353–408.

12. Chapman D. The polymorphism of glycerides Chem Rev 1962; 62:433–456.

13. Small DM. The physical chemistry of lipids. New York: Plenum Press, 1986:345.

14. Garti N, Sato K. Crystallization and polymorphism of fats and fatty acids. New York: Marcel Dekker:1988.

15. Larsson K. Lipids—molecular organization, physical functions and technical applications. Dundee: The Oily Press:1994.

16. Vand V, Bell IP. A direct determination of the crystal structure of the β form of trilaurin Acta Cryst 1951; 4:465–469.

17. Jensen LH, Mabis AJ. Refinement of the structure of β-Tricaprin Acta Cryst 1966; 21:770–781.

18. Doyne TH, Gordon JT. The crystal structure of a diacid triglyceride J Amer Oil Chem Soc 1968; 45:333–334.

19. Bunn CW. The crystal structure of long-chain normal paraffin hydrocarbons. The shape of the $>CH_2$ group Trans Faraday Soc 1939; 35:482–491.

14

The Functionality of Milk Fat Fractions in Confectionery and Plastic Fats

ALEJANDRO G. MARANGONI

Department of Food Science
University of Guelph
Guelph, Ontario, Canada

1. INTRODUCTION

The physical properties of chocolate are largely determined by the physical properties of the underlying fat phase [1]. In milk chocolate, cocrystallization of cocoa butter triacylglycerols (TAGs) and milk fat TAGs takes place; this cocrystallization is a key factor influencing the appearance and physical properties of milk chocolate [2]. However, the amount of milk fat that can be added to chocolate is limited by the thermodynamic incompatibility between milk fat and cocoa butter TAGs in the solid state. Because of molecular geometric constraints, as well as environmental factors that influence the kinetics of crystal-

lization, milk fat and cocoa butter TAGs do not form mixed crystals—they crystallize as separate milk fat and cocoa butter solids. This thermodynamic incompatibility results in the formation of a eutectic—a decrease in the melting point of the cocoa butter–milk fat mixture below the melting point of either of the two components. The formation of this eutectic, therefore, leads to a decrease in the hardness of the milk chocolate [3–10]. The exact amount of milk fat that can be added to chocolate before the functional properties of the material are significantly and adversely affected will depend on processing conditions, such as tempering times and temperatures. Reddy et al. [8] reported the successful production of milk chocolates containing 40% (w/w of the total fat) milk fat with good gloss and demolding properties.

Besides the obvious advantages of adding milk fat to chocolate, milk fat is known to reduce the incidence of bloom formation in chocolate. Fat bloom is a defect of chocolate that results in a white-gray appearance and crumbly texture. Addition of milk fat and milk fat fractions is known to decrease the incidence of bloom in chocolate [10–13]. Bloom formation is a problem mainly associated with dark chocolate. Some manufacturers, therefore, add 2–3% milk fat to dark chocolate to control hardness and delay bloom formation [14].

Milk fat is a complex mixture of several hundred different triacylglycerols with an extremely heterogeneous fatty acid composition [15]. Undoubtedly, it is one of the most complex fats found in nature. The physical properties of milk fat, including melting behavior, solid fat content (SFC), and polymorphism, are not only dependent on the physical and chemical properties of the constituent TAGs, but also on the interaction between these constituent TAGs. For these reasons, several studies have been performed in the past to understand how TAG structure influences phase behavior and polymorphism of milk fat [16–21]. A typical melting curve of untempered native milk fat determined using differential scanning calorimetry (DSC) shows three endothermic peaks, corresponding to high- (HMF) ($>50°C$), medium- (MMF) (35–40°C) and low- (LMF) ($<15°C$) melting fractions [18]. From DSC measurements (ratios of enthalpies), Timms [18] determined

that milk fat contains 11% HMF, 23% MMF, and 66% LMF [18]. Marangoni and Lencki [20] reported 12% (w/w) HMF, 33% (w/w) MMF, and 55% (w/w) LMF yields from solvent fractionation experiments. These fractions are chemically distinct, with HMF containing principally long-chain saturated fatty acids, MMF containing two long-chain saturated fatty acids and one short, or *cis*-unsaturated, fatty acid, and LMF containing one long-chain saturated fatty acid and two short-chain, or *cis*-unsaturated, fatty acids [18,20].

Knowledge of the chemical composition, phase behavior, and polymorphism of these fractions and their mixtures, and how their properties influence each other, will help us to better understand, predict, and control the physical properties of milk fat and mixtures of milk fat with other fats. To obtain this understanding, milk fat must first be efficiently separated into three fractions and the phase behavior and polymorphism of the individual fractions determined. Timms [18] fractionated milk fat into three fractions using acetone as a solvent and proved that HMF, MMF, and LMF were, in fact, distinct fractions (at the time, MMF was believed to be a solid solution of HMF and LMF). He also studied the polymorphism of these fractions, and the effects of LMF addition to HMF (50% LMF) and MMF (75% LMF). Marangoni and Lencki [20] fractionated milk fat into three major fractions using ethyl acetate as the solvent and studied the binary and ternary phase behavior of mixtures of these three fractions.

Isosolid diagrams are useful tools in the study of the phase behavior of mixtures of natural fats [19]. These isosolid diagrams have been used in the study of the phase behavior of mixtures of confectionery fats with milk fat and milk fat fractions [3,4,10,22,23]. The type of solution behavior can usually be discerned with the aid of these diagrams. Their main use in this area has been in the identification of eutectics in mixtures of cocoa butter and cocoa butter substitutes with milk fat and milk fat fractions. This procedure constitutes a useful way of qualitatively judging the compatibility of fats.

The phase behavior of mixtures of cocoa butter and milk fat, fractionated, and interesterified milk fat was originally studied by Timms [3,4]. More recently, the phase behavior of

binary and ternary mixtures of confectionery fats with milk fat and milk fat fractions has also been determined [7,10,23]. A better understanding of the complex interactions between milk fat TAGs, cocoa butter TAGs, and palm kernel stearin TAGs, and the resulting macroscopic properties of the blends (melting behavior, bloom formation, softening) has been obtained from these studies.

Because of the very high propensity of milk fat triglycerides to form mixed crystals [16,20], fractionation processes based on melt crystallization are not very efficient. Milk fat fractions obtained from the melt have different properties than those obtained by solvent crystallization. It would not be possible to do justice to the large field of milk fat fractionation in this short report. The readers are directed to the comprehensive work of Kaylegian and Lindsay [24] on milk fat fractionation and fraction utilization in food products. It is the purpose of this research to study the phase behavior of solvent fractionated milk fat fractions–cocoa butter mixtures in order to evaluate their potential utilization as ingredients in confectionery products and plastic fats.

MATERIALS AND METHODS

Multiple-Step Solvent Fractionation

Anhydrous milk fat (AMF) (200 g) was melted above 80°C, cooled to 40°C, and dissolved (1:4 w/w) in room temperature ethyl acetate (Fisher Scientific, St. Louis, MO). The mixture was then transferred to a glass bottle and placed in a thermostated water bath at 5°C for one hour. The mixture was mixed by inversion every 5 minutes and vacuum-filtered at 5°C using a Buechner funnel. A fast filtering Whatman #1 filter paper was used for this purpose. The collected crystal mass was immediately washed with 200 mL of 5°C ethyl acetate. The crystal mass was completely white and devoid of entrained material after this process. This fraction will be referred to as the HMF. The filtrate-plus-washes were transferred to a glass bottle, which was then placed in a stainless steel bucket filled with ethylene glycol (for improved heat transfer) in a freezer

at −28°C for one hour. The mixture was mixed by inversion every 10 minutes and vacuum-filtered at −28°C using a Buechner funnel. A fast filtering Whatman #1 filter paper was used for this purpose. The collected crystal mass was immediately washed with 400 mL of −28°C ethyl acetate. The crystal mass was completely white and devoid of entrained material after this wash. This fraction will be referred to as the MMF. The wet crystal masses were spread as a thin film on stainless steel trays and the excess solvent allowed to evaporate overnight at room temperature in a fume hood. The excess solvent present in the −28°C filtrate and washes was removed by vacuum distillation in a rotary evaporator at 40°C. This yellow liquid was then spread as a thin film on a stainless steel tray and the solvent allowed to evaporate overnight at room temperature in a fume hood. This fraction will be referred to as the LMF.

Chemical and Physical Characterization of the Milk Fat Fractions

Solid fat content was determined by pulsed nuclear magnetic resonance (pNMR) using a Bruker PC20 Series NMR Analyzer (Bruker, Milton, ON, Canada) according to the American Oil Chemists' Society (AOCS) Official Method Cd16-81. Dropping point and hardness index determinations were determined as described in Rousseau et al. [25] at 22°C. Differential scanning calorimetry was carried out as previously described [26] using a Dupont 2090 DSC instrument (TA Instruments, Mississauga, ON). Samples were melted at 60°C in DSC aluminum pans for 30 minutes, cooled at a rate of 5°C per minute to −40°C, and immediately heated at a rate of 5°C per minute until the material was completely melted again. Two to three replicate experiments were carried out simultaneously and the averages and standard deviations reported.

Phase Equilibrium Studies

Mixtures (w/w) of HMF, MMF, and LMF with cocoa butter were prepared in 10% increments from 0% to 100%. The solid fat content (SFC) and dropping points of the mixtures were determined from 0°C to 55°C in 5°C increments. A point-to-

point spline curve was fitted to the data for interpolation purposes using the software package GraphPad Prism 2.0 (GraphPad Software, San Diego, CA, USA). Isosolid SFC temperatures, as a function of blend composition, were derived from the data and used in the construction of the binary phase diagrams, from 100% SFC (solidus line) to 0% SFC (liquidus line) in 5% SFC intervals. Two to three replicate experiments were carried out simultaneously and the averages and standard deviations reported.

RESULTS AND DISCUSSION

The SFC vs. temperature profiles of the HMF, MMF, and LMF fractions in milk fat, anhydrous native milk fat (AMF), and cocoa butter (CB) are shown in Figure 1. Both the HMF and MMF have narrow melting ranges, and the LMF is completely liquid above 0°C. The dropping points of the HMF, MMF, and LMF were, respectively, 51.7°C, 30.4°C, and 12.5°C, while that of native AMF was 34.3°C and cocoa butter, 27.6°C. Of particular interest is the similarity between the melting profiles of cocoa butter and MMF.

The fatty acid and triacylglycerol compositions of the three milk fat fractions, AMF, and CB are presented in

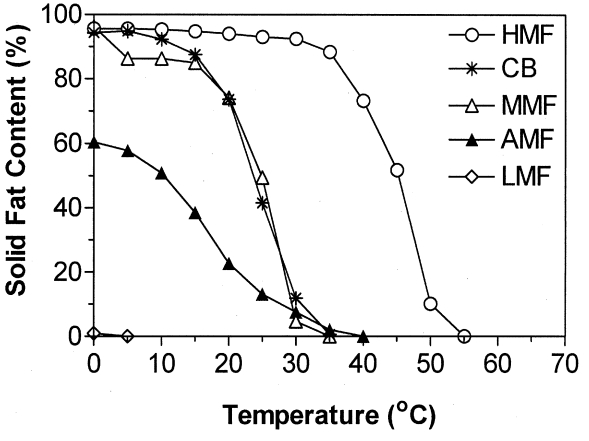

Figure 1 Solid fat content – temperature profiles for the different fats used in this study.

Tables 1 and Tables 2, respectively. Table 3 shows the region-specific distribution of fatty acids within TAG molecules in AMF, HMF, MMF, and CB. The characteristic feature of CB is the saturated-unsaturated-saturated (SUS) structure of its TAGs, where positions sn-1,3 are usually occupied by palmitic or stearic acids, while position sn-2 is almost exclusively occupied by oleic acid. For our purposes, HMF can be considered as a long-chain trisaturate. The conformation of TAG molecules within a crystal is reminiscent of a tuning fork, with fatty acids at positions sn-1,3 oriented parallel to the direction of the long axis of the unit cell. In this conformation, the fatty acid at position sn-2 is also oriented parallel to the direction of the long axis of the unit cell, resulting in a tuning fork–like TAG structure. One could then possibly predict a strong molecular interaction along the long molecular axis formed by the sn-1 and sn-3 fatty acid chains. Using computer modeling, it is also possible to predict favorable interactions between the sn-2

Table 1 Fatty Acid Composition (%w/w) of Ethyl-Acetate Fractionated Anhydrous Milk Fat (AMF) Fractions, AMF, and Cocoa Butter (CB)

Fatty Acid	HMF	MMF	LMF	AMF	CB
4:0	–	4.78	5.24	4.51	–
6:0	0.19	3.50	3.80	3.12	–
8:0	0.34	1.45	2.03	1.64	–
10:0	1.74	3.18	4.43	3.86	–
10:1	0.09	0.47	0.67	0.80	–
12:0	3.60	3.06	4.78	4.07	–
14:0	15.40	11.82	11.14	10.99	–
14:1	0.84	1.25	2.07	1.88	–
15:0	1.77	1.51	0.88	1.46	0.1
16:0	42.50	39.46	19.84	28.73	26
16:1	1.69	1.70	3.59	3.12	0.2
17:0	0.92	0.91	0.83	0.40	–
18:0	20.55	13.63	6.00	10.45	35
18:1	9.30	12.31	29.61	20.92	34
18:2	0.54	0.44	2.17	1.86	3.5
18:3	0.39	0.23	1.38	1.65	–
20:0	0.20	0.50	1.57	0.60	0.6

Table 2 Triglyceride (TAG) Composition (%w/w) of Ethyl-Acetate Fractionated Anhydrous Milk Fat (AMF) Fractions, Native AMF, and Cocoa Butter (CB)

Carbon #	HMF	MMF	LMF	AMF	CB
22	–	0.06	–	0.24	–
24	–	0.72	1.02	0.84	–
26	–	0.24	0.6	0.37	–
28	–	0.17	1.26	0.60	–
30	–	0.18	2.37	1.04	–
32	0.20	0.62	4.74	2.64	–
34	0.64	4.94	8.16	6.40	–
36	1.05	18.18	13.37	14.04	–
38	0.73	17.59	18.72	14.73	–
40	0.96	11.14	14.73	10.78	–
42	3.23	8.90	7.66	7.69	–
44	9.23	6.98	5.66	6.91	–
46	19.13	6.10	4.80	7.42	–
48	25.67	7.84	4.34	8.63	0.1
50	24.00	9.79	5.14	9.60	16.5
52	12.25	6.04	6.28	6.42	45.8
54	1.03	0.57	1.18	1.68	36.1
56	–	–	–	–	1.5

Table 3 Fatty Acid Distribution (mol%) of HMF, MMF, AMF and CB

Fatty Acid	HMF		MMF		AMF		CB	
	sn-1+3	sn-2	sn-1+3	sn-2	sn-1+3	sn-2	sn-1/3	sn-2
4:0	—	—	20.0	—	—	18.4	—	—
6:0	0.5	1.3	0.4	1.0	—	4.2	—	—
8:0	1.7	8.5	1.1	2.6	—	2.2	—	—
10:0	0.8	5.3	1.7	3.0	4.1	3.9	—	—
12:0	3.4	7.5	3.0	5.6	8.3	3.5	—	—
14:0	11.6	15.9	9.1	16.4	19.2	18.8	—	—
16:0	38.0	30.0	30.0	45.8	35.7	20.4	34/37	2
18:0	28.2	15.3	15.3	17.3	11.5	9.4	50/53	2
18:1	15.9	16.2	20.2	8.2	21.0	19.3	12/9	87
18:2	—	—	—	—	—	—	1/–	9
18:3	—	—	—	—	—	—		

oleic acid in CB TAGs and the sn-1 or sn-3 long-chain saturated fatty acids in the HMF TAGs (results not shown). In both CB and HMF TAGs, the long molecular axis is formed by long-chain saturated fatty acids. Intermolecular London dispersion forces would therefore be strong, and mixed crystal formation plausible. One could also envision that, if positions sn-1 or sn-3 would be occupied by short chain fatty acids or oleic acid, as in the case of MMF TAGs, intermolecular interactions would be hindered and mixed crystal formation would be less likely to occur.

Figure 2 shows DSC crystallization and melting thermograms of HMF, MMF, and LMF, respectively. The purity of the fractions is testament to the efficiency of the ethyl-acetate solvent fractionation process. This kind of fraction purity is not achievable using dry fractionation (melt crystallization) protocols.

A eutectic occurs when the melting point of a mixture is below the melting point of either of the individual components. Figure 3 shows the dropping points for mixtures of HMF with MMF, HMF with LMF, and MMF with LMF. On average, these mixtures displayed monotectic solution behavior. The situation for CB-AMF and milk fat fraction mixtures was, however, different. Changes in dropping points as a function of mixture composition are shown in Figure 4. Evident eutectics were detected in the range 0–30% AMF-CB and 0–60% MMF-CB. No eutectics were observed for HMF-CB mixtures, in contrast to work reported by Bystrom and Hartel [7], who reported the formation of a strong eutectic between CB and HMF. This effect was probably due to the fact that fractions used in their study were obtained via melt crystallization and significant amounts of MMF were probably present (discussed later). In order to confirm these findings, isosolid diagrams were generated for the different mixtures.

These isosolid diagrams for AMF-CB, MMF-CB, and HMF-CB mixtures are shown in Figure 5. A slight eutectic formation was evident in the AMF-CB system (Fig. 5*C*), while extreme thermodynamic incompatibility was evident in the MMF-CB mixtures (Fig. 5*B*). From the isosolid diagram, it was obvious that any mixture of CB and milk fat's MMF formed a

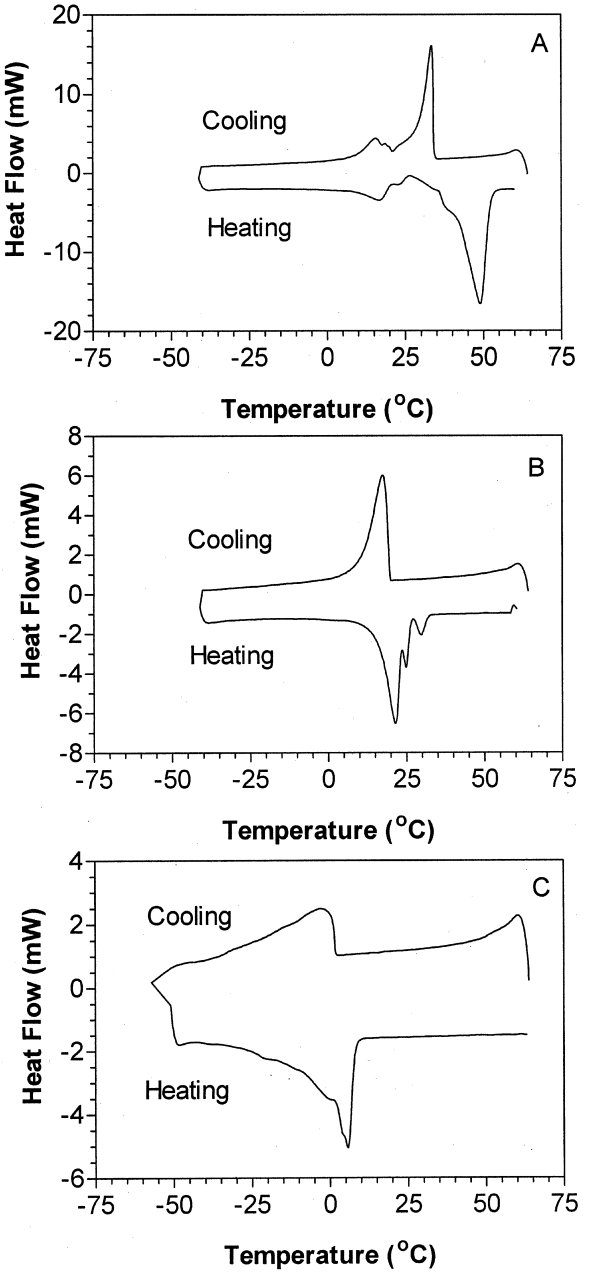

Figure 2 Differential scanning calorimetric thermograms for the crystallization (upon cooling) and melting (upon heating) of HMF (**A**), MMF (**B**) and LMF (**C**).

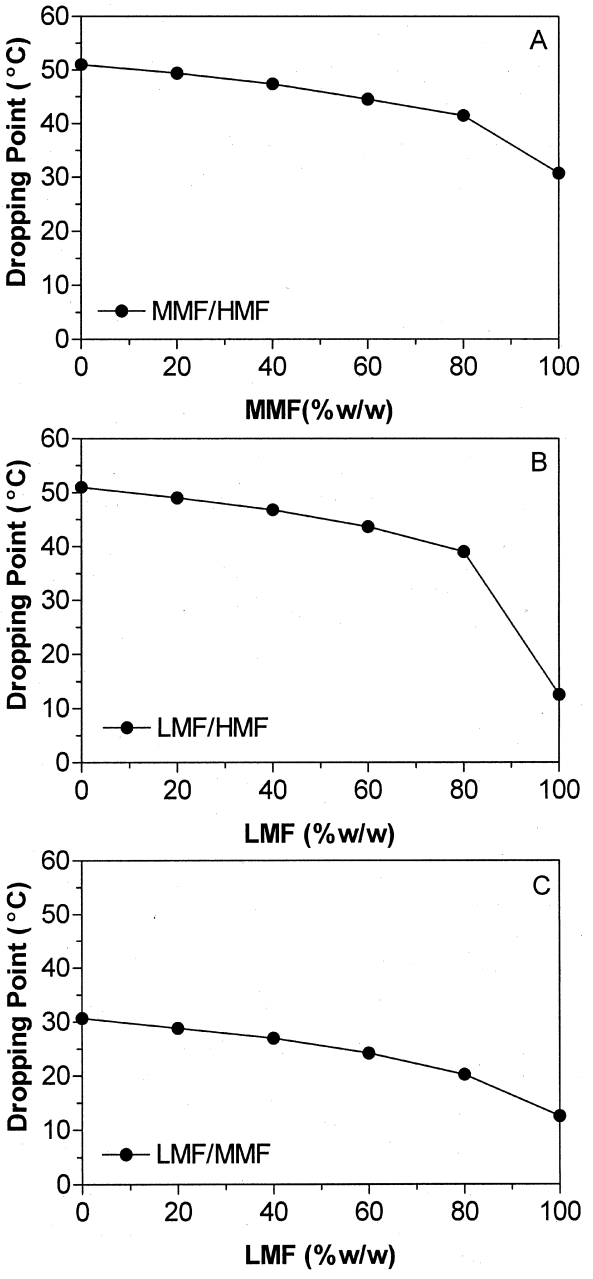

Figure 3 Changes in the dropping point of fraction mixtures as a function of composition.

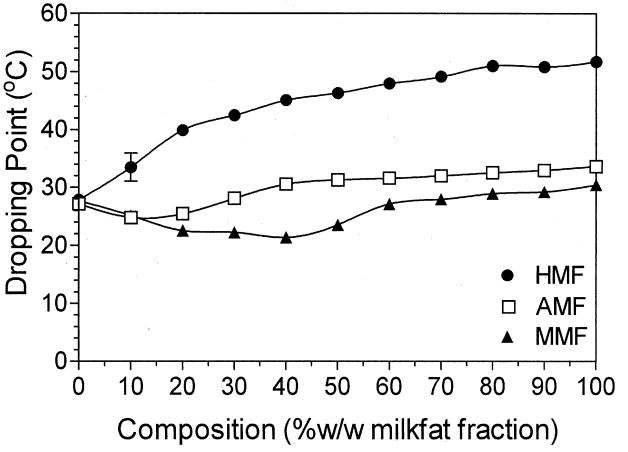

Figure 4 Changes in dropping point as a function of composition for mixtures of cocoa butter with milkfat (AMF) and milkfat fractions (HMF, MMF).

eutectic. No eutectics were formed between cocoa butter and milk fat's HMF (Fig. 5*A*). The patterns observed for the CB-HMF system are reminiscent of monotectic, partial solid solution formation [19], where a slight amount of thermodynamic incompatibility between the two components is evident. Kaylegian et al. [22] reported similar behavior for CB-HMF and CB-MMF mixtures using milk fat fractions obtained using acetone fractionation.

The dropping-point data and the isosolid diagrams agreed qualitatively. HMF and CB TAGs are thermodynamically compatible and no eutectic is formed. MMF TAGs are, however, extremely incompatible with CB TAGs. The eutectic in the AMF-CB mixtures most likely arises from the incompatibility between MMF and CB. Our results disagree with the data reported by Bystrom and Hartel [7], who reported on the thermodynamic incompatibility between HMF obtained via a dry fractionation process and cocoa butter. Most likely, their HMF fraction was contaminated with MMF, giving rise to the reported patterns. Work by the same group on the same year [13] reported that HMF obtained by solvent fractionation did not decrease hardness of cocoa butter, probably suggesting

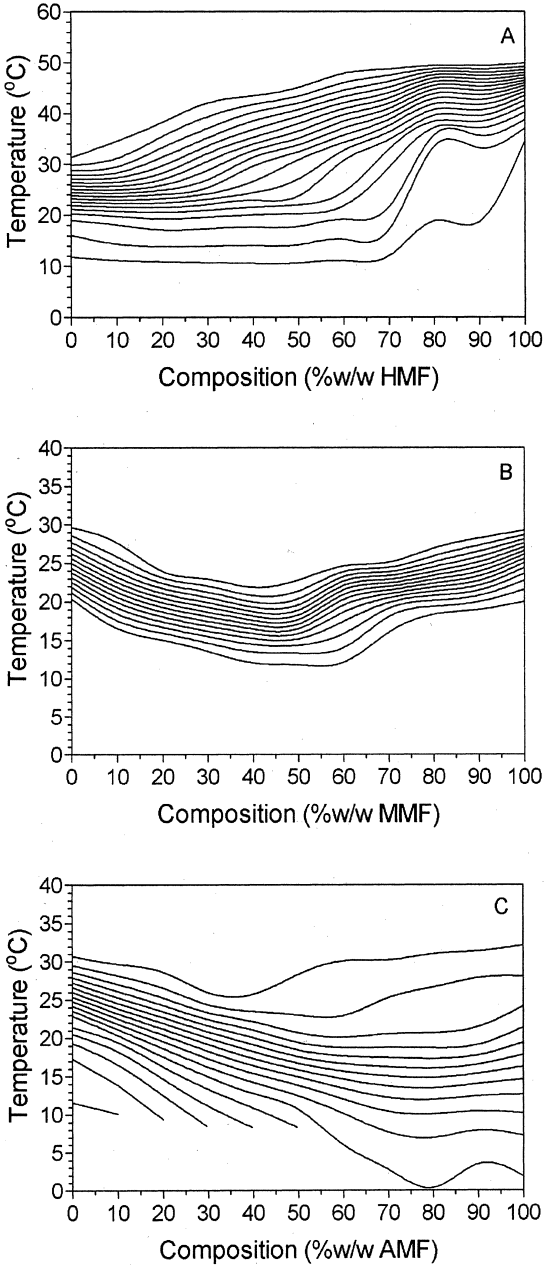

Figure 5 Isosolid diagrams for mixtures of cocoa butter with A)HMF, B)MMF, and C) AMF.

that eutectics were not formed for cocoa butter mixtures containing HMF obtained via solvent fractionation.

Figure 6 exemplifies the problem of the addition of milk fat and milk fat fractions to cocoa butter. After 24 hours of crystallization at 22°C, addition of 10% and 40% (w/w) AMF or MMF to cocoa butter significantly decreased the hardness of the material, while HMF addition did not. After 48 hours of tempering, 40% cocoa butter mixtures containing AMF or MMF were still very soft, while mixtures containing 10% AMF or MMF did not appear softer than control CB anymore. Obviously, further crystallization, recrystallization and/or polymorphic transformation, and fat crystal network setting of the mixtures occurred between 24 and 48 hours, erasing any effects of AMF and MMF addition on hardness of cocoa butter. Our results disagree with those of Full et al. [9], who reported a decrease in hardness of chocolate containing HMF. Again, this effect is probably due to MMF contamination of the HMF fraction. Dry-melt crystallization-based fractionation of milk fat does not produce fractions that enhance the functionality of confectionery products. Lohman and Hartel [13] have clearly shown that the addition of HMF obtained via solvent fractionation does not decrease the hardness of cocoa butter. As well,

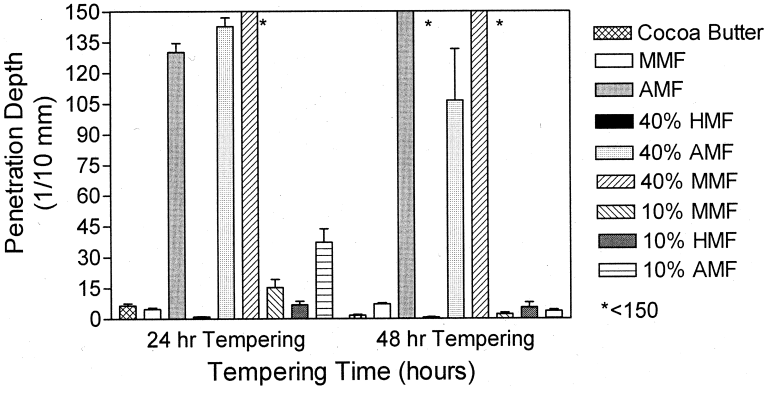

Figure 6 Changes in cone penetration depth as a function of fat composition and tempering time at 22°C.

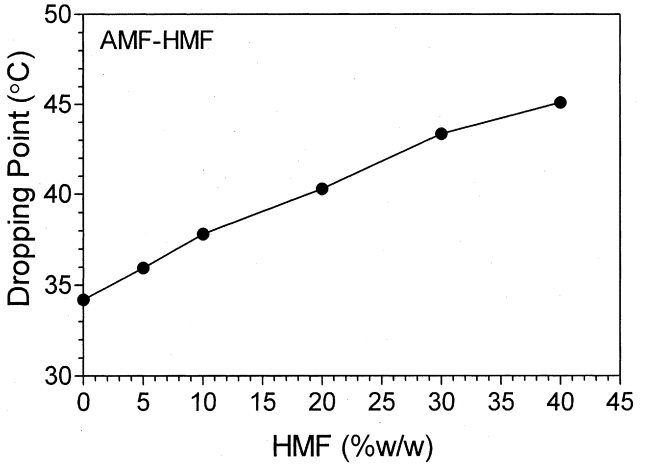

Figure 7 Increases in the dropping point of milkfat (AMF) as a function of HMF addition.

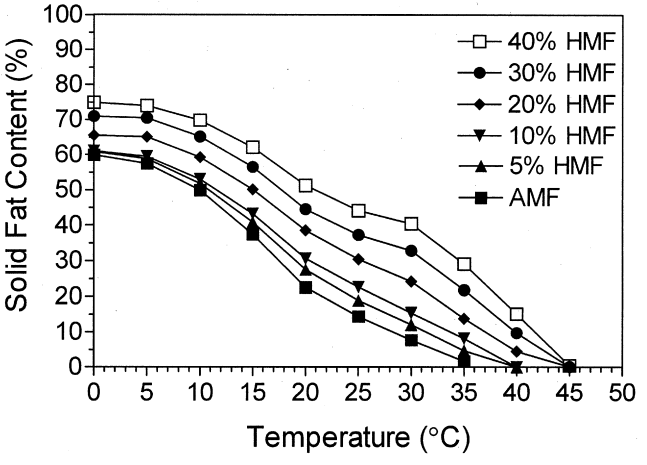

Figure 8 Increases in the solid fat content of milkfat (AMF) as a function of HMF addition.

these authors also clearly demonstrate the ability of HMF to delay the incidence of bloom formation in chocolate, and their equivalent to our MMF and LMF to enhance the rate of bloom formation. It would seem that the use of HMF obtained via dry fractionation (melt crystallization) is not a good idea since it forms eutectics with cocoa butter [7] and decreases the hardness of chocolate [9]. As far as the MMF is concerned, work in our laboratory has clearly shown that MMF can be used as a cocoa butter replacer. It is possible to manufacture high-quality confections using MMF as the sole confectionery fat.

Another possible application for milk fat fractions is in the manufacture of plastic fats. Milk fat's HMF can be added to milk fat to increase the dropping points and solid fat content (Figs. 7 and Figure 8, respectively). Increasing the SFC and dropping point of AMF would allow for the manufacture of butter for consumption in warmer countries or in situations where butter would be kept at room temperature for extended periods of time.

CONCLUSIONS

Milk fat solvent fractionation constitutes an interesting strategy to increase the utilization of milk fat and create new and innovative products whose physical properties are dependent on the presence of a milk fat fat crystal network underlying structure. HMF can be successfully used to prevent bloom formation in chocolate, while AMF is added to chocolate in the manufacture of milk chocolate to control hardness and delay bloom formation in dark chocolate. HMF can also be utilized as a hardstock in the manufacture of high-melting butter. However, the phase behavior of mixtures of milk fat and milk fat fractions with different fats must be determined in order to be able to judge their suitability for inclusion in specific fat blends.

REFERENCES

1. Jeffrey MS. The effect of cocoa butter origin, milk fat and lecithin levels on the temperability of cocoa butter systems Mfg Confectioner 1991; 71:76–82.

2. Koyano T, Hachiya J, Sato K. Fat polymorphism and crystal seeding effects on fat bloom stability of dark chocolate Food Structure 1990; 9:231–240.

3. Timms RE. The phase behavior of mixtures of cocoa butter and milk fat Lebensm Wiss Technol 1980; 13:61–65.

4. Timms RE, Parekh JV. The possibilities for using hydrogenated, fractionated or interesterified milk fat in chocolate Lebensm Wiss Technol 1980; 13:177.

5. Barna CM, Hartel RW, Metin S. Incorporation of milk-fat fractions into milk chocolates Manufacturing Confectioner 1992; 72:107–116.

6. Reddy SY, Dimick PS, Ziegler GR. Compatibility of milk fat fractions with cocoa butter determined by differential scanning calorimetry INFORM 1994; 5:522.

7. Bystrom CE, Hartel RW. Evaluation of milk-fat fractionation and modification techniques for creating cocoa butter replacers Lenbensm Wiss Technol 1994; 27:142–150.

8. Reddy SY, Full NA, Dimick PS, Ziegler GR. Tempering method for chocolate containing milk fat fractions J Amer Oil Chem Soc 1996; 73:723–727.

9. Full NA, Reddy SY, Dimick PS, Ziegler GR. Physical and sensory properties of milk chocolate formulated with anhydrous milk fat fractions J Food Sci 1996; 61:1068–1084.

10. Hartel RW. Application of milk-fat fractions in confectionery products J Amer Oil Chem Soc 1996; 73:945–953.

11. Kleinert J. Studies on the formation of fat bloom and methods of delaying it Rev Internat Choco 1961; 16:201–219.

12. Dimick PS, Thomas LN, Versteeg C. Potential use of fractionated anhydrous milk fat as a bloom inhibitor in dark chocolate INFORM 1993; 4:504.

13. Lohman MH, Hartel RW. Effect of milk-fat fractions on fat bloom in dark chocolate J Amer Oil Chem Soc 1994; 71: 267–276.

14. Minifie BW. Chocolate, cocoa and confectionery. 3rd ed. New York: Van Nostrand Reinhold, 1989.

15. Gresti J, Bugaut M, Maniongui C, Bezard J. Composition of molecular species of triacylglycerols in bovine milk fat J Dairy Sci 1993; 76:1850–1869.

16. Mulder H. Melting and solidification of milk fat Neth Milk Dairy J 1953; 7:149–176.

17. deMan JM. Polymorphism in milk fat Dairy Science Abstracts 1963; 25(6):219–221.

18. Timms RE. The phase behavior and polymorphism of milk fat, milk fat fractions and fully hardened milk fat Australian J Dairy Technol 1980; 35:47–52.

19. Timms RE. Phase behavior of fats and their mixtures Prog Lipid Res 1984; 23:1–38.

20. Marangoni AG, Lencki RW. Ternary phase behavior of milk fat fractions J Agric Food Chem 1988; 46:3879–3884.

21. Grotenhuis ET, van Aken GA, Malssen KF, Schenk H. Polymorphism of milk fat studied by differential scanning calorimetry and real-time X-ray powder diffraction J Amer Oil Chem Soc 1999; 76:1031–1039.

22. Kaylegian KE, Hartel RW, Lindsay RC. Applications of modified milk fat in food products J Dairy Sci 1993; 76:1782–1796.

23. Ali AR, Dimick PS. Melting and solidification characteristics of confectionery fats: anhydrous milk fat, cocoa butter and palm kernel stearin blends J Amer Oil Chem Soc 1994; 71:803–806.

24. Kaylegian KE, Lindsay RC. Handbook of milk fat fractionation technology. Champaign. IL: AOCS Press:1995.

25. Rousseau D, Hill AR, Marangoni AG. Restructuring butterfat through blending and chemical interesterification. 3. Rheology J Amer Oil Chem Soc 1996; 73:983–989.

26. Rousseau D, Forestiere K, Hill AR, Marangoni AG. Restructuring butterfat through blending and chemical interesterification.1. Melting behavior and triacylglycerol modifications J Amer Oil Chem. Soc 1996; 73:963–972.

15

Liquid-Multiple Solid Phase Equilibria in Fats: Theory and Experiments

L. H. WESDORP, J. A. VAN MEETEREN, S. DE JONG, R. V.D. GIESSEN, P. OVERBOSCH, P. A. M. GROOTSCHOLTEN, M. STRUIK, E. ROYERS, and A. DON

Unilever Foods Research Centre Vlaardingen,
Vlaardingen, The Netherlands

TH. DE LOOS, C. PETERS, and I. GANDASASMITA

Department of Applied Thermodynamics
Delft University of Technology,
Delft, The Netherlands

1. INTRODUCTION AND PROBLEM DEFINITION

It is important for the production of fat containing food products to control the melting and solidification behaviour of edible oils and fats. The objective of this work is to develop a method to predict the melting range and solid phase composi-

tion of fats from their overall composition. Fats consist of triacylglycerols (TAGs), which show polymorphism in the solid phase. The polymorphic behaviour is reviewed. The nomenclature for TAGs and groups of TAGs used in this work is explained. Existing methods for solid phase prediction are discussed.

1.1 SOLID-LIQUID PHASE EQUILIBRIA AND FATS

The fact that many languages have different words for the solid and liquid state of mixtures of triacylglycerols (triglycerides) indicates that the solid liquid phase behaviour of TAGs is something everyone encounters in daily life. Coconut "oil" can be conveniently used as table oil in many tropical countries, while in Northwest Europe it is considered a stone hard "fat".

Edible oils and fats usually consist of more than 95% of a complex mixture of triacylglycerols (TAGs). Typically an edible oil or fat can contain more than 500 different TAGs. Edible oils and fats therefore do not possess a distinct melting point, but exhibit a long melting range.

This melting range is one of the main factors determining the properties of fat containing food products, like fat spreads, dressings, chocolate, cakes, ice cream and cookies. A fat spread, for example, must contain enough liquid fat at refrigerator temperature in order to make it a spreadable, soft solid. At ambient temperature it still must contain enough solid fat to prevent the spread from becoming pourable and oiling out. To give the spread a nice taste, the fat should be liquid at mouth temperature [1]. (Figures 1 and 2).

A fat with an optimal melting range for a particular application is obtained by carefully blending natural and modified oils and fats. Of course the edible fats industry likes to be able to blend fats to a constant melting range regardless of the raw materials used. Other applications, like chocolate, require a fat with a very specific TAG-composition, which is often obtained by fractional crystallization of natural fats like palm oil. Simulation of this fractionation process requires calculation of the dependence of the crystal composition on process conditions. Both melting range and phase composition of a fat are

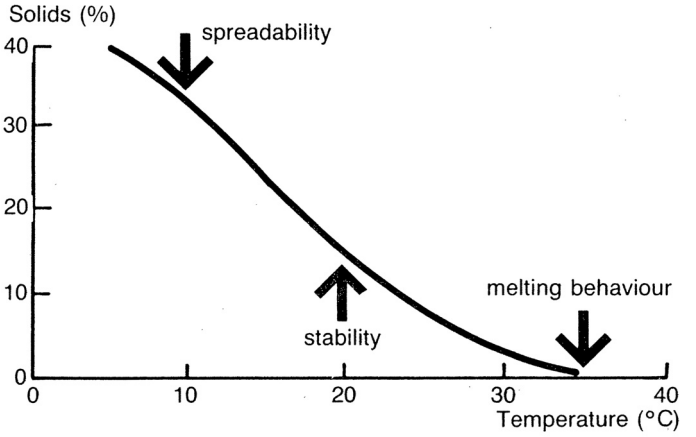

Figure 1 Requirements for the melting range of a fat spread.

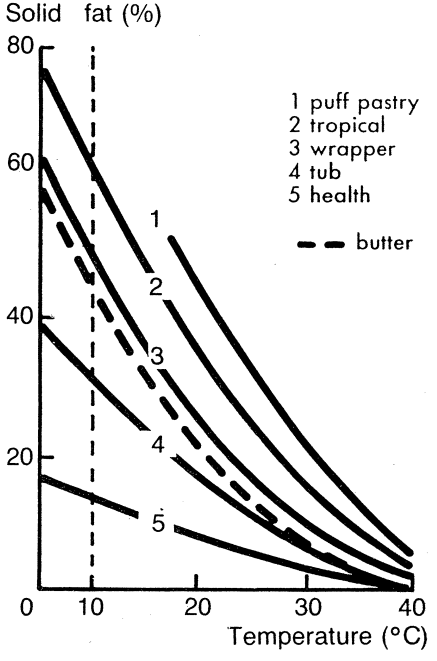

Figure 2 Melting ranges of some types of fat spreads.

primarily determined by the solid-liquid phase equilibrium in the fat. Describing the phase behaviour of edible oils and fats is therefore a necessity for the edible fats industry.

The objective of this work is to develop a method that enables prediction of the melting range and the solid phase composition of edible oils and fats.

1.2 TRIACYLGLYCEROLS: NOMENCLATURE

Edible oils and fats consist mainly of triacylglycerols (TAGs). For convenience TAGs will be identified by a 3-letter code in this work. Each of the three characters in the code represents one of the fatty acids that is esterified with the glycerol. So glycerol-1-palmitate-2, 3-disterate will be represented by PSS. The middle character always indicates the fatty acid that is esterified on the 2-position of the glycerol. The characters used to represent the fatty acids are given in Table 1.

It is sometimes convenient to be able to refer to groups of TAGs. Table 2 defines a set of letter-codes that represent a number of fatty acids.

Hence the TAG-group h_3 contains all TAGs that can be made from the four long chain fatty acids, like SSS, PPP, SPP, PPS, PSP, AAA, BBB, ASA, ASB, etc., while hOh stands for all TAGs having oleic acid on the 2-position and one of the

Table 1 Characters Used for Representing Individual Fatty Acids

Code	Fatty acid	Code	Fatty acid
2	Acetic acid	P	Palmitic acid (hexadecanoic acid)
4	Butyric acid	S	Stearic acid (octadecanoic acid)
6	Hexanoic acid	O	Oleic acid (cis-9-octadecenoic acid)
8	Octanoic acid	E	Elaidic acid (trans-9-octadecenoic acid)
C	Capric acid (decanoic acid)	l	Linoleic acid (cis-cis-9, 12-octadecadienoic acid)
L	Lauric acid (dodecanoic acid)	A	Arachidic acid (eicossanoic acid)
M	Myristic acid (tetradecanoic acid)	B	Behenic acid (docosanoic acid)

Table 2 Letter Codes Used for Representing Groups of Fatty Acids

Code	Fatty acids
m	medium chain fatty acids (8+C+L+M)
h	long chain saturated fatty acids (P+S+A+B) ("hydrogenated")
u	cis-C18 unsaturated fatty acids (O+l+linolenic acid)

four long chain fatty acids on the 1- and the 3-position of the glyceryl group like: SOS, POP, POS, AOS, etc.

1.3 TRIACYLGLYCEROLS: POLYMORPHISM

The existence of a number of alternative crystal structures is a characteristic property of all lipids (alkanes, fatty acids, soaps, methyl esters of fatty acids, and TAGs) [2]. This is due to the fact that there are a number of different possibilities of packing the long hydrocarbon chains into a crystal lattice. This phenomenon is called polymorphism and each different crystal structure is called a polymorphic form or modification of the lipid. Two types of polymorphism occur in lipids. When each form is thermodynamically stable in a definite range of temperature and pressure, it is called enantiotropic polymorphism. Each enantiotropic polymorph transforms into another polymorph at the transition temperature. The opposite case, when only one polymorphic form is thermodynamically stable, is called monotropic polymorphism. TAGs show monotropic polymorphism, while long chain odd alkanes show enantiotropic polymorphism (see Section 15.9)

The polymorphism of TAGs was first observed in 1853 by Duffy [3], but only in the early 1960s some agreement was reached about the number, structure and nomenclature of the different polymorphic forms of TAGs [4,5]. They occur in three different basic polymorphic forms, α, β' and β, which are characterized by a particular carbon chain packing and stability. Recent accurate experimental techniques, combined with better purity of the samples, have brought about a new controversy about the existence, number and nomenclature of submodifications of each polymorphic form [6–12].

It is not the objective of this work to enter into a discussion on submodifications. However the subject of this work, phase equilibria in TAGs, requires an opinion on TAG polymorphism.

1.3.1 Basic polymorphic forms of TAGs

This work will use the nomenclature proposed by Larsson [2,5] in the form applied by de Jong [13]. Basically the fatty acid chains of TAGs can be packed into three main polymorphic forms, characterized by the short spacings in the X-ray diffraction pattern, namely:

1. The α-modification, characterized by only one strong short-spacing line in the X-ray diffraction pattern near 0.415 nm. In the α-modification the chains are arranged in a hexagonal chain packing, without an order to the zig-zag chain planes. The chains do not have an angle of tilt. (Figure 3*a*).
2. The β′-modification, characterized by two strong short-spacing lines in the X-ray diffraction pattern near 0.38 nm and 0.42 nm. It also has a doublet in the 720 cm^{-1} region of the infrared absorption spectrum. The chain packing in the β′-modification is orthorhombic, with a perpendicular arrangement of the zig-zag chain planes. The chains have an angle of tilt between 50° and 70° (Figure 3*b*).
3. The β-modification, characterized by a strong short-spacing line in the X-ray diffraction pattern near 0.455 nm and a number of other strong lines around 0.36–0.39 nm. The β-modification is the most densely packed polymorph. The chains are arranged in a triclinic chain packing, with a parallel arrangement of the zig-zag chain planes. The chains have an angle of tilt between 50° and 70°C (Figure 3*c*)

Figure 3 Schematic representation of orientation of the TAGs in their three basic polymorphic forms, together with the respective chain packing subcell. One zig-zag is seen in the direction of the hydrocarbon chains, open circles are hydrogen, filled circles carbon [18].

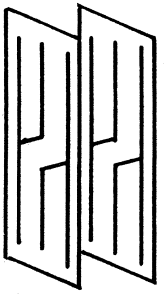

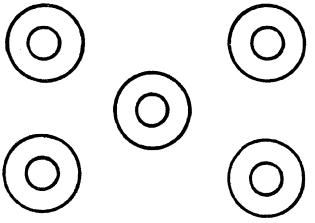

a: **α**: unstable, lifetime < 60 s.
present during process

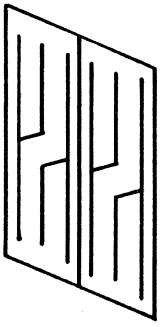

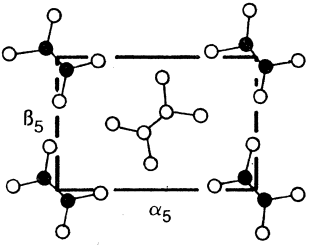

b: **ß′**: metastable (>60 s -> years)
present in products

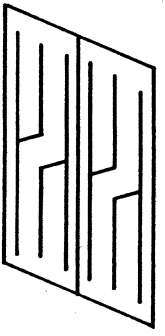

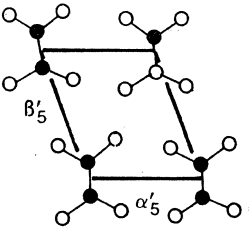

c: **ß**: stable

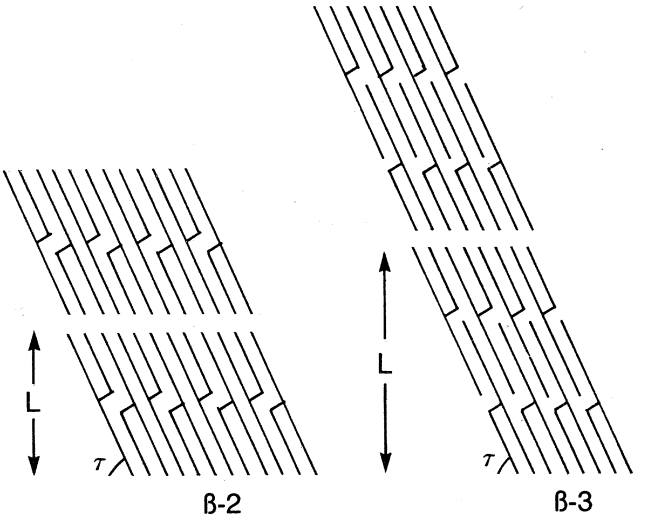

Figure 4 β-2 and β-3 arrangements of TAGs [13].

Based on the arrangement of the TAGs themselves in the crystal, two forms can be distinguished for each modification: a form with layers made up of two fatty acid chains and one with layers of three fatty acid chains (Figure 4). These forms are characterized by their long spacing in the X-ray diffraction pattern. To distinguish between the two forms, a suffix is added to the symbol that indicates the modification, e.g., β-2 and β-3.

The −2 forms are the most stable and the −3 forms are therefore only found for TAGs of which the chain packing in the −2 form would be very unfavourable: in TAGs with cis-unsaturated fatty acids and in TAGs in which the fatty acid chains differ by 6 or more.

1.3.2 Submodifications

If submodifications exist, they will be indicated by a subscript in order of decreasing melting point, e.g., β_1-2 and β_2-2.

Saturated TAGs

De Jong [13] has done an excellent, extensive study of molecular packing possibilities in the β-modification. He

shows that in theory a β-2 forming TAG can crystallize in at least two but often three different β-2 submodifications. For the β-3 modification two submodifications are possible. He found that in practice each TAG only occurs in one of these submodifications, although different TAGs crystallized in different submodifications.

Simpson and Hernqvist [6,7] reported simultaneously the existence of two β′-submodifications for saturated TAGs, and somewhat later Hagemann [8] managed to distinguish even three β′-submodifications, two α submodifications, and two β-submodifications in his DSC thermograms. The submodifications were never obtained as pure solid phases on their own, but they rapidly transformed to the most stable submodification. Consequently, reliable melting points or heats of fusion could not be determined. The X-ray diffraction patterns of the submodifications show only very subtle differences. The pattern of a less stable submodification has much broader peaks and shows less details than that of the most stable submodification.

Rapid polymorphic transitions used to be hard to study by X-ray. The polymorphic transition takes 5 minutes, while one X-ray scan takes 15 minutes. This makes the unambiguous identification of very unstable submodifications difficult. Very recent experimental techniques allow so-called time resolved X-Ray diffraction and neutron scattering studies [12,14]. These new techniques need only 5 seconds for a scan, which means that the actual order of events during a polymorphic transition can be followed.

Kellens et al. [12] find that the polymorphic transitions take place in a very specific order. Re-ordering along the three different crystallographic axes is not achieved simultaneously but takes place sequentially. This is in agreement with computer simulation results of Hagemann [15], who showed that, due to sterical hindrance, the minimal energy path for the rearrangement in the crystal packing follows a very specific order of events. Also Sato [10] has observed this phenomenon. Kellens states that melting the crystal in a transitional state, where it has not yet reached full crystallinity, can very well

result in DSC-thermograms similar to those from which Hagemann concluded the existence of unstable submodifications.

Kellens et al. also show that the melting entropies of Hagemann's and Hernqvist's submodifications are far too low to identify these submodifications as one of the differently packed β′ and β forms of de Jong [13]. Moreover, they found that the height of the shoulder or small prepeak in the DSC-thermogram did not increase upon increasing scan rate, which is contradictory to the existence of an unstable submodification that rapidly transforms into a more stable one.

Hagemann could not show during all his experiments that the recrystallization from α to one of the β-forms was actually complete. The observed less stable β_2-form can therefore also be explained as the melting peak of the β-form in the presence of a little bit of liquid.

Kellens final conclusion is that these submodifications may very well not be separate polymorphic forms in a thermodynamic sense, but transitional variants with lower crystal perfection and crystallinity.

Due to the serious doubts that one may have on the actual occurrence of a large number of submodifications of saturated TAGs and the plausible alternative explanations available, this work assume that only the three basic modifications occur.

Unsaturated TAGs

Only the polymorphism of hOh-type TAGs has been studied in more detail, because of their importance for explaining the phase behaviour of cocoa butter. As before, there is no agreement at all on the existence, properties and number of submodifications.

Perhaps the best results come from Sato [10]. His X-ray diffraction results show very convincingly a fourth polymorph, the γ-modification, characterized by two strong short spacings, at 0.470 nm and 0.390 nm and a weaker one at 0.45 nm, characteristic for orthorhombic chain packing with parallel orientation of the chain zig-zag planes. The thermodynamic properties are almost that of the perpendicular orthorhombic β′-modification. This γ-modification is of little practical importance, it is less stable than the α-modification and converts readily into the β′-modification. It is not observed in mixtures.

This γ-modification is also known under the names β″, sub-β-3, L_2, and form 4. This chapter will use Sato's nomenclature.

Sato, and other authors, also found 2 β′ and 2 β-submodifications, which hardly differ in X-ray pattern and stability. The existence and properties of β′-submodifications, which only occurred in POP and not in SOS and BOB, strongly depend on the level of impurities.

Therefore similar doubts arise for the existence of these submodifications as for Hagemann's submodifications of saturated TAGs. This work will only consider one β′-modification, having properties of the most stable of the β′-submodifications that are reported.

The existence of two β-submodifications is quite certain [10], as they can actually be obtained in pure form. The transition to the most stable form is extremely slow and takes several weeks. X-ray diffraction shows that the differences in structure must be minor. De Jong [13] suggests that the forms only differ in layer stacking. The most stable β_1-3 form has in this view a slightly higher symmetry and a heat of fusion that is only 1 kJ/mol more. This explains why the most stable form takes so long to form and why the 2 β-forms are only observed in pure components and mixtures of hOh-TAGs that are nearly isomorphous, like cocoa butter. In more complex mixtures that contain high amounts of hOh-type TAGs, like palm oil [16] and the mixtures that Hernqvist used [17], only one β-form is observed. Therefore, for most practical purposes the possible existence of β-submodifications can be neglected. However, for systems with very high concentrations (>80%) of one hOh-type TAG, we need to be aware of the possible occurrence of β-submodifications.

Conclusion

The discussion on submodifications is still very confusing and clear evidence has not been put forward for their existence, nor is there any agreement about their properties. In most cases, alternative explanations, like those of Kellens [12], are possible for the observed changes in X-ray patterns and the shoulders and shifts in the DSC-thermograms. This work it will therefore assume that each TAG crystallizes in three different polymorphic forms only.

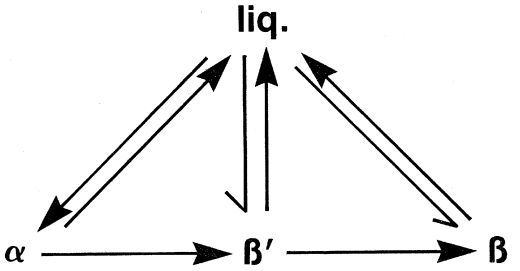

Figure 5 Simple picture of the possible polymorphic transitions in TAGs.

1.3.3 Stability

The α modification is the least stable and it converts within several minutes into the β′-modification. The α-form is found in edible fat products during their preparation.

The β′-modification is the stable modification for odd-chain TAGs and a number of even chain TAGs (like PSP). In other TAGs it converts into the β-modification within several minutes to hours. In mixtures this transition is often delayed to several months or years. It is therefore the modification that is encountered most frequently in normal edible fat products.

The β-modification is the stable modification. It only occurs in edible fat products during their lifetime, if the fat is composed of TAGs that are nearly isomorphous, like hardened rape-seed oils [18] and cocoa butter [16].

All three modifications can be obtained directly from the liquid, by varying the degree of supercooling. The transformation of α to β however, always takes place via the β′-modification [12,15,17] (Figure 5).

1.4 METHODS FOR PREDICTING SOLID PHASE COMPOSITION AND QUANTITY

The objective of this work is to develop a method to predict the melting range and composition of the solid phase of edible oils and fats from the overall composition of the fats. If the exact molecular composition of a fat is known, prediction of

its properties is in principle possible. The vegetable oils and fats became only analytically accessible by the progress in high performance liquid chromatography (HPLC) techniques made during the last 10 years, while the analysis of animal oils and fats is still troublesome. Besides, the theoretical understanding of solid-liquid phase equilibria in multicomponent systems was not at all adequate to deal with even very simple oils. Nevertheless, some (semi) empirical methods for prediction of solid phase content were developed. They will be briefly discussed in this section.

1.4.1 Linear programming/multiple regression

This method is frequently used in industry [16]. The composition of the fat blend is defined in terms of the natural and modified oils of which it is made (e.g., 50% palm oil, 50% bean oil). The solid phase content of the mixture is expressed as a linear function of the concentration of these components:

$$\%S = k_1 x_{oil1} + k_2 x_{oil2} + \cdots \quad (1)$$

The coefficients k are obtained by multiple linear regression on the data of a number of mixtures. For limited ranges of compositions and solid phase contents this method is very useful. It does have disadvantages:

1. The predictive equation has no theoretical basis at all. Extrapolation outside the range of experimental data is not possible and gives dangerously erroneous results.
2. The equations cannot be easily extended to incorporate new component fats. The complete regression analysis and experimental work must be repeated and all coefficients will change.
3. Understanding is not obtained about the actual phase behaviour, which implies that a solution can not be found for undesired recrystallization phenomena and other crystallization phenomena that may be observed in practice. Polymorphism is neglected.

1.4.2 Excess contribution method

Timms [16] shows the application of an empirical method developed by Nyvlt [18] to fats. The method is an extension of the multiple linear regression method of Section 15.1.4.1. The solid phase content is expressed as:

$$\%S = \sum_{i=1}^{n} \%S_i . x_i + \sum_{j=1}^{n} \sum_{i=1}^{j-1} I_{ij} . \frac{x_i x_j}{x_i + x_j} \quad (2)$$

The concentrations x are weight fractions of the constituing oils, the binary interactions it must be determined from measurements of a number of mixtures of the two oils concerned. The advantages over the linear method are two-fold:

1. The equation is in principle valid over larger concentration ranges
2. If a new component fat is to be added, only the binary mixtures with all other component fats have to be measured in order to determine the interaction parameters. All other interactions remain unaffected.

Timms [16] shows that the predictions are considerably worse than with the linear method, with deviations of 30% around the measured values. Again the model is totally empirical, the meaning of the parameters is unclear and it offers no real insight in the underlying crystallization phenomena.

1.4.3 TAGs Inductors de Crystallization Method

The first method that attempts to predict solid phase content from TAG-composition is the TAGs Inductors de Crystallization Method (TGIC-method) of Perron [19]. He assumes that:

A crystallized fat consists of a number of solid phases in equilibrium with each other and with the liquid phase present.

Each solid phase consists mainly of one TAG, called the TGIC. All solid phases contain impurities, which modify its melting point and heat of fusion.

Upon heating, each solid phase melts independently. The fraction of the solid phase that has disappeared at a

certain temperature is given by a point on a Kessis-curve. A Kessis-curve is a general mathematical representation of a DSC or DTA melting peak of a single component in a liquid solvent. By adjustment of the parameters it can be used to describe a measured DSC-curve, including the thermal lag.

The solid phase content at a certain temperature can be obtained from an addition of all contributions from the Kessis-curves of each TGIC at that temperature.

Although Perron's notion of a number of coexisting solid phases is correct, the method he has developed is not sound at all:

1. His selection of the number and composition of the coexisting solid phases has no physical ground.
2. There is no reason why the solid phases should melt according to a Kessis curve. Moreover, the width of the Kessis curve is normally determined by the DSC apparatus and the scan rate selected. It is therefore not a property of the fat and any assumption about the width of such a curve is arbitrary.

The criticism Timms [16] applied to an earlier version of Perron's TGIC-method is still valid. Contrary to the two empirical methods mentioned, the method is not even useful for practical purposes.

1.4.4 The Classification of TAGs method

Wieske [20] proposed a method in which he groups the TAGs into all possible TAG-groups that can be formed from elaidic acid (E) and the three fatty acid groups of Section 15.1.2, h,m, and u. These TAG-classes are supposed to form separate solid phases in a crystallized fat. The fraction of each class that has not crystallized is given by the Hildebrand-equation, assuming an average melting point and heat of fusion for each TAG-class. The Hildebrand equation reads:

$$\ln x_i^L = \frac{\Delta H_{f,i}}{R}\left(\frac{1}{T_{f,i}} - \frac{1}{T}\right) \tag{3}$$

This method has a physical background. It assumes that an oil can be considered as a mixture of a limited number of pseudo components that do not form mixed crystals. However, the predictions from this method are of a similar poor quality as those of the excess contribution method. Wieske's choice of the pseudo-components, as well as the assumption of solid immiscibility, and the selection of melting points and heats of fusion can be criticized. This method neither offers any understanding of the actual, underlying solid-liquid phase behaviour of TAGs.

1.4.5 Other TAG-based methods

Several attempts have been made to find an empirical correlation between the TAG-composition of a fat and its solid phase content [20,21]. None of these attempts was very successful. Moreover, the methods have the same disadvantages as the linear method of Section 15.1.4.1.

1.5 CONCLUSION

The objective of this work is to develop a method that predicts the melting range and solid phase composition in an edible oil from the overall fat composition.

Existing predictive methods have no sound physical basis, are not generally applicable and offer no understanding at all of the actual solid-liquid phase behaviour of TAGs.

TAGs show polymorphism in the solid phase. This work will assume that each TAG crystallizes in three different polymorphs only: the unstable α-modification, the β'-modification, and the stable β-modification.

Due to their poor analytical accessibility, animal fats will not be considered in this work.

2. APPROACH TO THE PROBLEM

The ultimate amount and composition of the solid phase in a fat are determined by the position of the thermodynamic equilibrium solely, but the crystallization process may lead

to significant deviations from the equilibrium composition in practical situations. Yet it appears that the starting point for any general predictive method of solid phase content in fats is a description of the solid-liquid phase equilibrium for all three polymorphic forms in which fats can crystallize. The thermodynamic equations that describe these equilibria are worked out. A number of steps is identified that need to be taken before a complete thermodynamic description can be obtained.

2.1 SOLID-LIQUID EQUILIBRIUM THERMODYNAMICS

In the end, the amount and the composition of the solid phase in a crystallized fat will be determined by the position of the solid-liquid phase equilibrium in that fat. Therefore a general method for prediction of the solid fat content and the fat crystal composition from the fat composition must be based on a description of the solid-liquid phase equilibrium thermodynamics in TAGs.

Fats are mixtures of many different TAGs. It is known that many pairs of TAGs only show limited miscibility in the solid phase [16]. Therefore it is very likely that "solid fat" often will consist of a number of different coexisting solid phases. These solid phases do not necessarily have the same polymorphic form. A thermodynamic description of this complicated liquid-multiple solid equilibrium can be developed as follows.

Suppose a crystallized fat in equilibrium consists of N components and contains P phases (a liquid phase and P-1 solid phases). The phase equilibrium must satisfy the following equations [22]:

1. The condition of thermodynamic equilibrium: the chemical potential of each component i in each phase must be equal to that in any other phase

   $$\mu_i^{solid} = \mu_i^{liquid} \tag{4}$$

   for each solid phase.
   This equation can be worked out for solid/liquid equilibria as:

$$\mu_i^{0.S} + RT \ln y_i^S x_i^S = \mu_i^{0,L} + RT \ln y_i^L x_i^L \quad (5)$$

γ is the activity coefficient, and x the mol fraction.

$$\ln\left(\frac{\gamma_i^S x_i^S}{\gamma_i^L x_i^L}\right) = \frac{1}{RT}(\mu_i^{0,L} - \mu_i^{0,S}) \quad (6)$$

$$\ln\left(\frac{\gamma_i^S x_i^S}{\gamma_i^L x_i^L}\right) = \frac{\Delta H_{f,i}}{R}\left(\frac{1}{T} - \frac{1}{T_f}\right) - \frac{\Delta c_{p,i}}{R}\left(\frac{T_{f,i} - T}{T}\right) + \frac{\Delta c_{p,i}}{R} \ln \frac{T_{f,i}}{T} \quad (7)$$

With $\Delta c_p = 0.2$ kJ/mol and $T_f - T$ never greater than 70 and usually between 0 and 20 the terms with Δc_p are comparatively small and tend to cancel due to their opposite sign. As an approximation they can therefore be neglected and there remains:

$$\ln\left(\frac{\gamma_i^S x_i^S}{\gamma_i^L x_i^L}\right) = \frac{\Delta H_{f,i}}{R}\left(\frac{1}{T} - \frac{1}{T_f}\right) \quad (8)$$

2. The mole balance: the sum of the amount of each compound i in each phase f, present in fraction Φ^f, must be equal to the overall amount of i, z_i: (P is the total number of phases)

$$\sum_{f=1}^{P} x_i^f \ \Phi^f = Z_i \quad (9)$$

3. The stoichiometric condition: the sum of the concentrations of the components in each phase must be equal to 100%:

$$\sum_{i=1}^{n} x_i^f = 1 \quad (10)$$

For P phases this results in PN + P equations with PN + P unknowns. (P*N mol fractions x and the quantity of P phases). This set of equations can in principle be solved to obtain the number of phases, the phase quantities and the composition of each phase from the overall composition and the temperature.

However, in order to solve these equations four things are needed:

1. Values for the pure component properties: the heat of fusion and the melting point.

2. Knowledge of the activity coefficients in the liquid phase.
3. Knowledge of the activity coefficients in the solid phase.
4. A method to solve this complex set of non-linear equations.

Each of these points will be handled in separate sections of this chapter, so that in the end a full description of the liquid-multiple solid equilibrium in fats will evolve.

2.2 KINETICS OF CRYSTALLIZATION

Although the ultimate amount of solid phase and the solid phase composition are determined by thermodynamics solely, it is well known that due to the extremely slow diffusion rate in solids the equilibrium state is not always reached in practical situations [23]. Hence both crystal composition and amount of solid phase that are observed may deviate considerably from what is predicted by thermodynamics. To avoid possible pitfalls the effect of kinetic factors on the amount and composition of the solid phase of fats should be considered.

2.2.1 Polymorphism and kinetics of crystallization

When fats crystallize, they usually first crystallize in the most unstable polymorph, the α-modification, followed by slow recrystallization to more stable polymorphs. Direct crystallization into the β′ or β-modification only takes place under conditions where little or no supercooling of the less stable modification is present. Palm oil crystallizes into the α-modification when supercooled to 10°C, into the β′-modification when cooled to 25°C, and into the β-modification when crystallized at 32°C [24]. In all three cases the thermodynamically most stable state is the β-modification.

Obviously solid fat content and crystal composition calculated for the β-modification using thermodynamics are poor predictions if the fat has crystallized in another polymorphic form. For a lot of practical situations the most stable thermo-

dynamic state is irrelevant: the residence time in the process line after the onset of fat crystallization is only a few minutes for many edible fat products, so the unstable α-modification is the phase that should be considered. During the life of most edible fat products, the recrystallization to the β-modification does not take place: the product is already consumed while it is still in the β′-modification.

In spite of their limited lifetime, the β′-modification and even the α-modification may coexist very well during their existence in thermodynamic equilibrium with the liquid oil. Hence thermodynamics can be applied to predict the amount and composition of these intermediate solid phases. Application of equilibrium thermodynamics to unstable states is quite common: a mixture of benzene and air is not thermodynamically stable but should disintegrate into carbon dioxide and water, yet a vast amount of literature exists about vapour-liquid phase equilibria with benzene.

2.2.2 Shell formation

If a fat is slowly cooled while it is crystallizing, shell formation may occur. At each instant during the crystallization process the surface of the growing crystals has the equilibrium composition. As temperature decreases, the equilibrium composition changes, but the composition of the inner part of the crystal does not change due to the low solid state diffusion rate. An inhomogeneous solid phase results, having a concentration gradient from the center of the crystals outwards. The solid phase composition deviates from the equilibrium composition. It is reported that the solid fat content can decrease to only 80% of the equilibrium value [16] due to shell formation.

If diffusion limitations do not occur during crystallization, shell formation can be prevented by crystallizing isothermally. The rate determining step in normal fat crystallization is the surface incorporation [24,25]. Indeed, when the crystal composition of an isothermally crystallizing fat is plotted against the reaction coordinate, shell formation seems absent (Figure 6).

Phase equilibrium thermodynamics will only give a reliable prediction of the solid phase composition and content if

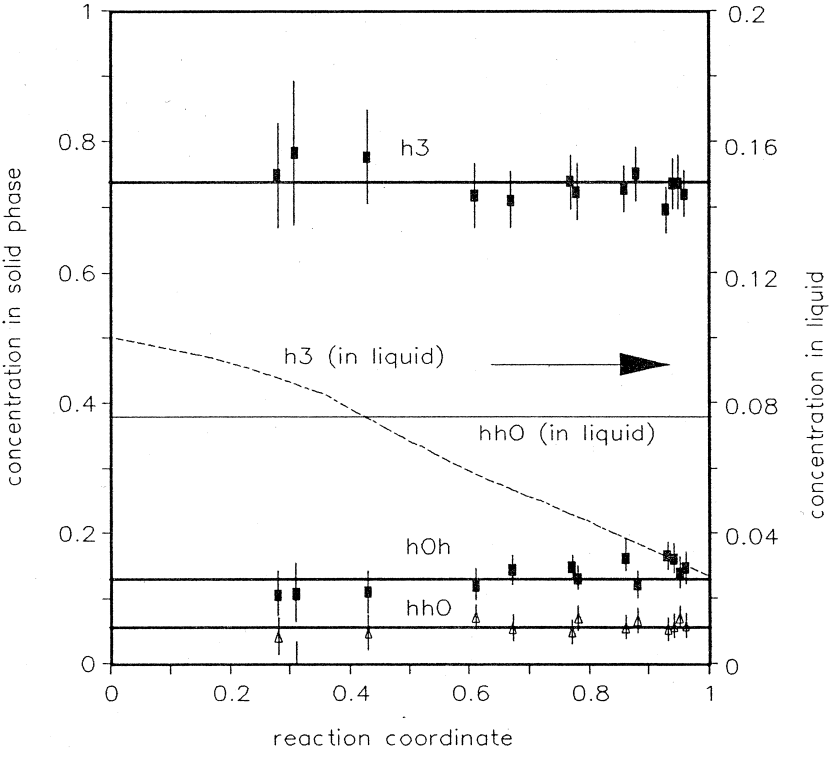

Figure 6 Composition of fat crystals from palm oil against the reaction coordinate of crystallization at 30°C. (Overall palm oil composition: h_3 – 0.1, hOh – 0.295, hhO – 0.075, hlh – 0.104, hOO – 0.246, liquid – 0.176.). The palm oil was heated to 80°C, rapidly cooled to 30°C and stored in a stirred tank. At regular time intervals over totally 21 hrs samples were taken. The solid fat content of the sample was measured and a small amount of liquid phase was rapidly filtered off and analysed by $AgNO_3$–HPLC. Crystal composition is calculated from overall composition, solid fat content and the TAG analyses of the liquid phase of the samples. The error margin is indicated.

shell formation is absent. However, the effect of shell formation on solid phase content can be calculated from the equilibrium composition as a function of temperature, as will be shown in Section 15.9.

2.2.3 Poor crystallinity

If fat is crystallizing rapidly, it may result in poorly packed crystals. The clear point of such poorly packed solid phases may be considerably lower than the clear point predicted by thermodynamics. Through recrystallization these badly packed crystals can rearrange into well packed crystals. The results of Gibon [11] show that without the presence of a liquid phase badly packed crystal forms may persist for years. However recrystallization via the liquid phase can occur relatively easily [23]. Norton [26] shows that partially hydrogenated palm oil initially crystallizes in a very badly packed β′-form, but that in the presence of about 50% of a liquid oil it only takes a few hours to rearrange into well packed crystals. Also the rate of polymorphic transitions was observed to be much larger in the presence of liquid [27].

Most fats used in edible fat products only contain 0–40% of solid fat that is purposely crystallized into very small (1 μ and less) crystals. Deviations from thermodynamic predictions due to bad crystal packing will therefore be of minor influence.

2.3 CONCLUSION AND APPROACH TO THE PROBLEM

The ultimate amount and composition of the solid phase in a fat are determined by the position of the thermodynamic equilibrium solely. The set of equations that describe a solid liquid phase equilibrium can be solved, if a number of requirements is fulfilled.

For prediction of the amount and the composition of the solid phase that can crystallize from an oil in practical situations, calculation of the most stable state by solid-liquid phase equilibrium thermodynamics is insufficient. The solid-liquid phase equilibria of unstable polymorphic forms must be considered as well.

The crystallization route that is followed may lead to inhomogeneous solid phases, of which amount and composition can deviate significantly from the equilibrium composition. Yet in order to calculate the effect of the crystallization process on the solid phase composition the equilibrium solid phase composition as a function of temperature must be known.

From this it is clear that for a prediction of the amount and composition of the solid phase in fats as a function of temperature the first requirement is a good description of the solid-liquid phase equilibrium for all three modifications in which fats crystallize. This work will therefore concentrate upon the development of this description for liquid-multiple solid phase equilibria in fats. The end of this chapter will briefly come back to the influence of the crystallization process.

In Section 2.1 it was shown that for the description of the solid liquid phase equilibrium four steps must be taken, namely:

1. Find a method to solve the complex set of non linear equations that describe the liquid-multiple solid phase equilibrium
2. Find values for the pure component properties: the heat of fusion and the melting point for all of the hundreds of TAGs involved.
3. Predict the activity coefficients of TAGs in the liquid phase.
4. Predict the activity coefficients in all possible solid phases.

These steps, in the order in which they are listed, are the subjects of the next chapters of this work.

3. FLASH CALCULATIONS

Solving the set of nonlinear equations that describe both the phase equilibrium between a liquid phase and a number of solid solutions in order to obtain the number and amount of coexisting phases and the composition of each phase present

from a given overall composition and temperature is called a "solid flash" calculation. There is not any literature on such solid flash calculations. This section will try to alter the best existing algorithms for vapour/liquid flash calculations so that they can deal with polymorphism and a number of solid solutions.

3.1 INTRODUCTION

A flash calculation requires the simultaneous solution of the set of nonlinear equations (Eq. 8–10). As this set cannot be solved analytically, an iterating procedure has to be used, that involves the following steps:

1. First make a estimate of the number of phases that will be present, the amount of phases and their composition.
2. Calculate the activity coefficients.
3. Make a new estimate, applying Eq. (4–9), using the activity coefficients of 2.
4. Repeat steps 2–3 until a convergence criterion is met.
5. Perform a stability test to check whether the initial estimate of the number of phases is correct. If not, an extra phase is added with an estimate of its composition.
6. Repeat steps 2–4 until convergence is obtained and a stability criterion is met.

Whether quick convergence is obtained in steps 2–3 depends on the quality of the initial estimate and on the reliability of the stability test. If the initial estimate is poor, convergence may be slow, to a local, rather than a global minimum or to a trivial solution with two phases having the same composition. A poor stability test will lead to an incorrect number of phases. A robust convergence procedure leads to the solution, even with a poor initial estimate. It follows that for composing a flash algorithm for fats, one needs:

1. A procedure to test the phase stability and provide an initial estimate for the phase compositions.

2. An iterating procedure to solve the phase equilibrium and mass balance equations.

3.2 INITIAL ESTIMATES AND STABILITY TESTS

There are no algorithms that directly give an estimate of the total number of phases that coexist. All methods start with assuming a single phase, either liquid or vapour. A simple calculation of the overall Gibbs energy learns which of the two is the most stable. For fats, the equivalent procedure is a comparison between the molar Gibbs energy of the fat in the liquid state and those in the α, β′ and β polymorphic forms:

$$g^f = \sum_{i=1}^{n} z_i \, (\mu_i^{0,\,f} + RT \ln \gamma_i^f z_i) \tag{11}$$

For convenience, in the remainder of this chapter the chemical potential in the pure liquid reference state arbitrary to 0, so that Eq. (12) reduces for the liquid state to:

$$\frac{g^L}{RT} = \sum_{i=1}^{n} z_i (\ln z_i) \tag{12}$$

and for the 3 solid states to:

$$\frac{g^m}{RT} = \sum_{i=1}^{n} z_i \left(\frac{\Delta H_f^m}{R} \left(\frac{1}{T} - \frac{1}{T_f^m} \right) + \ln \gamma_i^m z_i \right) \tag{13}$$

(with m = α, β′ or β and neglecting all terms with Δc_p)

The phase that has the lowest molar Gibbs energy is the starting point for the stability test. The stability test checks whether addition of a new phase giving a decrease in the overall Gibbs energy is possible. Two types of stability tests for multicomponent, multiphase systems can be found in literature: methods using a "splitting component" and methods based upon the tangent plane criterion of Gibbs.

3.2.1 Splitting component method

An example of this method is that of Gautam and Seider [28]. Shah [29] uses a nearly similar procedure. Asselineau [30] proposes a simpler procedure where the "splitting component" has to be known beforehand. That is not the case for fats. Gautam and Seider first search all phases to locate the

component with the highest activity. That component is named the "splitting component". Secondly, the phase in which the splitting component is found is searched for the component that has the highest activity in a binary mixture with the splitting component, taking concentrations proportional to those in the splitting phase. Next, these two components are distributed over two trial phases by solving Eq. (8–10) for this binary system using the well known two phase flash Eq. (22) (Box 1), starting with two pure phases.

If this calculation results in a split then the remaining components are distributed over the two trial phases in order of decreasing binary activity with the splitting component. The distribution coefficients that are needed are obtained using the composition of the trial phases calculated so far for getting the activity coefficients.

Box 1: If an initial amount S is assumed for the first trial phase, then Eq. (8–10) (the material balance combined with the phase equilibrium equation) give:

$$x_i^B = \frac{z_i}{1+S(K_i^{AB}-1)} \tag{14}$$

and

$$x_i^A = \frac{z_i K_i^{AB}}{1+S(K_i^{AB}-1)} \tag{15}$$

K is the distribution constant x^A/x^B that follows directly from Eq. (8).

Subsequently a function f(S) is defined:

$$f(S) = x_1^B + x_2^B - x_1^A - x_2^A = \sum_{i=1}^{2} \frac{z_i(1-K_i^{AB})}{1+S(K_i^{AB}-1)} \tag{16}$$

The equilibrium value for the phase split S is determined by calculating the zero of this function by a Newton Raphson iteration:

$$S_n = S_{n-1} - \frac{f(S)_{n-1}}{\left(\frac{\mathrm{d}f(S)}{\mathrm{d}S}\right)_{n-1}} \tag{17}$$

When S is found, the mole fractions are calculated and next the values of the distribution constants K are recalculated, using the new values for x. If the new K-values differ too much form the old ones, the function f(S) is solved again, using the new values of K. If the value of S is not between 0 and 1, the split is considered unsuccessful.

$$K_i^{A,B} = \frac{x_i^A}{x_i^B} = \frac{\gamma_i^B}{\gamma_i^A} \tag{18}$$

This procedure is repeated, taking the component with the second highest activity as splitting component etc. The Gibbs energy of all these trail splits is compared and that one with the lowest Gibbs energy is taken as initial estimate for a subsequent iterating procedure. If none of the binary flashes is successful, no trial phases can be formed and the solution is considered stable.

This procedure can be easily extended to deal with polymorphism in the solid phase. The number of trial splits needs to be extended: instead of one binary flash at each trial split four flashes need to be considered, e.g., if a component in a β phase had been selected as "splitting" not only a β-β split but also β-β′ split, a β-α split, and a β-liquid split must be considered. For a P phase N component system maximally 4P(N-1) trial splits must be evaluated.

3.2.2 Michelsen's tangent plane criterion method

The second approach is based on an extension of the well-known tangent plane criterion of Gibbs [22] for phase stability to the multicomponent, multiphase situation. The tangent plane criterion says that if the tangent to the Gibbs free energy curve at the solution at no point lies above the Gibbs free energy curve then the Gibbs free energy is at a global minimum. The mixture is stable and will not show further demixing. In Figure 7 the tangent to the Gibbs free energy curve at F lies partially above the curve: F is an unstable mixture and will demix in A and B. The tangent to the curve at G lies at no point above the curve and G represents a stable mixture.

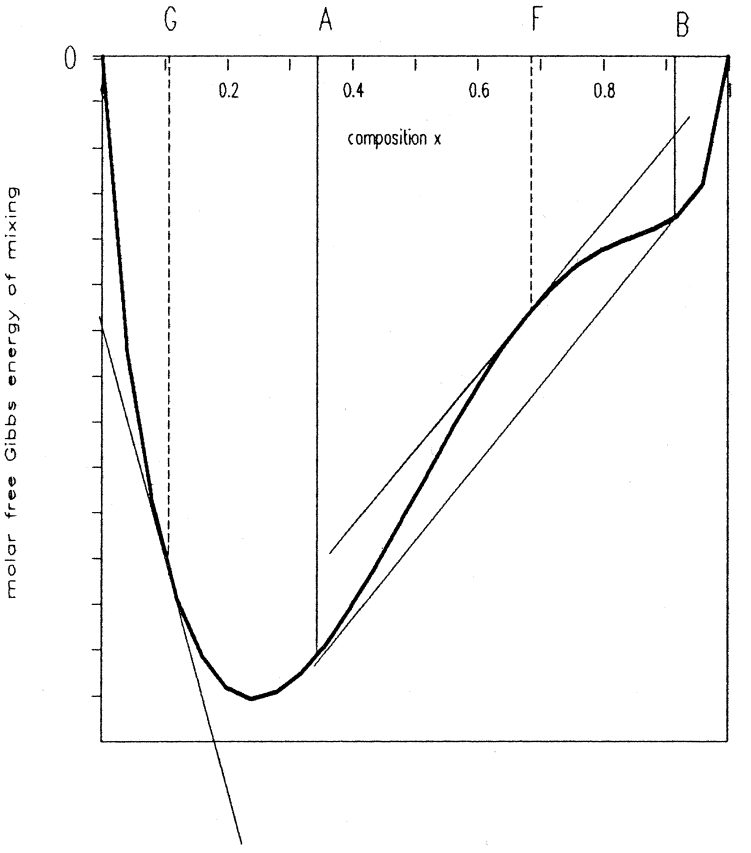

Figure 7 Gibbs free energy of mixing as a function of composition

The general formulation of the tangent plane criterion is presented by Michelsen [31] and the parts of interest for this work will be given next.

The total Gibbs energy of an original P-fase system ($P \leq 1$), apparently in equilibrium ($\mu_l^A = \mu_i^B$) and to be tested for stability is

$$G^{(I)} = \sum_{j=1}^{P} \sum_{i=1}^{n} n_i^j \, \mu_i^j = \sum_{i=1}^{n} n_i \, \mu_i^{(I)} \tag{19}$$

A different phase split into $L = P + 1$ phases with mole fractions y_i^j and totally N_1 mole in phase has a Gibbs energy of:

$$G^{(II)} = \sum_{j=1}^{L} \sum_{i=1}^{n} N_j \, y_i^j \, \mu_i^j \tag{20}$$

The energy difference between the two situations is:

$$\begin{aligned} G^{(II)} - G^{(I)} &= \sum_{j=1}^{L} \sum_{i=1}^{n} N_j \, y_i^j \, \mu_i^j - \sum_{i=1}^{n} n_i \, \mu_i^{(I)} \\ &= \sum_{j=1}^{L} \left(\sum_{i=1}^{n} y_i^j (\mu_i^j - \mu_i^{(I)}) \right) = \sum_{j=1}^{L} N_j \, F_j \end{aligned} \tag{21}$$

A phase split into L phases will occur if the Gibbs energy change is negative. That can only be so if at least one of the F_j is negative. Hence the stability criterion becomes: a system is stable if for any extra trial phase L with trial composition y

$$F_L = \sum_{i=1}^{n} y_i^L (\mu_i^L - \mu_i^{(I)}) \geq 0 \tag{22}$$

This is the general form of the tangent plane criterion.

F_L is positive for any composition y if the minimum of F_L is positive. The composition of the extra phase L at that minimum of F_L is found by simple differentation of F_L to the n-1 independent mole fractions y_i and setting all derivatives to O:

$$\begin{aligned} \frac{\partial F_l}{\partial y_i} &= \frac{\partial \left((\mu_n^L - \mu_n^{(I)}) + \sum_{i=1}^{n-1} y_i [(\mu_i^L - \mu_i^{(I)}) - (\mu_n^L - \mu_n^{(I)})] \right)}{\partial y_i} \\ &= (\mu_i^L - \mu_i^{(I)}) - (\mu_n^L - \mu_n^{(I)}) = 0 \end{aligned} \tag{23}$$

which gives $\mu_i - \mu_i^{(I)} = \mu_j - \mu_j^{(I)} = K$, a constant. The minimum of F should be greater than zero for stability

$$F(\min) = \Sigma \, y_i \, K = K \geq \mathrm{O} \tag{24}$$

It is often simpler to deal with activity coefficients rather than chemical potentials. The activity coefficients of the trial phase L are introduced with the help of Eq. (5):

$$k = \frac{K}{RT} = \frac{\mu_i^{0,L} - \mu_i^{(I)}}{RT} + \mathrm{In} \, \gamma_i^L + \ln \, y_i^L \tag{25}$$

If addition to a trial phase L gives a negative value of k, then the addition of an infinitesimal amount of phase L (infinitesimal, in order not to change composition of the other phases and so $\mu^{(I)}$) will lower the Gibbs energy. The original situation was unstable. The composition of the trial phase L with mini-

mum value for k can be found from an initial estimate of L by iterating:

$$\ln (y_i^L e^{-k}) = \frac{\mu_i^{(I)} - \mu_i^{0,L}}{RT} - \ln \gamma_i^L \tag{26}$$

From the calculated values of $y_i = \frac{y_i^L e^{-k}}{\sum_i y_i^L e^{-k}}$. If the denominator in this equation is smaller than 1, it corresponds to $k > 0$ and so to stability.

If there is no minimum of K located on the plane between the initial estimate of the trial phase and one of the existing phases, the iteration procedure converges to a trivial solution, in which the trial phase has the same composition as one of the existing phases. Therefore a number of initial estimates is necessary, to ensure that the minimum of K is found if it exists.

Michelsen recommends to take a pure phase of each component as initial estimate plus a trial phase with a composition that is the average of the composition of all phases present. He has shown that the iterations needn't be continued to convergence: for each initial estimate four iterations suffice. The trial phase with the most negative value of K is used as the initial estimate for the new phase, which will form after the split. If no negative values of K are found for all initial estimates, then only the one with the least positive value of K is converged. If this trial phase still yields positive values of K, then the original situation is considered stable.

Sometimes the authors found in highly nonideal systems after four iterations a phase with a negative K, indicating instability. But upon continuing iterations to convergence it occurred that K turned greater than O, indicating stability. Stopping after 4 iterations would have led to a false conclusion. Therefore always converge the trial phase that has the smallest K after four iterations.

Michelsen's stability test can be applied to solid liquid equilibria in TAGs simply by increasing the number of initial estimates for the trial phases: pure β, β′ and α phases of each component plus a β, a β′, an α, and a liquid phase (if not already present) with a composition being the average of all phases

already present. In a N component P phase system maximally 3N + 4 trial phases must be considered, about a factor P less than with the splitting component approach.

Michelsen's stability test has the advantage of being derived from the proven thermodynamic tangent plane criterion and requiring only a small number of trial phases, while the method of Gautam and Seider and like methods have no fundamental guarantee that phase instability is always detected. However in Michelsen's procedure the true minimum of K may be overlooked because of the selection of starting values for the trial phases. The algorithm of Michelsen and a number of algorithms similar to that of Gautam and Seider have been tested on several different vapour liquid and vapour liquid-liquid-liquid equilibria [32]. Generally Michelsen's algorithm proved to be the most reliable. In this chapter the performance of both methods with solid liquid equilibria in fats will be tested.

3.3 ITERATING PROCEDURES

Once a good initial estimate of the number of phases, their polymorphic form, and their composition is obtained, the equilibrium composition and phase quantities can be calculated by solving Eq. (8–10). The iterating procedures to solve these phase equilibria and mass balance equations fall into two categories:

1. The direct substitution methods
2. Methods involving the minimisation of the Gibbs Free Energy.

3.3.1 Direct substitution

This is the multiphase multicomponent analogue of the two-phase two-component flash equation, described in section 15.3.2.1 (Eq. 15 and 16).

The function f(S) is redefined for the P phase analogue as a set of P-1 equations:

$$\sum_{i=1}^{n} \frac{z_i(K_i^{mP} - 1)}{1 + \sum_{f=1}^{P-1} \Phi_f (K_i^{fP} - 1)} = 0 \quad (m = 1,2..P-1) \tag{27}$$

m ranges from 1 to P–1. K^{mP} is the distribution coefficient of a component over the phases m and P.

The solution of these sets of equations to obtain the P-1 phase fractions is carried out by Newton Raphson iteration. Then using these phase fractions new compositions are obtained. Next, new values for the distribution constants are calculated with the appropriate thermodynamic models. If these new values do not agree with the previous ones within a certain tolerance, the set equations is solved again for the P–1 phase fractions, using the new values of K.

Direct substitution is a very fast and reliable method for phase equilibria where the values of the activity coefficients do not depend strongly on the phase composition. It therefore seems most suited for calculating α phase equilibria, where all activity coefficients are 1 (see Section 15.5) and the values of K only depend on temperature, so that only one iteration will be sufficient.

When the activity coefficients strongly depend on the phase composition and/or when phase envelopes are very narrow, like it is often the case in the β and β′ modification, the direct substitution method converges very slowly. Examples of the need for several hundreds of iterations are known [31,33]. Various acceleration procedures exist, the General Dominant Eigenvalue method (GDEM) of Crowe and Nishio [33] being recommended by Michelsen [31] and by Swank and Mullins [32]. Even with these methods, convergence is not always obtained in the case of vapour-liquid equilibria, and other methods had to be used [31].

For systems that three GDEM acceleration steps are sufficient, each after five iterations and using more than two eigenvalues, even when more than three phases were present, offered no significant improvement in acceleration. This is in agreement with the findings of Michelsen and Swank & Mullins [31,32].

3.3.2 Gibbs free energy minimisation

The other method to solve the phase equilibrium and material balance equations is to minimize the Gibbs free energy. When the Gibbs energy is at its minimum the requirement for equi-

librium, equation (12), is satisfied. The problem can hence be reformulated for a N component, P phase system as:

Find the minimum of:

$$G_{\vec{n}} = \sum_{j=1}^{P} \sum_{i=1}^{N} n_i^j \, \mu_i^j = \vec{n} \cdot \vec{\mu} \tag{28}$$

subject to the constraints of the mass balance and the requirement of all $n_i^j \geq 0$

The two vectors are defined as:

$$\vec{n} = \begin{pmatrix} n_1^1 \\ n_2^1 \\ \cdot \\ \cdot \\ \cdot \\ n_N^P \end{pmatrix}, \qquad \vec{\mu} = \begin{pmatrix} \mu_1^1 \\ \mu_2^1 \\ \cdot \\ \cdot \\ \cdot \\ \mu_N^P \end{pmatrix} \tag{29}$$

The Gibbs free energy can be minimized by several variations on Newton's method (Box 2).

Two things should be added to the standard Newton method:

1. The solution should be within the constraints imposed by the mass balance and not result in negative concentrations.
2. It should be verified that the extreme obtained is actually a minimum and not a maximum or a saddle point.

The mass balance Eq. (9) can be equivalently formulated for each component i as:

The elements i of the vector $\vec{\Delta n}$ should obey

$$\sum_{j=1}^{P} \Delta n_i^j = \mathrm{O} \tag{30}$$

Box 2: The Gibbs free energy close to an initial estimate of the solution is given by a Taylor expansion:

$$\begin{aligned} G_{\vec{n}+\vec{\Delta n}} &= G_{\vec{n}} + \vec{\nabla G_{\vec{n}}} \cdot \vec{\Delta n} + \frac{1}{2} \vec{\Delta n}^T \cdot \nabla^2 G_{\vec{n}} \cdot \vec{\Delta n} \\ &= G_{\vec{n}} + \sum_{j=1}^{P} \sum_{i=1}^{N} \frac{\partial G_{\vec{n}}}{\partial n_i^j} \Delta n_i^j + \frac{1}{2} \sum_{j=1}^{P} \sum_{i=1}^{N} \sum_{k=1}^{P} \sum_{h=1}^{N} \frac{\partial^2 G_{\vec{n}}}{\partial n_i^j \partial n_h^k} \Delta n_i^j \Delta n_h^k \end{aligned} \tag{31}$$

Since the first term of this equation is constant, the minimum Gibbs energy is obtained when the two right hand sideterms $\Phi_{\overrightarrow{\Delta n}} = \overrightarrow{\nabla G_{\overrightarrow{n}}} \cdot \overrightarrow{\Delta n} + \frac{1}{2}\, \overrightarrow{\Delta n^T} \cdot \nabla^2 G_{\overrightarrow{n}} \cdot \overrightarrow{\Delta n}$ have a minimum. The minimum of this quadratic function Φ is easily calculated by setting its derivative to zero:

$$\nabla^2 G_{\overrightarrow{n}} \cdot \overrightarrow{\Delta n} = -\overrightarrow{\nabla G_{\overrightarrow{n}}} \tag{32}$$

This set of linear equations in Δn_i^j is readily solved and the resulting vector $\overrightarrow{\Delta n}$ is called the Newton direction. $\overrightarrow{n} + \overrightarrow{\Delta n}$ is an improved estimate of the composition at the minimum.

Next step would be to calculate new values for $\overrightarrow{\nabla G}$ and $\nabla^2 G$ at this improved estimate, determine the Newton direction from this point and repeat this until convergence is obtained.

This set of N linear constraints can be used to eliminate N variables from Eq. (33), so that indeed the mass balance is satisfied. Box 3 following describes a general way of doing this.

Non negative values for the mole numbers can be assured by introduction of a so called step size λ. The new estimate for the composition is set to: $\overrightarrow{n} + \lambda\, \overrightarrow{\Delta n}$. The step size λ is taken as the largest possible value not exceeding 1 that:

- still results in a new estimate of the solution in which all mole numbers n_i^j are greater than a small positive number δ and
- gives a decrease in Gibbs free energy.

Box 3: The set of linear mass balance constraints can be alternatively formulated as:

$$A \cdot \overrightarrow{\Delta n} = \overrightarrow{0},\ A = (I_1\, I_2 \cdot\cdot I_p) \tag{33}$$

The (P*N) x N matrix A consists of P identity matrices with dimension N.

If a second matrix Z of which its columns form a basis for the set of all vectors orthogonal to the rows of A is defined, then any vector $\overrightarrow{\Delta n} = Z \cdot \overrightarrow{\Delta n^z}$ will satisfy the mass balance constraints: $A \cdot \overrightarrow{\Delta n} = A \cdot Z \cdot \overrightarrow{\Delta n^z} = \overrightarrow{O} \cdot \overrightarrow{\Delta n^z} = \overrightarrow{O}$. Such a matrix Z of which the columns are orthogonal to the rows of A is:

$$Z = \begin{pmatrix} I_1 & I_2 & \cdot & \cdot & I_{p-1} \\ & & & -I_u & \end{pmatrix} \tag{34}$$

in which I is an identity matrix of dimension N and I_u is an identity matrix of dimension (N − 1) *P.

If $\overrightarrow{\Delta n}$ in Eq. 32 is substituted by $\overrightarrow{\Delta n^z}$, then the solution to the constrained problem of Eq. 32 is given by:

$$\nabla^2 G^Z_{\overrightarrow{n}} \cdot \overrightarrow{\Delta n}^Z = -\overrightarrow{\nabla G_{\overrightarrow{n}}}^Z, \quad \nabla^2 G^Z = Z^T \cdot \nabla^2 G \cdot Z$$
$$\overrightarrow{\nabla G}^Z = Z^T \cdot \overrightarrow{\nabla G} \tag{35}$$

The solution $\overrightarrow{\Delta n^z}$ is transformed to the original $\overrightarrow{\Delta n}$ by multiplication with Z.

The value that is chosen for δ depends on the precision of the computer used. In this way is guarantied, that no negative mole numbers will occur and that the calculations remain numerically stable. λ should differ form unity only in the first few Newton iterations.

A Newton direction that points to a minimum in the Gibbs energy is only obtained when the matrix of the second derivative of the Gibbs energy to all mole numbers, $\nabla^2 G_{\overrightarrow{n}}$, the so called Hessian, is positive definite, i.e., has only positive eigenvalues. In case of activity coefficients only slightly different from 1 this is so. However, in case of solid β and β′ phases it is not necessarily true. If the Hessian is not positive definite, the iterations may converge to a maximum in the Gibbs energy or even not converge at all.

Gautam and Seider [28] solve this problem by ignoring the second derivative of the excess Gibbs energy (ignoring the compositional derivatives of the activity coefficients). This is called the "Rand method." The Hessian is in that case always positive definite. Because of the inaccurate Hessian used, the Rand method will converge slower than when the full-second derivative had been used.

Michelsen [31] recommends the method of Murray [34]. In cases where the Hessian is not definite an approximate Hessian is calculated that is positive definite and looks as much as possible like the original Hessian (Box 4).

Instead of using the original Hessian, the modified Hessian is subsequently used when solving Eq. (33); then the resulting Newton direction always points to smaller values of the Gibbs energy.

Box: 4: The Hessian is decomposed by a so-called Cholesky decomposition into a lower triangular matrix L and a diagonal matrix D:

$$\nabla^2 G = L \cdot D \cdot L^T \tag{36}$$

The j-th column of the L matrix is defined from the previous columns by the equations:

$$d_j = \nabla^2 g_{jj} - \sum_{s=1}^{j-1} d_s \, l_{js}^2 \tag{37}$$

$$l_{ij} = \frac{1}{d_j}\left(\nabla^2 g_{ij} - \sum_{s=1}^{j-1} d_j \, l_{js} \, l_{is}\right) \tag{38}$$

If the Hessian is positive definite, all the elements of the diagonal of D are positive. In the other case, the decomposition results in a matrix D with some negative elements and a matrix L with sometimes extremely large values. Murray's method modifies the elements of the L and D matrix during decomposition, if during decomposition an element d_j becomes smaller than a small positive number Δ, d_j is replaced by Δ. The value of delta is determined by computer precision. If, by using this value of d_j for the calculation of the next column of L, one of the values of the elements of L next exceeds a certain maximum, the value of d_j is increased such that the elements of L will be below that maximum. The maximum of the elements of the column of L to be calculated is given by

$$l_{ij}^2 \leq \frac{1}{d_j} max\left(j, \frac{\xi}{\sqrt{N^2-1}}, \in_m\right) \tag{39}$$

γ is the largest diagonal element of the Hessian, $\in$ is the largest off-diagonal element of the Hessian and $\in_M$ is the precision of the computer used.

Using the modified forms of the L and D matrices, a modified Hessian is calculated. This modified Hessian is

positivedefinite. The decomposition and recombination of the original Hessian is numerically stable. The resulting modified Hessian is a very close positive definite approximation of the original Hessian.

3.3.3 Removal of phases

Occasionally it is necessary to remove one of the phases while solving the flash equations. This can occur in cases where initially a liquid phase is most stable, next a phase split occurs into liquid and β, thereafter a second split into liquid, β and β′ and during subsequent iterations the amount of liquid starts to approach zero. Calculations become increasingly inaccurate in that case. Therefore if the amount of one of the phases present drops below 5% during iterations, it is examined whether two phases can 'coalesce' such that a reduction in Gibbs energy is obtained. In that case iterations are continued with a reduced number of phases.

3.4 COMPARING METHODS

3.4.1 Criteria

The procedures that were outlined and modified in the previous section have to be compared on their performance with multicomponent multiphase solid-liquid flashes. Unfortunately, experimental data does not exist in which the number of coexisting solid phases and their composition is known. It is probably impossible to obtain such data for TAG-systems. As an alternative the following procedure is adopted.

Both stability tests are applied and the initial estimates are converged using all three convergence methods. Criteria for performance of the stability tests are:

1. Indication of instability where this is not the case: the test indicates instability and results in a phase split while during subsequent convergence this phase is removed again.
2. Failure to predict instability: one test indicates instability, the other doesn't, while the resulting converged phase split indeed has a reduced Gibbs free energy.
3. Number of iterations needed to converge the initial estimate.

Performance criteria for the convergence methods are:

1. Convergence.
2. The total computing time to reach convergence.

As test cases the following systems were considered:

1. Fully hardened palm oil (PO58), a 6 component system containing all TAGS that can be formed from palmitic and stearic acid, at temperatures between 40 and 70°C.
2. A ternary system of SSS, PPP and SES, where two components that are completely immiscible in the solid phase are combined with a component that is partially miscible with both. Temperature is varied between 50 and 75°C.

As description of the excess Gibbs energy both the 2-suffix and the 3-suffix Margules equation were used (see Section 15.7). The necessary binary interaction coefficients were obtained by fitting the data of de Bruijne [35, Section 15.7]. Calculations were performed three times, first only allowing the formation of the α- modification, secondly only allowing the β′-modification and finally allowing all modifications.

Swank and Mullins [32] performed a similar exercise with a number of vapour-liquid phase equilibria. They judged Michelsen's stability test as the most reliable and direct substitution as the quickest convergence method. However not all problems could be solved by direct substitution.

A combination of Michelsen's stability test plus a Murray minimisation always lead to the correct solution.

3.4.2. Test Results

A computer program was written in Turbo Pascal 5.0 for MS-DOS PCs that implements the two initial estimate and stability test procedures and the three methods to solve the flash equations.

The stability test of Michelsen clearly performs better than the algorithm of Gautam and Seider. It is faster and more reliable; especially in the ternary test system the splitting component approach indicates instability, where this is not the case.

Table 3 Average Time Per Flash (of 60 flashes) for the Test Systems (on a Compaq 386/25 PC under MS DOS)

System	Number of phases	Direct substition	Rand	Murray
PO58 (α form)	2	0.1 s	0.3 s	0.3 s
PO58 (β′, 2 suffix)	3	0.5 s	no conv.	0.8 s
PO58 (β′, 3 suffix)	3	no conv.	no conv.	1.4 s
PO58 (β' + β, 2 suffix)	4	no conv.	no conv.	2.0 s
PO58 (β' + β, 3 suffix)	5	no conv.	no conv.	2.7 s
(SSS/PPP/SES) α	2	0.08 s	0.12 s	0.12 s
(SSS/PPP/SES) β′	2	0.16 s	0.3 s	0.12 s
(SSS/PPP/SES) β	3	0.16 s	0.2 s	0.24 s

Both tests where perfectly able to deal with polymorphism in the solid phase. The coexistence of a number of stable β and β′ phases in PO58 was obtained without problems.

The three convergence algorithms are compared in Table 3.

"No conv." in the table means that convergence to a gradient norm of 10^{-12} was not obtained within 50 iterations. Except for the α phase and cases where no convergence was obtained, direct substitution converged within 6–25 iterations, while the Murray method needed 2–6 iterations.

For α phase calculations (in Section 15.5 is shown that miscibility in the α-modification is ideal, so only one solid phase plus a liquid phase are present) direct substitution is especially for larger systems (N = 6–50) the quickest method that will converge safely.

The Rand Method has, as expected, problems with converging in highly non-ideal systems and in systems where the initial estimate contains concentrations close to zero. Performance is inferior to both other methods.

The Murray method always resulted in a reasonably fast and safe convergence and is therefore the best method to be used for the β′ and β modifications, where demixing in the solid phase can occur. It is slower than the direct substitution method but more reliable.

These conclusions are in line with those of Michelsen: for vapour-liquid flashes with one liquid phase he advises the

direct substitution method, while for VLL and VLLL flashes a Murray minimisation works out better.

For flash calculations in fats it is therefore recommended to use Michelsen's stability test for initial estimates and Murray minimisation of the Gibbs Free energy for obtaining the final solution. For the α modification the direct substitution method should be used.

3.5 CALCULATION OF DIFFERENTIAL SCANNING CALORIMETRY CURVES

Differential Scanning Calorimetry (DSC) is one of the most frequently used techniques to study the solid phase behaviour of TAGs.

With DSC the apparent heat capacity of a sample is measured as a function of the temperature. It is often used as a tool to characterize a crystallized fat [36–39] and slowly replaces the more traditional methods for quality control of Cocoa Butter Equivalents and Replacers [40]. Comparison of experimental and calculated DSC-curves enables a better interpretation of those curves.

Make the simplifying approximation that the heat capacity of solid and liquid fat is equal, then the equilibrium DSC curve at infinitive slow scanning rate of any fat mixture can be calculated from:

$$c_p^{\text{apparent}} = c_p + \left(\frac{\partial H}{\partial T}\right)_n$$
$$H = H^E + \sum_{j=1}^{P}\sum_{i=1}^{N} n_i^j H_i^{0,j} \tag{40}$$

For convenience, set H (liquid) to zero for each component, which implies that H^0 becomes equal to the heat of fusion of the pure component in that modification. Another assumption is to neglect the excess entropy, which will be most likely comparatively small. The DSC curve can then be calculated from:

$$c_p^{\text{apparent}} = c_p + \frac{\partial G^E}{\partial T} + \sum_{j=1}^{P}\sum_{i=1}^{N} H_i^j \frac{\partial n_j^i}{\partial T} \tag{41}$$

The two partial derivatives in this formula are easily obtained by numerical differentiation, which requires two flash calcula-

tions for each point on a DSC curve. Calculations are speeded up considerably when the outcome of the flash calculation for one point is used as initial estimate for calculation of the next point.

Norton [41] constructs a DSC curve by using the Hildebrand equation for calculating the partial derivatives. The applicability of this approach is rather limited, because the Hildebrand equation describes only the phase behaviour of pure (= completely demixed) solid phases. Solid phase miscibility has a large influence on the shape of a DSC curve as is shown in Figure 8 for the ternary system 25 MPM/ 25 PPO/ 50 000 in the β′ form. This system cannot be described by the Hildebrand equation.

As will be shown in Section 15.7, the ternary of Figure 8 can be described by the 2-suffix Margules equation in which the binary interaction coefficient $A_{MPM-PPO}$ is 1.8 ± 0.3. Although no demixing of the solid phase takes place, still two peaks occur in the DSC curve. In literature the appearance of two peaks in DSC-thermograms of a fat is often used as

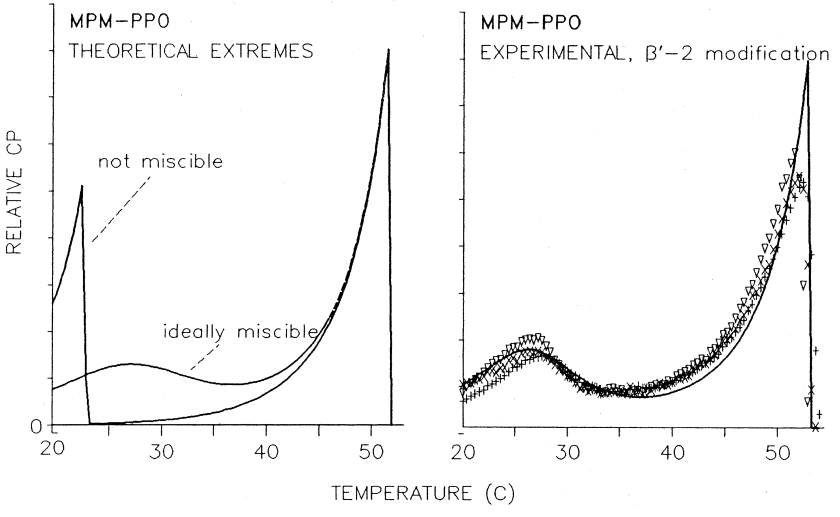

Figure 8 DSC – melting curves of a mixture of 25% MPM, 25% PPO and 50% 000 left: theoretical extremes: ideal and no solid state miscibility right: experimental (points) and calculated (line) curves.

indication for the presence of two solid phases [16,34,36,42]. In fact, it only indicates the presence of two groups of TAGs in the fat that have a clear difference in melting point, but may have cocrystallized.

Figure 8 also shows that DSC, together with the calculation procedures of this report form an elegant method for determination of binary interaction parameters and verification of excess Gibbs energy models.

3.6 CONCLUSION

A flash calculation consists of two parts: a stability test that gives an initial estimate of the phase compositions when it detects that a phase split can occur, and a convergence method that determines the phase compositions and phase quantities at equilibrium starting from the initial estimate. As no procedures for solid-liquid flashes were available, several existing methods for vapour-liquid flashes were adapted and tested for their performance with solid liquid flashes in fats.

1. The best stability test is the so-called stability test of Michelsen, that, with some small changes, can perfectly handle solid fats and polymorphism.
2. Only in case of the α modification (ideal solid miscibility) the normal direct substitution method for solving the flash equation gives a quick, reliable result.
3. For the β' and β modification (highly nonideal solid phases) direct substitution is unreliable. The flash problem can better be solved with a Gibbs free energy minimisation using Murray's method (a modified Newton method). This method is somewhat slower but very reliable.
4. Flash calculations can be applied for simulation of DSC curves of fat blends.

4. PURE COMPONENT PROPERTIES

For a thermodynamic description of the solid liquid phase equilibrium in a fat, the enthalpy of fusion and melting point of each modification of each TAG in the mixture are needed. These pure component properties can impossibly be measured

for all TAGs. Therefore correlations between structural characteristics and the properties must be developed. Existing correlations for heat of fusion and melting point are only reliable for mono-acid TAGs. Therefore, after having appended literature data with a set of experimental data, correlations for the heats of fusion and the melting points of TAGs in the α, β′ and β-modification are developed.

4.1 LITERATURE DATA AND CORRELATIONS

4.1.1 Correlating enthalpy of fusion and melting points of lipids

It is often assumed [2,43–53] that the enthalpy and entropy of fusion of lipids (alkanes, fatty acids, methyl esters, TAGs) can be seen as the sum of a contribution of the hydrocarbon chains that depends linearly on the chain length and a contribution of the end and head groups that is independent of chain length (Eq. 42 and 43, Figure 9).

$$\Delta H_f = hn + h_0 \tag{42}$$

$$\Delta S_f = sn + s_0 \tag{43}$$

n is the carbon number of the component.

In this view, the incremental hydrocarbon chain contributions h and s do not depend on the nature of the compound but only on the way the hydrocarbon chains are packed: h and s are universal lipid constants that only depend on the

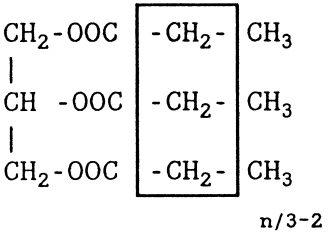

Figure 9 Schematic representation of the head group, the hydrocarbon chain and the end group of a TAG.

Table 4 Values for the Incremental Hydrocarbon Chain Contribution to the Enthalpy of Fusion (h) and the Entropy of Fusion (s). Numbers in Superscript are References

Compound	Polymorph	h (kj/mol CH_2)	s (J/K, mol CH_2)
n-alkanes	α	2.64[1], 2.5[2],	6.4[1], 6.0[2]
TAGs	α	2.5[3], 3.4[11], 3.6[12]	6.1[3]
n-alkanes	β'	3.2[1], 3.8[2], 3.98[4], 3.86[5]	7.7[1], 9.7[2], 9.52[4]
Methylesters	β′	3.78[6]	9.2[6]
TAGs	β′	3.87[3], 3.25[7]	9.8[3]
n-alkanes	β	4.11[1], 4.12[8]	9.9[1], 9.89[8]
Methylesters	β	4.28[6]	10.3[6]
Fatty acids	β	4.2[9], 4.3[7]	11.1[7]
Diglycerids	β	4.28[7]	10.5[7]
Monoglycerides	β	4.28[7]	10.5[7]
TAGs	β	4.28[7], 4.20[3]	10.5[3], 10.6[7]

polymorphic form in which the lipid has crystallized. This is experimentally confirmed (Table 4). Only the values for h of Bailey [52] and de Bruijne [53] for the α-modification of TAGs deviate. Perron [45] showed that these numbers were derived from very unreliable data.

The end group contributions h_0 and s_0 are specific to each class of lipids. Correlating the properties of alkanes and methylesters results in different values for h_0 and s_0 for these two groups of components.

The melting point T is simply given by the ratio of the enthalpy and entropy of fusion:

$$T_f = \frac{\Delta H_f}{\Delta S_f} = \frac{hn + h_0}{sn + s_0} \tag{44}$$

Expanding the denominator in this equation into a power series of 1/n gives:

$$T_f = \frac{h}{s}\left(1 + \left(\frac{h_0}{h} - \frac{s_0}{s}\right)\frac{1}{n} - \frac{s_0}{s}\left(\frac{h_0}{h} - \frac{s_0}{s}\right)\frac{1}{n^2} + \ldots\right) \tag{45}$$

This equation can be cut off after the second or the third term:

$$T_f = T_\infty\left(1 + \frac{A}{n} - \frac{AB}{n^2}\right) \tag{46}$$

$$T_f = T_\infty\left(1+\frac{A}{n}\right) \tag{47}$$

The constants T_∞, A and B are given by:

$$T_\infty = \frac{h}{s}, \quad A = \frac{h_0}{h} - \frac{s_0}{s}, \quad B = \frac{s_0}{s} \tag{48}$$

This implies that if the melting points of a class of lipids have been correlated, only one data point for the enthalpy of fusion is in principle sufficient to obtain a correlation for the enthalpy of fusion of the complete class of lipids.

Eq. (44) has successfully been used by Zacharis [51] to correlate the melting points of a large number of lipids: n-alkanes, methyl-esters, ethylesters, fatty acids, mono-acid mono- di- and tria-cylglycerols, phosphoglycerides, and dicarboxylic acids. He has found values for T_∞ that vary between 390 K and 410 K.

4.1.2 Data and correlations for TAGs

The main difficulty in the development of correlations for the thermal properties of TAGs is that TAGs is that TAGs do not belong to one class of lipids in the sense of Section 15.4.1.1. Not all TAGs share the same end-group. This becomes clear when a saturated TAG is formally denoted by the lengths p, q and r of its three fatty acid chains, i.e., p.q.r. P is always the shortest of the fatty acid chains on the 1- and 3-position of the glyceryl group. For example, myristoyl-stearoyl-palmitoyl-glycerol (MSP) is denoted as 14.18.16. The chain length differences x and y are defined as follows:

$$x = q - p$$

$$y = r - p$$

Only TAGs having the same value of x and y belong to a family of TAGs that share the same end-group. For TAGs that differ in x and y the value of the head and end group contributions h_0 and s_0 from Eq. 39 and 40 are different.

The dependency of the 'head and end group' contributions h_0, s_0, A and B from x and y and from the presence of unsaturation in the hydrocarbon chains must be accounted for in the

development of general correlations for all TAGs. In this work this will be accomplished by the addition of two extra terms to Eq. 39 and 40.

$$\Delta H_f = hn + h_0 + h_{xy} f_{xy} + h_{unsat} f_{unsat} \quad (49)$$

$$\Delta S_f = sn + s_0 + s_{xy} f_{xy} + s_{unsat} f_{unsat} \quad (50)$$

The functions f_{xy} and f_{unsat} should account for the effects on the thermodynamic properties of differences in chain length and degree of unsaturation. Their functional form cannot a priori be established.

Literature

The literature on the enthalpy of fusion of TAGs was reviewed up to 1975 by R.E. Timms [49]. Timms provided the enthalpy of fusion of 42 triglycerides, 19 saturated (16 beta and 3 beta′) and 23 unsaturated TAGs. The data were correlated using Eq. 39:

$$\Delta H_f^{\beta} = 4.28n - 32.6 \text{ kJ/mol} \quad (51)$$

$$\Delta H_f^{\beta'} = 0.76\ \Delta H_f^{\beta} \quad (52)$$

For mixed acid saturated TAGs the enthalpy of fusion should be reduced by 18.3 kJ/mol. The enthalpy of fusion of unsaturated TAGs was described by setting an effective carbon number for each unsaturated fatty acid (O = 10.4, E = 13.9, Li = 8.9). The root mean square error between experimental and predicted data is 4.3 kJ/mol. The values for h agree with those reported for other compounds (Table 4).

Since 1975 various data on the enthalpy of fusion of the stable beta modification of saturated fatty acids were reported [8,10,45,54–63]. The majority of these data concern mono-acid TAGs. There is only one observation for the α-enthalpy of fusion of a mixed acid saturated TAG (PSP, [56]). The data for the β′-modification of saturated TAGs mainly concern PSP and LML. Some data on the mono-acid saturated TAGs are available, but they show large deviations [8,45,59], which are ascribed to the existence of a second, less stable β′-form. Only the data for the most stable β′-form were taken. The number

of data for the lesser stable forms was too small and and the data showed no consistency.

The data of Hagemann [54] for AAA to 30.30.30 for the ′ form and for BBB to 26.26.26 for the -form look very unreliable: the enthalpy of fusion levels off and starts to decrease with increasing carbon number, which is in contradiction to the generally observed trend in lipids. The same holds for the data of Perron [59] for the ′-form of AAA and BBB, which is also admitted by Perron in a later article [45].

The data reported by Garti, Schlichter and Sarig [56] for all modifications differ completely from all other values reported. Therefore they are disregarded in this report.

Perron [48] has carried out the most extensive work on development of correlations for the enthalpy of fusion and melting points of TAGs since Timms. His correlations for the enthalpy of fusion of mono-acid TAGs are:

$$\Delta H_f^{\alpha} = 2.5n - 27.5 \text{ kJ/mol} \tag{53}$$

$$\Delta H_f^{\beta'} = 3.87n - 19.2 \text{ kJ/mol} \tag{54}$$

$$\Delta H_f^{\beta} = 4.20n - 29.9 \text{ kJ/mol} \tag{55}$$

Perron modelled the enthalpy of fusion of an unsaturated TAG as that of the corresponding saturated TAG minus a contribution of the double bonds:

$$\begin{aligned} &\Delta H_f(\text{unsat}) = \Delta H_f(\text{sat}) - 115\,(1 - e^{-0.706\Delta}) \\ &\Delta = \text{number of double bonds in the TAG.} \end{aligned} \tag{56}$$

Perron's values for h agree very well with those for other compounds given in Table 4.

Perron did not give relations for the enthalpy of fusion of mixed acid TAGs. However, he correlated the α and β-melting points of 19 different TAG families using Eq. (44). It resulted, as expected, in large fluctuations of the constant A.

The total collection of data from literature and from the database of Unilever Research Vlaardingen resulted in 152 values for the enthalpy of fusion and 944 melting points. Many of these data are multiple measurements for the same TAG. The polymorphic form of the solid phase is not always given.

Table 5 Number of TAGs for Which Melting Points and Enthalpies of Fusion are Available in Literature

	ΔH_f			T_f		
	α	β′	β	α	β′	β
Saturated	10	10	30	65	54	87
Unsaturated	8	11	16	50	47	49

The number of different TAGs for which data are available is much less (Table 5).

Conclusion

There is a disappointing lack of data for the heat of fusion of TAGs. The heat of fusion data that are available for the unstable modifications are mainly for mono-acid TAGs. Consequently the correlations that have been developed are only valid for mono-acid TAGs. An experimental program is required before these correlations can be extended to mixed acid TAGs.

A considerable amount of melting points that is reasonably well spread over the modifications and TAG-families is available. Correlations have been developed for a number of individual TAG-families, but a general correlation is not available. This correlation will be developed in Section 15.4.3.

4.2 EXPERIMENTAL WORK

The enthalpy of fusion and melting points of 42 saturated mixed acid TAGs and 9 unsaturated TAGs were determined for all three polymorphic forms. The pure TAGs were taken from the stock of reference materials of Unilever Research Vlaardingen. Their purity exceeds 95%.

The experimental program was carried out on a Perkin Elmer Differential Scanning Calorimeter (DSC-7). This DSC-7 is equipped with a TAG 7/3 datalogger and a liquid nitrogen Cooling Accessory. Control of the apparatus is achieved by

means of a PE computer. A more extensive description of DSC is given in Section 15.7.

The thermal data for each modification were obtained by the following procedures:

The data for the β-modification were obtained from the melting curve of the samples as they were delivered, so after several months to years of storage at room temperature.

The α-modification was obtained by rapidly quenching the TAGs from 10°C above the β-melting point to at least 20°C below the α-melting point. The enthalpy of fusion was obtained from the cooling curves. The melting curves were normally not suited for determination of α-thermal data, as the α-melting peak interfered with the β′ and β-crystallization peaks.

The β′-modification was most difficult to prepare as a pure substance; interference of the β′-melting peak with the α-β′ or the β′-β recrystallization peaks was often obtained. Although the authors did not always succeed in preparing pure β′, in general one of the two following methods gave good results:

1. The TAG was crystallized into the α-modification by quenching. Next it was heated till α-melting set in and stabilised at that temperature for, depending on the TAG used, 1 minute to 1 hour. The melting curve was taken.
2. If a β′-β-transition interfered in procedure A, the TAG was melted to 10°C above the β-melting point, rapidly cooled to 1 or 2°C above the α-melting point and stabilized for 30 minutes to 1 hour. The melting curve was taken.

The results are reported in Appendix 1, marked by a *.

4.3 DEVELOPMENT OF THE CORRELATION.

In the development of the correlations, data for TAGs containing acetic acid, butyric acid and hexanoic acid are not used. The chain length of these fatty acids is so short, that they cannot be looked upon as long chain hydrocarbons.

4.3.1 Saturated TAGs

Melting enthalpy

If the data for mono-acid TAGs are regressed against the carbon number n (Eq. 39), leaving out data that have a residual more than two times the root mean square error (RMSE) of the regression through all mono-acid data, we obtain:

$$\Delta H_f^{\alpha} = 2.4\ n - 17.6 \text{ kJ/mol, RMSE} = 4.6,\ r^2 = 0.98 \quad (57)$$

$$\Delta H_f^{\beta'} = 3.95\ n - 59.2 \text{ kJ/mol, RMSE} = 4.7,\ r^2 = 0.97 \quad (58)$$

$$\Delta H_f^{\beta} = 4.13\ n - 27.6 \text{ kJ/mol, RMSE} = 6.1,\ r^2 = 0.97 \quad (59)$$

The RMSE is in the order of magnitude of the experimental error (5–8 kJ/mol) and the values of the constants h agree with those of Perron [45] and those for other lipids, given in Table 4.

If all data are used for a regression of ΔH_f against the carbon number, the values of the incremental chain contribution h do not change significantly, but the RMSE goes up to 20 and the correlation coefficient decreases to 0.7. A RMSE of 20 is too large for a reliable correlation and a correction term for chain length differences must be introduced.

It cannot be assumed that the end group contribution and the variables x and y that define a TAG-family are neatly cor-

Table 6 Parameters that Result When Eq. 57 is Fitted to the Experimental Melting Enthalpy Data of Saturated TAGs. (s.e. = standard error in estimate)

	α-modification		β′-modification		β-modification	
Parameter	Estimate	s.e	Estimate	s.e	Estimate	s.e
h	2.39	0.1	4.17	0.2	4.03	0.1
h_0	−16.3	5	−68.4	8	−24.4	4
h_x	1.98	0.3	17.3	1.6	2.16	0.4
h_{x2}	−0.54	0.07	−3.25	0.3	−0.63	0.07
h_{xy}	–		−1.07	0.3	–	
h_y	–		−9.03	1.2	−7.28	0.5
h_{y2}	−0.64	0.08	–		–	
RMSE	5.2		6.0		7.1	

related. Neither is there any function f_{xy} that is self-evident for use. When the residual error of data predicted by the mono-acid relation with the experimental data are plotted against x and y, it becomes clear that the end group contribution and (x,y) are correlated. The enthalpy of fusion drops more or less quadratically when the difference in chain lengths, represented by x and y, increases. X and y behave similarly and their effect seems additive. From the data for the β-modification it can be seen that the effect of x and y levels off at values of x or y of 6 and more. This is probably associated with the transition from the β-2 form to the β-3 form. At large x or y the -3 forms become more stable than the corresponding -2 forms.

A function that can describe the influence of chain length differences on the melting enthalpy that is observed is a general quadratic function:

$$\Delta H_f = hn + h_0 + h_x x + h_{x2} x^2 + h_{xy} xy + h_y y + h_{y2} y^2 \quad (60)$$

In order to introduce the levelling-off at high x or y, a cut-off value of 6 is used in the calculations in stead of the real value of x or y when x or y exceeded 6. The resulting fit to the experimental data was very good: a RMSE nearly equal to that of a fit to the mono-acid data only was obtained. Melting enthalpies deviating more than 20 kJ/mol from the model predictions were rejected. The resulting values for h are in agreement with those of other lipids given in Table 4.

Melting points

If Eq. (43) is used to fit the mono-acid data, it results in a RMSE of 1.5°C for the α- and β-modification and 3°C for the β′-modification. This compares very well to the experimental error in the melting points of 1–2°C. The RMSE increases to 7–10°C when Eq. (43) is fitted to all data of saturated TAGs. A closer look to the differences between experimental melting points and those predicted by the fit to the mono-acid data suggests a quadratic relationship between x and y and the model parameters A and B:

$$\begin{aligned} A &= A_0 + A_x x + A_{x2} x^2 + A_{xy} xy + A_y y + A_{y2} y^2 \\ B &= B_0 + B_x x + B_{x2} x^2 + B_{xy} xy + B_y y + B_{y2} y^2 \end{aligned} \quad (61)$$

Table 7 Parameters that Result When Eq. (44) and (58) are Fitted to the Experimental Melting Points of Even Saturated TAGs

Parameter	α	β′	β
A_0	−9.0581	−8.4543	−8.0481
A_x	0.00290	−0.10360	0.074130
A_{x2}	−0.0619116	−0.018881	−0.0348596
A_{xy}	0.115128	0.0739411	0.00771420
A_y	−0.453461	−0.49721	−0.404136
A_{y2}	−0.005827	0.0115995	0.0111938
B_0	−4.4841	−0.26501	2.66923
B_x	−0.00111	0.54997	−0.31675
B_{x2}	0.148938	0.074136	0.085967
B_{xy}	−0.365917	−0.340928	0.040642
B_y	1.41154	2.34238	0.55040
B_{y2}	−0.001766	−0.135735	−0.000945
T_∞	401.15	401.15	401.15
RMSE	2.3°C	2.9°C	3.0°C

If the model of Eq. (57) is fitted to the data, the RMSEs that result are most satisfying. A subdivision of the modifications into their −2 and −3 forms (β-2 and β-3, etc.) does not give an improved fit.

The values for T_∞ are in agreement with the values that were found by Zacharis [51].

Simultaneous fit of melting points and melting enthalpies.

Although the empirical relations that were derived are perfectly useful as such, a few unsatisfying aspects must be mentioned:

1. According to Eq. (45) the values for the parameters of relationship [49] for the melting enthalpy can be derived from the parameters values of relation 43 plus 58 for the melting point. If this is actually done so, the resulting parameters for the melting enthalpy are completely different from those given in Table 6. The melting enthalpies that are calculated in this way do not at all agree with the experimental data. Appar-

ently the parameters of Table 7 are not consistent with those in Table 6.

2. The melting enthalpy data for the β-modification showed clearly that the influence of x and y levels off when x or y are greater than 6. The melting points did not seem to show such effect. However, if the correlation for the melting points extrapolated to extreme values of x or y, absurd results are obtained, indicating that levelling off of the influence of x and y should be introduced.

Therefore, this section will attempt to derive a unified model for both the enthalpies of melting, the entropies of melting and the melting points of saturated TAGs, by fitting the ΔH_f and T_f data simultaneously.

The function f_{xy}, as defined in Eq. (46) and (47) should account for the observed decrease in melting enthalpies and melting points as differences between the three chain lengths increase. It should be chosen in such a way that this effect does not grow indefinitely with increasing x and/or y but levels off. The general quadratic relations with cut-off value, which were previously used, did not perform well. The function finally arrived at is:

$$f_{xy} = 2 - \exp\{-\left(\frac{x - x_0}{k_x}\right)^2\} - \exp\{-\left(\frac{y}{k_y}\right)^2\} \tag{62}$$

which increases from 0 (for small values of both x and y) via 1 (for a large absolute value of either x or y) to 2 (for large values of both x and y). We have investigated a more complex variation of this function, namely:

$$f'_{xy} = 2 - \left(1 + \frac{1}{2}\delta\right)\exp\{-\left(\frac{x' - x_0}{k_x}\right)^2\} - \left(1 - \frac{1}{2}\delta\right)\exp\{-\left(\frac{y' - y_0}{k_y}\right)^2\} \tag{63}$$

with

$$x' = \cos\Theta\, x + \sin\Theta\, y$$
$$y' = \cos\Theta\, y - \sin\Theta\, x$$

The more general function (Eq. 60) allows for a rotation over an angle Θ of the (x, y)-axes to (x′, y′)-axes, a difference in scaling along these directions (k_x and k_y instead of a common k), a non-zero offset y_o, and a relative difference in the maximal effects along the two directions expressed by the parameter δ. It appeared, however, that Eq. (59), which is a special case of the more general Eq. (60) (viz. $\Theta = 0$, $k_x = k_y = k$, $y_o = 0$, $\delta = 0$) gave a satisfactory fit to the data. Therefore, the results reported further on refer to this simpler model.

One must also take into account the possible effect of asymmetry on melting points. This is done by including an additional Rln2 term in the expression for the melting entropy to distinguish symmetric ($y = 0$) from asymmetric ($y \neq 0$) TAGs. The work of de Jong and van Soest has shown that for the -phase the inclusion of such a term is appropriate [64,65]. In the β-modification random mixing of the two mirror images is not possible. For the loosely packed α-phase we do not expect that this term is needed. The ′ -phase takes an intermediate position and it is not clear beforehand whether the inclusion of the Rln2 term will improve or worsen the fit.

Finally, consider the phenomenon of melting point alternation: odd mono-acid TAGs tend to melt systematically lower than expected on the basis of interpolation from even mono-acid TAGs. Again, anticipate that allowance for this effect will improve the fit for melting points of -phase TAGs. For the α-phase TAGs, do not expect any benefit and it is not known for the ′ -phase TAGs.

The full expressions for the enthalpy and entropy of melting then read:

$$\Delta H_f = hn + h_o + h_{xy} f_{xy} + h_{odd}.odd \tag{64}$$

$$\Delta S_f = sn + s_o + S_{xy} f_{xy} + S_{odd}.\, Odd + R \ln 2.asym \tag{65}$$

Here “asym” and “odd” are indicator variables taking the value 1 (“true”) when an asymmetric TAG or an odd TAG is involved and the value 0 (“false”) otherwise. An TAG is considered “odd” when at least one of the fatty acid chains has an odd number of carbon atoms

The eight parameters h_o, h_n, S_o, S_n, h_{xy}, S_{xy}, k and x_o were estimated by simultaneously fitting the ΔH_f-model, Eq. (59) and (61), to observed melting enthalpy data and the T_f-model based on Eq. (41), (59), (61), and (62) to observed melting points. The models were fit using weighted non linear least-squares regression taking a factor 6 for the ratio of the variances of melting enthalpies and melting points.

Enthalpies of fusion deviating more than 20 kJ/mol from the model fit have been rejected. Exclude all melting points which could not be fit well, i.e., that deviated more than 10 degrees. In all, the enthalpies of some 40 TAGs and the melting points of about 70 TAGs were fitted for the a-, ′- and -phase separately.

The main results are collected in Appendix 1. Measured values are averaged over several observations with the number of independent observations given in the column labelled FREQ. Zero FREQ values refer to cases excluded from the estimation procedure. The heats of fusion that were measured in this work are separately listed. The estimated parameter values along with their standard errors are given in Table 8.

Table 8 Estimates and Standard Errors of the Parameters from Eq. (61) and (62) When Simultaneously Fitted to Melting Points and Melting Enthalpies of All Saturated TAGs

	α-modification		β′-modification		β-modification	
Parameter	Estimate	s.e.	Estimate	s.e.	Estimate	s.e
h_0	−31.95	3.00	−35.86	5.88	−17.16	4.83
h	2.70	0.07	3.86	0.13	3.89	0.10
s_0	−19.09	10.56	−39.59	19.28	31.04	15.81
s	6.79	0.25	10.13	0.42	9.83	0.34
h_{xy}	−13.28	2.42	−19.35	2.81	−22.29	2.08
s_{xy}	−36.70	7.79	−52.51	8.76	−64.58	6.45
k	4.39	0.50	1.99	0.24	2.88	0.35
x_0	1.25	0.27	2.46	0.19	0.77	0.27
t_∞	397	4.1	381	3.6	395	3.3
h_{odd}	–	–	–	–	2.29	0.44
RMSE (ΔH H)	8.6		9.2		10.3	
RMSE (T)	2.5		3.7		3.7	

It turned out that the inclusion of the symmetry/asymmetry term (Rln2) improved the fit for the -phase in contrast to the α-phase and the ′-phase where the fit became worse. A similar result was obtained for the even/odd term: no significant improvement for the α- and ′-phase and a much better fit for the -phase odd TAGs.

The resulting RMSEs for the melting points are only slightly more than those obtained by fitting the melting points solely. The RMSEs for the melting enthalpy have increased by 50%, but are still acceptable when compared to the experimental error of 5–7 kJ/mol. The values for h and s agree very well with those of other lipids, given in Table 4. The values for h_{xy}, which represent the maximum decrease in ΔH_f that is caused by chain length differences and which are likely to be related to the enthalpy difference between the β-2 and β-3 form of a mono-acid TAG, compare well with the stability difference between the two forms that was calculated by de Jong [13] (10–20 kJ/mol). The values of h_{xy} and s_{xy} increase from α to β, in accordance with the expectation that the influence of chain length differences is more pronounced in a more densely packed polymorph. In the β-modification the influence of x and y levels off at x or y = 6 (2k), as was found previously.

A much more consistent correlation has been obtained at the expense of only a relatively small increase of the RMSEs.

4.3.2 Unsaturated TAGs

Melting enthalpy

The authors have chosen to model the effect of unsaturation on the melting enthalpy of a TAG as a correction to the melting enthalpy of the corresponding saturated TAG (Eq. 46). The model proposed by Perron [48] did not perform very well; it resulted in a RMSE of more than 24 kJ/mol. After having investigated several other functions, the following model evolved:

$$\Delta H_f^{unsat} = \Delta H_f^{sat} + h_o n_o + h_E n_E + h_l n_l \quad (66)$$

Here n_o stands for the number of oleic chains, n_E stands for the number of elaidic chains and n_1 for the number of linoleic

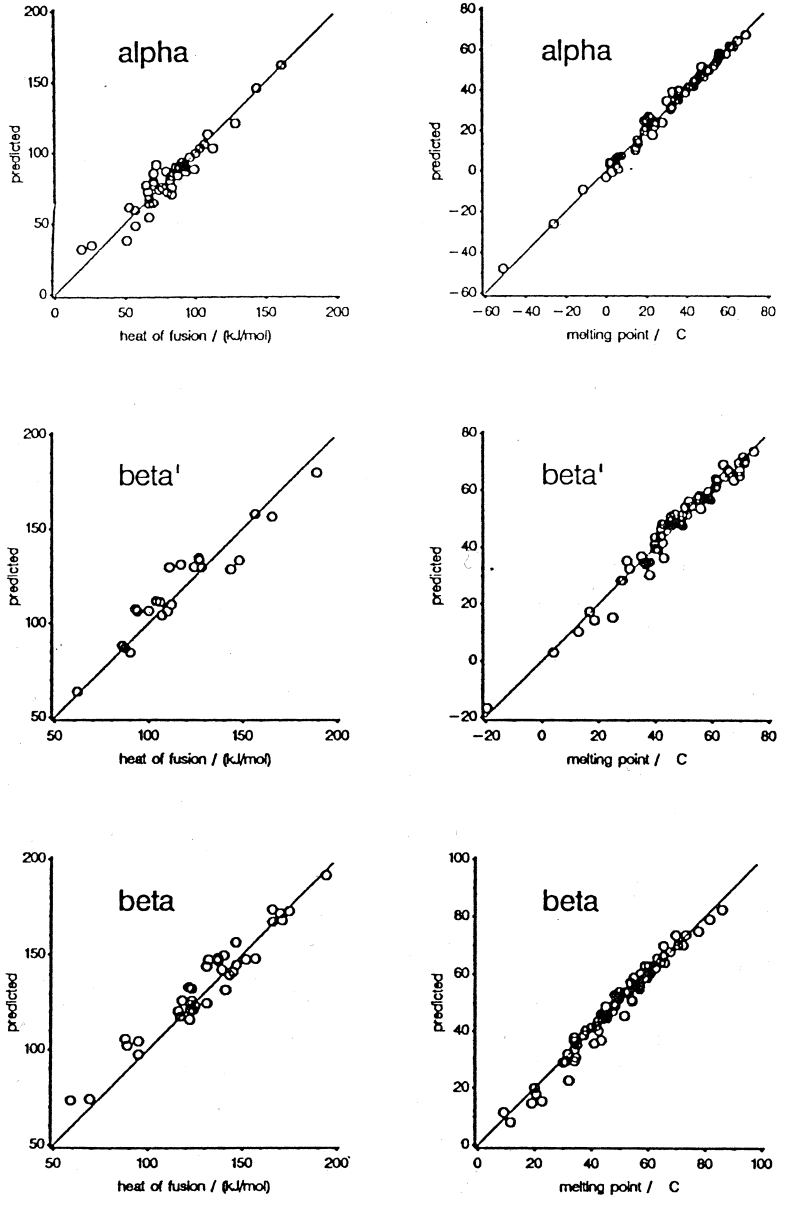

Figure 10 Values of the melting enthalpy and the melting points of saturated TAGs, calculated using the relations 62 and 63 plotted against the experimental data.

chains in the TAG. ΔH_f^{sat} is the melting enthalpy of the corresponding saturated TAG that can be obtained from the data in Table 6 or Table 7.

The authors have fitted this model for the α, β′ and β modifications. The complete data set contained over 80 melting enthalpies of only 16 different TAGs: 20 observations for 12 TAGs in the α-modification, 21 observations for 13 TAGs in the β′-modification, and 44 observations for 16 TAGs in the β-modification. The authors rejected data that deviated more than 30 kJ/mol from the predicted values. The data and the predictions are given in Appendix 1. (See also Figure 10.) The resulting parameters are given in Table 9.

The values of the parameters that were obtained for the β-modification agree very well with the effective carbon numbers that Timms derived for the unsaturated fatty acids. The large RMSE for the β′-modification is solely due to the β′-melting enthalpy of POP (104 kJ/mol vs a predicted value of 128 kJ/mol). If POP is left out the RMSE decreases to 9.7, while the parameter values do not change. POP is the only cis-unsaturated TAG in the data set that crystallizes in the β′-2 form [10], which may explain its deviating behaviour.

There is a lack of data for the unstable modifications of TAGs with linoleic acid, so that the model parameter h_1 for these modifications could not be calculated. The parameter that describes the effect of the fatty acid that is most similar to

Table 9 Estimates and Standard Errors of the Parameters of Eq. (63) Fitted to the Melting Enthalpies of Unsaturated TAGs. s.e = standard error. Values in Brackets were Guessed, Due to Lack of Data

	α-modification		β′-modification		β-modification	
Parameter	Estimate	s.e.	Estimate	s.e.	Estimate	s.e
h_O	−31.7	1.8	−28.3	1.8	−30.2	1.4
h_E	−11.7	1.3	(−15.9)		−15.9	0.9
h_I	(−37.7)		(−37.7)		−37.7	2.5
RMSE	8.3		22		11.1	

linoleic acid, h_0, is nearly independent from the modification. Assume that this also holds for h_1.

A good fit to the available data was altogether obtained; the RMSEs are nearly equal to those of the saturated TAGs. A better general model can only be developed if more experimental data are made available, over a wider range of carbon numbers, including linoleic acid and including mixed unsaturated fatty acid TAGs.

Melting point

An approach to model the melting points of unsaturated TAGs is start from a model for the saturated TAGs and add a correction term that accounts for the presence of O, E, l and linolenic acid (le) (Eq. 46, 15). After exploring various simpler models it was learned that it was necessary to model interactions between unsaturated chains. The final model giving the best results is Eq. (44) for which A is given by:

$$\begin{aligned} A = {} & A_{sat} + A_O n_O + A_E n_E + A_l n_l + A_{le} n_{le} \\ & + A_{OO} n_{OO} + A_{EE} n_{EE} + A_{ll} n_{ll} + A_{lele} n_{lele} \\ & + A_{Ol} n_{Ol} + A_{Ole} n_{Ole} + A_{lle} n_{lle} \end{aligned} \tag{67}$$

and for which B is given by the much simpler expression:

$$B = B_{sat} + B_O n_O + B_l n_l + B_{le} n_{le} \tag{68}$$

Here, for example, no stands for the number of oleic chains in the TAG and n_{ol} for the number of 0–1 pairs. A_{sat} and B_{sat} can be obtained from Table 7 and Eq. (58) or from Table 8, using Eq. (45) and (60–62).

The authors have fit this model for the α, β′ and β modifications. The complete data set contained over 120 melting points of cis-unsaturated TAGs, of which 18 were left out, because they involved unsaturated fatty acids other than o, l and le. Of the remaining 102 melting point data, 13 were associated with the α-modification, 16 with the β′-modification, 13 with the β-modification while for 60 data points the modification was not specified. The modification was not known for 13 of the 47 melting points of the trans containing TAGs.

In these cases the authors chose to assign the melting point to that modification, which gave the best fit. This assignment had to be done in an iterative manner using the results

of the previous regression to determine the best modification input for the next regression analysis and carrying this process through till internal consistency was achieved. This laborious procedure can be viewed as a Maximum Likelihood estimation of both the melting point/structure relationship and the unknown modifications. The data and the resulting assignments are given in Appendix 1. Data deviating more than 10°C from the predicted value were disregarded. The parameters are given in Table 10.

The standard deviations are only slightly larger than those for the saturated TAGs. We do not expect that these values can be substantially improved by another model. It should be realized that the reliability of the input data probably varies considerably. The data have been collected from literature spanning nearly a century. The authors have screened the data to some extent and discarded a number of a priori very unlikely cases. In general, however, it is very difficult to assess the quality of the data reported. Thus, some of the input

Table 10 Estimates and Standard Errors of the Parameters in Eq. (64) and (65) Fitted to the Melting Points of Unsaturated TAGs

	α-modification		β′-modification		β-modification	
Parameter	Estimate	s.e.	Estimate	s.e.	Estimate	s.e
A_O	3.46	0.39	2.20	0.36	2.93	0.24
A_E	1.38	0.16	1.34	0.22	1.68	0.11
A_l	3.35	0.66	2.5	1.1	4.69	0.50
A_{le}	4.2	2.1	2.2	2.1	5.2	1.9
A_{OO}	0.11	0.16	−0.27	0.14	−0.89	0.10
A_{EE}	0.01	0.19	−0.04	0.34	−0.40	0.13
A_{ll}	3.68	0.87	−0.55	0.26	−1.21	0.17
A_{lele}	1	1.9	−1.51	0.92	−1.38	0.60
A_{Ol}	−0.53	0.24	1.0	0.32	−0.71	0.15
A_{Ole}	−0.83	0.34	−0.76	0.22	−0.69	0.18
A_{lle}	3.0	1.3	−1.12	0.36	−0.73	0.52
B_O	0	1.6	−4.3	1.5	−3.7	0.8
B_l	5.4	2.3	−7.8	5.3	−1.5	1.6
B_{le}	2.6	8	−13.7	11.8	−1.8	7.0
RMSE	3.2°C		4.1°C		2.6°C	

data may have a substantial error and this will cause some lack of fit.

In future work we will extend the number of available melting enthalpy data and attempt to correlate the melting enthalpy and melting points of unsaturated TAGs simultaneously.

4.4 Conclusion

A compilation of literature data of melting points and melting enthalpies of TAGs was made. This data set was extended by measurements of melting enthalpies of 51 mixed acid saturated and unsaturated TAGs in all three modifications.

Reliable relations were developed that give the melting point and melting enthalpy as a function of the carbon number, chain length differences and degree of unsaturation for the α, β' and β-modification.

5. MIXING BEHAVIOUR IN LIQUID STATE

Before a study on solid TAG phases that are in equilibrium with a liquid TAG phase, can be started, knowledge of the mixing behaviour of TAGs in the liquid state is required. Although it is generally assumed that TAGs mix ideally in the liquid state, experimental evidence is lacking. Therefore the activity coefficients in mixtures of TAGs in the liquid state are measured using Gas-Liquid Chromatography with a liquid stationary TAG phase. The results are compared with activity coefficients calculated with the UNIFAC group contribution method.

5.1 LITERATURE

It is generally stated in literature on the phase behaviour of TAGs that the miscibility of TAGs in the liquid state is ideal [16,66,67]. Yet the experimental evidence on which this conclusion is based is only very minor:

1. In dilatation experiments on pure TAGs and binary mixtures of TAGs no volume effect was observed

[67,68]. However, although ideal miscibility implies a zero excess volume of mixing, the opposite is not necessarily true.

2. For liquid alkanes it was found that the heat of mixing is less than 0.1 kJ/mol [44,66], even for hydrocarbons considerably differing in chain length. Compared to the heat of fusion this heat of mixing is negligible. It was reasoned that if alkanes have almost no heat of mixing, then TAGs, which are chemically very similar to alkanes, will also have no heat of mixing. Again, ideal miscibility implies the absence of a heat of mixing, while the reverse is not necessarily true.
3. Mixtures of high melting saturated TAGs and liquid unsaturated TAGs were often found to obey the Hildebrand solubility equation (Eq. 66).

$$\ln x_i^L = \frac{\Delta H_f}{R}\left(\frac{1}{T_f} - \frac{1}{T}\right) \tag{69}$$

It is stated that therefore liquid mixtures of TAGs are ideal and if the Hildebrand equation is not obeyed, it is often ascribed to liquid phase non-ideality [27,66]. The Hildebrand equation assumes no solid phase miscibility and ideal liquid phase miscibility. In Sections 15.6 and 15.7 it will be shown that TAGS do show solid phase miscibility. Whether the Hildebrand equation is obeyed or not is therefore no indication for ideality of the liquid state, as the solid state behaviour may not be disregarded.

Summarizing, it is clear that the evidence for ideal miscibility of liquid TAGs is not very convincing. Yet, before any description of solid-liquid phase behaviour and non ideality in the solid phase can be given, the mixing behaviour of TAGs in the liquid state needs to be known. In the next sections measurements of activity coefficients of TAGs in the liquid state are reported and compared with activity coefficients that are estimated using the UNIFAC group contribution method.

5.2 MODEL CALCULATIONS

In order to enable the estimation of activity coefficients in mixtures for which no experimental data are available, Freden-

Table 11 Activity Coefficients in the Liquid Phase for Binary Mixture of SSS with MMM and 8C8, Calculated with UNIFAC

SSS [1] and MMM [2]			SSS [1] and 8C8 [2]		
T (°C)	x_1	y_1	T (°C)	x_1	y_1
100	0.25	1.007	100	0.25	1.091
100	0.50	1.003	100	0.50	1.020
100	0.75	1.000	100	0.75	1.004
120	0.25	1.006	120	0.25	1.079
120	0.50	1.002	120	0.50	1.022
120	0.75	1.000	120	0.75	1.003

slund, Rasmussen and coworkers developed the UNIFAC method [69]. The UNIFAC method was shown to perform quite well in phase equilibrium calculations for many hydrocarbon systems [70].

The basic idea of the UNIFAC method is that although there are thousands of different chemical components of interest for the chemical technology, the number of functional groups that constitute these compounds is much smaller. A natural oil contains thousands of different TAGs, but it only consists of CH_3–, –CH_2–, –CH–, –CH=CH–, –OH and

Table 12 Activity Coefficients in the Liquid Phase for Binary Mixtures of MMM with 8C8, Calculated with UNIFAC

MMM [1] and 8C8 [2]		
T (°C)	x_1	y_1
100	0.25	1.046
100	0.50	1.015
100	0.75	1.003
120	0.25	1.041
120	0.50	1.014
120	0.75	1.002

CH_2COO– functional groups. UNIFAC assumes that the activity coefficient of each component in the mixture is a function of the individual contributions of the components' functional groups. Therefore activity coefficients can be calculated from a limited number of parameters for the functional groups. An excellent and clear description of the method is given by Fredenslund [69].

The activity coefficients of TAGs in a set of TAG mixtures were calculated: in 3 binary mixtures of SSS and MMM, 3 binary mixtures of MMM and 8C8, 3 binary mixtures of SSS and 8C8 and in a mixtures of the 6 main TAGs and the 2 main partial glycerides occurring in palm oil. The authors used a computer program and a database that were obtained from the department of prof. J.M. Prausnitz (University of California, Berkeley) for the calculations.

The results confirm the assumption made in literature and show that the activity coefficients of all TAGs are unity, so ideal mixing of TAGs is predicted. In view of the chemical similarity between all components, this is not too surprising. The two partial glycerides are predicted to have activity coefficients considerably larger than unity, as may be expected for polar compounds in an a-polar solvent.

Table 13 Activity Coefficients in the Liquid Phase for the 6 Main TAGs and the 2 Main Partial Glycerides of Palm Oil at 50°C, Calculated with UNIFAC

Palm oil without partial glycerides			Palm oil with partial glycerides		
Component	x	y	Component	x	y
PPP	0.08	0.9974	PPP	0.08	1.0005
POP	0.26	0.9997	POP	0.26	1.0018
PPO	0.14	0.9997	PPO	0.12	1.0018
PLP	0.10	1.0004	PLP	0.08	1.0008
POO	0.25	0.9998	POO	0.23	1.0009
OOO	0.17	0.9982	OOO	0.17	0.9982
mono-P	–	–	mono-P	0.01	4.2000
di-P	–	–	di-P	0.05	1.3518

5.3 EXPERIMENTS

5.3.1. Method for determination of activity coefficients of mixtures of non-volatile liquids

Activity coefficients in the liquid phase are often determined by measuring to what extent the vapour pressure of a liquid mixture deviates from Raoults' law.

$$p_i = p_i^* x_i^L \tag{70}$$

However, the vapour pressure of TAGs is less than 1 Pa at temperatures between 0°C and 80°C, the temperature region in which solid fat crystallizes. This is unmeasurably small and therefore another method for determination of activity coefficients must be developed.

A well-known method for determination of activity coefficients at infinite dilution of volatile compounds in non-volatile liquids is the use of gas-liquid chromatography (GLC). The nonvolatile liquid is used as stationary phase and the volatile component is injected into the carrier gas stream. The activity coefficient is calculated from the retention time. The GLC method is discussed in many textbooks on gas chromatography (Box 5; [71,72])

Box 5: The net retention volume of a injected sample is defined as the product of the net retention time and the flow rate of carrier gas, corrected for the pressure drop over the chromatographic column:

$$V_n = t_n \Phi_V \cdot \frac{3_V \left(\frac{p_{\text{in}}}{p_{\text{out}}} \right)^2}{2_V \left(\frac{p_{\text{in}}}{p_{\text{out}}} \right)^3} \tag{71}$$

The specific retention volume is defined as the net retention volume per unit mass of liquid stationary phase at 273.15°C. It is given by:

$$V_g = \frac{273.15 V_n}{m_L T} \tag{72}$$

It is assumed that:

the sample concentration in mobile and stationary phase always have the equilibrium values and
that the sample volume is very small in comparison with mobile and stationary phase volume (infinite dilution).

In that case the mol fraction of the sample that is in the mobile phase must be equal to the ratio of the volume of the mobile phase and the retention volume (= net retention volume + mobile phase volume). The equilibrium distribution coefficient of the sample over mobile (L) and stationary phase (G) is therefore given by:

$$K_{LG} = \frac{x^L}{x^G} = \frac{V_n}{n_L} \cdot \frac{n_G}{V_G} \tag{73}$$

The condition for equilibrium between stationary and mobile phase for infinite sample dilution is (if the mixture of carrier gas and sample behaves ideally):

$$px^G = p^* \gamma^\infty x^L \tag{74}$$

By rearranging the latter two equations one obtains an expression for the activity coefficient at infinite dilution of the sample in the stationary phase as a function of net retention volume.

$$\gamma^\infty = \frac{n_L}{p^* V_n} \cdot \frac{pV_G}{n_G} \tag{75}$$

The last term in this equation reduces to RT if the ideal gas law may be applied to a mixture of a carrier gas and a sample.

When the influence of the pressure drop over the column and the non-ideality of the mobile gas phase are taken into account, a correction term must be added to Eq. (72). Replacing the net retention volume by the specific retention volume and the vapour pressure by the corrected vapour pressure according to Prausnitz [22], Desty [71] obtains the following corrected expression for the activity coefficient at infinite dilution:

$$\ln \gamma^{\infty} = \ln\left(\frac{273.15R}{p^{*} V_g M_L}\right) - p^{*}\left(\frac{B_{11} - v}{RT}\right) \tag{76}$$

The second virial coefficient B11 and the molar volume v of the liquid probe at the measuring temperature can be obtained from one of the correlations based on the principle of corresponding states given in Prausnitz [22] and Smith [73].

Although the correction term is significant for the activity coefficients at infinite dilution of the samples, that are used in this work, it is of no influence on the calculated interaction between the non-volatile components in the stationary phase, as will be clear from Eq. (77) and (82) in the next section. In that case the correction term can therefore be neglected.

Desphande et al. [74] have extended the use of this GLC method, using so-called "probes" to measure the interaction between two non volatile liquids:

First, two GLC columns are prepared, each containing a pure non volatile liquid as stationary phase and the activity coefficient of a volatile "probe" in these two pure stationary phases is determined by the method outlined above.

Next a number of GLC columns is prepared, containing mixtures of the two non-volatile components as stationary phase. The activity coefficients of the probe in these mixed stationary phases are determined.

The interaction between the two non volatile components will affect their affinity for the probe, which will be expressed in the retention time of the probe. The interaction between the two liquid components can therefore be obtained by comparing the activity coefficients of the probe in the pure liquids with those in mixtures of the liquid components.

For simple regular solutions this can be worked out as follows: A system of two non-volatile components [1] and [2] and a probe [pr] are considered. The activity coefficient of the probe in a mixture of the two other components is given by: [22]

$$RT \ln \gamma_{pr,\,12} = A_{pr,1}\, x_1^2 + A_{pr,2}\, x_2^2 + (A_{pr,1} + A_{pr,2} - A_{1,2})\, x_1\, x_2 \tag{77}$$

At infinite dilution we obtain for a binary system of the probe and one of the non-volatile components:

$$RT \ln \gamma^{\infty}_{pr,1} = A_{pr,1} \tag{78}$$

and for the complete ternary mixture:

$$RT \ln \gamma^{\infty}_{pr,12} = A_{pr,1}\, x_1 + A_{pr,2}\, x_2 - A_{1,2}\, x_1\, x_2 \tag{79}$$

The interaction between the two nonvolatile components can now be determined from the experimental activity coefficients at infinite dilution of the probe by:

$$\frac{A_{1,2}}{RT} = \frac{x_1 \ln \gamma^{\infty}_{pr,1} + x_2 \ln \gamma^{\infty}_{pr,2} - \ln \gamma^{\infty}_{pr,12}}{x_1 x_2} \tag{80}$$

It is clear that this elegant method can be applied straightforwardly to TAGs. The result should be independent from the probe used. If indeed TAGs mix ideally, the interaction coefficient A_{12} must turn out to be zero.

5.3.2 Experimental work

The mixing behaviour of the binary SSS-MMM and of the binary SSS-8C8 was studied. The TAGs were obtained from Dr. A. Fröhling of Unilever Research Vlaardingen and were GC-pure.

Experimental procedure

The stationary phases were prepared by mixing a predetermined amount of the carrier material Chromosorb W (80–100 mesh, acid washed, DCMS treated) that was suspended in chloroform, with a predetermined amount of the TAG or TAG mixture, dissolved in chloroform. The chloroform was slowly evaporated at 60°C under occasional stirring. The last remnants of chloroform were removed by heating 3 hours at 80°C. It was checked by weighing whether no loss of carrier material or TAGs had occurred. The stationary phase was brought into a glass column of 1 m. length and 2 mm diameter and the column was conditioned for 10 hours at 150°C. Measurements were carried out at the Technical University of Delft [75] in a modified VARIAN 3700 gaschromatograph with a thermal conductivity detector. The retention times were determined with a VARIAN CDS-11 integrator. Helium was used as carrier gas.

In order to confirm that that the probe that is used has no influence indeed on the calculated TAG-TAG interaction, measurements were repeated using eight different probes:

1. n-pentane
2. n-hexane
3. n-heptane
4. 2-methyl-pentane
5. 3-methyl-pentane
6. benzene
7. toluene
8. cyclohexane

All measurements were repeated at 2 carrier gas flow rates (17 and 38 ml/min) and with two columns, containing 10% and 20% of the stationary phase on carrier. About 0.1 μl of the probe was injected.

Measurements

The specific retention volumes of the 8 probes were determined at 82, 92, 102, 112, 123 and 133 °C for the following stationary phases: (concentrations in mol fractions)

SSS	0.4487 SSS, 0.5513 MMM	0.1557 SSS, 0.8443 8C8
MMM	0.7116 SSS, 0.2884 MMM	0.3593 SSS, 0.6407 8C8
8C8		0.6023 SSS, 0.3977 8C8

The results are given in Appendix 2. The average experimental error in the retention volumes is 3%.

5.3.3 Results and discussion

The activity coefficients at infinite dilution of the probes can be calculated from the specific retention volumes with Eq. (73). It turns out that they do not depend on temperature, as is illustrated for some of the probes and some stationary phases in Figure 11. The variation as a function of temperature is less than the experimental error of 3% in the activity coefficients. This indicates that the probe-TAG mixtures behave athermal, i.e., that the excess Gibbs energy is nearly equal to the excess entropy of mixing.

Because a dependency on temperature was not found, the averages over all temperatures of the activity coefficients are used in further discussions. They are given in Table 14.

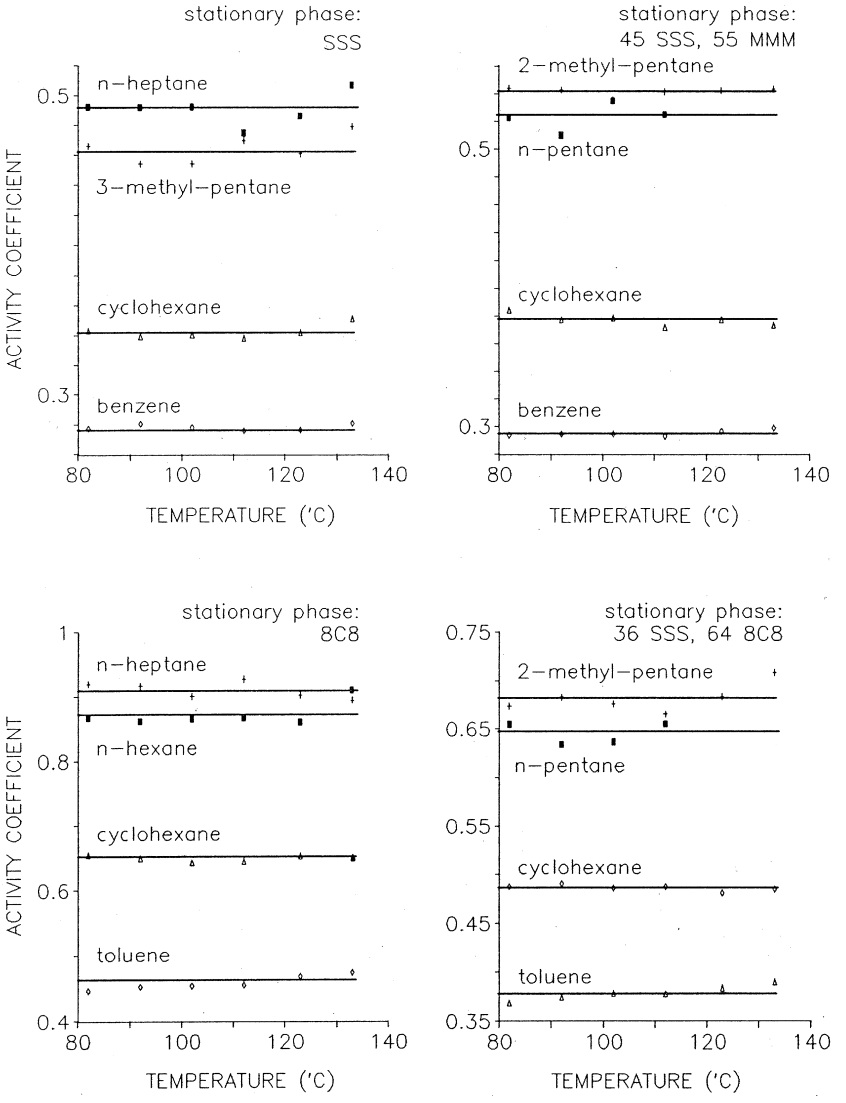

Figure 11 Activity coefficients at infinite dilution of a number of different probes in stationary TAG phases as a function of temperature

Table 14 Average Activity Coefficients at Infinite Dilution of Several Probes in a Number of Liquid TAG Mixtures Determined by GLC. The Experimental Error in the Activity Coefficients is 3%. Concentrations in Mol Fractions

x_{SSS}	1			0.449	0.712	0.156	0.359	0.602
x_{MMM}		1		0.551	0.288			
x_{8C8}			1			0.844	0.641	0.398
PROBE								
n-pentane	0.45	0.55	0.85	0.52	0.49	0.75	0.65	0.56
n-hexane	0.47	0.57	0.87	0.52	0.50	0.75	0.66	0.57
n-heptane	0.49	0.59	0.91	0.54	0.52	0.78	0.69	0.60
2-methyl-pent.	0.49	0.59	0.90	0.54	0.52	0.77	0.68	0.59
3-methyl-pent.	0.46	0.56	0.87	0.52	0.49	0.73	0.66	0.56
Benzene	0.28	0.32	0.43	0.30	0.29	0.39	0.36	0.32
Toluene	0.29	0.33	0.46	0.31	0.31	0.41	0.38	0.34
Cyclohexane	0.34	0.41	0.65	0.38	0.37	0.55	0.49	0.42

The interaction coefficients between the TAGs for the regular solution theory can now be calculated using Eq. (77). The results are given in Table 15.

The results for the binary SSS-MMM clearly indicate that within experimental error these two TAGs mix ideally. The results are very consistent for both binary mixtures and all probes used.

The results for the binary SSS-8C8 clearly indicate that this binary does not mix ideally in the liquid phase. The interaction parameters significantly differ from zero. And even worse, they also depend on the concentration of the TAGs. The simple regular solution model is therefore not a correct description for the non ideal behaviour of this binary pair.

Interpretation with the Flory-Huggins theory

The main difference between MMM and 8C8 is their difference in molecular size. This must be the cause of the large differences found in mixing behaviour with SSS. An excess Gibbs energy model that accounts for such size differences is the Flory-Huggins theory for polymer solutions 89. According to this theory the activity coefficient in the ternary system of probe [pr] and the two TAGs [1] and [2] is:

Table 15 Regular Solution Interaction Parameters A_{12}/RT for the Interaction Between the TAGs Determined from GLC Results, Using Different Probes. Experimental Error in the Parameters is 0.1. Concentrations in Mol Fractions

x_{SSS}	0.449	0.712	0.156	0.359	0.602
x_{MMM}	0.551	0.288			
x_{8C8}			0.844	0.641	0.398
PROBE					
n-pentane	−0.15	−0.11	−2.61	−0.99	−0.58
n-hexane	0.03	−0.03	−2.23	−0.93	−0.47
n-heptane	0.01	−0.04	−2.29	−0.98	−0.50
2-methyl-pent.	−0.01	−0.02	−2.25	−0.94	−0.48
3-methyl-pent.	−0.02	−0.03	−2.29	−1.01	−0.47
Benzene	0.05	−0.02	−1.69	−0.73	−0.36
Toluene	0.02	−0.06	−1.77	−0.79	−0.41
Cyclohexane	0.03	−0.05	−2.41	−0.99	−0.50
Average	−0.01	−0.05	−2.19	−0.92	−0.47
Stand. dev.	0.06	0.03	0.29	0.10	0.06

$$\ln \gamma_{pr,12} = \ln\left(\frac{v_{pr}}{x_{pr}v_{pr} + x_1 v_1 + x_2 v_2}\right) + \left(1 - \frac{v_{pr}}{v_1}\right)\phi_1 + \left(1 - \frac{v_{pr}}{v_2}\right)\phi_2 + \chi_{pr,1}\phi_1^2 + \chi_{pr,2}\phi_2^2 + (\chi_{pr,1} + \chi_{pr,2} - \chi_{1,2})\phi_1\phi_2 \tag{81}$$

The volume fraction ϕ_1 is defined as:

$$\phi_i = \frac{x_i v_i}{\sum_{j=1}^{N} x_j v_j} \tag{82}$$

in which v_i represents the molar volume.

At infinite dilution we obtain for a binary system of the probe and one of the TAGs:

$$\ln \gamma_{pr,1}^{\infty} = \ln\left(\frac{v_{pr}}{v_1}\right) + \left(1 - \frac{v_{pr}}{v_1}\right) + \chi_{pr,1} \tag{83}$$

and for the complete ternary mixture:

$$\ln \gamma^{\infty}_{pr,12} = \ln\left(\frac{v_{pr}}{x_1 v_1 + x_2 v_2}\right) + \left(1 - \frac{v_{pr}}{v_1}\right)\phi_1 + \left(1 - \frac{v_{pr}}{v_2}\right)\phi_2 + \chi_{pr,1}\phi_1 + \chi_{pr,2}\phi_2 - \chi_{1,2}\phi_1\phi_2 \quad (84)$$

The Flory-Huggins interaction parameter χ_{12} for the two TAGs can be determined from the experimental activity coefficients at infinite dilution by:

$$\chi_{12} = \frac{\phi_1\left(\ln \gamma^{\infty}_{pr,1} - \ln\left(\frac{v_1}{x_1 v_1 + x_2 v_2}\right)\right) + \phi_2\left(\ln \gamma^{\infty}_{pr,2} - \ln\left(\frac{v_2}{x_1 v_1 + x_2 v_2}\right)\right) - \ln \gamma^{\infty}_{pr,12}}{\phi_1\phi_2} \quad (85)$$

When the molecular volumes of the two TAGs are equal, the Flory-Huggins interaction parameter χ becomes equal to the regular solution interaction parameter A_{12}/RT and Eq. (82) reduces to Eq. (77) for the regular solution theory. The Flory-Huggins interaction parameters are given in Table 16.

The interaction parameters of both binaries do not depend on the probe used and not on the concentration of the two TAGs in the binary mixture. The values of interaction parameters, -0.04 ± 0.1 for SSS-MMM and 0.07 ± 0.1 for SSS-8C8, do not differ significantly from zero, which implies that the TAGs have no specific interaction in the mixtures. The deviation from ideality that was found for SSS-8C8 is entirely explained by the extra entropy of mixing that arises from the large difference in molecular size of the two TAGs. The activity coefficients at infinite dilution of the three possible binary TAG mixtures, calculated with Eq. (80), and in agreement with measurements, are given in Table 17.

Implications for natural edible oils

The results imply that deviations from ideal miscibility only become noticeable when an oil contains reasonable amounts of TAGs that have a carbon number that differs more than about 10 with the average carbon number of the mixture.

Table 16 Flory – Huggins Interaction Parameters X_{12} for the Interaction Between the TAGs Determined from GLC Results, Using Different Probes. Experimental Error in the Parameters is 0.1. Concentrations in Mol Fractions

x_{SSS}	0.449	0.712	0.156	0.359	0.602
x_{MMM}	0.551	0.288			
x_{8C8}			0.844	0.641	0.398
PROBE					
n-pentane	−0.17	−0.15	−0.07	−0.02	−0.08
n-hexane	0.01	−0.05	0.17	0.04	0.05
n-heptane	−0.01	−0.06	0.17	0.02	0.04
2-methyl-pent.	−0.02	−0.04	0.21	0.06	0.08
3-methyl-pent.	−0.04	−0.05	0.24	0.02	0.11
Benzene	0.05	−0.03	0.14	0.04	0.09
Toluene	0.01	−0.07	0.14	0.01	0.04
Cyclohexane	0.01	−0.07	0.17	0.04	0.07
Average	−0.02	−0.07	0.15	0.03	0.05
Stand. dev.	0.06	0.03	0.09	0.02	0.06
Total av.		−0.04		0.07	
Stand. dev.		0.05		0.08	

In normal vegetable oils and fats the differences in molecular size of the TAGs are of the order of the differences between MMM and SSS. For practical purposes liquid vegetable oils can therefore be treated as ideal mixtures of TAGs.

In animal oils and fats, like fish oil, butter fat and edible tallow, the spread in molecular size of the TAGs is much larger, although the concentrations of very small and very large TAGs

Table 17 Activity Coefficients at Infinite Dilution of the Three TAGs Studied, Calculated Using the Flory-Huggins Theory for the Excess Entropy of Mixing (Eq. 80)

	$\ln\gamma^{\infty}_{I,SSS}$	$\ln\gamma^{\infty}_{I,MMM}$	$\ln\gamma^{\infty}_{I,8C8}$	$\gamma^{\infty}_{I,SSS}$	$\gamma^{\infty}_{I,MMM}$	$\gamma^{\infty}_{I,8C8}$
SSS	–	–0.02	–0.16	1	0.98	0.85
MMM	–0.03	–	–0.07	0.97	1	0.93
8C8	–0.24	–0.09	–	0.79	0.91	1

are limited. Treating these oils as ideal mixtures may, depending on the situation, lead to errors of about 10–15% in calculation results.

This chapter considers the TAGs that occur in normal vegetable oils and fats. The liquid TAG phase may therefore safely be treated as an ideal mixture.

5.4 CONCLUSION

TAGs that differ not too much in molecular size mix ideally in the liquid state.

The deviation from ideality that becomes noticeable at differences in carbon number greater than about 15–20, can entirely be ascribed to the extra entropy of mixing that occurs in mixtures of molecules that differ considerably in size. No specific TAG – TAG interactions were found.

In the liquid state the vegetable oils that are normally used in the edible fats industry may be treated as ideal mixtures of TAGs.

6. MIXING BEHAVIOUR IN THE ALPHA MODIFICATION

Contrary to the β and β′-modification, in the α-modification the fatty acid chains still appear to oscillate and rotate with considerable molecular freedom. The formation of mixed crystals will therefore hardly disturb the α-crystal packing. As a consequence, mixing in the alpha phase may be nearly ideal. With this assumption α-melting ranges of a number of common fat blends are calculated and compared with experimental data.

6.1 EVIDENCE FOR PARTIAL RETAINED CHAIN MOBILITY IN THE α-MODIFICATION

Not only TAGs, but many lipids, like alkanes, n-alcohols and simple esters solidify upon quick cooling from the melt in a crystal form with hexagonal chain packing, which for TAGs is called the α-modification. In 1932 it was suggested by Müller [76] that the hexagonal polymorph of n-alkanes has complete

rotational disorder of the chains in the crystal. Therefore the hexagonal polymorph of n-alkanes has been called the "rotator phase". At present the rotational disorder in the rotator phase of n-alkanes has been extensively studied and is well established [2,43,44,46]. A curious property of lipid crystals in the rotator phase is their plasticity. Due to this property esters occurring in this form have been called waxes.

Contrary to n-alkanes, the chains in the α-modification of TAGs cannot have complete freedom of rotation. For sterical reasons chain mobility near the glyceryl group must be restricted. Yet the heat of fusion and the entropy of fusion of the α-modification of TAGs correspond closely to that of the rotator phase of alkanes. Moreover, the entropy of fusion is only 60% of that of the very crystalline β and 75% of that of the β′-modification, indicating that in the remaining part of the molecule still considerable disorder must exist (Table 18).

The melting dilatation (the volume increase upon melting) of the α-modification is only 60–70% of that of the β-modification [77]. This clearly demonstrates a less dense packing of the TAG molecules in the α-modification.

In pulse NMR for the determination of solid fat content [78] the so-called f-factor, which is inversely proportional to the relaxation time, is only 1.2–1.3 for the α-modification, compared to 1.4–1.5 for the β′-modification and about 1.6 for the β-modification. This indicates a more disordered and liquid-like packing of the fatty acid chains in the α-modification.

Table 18 Enthalpy and Entropy of Fusion of Some TAGs and Some N-alkanes

	ΔH_f KJ/mol			ΔS_f J/mol,K		
TAG-name	α	β′	β	α	β′	β
MMM	84	107	145	275	334	440
PPP	98	132	169	309	399	501
SSS	113	156	193	343	464	561
n-C19	45	60	–	147	197	–
n-C21	48	63	–	153	203	–

Hernqvist and Larsson [7] observed that the long spacing of the α-modification of SSS depends on temperature. A temperature dependence of the same order of magnitude was one of the main arguments for V. Luzatti et al. in their classical work on liquid crystallinity [79] to suggest a liquid state of hydrocarbon chains in liquid crystals. Hernqvist and Larsson also measured RAMAN spectra of TAGs. The β′ and β-modification showed sharp peaks at 1065 and 1130 cm-1 (C–C stretching vibrations), while liquid TAGs have a broad band near 1090 cm-1. The RAMAN spectra of the α-modification had a significant liquid-like character.

The most convincing evidence for chain mobility comes from Norton [27]. He concludes from high resolution CP/MAS ^{13}C-NMR spectra of the liquid state and the three polymorphs of SSS and PPP, that in the α-modification, like in the liquid phase and contrary to the β′- and β-modification, the 1 and 3 position of the glycerol are equivalent. He was able to study molecular motion by application of 'interrupted decoupling' (switching of the ^{13}C–^{1}H decoupling for a short time, which suppresses the signal of immobile protonated carbons). The results clearly show that the mobility of the fatty acid chains near the glyceryl group are very limited in all three polymorphs. In the α-modification the main hydrocarbon chain still possesses some mobility, while the carbons near the methyl end plane are very mobile. Main chain mobility is still present to some extent in the β′-modification, while the β-modification shows no main chain mobility. Even in the β-modification the methyl end group has retained some mobility.

The good correspondence with the rotator phase of alkanes and all facts that are mentioned above clearly support the view of Hernqvist [17] on the α-modification. In the α-modification, close to the methyl end plane the fatty acid chains are disordered like in lamellar liquid crystalline phases. Close to the glyceryl group, chain mobility is absent (Figure 12).

6.1.1 Supercooling of the α-modification

One of the other arguments that is often mentioned in favour of chain mobility in the α-modification is the observation of van

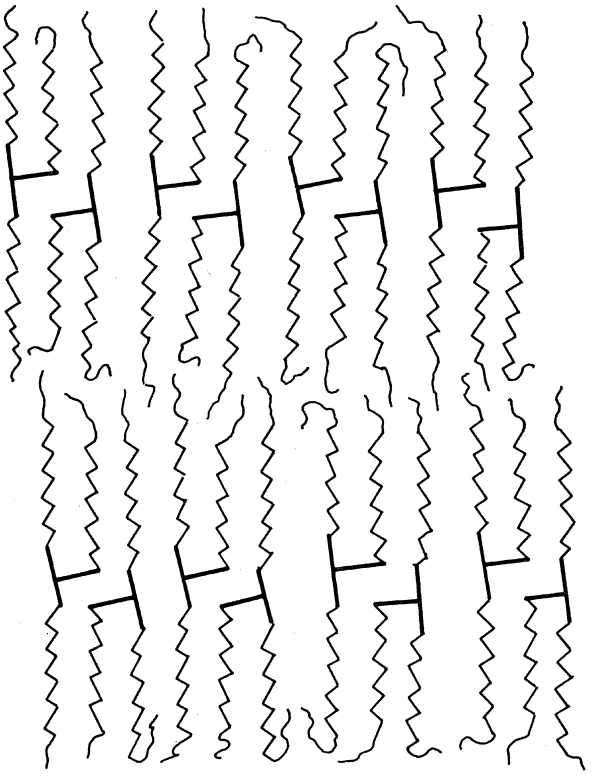

Figure 12 Chain disorder in the α-modification

den Tempel [80] that the α-modification, like lamellar liquid crystalline phase, cannot be supercooled [76].

This is not entirely correct. In oil-in-water emulsions with a relatively small average droplet size supercooling of the α-modification could be obtained. Moreover, there is a whole class of very slowly crystallizing fat blends with a specific TAG composition, in which even in a bulk phase under shear supercooling of the α-modification could be obtained. Crystallization to equilibrium was extremely quick and took place in about 1 minute. A noticeable transition to the β′-modification only occurred after about 1 hour.

In all other fat blends investigated, the authors could not obtain supercooling of the α-modification in sheared bulk

phases. This effect in the experiments is described in Section 15.6.2.

6.1.2 Excess Gibbs energy in the α-modification

In normal crystalline phases ideal mixing is only found when the components that are mixed, are nearly isomorphous [23]. In all other cases incorporation of a second component causes disturbances in the extremely regular crystal lattice, leading to nonideal mixing. However, the α-modification may be an exception. The large degree of liquid-like disorder that exists, especially in the methyl end-plane region, may very well enable the incorporation of TAGs with considerably longer or shorter fatty acid chains into the crystal "lattice", without causing much extra disorder or misfittings. In other words, the excess Gibbs energy of mixing is likely to be very small, or even zero in the α-modification.

There exists some evidence in literature that in the α-modification of TAGs considerable solid solubility occurs [27,34], but the data are too inaccurate and too scarce to allow any quantification. However, the phase diagrams of the rotational phase-liquid equilibrium of n-alkanes [44] indicate clearly that mixing in the rotational phase must be nearly ideal at atmospheric pressure. The topic will come back to the solid-liquid phase behaviour of n-alkanes in Section 15.9.

Assume that TAGs mix ideally in the α-modification and with this assumption the α-melting range of a fat can be predicted. In the next section it will be investigated whether such predicted α-melting ranges agree with the experimental melting ranges.

6.2 COMPARISON OF EXPERIMENTAL AND CALCULATED α-MELTING RANGES.

6.2.1 Experimental procedure

The α-modification is extremely unstable. In normal fats it transforms to the β′-modification within 3–20 minutes. This instability poses some problems in the determination of α-phase equilibria. The normal thermal techniques for studying

solid-liquid equilibria, like DSC and DTA, are too slow. A faster method must be defined.

The fact that it is very hard to supercool the α-modification in a bulk fat phase that is subjected to shear, while it is very easy to supercool the β′- and β-modification under those conditions, can be used to determine the α-melting range of a fat blend. The following procedure takes advantage of this phenomenon:

1. About 2 kg of the fat blend is heated in a stirred tank to a temperature at least 10°C above the slip melting point of the fat. Next the fat is circulated through a gear pump, two lab-scale scraped surface heat exchangers (SSHE) for cooling and a tubular heat exchanger for remelting, in the set-up depicted in Figure 13. The volume of the SSHEs is 18 ml, the total cooling surface 7.10^{-3} m^2. As coolant ethanol is used at temperatures between 5 and −20°C. Samples can be taken directly after the SSHEs. The solid fat content of these samples can be measured in a Bruker Minispec p120i pulse NMR device. The NMR is operated with a 90_x-τ-90_y pulse sequence, that not only gives the solid fat content, but also the f-factor, a number

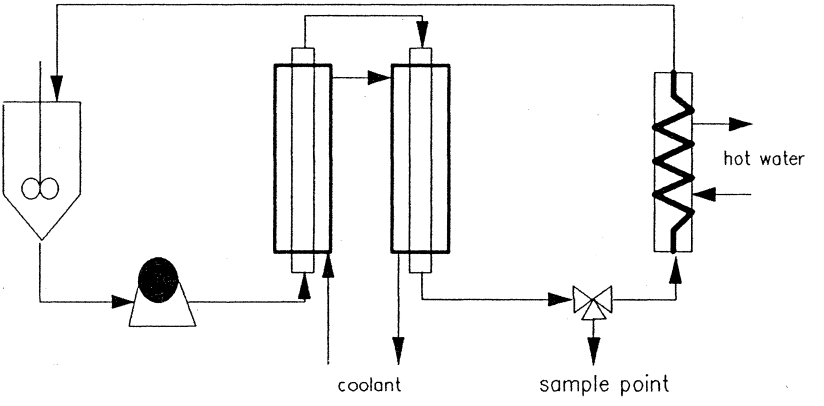

Figure 13 Experimental set-up with two SSHEs and a remelter for measurements of α-melting ranges.

that is characteristic for the modification in which the fat has crystallized [80].

2. The fat is cooled in the SSHEs to 1°C below its α-cloud point. Next the throughput is increased, while keeping the SSHE exit temperature constant, until no decrease in solids content is observed upon further increase of throughput. Usually this is obtained at about 16 kg/hr (4.4 g/s). Thus is made sure that the transition to the β′-modification has not yet started in the SSHEs and that the solid phase is still completely in the α-modification. Sample temperature and solid phase content are recorded.
3. Next the fat temperature is decreased in steps of about 2°C. When the solid phase content and temperature have stabilised, a sample is taken and the solid phase content and temperature are recorded. 8 data points are usually taken in duplo for each fat blend.
4. The plot of solids content against temperature is called an α-line and represents the α-melting range of the fat blend.

During experiments the pulse NMR always returned f-factors of about 1.25. An f-factor of 1.25 is indicative for the α-modification.

It may be argued that the α-line obtained in this way, is not a line representing the α-liquid-phase equilibrium, but a line representing the maximum possible supercooling of the fat under the conditions used. Such lines of maximal supercooling usually depend strongly on the specific conditions, like impeller speed, that are applied [81,82]; Figure 14*a*). However the α-lines, which were measured, were found to be totally independent of the rotational shaft speed of the SSHEs, coolant temperature and throughout, once the throughput was high enough to prevent the formation a β′-phase in the SSHE (Figure 14*b*).

Nine fat blends were selected that cover the area of compositions and melting ranges normally occurring in household and industrial fat spreads. The TAG compositions of the fat blends were obtained by calculation from average TAG compo-

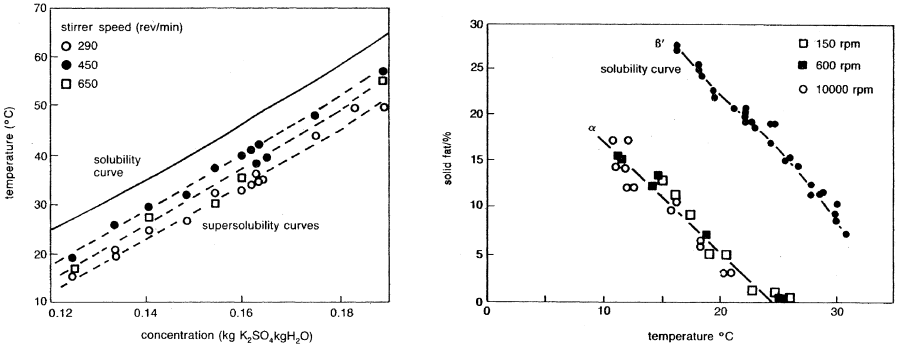

Figure 14 Effect of crystallizer impeller speed on the position of the supersolubility curve. a. Left: Potassium Sulphate [81] b. Right: A mixture of soybean oil and hardened soybean oils.

sitions of the fat blend components. The average TAG compositions of the fat blend components, like sunflower oil or hardened palm oils, were taken from the Edible Fats Database of Unilever Research Vlaardingen (Table 19).

6.2.2 Calculations

The α-melting ranges were calculated using the standard multicomponent 2-phase flash algorithm and Michelsen's stability test for the initial estimate, both described in Section 15.3. Ideal mixing in the solid and in the liquid phase was assumed, therefore all activity coefficients were unity. The TAG-compositions from Table 8 were used, while all pure component properties were estimated using the correlations developed in Section 15.4.

6.2.3 Results

The results of the calculations and the measurements are given in Figures 15–17.

The outcome is very surprising: it appears possible to predict the behaviour of the extremely unstable α-modification by phase equilibrium thermodynamics. The agreement between predictions and measurements is striking.

Table 19 Summarized TAG Compositions of 9 Fat Blends of Commerical Fat Spreads

TAG	1	2	3	4	5	6	7	8	9
SSS				0.005	0.002			0.002	0.010
S_2P				0.009	0.005	0.001		0.004	0.020
SP_2	0.006	0.002	0.006	0.006	0.005	0.011	0.002	0.003	0.014
PPP	0.011	0.004	0.019	0.001	0.002	0.032	0.004		0.003
SES		0.001			0.007		0.002	0.004	0.025
PES	0.006	0.009			0.012	0.002	0.006	0.006	0.034
PEP	0.018	0.020			0.007	0.001	0.009	0.002	0.011
SSE		0.002			0.007		0.003	0.008	0.025
PSE	0.002	0.006			0.011	0.002	0.009	0.012	0.034
PPE	0.006	0.009			0.006	0.002	0.010	0.005	0.011
P_2m	0.004		0.001	0.006	0.002	0.004			0.004
PSm	0.002			0.020	0.004				0.013
S_2m				0.010	0.002				0.009
SOS	0.001	0.001	0.003	0.001	0.003	0.001	0.001	0.002	0.007
POS	0.020	0.015	0.052	0.002	0.007	0.021	0.004	0.004	0.010
POP	0.078	0.057	0.230	0.001	0.004	0.090	0.005	0.002	0.004
SlS			0.001	0.002	0.002			0.001	
PlS	0.008	0.005	0.009	0.004	0.004	0.008	0.003	0.003	0.002
PlP	0.027	0.014	0.035	0.003	0.003	0.029	0.004	0.002	0.002
SSO		0.001		0.002	0.003	0.001	0.002	0.005	0.007
PSO	0.010	0.007	0.008	0.004	0.008	0.013	0.006	0.009	0.010
PPO	0.033	0.016	0.031	0.003	0.005	0.052	0.007	0.004	0.004
SSl	0.001		0.001	0.003	0.002			0.002	0.001
PSl	0.011	0.005	0.005	0.008	0.005	0.007	0.005	0.006	0.003
PPl	0.030	0.009	0.009	0.006	0.004	0.020	0.007	0.005	0.004
SE_2	0.002	0.018			0.041	0.010	0.031	0.027	0.084
PE_2	0.009	0.034			0.036	0.014	0.050	0.021	0.056
Pm_2	0.013			0.011	0.001				0.002
Sm_2	0.003			0.018	0.001				0.004
EEE	0.003	0.037			0.059	0.020	0.063	0.021	0.047
mmm	0.014			0.007					
SmE					0.010				0.034
PmE					0.012				0.022
E_2m					0.017			0.001	0.034
SEO	0.002	0.018			0.029	0.010	0.031	0.031	0.054
PEO	0.010	0.034			0.035	0.014	0.049	0.025	0.036
SEl		0.002			0.023	0.001	0.004	0.003	0.005
PEl	0.001	0.004			0.021	0.002	0.006	0.003	0.004
SmO	0.002			0.005					
PmO	0.012			0.003					
mOm	0.006								
mlm	0.001								
mmO	0.013			0.002					
mml	0.003			0.001					
E_2O	0.004	0.055			0.049	0.030	0.094	0.037	0.053
E_2l		0.007			0.058	0.004	0.012	0.004	0.005
SO_2	0.20	0.007	0.009	0.008	0.021	0.013	0.004	0.012	0.009
PO_2	0.120	0.039	0.049	0.012	0.028	0.101	0.011	0.014	0.010
liquid	0.485	0.560	0.530	0.836	0.437	0.481	0.557	0.706	0.272

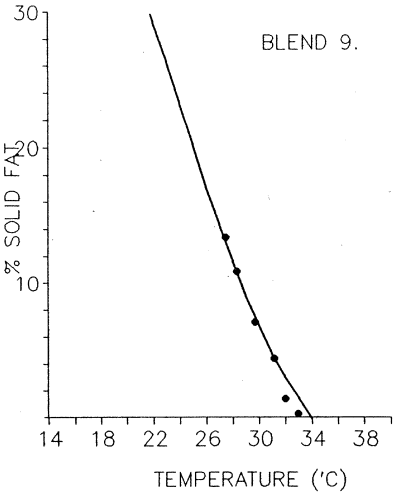

Figure 15 Measured (points) and calculated (lines) α-melting ranges of several commercial fat blends. The number corresponds to the composition given in Table 19.

6.3 CONCLUSION

A good description of the phase behaviour of TAGs in the very unstable α-modification is obtained when it is assumed that TAGs form ideal solid solutions in the α-modification.

7. MIXING BEHAVIOUR IN THE BETA′ AND BETA MODIFICATIONS

The miscibility of TAGs in the β′- and β-modification is highly non ideal. It is attempted to describe this non ideal mixing with the simplest possible excess Gibbs energy models. A compilation of existing binary T, x, y solid-liquid phase diagrams is used to determine the binary interaction parameters that occur in these models. A new method is developed to determine binary interaction parameters from a single, complete DSC melting curve of ternary mixtures. Some ternary phase diagrams are considered.

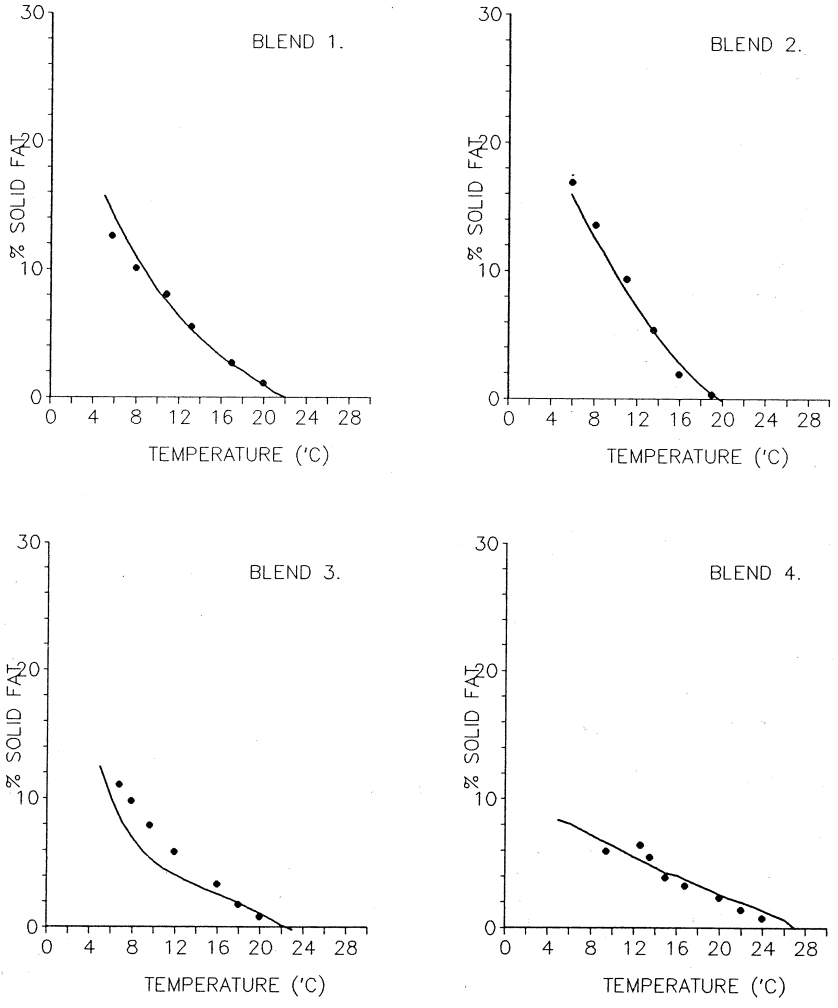

Figure 16 Measured (points) and calculated (lines) α-melting ranges of several commercial fat blends. The number corresponds to the composition given in Table 19.

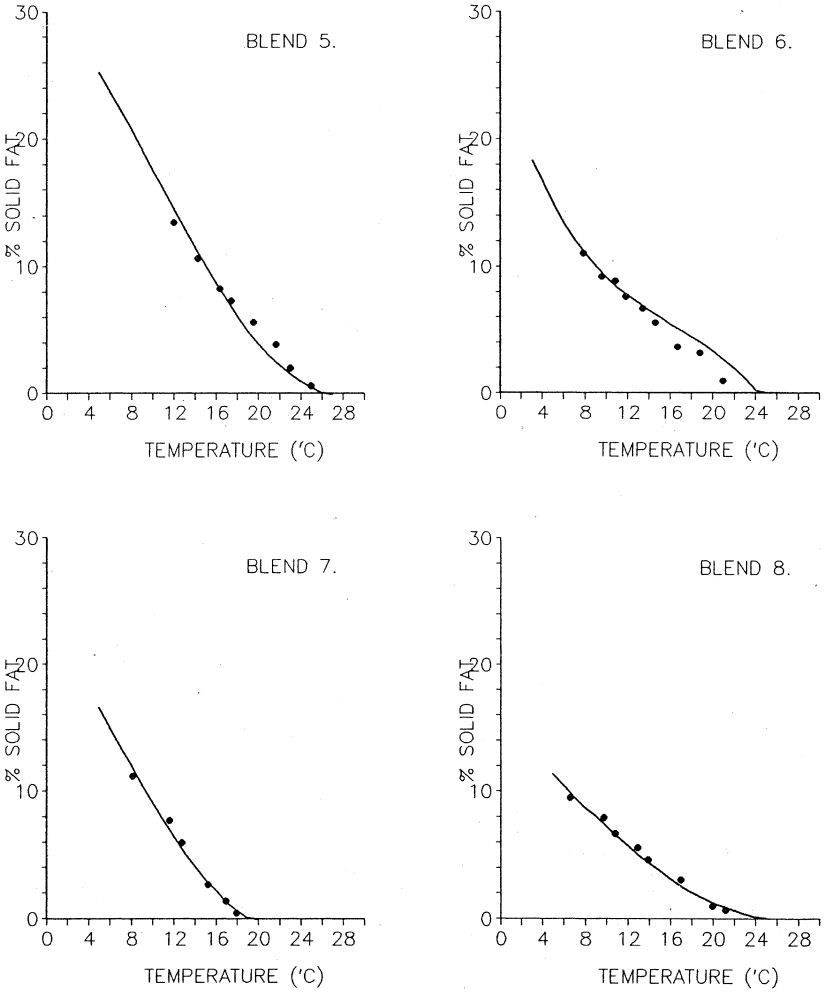

Figure 17 Measured (points) and calculated (lines) α-melting ranges of several commercial fat blends. The number corresponds to the composition given in Table 19.

7.1 EXCESS GIBBS ENERGY

It is well known [16,34] that the mixing behaviour of TAGs in the β′ and β-modification is highly non ideal. Therefore, in order to be able to solve the 'solid-flash' problem of chapter 3, we need to know the activity coefficient of each TAG in the β′- or β-solid phase as a function of the phase composition. Usually this is obtained from an excess Gibbs energy model:

The Gibbs energy of a phase is given by [22]:

$$G = \sum_{i=1}^{N} n_i \mu_i = G^{\text{ideal}} + RT \sum_{i=1}^{N} n_i \ln \gamma_i \tag{86}$$

when Eq. (5) is used for the chemical potential. The excess Gibbs energy of this phase is subsequently defined as:

$$G^{\text{E}} = G - G^{\text{ideal}} = RT \sum_{i=1}^{N} n_i \ln \gamma_i \tag{87}$$

As the chemical potential is by definition the partial molar Gibbs energy, it follows that an activity coefficient is a partial molar excess Gibbs energy:

$$\mu_i = \left(\frac{\partial G}{\partial n_i} \right)_{P,T,n_j} \quad \Rightarrow \quad RT \ln \gamma_i = \left(\frac{\partial G^E}{\partial n_i} \right)_{P,T,n_j} \tag{88}$$

This implies that once a model for the excess Gibbs energy has been formulated, the activity coefficients, needed for solving the set of equilibrium Eq. (4–8) to obtain the number of phases and the amount and composition of each phase present, are readily obtained.

7.1.1 Excess Gibbs energy models

Hardly any literature on excess Gibbs energy models for solid mixtures is available. In thermodynamic calculations it is nearly always assumed that solid phases are pure phases. Deviations between experiments and calculations are explained with "mixed crystal formation", but without any quantification.

Kitaigorodskii [83] and Haget [84] propose a parameter, the "degré d'isomorphisme crystallin" that expresses how well a molecule will fit into the crystal of another compound. The parameter was successfully used for qualitatively predicting complete, partial, or no miscibility in the solid phase

of mixtures several substituted naphthalenes, but could not be used for quantitative predictions.

In a few cases existing liquid phase excess Gibbs energy models were applied to solid mixtures: a regular solution model for petroleum waxes [85–87], van Laar and Wilson Eq. (112) for sodium carbonate and sodium sulphate [88]. General guidelines cannot be distilled from literature.

The excess Gibbs energy of a pure phase is zero: $G^E = 0$ (if $x_i \rightarrow 1$). The simplest relation meeting this requirement is the regular solution or two suffix Margules model. For a binary system it is given by [22]:

$$g^E = A_{12}\, x_1\, x_2 \rightarrow RT \ln \gamma_1 = A_{12}\, x_2^2 \tag{89}$$

and for multicomponent system by:

$$\begin{aligned} g^E &= \sum_{i=1}^{N} \sum_{j=i+1}^{N} A_{ij} x_i x_j \\ RT \ln \gamma_i &= -g^E + \sum_{j=1,\, j \neq i}^{N} A_{ij} x_j \end{aligned} \tag{90}$$

It contains one interaction parameter per binary.

Usually the very regular crystal lattice of a pure component will be disturbed when a molecule of another size is incorporated. This results in a positive excess Gibbs energy. Therefore normally the interaction parameters A_{12} in the solid phase will be positive and the activity coefficients will be greater than unity.

The two suffix Margules equation is symmetric: a mixture of 10% PPP and 90% SSS would have the same excess Gibbs energy as a mixture of 10% SSS with 90% PPP. However, symmetric behaviour in the solid phase is unlikely; the effect of incorporating a large molecule in a crystal lattice of smaller molecules probably differs from the effect of the reverse case. The two suffix Margules equation is therefore not the most obvious excess Gibbs energy model to be used for solid fats.

The simplest models, able to describe demixing, that can account for the expected asymmetric behaviour are the van Laar and the three suffix Margules equations. Both contain two interaction parameters per binary pair. More complex models are not justified [22]: they require very accurate and extensive data, which are not available for TAGs and in view

of the experimental difficulties probably impossible to obtain. Because of its somewhat wider versatility [22] the 3-suffix Margules equation is used in this work. For a binary system it is given by:

$$\begin{aligned} g^{\mathrm{E}} &= (A_{21}x_1 + A_{12}x_2)x_1x_2 \\ RT\ln\gamma_1 &= x_2^2[A_{12} + 2(A_{21} - A_{12})x_1] \\ \ln\gamma_1^{\infty} &= \frac{A_{12}}{RT} \quad , \quad \ln\gamma_2^{\infty} = \frac{A_{21}}{RT} \end{aligned} \tag{91}$$

The main disadvantage of 3-suffix Margules equation (and also of the van Laar equation) is its lack of a rational base for extension to multicomponent systems. An extra assumption has to be made. Assuming that an i, j pair in the multicomponent system gives the same contribution to g^{E} as in the binary mixture at the same relative concentrations [89], then the multicomponent 3-suffix Margules equation becomes:

$$\begin{aligned} g^{E} &= \sum_{i=1}^{N}\sum_{j=i+1}^{N}\left(A_{ij}\frac{x_j}{x_i + x_j} + A_{ji}\frac{x_i}{x_i + x_j}\right)x_ix_j \\ RT\ln\gamma_i &= -g^{E} + \sum_{j=1,j\neq i}^{N} x_j\left(\frac{A_{ji}(x_i^2 + 2x_ix_j) + A_{ij}x_j^2)}{(x_i + x_j)^2}\right) \end{aligned} \tag{92}$$

When both interaction parameters are equal, the equations reduce to the 2-suffix Margules equations.

7.1.2 Regular or athermal?

The parameters in the Margules equations are usually taken to be independent of temperature. This is equivalent to assuming that the excess entropy equals zero. Mixtures with this behaviour are called regular. The opposite case is assuming that the excess enthaply is zero. Mixtures with this property are called athermal. The interaction parameters are inversely proportional to temperature. In reality the situation usually lies in between: both excess enthalpy and entropy deviate from zero.

The data of Haget and Chanh [84] for substituted naphtalenes in the solid state as well as the data of Maroncelli [90] and Snyder for n-alkanes in the solid state suggest that

these mixed solid phases of chemically very similar compounds show nearly regular behaviour. The temperature differences that are considered in this chapter, are probably too small to be able to discriminate between both extreme situations. The authors could not obtain any improvement of fit to binary phase diagrams of TAGs by replacing the assumption of regular behaviour with athermal mixing. Therefore it is arbitrarily assumed in this work that TAGs form regular mixtures.

7.1.3 Phase diagrams

The solid-liquid phase behaviour of two components is usually represented by a T, x, y phase diagram. Figures 18*a* and 18*b* illustrate the types of binary T, x, y phase diagrams that can be obtained assuming an ideal liquid phase (Section 15.4) and a nonideal solid phase that is described by the 2- or the 3-suffix Margules equation.

The following aspects feature:

1. The eutectic composition is determined almost completely by the difference in melting point of the two components when the 2-suffix Margules equation is used. Using the 3-suffix Margules equation the eutectic composition can still be shifted about 0.05 mol fraction in both directions.
2. Peritectic diagrams cannot be obtained using the 2-suffix Margules equation.
3. The position of the liquidus is hardly influenced by the magnitude of the interaction coefficients:

if the value of the interaction coefficients A/RT exceeds 4.
if the difference between the melting points of the components is more than about 15°C.

In the first case, that of a eutectic diagram, the magnitude of the interaction coefficients only influences the position of the solidus at mole fractions less than 0.1 or greater than 0.9. In the second case the position of the solidus hardly depends on the value of the interaction parameters at mole fractions of the lowest melting component less than or equal to 0.5. Only at very low concentrations of the highest melting component there is influence of the interaction parameters on the li-

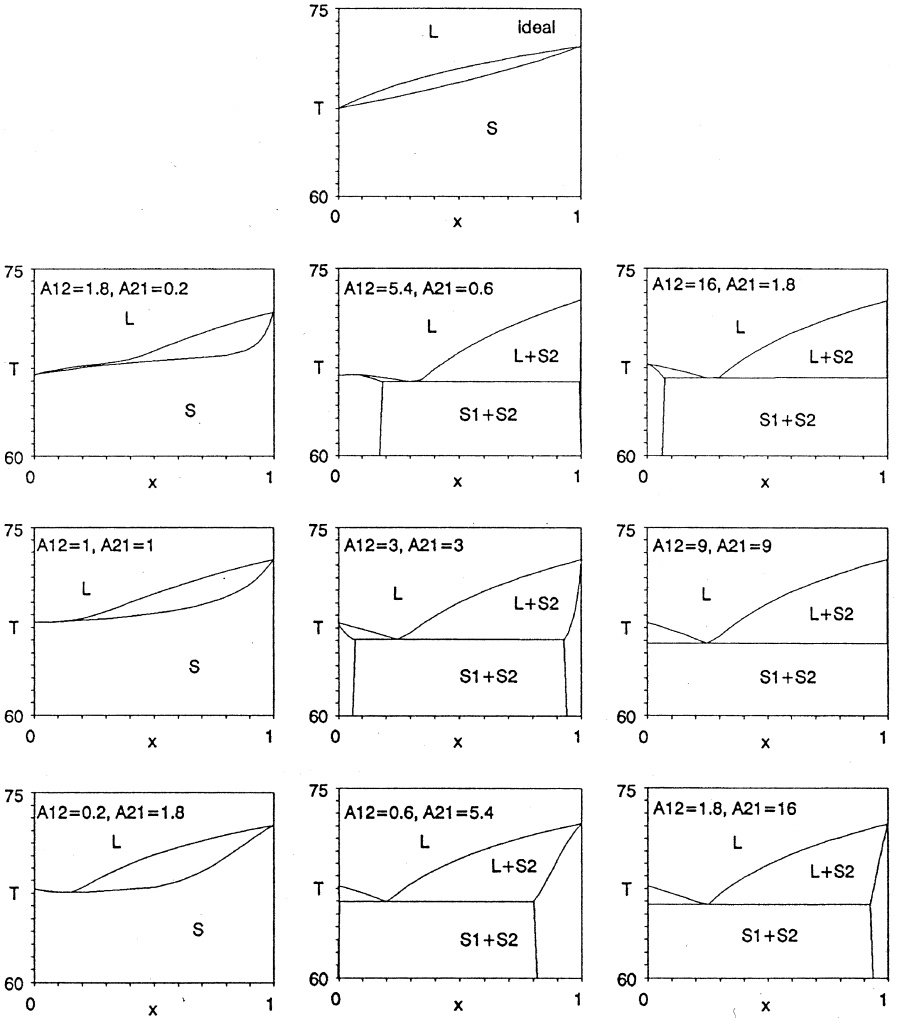

Figure 18a Theoretically possible T, x, y solid-liquid phase diagrams of PSS-SSS calculated using the 3-suffix Margules equation. The values of the binary interaction parameters are indicated.

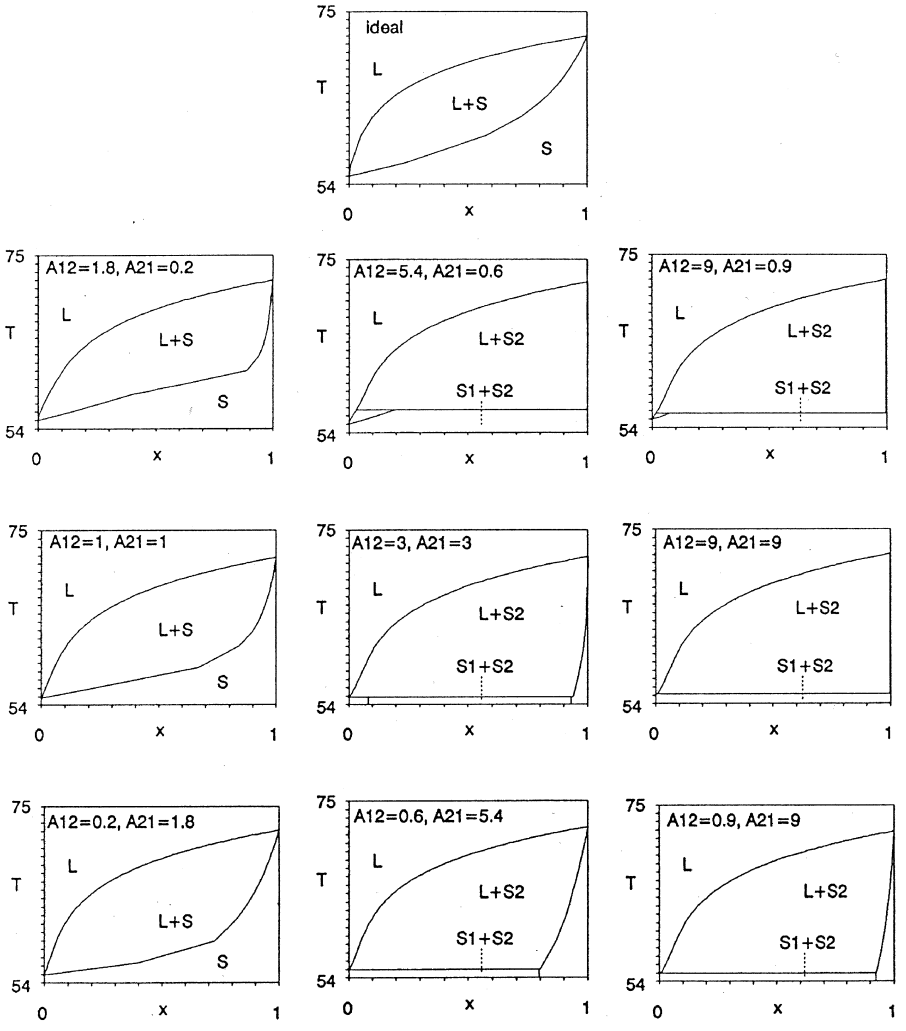

Figure 18b

quidus. However in this region the experimental errors are normally most pronounced.

According to Timms [16] four types of phase diagrams are observed for TAGs: monotectic with continuous solid solubility, eutectic, monotectic with partial solid solubility, and peri-

tectic diagrams. Only the 3-suffix Margules equation is able to describe all these diagrams.

Nomenclature

Henceforth the liquidus and solidus that are obtained when ideal mixing in the solid phase is assumed will be called ideal liquidus and ideal solidus. The interaction parameters of the excess Gibbs energy models are zero. The liquidus and the solidus that are obtained in the opposite case, when no mixing in the solid phase occurs, will be called eutectic liquidus and eutectic solidus. Then the interaction parameters of the G^E models are infinite, which is in practice equivalent to values of A/RT greater than or equal to 9.

The eutectic liquidus is also obtained from the well known Hildebrand equation, Eq. (39), which assumes the absence of mixed solid phases. In literature this liquidus is often referred to as the ideal solubility line, in spite of the highly non ideal solid phase behaviour that is implicitly assumed.

A point on the liquidus is called the clear point and a point on the solidus will be referred to as the softening point of a mixture.

Use of phase diagrams to determine interaction parameters

Experimental binary phase diagrams of TAGs can be used to determine the interaction parameters that occur in an excess Gibbs energy model. Using a fitting procedure the interaction parameters are adjusted until the calculated and measured phase behaviour agree.

There is one important limitation: in the aforesaid cases where the position of the liquidus hardly depends on the magnitude of the interaction parameters, it will be very hard to obtain reliable values of those interaction parameters from a phase diagram. That would require a number of solidus points at mole fractions less than 0.1 and greater than 0.9. Such data points are seldom available.

Therefore, the use of phase diagrams to determine interaction parameters is in practice limited to binaries of components that still show considerable solid miscibility and that differ less than about 15°C in melting point. It is possible to

fit the phase diagram of other binaries, however without learning much of the performance of the G^E model that is applied.

7.2 EXPERIMENTAL PHASE DIAGRAMS OF TAGS

7.2.1 Measuring phase diagrams

Rossell [91] reviews all phase diagrams of TAGs that were published before 1967. Although he gives no quantitative interpretation of the phase diagrams, he recognizes the main problems that occur when determining a binary solid-liquid T, x, y phase diagram:

1. Impurities,
2. Incomplete and incorrect stabilisation,
3. Other experimental errors.

Impurities

Impurities generally lead to an increase of the observed melting range and may cause an erroneous picture of mutual solid solubility. The position of both liquidus and solidus are affected by the presence of impurities. Good determination of TAG purity by GLC, TLC, or HPLC is only possible since about 1965. Therefore older data may be suspect.

Stabilization

Due to the extremely low diffusion rates in the solid phase lengthy stabilization procedures are required to ensure that the solid phase composition has its equilibrium value. The polymorphic behaviour of TAGs complicates the stabilization even more. Part of the solid phase may persist in an unstable polymorphic form with a deviating equilibrium composition. Except for the combination of very short stabilization with very quick measurements, the position of the liquidus usually does not depend very strongly on the stabilization procedure. The small amount of solid phase at temperatures just below the clear point can relatively easily recrystallize via the liquid phase to the equilibrium solid phase composition. Stabilization strongly influences the position of the solidus.

Proper stabilization requires lengthy schemes of temperature cycling between clear point and softening point. These can take several months to a year.

Often the mixtures are stabilized by long storage at a temperature several degrees below the softening point. This procedure is certainly not sufficient; in this way unstable polymorphic forms are "frozen". It was shown that they could persist several years [92].

Other experimental problems

In older reports the technique usually applied for measuring phase diagrams is the thaw-melt technique with visual observation of softening and clear points. Visual observation of clear points and especially of softening points is very inaccurate and large errors both in liquidus and solidus may occur.

The method most applied at present is some form of thermal analysis, Differential Thermal Analysis (DTA) or Differential Scanning Calorimetry (DSC). Problems that can occur when using DSC are:

1. Thermal lag because of a large sample size or scan rate. The softening point remains in place, but the observed clear point is shifted to a higher temperature. It becomes more difficult to detect small heat effects.
2. Failure to detect melting peaks. Combination of a large ($> 15°C$) difference in melting point, low concentration of one of the components, and some solid solubility leads to broad, diffuse humps rather than sharp melting peaks in the DSC thermogram. The determination of the exact starting and end temperature of these humps is very difficult. The hump itself is easily overlooked. A set of false liquidus and solidus points results.

An alternative method, that is sometimes applied, is measurement of the solid phase content of a set of binary mixtures at different temperatures by wide range pulse NMR (or before 1970 by dilatometry) [91]. The phase diagram can be constructed from the resulting melting lines or solubility curves [40,93]. This method is much more time consuming than the thermal methods. Due to the inaccuracy of the measurements (0.7% solids) the solidus and liquidus are obtained with a relatively large experimental error.

An illustration

The influence of the experimental problems on the quality of the phase diagram is illustrated in Figure 19. Two sets of simulated (Section 15.3) DSC curves of the binary POP-PEP are given. The first set was generated using the 2-suffix Margules equation with A/RT of 3, resulting in a mutual solid solubility of about 15%. For the second set the 3-suffix Margules equation was used with $A_{pop\text{-}pep}/RT$ of 0 and $A_{pep\text{-}pop}/RT$ of 6, resulting in zero solubility of PEP in solid POP and 50% solubility of POP in solid PEP. Moreover 3% of impurities, a thermal lag of 0.2°C, and 3% random noise were included. These levels of impurities, thermal lag and noise are quite normal for literature data on TAGs.

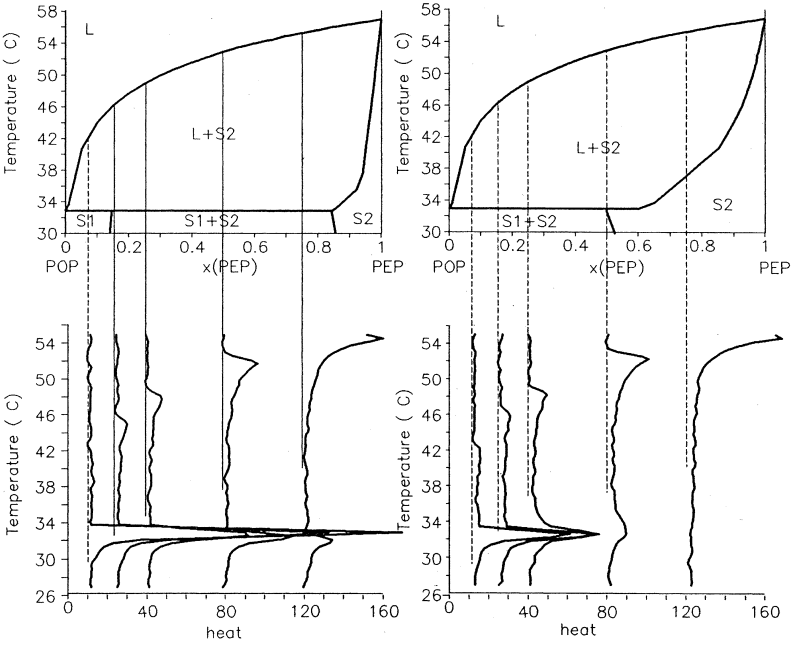

Figure 19 Simulated DSC melting curves (bottom) and binary phase diagrams (top) for a number of different mixtures of POP and PEP. The trajectory through the binary phase diagram that is followed is indicated for each mixture. *left:* Simulation with $A_{12} = A_{21} = 3$ *right:* Simulation with $A_{12} = 0$ and $A_{21} = 6$

Perfect (i.e., in absence of thermal lag, impurities, etc.) measurements on the first system would result in DSC curves with a sharp spike at the eutectic temperature followed by a broader hump that ends abruptly at the clear point. Due to the presence of impurities and thermal lag the eutectic spike is broadened to 2–4 degrees. This causes an uncertainty in the position of the solidus of the same size, while the shape of the solidus remains correct.

In the second system the sharp spike at the eutectic temperature disappears and is replaced by a broad hump at PEP concentrations over 50%. The onset of this hump is hard to determine exactly. At 75% PEP, the hump becomes very broad. In the simulated curve it is no longer detectable. The softening point of this mixture is 36°C. However, the softening point that one would read from the simulated DSC-curve is the onset of the second melting peak, at about 46°C, a difference of 10°C

The influence that the experimental errors can have the measured phase diagram becomes clear in Figure 20. In this figure the simulated phase diagram is plotted together with pseudo-experimental solidus and liquidus points that are determined form the simulated experimental. DSC-melting

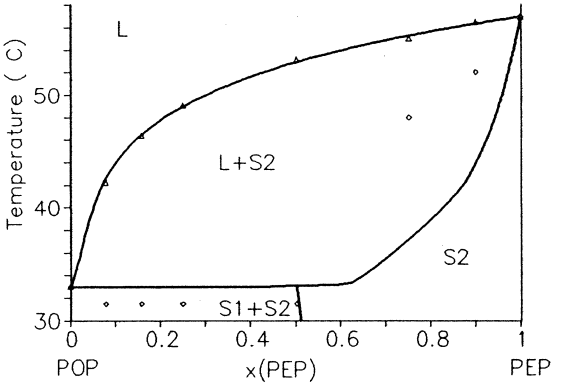

Figure 20 Solidus and liquidus points read from the simulated DSC curves of Figure 19 together with the phase diagram that formed the basis for the simulation of the DSC curves.

curves. The original simulated liquidus and the experimental liquidus points correspond very well, but the solidus points deviate considerably from the original solidus. At the POP side of the diagram the experimental points lie far under the original solidus, while they are positioned above the ideal solidus at the PEP side of the phase diagram.

The POP-PEP binary was measured by Lovergren [66]. As in the simulated DSC curve, it is impossible to detect a start melting point between 30 and 40°C in Lovegren's curve for 75% PEP. Whatever the solubility of POP in PEP would be, the start melting point would have to lie in this temperature range, which implies that the softening point that is read from this curve is wrong.

Solidus points that lie below the eutectic solidus at the side of lowest melting component and suddenly shift to values far above the ideal solidus on the other side of the phase diagram, are frequently reported for TAGs with a large difference in melting point [91]. Often, in about half of the cases, contradicting reports exist, showing no solidus points that lie above the ideal solidus. An example form the data of Kerridge for SSS-LLL [94], that are in contradiction to the data of Lutton [95].

A thermodynamic consistency test on the data is not possible. Heats of mixing, that are needed to check if the isobaric, non isothermal Gibbs-Duhem equation is obeyed, are not available.

Compound formation, that would explain a solidus that lies above the ideal solidus is very unlikely: compound formation is only known between pairs of TAGs made up of the same fatty acids, but attached to different positions of the glycerol group (like POP and PPO). The binaries for which deviating solidi are reported normally have a large difference in melting point, which stems from large differences in size or shape. It is therefore much more likely that the deviations are caused by impurities, improper stabilisation and failures in detecting the true softening point.

7.2.2 Literature overview

It is clear that the determination of solid-liquid T, x, y phase diagrams is a tedious and unrewarding job, which is probably

the reason why since Rossell's review [91] so few phase diagrams were reported.

De Bruijne and Knoester [66] have published the phase diagrams of all binary combinations of TAGs with palmitic (P) and stearic (S) acid. They put much effort in stabilization and purification. Their data seem therefore of good quality. They always expected the sharp double peaked DSC-curve that is characteristic for eutectic behaviour. Therefore they missed the solidus in those cases where due to solid solubility the DSC melting curve had another shape.

De Bruijne also determined the phase diagrams of tribehenate (BBB) with tristearate (SSS) and tripalmitate (PPP) [96], and of POP with PPO in the β′-modification [92]. Unfortunately these diagrams are only of little value as hardly any stabilization was used.

Perron [97] and coworkers have also measured the systems of de Bruijne. They do not report any purity of their TAGs and did not stabilize the mixtures at all. Their DSC curves are full of polymorphic transitions, partially overlapping with melting peaks. They report β′-stable PSS and PPS while these TAGs are known to be beta stable [11,66]. Consequently, the resulting diagrams can better be disregarded.

In later work Perron [60] again reports some of these phase diagrams (SSS-PSP, PSP-SPP, SSS-SPP), but now with very pure components and a longer stabilisation procedure.

Gibon [11] also measured the same systems and those of some of the TAGs occurring in palm oil (POP, PPO, OPO, POO). Although she worked with very pure samples, she put no effort at all in stabilization. Most of her phase diagrams are therefore, like the early Perron work, useless for our purpose. Gibons work is continued by De Smedt [98] with TAGs that contain elaidic acid (SES, SSE, PEP, PPE, EPE), but unfortunately in the same manner.

Krautwurst [99] gives the binary diagram of PPP-MMM and some data of the ternary PPP-MMM-LLL. He does not give purities and followed a reasonable stabilisation procedure.

The binary SSS-trioctanoate (888) was determined by Barbano [100] with a stabilization of 23 months and very pure TAGs.

Grootscholten [93] determined the liquidi of SSS-SES, SSS-SSE, SSE-SES, SSS-SEE and of PPP and SSS with OOO using a reasonable stabilisation procedure.

Smith [40] reports the only known good quality ternary diagram: a well stabilized ternary diagram of POP/SOS/POS in their most stable polymorphic form determined by NMR.

Lovegren [66] gives the DSC melting curves of the binary POP-PEP after several stabilization procedures, from which a diagram can be constructed.

Norton [27] gives some liquidus points of PPP and SSS with OOO determined by DSC. His end melting peaks show a strange tail for which the reason is not clear.

Only Grootscholten interpreted his phase diagrams applying an activity coefficient approach [101]. All other authors only state, if something, whether their data deviate from the Hildebrand equation (eutectic liquidus and solidus).

Also outside the area of edible oils and fats phase diagrams of organic compounds that show similar phase behaviour as TAGs, like substituted naphthalenes [84] or sulfolane with compounds as dimethysulfoxide and dioxane [102] are only interpreted with the Hildebrand equation for pure solids. Solid solutions have not been described quantitatively. Related phase diagrams, between a liquid crystalline phase and a gel phase of phospholipids (e.g., stearyl-palmityl-glycero-phosphocholine and dimyristyl-glycero-phosphocholine, 2 lecithins) have been described quantitatively with the 2-suffix Margules equation. In these systems stabilization is considerably less important. Values of A/RT between 0 and 1.5 are found [103].

7.2.3 Fitting experimental phase diagrams

The ability of the 2-suffix and 3-suffix Margules equations to describe non ideal mixing in solid fats was tested by fitting these G^E models to the experimental binary phase diagrams. The Simplex method [104] was used for parameter adjustment.

In Section 15.7.3.1 it was concluded that solidus data may be very inaccurate. Therefore only the liquidus was fitted.

Clear points were calculated using Michelsens' stability test (Section 15.3). This guaranteed that the solid phase was in the right polymorphic form. Next the solidus data were used to fine-tune the interaction parameters within the error margin that resulted from the fit to the liquidus.

As pointed out in Section 15.2.2.2, accurate values of binary interaction parameters can only be obtained from binaries of components that have a small difference in melting point and a reasonable mutual solid solubility. Typically the requirements are: an interaction parameter A/RT less than 3 and a difference in melting point less than 15°C. For all other cases only rough indications of the values of the interaction parameters can be given, using the solidus points that are available.

The phase diagram was rejected as a whole if:

- the reported melting points differ more than 4°C from the accepted values
- the reported liquidus lies on average more than 2°C above the ideal liquidus or more than 2°C below the eutectic liquidus.
- the eutectic composition differs 0.08 mol fraction or more from the composition that follows from the melting points alone.

Solidus points that lie more than 3°C above the ideal solidus were neglected: as is outlined in Section 15.7.3.1, it is likely that the actual softening point was not detected in the experiments. When published or when a lab journal was still available, the original data were used, but usually the data had to be read from the graphs in the publications (Appendix 4).

7.2.4 Saturated TAGs

SSS, SSP, PSP, SPS, PPS and PPP

These are the TAGs that occur in fully hydrogenated vegetable oils as palm oil, soybean oil, sunflower oil, rape seed oil and safflower oil (Figures 21–25). The interaction parameters and residual errors in predicted liquidus lines (the square root of the quotient of the sum of squared errors and the number of degrees of freedom) are given in Table 20, the phase diagrams in Figures 21–25.

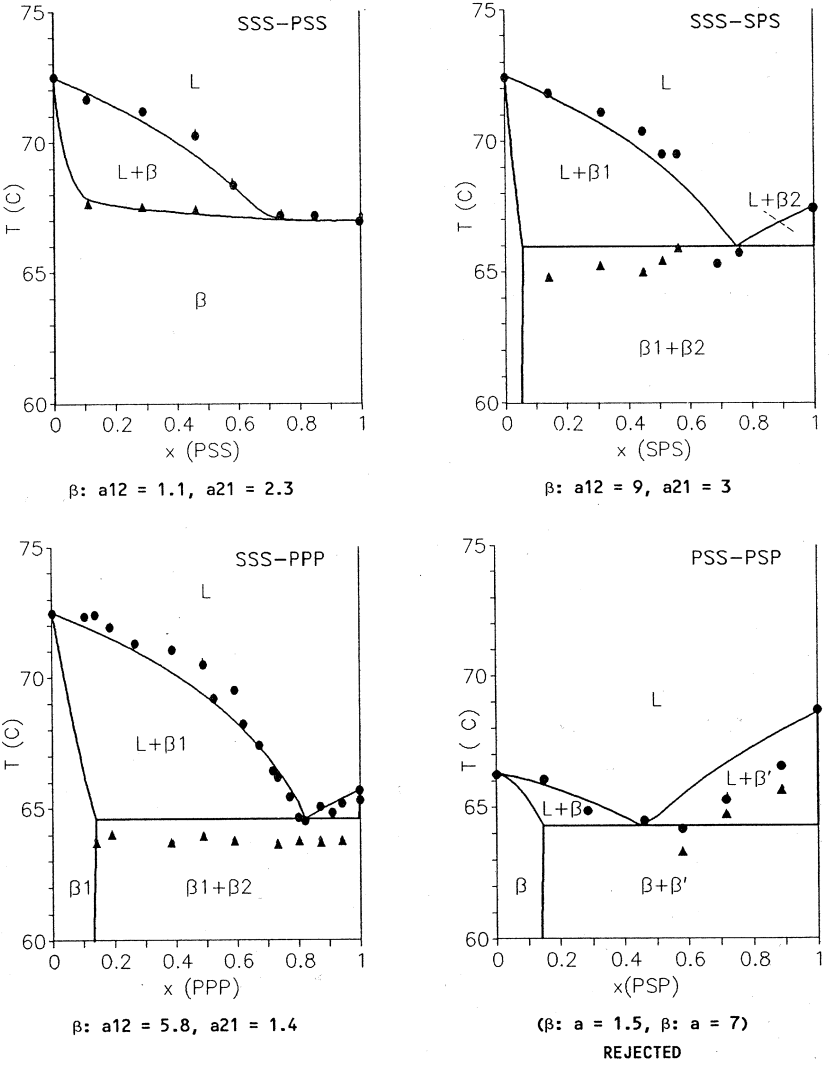

Figure 21 T, x, y diagrams of TAGs from Table 20. Experimental data (circles : clear points; triangles: softening points) and best fit (lines) with the 2- or 3-suffix Margules equation. (a = A/RT).

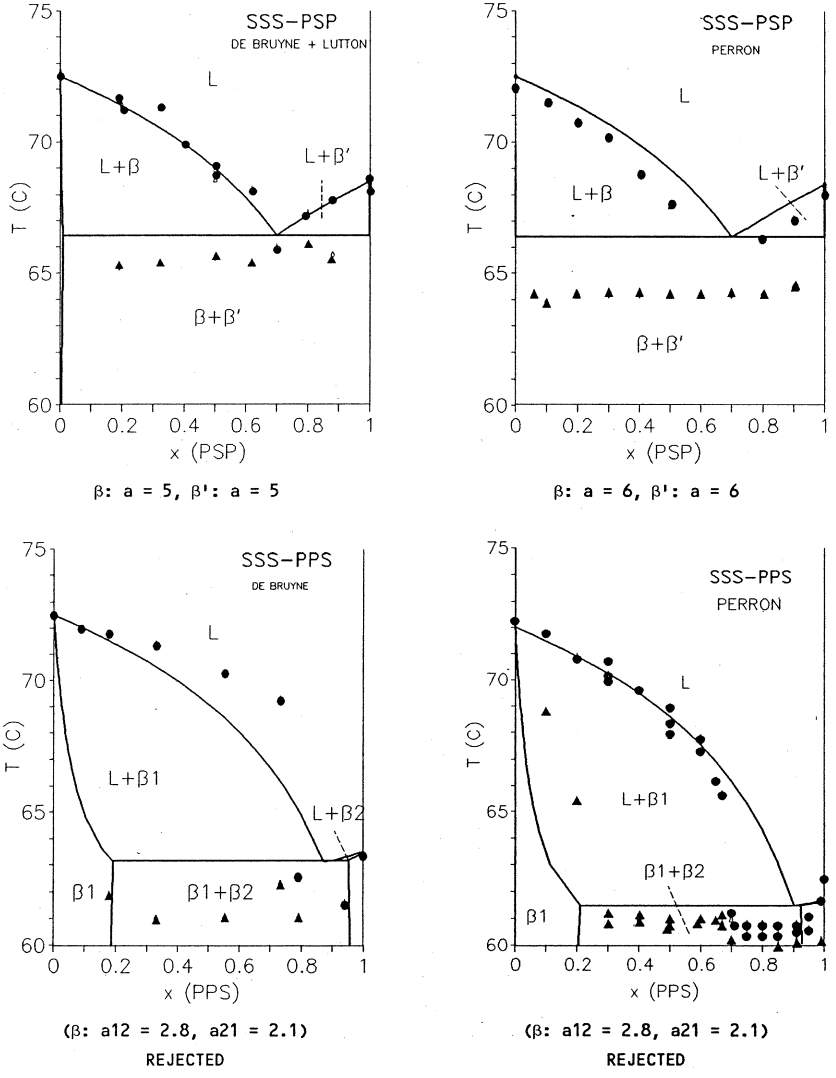

Figure 22 T, x, y diagrams of TAGs from Table 20. Experimental data (circles : clear points; triangles: softening points) and best fit (lines) with the 2- or 3-suffix Margules equation. (a = A/RT).

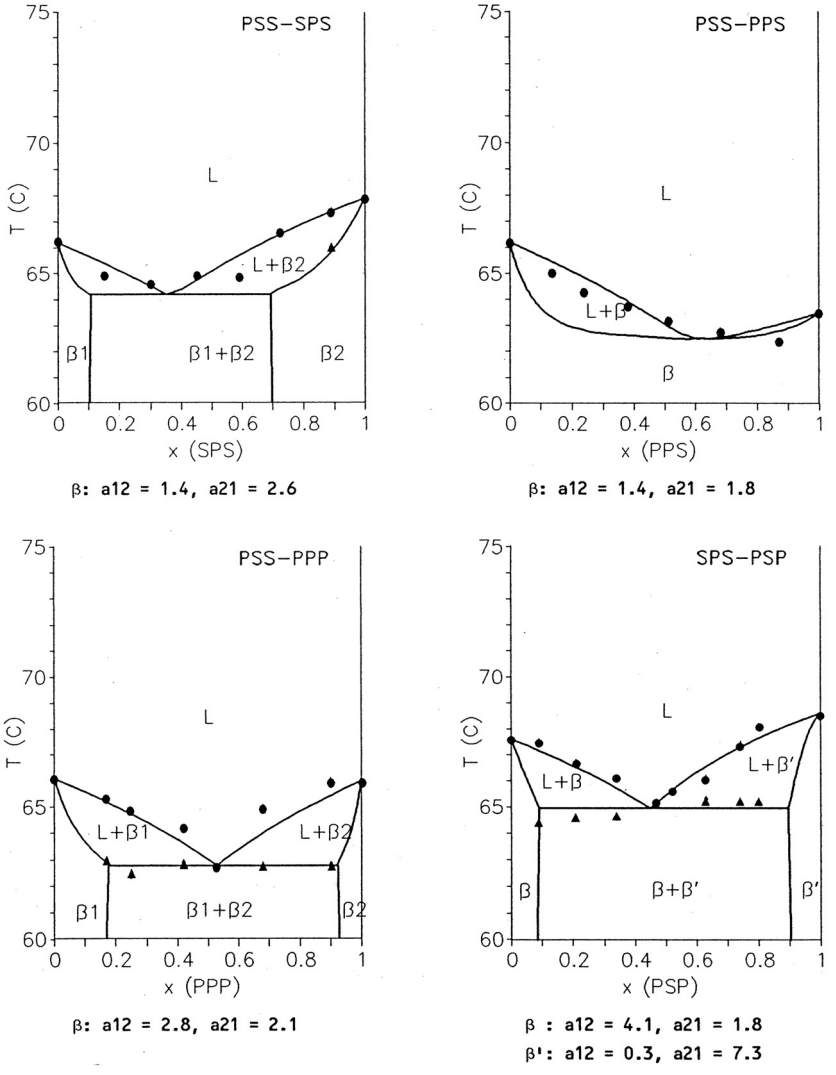

Figure 23 T, x, y diagrams of TAGs from Table 20. Experimental data (circles : clear points; triangles: softening points) and best fit (lines) with the 2- or 3-suffix Margules equation. (a = A/RT).

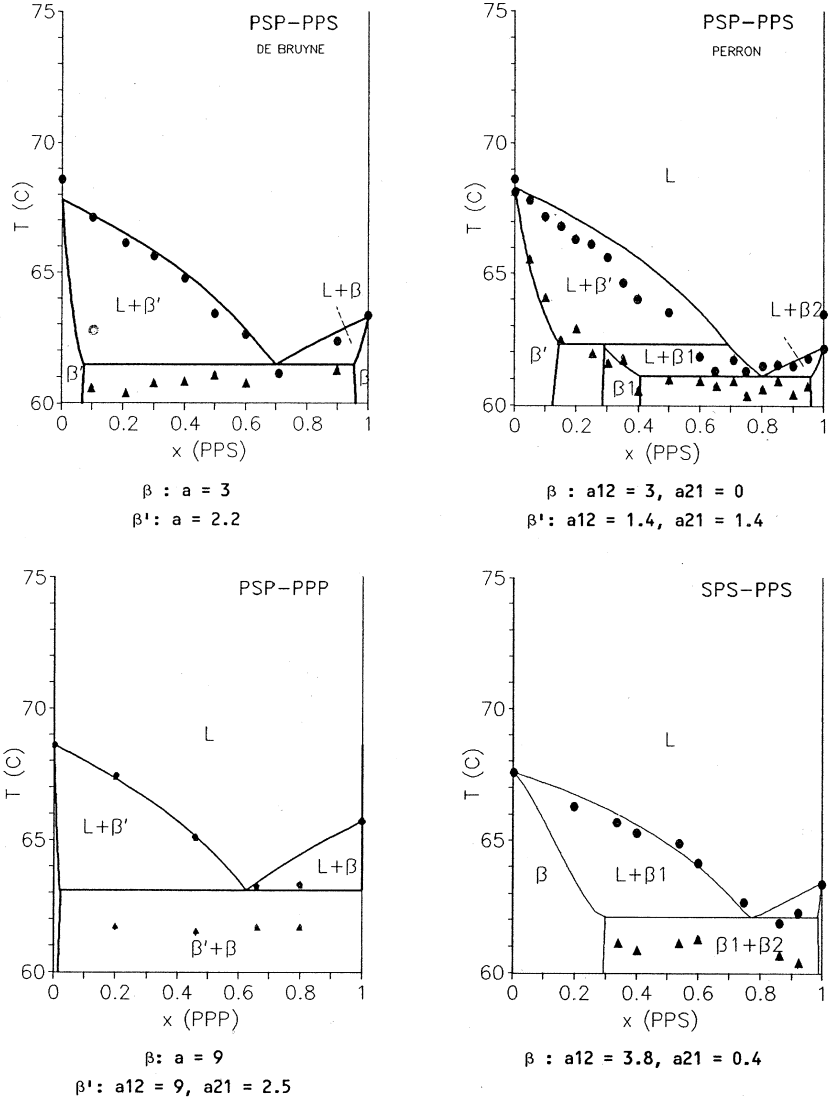

Figure 24 T, x, y diagrams of TAGs from Table 20. Experimental data (circles : clear points; triangles: softening points) and best fit (lines) with the 2- or 3-suffix Margules equation. (a = A/RT).

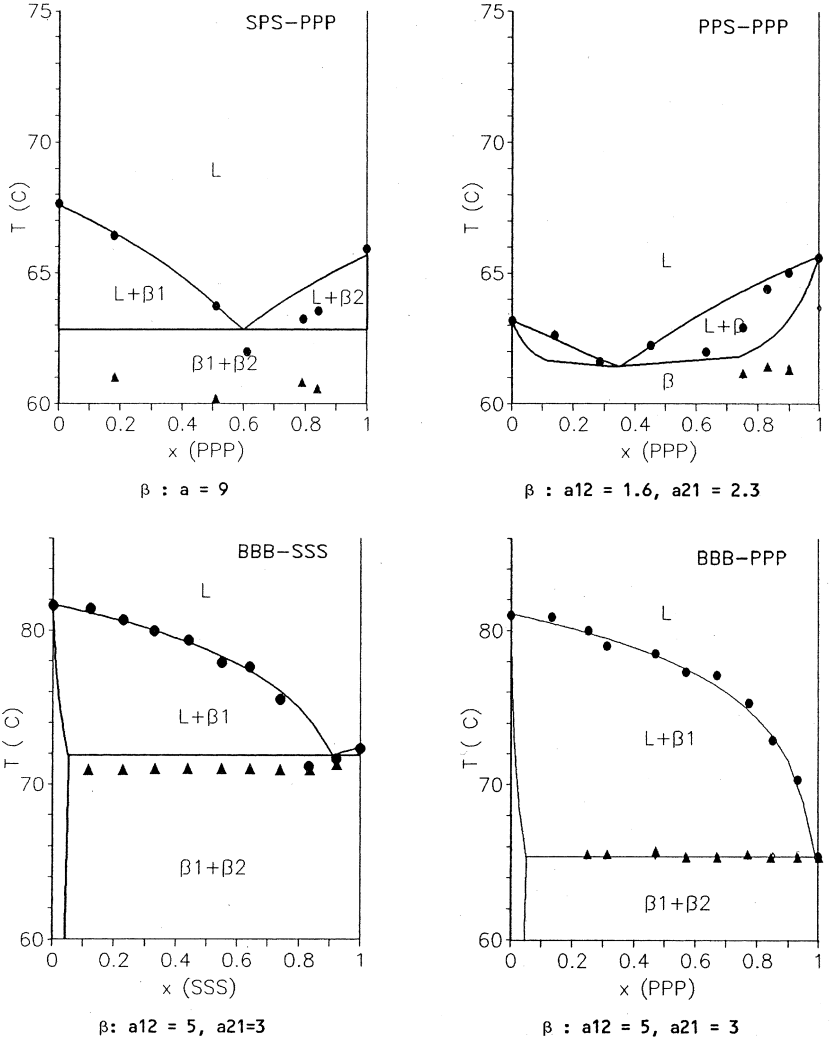

Figure 25 T, x, y diagrams of TAGs from Tables 20 and 21. Experimental data (circles : clear points; triangles: softening points) and best fit (lines) with the 2- or 3-suffix Margules equation. (a = A/RT).

Table 20 Binary Interaction Parameters for the P/S TAGs and Root Mean Square Error Between Experimental Points and Fitted Liquidus. (Standard error in the constants is 0.5, when two sets of constants are given, the first are values for the beta and the second set is for tbe beta′ modification). Data from A = de Bruijne [98], B = Lutton [97], C = Perron [99]

	2-suffix Margules		3-suffix Margules			
Binary	A/RT	rmse	A_{12}/RT	A_{21}/RT	rmse	Ref
SSS-PSS	1.6	0.3	1.1	2.3	0.3	A
SSS-PSP	3–7	0.3	3–7	3–7	0.4	A/B
β′	3–7		3–7	3–7		
SSS-SPS	3–9	0.7	3–9	2–4	0.8	A
SSS-PPS	>2.2 ?	1.7	–	–	–	A
SSS-PPP	3	0.8	5.8	1.4	0.7	A/B
PSS-PSP	1.5?	1.2	–	–		A
β′	7?		–	–		
PSS-SPS	2.0	0.4	1.4	2.6	0.3	A
PSS-PPS	1.6	0.4	1.4	1.8	0.5	A
PSS-PPP	2.2	0.5	2.8	2.1	0.5	A
PSP-SPS	1.4	0.3	1.8	1–6	0.3	A
β′	1.0		2–7	0.3		
PSP-PPS	3–9	0.9	3–9	1–9	0.9	A
β′	2.2–9		1–9	2.2–9		
PSP-PPP	3–9	0.7	0–9	3–9	0.8	A
β′	0–9		0–9	0–9		
SPS-PPS	2.0	0.6	3–5	0.4	0.4	A
SPS-PPP	5–9	0.8	5–9	5–9	0.8	A
PPS-PPP	1.9	0.7	1.6	2.3	0.7	A
Perron:						
SSS-PSP	5–9	0.7	5–9	5–9	0.8	C
	5–9		5–9	5–9		
SSS-PPS	2.1 ?	2.4	–	–	2.4	C
PSP-PPS	–	–	3	0	–	C
		1.4	1.4			

Taking into account that the experimental error that is claimed is 0.3–0.4°C, the fit to the data is usually most satisfying. In spite of this good fit, the experimental error causes a rather large uncertainty in the interaction parameters. The uncertainty is even larger in the case of PSP. PSP crystallizes in the β′ modification, and the phase diagrams are therefore mixed β-β′. Consequently the 3-suffix Margules parameters determined from these diagrams that indicate the solubility in β-PSP and in the β′ modification of the other TAG will show a very large error.

The data of Lutton [95] and de Bruijne [96] for SSS-PPP are in good agreement, while the data of the other authors mentioned by Rossell (Kerridge, Kung, Joglekar) disagree and cannot be fitted at all.

Lutton's and de Bruijne's data for SSS-PSP also agree very well. Both deviate from the data of Perron [60], which show a greater discrepancy between solidus and liquidus. When fitting the G^E models to Perron's data, the residual error is much larger, but similar interaction coefficients are obtained.

The diagrams of SSS-PSS, SSS-PSP, PSS-SPS, PSS-PPS, PSS-PPP, SPS-PSP, and SPS-PPS are perfectly acceptable and are described rather well.

The 3-suffix-Margules parameter $A_{SSS\text{-}SPS}$ is inaccurate, due to lack of data on the SPS side of the diagram. The same holds for the PPP side of the PSP-PPP diagram.

The data for SSS-PPS of de Bruijne are poor; part of the data lies above the ideal liquidus, while the data points on the PPS side of the diagram lie below the eutectic liquidus. The solidus points indicate that the 2-suffix Margules interaction parameter should exceed 2.2. The liquidus of Perron for this binary is somewhat better, although it still does not meet the acceptance criteria of Section 15.3.3; on average the liquidus lies more 2°C below the eutectic liquidus.

At the PSP side of the PSS-PSP diagram the experimental clear points also lie far below the eutectic liquidus, indicating poor the quality of the data. Best fit to the PSS side of the diagram gives an A(β)/RT of 1.5 for this system.

The liquidi of Perron and de Bruijne for the system PSP-PPS agree very well, the solidi are in complete disagreement. Best fit to the clear points results in a nearly eutectic solidus, in agreement with de Bruijne's results. The best fit to the complex solidus of Perron, that shows a peritectic and an eutectic, results in a liquidus that fits poorly to the data.

In the diagram of PPS-PPP there are two data points on the PPP side that lie more than 1 degree below the eutectic liquidus. Those points were given very low weight during fitting. The same occurs in the diagram of SPS-PPP, resulting in a very inaccurate 3-suffix Margules parameter for the solubility of SPS in PPP.

Saturated mono acid TAGs

The melting points most of these TAGs differ considerably. Therefore no exact values for the interaction parameters can be obtained. In this case fitting is merely a check whether the reported liquidi agree with expectations (Table 21, Figures 25 and 26).

Indeed all liquidi are described very well. The data of Kerridge and Barbano contain solidus points that lie far above the ideal solidus.

Table 21 Binary Interaction Parameters and Root Mean Square Error Between Experimental Points and Fitted Liquidus for Saturated Mono Acid TAGs. Data from A =De Bruijne [92, 96], B= Lutton [95], C=Kerridge [94], D= Barbano [100], E= Krautwurst [99]. Standard Error in the Parameters is 0.5, Unless Otherwise Indicated

	2-suffix Margules		3-suffix Margules			
Binary	A/RT	rmse	A_{12}/RT	A_{21}/RT	rmse	Ref
BBB-SSS	3–9	1.0	4–9	2–9	1	A
BBB-PPP	3–9	0.5	3–9	2–9	0.5	A
SSS-PPP	3	0.8	5.8	1.4	0.7	A/B
SSS-LLL	3–9	0.9	3–9	3–9	0.9	B/C
SSS-888	3–9	2.4	3–9	0–9	2.4	D
PPP-MMM	3–9	0.3	3–9	2–9	0.3	E
PPP-LLL	3–9	0.3	5–9	2–9	0.3	B/C

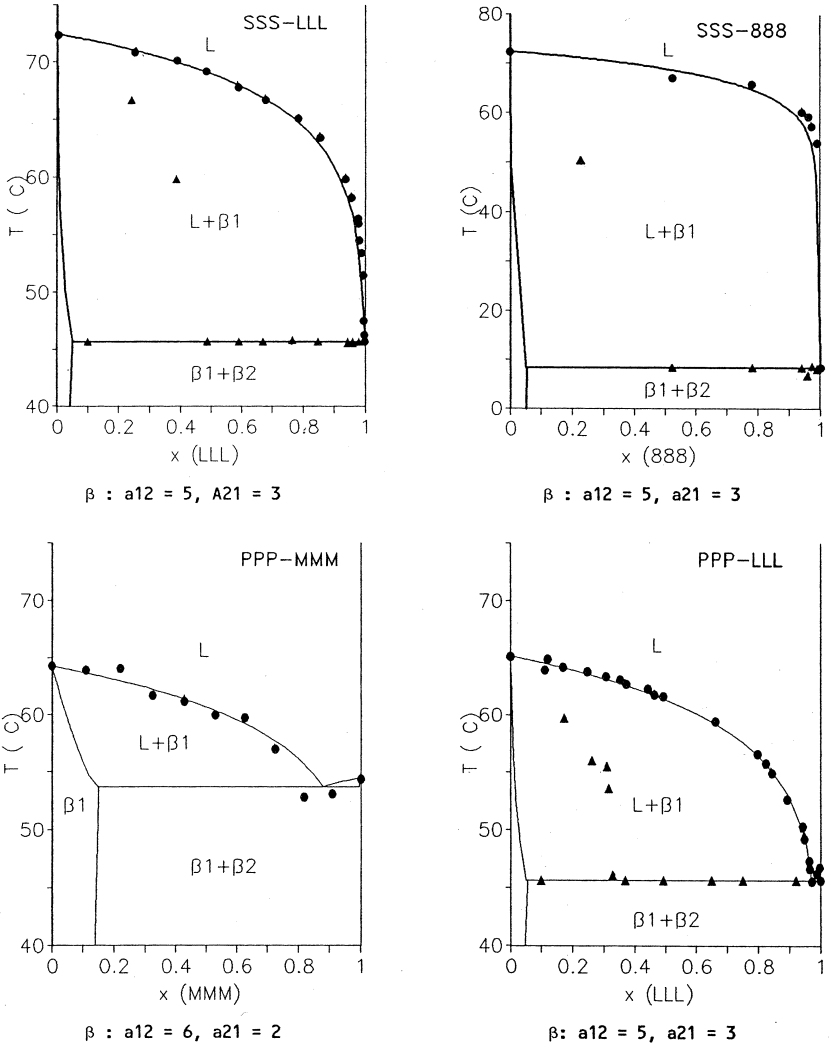

Figure 26 T, x, y diagrams of TAGs from Table 21. Experimental data (circles : clear points; triangles: softening points) and best fit (lines) with the 2- or 3-suffix Margules equation. (a = A/RT).

Lutton's data for the systems with LLL confirm that these solidus points are indeed not right. The available solidus points indicate that in all systems solid solubility is only very limited.

7.2.5 Saturated TAGS + trans TAGs

The similarity between elaidic acid and stearic acid is reflected in the nearly ideal miscibility of SSE and SES with SSS (Figures 27 and 28).

The interaction parameters for PPP-SSE are very similar to that of PPP and SSS. However, the data of Kung for this system look unreliable: there is a very poor correspondence between liquidus and solidus and the liquidus lies well below the eutectic liquidus near the eutectic point. Therefore the interaction parameters cannot be very reliable either.

Clement's data for PPP-EEE had to be disregarded: the liquidus and solidus lie too far above the ideal liquidus and solidus. Simultaneously Clements measured the system LLL-EEE, using the same technique and batch of EEE. The data are therefore suspect. The fit to these data is with a residual error of 20%—rather poor. The interaction coefficients for EEE-LLL should therefore not be taken too seriously.

Table 22 Binary Interaction Parameters and Root Mean Square Error Between Experimental Points and Fitted Liquidus for Saturated +trans Containing TAGs. Data from A=Grootscholten [93], B=Kung [106], C=Clements [107]. Standard Error in the Constants is 0.5, Unless Otherwise Indicated

	2-suffix Margules		3-suffix Margules			
Binary	A/RT	rmse	A_{12}/RT	A_{21}/RT	rmse	Ref
SSS-SES	0.4	0.2	0	0.8	0.2	A
SSS-SSE	0.4	0.7	0.1	0.7	0.5	A/B
PPP-SSE	–	–	1?	9?	0.9	B
PPP-EEE	–	–	–	–	–	C
LLL-EEE	–	–	2.8?	0?	–	C

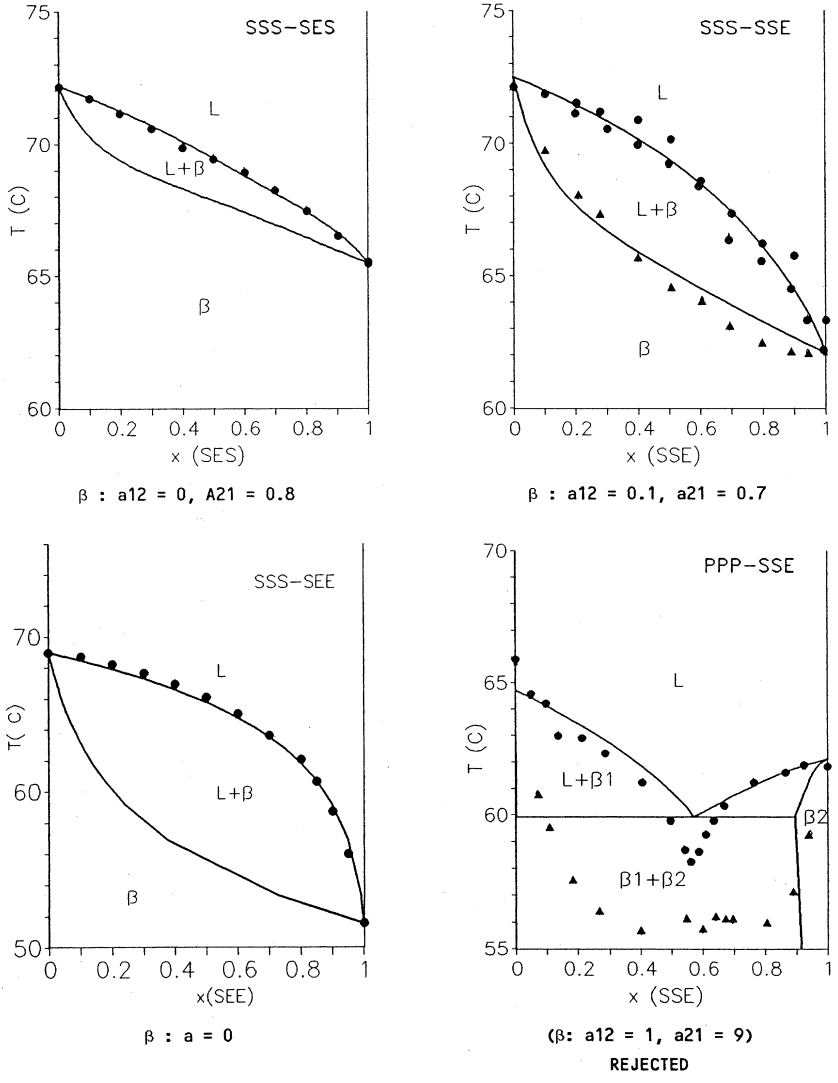

Figure 27 T, x, y diagrams of TAGs from Table 22. Experimental data (circles: clear points; triangles: softening points) and best fit (lines) with the 2- or 3-suffix Margules equation. (a = A/RT).

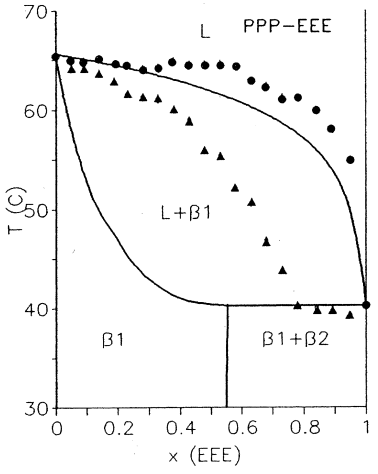

REJECTED

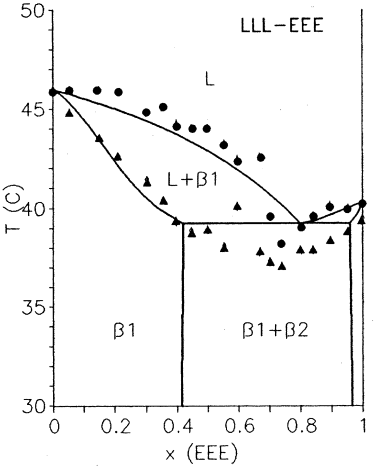

(β : a12 = 0, a21 = 2.8)
REJECTED

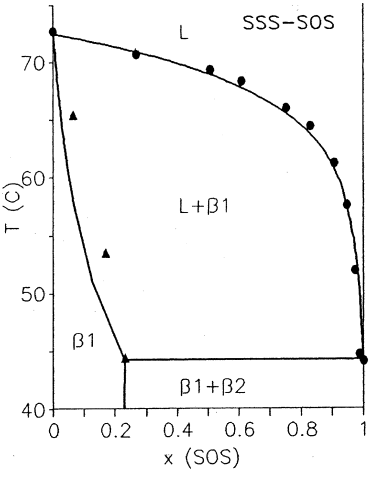

β-2 : a = 1.5
β-3 : a = 1.5

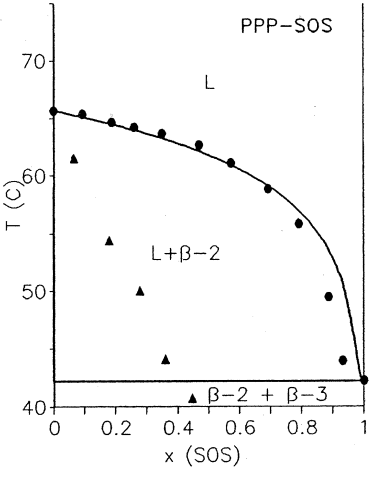

β-2: a = 1.5
β-3: a = 3
REJECTED

Figure 28 T, x, y diagrams of TAGs from Tables 22 and 23. Experimental data (circles: clear points; triangles: softening points) and best fit (lines) with the 2- or 3-suffix Margules equation. (a = A/RT).

7.2.6 Saturated TAGs + mono- and di-unsaturated TAGs

Due to the large differences in melting points, it will only be possible to get a coarse indication of the magnitude of the interaction parameters (Figures 28 and 29).

A complicating factor in the interpretation of these phase diagrams is the fact that the saturated TAGs crystallize in the β-2 modification, while the cis-unsaturated TAGs crystallize in the β-3 modification. Complete miscibility of a saturated and a cis-unsaturated TAG is impossible: an intermediate β′-2/β′-3 structure is not feasible. In thermodynamic calculations the two β′-forms must therefore be treated as separate modifications, just like the β′ and β-modification. This requires β-3 melting points and enthalpies of fusion of β-2 stable TAGs and vice versa. In line with the findings of de Jong [13] and the observations in Section 15.4, the melting point of the β-form that does normally not occur in the pure substance lies 3°C below the normal β-melting point, while the enthalpy of fusion is 90% of that of the normal β-enthalpy of fusion.

The liquidi of SSS-SOS (Lutton) and of PPP-POO (Gibon) are described very well. In those cases also good correspondence with the solidi could be obtained.

Table 23 Binary Interaction Parameters and Root Mean Square Error Between Experimental Points and Fitted Liquidus for the saturated + Unsaturated TAGs. Data from A=Lutton [93], B= Kung [106], C=Kerridge [94], D=Gibon [11]. Standard Error in the Constants is 0.5, Unless Otherwise Indicated

	2-suffix Margules			
Binary	Aβ-2/RT	Aβ-3/RT	rmse	Ref
SSS-SOS	>1.5	>1	2	A
PPP-SOS	>1	>1	4	B
PPP-POP	>1.3	>1	3.6	C
PPP-POO	1.5	4 (β′-3)	1	D

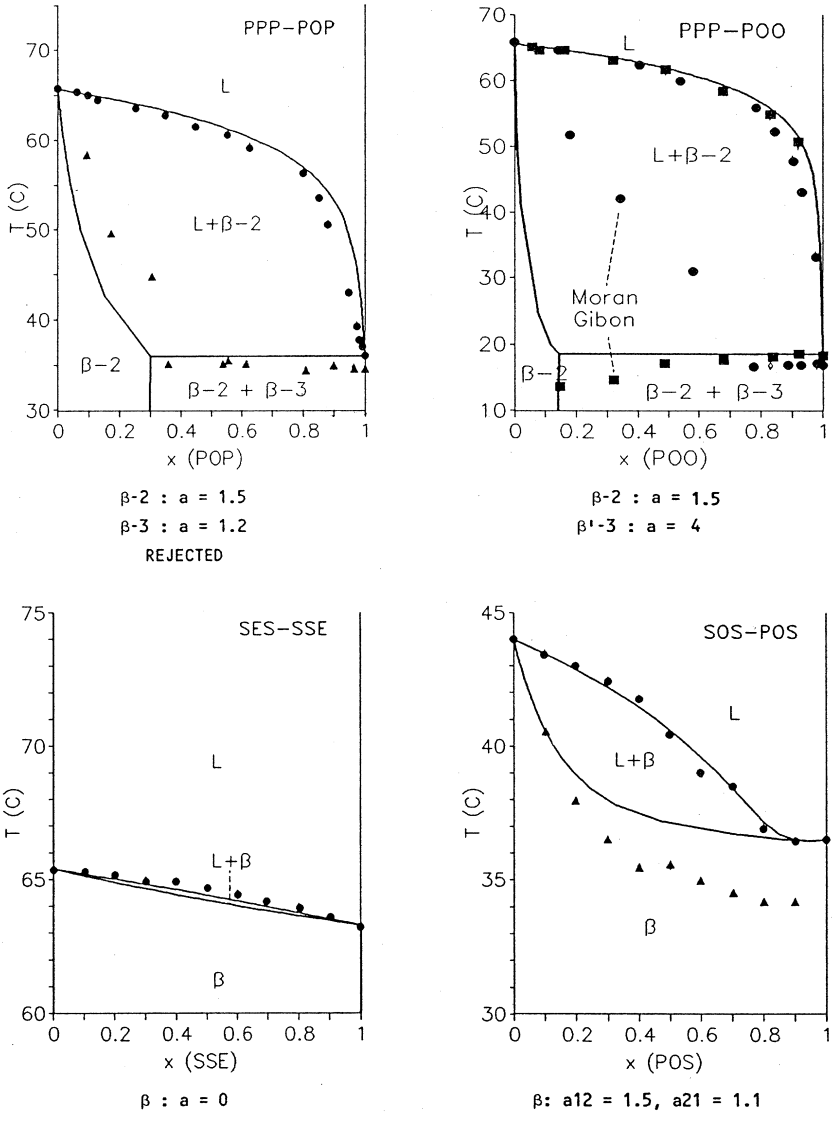

Figure 29 T, x, y diagrams of TAGs from Tables 23 and 24. Experimental data (circles: clear points; triangles: softening points) and best fit (lines) with the 2- or 3-suffix Margules equation. (a = A/RT).

The liquidi of PPP-SOS [106], PPP-POP [94], and the data for PPP-POO of Morancelli [90] are rejected: do not meet the criteria of Section 15.7.3.3: the liquidus lines lie too far below the eutectic liquidus and large parts of the solidus lines are found far above the ideal solidus.

7.2.7 Unsaturated TAGs

Mono unsaturated TAGs

SSE and SES show ideal miscibility, in line with the good solid solubility of both components in SSS. Elaidic acid behaves like stearic acid (Figures 29 and 30).

Smith determined solidus and liquidus in independent experiments using NMR. His liquidi of POS-POP, SOS-POP, and SOS-POS, which he obtained after extensive temperature cycling, fit very well. Smith's cycling procedure was less suited for obtaining a reliable solidus, and consequently the correspondence between the solidus and liquidus data is not perfect.

The diagrams of SOS-SSO and POP-PPO could not be fitted. For both systems there is evidence for formation of a 50–50 compound [16], leading to a maximum in the liquidus lines. The β′-liquid phase diagrams for POP-PPO given by Morancelli [90] and de Bruijne [92] are in complete disagreement. Morancelli obtained an eutectic at 15% POP, while de Bruijne found an eutectic near 50% POP, in agreement with the eutectic composition that is expected from calculations. Phase diagrams in the unstable β′-modification are suspect: during slow scanning in the DTA or DSC equipment the transition to a more stable modification will occur very easily when a large amount of liquid phase is present. Consequently, not all clear points may be those of the unstable modification.

The binary POP-PEP is another example of a phase daigram of two TAGs, that crystallize in differerent β-forms: PEP crystallizes into the β-2 form, while POP crystallizes into the β-3 form.

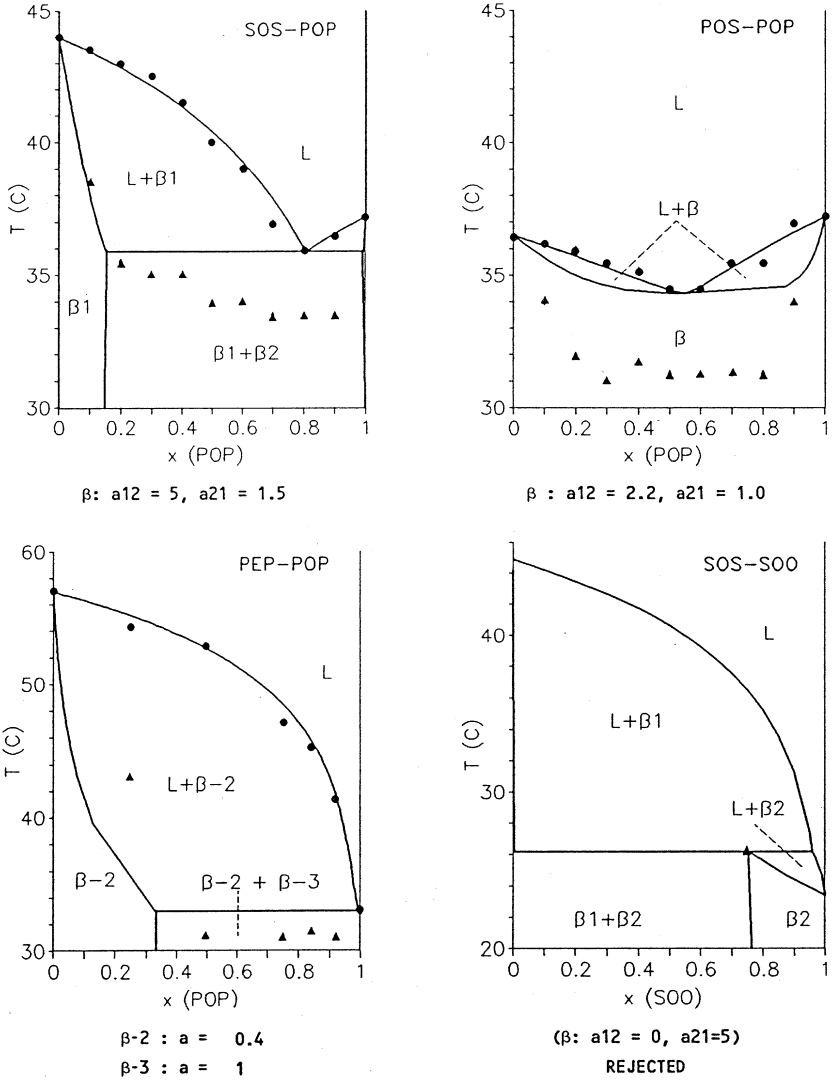

Figure 30 T, x, y diagrams of TAGs from Tables 24 and 25. Experimental data (circles: clear points; triangles: softening points) and best fit (lines) with the 2- or 3-suffix Margules equation. (a = A/RT).

Other unsaturated TAGs

All phase diagrams reported for these TAGs seem very unreliable (Figures 30 and 31). Rossell [91] gives three diagrams of SOS-SOO, from McGowan, Morancelli, and Rossell. The three diagrams all disagree and have liquidi far below the eutectic liquidus. Therefore they are unreliable. There is one similarity: all diagrams have peritectic point at 24% SOS and about 27°C. This peritectic point can be obtained using the values of the interaction parameters given in Table 24.

The liquidus data of Gibon for PPO-POO are described by the eutectic liquidus. The data were obtained after a stabilisation at room temperature for a year. The mixtures are still partially liquid at room temperature and it may be assumed that sufficient recrystallization had occurred to render a reasonable liquidus. The solidus was obtained directly after crash cooling and is therefore unreliable. Moran gives for PPO-POO a liquidus far below the eutectic liquidus. His data were therefore not further used.

Both diagrams of Morancelli for POP-POO also have a liquidus below the eutectic liquidus and were therefore disregarded. In Gibon's DSC curves for POP-POO the final melting peak overlapped with a $\beta' - \beta$ transition. Stabilisation has been insufficient.

The data of Morancelli for PPO-OPO are very well described by the eutectic liquidus, but the solidus again lies far above the ideal solidus.

Morancelli reported two diagrams for POO-OPO, of which the one given in Figure 14 has an eutectic composition where it is expected, at about 50% POO. Strangely enough Morancelli judged his other diagram, with a eutectic at 17% POO, more reliable. The correspondence with the solidus is poor in both cases.

Morancelli's diagram for POP-OPO has to be disregarded: the liquidus lies far below the eutectic liquidus. Morancelli explained this by assuming compound formation, but if a compound would have formed, part of the liquidus certainly had to be situated above the eutectic liquidus.

It seems that most of Morancelli's data are not reliable, which arouses doubts about the two diagrams of Morancelli

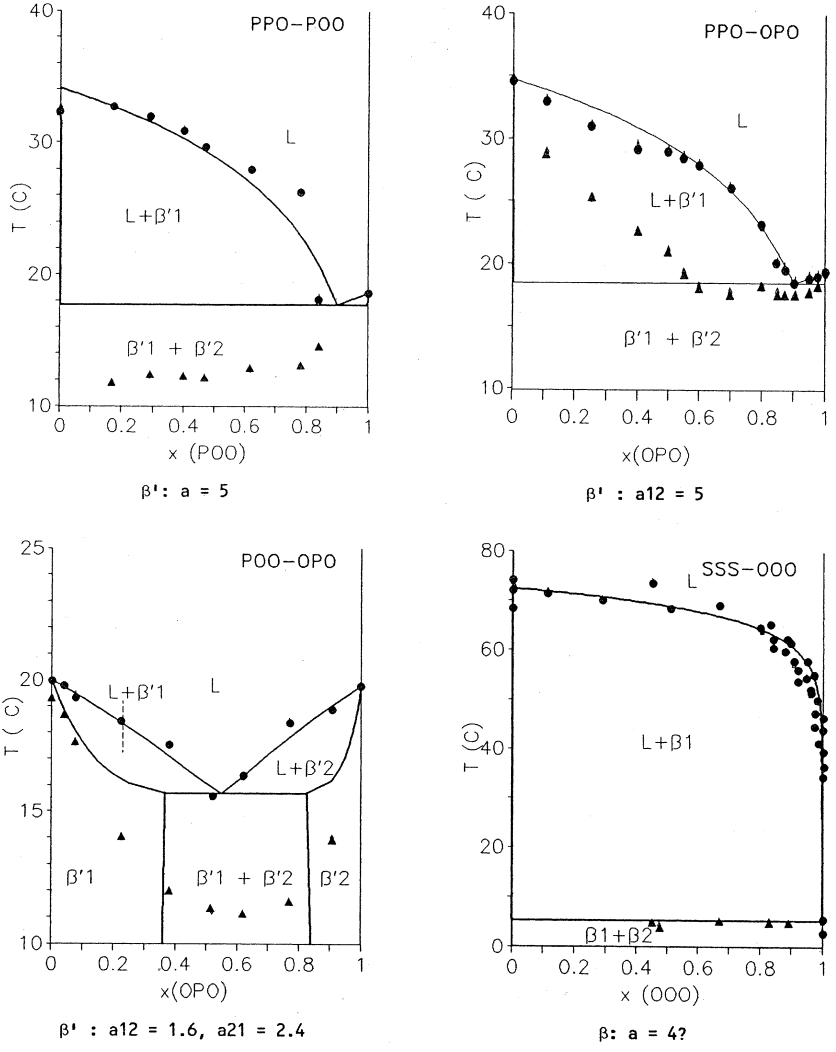

Figure 31 T, x, y diagrams of TAGs from Tables 25 and 26. Experimental data (circles: clear points; triangles: softening points) and best fit (lines) with the 2- or 3-suffix Margules equation. (a = A/RT).

Table 24 Binary Interaction Parameters and Root Mean Square Error Between Experimental Points and Fitted Liquidus for Mono-unsaturated TAGs. Data from A = Grootscholten [101], B = Freeman [108], C = Smith [40], D = Lovegren [66], E = Morancelli [90]. Standard Error in the Constants is 0.5, Unless Otherwise Indicated

	2-suffix Margules		3-suffix Margules			
Binary	A/RT	rmse	A_{12}/RT	A_{21}/RT	rmse	Ref
SES-SSE	0	0.2	0	0	0.2	A
SOS-SSO	–	–	–	–		B
SOS-POS	1.3	0.2	1.5	1.1	0.2	C
SOS-POP	3.6–6	0.3	5	1.5	0.3	C
POS-POP	1.6	0.5	2.2	1.0	0.4	C
POP-PPO	–		–	–	–	E
POP-PEP	0.4 ± 1	0.9	–	–	–	D
β-3:	1 ± 0.8					

(PPO-OPO and POO-OPO) that did meet the acceptance criteria of Section 15.7.3.3.

Triolein

Indeed, all data lie reasonably well on the calculated liquidus, the data of Grootscholten being slightly better than those taken from Rossell (Figures 31 and 32) [91].

Table 25 Binary Interaction Parameters and Root Mean Square Error Between Experimental Points and Fitted Liquidus for Unsaturated TAGs. Data from A = Rossell [91], B = Morancelli [90], C = Gibon [11]

	2-suffix Margules		3-suffix Margules			
Binary	A/RT	rmse	A_{12}/RT	A_{21}/RT	rmse	Ref
SOS-SOO	–		0?	5?	–	A
PPO-POO(β′)	1–9?	1.7	1–9?	1–9?	1.7	C
PPO-OPO(β′)	5–9 ?	0.6	4–9 ?	2–9 ?	0.6	B
POO-OPO(β′)	2.0 ?	0.3	1.6 ?	2.4 ?	0.3	B

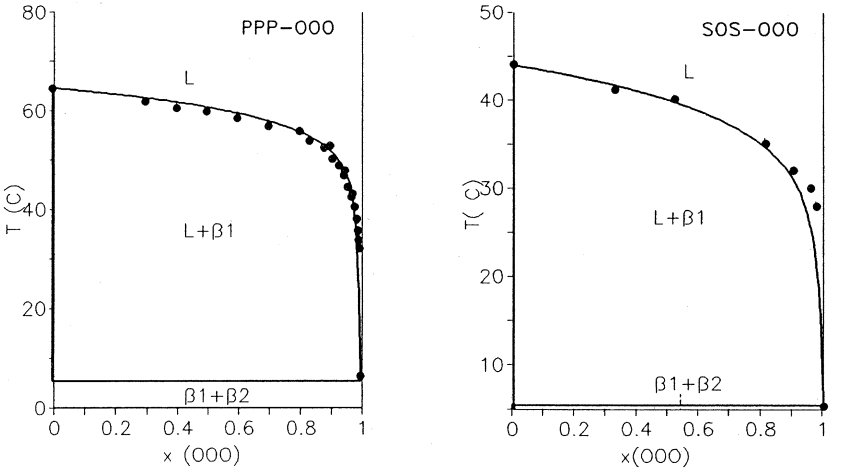

Figure 32 T, x, y diagrams of TAGs from Table 27. Experimental data (circles: clear points, triangles: softening points) and calculated lines.

In these diagrams, the difference in melting points is so large that the ideal and eutectic liquidus and solidus almost coincide.

Fitting is in this case merely a test of the quality of the data and does not give much information about the extent of non-ideal mixing.

Table 26 Binary Interaction Parameters and Root Mean Square Error Between Experimental Points and Fitted Liquidus for Triolein. Data from A = Rossell [91] and B = Grootscholten [93]

	2-suffix Margules		3-suffix Margules			
Binary	A/RT	rmse	A_{12}/RT	A_{21}/RT	rmse	Ref
SSS-OOO	0–9	4	–	–		A/B
PPP-OOO	0–9	3	–	–		A/B
SOS-OOO	0–9	2	–	–		A

7.2.8 Summarizing

Nearly 120 phase diagrams were considered:

- 84 had to be rejected because they were clearly not correct.
- The liquidus lines were fitted very well for 34 of the remaining 36 phase diagrams. The average deviation from the experimental curves was only 7% of the difference between maximal and minimal liquidus temperature.
- In two cases no fit could be obtained, which was attributed to compound formation that was not accounted for in the thermodynamic modelling.
- The experimental softening points lay far above the ideal solidus at the side of the higher melting component in five of the 34 remaining diagrams. These five binaries all concerned TAGs with a large difference in melting point. It was made plausible that this deviation was due to an experimental error. Experimental evidence that confirmed this exists for two of the five binaries.
- The difference between the melting points of two components was less than 15°C in 24 of the 34 binaries that remained. Eleven of these 24 diagrams were almost completely eutectic. This implies that only in 13 diagrams the interaction parameters have a clear influence on the shape of the liquidus. Therefore these 13 diagrams are the most demanding test cases for the performance of the excess Gibbs energy models.

The average root mean square error between measured and fitted liquidus for these 13 remaining diagrams is 0.4°C. This is approximately the experimental error that is claimed. It is impossible to obtain very accurate values of the interaction parameters with an experimental error of this magnitude.

Based on the available data it is not possible to express a preference for one of the two excess Gibbs energy models used. Hardly any improvement in fit was obtained when the 3-suffix Margules equation was used. Peritectic diagrams that could not be described using the 2-suffix Margules equation, had to be disregarded. Generally the experimental softening points were better described with the 3-suffix Margules equation.

7.3 AN ALTERNATIVE TO PHASE DIAGRAM DETERMINATION

7.3.1 How to proceed?

The evaluation of all available phase diagrams of TAGs in Section 15.7.3 has resulted in interaction coefficients for only 35 binaries. The uncertainty in these interaction parameters is considerable, due to the large experimental error in the diagrams.

Interaction parameters were almost exclusively obtained for the β-modification. However, it is of much greater importance to know the parameters for the polymorph that is normally found in edible fat products, the β′-modification.

The determination of binary interaction parameters that occur in an excess Gibbs energy model by fitting this model to experimental binary T, x, y solid liquid phase diagrams has a number of very serious drawbacks:

It is extremely troublesome, time consuming and probably almost impossible to determine accurate phase diagrams. It takes months to years before the samples have been stabilized properly, minor impurities have large effects, and the true start and end melting point of a mixture are very hard to determine.

Relatively small experimental errors in the position of the liquidus and solidus lead to large uncertainty in the interaction parameters that are determined from the diagrams. It is questionable whether more accurate β-data can be obtained by determining binary solid-liquid phase diagrams.

It is not possible to measure reliable phase diagrams of unstable modifications, like a binary β′-phase diagram of β-stable TAGs.

Determination of binary interaction parameters from phase diagrams is only feasible for TAGs that differ less than about 15°C in melting point. At larger melting point differences, the position of liquidus and solidus becomes too insensitive to the value of the interaction parameters.

Determining phase diagrams of TAGs to obtain binary interaction parameters is therefore not practical and another method has to be defined.

7.3.2 Formulation of an alternative method

The problem of the extremely long stabilization times can probably be solved.

In a solid binary system, diffusion rates are extremely low, so that unstable modifications and crystals with a non-equilibrium composition have been shown to persist for years [11]. But if a surplus of a liquid TAG is added to the binary system, things become different. The phase diagram of such a ternary system (PSP/SEE/OOO) is shown in Figure 33. When the temperature is sufficiently above the melting point of the liquid component (OOO), the solidus surface in the diagram

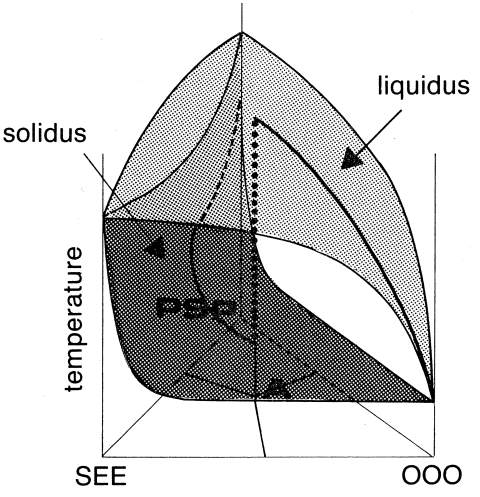

Figure 33 Schematic ternary phase diagram of the system PSP/SEE/OOO in the β′-modification. The softening point surface is dark shaded, while the clear point surface is light shaded. The lines indicated with solidus and liquidus represent the composition of the solid and liquid phase of a mixture with composition A while it is being melted.

coincides with the binary side plane of the two crystallizing TAGs (PSP and SEE), even when ideal mixing in the solid phase occurs. The concentration of the liquid component in the solid phase is then negligible. The solid phase in this ternary system is still a binary mixture.

If the fat is crystallized in very small (< 1 μm) crystals, to create a large exchange surface with the liquid phase, then the solid fat can recrystallize relatively easily via the liquid phase to its equilibrium composition and modification [23,27].

Phase diagrams are usually determined by measuring the softening and clear point of a set of mixtures using DSC. Due to impurities and thermal lag that occur both points can only be determined with an accuracy of about 0.2–1°C.

In fact this application of DSC does not use all available information: a DSC-curve of a mixture is taken and next the two most undefined points on the curve, its start- and end-point, are used, while everything in between, that contains lots of information about the phase behaviour of the binary system, is wasted. If the complete DSC curve is used for determination of the interaction parameters, rather than only 2 points, it should be possible to increase the accuracy of results with considerably less measurements. In Section 15.3, a method to simulate the effect of non ideal mixing in the solid phase on the shape of DSC-curves was defined. This method can be applied to fit a complete DSC curve by adapting the binary interaction parameters.

The method for determinating interaction parameters that evolve, is to fit the complete DSC-curve of a binary mixture, to which a surplus of a liquid TAG is added. The liquid TAG assures shorter and better stabilization. The use of the complete curves reduces experimental error, reduces the number of measurements and removes the limitation to binary pairs that have a difference in melting point less than 15°C.

7.3.3 DSC curves of binary systems dissolved in a liquid TAG.

Figure 34 on the following page gives the types of DSC-curves that can be obtained for TAGs that differ considerably in melt-

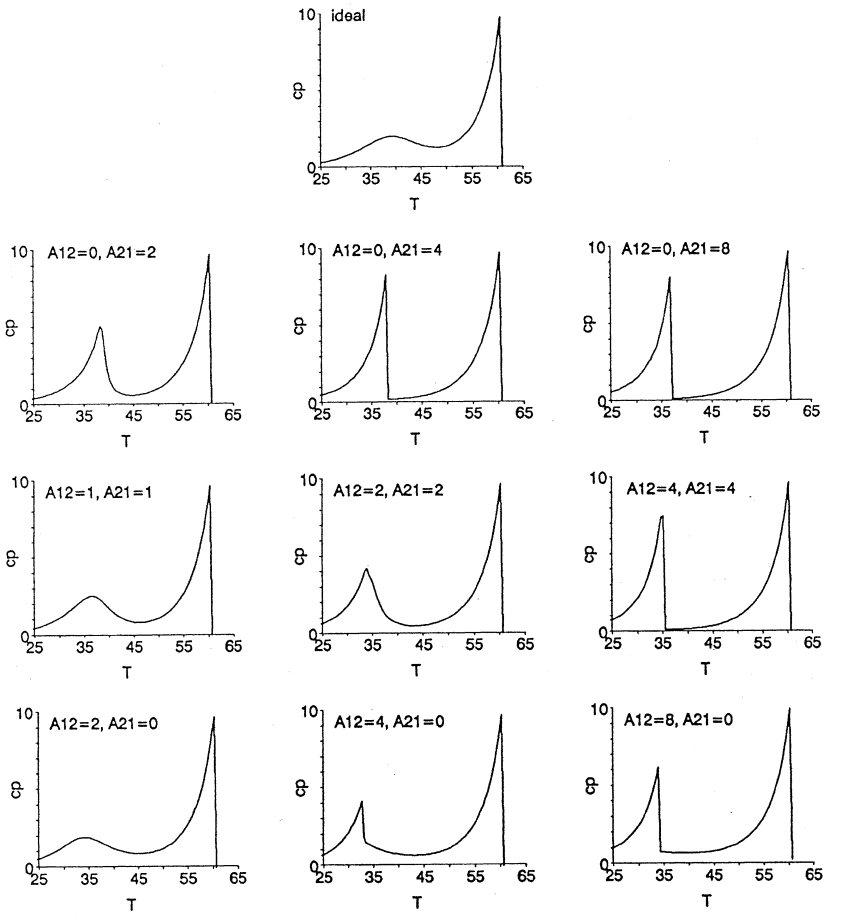

Figure 34 Theoretically possible DSC-melting curves of a ternary mixture of 25% PSP, 25% SOS and 50% 000 crystallized in the β′-2 modification. The curves are calculated using the 3-suffix Margules equation. The values of the binary interaction parameters are indicated.

ing point by application of the 3-suffix Margules equation. Although in this situation the position of liquidus and solidus in the binary phase diagram are nearly invariant, still considerable differences in curve shape are obtained.

The following aspects feature:

1. All curves contain two melting peaks. The shape of the final melting peak and the start of the first melting peak are hardly influenced by the values of the interaction parameters. This is in line with the invariance of the phase diagram. However, the shape of the first melting peak and the height of the plateau in between the two peaks depend very much on the values of the interaction parameters.
2. The first melting peak ends sharply if demixing in the solid state occurs.
3. If no demixing occurs, the complete shape of the first melting peak is indicative for the value of the interaction parameters, which implies that the interaction parameters can be determined very accurately.
4. If demixing occurs, the height of the plateau just after the first peak is indicative for the magnitude of the interaction parameters. This implies that in these cases the interaction parameters can be determined less accurately, due to the influence of noise and the uncertainty in the baseline.
5. Above values of $A/RT = 4$ the curve shape does not depend on the magnitude of the interaction parameters any more. However, as at $A/RT = 4$ already nearly complete solid phase immiscibility occurs, this is not a real problem.
6. For the 2-suffix Margules equation peak shape and peak position are closely related: upon increasing magnitude of the interaction parameters the first melting peak becomes sharper and shifts towards lower temperatures. Therefore 2-suffix Margules parameters can be determined very easily. Bringing in asymmetric behaviour with the 3-suffix Margules equation allows shifting of sharp peaks to higher tem-

peratures and of broad humps towards lower temperatures. In fact, if the component with the highest melting point is [1] and the other [2], then the shape of the first melting peak is mainly determined by A_{21} and its position mainly by A_{12}. The 3-suffix Margules parameters determined from the curves will necessarily have a larger error, as the uncertainty in the melting points of 1–1.5°C has to be taken into account now.

7.3.4 What experiments?

In most edible fat products the fat has crystallized into the β′ modification. There are no reliable data available about miscibility in the β′ modification.

For fat fractionation calculations it is important to know the solubility of mono-unsaturated TAGs in the solid phase of saturated TAGs both in the β′ and in the β modification. It was shown in Section 15.7.3 that the scarce information that exists is unreliable.

In edible fat products mostly hydrogenated fats, which are rich in elaidic acid, are used. Except for S_2E in SSS there is no information available about the phase behaviour of TAGs that contain elaidic acid.

Of the many systems that can be studied, it seems therefore most relevant to determine interaction parameters for the β′-modification of systems where mono-unsaturated and trans-containing TAGs are combined with saturated TAGs.

In order to enable the determination of β′-interaction parameters, assure that during determination of the DSC-curve, which must be taken at low scan rates in order to reduce thermal lag, no transition to the β-modification will occur. Near the clear point the solid phase usually almost completely consists of the component with the highest melting point. If this component is β-stable, than a transition is very likely. However, if for this component a β′-stable TAG is taken, the chances of keeping the system sufficiently long into the β′-modification to allow a measurement are much higher. Moreover, even if in this case a solid phase in the β-modification, rich in the crystallizing component with the lower melting

point, comes about, the DSC curve will still contain a melting peak of a mixed β′-phase that holds information about the miscibility in the β′-modification.

In view of this, the authors have selected a number of systems, of a β′ stable saturated TAG and a number of mono- and di-unsaturated TAGs, including some that contain elaidic acid:

PSP with SOS, SSO, POP, PPO, PEE, EPE, SEE, ESE and EEE.

MPM with SOS, SSO, POP, PPO, PEE, EPE, SEE, ESE and EEE.

These systems allow the study of the influence of a difference in size as well as the influence of position and nature of the unsaturated chains. The data themselves are relevant for normal edible fat products.

7.4 EXPERIMENTAL

7.4.1 Principles of DSC

With DSC two cups, one containing a few milograms of the sample to be investigated and the other containing an inert reference material, are placed in two identical microfurnaces. Both furnaces are mounted in cavities of a large aluminium block or heat sink. The aluminium block is kept at a constant temperature, well below the temperature range of the experiment. In the base of each furnace are two identical platinum resistance elements. One is used to provide heat to the furnace, the other that is mounted directly under the furnace base, serves as temperature sensor (Figure 35).

The equipment is controlled by two control loops: an average temperature control or scan loop that enables simultaneous heating of both microfurnaces at a constant heating rate (in °C/min). The other loop is a differential temperature control loop from which the instrument output signal is obtained. This loop adjusts the heat flow to one of the furnaces if a process in one of the samples takes place that gives out or takes up heat, such that the temperature difference between the two cups always remains zero.

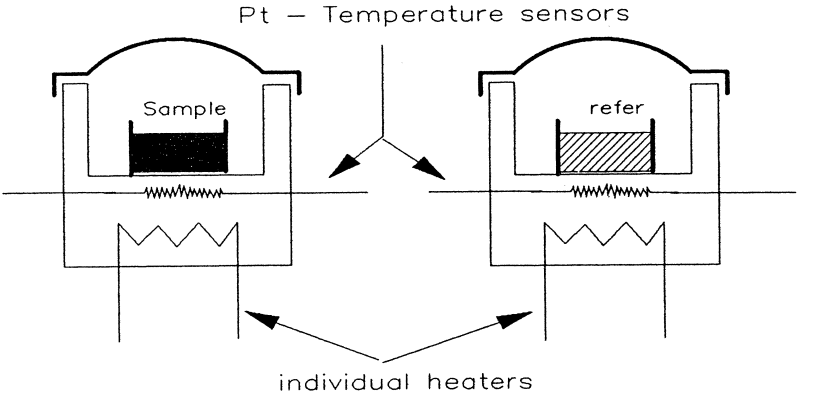

Figure 35 Schematic view of a DSC apparatus

The difference in the amount of energy that must be supplied to the samples to heat both at the same rate plotted as a function of temperature is the DSC-curve. It is directly proportional to the apparent heat capacity of the sample as a function of temperature.

DSC is often confused with DTA, Differential Thermal Analysis. In DTA both samples are heated in the same microfurnace with a constant heat flow. The temperature difference that occurs between the samples, when the sample gives out or takes up heat, is recorded, the DTA-curve. The DTA-curve contains essentially the same information as DSC-curves. With DTA fast heating and cooling rates as well as isothermal measurements are not possible and heat effects are derived quantities rather than directly measured quantities. However DTA is technically less complex.

7.4.2 Thermal lag

The main problem in the use of DSC-curves is the thermal lag that occurs. During scanning the temperature of the inner part of the sample lags behind that of the apparatus. This thermal lag can completely disturb the shape of the DSC curve at large sample sizes and scan rates (Figure 36).

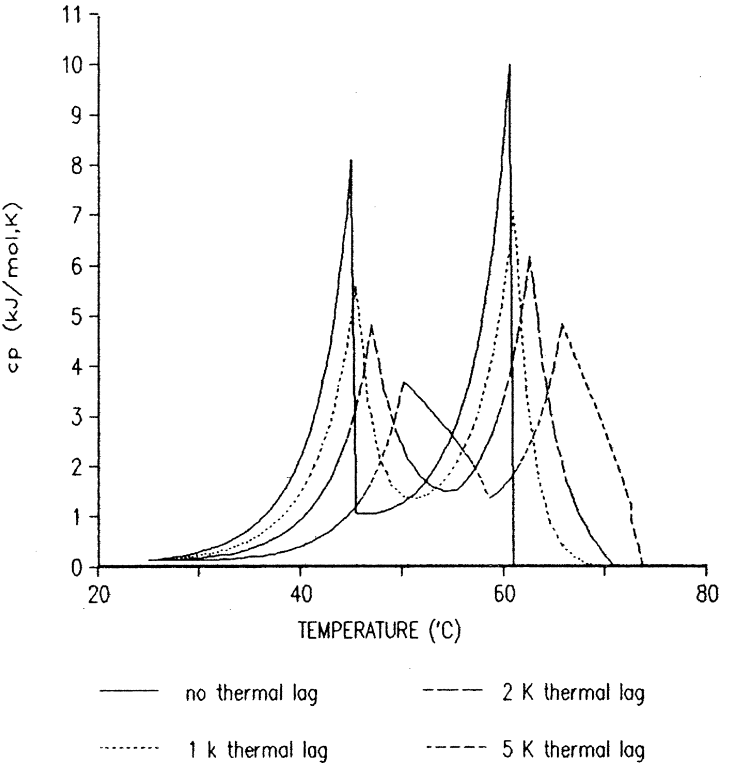

Figure 36 Influence of thermal lag on the curve shape of the system 25% PSP, 25% SEE, 50% 000. (simulated curves)

It is best to check for the presence of thermal lag by obtaining the steepness of the peak at the end melting point. Ideally this should be a straight line perpendicular to the temperature axis. At very low scanning rate or small sample size thermal lag is negligible, but the DSC signal becomes very weak, leading to noisy DSC curves. In the experimental procedure the right balance between thermal lag and sensitivity must be found by trial and error.

7.4.3 Experimental procedure

The work was largely carried out using a Perkin Elmer DSC-2, equipped with an IBM-AT for data acquisition and control

of the apparatus by means of software developed at the Department for Thermal Analysis of the Unilever Research Vlaardingen. Some work was done on a Perkin Elmer DSC-7, which is mechanically equivalent, but equipped with more advanced Perkin Elmer machinery for data-acquisition and control, making it more sensitive. The heat sink was cooled with a solid CO_2/acetone mixture (DSC-2) or liquid nitrogen (DSC-7). The equipment was calibrated using pure Indium (T_f = 156.6°C) and Gallium (T_f = 29.8°C).

About 10 mg of a sample was weighed into an aluminium cup, that was closed and sealed. The sample was inserted into the apparatus, melted at 80°C and kept for 10 minutes at that temperature to prevent possible memory effects. Next the sample was cooled at 20°C/min to 5°C below the temperature where the melting of a fully eutectic β′-phase would take place. The sample was stabilized for 1 minute at that temperature and subsequently heated at 1–2°C/min. The melting curve was recorded. This procedure is repeated several times with varying stabilization time: 1 minute stabilisation, 5 minutes, 15 minutes, 1 hour, 3 hours, 24 hours, a week, and a month.

Usually stabilization times less than 1 hour resulted in melting curves of the β′ modification, sometimes disturbed by a transition to the β modification. Longer stabilisation times mostly lead to a 3-phase β-β′-Liquid system.

Stabilization longer than a week usually did not result in changes any more. To verify that indeed crystallization had taken place in the right polymorphic form X ray diffractograms were taken after the same cooling and stabilization procedure for some of the mixtures.

The influence of stabilization time on the polymorphic form in which crystallization has taken place is illustrated in Figure 37 for the system PSP/SEE/OOO. The shortest stabilization time only shows melting peaks of β′-crystal phases. After somewhat longer stabilization a β-melting peak starts to appear as a shoulder, while in the completely stabilised sample a sharp melting peak of a SEE-rich β-phase is present next to a melting peak of a PSP-rich β′ phase.

At the sample size and scan rate used thermal lag may be neglected: the curve shape does not change significantly

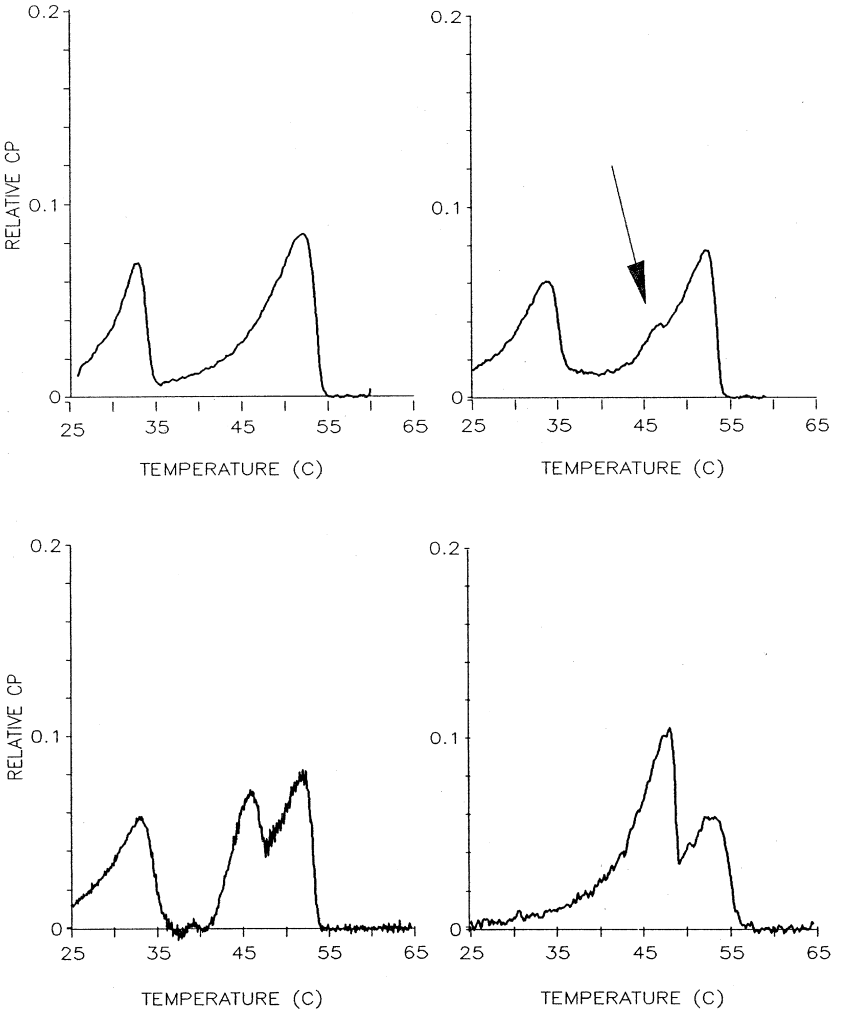

Figure 37 Measured DSC-curves of ternary mixtures of 25% MPM% with ±25% ESE and ±′50% 000. Note the appearance of a melting peak of a seperate ESE-rich β-phase at 46°C and the disappearance of the melting peak of an ESE-rich β′-phase at 34°C upon increasing stabilisation time. *top left* = 1 min 20°C *top right* = 15 min 20°C *bottom left* = 60 min 20°C *bottom right* = 7 days 20°C

when the scan rate is further decreased, while the noise increases. Normally a scan rate of 2.5°C/min was used, sometimes, if no β′-β transition occurred and the noise level was acceptable a scan rate of 1.25°C/min was used.

The TAGs were obtained from Dr. A. Fröhling of the section Organic Chemistry of Unilever Research Vlaardingen. They were pure on TLC. To remove oxidation products and partial glycerides the unsaturated TAGs were treated over a silica column. The TAGs were as extra purification recrystallized from hexane. To prevent oxidation during measurements and storage 0.01% of BHA was added as antioxidant. The GLC and HPLC analysis results of the TAGs are given in Appendix 3.

Determination of interaction parameters

The interaction parameters were determined from the measured curves by adapting the parameters using a Simplex procedure until the sum of squared errors between the calculated and measured curve are minimal. Heats of fusion and melting points are obtained from the correlations of Section 15.4. As the melting points from the correlations, as well as experimental melting points, have an accuracy of about 1°C, we allowed the fitting procedure to vary the melting point maximally ± 1°C around the value from the correlation. Both calculated as well as measured curves are normalized such, that the area under the curves from 25°C up to the clear point equals unity. To reduce calculation time the number of data points was reduced to one per 0.4°C. One iteration required about 40–60 s on a Compaq 386/25 PC under MS-DOS.

7.5 RESULTS

7.5.1 PSP and MPM with ESE and SEE

The measurements that were carried out and the results of the fitting procedure are given in Table 27 and Figures 38 and 39.

The fit to the measured curves is most satisfactory. The minor overshoot of the calculated curves at the top of sharp peaks must be ascribed to the inertness of the measuring tech-

Table 27 DSC Measurements and 2-suffix Margules Parameters for the Highest Melting Binary Pair Determined from these Measurements. (composition in mole fractions, temperatures in °C, time in minutes, unless otherwise indicated: d = days)

Modification	PSP	MPM	SEE	ESE	OOO	Scan rate (K/min)	Stabilization time (min)	Stabilization temp. (°C)	A/RT
β′	0.26		0.25		0.49	2.5	15–180	20	0 ± 0.2
β′		0.28	0.24		0.48	2.5	1–15	20	3.0 ± 0.2
β′	0.26			0.24	0.50	2.5	1–180	20–25	0 ± 0.2
β′		0.27		0.23	0.50	2.5	1–15	20	3.0 ± 0.2
β	0.26		0.25		0.49	2.5	14d	20	≥ 2.5
β		0.28	0.24		0.48	2.5	1d–3d	20	≥ 2.5
β	0.26			0.24	0.50	1.25	5d–28d	20–25	≥ 2.0
β		0.27		0.23	0.50	1.25	60–7d	20	2 ± 1

nique, due to factors like thermal lag and the sampling time of the A/D converter in the DSC-2.

Only the 2-suffix Margules parameters are given, as no improvement of fit could be obtained by application of the 3-suffix Margules equation. While the interaction parameters for the β′-modification are indeed very accurate, the interaction parameters for the β-modification are only rough estimates. In combination with a β′-stable TAG a solid phase split, leading to a DSC-curve with two sharp peaks, will always occur. Only the position of the peak at the lower temperature end of the curve is indicative for the magnitude of β-interaction parameter, while its shape does not change.

The behaviour of ESE and SEE is exactly the same, which is in correspondence to the close similarity of elaidic and stearic acid. Both mix ideally with PSP in the β′-modification, but show a solid solubility less than 15% in the β-modification. With MPM the solubility in the β′-modification is reduced to only 7%, showing the influence of the increased difference in molecular size.

X-ray diffractograms for PSP-SEE-OOO are in line with these DSC observations: initially a typical β′ diffraction pattern is obtained, with two strong maxima at 3.80 Å and 4.20 Å, which are characteristic for the β′-modification and a single long spacing, indicating the existence of only one crystalline

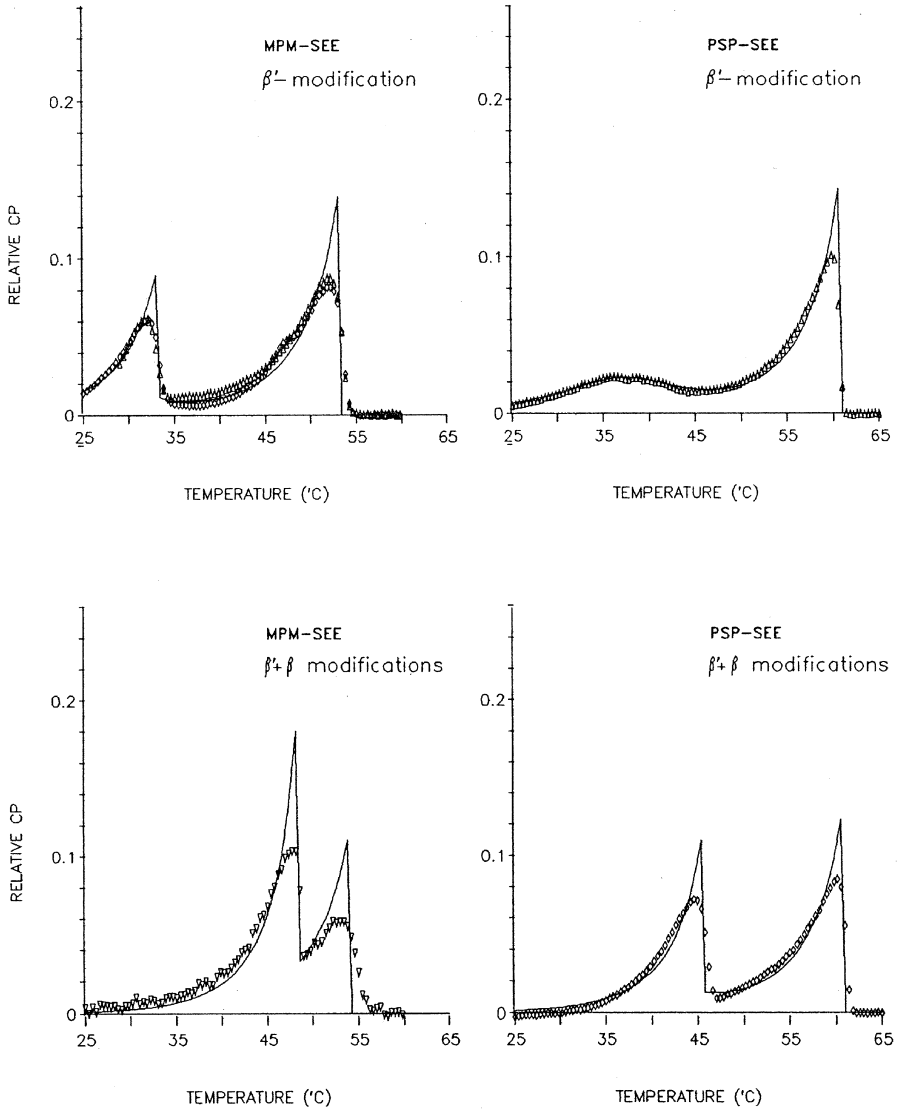

Figure 38 Measured (dots) and fitted (lines) DSC-curves of ternary mixtures of ±25% PSP or MPM% with ±25% SEE and ±50% 000. The modification(s) in which crystallization has taken place is indicated.

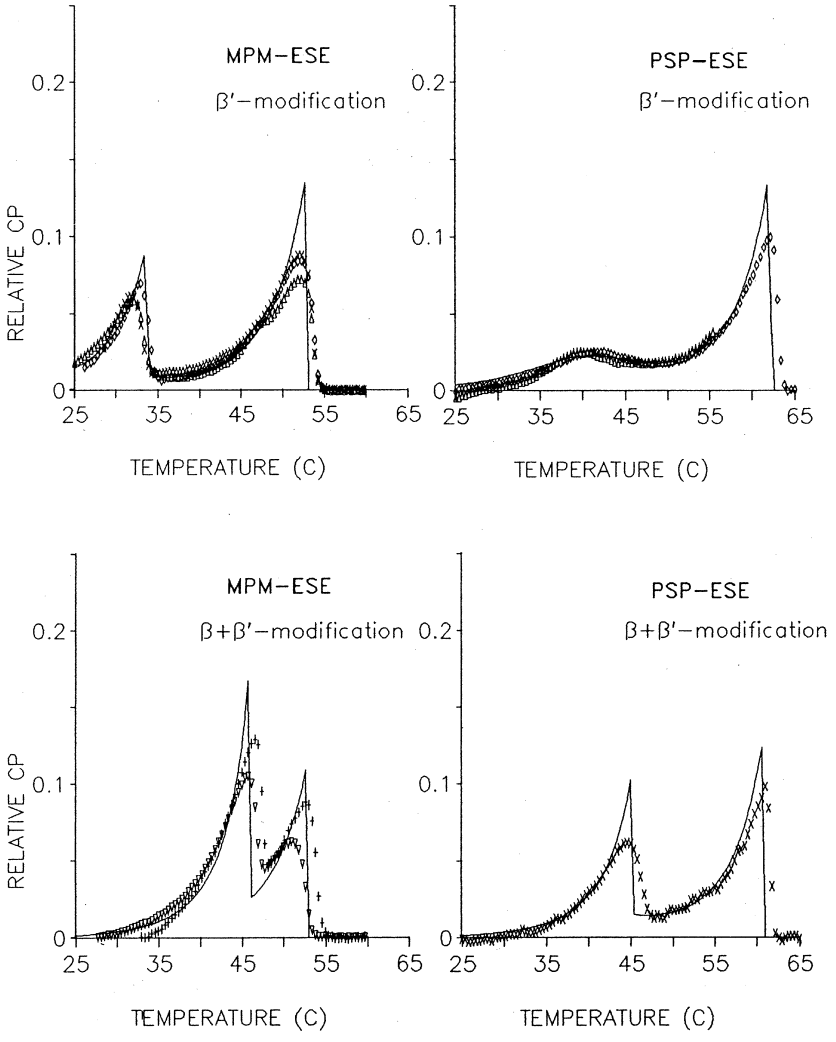

Figure 39 Measured (dots) and fitted (lines) DSC-curves of ternary mixtures of ±25% PSP or MPM% with ±25% ESE and ±50% 000. The modification(s) in which crystallization has taken place is indicated.

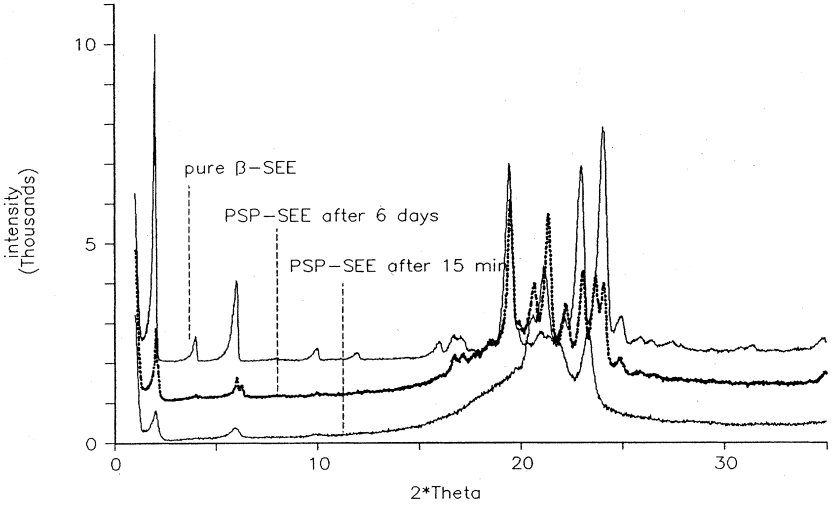

Figure 40 X-ray diffractograms of the mixture 25% PSP- 25% SEE- 50% 000, after 15 minutes and 6 days of stablization at 20°C. The diffractogram of pure -SEE is also given.

phase. The diffraction pattern differs from that of pure PSP, indicating that a single mixed β′-phase indeed exists, in agreement with the complete miscibility derived form the DSC results (Figure 40).

After one day the diffraction pattern has changed. The β′-short spacings are still present, but also a short spacing at 4.55 Å has come up, which is characteristic for the β-modification. The long spacing has doubled, indicating the presence of a second crystalline phase. The DSC-results are confirmed again: after long stabilization a β-phase coexists with a β′-phase. The positions of the extra β-diffraction peaks correspond closely to those of pure SEE, in agreement with the prediction of a nearly pure β-SEE phase, which can be derived from the DSC curve.

7.5.2 PSP and MPM with EPE and PEE

The measurements that were carried out and the results of the fitting procedure are given in Table 28 and Figures 41 and 42.

Table 28 DSC Measurements and 2-suffix Margules Parameters for the Highest Melting Binary Pair Determined from these Measurements (composition in mole fractions, temperatures in °C, time in minutes, unless otherwise indicated: d = days)

Modification	PSP	MPM	PEE	EPE	OOO	Scan rate (K/min)	Stabilization time (min)	Stabilization temp. (°C)	A/RT
β′	0.26		0.25		0.49	0.62	14d	15	0 ± 0.2
β′		0.28	0.24		0.48	2.5	1–5	5–15	1.8 ± 0.5
β′	0.26			0.25	0.49	2.5	7d	15	2.0 ± 0.5
β′		0.27		0.25	0.48	1.25	3d	20	2.3 ± 0.5
β	0.26		0.25		0.49	0.62	30d	15	noβ
β		0.28	0.24		0.48	2.5	15–10d	15	≥2.5
β	0.26			0.25	0.49	2.5	7d	15	≥2.5
β		0.27		0.25	0.48	1.25	3d	20	≥ 3

Naturally palmitic and elaidic acid do not show the similarity in behavior that elaidic and stearic acid do. Consequently PEE and EPE can be expected to show differences in mixing behavior. This is indeed observed: while PEE shows a complete miscibility with both PSP and MPM in the β′-modification, EPE shows only limited solubility.

PEE shows a very interesting behavior. The system PSP/PEE/OOO has remained in the β′-modification, even after a month of stabilization. This is confirmed by the X-ray results for this system. Looking at the results obtained for SEE, ESE and EPE, a realistic estimate for the PSP-PEE β-interaction parameter is A/RT = 3. In that case, calculations show that this system is β′-stable at all temperatures, although PEE itself is β-stable: the extra stability of the β-modification is not enough to compensate for the large excess Gibbs energy of a solid phase in that modification. A nearly pure β-PEE phase will only crystallize when the ratio PSP/PEE in the system drops below 0.5. But even for such mixtures the driving force to β is very low, making a speedy recrystallization unlikely. After one week of stabilization of such a mixture only a minor broadening of the first β′-melting peak at the position where a β melting peak would occur, was observed.

The system MPM/PEE/OOO does crystallize into the β-modification. Contrary to PSP and PEE, MPM and PEE show

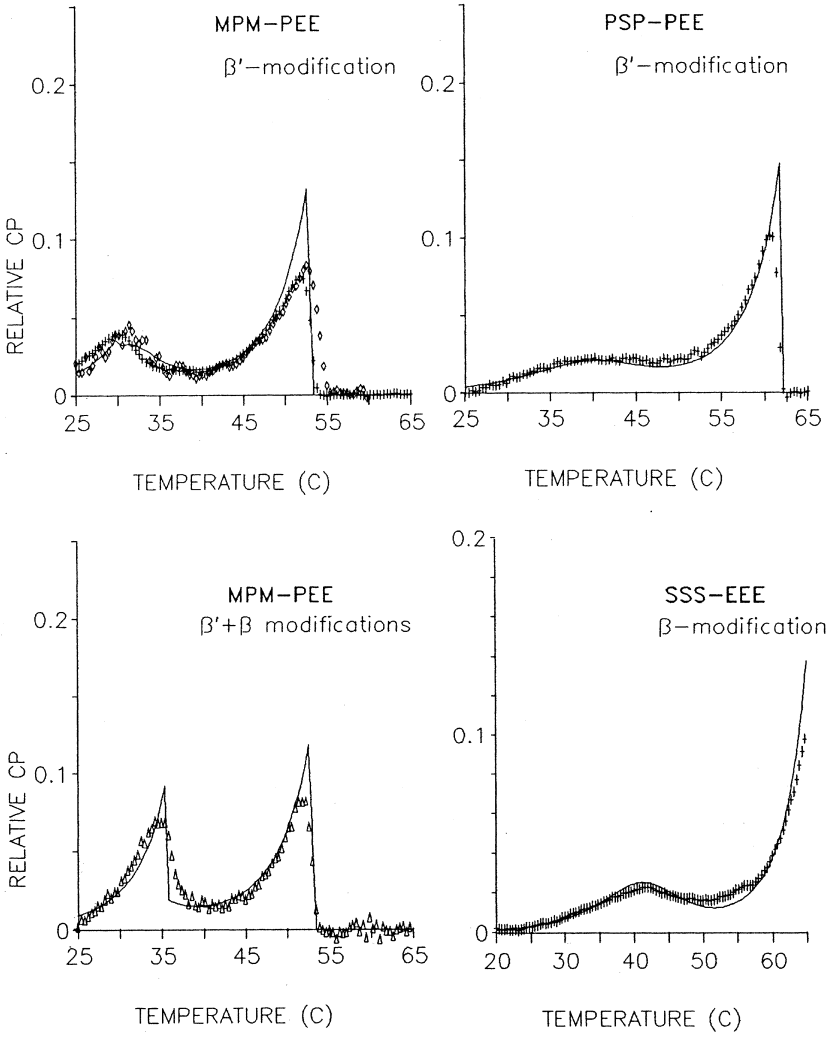

Figure 41 Measured (dots) and fitted (lines) DSC-curves of ternary mixtures of ±25% PSP or MPM% with ±25% PEE and ±50% 000 and of a mixture of 25%, SSS, 25% EEE and 50% 000. The modification(s) in which crystallization has taken place is indicated.

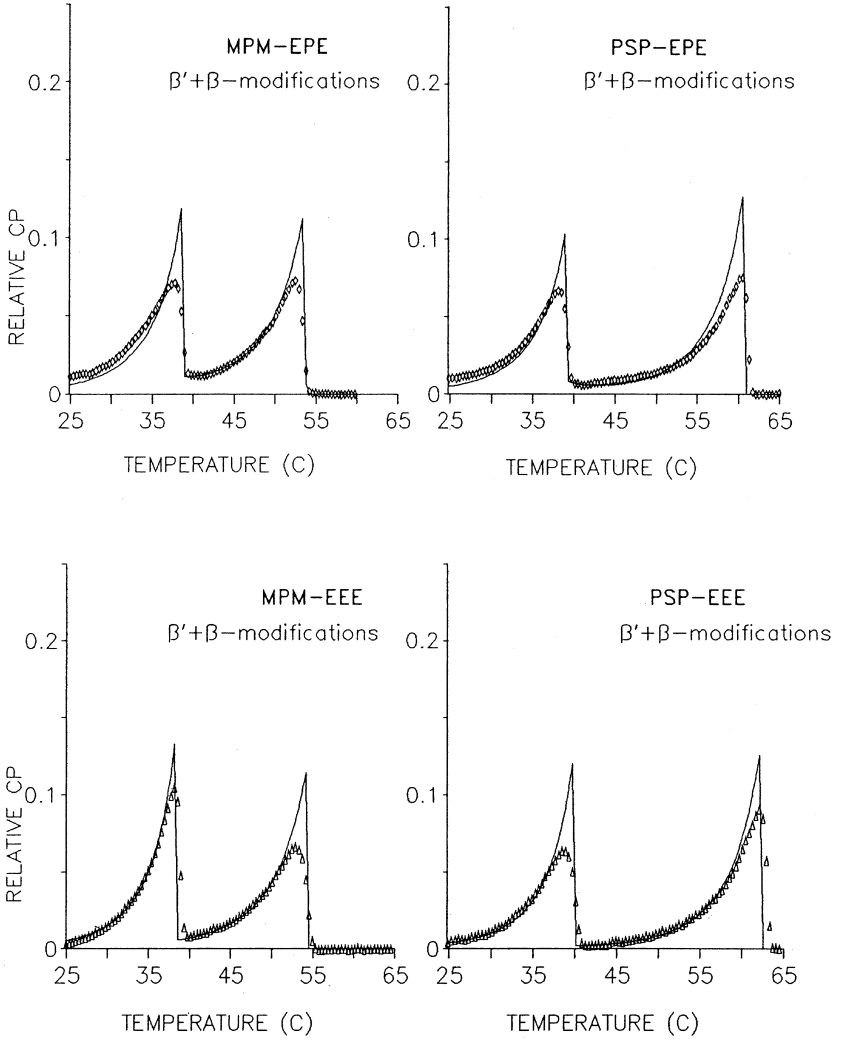

Figure 42 Measured (dots) and fitted (lines) DSC-curves of ternary mixtures of ±25% PSP or MPM% with ±25% EPE or EEE and ±50% 000. The modification(s) in which crystallization has taken place is indicated.

non-ideal mixing in the β′-modification, and therefore the difference in excess Gibbs energy between the two modifications is not large enough to counterbalance the stability difference. The same holds for the PSP/EPE/OOO system that was studied.

Even without stabilization the DSC-curves of the systems with EPE showed exothermic peaks of the β′-β-transition. A complete β′-melting curve can therefore not be obtained. The estimate for the β′-interaction parameter is based on the shape and height of the plateau just after the first melting peak in the curve of a completely stabilised sample.

7.5.3 PSP and MPM with EEE

The measurements that were carried out and the results of the fitting procedure are given in Table 29 and Figures 41 and 42.

These systems all recrystallized quickly into the β-modification. Even without stabilization, the melting curves of the β′-modification were disturbed by exothermic peaks of the β′-β-transition. Therefore the values of the β′-interaction parameters had to be estimated from the height of the plateau just after the first melting peak. The plateau height is nearly zero.

For a reliable determination of the β′-interaction parameter the β′-melting point of EEE is required. The authors were not able to determine a β′-melting point of their EEE sample, only an α and a β-melting point were found. This is in line

Table 29 DSC Measurements and 2-suffix Margules Parameters for the Highest Melting Binary Pair Determined from these Measurements. (composition in mole fractions, temperatures in °C, time in minutes, unless otherwise indicated: d = days

Modification	PSP	MPM	PEE	OOO	Scan rate (K/min)	Stabilization time (min)	Stabilization temp. (°C)	A/RT
β′	0.26		0.25	0.49	2.5	1–7d	15	0 ± 1
β′		0.27	0.25	0.48	2.5	30–70	15–20	≥ 2 ?
β	0.26		0.25	0.49	2.5	1–7d	20	≥ 2.0
β		0.27	0.25	0.48	2.5	30–70	15–20	≥ 2.0

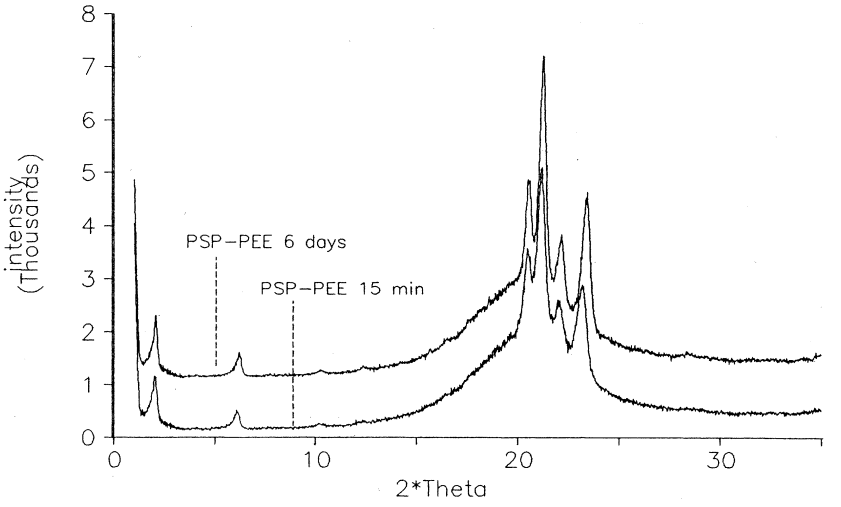

Figure 43 X-ray diffractograms of the mixture 25% PSP- 25% PEE- 50% 000, after 15 minutes and 6 days of stablisation at 20°C.

with the findings of Hagemann [103] and earlier authors [109], who also could not detect a β′-melting point of EEE. A very old report of Malkin [110] gives 37°C for the β′-melting point. This value does not compare well with the data of Hagemann [103] for a number of glycerol tri-trans-octadecenoates. Hagemann found a steady decrease in the β′-melting point from 43°C for trans-17-octadecenoic acid to 28°C for trans-11-octadecenoic acid. Extrapolating the data of Hagemann to trans-9-octadecenoic acid (E) results in a β′-melting point of 27–28°C for EEE.

If 37°C is used as β′-melting point of EEE, than the 2 suffix Margules interaction parameter for PSP-EEE in the β′-modification must be greater than 2.5 in order to explain a zero plateau height. If a melting point of 27°C is used, A/RT (PSP-EEE) = 0 ± 1.

From binary phase diagrams we concluded that SSS mixes nearly ideally with SES, SSE and SEE in the β-modification (Section 15.7.3). In addition to the DSC-curve of PSP-EEE-OOO we also determined the curve of SSS-EEE-OOO in

the β-modification (Figure 41). The result is not very surprising: SSS and EEE also mix ideally in the β-modification. Clearly the elaidic and stearic acid chains behave more or less equivalent, which is confirmed by our findings for PSP-SEE and PSP-ESE for both β′- and β-modification.

If S and E behave equivalent, then the interaction parameter for the binary PSP-EEE should be equal to those of PSP-SEE and PSP-ESE. As the latter parameters both equal zero, expect that A/RT (PSP-EEE) will also be zero. This implies that the β′-melting point of EEE must be 27 ± 2°C, and that Malkins' value for the β′-melting point of EEE, 37°C, is not right.

7.5.4 PSP and MPM with cis-unsaturated TAGs

The measurements of mixtures of PSP and MPM with SSO, PPO, SOS and POP resulted in more complicated curves than those of the previous mixtures. Contrary to the previous TAGs, which all crystallized into the β′-2 and β-2 modification, most cis-unsaturated TAGs crystallize into the β′ and β-3 modification. Only POP crystallizes into the β′-2 form (Table 30).

The formation of a continuous solid solution between a component that crystallizes into the β′-2 form and a component that crystallizes into the β′-3 form seems on structural grounds impossible: an intermediate β′-2/β′-3 structure is not feasible. In thermodynamic calculations the two β′-forms must therefore be treated as separate modifications, just like the β′ and β-modification.

This has two implications:

1. The DSC curve of the β′-modification of a mixture of a β′-2 and a β′-3 forming TAG must always contain

Table 30 Polymorphic Forms of the Cis Unsaturated TAGs [10, 109]

PSP	β′-2		MPM	β′-2	
SOS	β′-3	β-3	PPO	β′-3	
SSO	β′-3		POP	β′-2	β-3

two sharp peaks, because demixing in the solid phase will occur even when the components mix ideally both in the β′-2 as in the β′-3 phase.

2. For calculation of the interaction parameters the heat of fusion and the melting point of a hypothetical β′-2 form of the β′-3 forming TAG and of the hypothetical β′-3 form of the β′-2 forming TAG must be known. These hypothetical pure component properties cannot be measured. They must be estimated, which will cause a considerable uncertainty in the value of the interaction parameters.

Quite surprisingly, after short stabilization of the MPM-SSO-OOO and MPM-PPO-OOO mixtures, DSC curves in which the first melting peak is a broad hump were obtained, rather than the sharp peak that was expected for these β′-2/β′-3 mixtures. After prolonged stabilization a clear polymorphic transition was observed, and finally the expected DSC curves with two sharp peaks were obtained. The final melting peak remained in place during this transition. The broad hump indicates that initially crystallization must have taken place into a single, mixed solid phase, which has to be in the β′-2 modification. The final, stable, separate PRO- or SSO-rich β′-3 phase is only formed later. This behaviour confirms the assumption that the -2 and -3 forms must be treated as separate, independent modifications, that needn't always occur in pure components. The order of the polymorphic transitions that is observed is therefore:

$$\alpha \rightarrow \beta' - 2 \rightarrow \beta' - 3 \tag{93}$$

From the work of de Jong [13] it can be concluded that the melting point of a hypothetical β-3 modification of PSP and MPM is about 3 degrees less than the melting point of a hypothetical β-2 form of these TAGS. In analogy to the β modification, assume that the β′-3 melting points of MPM and PSP also lie 3°C below their experimental β′-2 melting points. Based on the enthalpy of fusion data of chapter 4 we conclude that the heat of fusion of the β′-3 form is about 90% of that of the β′-2 modification.

Similarly it is assumed that the heat of fusion of the hypothetical β′-2 form of SSO, PPO and SOS is 90% of that of the β′-3 modification. If the 2-suffix Margules equation is used, the melting points of the β′-2 modification of these TAGs can be calculated from the β′-2 DSC curves of the mixtures with MPM:

$$\text{SSO} : T_f(\beta'\text{-}2) = 39 \pm 0.5°C \; (T_f(\beta'\text{-}3) = 42°C)$$
$$\text{SOS} : T_f(\beta'\text{-}2) = 29 \pm 2°C \; (T_f(\beta'\text{-}3) = 36.5°C)$$
$$\text{PPO} : T_f(\beta'\text{-}2) = 31 \pm 0.5°C \; (T_f(\beta'\text{-}3) = 34°C)$$

The measurements that were carried out and the results of the fitting procedure are given in Tables 31 and 32 and Figures 44–47.

The broad first melting peaks in the β′-2 DSC curves of PSP-POP and PSP-SSO have maxima, that lie several degrees above the temperature where these maxima should be situated when A/RT = 0. These DSC curves could only be fitted with the 3-suffix Margules equation, using negative values for A_{PSP_POP} and A_{PSP_SSO} (Table 33). Apparently the β′-2 form of POP and SSO is enormously stabilised by the presence of PSP, their almost exact saturated counterpart. Calculations show that this stabilizing effect makes the mixture β′-2 stable. Indeed no transition to the β-modification (POP) or the β′-3 modification (SSO) was observed, even after long stabilisation.

Table 31 DSC Measurements and 2-suffix Margules Parameters for the Highest Melting Binary Pair Determined from these Measurements (composition in mole fractions, temperatures in °C, time in minutes, unless otherwise indicated: d = days)

Modification	PSP	MPM	SOS	SSO	OOO	Scan rate (K/min)	Stabilization time (min)	Stabilization temp. (°C)	A/RT
β′ −2	0.32		0.19		0.49	2.5	15	5	0 ± 0.3
β′ −2		0.29	0.23		0.48	2.5	1	5	2 ± 0.7
β′ −2	0.26			0.24	0.50	2.5	1–7d	10	no fit
β′ −2		0.28		0.24	0.48	1.25	1–60	15	2 ± 0.2
β′ −3	0.32		0.19		0.49	2.5	15	5	0 ± 0.5
β′ −3		0.29	0.23		0.48	1.25	8d	10	1.7 ± 0.7
β′ −3		0.28		0.24	0.48	1.25	3d	15	2 ± 0.5
β	0.32		0.19		0.49	1.25	1d	28	1.5 ± 0.5
β		0.29	0.23		0.48	1.25	8d	10	1.0 ± 0.5

Table 32 DSC Measurements and 2-suffix Margules Parameters for the Highest Melting Binary Pair Determined from these Measurements. (composition in mole fractions, temperatures in °C, time in minutes, unless otherwise indicated: d = days)

Modification	PSP	MPM	POP	PPO	OOO	Scan rate (K/min)	Stabilization time (min)	Stabilization temp. (°C)	A/RT
β′ −2	0.26		0.26		0.48	1.25	15–7d	10	no fit
β′ −2	–	0.29	0.23		0.48	2.5	1	5	0.8 ± 0.2
β′ −2	0.25			0.28	0.47	1.25	7d	15	−1.5?
β′ −2		0.28		0.25	0.47	1.25–2.5	1–60	10	0.8 ± 0.4
β′ −3	0.25			0.28	0.47	1.25	26d	5	–
β′ −3		0.28		0.25	0.47	1.25–2.5	7d	10	−0.2 ± 0.4
β	0.26		0.26		0.48	–	–	15	no β
β		0.29	0.23		0.48	1.25	7d	5	3.5 ± 1

The stabilising effect seems also present in the curves of PSP-PPO and PSP-SOS. In these case an exact determination of the β′-2 state was not possible: a β′-2/β′-3 transition always disturbed the DSC curve. The shape of the PSP-PPO-OOO melting curves above 35°C suggest A/RT = −1.5.

The 2-suffix parameters for the β-modification of the mixtures with SOS are very low, compared to those for the β′-modification. It is possible to use 3-suffix Margules β-interaction parameters that are more in line with the results for the β′-modification for the description of the curve (Table 33). However, they have no statistical significance.

7.6 DISCUSSION

7.6.1 The use of DSC-melting curves

The results show that it is possible to use DSC melting curves of ternary mixtures to determine binary interaction param-

Table 33 2- and 3-suffix Margules Parameters for Some of the Systems of Table 31 and 32

System	Modification	A/RT	A_{12}/RT	A_{21}/RT
PSP-POP	β′ −2	–	−3 ± 1	0 ± 0.5
PSP-SSO	β′ −2	–	−2 ± 1	0 ± 0.5
PSP-SOS	β	1.5 ± 0.5	1.5 ± 0.5	3 ± 1.5
MPM-SOS	β	1.0 ± 0.5	0.5 ± 1	3 ± 2

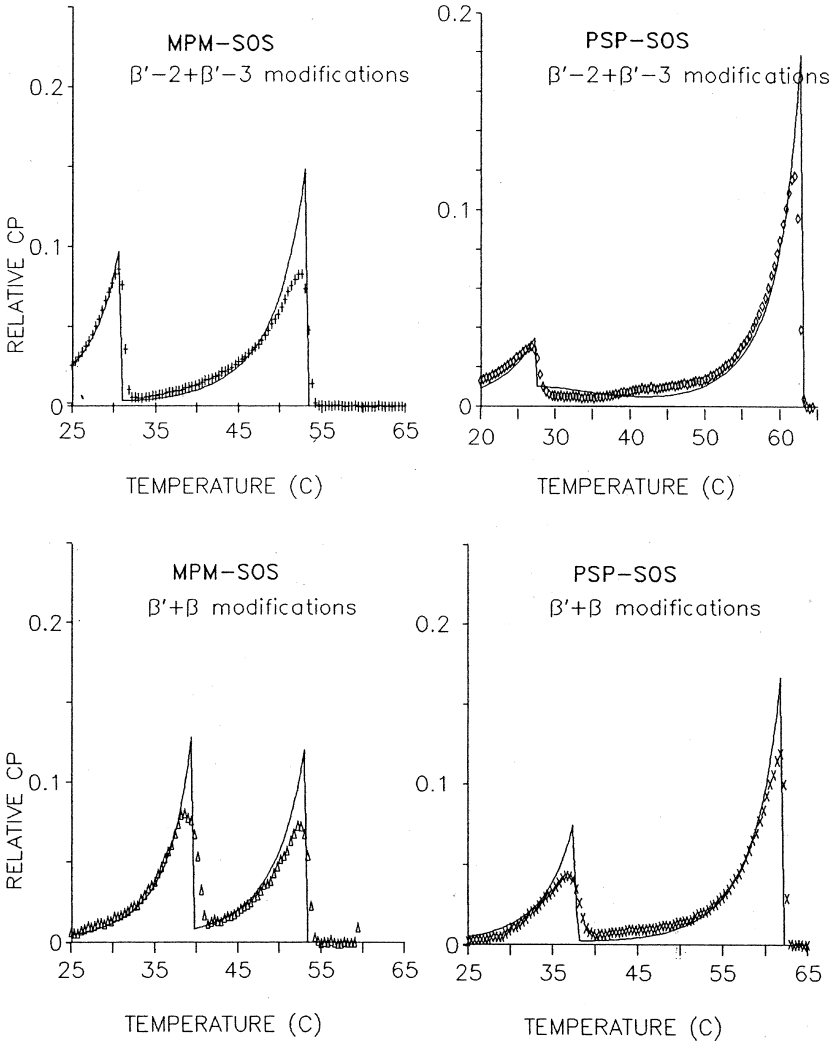

Figure 44 Measured (dots) and fitted (lines) DSC-curves of ternary mixtures of ±25% PSP or MPM% with ±25% SOS and ±50% OOO. The modification(s) in which crystallization has taken place is indicated.

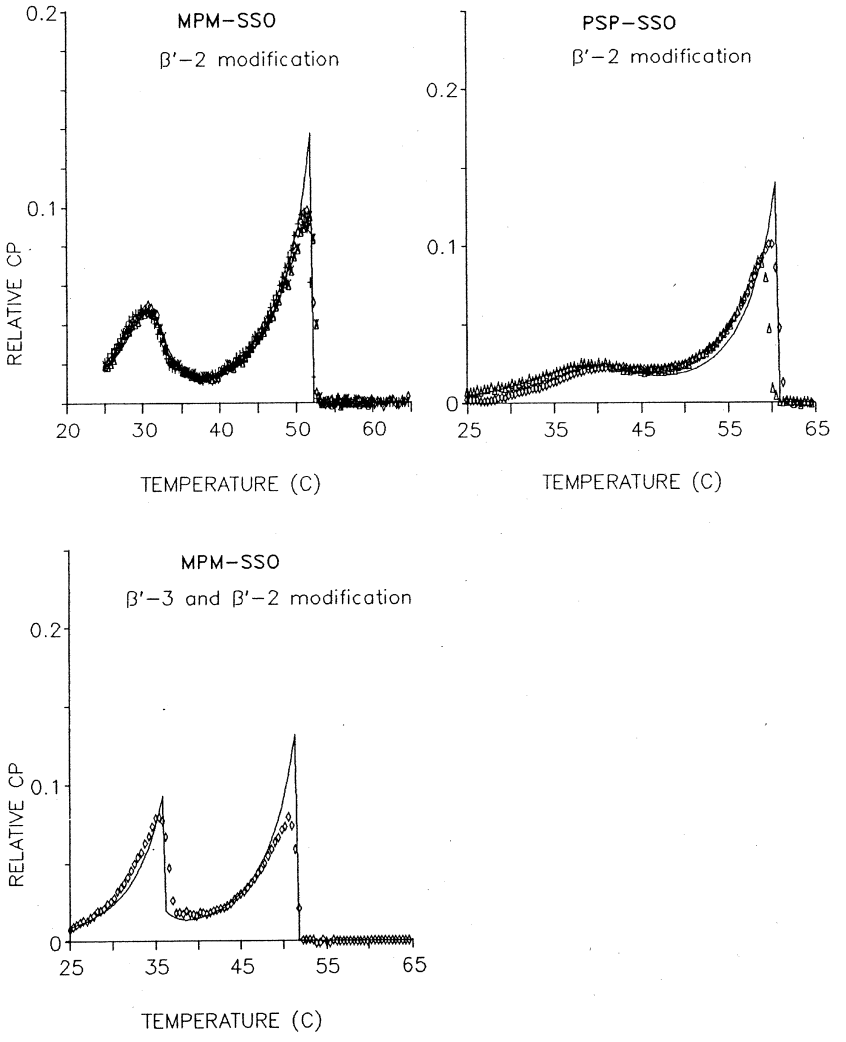

Figure 45 Measured (dots) and fitted (lines) DSC-curves of ternary mixtures of ±25% PSP or MPM% with ±25% SSO and ±50% OOO. The modification(s) in which crystallization has taken place is indicated.

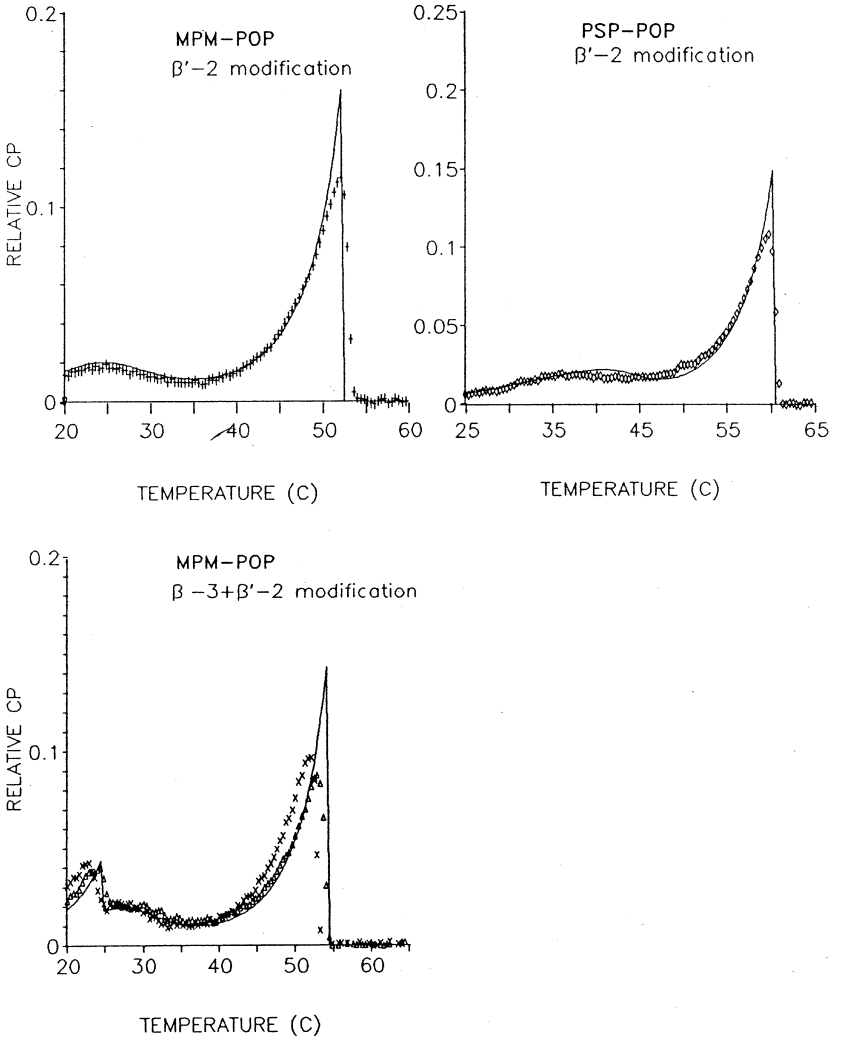

Figure 46 Measured (dots) and fitted (lines) DSC-curves of ternary mixtures of ±25% PSP or MPM% with ±25% POP and ±50% OOO. The modification(s) in which crystallization has taken place is indicated.

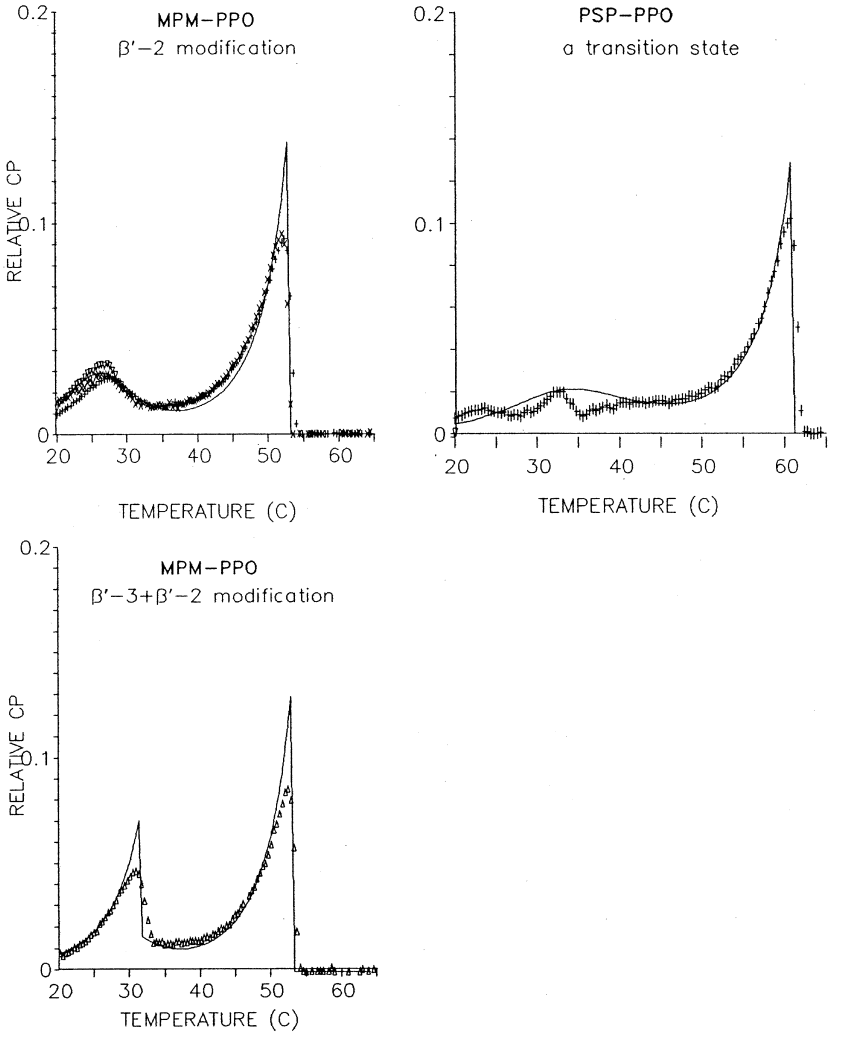

Figure 47 Measured (dots) and fitted (lines) DSC-curves of ternary mixtures of ±25% PSP or MPM% with ±25% PPO and ±50% 000. The modification (s) in which crystallization has taken place is indicated.

eters. This method is much quicker and more reliable than the determination of a phase diagram. It allows the study of phase behaviour in unstable modifications. Thus we have obtained a new, powerful and versatile method for studying the solid liquid phase behaviour.

The 3-suffix Margules equation

The 3-suffix Margules interaction parameters can be obtained from the combination of peak shape and peak position in the DSC melting curve. This dependency on exact peak position implies that the uncertainty in the melting points of the pure components of about 1°C will translate itself into an error in the 3-suffix Margules parameters of about 0.5. Due to this uncertainty in the parameters, asymmetric behaviour in systems that show only small differences in the two parameters cannot be detected. In those cases the 2-suffix Margules equation performs equally well. In this work TAGs were studied that show considerable differences in stereochemical nature. Yet only in the most extreme case, for TAGs with oleic acid, which crystallize in very different lattices, clear asymmetric behaviour and the need for using the 3-suffix Margules equation was apparent.

7.6.2 Binary interaction parameters

The β′-modification

For the first time reliable information about mixing behaviour in the β′-modification has been obtained. On average solid solubility in the β′-modification is higher than in the β-modification, but contrary to the α-modification non ideal mixing can occur.

The influence of size differences is clear: none of the unsaturated TAGs mixes very well with the smaller TAG MPM, while often even ideal miscibility is found with PSP, which is about similar in size. The position of the fatty acid chains on the glycerol influences the mixing behaviour with MPM only very slightly, the size difference dominates. But when the size difference is small, the chain position is of great influence, as can be seen from the data on PSP-PEE vs. PSP-EPE, PSP-

SSO vs. PSP-SOS, and PSP-PPO vs. PSP-POP. It is not clear why these relatively small differences can have such large effects on mixing behaviour. Simulation of the disturbance of a crystal lattice by insertion of another TAG using molecular mechanics, may help to create understanding. This will be attempted in Section 15.8.

The β-modification

Due to the use of β′-stable TAGs as the highest melting component in the systems that were studied by DSC, β-interaction parameters could only be determined very roughly from the position of the first melting peak. That means that the uncertainty in the melting points already has to be taken into account in the 2-suffix Margules parameters, while the determination of statistically significant 3-suffix Margules parameters is impossible.

However, as illustrated for the system SSS and EEE, determination of accurate interaction parameters for the β-modification from DSC-curves is very well possible if a β-stable TAG is used as highest melting component.

In the survey of the binary phase diagrams complete solid misciblity was only found for pairs of TAGs that are very similar in size, like SSS and PSS. Our DSC results are in line with this finding. In Section 15.8 the data will be used in an attempt to find a relation between the influence of structural differences of TAGs and the magnitude of the interaction parameters.

7.6.3 Kinetics

It is striking how strongly the kinetics of transformation from β′ to β depend on the miscibility in the β′-modification: if the components mix very well in the β′-modification, the transformation takes at least several days, while if solid phase immiscibility occurs, it takes only a few seconds to an hour to complete the transformation.

The explanation is two-fold:

The combination of poor β-phase miscibility and nearly ideal mixing in the β′-modification reduces the Gibbs energy

difference between the two modifications, which is the driving force for recrystallization.

It also leads to a β′-solid phase composition that is completely different from that in the demixed β-modification, which makes the transformation kinetically much more difficult. In the case of poor β′-phase miscibility the solid phase composition is nearly equal to that in the β-modification, so that the barrier for the transformation is much smaller.

7.7 TERNARY SOLIDS

Although the DSC melting curves of Section 15.7.6 were measured using ternary mixtures, the composition of the mixture and the temperature range of the experiment were selected such, that only a binary solid phase was present. This enabled the determination of binary interaction parameters in the solid phase.

Crystallized fats are normally multicomponent solid phases. The binary interaction parameters that were determined in this work can only be used for prediction of multicomponent phase behaviour if ternary, quaternary and higher interaction terms can be neglected. A way of checking this is comparing measured ternary phase diagrams with phase diagrams predicted from binary interaction parameters. In literature there are only a few ternary phase diagrams available: that of the Cocoa Butter (CB) TAGs SOS/POS/POP from Smith [40] and those of the palm oil TAGs PPP/POP/POO and PPP/PPO/POO from Gibon [11]. The data from Gibon are not very reliable, due to the very poor stabilisation procedure and the high DSC-scan rates that were used (Section 15.7.2). Calculated and measured ternary clear point curves for the three systems are given in Figures 48 and 49. For SOS-POS-POP also a diagram is given with the isotherms for 25% solids.

As can be seen the agreement between theory and experiment is very good for the SOS/POS/POP ternary, taking into account the error in the measurements of 1°C. Also the temperatures at which a mixture contains 25% solids are predicted within 1°C.

The PPP/POP/POO and PPP/PPO/POO ternaries also show good agreement between measurements and calcula-

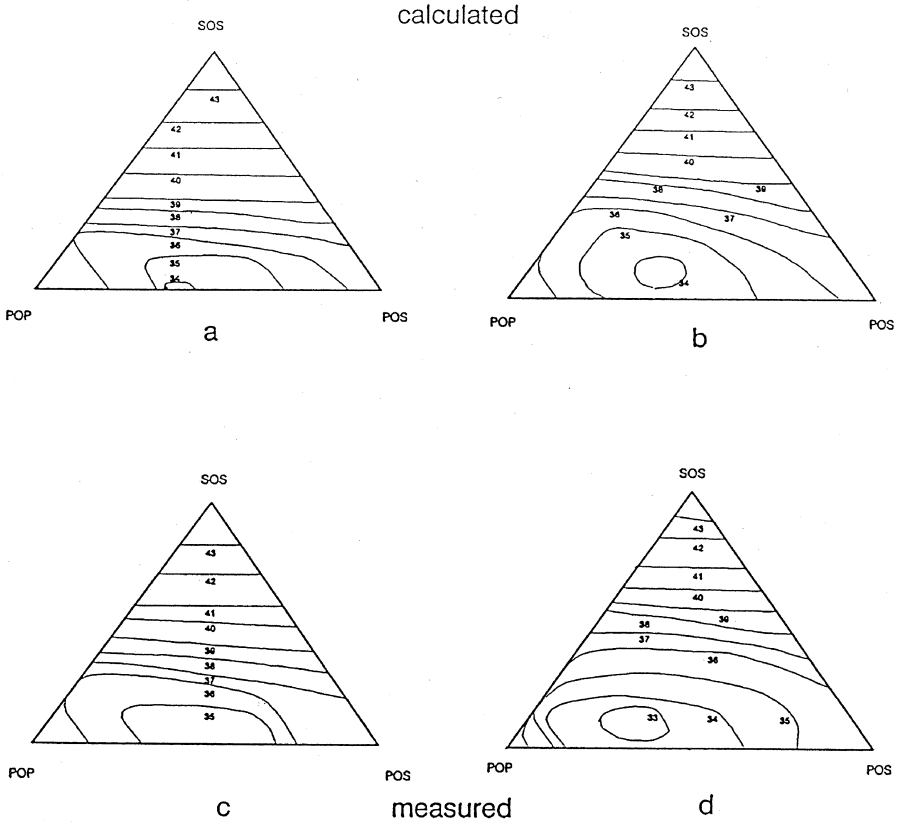

Figure 48 Calculated and measured ternary isosolids diagrams of SOS-POS-POP. Measured by Smith [40]. a and c: Clear point diagrams, b and d: isotherms with 25% solid fat.

tions. The agreement near the PPP corner at the PPP-POO side of the diagrams is somewhat less good. However, the clear points that are given by Gibon for this PPP/POO binary are probably not correct as they lie well below the eutectic liquidus.

The results suggest that the use of binary interaction parameters is indeed sufficient for the description of multicomponent TAG systems. In the authors' later work predictions were

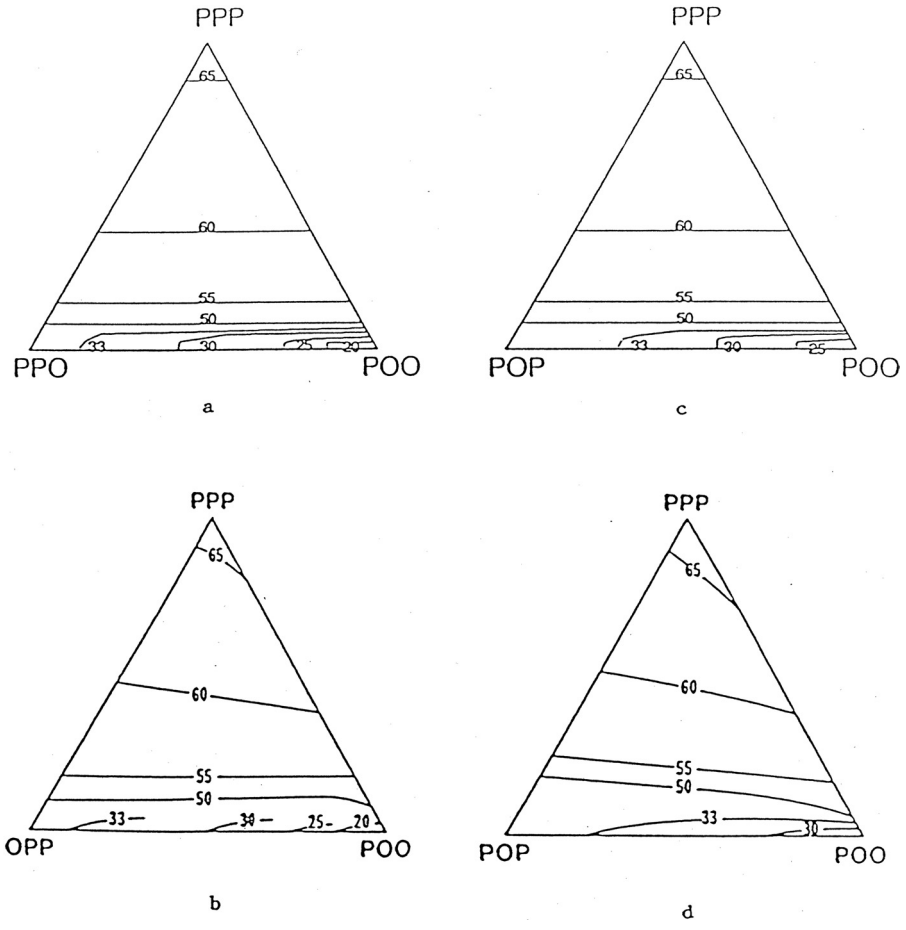

Figure 49 Calculated and experimental clear point diagrams of TAGS from palm oil. a and c: calculated, b and d : measured by Gibon [11].

also obtained using only binary interaction parameters (Section 15.9).

The clear point diagram for the CB-TAGs SOS/POS/POP may be used to define the possible compositions of CBEs (Cocoa Butter Equivalents). CBE's must have the same clear point as CB, and so all possible CBE compositions will be re-

stricted to the isotherm through the CB composition. The 25% isosolids diagram demonstrates that even for such difficult systems as SOS-POS-POP solids content can be predicted by application of solid-liquid equilibrium thermodynamics.

7.8 CONCLUSION

In the β and β′ modification TAGs show limited solid miscibility that can be described with rather simple models for the excess Gibbs energy: the 2- and 3-suffix Margules equation.

Eighty-four of the 120 binary phase diagrams of TAGs, that are available in literature, are rejected because they are clearly not correct. The solidus lines of most of the remaining 36 phase diagrams show large inconsistencies. The majority of these phase diagrams were measured after 1971. The 36 phase diagrams can be described within experimental error both by the 2- and by the 3-suffix Margules equations.

The excess Gibbs energy models contain binary interaction parameters. The large experimental errors in the binary phase diagrams lead to a very large inaccuracy in the interaction parameters that are determined from these diagrams.

Due to the serious drawbacks in the use and determination of binary phase diagrams, a new method for the study of solid-liquid phase behavior has been defined. It is possible to obtain quantitative information about mixed crystal formation from a single, complete DSC melting curve of a ternary system, consisting of two crystallizing TAGs and one liquid TAG.

The method is much quicker, more reliable, and more versatile than the traditional study of phase behaviour of TAGs via binary phase diagrams.

For the first time accurate information was obtained about the degree of mixed crystal formation in the β′-modification. Generally solid phase miscibility is higher in the β′-modification than in the β-modification. Large differences in molecular size reduce solid phase miscibility. Also the position of the fatty acid on the glyceryl-group has a great influence on solid phase miscibility.

Surprisingly the mixing behaviour of TAGs in the solid phase can usually be described with sufficient accuracy by the

very simple regular solution model or 2-suffix Margules equation. Only in a few cases the use of the more complex 3-suffix Margules equation was required.

Ternary systems could be described with binary interaction parameters only.

Kinetics of recrystallization showed a clear relation with the calculated thermodynamic driving force and the degree of rearrangement of the solid phase that is required.

8. PREDICTING INTERACTION PARAMETERS

Now that it has been shown that the mixing behaviour of TAGs in the α, β' and β-modification can be described with rather simple excess Gibbs energy models, there remains only one step to be taken: finding a procedure for predicting the binary interaction parameters for any pair of TAGs. Therefore, the relation between geometrical differences and the magnitude of the interaction parameter is studied. Molecular mechanics are used to obtain an impression of the lattice distortions that are brought about by incorporation of guest TAGs in a lattice of a host TAG. Finally a first, empirical, set of rules is given for prediction of the binary interaction parameters.

8.1 ARE INTERACTION PARAMETERS RELATED TO STRUCTURAL DIFFERENCES?

In the conclusion of Section 15.2, four steps were mentioned that had to be taken to obtain a description of the liquid-multiple solid phase equilibria in fats. Those four steps were the subject of the preceding sections. It was concluded that the solid-liquid phase equilibrium in a TAG mixture can be described, provided the binary interaction parameters for all possible pairs of TAGs in the mixture are known. The large number of TAGs in a natural oil makes it impossible to determine the parameters experimentally. Therefore a method must be developed for predicting these binary parameters. Fortunately TAGs are chemically very similar, so the degree of nonideal mixing will only be determined by sterical effects. In the next

sections it will be attempted to find a relation between the binary interaction parameters and structural differences.

8.1.1 Degree of isomorphism

In his work on mixed crystals Kitaigorodskii [111] investigated the solid miscibility of several hundreds of pairs of organic compounds. Based on this investigation he formulated his "major rule of substitutional solid solubility" of organic compounds:

1. Solid solubility is determined by geometric factors if:

   there is no electron transfer between the two components to be mixed,
   the components to be mixed have no permanent dipole moments and
   the components to be mixed do not form strong hydrogen bridges.
2. If solid solubility is solely determined by geometrical factors, then two components will only mix in the solid state if their 'degree of isomorphism' exceeds 0.85.

   The degree of isomorphism $\in$ is defined as follows: superimpose the molecules of the components so as to maximize the intermolecular overlap. Let the volume of the non-overlapping parts be V_{non} and the volume of the overlapping parts v_0. Then the 'degree of isomorphism' or 'coefficient of geometrical similarity' is given by:

   $$\in = 1 - \frac{\upsilon_{non}}{\upsilon_0} \tag{94}$$
3. In addition to this second condition, complete solid state miscibility in any proportion is only possible if the molecular packing in the crystal of the pure components is similar, the crystals have the same symmetry and the atoms occupy the same crystallographic positions.

Generally, Kitaigorodskii's rule gives a correct prediction of the occurrence of fully eutectic behaviour and the presence of

a miscibility gap. However, the reverse is not true: sometimes a miscibility gap is found, even though Kitaigorodskii's rule has predicted a good solid state miscibility. The reason for this is that when a guest molecule is inserted in a host lattice, then, depending on the nature of the guest molecule, its protruding part may occupy a lattice site in an area where packing is very dense. Obviously, solid solubility will be considerably less than in the case of a guest molecule of the same size that protrudes into a loosely packed area. Therefore, generally, Kitaigorodskii's rule can only be used for qualitative statements on solid phase miscibility.

According to Kitaigorodskii quantitative predictions of solid solubility can be obtained by calculating the lattice distortion:

1. An impurity is placed in an undistorted lattice of the pure component.
2. The difference in interaction energy of the impurity with the lattice and of the host with the lattice is calculated.

   The simplest approach is to leave the host lattice completely undisturbed and calculate the conformation of the impurity that gives minimal interaction energy.

   A more sophisticated approach is to allow also some conformational changes in the host lattice near the impurity ("crystal elasticity"). Unfortunately, this increases computing time enormously.

The lattice distortion obtained in this way can be used to calculate the excess Gibbs energy and hence the maximum solid solubility. The results are reasonable estimates of the maximum solid solubility. Surprisingly, Kitaigorodskii only calculates the maximal solid solubility and does not use this information to calculate a complete binary phase diagram. Most of these complex computer calculations were carried out for relatively simple atomic crystals. Only one example of molecular crystals is mentioned (diphenyl-dipyridyl).

In mixtures of TAGs, the lattice distortion always occurs on the same lattice sites, the methyl-end-plane region, and is

always caused by the same functional group: CH_2–CH_3. Because of this, it may very well be that the degree of isomorphism correlates much better with the solid solubility of TAGs than with that of an arbitrary pair of organic substances.

The condition for complete solid state miscibility of Kitaigorodskii's rule implies that complete solid solubility in the equilibrium state cannot occur when two TAGs differ in their most stable polymorphic form, like PSP and SSS. This was already implicitly assumed in all previous calculations by treating the polymorphic forms as different states of the substance, equivalent to the liquid and gas state. However, this condition also implies that complete miscibility cannot occur in mixtures of two TAGs that crystallize in different submodifications, as is the case in a mixture of a β-3 forming TAG and a β-2 forming TAG.

In the next sections it will be investigated as to what extent the simple parameter $\in$ correlates with the interaction parameters of TAGs, whether it is possible to calculate the lattice distortion by impurities in TAG crystals and whether this lattice distortion can be used for prediction of interaction coefficients.

8.1.2 TAGs and the degree of isomorphism $\in$

There are two major lattice distortions that occur in TAG mixtures: those caused by differences in chain length and those caused by cis-unsaturated double bonds. Assume that the distortion in the lattice of a saturated TAG that is caused by a trans-double bond is negligible, in line with the nearly ideal miscibility that was found for SSS, SES, SSE, SEE and EEE. The two major distortions will be considered separately.

The β′-modification

In Table 34 the binary interaction parameters for the β′-modification of saturated and trans-unsaturated TAGs are listed together with the degree of isomorphism. As a matter of convenience v_{non} is the sum of the absolute differences in carbon number of each of three chains and for v_0 the sum of the carbon numbers of the smallest chain on each glyceryl position.

Table 34 Two Suffix Margules Parameters for the β′ —Modification and the degree of Isomorphism of Saturated and Trans-unsaturated TAGs (From Section 15.7)

Binary pair	A/RT	∈
PSP-PEE	0 ± 0.2	0.96
PSP-SEE	0 ± 0.2	0.92
PSP-ESE	0 ± 0.2	0.92
PSP-EEE	0 ± 2	0.92
PSP-EPE	2 ± 0.5	0.88
MPM-PEE	1.8 ± 0.5	0.82
MPM-EPE	2.3 ± 0.5	0.82
MPM-SEE	3 ± 0.2	0.77
MPM-ESE	3 ± 0.2	0.77
MPM-EEE	3 ± 2	0.77

The correlation between the degree of isomorphism ∈ and the binary interaction parameter is striking. In agreement with the results of Kitaigorodskii, the limit of complete miscibility, corresponding to A/RT = 2, is reached at ∈ = 0.85. Moreover, ideal miscibility is found if ∈ ≥ 0.92. The degree of isomorphism explains the large difference in miscibility with PSP that has been found for PEE and EPE in Section 15.7. Although the number of data is too small for a decisive statement, it seems possible to use ∈ for predicting the binary interaction parameters of pairs of these TAGs.

The correlation for cis-unsaturated TAGs will be less simple, as the cis-double bond disturbs the regular zigzag (trans configuration) of the saturated chains in the crystal lattice. From the cis-unsaturated TAGs that were studied in Section 15.7, only POP crystallizes in the β′-2 modification, while SOS, SSO and PPO are reported to crystallize in the β′-3 modification [10,11,109]. In Section 15.7 SSO and PPO initially seem to crystallize in a β′-2 form that does not exist in pure PPO and SSO. The values of the two or three suffix Margules equation interaction parameters for the β′-2 and β′-3 forms are listed in Table 35 together with ∈. The extra contribution of a cis-

Table 35 2- or 3-Suffix Margules Parameters for the β′-Modification and the Degree of Isomorphism of saturated and Cis-unsaturated TAGs. The Modification in which the Cis-unsaturated TAG has Crystallized is Given. A – Behind the Value of ∈ Indicates, that the Contribution of the Cis-double Bond is not Incorporated in the Value of ∈

Binary pair	Modification	A_{12}/RT	A_{21}/RT	∈
PSP-POP	β′-2	−3 ± 1	0 ± 0.5	1-
PSP-PPO	β′-2	−1.5 ± 1.5	−1.5 ± 2	0.92-
PSP-SSO	β′-2	−2 ± 1	0 ± 0.5	0.92-
MPM-POP	β′-2	0.8 ± 0.4	0.8 ± 0.2	0.86-
MPM-PPO	β′-2	0.8 ± 0.5	0.8 ± 0.3	0.86-
MPM-SSO	β′-2	2 ± 0.7	2 ± 0.2	0.77-
Binary pair	Modification	A/RT		
PSP-SOS	β′-3	0 ± 0.5		0.92-
MPM-PPO	β′-3	−0.2 ± 0.4		0.86-
MPM-SOS	β′-3	1.7 ± 0.7		0.77-
MPM-SSO	β′-3	2 ± 0.5		0.77-

double bond to ∈ is not incorporated in the number, but indicated by – (minus).

Here again, the limited amount of data for both β′-forms indicate that the degree of isomorphism is related to the magnitude of the binary interaction parameters. Surprisingly the miscibility of saturated and cis-unsaturated TAGs seems to be slightly better than that of saturated and trans-unsaturated TAGs with the same degree of isomorphism.

The β-modification

Most data for the β-modification that are available have a considerable error margin. Yet, as appears from Table 36, a correlation between degree of isomorphism and the binary interaction parameters seems present.

In line with expectations, the degree of isomorphism that is required for complete miscibility in the β-modification is higher than for the less densely packed β′-modification: in the β-modification A/RT = 2 is already reached when ∈ = 0.94, while miscibility in the β′-modification at ∈ = 0.94 is still

Table 36 2- and 3-suffix Margules Interaction Parameters and the Degree of Isomorphism for Binary Pairs of β-2 or β-3 Forming TAGs

Binary pair	Modification	A/RT	A_{12}/RT	A_{21}/RT	∈
SSS-SES	β-2	0.4 ± 0.5	0 ± 0.5	0.8 ± 0.5	1
SSS-SSE	β-2	0.4 ± 0.5	0.1 ± 0.5	0.7 ± 0.5	1
SSS-SEE	β-2	0 ± 1	0 ± 1	0 ± 1	1
SSS-EEE	β-2	0 ± 0.2	0 ± 0.2	0 ± 0.2	1
SES-SSE	β-2	0 ± 0.5	0 ± 0.5	0 ± 0.5	1
SSS-PSS	β-2	1.6 ± 0.5	1.1 ± 0.5	2.3 ± 0.5	0.96
SSS-SPS	β-2	> 3	> 3	> 2	0.96
PSS-PPS	β-2	1.6 ± 0.5	1.4 ± 0.5	1.8 ± 0.5	0.96
SPS-PPS	β-2	2 ± 0.5	3 − 5	0.4	0.96
PSP-PPP	β-2	> 3	> 3	> 1	0.96
PPS-PPP	β-2	1.9 ± 0.5	1.6 ± 0.5	2.3 ± 0.5	0.96
SSS-PSP	β-2	> 3	–	–	0.92
SSS-PPS	β-2	> 2.2 ?	–	–	0.92
PSS-SPS	β-2	2 ± 0.5	1.4 ± 0.5	2.6 ± 0.5	0.92
PSS-PPP	β-2	2.2 ± 0.5	2.8 ± 0.5	2.1 ± 0.5	0.92
SPS-PPP	β-2	> 5	> 5	> 5	0.92
PSP-PPS	β-2	> 3	> 3	> 1	0.92
PSP-SEE	β-2	> 2.5	–	–	0.92
PSP-ESE	β-2	> 2	–	–	0.92
PSP-EEE	β-2	> 2	–	–	0.92
SSS-PPP	β-2	3 ± 0.5	5.8 ± 1	1.4 ± 1	0.88
SPS-PSP	β-2	1.4 ± 0.5	> 1	1.8 ± 0.5	0.88
PSP-EPE	β-2	> 2.5	–	–	0.88
PPP-MMM	β-2	> 3	–	–	0.86
MPM-PEE	β-2	> 2.5	–	–	0.82
MPM-EPE	β-2	> 3	–	–	0.82
BBB-SSS	β-2	> 3	–	–	0.77
MPM-SEE	β-2	> 2.5	–	–	0.77
MPM-ESE	β-2	2 ± 1	–	–	0.77
PPP-LLL	β-2	> 3	–	–	0.67
BBB-PPP	β-2	> 3	–	–	0.63
SSS-LLL	β-2	> 3	–	–	0.50
SSS-888	β-2	> 3	–	–	0
SOS-POS	β-3	1.3 ± 0.5	1.5 ± 0.5	1.1 ± 0.5	0.96
POS-POP	β-3	1.6 ± 0.5	2.2 ± 0.5	1.0 ± 0.5	0.96
SOS-POP	β-3	> 3.6	5 ± 1	1.5 ± 1	0.92

ideal. The few data for the β-3 modification agree with those for the β-2 modification.

There are a few noticeable exceptions in the data set, all concerning SPS and PSP: in combination with each other the miscibility is better than could be expected from their low degree of isomorphism, while in combination with other saturated TAGs that have a high degree of isomorphism with these two TAGs, miscibility seems much less than expected.

Although SSS and SPS both crystallize in a β-2 lattice, according to de Jong [13], they crystallize into different β-2 submodifications. SSS, PSS, PPS and PPP crystallize into the β-2A submodification, while PSP and SPS both crystallize into the β-2B submodification. Although these submodifications are very similar, apparently the condition for complete solid miscibility of Kitaigorodskii's rule is not fulfilled. The β-2 submodifications should have been treated as independent polymorphs. The effect of treating the submodifications as independent polymorphs is illustrated in Figure 50 for A/RT = 1.8, a value in agreement with the other data of TAGs with a degree of isomorphism $\in = 0.96$. It is clear that the treatment as independent polymorphs gives a much better fit to the data.

Out of the four β-2 submodifications that occur, the β-2B submodification has the lowest packing density in the methyl

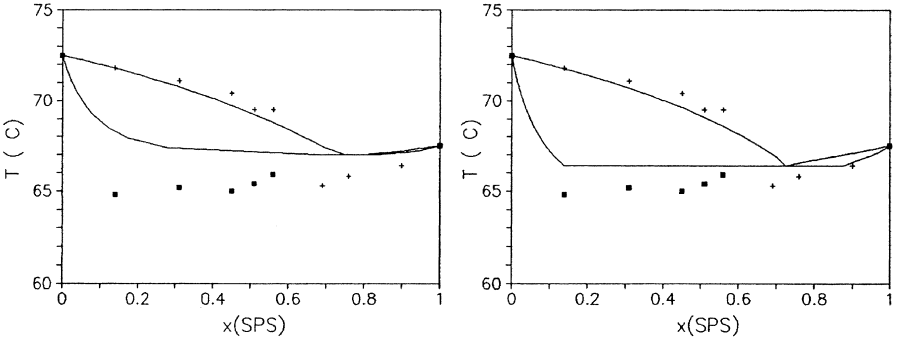

Figure 50 The influence of discontionuous miscibility in the β-2A and β-2B submodifications on the phase diagram of SSS-SPS. Left: continuous miscibility with A/RT = 1.8 Right: discontinuous miscibility with A/RT = 1.8 for both submodifications.

terrace area. This could explain the "too large" miscibility that was experimentally found for SPS-PSP.

Conclusions

Kitaigorodskii's major rule of substitutional solubility applies to TAGs.

Within one submodification, the degree of isomorphism correlates very well with the binary interaction parameters. Contrary to the general case of organic compounds, the use of the degree of isomorphism for an empirical prediction of interaction parameters between TAGs seems feasible.

It turns out that in the description of phase equilibria in TAGs not only the three basic modifications have to be considered as separate states, but also each subform of these three modifications. A practical problem in doing so, is the fact that only the heat of fusion and melting point of the most stable subform can be determined experimentally.

8.2 CALCULATION OF LATTICE DISTORTION

When the degree of isomorphism is used for predicting binary interaction parameters, it is implicitly assumed that the two suffix Margules equation gives an adequate description of the phase behaviour of TAGs. Although this is quite often true, it is not always the case. Moreover, the validity of the 2-suffix Margules equation is theoretically unlikely. There is no reason why an impurity with a protuberance will lead to a lattice distortion of the same magnitude as an impurity that causes a hole in the lattice, or why a protuberance of a constant size should cause a lattice distortion of the same magnitude regardless whether it is a protuberance of the fatty acid on 1, 2 or 3 position of the glycerol group. To get a clearer insight into this matter more sophisticated molecular considerations are required.

8.2.1 Equivalent distortions in the β-2 modification

All saturated TAGs and trans-unsaturated TAGs that were considered in this work crystallize in the β-2 modification. According to de Jong [13] and using his nomenclature, all monoacid TAGs, PSS, PPS, SES, SSE, SEE and EEE crystallize in

the β-2A submodification, while PSP, SPS and probably also PEP crystallize into the β-2B submodification. These two submodifications have the same angle of tilt, 60°, of the fatty acid chains, but differ in the shape of their methyl end plane. The β-2B modification is somewhat less densely packed it this area. Within one submodification the shape of the methyl terrace does not change, but the position of the 'steps' in the terrace is shifted (Figure 51).

In Figure 51 equivalent positions on the methyl terrace are marked by a circled 1, 2, or 3. Exchanging a molecule by a molecule of another TAG will corrupt the methyl end plane. If a PPP molecule is exchanged by PPS then an ethyl group is added to the first chain of a 'step' of the methyl terrace. The

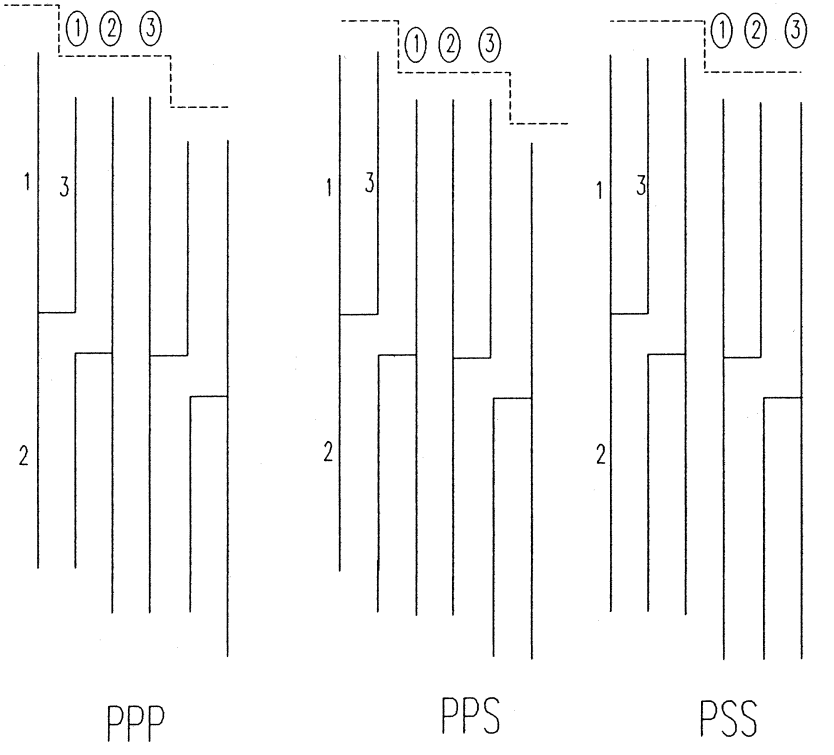

Figure 51 Equivalent positions on the methyl terraces of PPP, PPS and PSS (marked by a circled number).

distortion of the lattice caused by this addition will be called a (1,0,0) distortion, while that caused by removing an ethyl group from the same chain will be denoted as a (− 1,0,0) distortion. A (0,1,0) distortion is in this nomenclature the addition of an ethyl group to the chain in the middle of a 'step' in the methyl terrace. It is also possible to bring about a (1,0,0) distortion in a PPS crystal: by exchanging PPS with PSS. As the distortion to the lattice is exactly the same, the activity coefficients at infinite dilution of PPS in PPP and PSS in PPS must be equal. Therefore, according to equation 88, the 3-suffix Margules parameters $A_{PPS\text{-}PPP}$ and $A_{PSS\text{-}PPS}$ should be identical as well, which was found indeed ($A_{PPS\text{-}PPP} = 1.6$, $A_{PSS\text{-}PPS} = 1.4$). Table 37 lists all 26 different distortions to the lattice of β-2A and β-2B TAGs that can be caused by addition or removal of ethyl groups.

These 26 different distortions occur at only three levels of the degree of isomorphism.

A complicating factor is the asymmetry of the TAGs PPS and PSS: PPS causes a (1,0,0) distortion in PPP, while its mirror image SPP leads to a (0,0,1) disturbance. These two distortions are not necessarily equivalent.

Notwithstanding the fact that sometimes asymmetric TAGs are involved, a good agreement is found between the values of the three suffix Margules parameters of equivalent distortions (Table 38).

The 3-suffix Margules parameters for the binary SSS-PPS could not be determined because of poor data quality. If the effects of chirality are negligible, they should be the same as those of PSS-PPP.

The distortions of Table 38 are arbitrarily marked from A–Z for the β-2A submodification and from A′–Z′ for the β-2B submodification. Using these markers, the phase diagrams can be classified: for example SSS-PPP is a Z/A phase diagram. The binary interaction parameters for all Z/A phase diagrams should be the same, regardless of the excess Gibbs energy model used.

If chirality is neglected, the 15-phase diagrams can be classified into nine different groups. The value of the binary interaction parameter within a group seems to be constant.

Table 37 TAGs that Cause Equivalent Distortions When Inserted in the Crystal Lattice of the Six TAGs that can be Formed from P and S

Disturbance of methyl terrace		TAGs crystallizing in the β-2A modification				TAGs in the β-2B modification		
		PPP	SSS	PPS	PSS	PSP	SPS	∈
A	−1 −1 −1	MMM	PPP	MMP	MPP	MPM	PMP	0.88
B	−1 −1 0	PMM	SPP	MMS	MSP	MPP	PPP	0.92
C	−1 −1 1	SMM	APP	MMA	MAP	MPS	PSP	0.88
D	−1 0 −1	MPM	PSP	PMP	MPS	PPM	PMS	0.92
E	−1 0 0	PPM	SSP	PMS	MSS	PPP	PPS	0.96
F	−1 0 1	SPM	ASP	PMA	MAS	PPS	PSS	0.92
G	−1 1 −1	MSM	PAP	SMP	MPA	SPM	PMA	0.88
H	−1 1 0	PSM	SAP	SMS	MSA	SPP	PPA	0.92
I	−1 1 1	SSM	AAP	SMA	MAA	SPS	PSA	0.88
J	0 −1 −1	MMP	PPS	MPP	PPP	MSM	SMP	0.92
K	0 −1 0	PMP	SPS	MPS	PSP	MSP	SPP	0.96
L	0 −1 1	SMP	APS	MPA	PAP	MSS	SSP	0.92
M	0 0 −1	MPP	PSS	PPP	PPS	PSM	SMS	0.96
N	0 0 1	SPP	ASS	PPA	PAS	PSS	SSS	0.96
O	0 1 −1	MSP	PAS	SPP	PPA	SSM	SMA	0.92
P	0 1 0	PSP	SAS	SPS	PSA	SSP	SPA	0.96
Q	0 1 1	SSP	AAS	SPA	PAA	SSS	SSA	0.92
R	1 −1 −1	MMS	PPA	MSP	SPP	MAM	AMP	0.88
S	1 −1 0	PMS	SPA	MSS	SSP	MAP	APP	0.92
T	1 −1 1	SMS	APA	MSA	SAP	MAS	ASP	0.88
U	1 0 −1	MPS	PSA	PSP	SPS	PAM	AMS	0.92
V	1 0 0	PPS	SSA	PSS	SSS	PAP	APS	0.96
W	1 0 1	SPS	ASA	PSA	SAS	PAS	ASS	0.92
X	1 1 −1	MSS	PAA	SSP	SPA	SAM	AMA	0.88
Y	1 1 0	PSS	SAA	SSS	SSA	SAP	APA	0.92
Z	1 1 1	SSS	AAA	SSA	SAA	SAS	ASA	0.88

These structural considerations show clearly that there is no reason at all for the assumption that the interaction parameters for the binary pairs PSP-PPP (type P/E′) and PPS-PPP (type VN/M) should be the same, in spite of the fact that the degree of isomorphism of both pairs is 0.96. In the previous section it was found that the binaries with PSP and SPS are exceptions to the empirical 'rule' that the degree of isomorph-

Table 38 Three Suffix Margules Parameters for Some Equivalent Distortions (a = A/RT)

Code	Distortion			
P	(0,1,0)	$a_{PSP\text{-}PPP} = > 3$	$a_{SPS\text{-}PPS} = >3$	
U	(1,0,−1)	$a_{PSP\text{-}PPS} = > 3$	$a_{SPS\text{-}PPS} = 2.6$	
J	(0,−1,−1)	$a_{PPS\text{-}SSS} = 2.3$	$a_{PPP\text{-}PSS} = 2.1$	
M	(0,0,−1)	$a_{PSS\text{-}SSS} = 2.3$?	$a_{PPP\text{-}PPS} = 2.3$	$a_{PPS\text{-}PSS} = 1.8$
V	(1,0,0)	$a_{SSS\text{-}PSS} = 1.1$	$a_{PPS\text{-}PPP} = 1.6$	$a_{PSS\text{-}PPS} = 1.4$
Y	(1,1,0)	$a_{PSS\text{-}PPP} = 2.8$	$a_{SSS\text{-}PPS} = 2.3$?	

ism is related to the magnitude of the 2-suffix Margules parameter. This was explained by assuming that continuous miscibility cannot exist between the β-2A and β-2B modification, in spite of the close resemblance between the two β modifications. An alternative explanation is simply that the (0,1,0) distortion caused by PSP in PPP is not equivalent to the (1,0,0) distortion of PPS in PPP. This alternative explanation implies that the degree of isomorphism is too coarse a measure to correlate the interaction parameters.

Only calculation of the magnitude of the lattice distortions can decide which of the explanations is most likely.

Table 39 The P/S Binaries Classified in the Types Defined in Table 37, Together with the 2-suffix Margules Parameters. Where Asymmetric TAGs are Involved, a Three or Four Letter Code is Used, Indicating the Distortions Caused by Both Mirror Images

Binary	Type	A/RT	Binary	Type	A/RT
SSS-PSS	V/ME	1.6	SSS-PPP	Z/A	3
PSS-PPS	VX/MS	1.6			
PPS-PPP	VN/M	1.9	PSP-SPS	C′/I′	1.4
SSS-PSP	Q′/D	> 3	PSS-SPS	F′L/U	2
			PSP-PPS	U/F′H′	β′
SSS-SPS	N′/K	≥ 3			
PSS-PSP	N′/K′	β′	PSP-PPP	P/E′	β′
			SPS-PPS	P/E′	2
SSS-PPS	Y/BJ	≥ 2.3 ?			
PSS-PPP	QY/J	2.2	SPS-PPP	W/B′	> 5

8.2.2 β-2A lattice distortion calculations

The calculations were carried out using the programs Insight and Discover from Biosym. The program calculates the molecular configuration with minimal energy. The molecular energy is the sum of the internal energy from bond length stretching, bond angle stretching and torsion, and the non-bond-associated energy due to Coulomb and van der Waals forces.

The magnitude of a (1,0,0), a (0,1,0), and a (0,0,1) distortion to LLL have been calculated by comparison of the lattice energy of a pure LLL crystal with the lattice energy of an LLL crystal in which one molecule of an impurity [I] has been inserted per 54 molecules of LLL.

In the latter calculations we allowed the impurity to obtain the conformation with minimal energy, while the LLL molecules were fixed to the conformation that they have in a pure crystal. Calculations in which the complete impure crystal was allowed to rearrange went beyond the capacity of the program. The results are given in Table 40.

The order of magnitude of the crystal energy corresponds very well with the data of de Jong [13] for CCC.

The (0,1,0) lattice distortion, which is brought about by the β-2B-forming TAG LML, has the same order of magnitude as those caused by the two β-2A forming TAGs LLM and MLL. The very poor miscibility in the solid phase that was found experimentally for TAGs equivalent to LML and LLL can therefore only be explained by assuming that continuous miscibility between the β-2A and β-2B submodification is not pos-

Table 40 Lattice Distortions U/RT to a β-2A Crystal of LLL Caused by Impurities at Infinite Dilution in LLL

Type	Causedby	Distortion U/RT	U (distorted crystal) kJ/mol	U (pure "impurity") kJ/mol
(1, 0, 0)	LLM	1.0	258.9	270.1
(0, 1, 0)	LML	1.9	251.9	268.8
(0, 0, 1)	MML	3.6	255.0	270.1
(0, 0, 0)	LLL	0	253.8	253.8

sible, in line with the findings in the previous section. The magnitude of the lattice distortion U/RT agrees strikingly well with the magnitude of the interaction parameter A/RT = 1.8 that we obtained from the experimental data (Figure 50).

The (1,0,0) distortion caused by LLM is much smaller than the (0,0,1) distortion caused by its mirror image MLL. The effects of chirality may clearly not be disregarded. Here again, the average value of the distortions U/RT corresponds reasonably well to the values of the interaction parameter A/RT of 1.6–2.3 that were found experimentally.

The order of magnitude of the calculated distortions corresponds with that expected from the value of the interaction parameters. However, we would expect that the distortions calculated in this way would lead to a systematic overestimate of the interaction parameters. The actual distortion is smaller, because in reality some relaxation of the LLL lattice near the distortion will occur. Moreover, entropy effects are neglected. Apparently both effects are relatively small.

It has become evident that the lattice distortion calculations can be used to obtain good insight into the influence of structural differences on the solid state miscibility. We will continue this approach in future work. In view of the results obtained, the good performance of the 2-suffix Margules equation and the good correlation of the interaction parameter with the degree of isomorphism remain very surprising.

8.3 AN EMPIRICAL METHOD

Although Larsson and Hernqvist [7] have announced a detailed analysis of the crystal structure of the β′-modification, similar to that of de Jong [13] for the β-modification, at present the β′-crystal structure of TAGs is still not exactly known. The instability of the β′-modification and the inability to grow large single crystals are the main obstacles to be taken. The crystal structure of cis-unsaturated TAGs has not been unambiguously revealed either. This implies that it is not yet possible to study the influence of impurities on the β′-crystal lattice by molecular modelling. Fundamental insight in the relation between non-ideal miscibility of TAGs and structural differ-

ences can probably best be obtained form these lattice distortion calculations. While this is impossible, a semi-empirical approach to the problem of this chapter, finding a method to predict binary interaction parameters, has to be followed.

8.3.1 The method

The correlation between the degree of isomorphism, $\in$, and the 2-suffix Margules parameter within one submodification can serve as basis for such a semi-empirical predictive method. It is assumed that:

1. Within one submodification the 2-suffix Margules binary interaction parameter A/RT is:

   for a β′-modification:

   $$\in > 0.93 \; : \; \frac{A}{RT} = 0 \tag{95}$$

   $$\in \leq 0.93 \; : \; \frac{A}{RT} = -19.5 \in +18.2 \tag{96}$$

   and for a β-modification:

   $$\in > 0.98 \; : \; \frac{A}{RT} = 0 \tag{97}$$

   $$\in \leq 0.98 \; : \; \frac{A}{RT} = -35.8 \in +35.9 \tag{98}$$

2. Both 3-suffix Margules parameters are also given by Eq. (92–95), except for the β′-2 modification of a binary pair of which one of the TAGs belongs to the h_2u TAG-group. If the h_2u-type TAG is indicated by 2, then A_{21} is given by Eq. (92) and (93), while A_{12} follows from:

   $$\frac{A_{12}}{RT} = -21.7 \in +18.7 \tag{99}$$

3. If A/RT $>$ 8, A/RT $=$ 8 can be used in calculations. The relations were obtained by linear regression through the data of Tables 34–36. The correlation coefficient is 0.9, while the standard error in the esti-

mated interaction parameters is 0.3–0.5. The values of the regression constants clearly illustrate the better solid miscibility in the less densely packed β′-modification.

Interaction parameters within a submodification are useless if the pure component properties of the TAG, crystallized in that submodification, are not known. Often these properties cannot be measured, because the pure components do not occur in the desired submodification. Therefore the following additional assumptions are made in line with our observations in Section 15.4 and those of de Jong [13]:

4. The melting point of a hypothetical -3 form of a TAG that crystallizes into the β′-2 or β-2 form, is 3°C less than the melting point of the corresponding -2 form. The heat of fusion is 90% of that of the corresponding -2 form. Similarly the melting point of a hypothetical -2 forms of a TAG that crystallizes into the β′ -3 of β-3 form is 3°C less than that of the corresponding -3 form, while the heat of fusion is 90% of that of the -3 form.
5. Submodifications in the β′-modification are, if they exist, continuously miscible
6. It is only possible to form continuous solid solutions of two TAGs in the β-2 modification when they both crystallize in the same β-2 submodification. Table 41 lists the four different β-2 submodifications that occur in practice, using de Jong's nomenclature, representing a TAG according to the method defined in chapter 4 as (p.p + x.p + y) and thus indicating TAG-families by (x,y).
7. The melting point and heat of fusion of the hypothetical β-2 forms, which do not occur in the pure TAG, are assumed to lie 3°C below that of the stable β-2 form, while the heat of fusion is 90% of that of the stable form.

   Thermodynamic calculations now become extremely complicated, as the number of independent polymorphs that have to be considered, has increased

Table 41 Summary of the β-2 Submodfications in Which Different TAG-families (x,y) Crystallize

β-2 submodification			
A	B	C	D
(0, 0)	(−2, 0)	(4, 2)	(2, 2)
(0, 2)	(2, 0)	(4, 4)	
(2, 2)	(2, 4)		

with each extra assumption from 3 to 8. Because most binary pairs of TAGs that crystallize into different β-2 modifications are not completely miscible even when they would crystallize in the same submodification, often equivalent calculation results are obtained if assumption 7 is replaced by the following assumption:

8. In calculations only one β-2 polymorph can be used. However, if the two TAGs of a binary crystallize in different submodifications, the two suffix Margules parameter that is obtained from Eq. (94) and (95) is augmented by 1.

    The phase diagram of SSS-SPS (Figure 50) that was calculated allowing the occurrence of 2 β-2 modifications and A/RT = 1.8 in each submodification is nearly the same as the phase diagram given in Section 15.7 using only one β-modification and A/RT = 3.

The difference of 3°C between the melting point of the stable and hypothetical β′- and β-forms is a best guess, based on de Jong's findings for the melting points of saturated mono-acid TAGs in different submodifications. The value of 90% for the heat of fusion of hypothetical submodifications is a best guess that is based on the data, given in Section 15.4.

8.3.2 Discussion

It is obvious that the empirical method given is far from perfect, as it is based on a small number of data, which necessi-

tated a number of speculative assumptions. However, the underlying notion that only TAGs with a high degree of geometric similarity will mix well in a densely packed solid phase is most likely correct. Therefore, the main effects of structural differences on solid phase miscibility are covered by the method, although not always very precise. In order to improve the method, more data are required and a number of issues need to be solved:

1. There is still a lack of reliable data on binary interaction parameters of TAGs, both for the β′-modification and for the β-modification. Especially ona mixtures with cis-mono- and di-unsaturated TAGs more information is required.
2. The crystal structure of the β′-modification and its possible submodifications as well as the structure of the polymorphic forms of cis-unsaturated TAGs have to be known.
3. It must be established to what extent the structure of two submodifications must be different before continuous miscibility of the two submodifications cannot occur, so that treatment as independent polymorphs is necessary
4. If two submodfications need to be treated as independent polymorphs, a method must be developed to estimate the thermodynamic properties of those polymorphs that do not occur in the pure component.
5. To obtain insight in the magnitude of different lattice distortions more mixtures have to be studied by molecular modelling, not only in the β-modification, but also in the β′-modification.

In spite of its serious limitations, the empirical method in Section 15.9 will be tested to see how it performs in practical situations.

8.4 CONCLUSION

The nonideal mixing behaviour of TAGs in the solid phase can be explained by geometrical considerations.

Within one (sub)modification the binary interaction parameters show a clear correlation with the degree of isomorphism, as defined by Kitaigorodskii [111].

Based on the good correlation between degree of isomorphism and the 2-suffix Margules interaction parameter, a method has been defined that predicts the binary interaction parameters from structural differences.

The work that is required to improve this predictive method was outlined.

9. PRACTICAL APPLICATIONS

In the previous sections, all steps that are required to meet the objective of this work (prediction of melting ranges and solid phase composition of fats) have been taken. In this section, the method developed will be used for predictions in a number of practical situations: the prediction of melting ranges of margarine fat blends, the prediction of the composition of fat fractions obtained from fractional crystallization, and the understanding of recrystallization phenomena. Some examples outside the area of edible fats are considered as well. Finally the conclusions of this chapter are summarized.

9.1. PREDICTION OF MELTING RANGES

The primary objective of this chapter is the development of a general method to predict the melting range of a fat blend from its composition. In this section, we will investigate to what extent this objective has been attained.

In Section 15.6 it was shown that the α-melting ranges, or 'α-lines' of the fat blends of nine different commercial fat spreads could be predicted very well.

If the binary interaction parameters for the β′-modification are estimated with the procedure outlined in Section 15.8.3, it is in principle possible to calculate the β′-melting ranges of these fats as well. A complicating factor in the calculations is the large number of components, usually between 30 and 400 in these fats. Even if only four coexisting β′-phases are formed, the flash calculation of Section 15.3 must already

handle matrices with a 2000 × 2000 dimension, which will make the calculation procedure too slow for practical use.

To keep the calculations manageable, pseudocomponents are defined as follows: all components that are nearly isomorphous ($\in > 0.95$) and that differ 5°C or less in their β′-2 melting point are taken together as a new pseudocomponent that has the polymorphic behaviour and the size of the component that contributes most to the pseudocomponent. Components and pseudocomponents with a concentration less than 0.1% are neglected.

In this way blend 1–8 from Table 19 were reduced to 15–20 component mixtures. Only blend 9 remained too complex. The β′-melting ranges of these 15–20 component mixtures were calculated and plotted in Figure 52, together with the experimental values. The experimental values were obtained with wide range NMR of samples that were molten, kept for 1 hour at 80°C, rapidly cooled to 0°C, stabilised for 16 hours at 0°C and for 30 minutes at the temperature of measurement. With this procedure, one of the Unilever standard methods, most normal fat blends have crystallized completely.

Although the predictions show a larger deviation than those for the α-melting ranges, the agreement with the experimental data is still very good, in spite of the large simplifications that were made in the composition and in the estimation of the interaction parameters. The standard error of 3% solids compares well with the experimental error of 1% solids and the effects of kinetics of crystallization, that are normally estimated to be in the order of a few percent of solids.

Out of the empirical methods, mentioned in Section 15.1, only the multiple linear regression/linear programming method performs better, but only within the limited range of compositions for which this method is valid. As it is based on interpolations within a finely meshed raster of experimental data points, this is not too surprising.

Only for blend 3, which contains 23% of POP, the experimental points, determined with the standard method, lie far below the calculated line. Blend 3 is a typical example of a fat blend that shows extreme 'post-crystallization'. Post crystallization means that in the first week after production still a

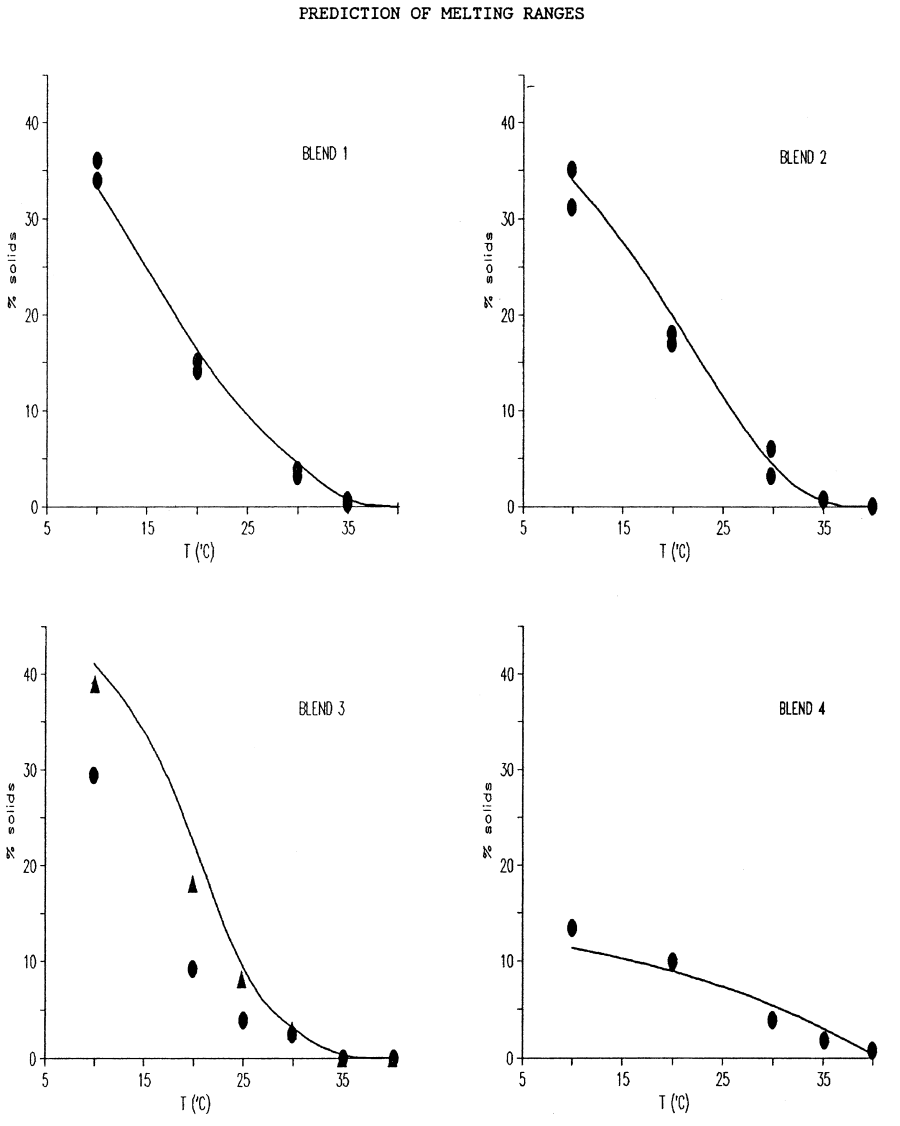

Figure 52a (a) Predicted (lines) and experimental (points) β′-melting ranges of several commercial fat blends. The numbers refer to the composition of the fat blend, given in Table 19. The 2-suffix Margules equation was used for the excess Gibbs energy. dots : solid phase measured with standard procedure triangles (blend 3 only): determined in a week-old margarine.

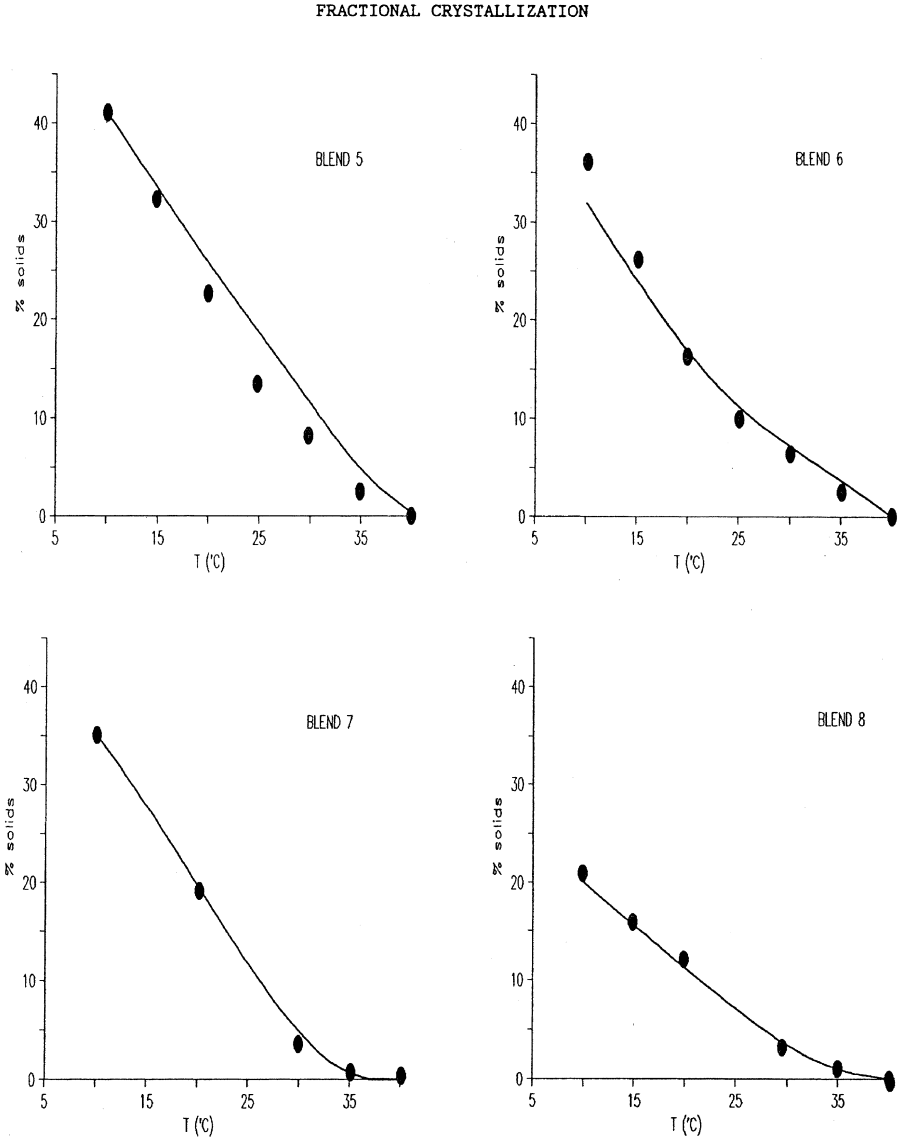

Figure 52b (b) Predicted (lines) and experimental (points) β′-melting ranges of several commercial fat blends. The numbers refer to the composition of the fat blend, given in Table 19. The 2-suffix Margules equation was used for the excess Gibbs energy

considerable amount of solid fat crystallizes. The solid fat content that was determined in a margarine sample of a week old is also plotted in Figure 52. Now the agreement with the calculated data is very good. Obviously, blend 3 has not crystallized completely when the standard procedure is used.

Thus it has been demonstrated that melting ranges of the practically relevant polymorphic forms of fat blends can be predicted by application of solid-liquid phase equilibrium thermodynamics.

9.2 FRACTIONAL CRYSTALLIZATION

The second objective of this chapter is the development of a method that predicts the solid phase composition of a fat at a certain temperature, in order to enable modelling of a fractional crystallization process. At present fractional crystallization is primarily used for fractionation of palm oil into palm olein, a liquid fraction of palm oil and palm stearin, a solid fraction.

Palm oil was heated to 80°C for 1 hour and subsequently cooled to the fractionation temperature. Five hours after the appearance of the first turbidity the palm olein was filtered off in a filter press at 12 bar. The separation efficiency (amount of olein that is obtained over the total amount of liquid phase that is present in palm oil) was determined. NMR showed that crystallization had taken place into the β-modification. The TAG compositions of the palm oil, the olein, and the stearin were analyzed by $AgNO_3$-HPLC [111]. The results are given in Table 42, together with the composition that was calculated, using the procedure as outlined above and the measured separation efficiency

The calculated data agree very well with the experimental ones. van Putte [24] states that palm oil crystallizes into the β′-modification when the crystallization takes place at 27°C or less, while above this temperature the β-modification is observed. In line with this observation, calculations show that in palm oil up to 25–26°C a stable β′-solid phase coexists with two β-solid phases, while above this temperature only β-solid phases remain.

Table 42 Experimental and Predicted Compositions of Palm Oil Fractions (Calculated for the most stable state, the β-modification)

	Fract. at 29 °C		Fract. at 32 °C	
	Measured	Calc.	Measured	Calc.
Palm oil				
h_3	8.8			
hOh	33.0			
hhO	7.1			
hlh	9.5			
rest	41.7			
Stearin				
h_3	45.3	46.2	54.7	53.3
hOh	25.4	29.3	21.5	17.2
hhO	6.1	4.1	5.5	4.3
hlh	5.3	4.9	4.3	4.7
rest	17.9	15.4	14.0	20.1
Olein				
h_3	2.2	0.1	2.8	0.2
hOh	34.4	33.7	34.7	35.8
hhO	6.1	7.8	5.9	7.6
hlh	10.6	10.5	10.1	10.3
rest	46.7	47.7	46.4	46.0

This example shows clearly that application of solid liquid phase equilibrium thermodynamics to fat fractionation processes is feasible.

9.3 RECRYSTALLIZATION PHENOMENA

9.3.1 The influence of precrystallization and temperature cycling

In Section 15.7, DSC-curves of mixtures of a crystallizing binary pair of TAGs in a surplus of a liquid TAG were determined. The samples were stabilized by rapid cooling to a stabilization temperature. In those experiments, stabilisation at temperatures below the onset of the first melting peak in the DSC thermogram in the end always resulted in the same DSC-curve, regardless of the stabilization procedure that was fol-

lowed. However, if a well stabilized sample was subjected to temperature cyclization by increasing the temperature from the stabilization temperature to a cycling temperature well above the onset of the first melting peak and backwards, then the DSC-curves that were measured directly after the cycling step often had a completely different shape. The effect even occurred at cycling rates as low as 0.6°C/min. It was not possible to fit such DSC-curves with the 2- or the 3-suffix Margules equation.

The shape of the curves of the cycled samples could be obtained using the well known concept of shell formation [23], which was already mentioned in Section 15.2. Upon heating the sample part of the solid phase dissolves. It is assumed that upon cooling the remaining crystals are covered with a layer of solid fat that is in equilibrium with the liquid phase that is present. This shell effectively keeps the inner part of the crystals from gaining the equilibrium composition.

The resulting DSC melting curve will be the sum of that a sample that has an overall composition equal to that of the liquid phase at the cyclisation temperature and the curve of the solid phase that remained at the cyclisation temperature. This DSC curve will deviate from the equilibrium curve at temperature below the cyclisation temperature. Figure 53*a* shows that this is exactly what is observed, while the curves in figure 53*b*, which are calculated assuming shell formation, confirm that shell formation can describes the observations.

Shell formation is much less likely with the isothermal stabilization procedure that is followed in this work: always a completely liquid sample is very quickly supercooled to the stabilization temperature. Therefore all solids are formed at the stabilization temperature.

Elaborate cyclization procedures were followed in order to obtain the binary phase diagrams given Section 15.7. The cycling effect described here offers another explanation for the large discrepancies between solidus and liquidus that were found: cyclization leads to the formation of a solid phase that starts to melt off at lower temperatures. After initial melting a solid phase that is enriched in the highest melting component remains.

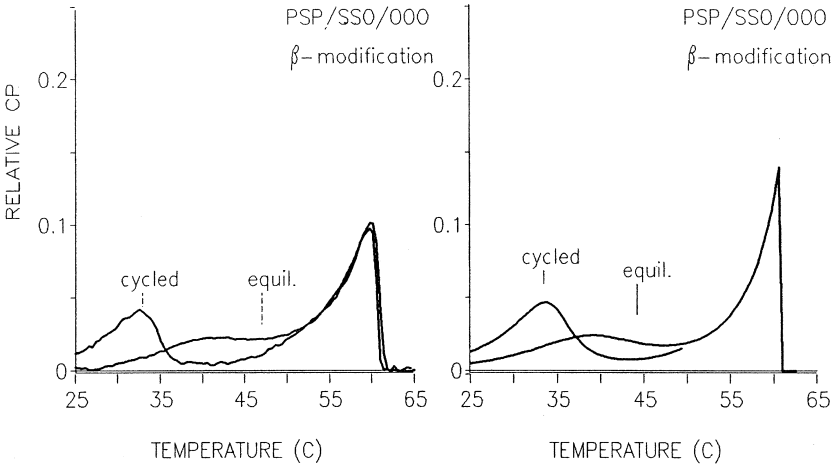

Figure 53 (a) 25% PSP/25% SSO/50% 000. Effect of cycling to 50°C on the DSC melting curve. Experimental curves, taken at 2.5°C/min. (b) Simulation of the effect of cycling to 50°C on the DSC melting curve of the system of Figure 30.

Shell formation also offers the explanation for the differences in fraction composition that are obtained with fractional crystallization of oils and fats when different cooling rates are used [112]: slow cooling to the fractionation temperature causes shell formation and so results in a solid phase that is enriched in the higher melting components, while quick cooling results in the equilibrium composition. This work enables the quantification of the magnitude of these effects.

Shell formation also plays a role in the normal margarine "votator" process. Fat spreads are usually prepared by quickly cooling and emulsifying a mixture of a molten fat blend and milk or water in a scraped surface heat exchanger or "A-unit". The supercooled emulsion is subsequently crystallized in a pin stirrer, or "C-unit". In many cases this is followed by further cooling and crystallization in second series of A and C-units [1], so that the complete votator process sequence becomes $A–C_1–A–C_2$. It is often impossible to complete crystallization in this second C-unit to the β′-equilibrium, even when a very

long residence time is provided. Upon storage, the equilibrium solids content will eventually be reached, resulting in a considerable posthardening and change of rheological properties. In fact, the two-step crystallization in this votator process is a build in cyclization step: in the first C-unit a solid phase is formed, which is encapsulated in the second C-unit with a solid phase of different composition.

The effect of this precrystallization on solids content can be quite dramatic, as is illustrated in Figure 54 for the PSP/SSO/OOO model blend that was used in Section 15.7: the difference in solid content between precrystallized and equilibrium situation can be as large as 10–15% solids. After the $A–C_1–A–C_2$ votator process the fat can only crystallize to a point on the lower solids line. But upon storage it will recrys-

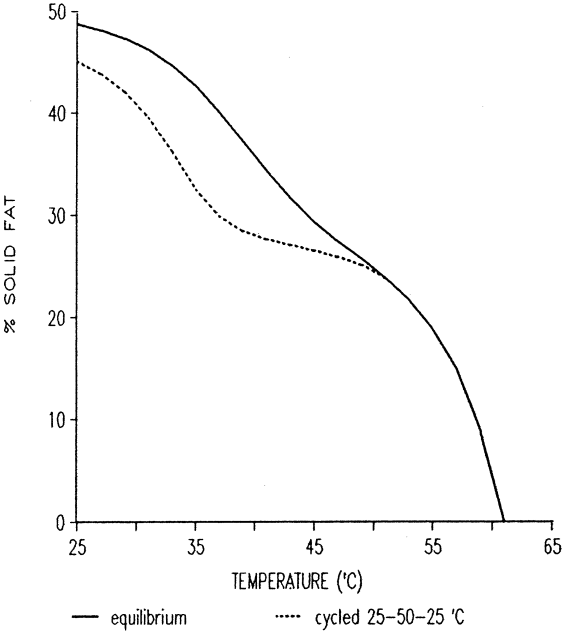

Figure 54 Calculated solids-temperature lines of the TAG-blend of Figure 53 (25% PSP/25% SSO/50% 000). Solid line = equilibrium line, dashed line = after precrystallization at 50°C.

tallize to the equilibrium composition in several weeks, which explains the increase in solids content and the rise in product hardness.

Fat blends in which the TAGs show considerable solid phase miscibility will be more sensitive to precrystallization effects than blends in which the TAGs show no solid phase miscibility.

9.3.2. Sandiness

A well known phenomenon is the development of sandiness in fat spreads with a fat blend containing only liquid oils and hydrogenated low erucic acid rape seed oil [113,114]. Sandiness is the development upon storage of large β-fat crystals in a product that initially had crystallized into the β′-modification. Those large crystals give a sensation to the consumer as if sand has been erroneously added to the product.

Hydrogenated rape seed oil consists for 95% out of TAGs from C18 fatty acids (E, O and S). The degree of isomorphism between these TAGs is 1, which implies ideal solid solubility both in the β′ and in the β-modification. In Section 15.7 it was found that the rate of recrystallization from β′ to the β-modification depends on the thermodynamic driving force and on the degree of rearrangement of the solid phase that is required. Because the rape seed TAGs mix ideally in both modifications, the thermodynamic driving force is the full stability difference between the two modifications, while virtually no change in solid phase composition has to take place.

In this reasoning, the tendency to develop sandiness can be reduced by additions of TAGs that reduce the thermodynamic driving force and increase the degree of rearrangement in the solid phase that is required. Such TAGs should mix nearly ideally with the TAGs from rape seed oil in the β′-modification, but must demix in the β-modification. TAGs that have a degree of isomorphism with the rape seed TAGs of about 0.92 and a melting point above 30°C fulfill this criterion. Candidates are therefore the TAGs P_2S, P_2E, P_2O, A_2S, A_2S, A_2O, and also BS_2, B_2E, and B_2O. The solubility of these inhibiting TAGs in the β-modification of the rape seed TAGs is according

to the findings in Section 8 nearly 10%. Therefore, expect that the β′-β transition in hydrogenated rape seed oil mixtures will be retarded considerably if the crystallizing TAGs in the fat blend consist for more than 10% of inhibiting TAGs. Hydrogenated rape seed oil already contains 5% of those TAGs, so that addition of only 5% of an inhibiting fat is required to retard sandiness.

TAGs with a degree of isomorphism with the rape seed TAGs of less than 0.86 are expected to have much less effect: they do not even cocrystallize with the rape seed TAGs in the β′-modification, so that still hardly any solid phase rearrangement is required for the formation of the β-modification.

Hydrogenated soybean oil has a TAG composition that is very similar to that of hydrogenated rape seed oils, but the concentration of sandiness inhibiting TAGs is higher: it varies from batch to batch around the critical value of 10%, which implies that depending on the batch of oil sandiness can occur. And indeed from time to time we have observed sandiness in products based on hydrogenated soybean oil.

Hydrogenated high erucic rape seed oil, contains depending on the hydrogenation procedure followed, more than 10% of inhibiting TAGs. Therefore sandiness is not so often observed in products of this rape seed oil breed [113,114].

Hernqvist already mentioned the possibility of addition of inhibiting TAGs, but he followed another reasoning and is not able to specify which TAGs and what amounts are required. By trial and error Hernqvist found no sandiness in a mixture of TAGs from rape seed and 20% PSP and he suggests that other inhibiting TAGs may exist. Indeed PSP belongs to the inhibiting TAGs mentioned.

9.3.3. Conclusion

The examples in this section have made clear that, although quantitative predictions are not always possible, the methods of this work help create understanding of recrystallization phenomena, which can directly be translated into practical methods to influence recrystallization.

9.4. APPLICATIONS OUTSIDE EDIBLE OILS AND FATS

9.4.1. Solid liquid phase behaviour of n-alkanes

Contrary to TAGs, which have only one thermodynamically stable polymorph ("monotropic polymorphism"), each polymorphic form of medium to long chain odd numbered n-alkanes is stable within a certain temperature and pressure region ("enantiotropic polymorphism"). Far below the melting point the β′-form is stable. However, from about 10°C below to melting point upwards the α-modification ("rotator phase") is the stable polymorph. Upon heating a β′-form of an odd numbered n-alkane, it will first transform to the α-modification at the so called transition temperature and finally melt at the α-melting point.

The enantiotropic polymorphism gives rise to most peculiar solid-liquid phase diagrams, of which an example is depicted in Figure 55. The phase diagram consists of three single phase regions, a liquid, an α-and a β′-region. The regions are separated by two two phase domains, a cigar-shaped α-L and a β′-α region with a minimum transition temperature [44,90]. Although on first sight the phase behavior seems completely different, remarkable agreement exists between the phase behaviour of TAGs and these n-alkanes.

The cigar-shape of the α-L region indicates that miscibility in the α-modification of these n-alkanes must be nearly ideal. This is in agreement with our findings for the α-modification of TAGs.

The shape of the β′-α region and the existence of a single phase β′-region suggest non ideal mixing in the β′-modification, with a value for a regular solution binary interaction parameter in the β′-modification around 1.3–1.8. This is the same order of magnitude of the interaction parameters that have been found for the β′-modification of a binary pair of TAGs with a degree of isomorphism of 0.89.

When these values are used to describe the mixing behaviour in the α- and β′-modification, the phase diagram of Figure 55 is obtained easily, applying the models and techniques used in this work for TAGs.

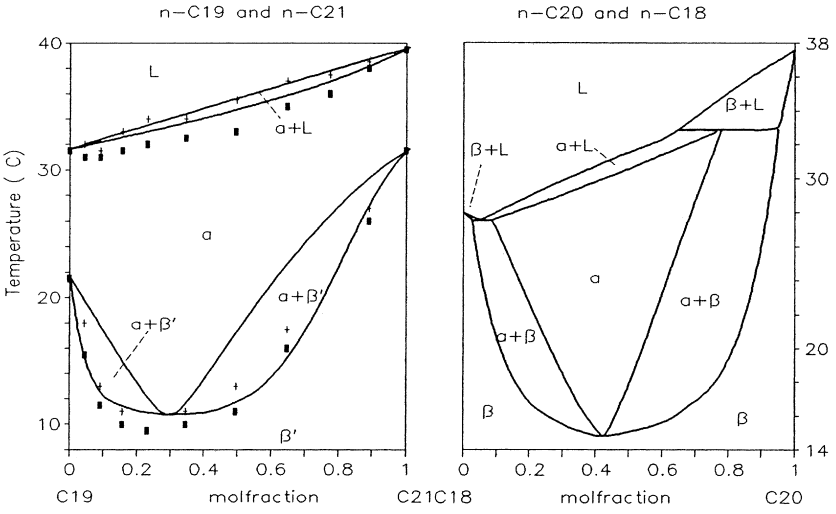

Figure 55 Phase diagrams of binary n-alkane mixtures. (a) (*left*): n-C19 with n-C21, points: data from Würflinger [44] lines : calculated with ideal α and liquid phase miscibility and non-ideal mixing in the β′-modification with 3-suffix Margules parameters $A_{19\_21}/RT = 0.4$ and $A_{21\_19}/RT = 1.7$. (b) (*right*): n-C18 with n-C20. Calculated assuming ideal miscibility in the α-modification and liquid phase and non ideal miscibility in the β′-modification with regular solution parameter $A/RT = 1.6$. The α-melting points were taken 1.5°C below the β-melting points.

The main problem in the calculations is the absence of values for the β′-melting points. The enantiotropic behaviour of these n-alkanes makes an experimental determination of β′-melting point impossible. However, they can be calculated from the measured β′-α-transition temperatures using the following expression:

$$T_{f,\beta'} = T_{\text{transition}} \cdot \frac{\Delta H_{\beta'}}{\Delta H_{\beta'} + \Delta H_{\alpha}\left(\dfrac{T_{\text{transition}}}{T_{f,\alpha}} - 1\right)} \tag{100}$$

The expression follows from the fact that at the transition temperature the Gibbs energy of the two polymorphs must be

equal. The differences in heat capacity are neglected. Calculated β′-melting points are listed in Table 42. Although the transition temperatures lie 10°C or more below the α-melting point, the calculated β′-melting points lie only 1 or 2 degrees below the α-melting point.

The table also shows that, in spite of the higher melting point, entropy and heat of fusion of the α-modification are only 70% of the β-values, which is in agreement with the values found for TAGs. In fact, a rise of only 5% in α-melting entropy would change the enantiotropic polymorphism into the normal monotropic behaviour that is observed for TAGs.

The phase diagram that is calculated from the values of Table 43 and the assumptions about the mixing behaviour in the various polymorphic forms is plotted in Figure 55*a*, together with the data of Würflinger. The agreement is striking, especially when taking into account that it must be almost impossible to determine the equilibrium α-β′-coexistence region correctly by experiment. It would require large rearrangements in the solid state within the time of measurement, while solid state diffusion is extremely slow.

Some even chain n-alkanes are just monotropic: the α-melting point lies just below the β melting point. Binary mix-

Table 43 Thermodynamic Data of Some Odd-chain N-alkanes. T in °C, H in kJ/mol and S in J/K, mol. (From Würflinger [44])

Carbon number	T_f, α	T_f, β′	ΔH_α	$\Delta H_{\beta'}$	ΔS_α	$\Delta S_{\beta'}$	T_{trans}
9	−53.5	−54.2	16	22	71	100	−56.0
11	−25.5	−28.1	22	29	90	118	−36.5
13	−5.4	−8.1	28	36	106	136	−18.0
15	9.9	7.3	35	44	123	157	−2.3
17	21.9	19.4	41	52	138	176	10.5
19	32.0	29.6	46	59	150	197	22.0
21	40.2	38.3	48	63	152	203	32.5
23	47.5	45.5	54	76	169	238	40.5
25	53.5	51.5	58	84	177	258	47.0
27	58.8	56.9	60	89	182	270	53.0
29	61.2	60.2	66	98	198	293	58.0

tures of those components are enantiotropic, which gives rise to interesting phase diagrams [44]. This type of phase diagrams, too, is obtained without problems, assuming ideal mixing in the α-modification and non ideal mixing in the β′-modification with $A_{12}/RT = 1.3–1.8$ (Figure 55*b*).

Thus it is illustrated that very simple excess Gibbs energy models, when combined with a proper treatment of polymorphism, can describe the main features of the complex solid-liquid phase behaviour of n-alkanes.

9.4.2. Petroleum waxes

In parallel with this chapter, a number of articles appeared from Won [85,86] and Hansen [87] on petroleum waxes. If mineral oils are brought from reservoir temperature and pressure to atmospheric conditions, sometimes a solid wax phase crystallizes, which causes fouling of the equipment and pipelines.

This wax phase is amorphous, so it is in complete rotational disorder. In line with our findings for the α-modification of TAGs and the rotator phase of alkanes, it can be expected that these wax phases behave like ideal solid solutions. Consequently it is possible to calculate the wax appearance point of these oils.

Indeed, Won and Hansen found that the melting range of these complex petroleum waxes was predicted correctly by assuming ideal solid phase miscibility.

9.4.3. β-substituted naphtalenes

Another class of components that show polymorphism are the β-substituted naphtalenes. Like the odd-chain alkanes, the polymorphism is enantiotropic, with a high temperature polymorph that shows some rotational disorder and more densely packed lower temperature polymorphs. Consequently the phase diagrams are very similar to those of the enantiotropic odd-chain n-alkanes. An extensive study of binary phase diagrams of these components has been made by Chanh and Haget [84,115,116]. Contrary to the n-alkanes, the rotational disorder in the high temperature α-polymorph is not very large, so that a fairly high degree of isomorphism is required

for ideal α-miscibility. In the more densely packed lower temperature polymorphs miscibility is even less ideal than in the α-modification, which in mixtures will lead to an extension towards lower temperatures of the region where the α-modification is stable. This is illustrated in Figure 56 for β-thionaphtalene and β-bromonaphtalene with a degree of isomorphism of 0.97. These components mix nearly ideally in the α-modification and highly non ideally in the other modifications. β-thionaphtalene and β-fluoronaphtalene, with a degree isomorphism of only 0.87 already show non ideal mixing in the α-modification.

Although Chanh et al. do not report pure component properties for each polymorphic form, so that calculation of the phase diagrams from their data is not possible, it is clear that

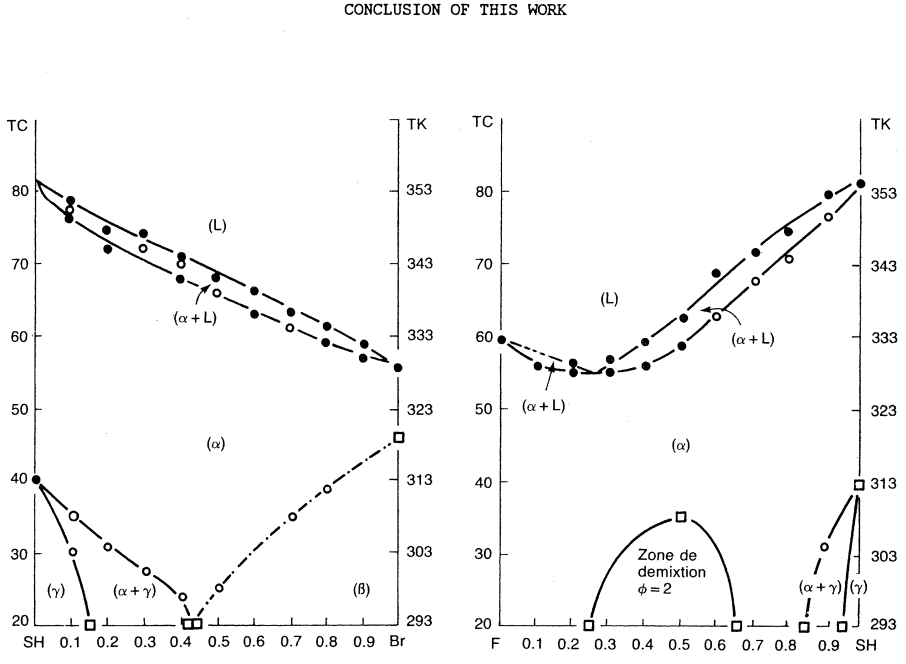

Figure 56 T, x, y binary phase diagrams of some β-substituted naphtalenes. *Left*: β-thionaphtalene and β-bromonaphtalene. *Right*: β-thionaphtalene and β-fluoronaphtalene.

the approach of this work offers a good starting point for the development of a description of the complex solid phase behaviour of this class of compounds.

9.5. CONCLUSION OF THIS CHAPTER

The objective of this chapter is the development of a predictive method for the melting range and the solid phase composition of edible oils and fats. We have shown that this objective can be attained by application of solid-liquid phase equilibrium thermodynamics to all three basic polymorphic forms in which TAGs crystallize.

In order to develop this thermodynamic description:

Existing multicomponent multiphase vapour liquid flash calculation algorithms have been adapted to deal with a number of mixed solid phases that show polymorphism.

The heat of fusion and the melting points of TAGs have been correlated with a number of structural parameters.

Liquid TAG mixtures and TAG mixtures in the α-modification have been treated as ideal mixtures.

The deviation from ideal miscibility in the β' and β-modification has been described by the two and the three suffix Margules equations.

A new method for the determination of the binary interaction parameters that occur in the two or three suffix Margules equation has been developed. The method is based upon the interpretation of the complete DSC melting curve of a mixture of the binary pair and a surplus of a liquid TAG. It is quicker, more versatile and more reliable than the use of binary T, x, y solid liquid phase diagrams.

The binary interaction parameters that occur in the 2- or the 3-suffix Margules equation have been correlated with the degree of isomorphism of the binary pair, a parameter that indicates geometrical similarity.

Now the thermodynamic framework has been set up, the main scope of future research in this area should be the development

of a more refined method to predict binary interaction parameters from structural differences.

SUMMARY

It is important for the production of fat containing food products to control the melting and solidification behavior of edible oils and fats. The properties of many food products, like margarine, reduced fat spreads, cake, ice-cream, and chocolate are to a large extent determined by the melting range of the fat that they contain. The objective of this chapter is to develop a method to predict the melting range and solid phase composition of fats from their overall composition. Unfortunately, at present the only empirical calculation methods available have only limited use. The ultimate amount and composition of the solid phase in a fat are determined by the position of the thermodynamic equilibrium solely, but the crystallization process may lead to significant deviations from the equilibrium composition in practical situations. Yet, it appears that the starting point for any general predictive method of the solid phase content is a description of the solid-liquid phase equilibrium.

Fats consist out of hundreds of different triacylglycerols (TAGs) that can basically crystallize in three forms: the unstable α-modification, the metastable β′-modification and the stable β-modification. The objective of this chapter requires the description of the solid-liquid phase equilibrium for all three polymorphic forms.

The thermodynamic equations that describe these equilibria are worked out in Section 15.2. To solve this set of equations to obtain the solid phase content and the solid phase composition, the following things must be known:

1. the melting enthalpies and melting points of pure TAGs.
2. the mixing behaviour in the liquid phase.
3. the degree of mixed crystal formation in the solid phases.

A method to solve the set of equations must be found as well.

In Section 15.3 the way to solve the thermodynamic equations is worked out. Several methods for flash calculations in multicomponent, multiphase gas-liquid systems are adapted for use with solid phases that show polymorphism. Michelsen's method for the initial estimate combined with a Gibbs free energy minimisation according to Murray perform best.

The melting enthalpies and melting points of pure TAGs are obtained from empirical relations, which are developed by correlating literature data and experimental data with a set of parameters that represent the TAG structure.

The mixing behaviour of TAGs in the liquid phase is studied in Section 15.5. From model calculations, literature data and determination of some liquid phase activity coefficients by means of gas liquid chromatography it appears that the TAGs mix essentially ideally in the liquid phase.

The fatty acid chains of the TAGs still possess considerable mobility in the unstable α-modification. This suggested the hypothesis of ideal miscibility in the α-modification. Surprisingly the α-melting ranges of a large number of commercial fats is predicted very well using this hypothesis.

Miscibility is clearly not ideal in the β′ and β-modification. Using binary T, x, y phase diagrams, of which some have never been published before, we show that it is possible to describe non ideal mixing in these polymorphic forms with the relatively simple 2- and 3-suffix Margules equations. As binary phase diagrams only give information about the β-modification and not about the much more important β′-modification, and as the majority of the existing phase diagrams is inconsistent, a new method is developed for quick determination of the binary interaction parameters in the models for nonideal behaviour. This method is based upon the interpretation of a single, complete DSC melting curve of a mixture of the two TAGs to be studied and a surplus of a liquid TAG. In this way, reliable data concerning the mixing behavior in the β′-modification have been obtained for the first time.

The binary interaction parameters that occur in the models for non ideal mixing show a correlation with a parameter, that indicates the degree of geometrical similarity. This

correlation is used to develop a practical method to predict the binary interaction parameters of two TAGs.

In Section 15.9 the methods developed in this chapter can be used for predicting melting ranges and the composition of the solid phase of fats. A better insight is obtained in the occurrence and prevention of undesired recrystallization phenomena that occur in fats. Also applications outside the world of edible fats are feasible.

LIST OF SYMBOLS

A interaction parameter
v volume of a molecule
$\in$ degree of isomorphism
L long spacing
R gas constant (J/K, mol)
T temperature (K)
T_f normal melting point (K)
%S solid phase content
$\times$ mole fraction
ΔH_f heat of fusion (kJ/mol) at Tf.
τ angle of tilt
c_p heat capacity (J/mol,K)
g molar Gibbs free energy (J/mol)
G Gibbs free energy (J)
N number of components
n number of moles (mol)
P number of phases
z overall mole fraction
γ activity coefficient
Φ phase fraction
μ chemical potential (J/mol)
k, K A constant
K^{AB} distribution constant
f a function
$n_{o,1,e}$ number of 0,1 or E chains
p shortest outer TAG-chain
q middle TAG chain
r longest outer TAG-chain

T_∞ hypothetical melting point of polyethelyne (K)
x p – q
y p – r
δ, θ constants
Δ number of double bonds
ΔS_f melting entropy (J/K, mol)
A Interaction parameter
B_{11} Second virial coefficient
K Molar distribution coefficient
m mass (kg)
M Molar weight (kg/mol)
P Pressure (Pa)
P* Vapour pressure of pure component
v Liquid molar volume (m^3/mol)
V Volume (m^3)
x mol fraction (mol/mol)
Y Activity coefficient
ΔH_f Heat of fusion (kJ/mol)
ϕ Volume fraction
Φ_v Volume flow rate (m^3/s)
χ Interaction parameter
A interaction coefficient.
a A/RT.
$\in$ Degree of isomorphism

APPENDIX 1. PURE COMPONENT DATA

Saturated TAGs

Table A1.1 Enthalpy of Fusion for the α-Modification of Saturated TAGs. Data Marked by a * Include Measurements from this Chapter. FREQ Indicates the Number of Measurements that has Been Averaged

X	Y	TAG	n	ΔH_f (kJ/mol)	Predicted	Residual	FREQ
−6	0	SLS	48	70.0	85.1	−15.1	1*
−6	2	PCS	44	80.0	71.8	8.2	1*
−4	0	PLP	44	65.0	76.6	−11.6	1*
−4	0	SMS	50	90.0	92.8	−2.8	1*
−4	2	PLS	46	70.0	79.5	−9.5	1*
−4	4	MCS	42	67.0	63.7	3.3	1*
−2	0	PMP	46	79.0	86.5	−7.5	1*
−2	0	SPS	52	103.0	102.7	0.3	1*
−2	2	PMS	48	93.0	89.4	3.6	1*
0	0	888	24	18.4	31.8	−13.4	3*
0	0	CCC	30	57.3	47.9	9.4	2*
0	0	LLL	36	69.8	64.1	5.7	3*
0	0	MMM	42	81.9	80.3	1.6	3*
0	0	PPP	48	95.8	96.5	−0.7	3*
0	0	SSS	54	108.5	112.7	−4.2	3*
0	0	BBB	66	143.2	145.1	−1.9	1
0	0	24.24.24	72	160.9	161.3	−0.4	1
0	2	88C	26	26.0	34.7	−8.7	1*
0	2	MMP	44	82.0	83.2	−1.2	1*
0	2	PPS	50	100.0	99.4	0.6	1*
0	4	LLP	40	67.0	67.4	−0.4	1*
0	4	MMS	46	87.0	83.6	3.4	1*
2	0	8C8	26	51.0	37.8	13.2	1*
2	0	CLC	32	67.0	54.0	13.0	1*
2	0	LML	38	83.0	70.2	12.8	1*
2	0	MPM	44	93.0	86.4	6.6	1*
2	0	PSP	50	112.2	102.6	9.7	2*
2	2	MPP	46	89.0	89.3	−0.3	1*
2	2	PSS	52	106.0	105.5	0.5	1*
2	4	LMP	42	74.0	73.5	0.5	1*
2	4	MPS	48	86.0	89.7	−3.7	1*
2	6	CLP	38	57.0	59.0	−2.0	1*
2	6	MPA	50	72.0	91.3	−19.3	1
4	0	MSM	46	99.0	87.8	11.2	1*
4	0	SBS	58	128.0	120.2	7.8	1*
4	2	MSP	48	91.0	90.7	0.3	1*

(Continued)

Table A1.1 Continued

X	Y	TAG	n	ΔH_f (kJ/mol)	Predicted	Residual	FREQ
4	4	LPP	44	83.0	75.0	8.0	1*
4	4	MSS	50	92.0	91.1	0.9	1*
6	0	LSL	42	66.0	72.2	−6.2	1*
6	0	MAM	48	88.0	88.4	−0.4	1*
6	4	LSP	46	76.0	75.5	0.5	1*
6	6	CPP	42	53.0	61.0	−8.0	1*
6	6	LSS	48	70.0	77.2	−7.2	1*

Table A1.2 Enthalpy of Fusion for the β′-Modification of Saturated TAGs. Data Marked by a * Include Measurements from this Work. FREQ Indicates the Number of Measurements that has Been Averaged

X	Y	TAG	n	ΔH_f (kJ/mol)	Predicted	Residual	FREQ
0	0	LLL	36	86.0	88.0	−2.0	1
0	0	MMM	42	106.0	111.1	−5.1	3*
0	0	PPP	48	126.5	134.3	−7.8	2*
0	0	SSS	54	156.5	157.5	−1.0	2*
0	2	MMP	44	100.0	106.5	−6.5	1*
0	2	PPS	50	124.0	129.7	−5.7	1*
0	4	LLP	40	90.0	84.4	5.6	1*
0	4	MMS	46	93.0	107.6	−14.6	1*
2	0	8C8	26	62.0	63.5	−1.5	1*
2	0	CLC	32	87.5	86.7	0.8	2*
2	0	LML	38	112.0	109.9	2.1	1*
2	0	MPM	44	127.0	133.0	−6.0	1*
2	0	PSP	50	165.5	156.2	9.3	4*
2	4	LMP	42	94.0	106.3	−12.3	1*
2	4	MPS	48	111.0	129.5	−18.5	1*
4	0	MSM	46	148.0	133.0	15.0	1*
4	0	SBS	58	189.0	179.4	9.6	1*
4	2	MSP	48	143.5	128.4	15.1	2*
4	4	LPP	44	110.0	106.3	3.7	1*
4	4	MSS	50	128.0	129.5	−1.5	1*
6	0	LSL	42	87.0	107.8	−20.8	0*
6	0	MAM	48	117.0	130.9	−13.9	1*
6	4	LSP	46	107.0	104.2	2.8	1*
6	6	LSS	48	104.0	111.6	−7.6	1*

Table A1.3 Enthalpy of Fusion for the β-Modification of Saturated TAGs. Data Marked by a * Include Measurements from this Work. FREQ Indicates the Number of Measurements that has Been Averaged

X	Y	TAG	n	ΔH_f (kJ/mol)	Predicted	Residual	FREQ
−10	0	S8S	44	141.0	131.7	9.3	1
−8	0	P8P	40	122.0	116.2	5.8	3
−8	0	SCS	46	143.0	139.5	3.5	2
−6	0	PCP	42	122.5	124.0	−1.5	2
−6	0	SLS	48	132.0	147.4	−15.4	2*
−6	2	PCS	44	125.0	123.3	1.7	1*
−4	0	PLP	44	121.5	133.1	−11.6	2*
−4	0	SMS	50	146.5	156.5	−10.0	2*
−4	2	PLS	46	123.0	132.4	−9.4	1*
−4	4	MCS	42	88.0	106.3	−18.3	1*
−2	0	PMP	46	137.0	148.3	−11.3	2*
−2	0	SPS	52	170.3	171.7	−1.4	4*
−2	2	PMS	48	152.0	147.6	4.4	1*
0	0	888	24	69.2	74.7	−5.4	4*
0	0	CCC	30	95.0	98.0	−3.0	5*
0	0	LLL	36	122.2	121.3	0.9	9*
0	0	MMM	42	146.8	144.7	2.1	8*
0	0	PPP	48	171.3	168.0	3.3	16*
0	0	SSS	54	194.2	191.3	2.8	20*
0	2	88C	26	59.0	73.9	−14.9	1*
0	2	LLM	38	116.0	120.6	−4.6	1
0	2	MMP	44	131.0	143.9	−12.9	1*
0	2	PPS	50	166.3	167.3	−1.0	4*
0	4	LLP	40	117.0	117.8	−0.8	1*
0	4	MMS	46	145.0	141.2	3.8	1*
2	0	PSP	50	166.0	173.6	−7.6	1
2	2	LMM	40	118.0	126.2	−8.2	1
2	2	MPP	46	140.0	149.6	−9.6	1*
2	2	PSS	52	175.0	172.9	2.1	3*
2	4	LMP	42	125.0	123.5	1.5	1*
2	4	MPS	48	137.0	146.8	−9.8	1*
2	6	CLP	38	95.0	105.0	−10.0	1*
2	6	MPA	50	122.0	151.6	−29.6	0*
4	4	LPP	44	146.0	119.0	27.0	0*
4	4	MSS	50	139.0	142.4	−3.4	1*
6	0	LSL	42	131.0	124.8	6.2	1*
6	0	MAM	48	157.0	148.1	8.9	1*
6	4	LSP	46	124.0	121.3	2.7	1*
6	6	CPP	42	89.0	102.8	−13.8	1*
6	6	LSS	48	123.0	126.1	−3.1	1*

Table A1.4 Melting Points of the α-Modification of Saturated TAGs. FREQ Indicates the Number of Measurements that has Been Averaged

X	Y	TAG	n	ΔH_f (kJ/mol)	Predicted	Residual	FREQ
−12	0	S6S	42	27.8	23.7	4.1	2
−10	0	P6P	38	14.6	10.2	4.4	2
−8	0	SCS	46	30.0	34.4	−4.4	2
−6	0	PCP	42	20.0	24.3	−4.3	2
−6	0	SLS	48	36.0	39.3	−3.3	2
−4	0	MCM	38	16.0	13.4	2.6	1
−4	0	PLP	44	32.6	31.4	1.2	2
−4	0	SMS	50	43.8	44.3	−0.5	4
−4	0	BSB	62	61.1	61.7	−0.6	1
−2	0	LCL	34	5.0	2.9	2.1	2
−2	0	MLM	40	24.0	23.7	0.3	1
−2	0	PMP	46	39.1	38.5	0.6	5
−2	0	SPS	52	50.7	49.4	1.3	6
−2	2	PMS	48	40.9	41.3	−0.4	2
−1	0	P.15.P	47	43.4	41.7	1.7	1
−1	0	s.17.s	53	53.1	51.8	1.3	1
0	0	888	24	−51.0	−47.8	−3.2	1
0	0	9.9.9	27	−26.0	−26.1	0.1	1
0	0	CCC	30	−11.5	−9.3	−2.2	2
0	0	11.11.11	33	2.0	4.2	−2.2	2
0	0	LLL	36	15.6	15.2	0.4	4
0	0	13.13.13	39	24.5	24.3	0.2	3
0	0	MMM	42	32.6	32.0	0.6	6
0	0	15.15.15	45	39.5	38.7	0.8	4
0	0	PPP	48	44.7	44.4	0.3	5
0	0	17.17.17	51	49.9	49.4	0.5	4
0	0	SSS	54	54.7	53.8	0.9	8
0	0	19.19.19	57	59.1	57.7	1.4	2
0	0	AAA	60	62.9	61.3	1.6	2
0	0	21.21.21	63	65.0	64.4	0.6	1
0	0	BBB	66	69.1	67.3	1.8	2
0	1	11.11.L	34	7.5	7.3	0.2	1
0	2	CCL	32	0.0	−3.2	3.2	1
0	2	LLM	38	19.0	19.4	−0.4	1
0	2	MMP	44	34.5	35.2	−0.7	3
0	2	PPS	50	46.4	46.9	−0.5	5
0	4	CCM	34	3.0	−0.8	3.8	2
0	4	LLP	40	20.0	21.4	−1.4	1

(*Continued*)

Table A1.4 Continued

X	Y	TAG	n	ΔH_f (kJ/mol)	Predicted	Residual	FREQ
0	4	MMS	46	35.6	37.0	−1.4	3
0	4	SSB	58	56.7	57.2	−0.5	2
0	6	CCP	36	2.0	3.2	−1.2	1
0	6	LLS	42	20.5	24.5	−4.0	2
0	8	CCS	38	32.0	9.6	22.4	0
0	10	66P	28	−7.4	−50.2	42.8	0
0	10	88S	34	5.0	−9.0	14.0	0
0	12	66S	30	6.8	−34.1	40.9	0
0	14	88B	38	26.0	9.0	17.0	0
0	16	66B	34	31.0	−9.1	40.1	0
1	0	P.17.P	49	48.2	46.5	1.7	1
1	0	S.19.S	55	55.5	55.4	0.1	1
2	0	CLC	32	6.0	0.8	5.2	1
2	0	LML	38	24.0	22.0	2.0	1
2	0	MPM	44	36.2	36.9	−0.7	3
2	0	PSP	50	47.2	48.0	−0.8	5
2	2	CLL	34	5.0	6.1	−1.1	1
2	2	LMM	40	22.0	25.7	−3.7	1
2	2	MPP	46	36.0	39.8	−3.8	1
2	2	PSS	52	50.1	50.4	−0.3	5
2	4	MPS	48	41.9	41.5	0.4	3
4	0	CMC	34	3.0	4.4	−1.4	1
4	0	LPL	40	19.0	24.7	−5.7	1
4	0	MSM	46	33.0	39.1	−6.1	1
4	0	SBS	58	56.0	58.2	−2.2	1
4	4	CMM	38	15.0	11.7	3.3	1
4	4	LPP	44	32.0	30.3	1.7	1
4	4	MSS	50	44.0	43.6	0.4	1
4	4	SBB	62	61.3	61.4	−0.1	1
6	0	CPC	36	6.0	6.9	−0.9	1
6	0	LSL	42	21.0	26.8	−5.8	1
6	0	PBP	54	47.4	51.4	−4.0	1
6	6	CPP	42	23.0	17.6	5.4	1
6	6	LSS	48	36.0	34.9	1.1	1
6	6	PBB	60	55.9	56.8	−0.9	1
8	0	CSC	38	34.0	11.5	22.5	0
8	8	CSS	46	42.5	26.6	15.9	0
12	0	6S6	30	0.0	−31.6	31.6	0

Table A1.5 Melting Points of the β′-Modification of Saturated TAGs. FREQ Indicates the Number of Measurements that has Been Averaged

X	Y	TAG	n	ΔH_f (kJ/mol)	Predicted	Residual	FREQ
−8	0	SCS	46	53.0	54.3	−1.3	1
−6	0	PCP	42	44.5	47.7	−3.2	2
−6	0	SLS	48	57.3	57.0	0.3	2
−4	0	MCM	38	40.0	39.4	0.6	1
−4	0	PLP	44	49.6	51.2	−1.6	2
−4	0	SMS	50	58.8	59.5	−0.7	3
−4	0	BSB	62	71.8	70.5	1.3	2
−2	2	PMS	48	56.1	53.5	2.6	1
0	0	888	24	−19.5	−16.7	−2.8	2
0	0	9.9.9	27	4.0	3.0	1.0	1
0	0	CCC	30	16.8	17.3	−0.5	2
0	0	11.11.11	33	27.9	28.2	−0.3	4
0	0	LLL	36	35.1	36.7	−1.6	9
0	0	13.13.13	39	41.8	43.6	−1.8	4
0	0	MMM	42	45.9	49.3	−3.4	5
0	0	15.15.15	45	50.8	54.1	−3.3	2
0	0	PPP	48	55.7	58.1	−2.4	6
0	0	17.17.17	51	61.5	61.6	−0.1	4
0	0	SSS	54	64.3	64.6	−0.3	7
0	0	19.19.19	57	65.6	67.3	−1.7	2
0	0	AAA	60	69.5	69.6	−0.1	2
0	0	21.21.21	63	71.0	71.7	−0.7	1
0	0	BBB	66	74.8	73.6	1.2	2
0	1	11.11.L	34	28.5	28.3	0.2	1
0	2	88C	26	5.5	−24.9	30.4	0
0	2	CCL	32	26.0	13.6	12.4	0
0	2	LLM	38	37.8	34.8	3.0	3
0	2	MMP	44	48.5	48.2	0.3	2
0	2	PPS	50	58.7	57.5	1.2	3
0	4	CCM	34	31.0	15.6	15.4	0
0	4	LLP	40	43.0	36.2	6.8	1
0	4	MMS	46	49.3	49.3	0.0	2
0	4	SSB	58	69.7	65.0	4.7	1
0	6	LLS	42	39.8	41.0	−1.2	2
0	8	CCS	38	38.0	30.2	7.8	1
0	10	66P	28	12.0	−22.2	34.2	0
0	10	88S	34	25.0	15.3	9.7	1
0	12	66S	30	17.0	−6.7	23.7	0

(*Continued*)

Table A1.5 Continued

X	Y	TAG	n	ΔH_f (kJ/mol)	Predicted	Residual	FREQ
1	0	P17P	49	61.2	60.9	0.3	2
1	0	S19S	55	69.8	66.7	3.1	1
2	0	8C8	26	18.5	14.3	4.2	1
2	0	CLC	32	37.7	34.5	3.2	2
2	0	LML	38	49.8	47.5	2.3	3
2	0	MPM	44	59.5	56.6	2.9	5
2	0	PSP	50	67.7	63.4	4.3	10
2	0	11.13.11	35	42.6	41.6	1.0	1
2	2	8CC	28	12.8	10.3	2.5	2
2	2	CLL	34	31.0	32.4	−1.4	1
2	2	LMM	40	42.0	46.4	−4.4	1
2	2	MPP	46	52.0	56.0	−4.0	1
2	2	PSS	52	61.8	63.0	−1.2	3
2	4	CLM	36	36.7	33.9	2.8	1
2	6	LMS	44	45.5	50.8	−5.3	1
2	8	CLS	40	40.0	43.4	−3.4	1
4	0	CMC	34	30.0	35.2	−5.2	1
4	0	LPL	40	46.7	48.2	−1.5	2
4	0	LPL	40	42.5	48.2	−5.7	1
4	0	MSM	46	55.2	57.2	−2.0	3
4	0	SBS	58	64.0	69.0	−5.0	1
4	4	CMM	38	38.0	34.7	3.3	1
4	4	LPP	44	49.5	48.1	1.4	1
4	4	MSS	50	58.3	57.4	0.9	2
4	4	SBB	62	71.5	69.4	2.1	1
4	6	LPS	46	47.0	51.5	−4.5	1
4	8	CMS	42	42.0	44.1	−2.1	1
6	0	CPC	36	36.0	34.8	1.2	1
6	0	LSL	42	43.0	48.0	−5.0	1
6	0	PBP	54	61.5	64.0	−2.5	1
6	6	CPP	42	41.0	39.3	1.7	1
6	6	LSS	48	51.4	51.4	0.0	8
6	6	PBB	60	66.1	66.2	−0.1	1
8	0	CSC	38	40.0	39.4	0.6	1
8	8	CSS	46	46.0	47.6	−1.6	1

Table A1.6 Melting Points of the β-Modification of Saturated TAGs. FREQ Indicates the Number of Measurements that has Been Averaged

X	Y	TAG	n	ΔH_f (kJ/mol)	Predicted	Residual	FREQ
−12	0	S6S	42	53.1	53.6	−0.5	2
−10	0	P6P	38	45.4	45.7	−0.3	3
−10	0	S8S	44	54.0	57.0	−3.0	5
−8	0	P8P	40	48.5	49.9	−1.4	1
−8	0	SCS	46	57.4	60.1	−2.7	4
−6	0	PCP	42	51.8	53.7	−1.9	2
−6	0	SLS	48	60.3	62.9	−2.6	3
−6	2	PCS	44	54.2	51.2	3.0	3
−4	0	MCM	38	43.5	46.0	−2.5	1
−4	0	PLP	44	53.9	57.2	−3.3	4
−4	0	SMS	50	63.3	65.6	−2.3	9
−4	2	PLS	46	57.0	54.9	2.1	2
−4	4	MCS	42	51.7	45.3	6.4	3
−2	0	C8C	28	20.0	19.9	0.1	1
−2	0	LCL	34	37.4	38.5	−1.1	3
−2	0	MLM	40	49.8	51.4	−1.6	2
−2	0	PMP	46	59.9	60.8	−0.9	6
−2	0	SPS	52	68.0	68.1	−0.1	8
−2	2	PMS	48	59.6	58.7	0.9	3
−2	4	MLS	44	54.5	50.9	3.6	2
−2	6	LCS	40	41.8	41.7	0.1	1
−1	0	P.15.P	47	56.5	57.7	−1.2	1
−1	0	S.17.S	53	65.7	64.9	0.8	2
0	0	888	24	9.1	11.4	−2.3	6
0	0	CCC	30	31.6	31.8	−0.2	8
0	0	LLL	36	45.7	45.9	−0.2	9
0	0	13.13.13	39	44.1	45.8	−1.7	5
0	0	MMM	42	57.1	56.2	0.9	10
0	0	15.15.15	45	54.6	55.5	−0.9	4
0	0	PPP	48	65.9	64.0	1.9	9
0	0	17.17.17	51	63.9	63.0	0.9	6
0	0	SSS	54	72.5	70.2	2.3	9
0	0	19.19.19	57	70.6	69.0	1.6	3
0	0	AAA	60	77.8	75.3	2.5	4
0	0	21.21.21	63	77.0	73.9	3.1	2
0	0	BBB	66	81.7	79.4	2.3	7
0	0	24.24.24	72	86.0	82.9	3.1	1
0	1	11.11.L	34	29.2	29.8	−0.6	2
0	2	88C	26	11.5	7.9	3.6	1
0	2	CCL	32	30.0	28.9	1.1	1
0	2	88C	26	11.5	7.9	3.6	1
0	2	CCL	32	30.0	28.9	1.1	1

(*Continued*)

Table A1.6 Continued

X	Y	TAG	n	ΔH_f (kJ/mol)	Predicted	Residual	FREQ
0	2	LLM	38	42.3	43.4	−1.1	4
0	2	MMP	44	53.3	54.1	−0.8	5
0	2	PPS	50	62.6	62.2	0.4	10
0	2	15.15.17	47	54.0	53.5	0.5	1
0	4	CCM	34	34.5	30.6	3.9	1
0	4	LLP	40	45.6	45.3	0.3	5
0	4	MMS	46	56.6	55.9	0.7	4
0	4	SSB	58	70.7	70.3	0.4	1
0	6	CCP	36	35.0	35.1	−0.1	1
0	6	LLS	42	45.1	48.7	−3.6	8
0	8	CCS	38	42.5	40.1	2.4	2
0	10	88S	34	31.0	29.3	1.7	2
0	12	66S	30	22.6	15.4	7.2	2
0	14	88B	38	38.0	40.1	−2.1	1
0	16	66B	34	34.0	29.3	4.7	1
2	0	8C8	26	20.5	17.9	2.6	1
2	0	CLC	32	34.0	36.4	−2.4	1
2	0	MPM	44	55.0	58.8	−3.8	1
2	0	PSP	50	65.3	66.2	−0.9	2
2	2	8CC	28	19.0	14.6	4.4	2
2	2	CLL	34	34.1	33.6	0.5	2
2	2	LMM	40	47.5	46.9	0.6	2
2	2	MPP	46	55.8	56.8	−1.0	4
2	2	PSS	52	64.4	64.4	0.0	9
2	4	LMP	42	48.5	48.8	−0.3	3
2	4	MPS	48	58.5	58.7	−0.2	5
2	6	LMS	44	49.0	52.0	−3.0	2
2	8	CLS	40	44.0	44.1	−0.1	1
4	0	CMC	34	34.0	37.7	−3.7	1
4	0	SBS	58	69.9	73.8	−3.9	2
4	4	CMM	38	43.5	36.7	6.8	1
4	4	LPP	44	54.4	50.5	3.9	4
4	4	MSS	50	60.9	60.5	0.4	6
4	4	SBB	62	73.5	73.9	−0.4	1
4	6	LPS	46	52.0	53.8	−1.8	1
4	8	CMS	42	45.0	45.7	−0.7	1
6	0	CPC	36	40.0	41.2	−1.2	1
6	0	LSL	42	49.8	53.8	−4.0	3
6	0	MAM	48	59.0	63.0	−4.0	1
6	0	PBP	54	65.5	70.0	−4.5	2
6	6	CPP	42	45.5	44.5	1.0	1
8	0	CSC	38	44.5	45.7	−1.2	1
8	8	CSS	46	48.3	52.8	−4.5	3
10	0	8S8	34	41.0	35.6	5.4	1
12	0	6S6	30	32.0	22.5	9.5	1

UNSATURATED TAGs

Table A1.7 Enthalpy of Fusion for the α-Modification of Unsaturated TAGs. Data Marked by a * Include Measurements from this chapter FREQ Indicates the Number of Measurements that has Been Averaged

X	Y	TAG	n	ΔH_f (kJ/mol)	Predicted	Residual	FREQ
−2	0	EPE	52	79	79	0	2*
0	0	SSO	54	71	81	−10	2*
0	0	SOS	54	73	81	−8	1
0	0	OOO	54	37	18	19	1
0	0	SEE	54	89	89	0	1*
0	0	EEE	54	78	78	0	1*
0	0	ESE	54	92	89	3	2*
0	2	PPE	50	118	88	30	0
0	2	PPO	50	53	68	−15	2*
2	0	PEP	50	122	91	31	0
2	0	POP	50	70	71	1	4*
2	2	POS	52	78	74	4	2
2	2	PEE	52	81	82	−1	2*

Table A1.8 Enthalpy of Fusion for the β′-Modification of Unsaturated TAGs. Data Marked by a * Include Measurements from this Chapter. FREQ Indicates the Number of Measurements that has Been Averaged

X	Y	TAG	n	ΔH_f (kJ/mol)	Predicted	Residual	FREQ
−2	0	SPO	52	126	117	9	1
0	0	SOS	54	111	129	−18	2
0	0	SOO	54	110	101	9	1
0	0	SSO	54	125	129	−4	2*
0	0	OOO	54	79	73	6	1
0	2	PPO	50	111	101	10	2*
2	0	PEP	50	135	140	−5	1*
2	0	POP	50	104	128	−24	6
2	2	PSO	52	111	123	−12	1
2	2	POS	52	114	123	−9	1
2	2	POO	52	95	95	0	1

Table A1.9 Enthalpy of Fusion for the β-Modification of Unsaturated TAGs. Data Marked by a * Include Measurements from this Chapter. FREQ Indicates the Number of Measurements that has Been Averaged

X	Y	TAG	n	ΔH_f (kJ/mol)	Predicted	Residual	FREQ
−2	0	SPO	52	126	117	9	1
−2	0	EPE	52	130	140	10	2
−2	0	OPO	52	126	111	14	1
0	0	EEE	54	148	144	4	11
0	0	ESE	54	155	160	−5	3
0	0	lll	54	84	78	6	1
0	0	SES	54	163	175	−12	2
0	0	SEE	54	155	160	−5	1
0	0	SOS	54	154	161	−7	5
0	0	OOO	54	100	101	1	5
0	2	PPE	50	157	151	6	3
0	2	SOA	56	158	160	−2	1
2	0	POP	50	140	143	−3	4
2	0	PlP	50	100	136	−36	0
2	0	PEP	50	150	158	−8	1
2	2	POS	52	150	143	7	2
2	2	PEE	52	134	141	−7	2

Table A1.10 Melting Points of the α-Modification of Unsaturated TAGs. FREQ Indicates the Number of Measurements that has Been Averaged, OMOD Indicates the Modification that was Originally Reported for the Melting Point

TAG	T_f (kJ/mol)	Predicted	Residual	FREQ	OMOD
CCE	15	8.9	6.1	1	?
COC	−16.4	−22.8	6.4	1	alpha
LLl	15.5	17	−1.5	1	?
Lll	−11.5	−15.6	4.1	1	?
MMl	20.5	22.2	−1.7	1	?
Mll	−8.5	−7.6	−0.9	1	?
MOM	11.7	4.8	6.9	2	alpha
PPO	18.4	16.8	1.6	4	alpha
PSl	36.5	32.6	3.9	1	?
PSO	25.9	21.3	4.6	2	alpha
PEP	39.4	35.6	3.8	2	alpha

(*Continued*)

Table A1.10 Continued

TAG	T_f (kJ/mol)	Predicted	Residual	FREQ	OMOD
PEE	22.8	26.1	−3.3	1	?
PlO	13.2	11.2	2	1	?
POP	16.6	17.6	−1	6	alpha
POS	19.6	21.3	−1.7	4	alpha
POl	13.3	11.2	2.1	1	?
SES	41.5	44	−2.5	2	alpha
SES	46.5	44	2.5	0	β′
SlS	37.9	37.3	0.6	3	?
SOS	22.9	27.2	−4.3	8	alpha
88E	3	5.4	−2.4	1	?
EPE	26	27	−1	1	alpha
EPE	32	27	5	0	β′
ESS	43	44	−1	1	?
ESE	34	32	2	1	alpha
EES	28.8	32	−3.2	1	alpha
EEE	15.8	19.1	−3.3	4	alpha
lPS	34.2	33.1	1.1	1	?
lPO	11.7	11.1	0.6	1	?
lSl	−3	0.2	−3.2	1	?
lSO	16.5	15.8	0.7	1	?
llO	−16.4	−15.6	−0.8	2	?
lleO	−24.7	−22.5	−2.2	1	?
lOO	−2.2	−5.7	3.5	1	?
leSl	−9.2	−7.9	−1.3	1	?
leSO	5.2	6.1	−0.9	1	?
lelS	−8.3	−7.9	−0.4	2	?
lelO	−22.4	−22.5	0.1	2	?
lelele	−44.6	−42.8	−1.8	1	al-
phaleleO	−17.8	−19.9	2.1	2	?
leOS	−2.5	6.1	−8.6	1	?
OPS	17.9	22.1	−4.2	2	alpha
OSS	30.3	27.2	3.1	6	alpha
OSO	1	−0.7	1.7	1	alpha
OleO	−15	−14.3	−0.7	1	?
OOO	−33.7	−28.8	−4.9	4	alpha

Table A1.11 Melting Points of the β′-Modification of Unsaturated TAGs. FREQ Indicates the Number of Measurements that has Been Averaged, OMOD Indicates the Modification that was Originally Reported for the Melting Point

TAG	T_f (kJ/mol)	Predicted	Residual	FREQ	OMOD
CCO	4.4	2.7	1.7	2	?
CEE	25	20.1	4.9	1	?
LLO	18	15.7	2.3	2	?
MOM	26.4	26.4	0	2	β′
PPl	26.5	24.9	1.6	1	?
PPO	34.6	34.2	0.4	8	β′
PSO	40	38	2	6	β′
PES	48.5	51.4	−2.9	1	?
Pll	−4.2	−2.9	−1.3	3	?
Plel	−7.5	−6.2	−1.3	1	?
Plele	−10.5	−10.2	−0.3	1	?
POP	33.2	34.8	−1.6	8	β′
SOS	37	42.2	−5.2	9	β′
SOS	43	42.2	0.8	0	β
ESS	56.7	54.9	1.8	1	?
ESE	43.2	45.1	−1.9	0	β
EEE	37	35.7	1.3	1β′	
lPl	−3	−2.3	−0.7	1	?
llS	2.5	3.8	−1.3	2	?
lll	−25.3	−25	−0.3	3	β′
lOS	−3.5	−1.2	−2.3	1	?
lOl	−39	−46.5	7.5	1	?
lePl	−4	−4	0	1	?
leSS	27.8	28.1	−0.3	2	?
lelle	−15.5	−15.5	0	1	?
lelel	−16.5	−15.5	−1	1	?
leOl	−28.5	−31.7	3.2	1	?
leOle	−11.1	−14.9	3.8	2	?
OSS	41.9	42.2	−0.3	10	β′
OSO	20.5	19.3	1.2	1	β′
OlS	−10.4	−1.2	−9.2	2	?
OleS	14.2	7.6	6.6	1	?
OOA	29.2	23	6.2	1	?
OOB	33.3	25.8	7.5	1	?
0.0.24	36.1	27.4	8.7	1	?
OOO	−10	−3.4	−6.6	5	β′

Table A1.12 Melting Points of the β-Modification of Unsaturated TAGs. FREQ Indicates the Number of Measurements that has Been Averaged, OMOD Indicates the Modification that was Originally Reported for the Melting Point

TAG	T_f (kJ/mol)	Predicted	Residual	FREQ	OMOD
CCl	−0.5	−9.7	9.2	1	?
CMO	13.9	16.8	−2.9	1	?
COC	−4.8	1.6	−6.4	0	β′
COC	5.9	1.6	4.3	2	β
COO	−0.3	5	−5.3	2	?
LLE	27	31.6	−4.6	1	?
LPO	29.5	24.6	4.9	1	?
LEE	35.5	38	−2.5	1	?
LOL	16.5	15.8	0.7	0	β′
LOO	5.1	4.7	0.4	3	?
MME	39.5	40.9	−1.4	1	?
MMO	23.9	22.4	1.5	2	?
MEE	40	39.8	0.2	1	?
MOM	28	28	0	2	β
MOP	27	30	−3	1	?
MOS	27	32.7	−5.7	1	?
MOO	12.8	8.3	4.5	4	?
PPE	50.2	50.1	0.1	3	?
PEP	55.3	53.7	1.6	4	β
PEP	53.9	53.7	0.2	0	β′
PEE	44.2	44.1	0.1	3	?
PlP	27.1	27.6	−0.5	2	β
PlS	24.5	28.8	−4.3	1	?
POP	37.2	37.6	−0.4	10	β
POS	31	38	−7	0	β′
POS	37.1	38	−0.9	8	β
POO	18.5	14.6	3.9	0	β′
SES	60.5	59.3	1.2	3	β
SleS	35.8	31.4	4.4	2	?
SOA	41.5	44	−2.5	1	β
EPE	44.5	46.9	−2.4	1	β
ESS	61.1	59.3	1.8	4	β
ESE	49.7	50.2	−0.5	2	β
EES	49.7	50.2	−0.5	5	β
EEE	42.2	44	−1.8	9	β
lSS	35.8	35.4	0.4	4	?
lll	−12.3	−14	1.7	6	β
leleS	−0.5	−0.5	0	1	?
lelele	−24.2	−23.5	−0.7	3	β
leOO	−13.1	−12	−1.1	2	?
OPS	40.2	41	−0.8	0	β′
OPO	19.6	17.9	1.7	3	β
OSO	23.9	22.7	1.2	4	β
OlO	−9.5	−7	−2.5	1	?
OOS	23.5	22.7	0.8	0	β′
OOO	4.8	6.1	−1.3	9	β
PEP	54	51.2	2.8	0	?

APPENDIX 2. SPECIFIC RETENTION VOLUMES OF SEVERAL PROBES IN STATIONARY PHASES OF LIQUID TAGS

Table A2.1 Specific Retention Volume in ml/g. Stationary Phase: SSS

T (°C)	82	92	102	112	123	133
n-pentane	16.856	13.332	10.611	8.567		
n-hexane	38.053	29.16	22.595	18.307	14.618	11.571
n-heptane	88.048	64.449	48.319	39.669	29.083	22.295
2-methyl-pent.	28.852	23.087	18.014	14.722	11.722	9.36
3-methyl-pent.	33.438	26.465	20.88	16.188	13.428	10.789
Benzene	88.658	65.532	50.591	39.684	31.332	24.767
Toluene	218.379	154.476	114.394	85.939	64.479	50.534
Cyclohexane	73.4	55.932	42.915	33.832	26.582	20.903

Table A2.2 Specific Retention Volume in ml/g. Stationary Phase: MMM

T (°C)	82	92	102	112	123	133
n-pentane	16.448	13.525	11.09	8.323		
n-hexane	39.175	30.356	23.319	18.389	14.449	11.715
n-heptane	90.897	66.559	50.618	38.246	29.328	23.399
2-methyl-pent.	30.691	23.922	18.619	14.482	12.019	9.926
3-methyl-pent.	34.607	27.125	21.358	16.77	13.487	11.41
Benzene	97.106	72.451	54.744	42.351	33.476	26.445
Toluene	235.44	169.84	123.941	91.414	69.741	53.632
Cyclohexane	74.389	57.106	44.007	34.218	26.791	21.699

Table A2.3 Specific Retention Volume in ml/g. Stationary Phase: 8C8

T (°C)	82	92	102	112	123	133
n-pentane	15.803	12.58	10.341	8.067		
n-hexane	37.093	28.536	22.103	17.575	14.291	11.052
n-heptane	84.266	61.824	47.214	36.302	28.01	22.596
2-methyl-pent.	28.69	22.432	17.473	13.829	11.433	9.33
3-methyl-pent.	33.008	25.125	19.726	15.558	12.576	10.561
Benzene	105.237	77.315	59	46.098	34.87	27.754
Toluene	250.008	177.156	130.416	97.67	72.598	55.754
Cyclohexane	68.781	52.18	40.569	31.692	24.866	20.14

Table A2.4 Specific Retention Volume in ml/g. Stationary Phase: 0.4487 SSS, 0.5513 MMM

T (°C)	82	92	102	112	123	133
n-pentane	15.772	12.92	10.023	8.432		
n-hexane	38.571	29.43	22.959	18.083	14.644	11.976
n-heptane	88.55	65.675	49.205	37.647	29.347	23.427
2-methyl-pent.	29.374	22.84	18.173	14.563	11.875	9.806
3-methyl-pent.	33.769	26.388	20.544	16.667	13.366	11.047
Benzene	93.42	69.591	53.302	41.705	32.528	25.958
Toluene	226.576	162.709	119.042	89.083	67.384	52.15
Cyclohexane	73.139	56.066	43.033	34.312	26.868	21.905

Table A2.5 Specific Retention Volume in ml/g. Stationary Phase: 0.7116 SSS, 0.2884 MMM

T (°C)	82	92	102	112	123	133
n-pentane	15.637	12.695	10.335	8.961		
n-hexane	37.808	29.054	22.138	18.762	14.216	11.513
n-heptane	87.566	64.7	48.113	38.308	28.667	22.664
2-methyl-pent.	29.191	22.873	17.671	14.681	11.656	9.642
3-methyl-pent.	33.639	26.154	20.204	16.969	13.17	10.806
Benzene	89.447	67.982	51.08	41.244	31.129	24.872
Toluene	216.024	157.377	114.093	88.601	65.358	50.193
Cyclohexane	71.81	55.042	42.012	34.242	26.328	21.026

Table A2.6 Specific Retention Volume in ml/g. Stationary Phase: 0.1557 SSS, 0.8443 8C8

T (°C)	82	92	102	112	123	133
n-pentane	16.106	12.78	10.684	7.576		
n-hexane	38.33	29.045	23.253	18.239	15.18	11.53
n-heptane	89.874	65.641	49.02	37.321	29.777	22.787
2-methyl-pent.	29.958	22.945	18.225	14.872	12.261	9.598
3-methyl-pent.	34.145	26.14	20.739	16.836	13.721	10.981
Benzene	103.725	76.097	58.447	44.336	35.324	27.454
Toluene	249.649	176.011	129.15	95.406	73.275	56.006
Cyclohexane	72.801	54.314	41.793	33.111	26.712	20.865

Table A2.7 Specific Retention Volume in ml/g. Stationary Phase: 0.3593 SSS, 0.6407 8C8

T (°C)	82	92	102	112	123	133
n-pentane	15.707	12.973	10.513	8.432		
n-hexane	38.224	29.198	22.737	18.077	14.426	11.369
n-heptane	88.634	63.696	48.437	37.146	28.879	22.157
2-methyl-pent.	29.616	22.65	17.992	14.799	11.769	9.388
3-methyl-pent.	33.493	25.654	20.25	16.368	12.962	10.658
Benzene	98.094	71.955	54.47	42.629	33.273	26.636
Toluene	235.818	166.864	121.852	91.705	68.986	52.84
Cyclohexane	72.015	53.896	41.858	32.677	26.331	21.08

Table A2.8 Specific Retention Volume in ml/g. Stationary Phase: 0.6023 SSS, 0.3977 8C8

T (°C)	82	92	102	112	123	133
n-pentane	16.053	12.907	10.38	8.446		
n-hexane	38.167	28.82	23.03	18.049	14.425	11.9
n-heptane	88.696	65.02	49.16	37.255	28.732	23.11
2-methyl-pent.	29.275	23.16	18.376	14.462	11.607	9.706
3-methyl-pent.	33.845	26.658	20.643	16.313	13.603	11.093
Benzene	93.481	70.449	53.696	41.189	32.5	26.462
Toluene	226.756	162.489	119.081	88.857	67.427	52.692
Cyclohexane	72.627	55.369	42.955	33.206	26.383	21.492

APPENDIX 3. PURITY OF THE TAGS USED IN SECTION 15.7

TAG	Purity (%)	Main impurities
SSS	99.6	–
PSP	99.3	–
MPM	>99.6	–
SEE	91.4	SES 8%
ESE	94.3	4.5% SSE, 1% SEO
PEE	91.1	8.6% PEP, PPE, EPE
EPE	89.8	9.1% PEP, PPE, PEE, 1.1% PEO
EEE	96.8	1.7% ESE, SEE
SOS	99.5	–
SSO	90.7	4% SOS, 3% SSE
POP	99.0	1% PEP
PPO	98.5	1.5% PPO

APPENDIX 4. BINARY PHASE DIAGRAMS OF TAGS - DATA

SSS-PSS			SSS-PSP			SSS-SPS		
X	Solidus	Liquidus	X	Solidus	Liquidus	X	Solidus	Liquidus
0.00	72.5	72.5	0.00	72.5	72.7	0.00	72.5	72.5
0.11	67.7	71.8	0.19	65.2	71.6	0.14	64.8	71.8
0.29	67.5	71.2	0.20		71.4	0.31	65.2	71.1
0.46	67.4	70.4	0.32	65.4	71.3	0.45	65.0	70.4
0.58		68.5	0.40		69.9	0.51	65.4	69.5
0.74		67.3	0.50		68.6	0.56	65.9	69.5
0.85		67.1	0.50	65.6	69.0	0.69		65.3
1.00	67.2	67.2	0.62	65.4	68.2	0.76		65.8
			0.70		66.0	0.90		66.4
			0.80	66.1	67.3	1.00	67.5	67.5
			0.88	65.7	67.8			
			1.00	68.4	68.4			
			1.00		68.7			

SSS-PPS			SSS-PPP			PSS-PSP		
X	Solidus	Liquidus	X	Solidus	Liquidus	X	Solidus	Liquidus
0.00		72.3	0.00	72.5	72.5	0.00	66.2	66.2
0.10	68.8	71.8	0.14	63.8	72.4	0.15		66.1
0.18	61.9	71.8	0.19	64.0	72.0	0.29		64.9
0.20	65.4	70.8	0.39	63.7	71.1	0.46		64.5
0.20		70.9	0.49	64.0	70.6	0.58	63.3	64.2
0.30	61.2	69.9	0.59	63.8	69.5	0.72	64.7	65.4
0.30	60.8	70.7	0.73	63.7	66.3	0.89	65.7	66.6
0.30		70.2	0.80	63.7	64.7	1.00	68.7	68.7
0.33	61.0	71.4	0.87	63.8	65.1			
0.40	61.1	69.6	0.94	63.8	65.2			
0.40	60.9		1.00	65.7	65.7			
0.50	61.0	68.9						

(*Continued*)

Appendix 4 Continued

SSS-PPS			PSS-SPS			SSS-SPS		
X	Solidus	Liquidus	X	Solidus	Liquidus	X	Solidus	Liquidus
0.50	60.8	68.3	0.00	66.3	66.3	0.00	66.1	66.1
0.50	60.6	67.9	0.15		64.9	0.14		65.0
0.55	61.0	70.3	0.30		64.6	0.24		64.3
0.59	60.8	67.3	0.45		64.9	0.38		63.8
0.60	61.0	67.8	0.59		64.9	0.51		63.2
0.65	60.9	66.2	0.72		66.6	0.68		62.8
0.67	60.8	65.7	0.89	66.0	67.4	0.87		62.3
0.67	61.1		1.00	67.9	67.9	1.00	63.5	63.5
0.70	59.5	61.0						
0.70	60.2	61.2						
0.71	59.6	60.7						
0.73	62.3	69.3						
0.75	59.7	60.4						
0.75	59.7	60.8						
0.79	61.0	62.5						
0.80	59.8	60.4						
0.80	59.6	60.8						
0.85		60.7						
0.85		60.0						
0.85		60.4						
0.91		60.8						
0.91		60.5						
0.91		60.2						
0.94		61.6						
0.95		60.6						
0.95		61.1						
0.99		60.2						
0.99		61.7						
1.00	63.4	63.4						

PSS-PPP			PSP-SPS		
X	Solidus	Liquidus	X	Solidus	Liquidus
0.00	66.1	66.1	0.00	68.5	68.5
0.17	63.0	65.3	0.20	65.2	68.1
0.25	62.4	64.9	0.26	65.2	67.4
0.42	62.9	64.2	0.37	65.3	66.1
0.53		62.7	0.48		65.6
0.68	62.8	65.0	0.53		65.2
0.90	62.8	66.0	0.66	64.6	66.1
1.00	66.0	66.0	0.79	64.6	66.7
			0.91	64.4	67.5
			1.00	67.6	67.6

(*Continued*)

Appendix 4 Continued

PSP-PPS (De Bruijne)			PSP-PPP			SPS-PPS		
X	Solidus	Liquidus	X	Solidus	Liquidus	X	Solidus	Liquidus
0.00	68.6	68.6	0.00	68.6	68.6	0.00	67.6	67.6
0.10	60.6	67.1	0.20	61.7	67.4	0.20		66.3
0.21	60.4	66.2	0.46	61.5	65.1	0.34	61.1	65.7
0.30	60.8	65.7	0.66	61.7	63.2	0.40	60.8	65.3
0.40	60.8	64.8	0.80	61.7	63.3	0.54	61.1	64.9
0.50	61.1	63.5	1.00	65.8	65.8	0.60	61.3	64.2
0.60	60.7	62.7				0.75		62.7
0.71	61.2	61.2				0.86	60.6	61.9
0.9	61.3	62.4				0.92	60.3	62.2
1.0	63.4	63.4				1.00	63.3	63.3

PSP-PPS (Perron)			SPS-PPP			PPS-PPP		
X	Solidus	Liquidus	X	Solidus	Liquidus	X	Solidus	Liquidus
0.00		68.2	0.00	67.7	67.7	0.00	63.2	63.2
0.05	65.6	67.8	0.18	61.0	66.5	0.14		62.7
0.10	64.1	67.5	0.51	60.2	63.8	0.29		61.6
0.15	62.5	66.9	0.61		62.0	0.45		62.3
0.20	62.9	66.4	0.79	60.8	63.3	0.63		62.0
0.25	61.9	66.2	0.84	60.6	63.6	0.75	61.1	63.0
0.30	61.6	65.6	1.00	66.0	66.0	0.83	61.4	64.4
0.35	61.8	64.7				0.90	61.4	65.1
0.40	60.6	64.1				1.0	63.7	65.7
0.50	60.9	63.5						
0.60	60.9	61.9						
0.65	60.7	61.3						
0.71	60.9	61.8						
0.75	60.4	61.3						
0.80	60.6	61.5						
0.85	60.9	61.6						
0.90	60.4	61.5						
0.95	60.7	61.8						
1.00	62.2	62.2						
		0.55						
		0.64						
		0.74						
		0.83						
		0.92						
		1.00						

BBB-SSS			BBB-PPP		
X	Solidus	Liquidus	X	Solidus	Liquidus
0.00	81.7	81.7	0.00	81.1	81.1
0.12	71.0	81.5	0.13	67.0	80.9
0.23	71.0	80.7	0.25	65.4	80.0
0.33	71.0	80.0	0.31	65.4	79.0
0.44	71.0	79.5	0.47	65.4	78.5
0.55	71.0	78.0	0.57	65.4	77.4
0.64	71.0	77.7	0.67	65.4	77.2
0.74	71.0	75.6	0.77	65.4	75.4
0.83	71.0	73.9	0.85	65.4	73.0
0.92	71.5	71.5	0.93	65.4	70.4
1.00	72.4	72.4	1.00	65.4	65.4

(*Continued*)

Appendix 4 Continued

SSS-LLL			SSS-888			PPP-MMM		
X	Solidus	Liquidus	X	Solidus	Liquidus	X	Solidus	Liquidus
0.00	72.6	72.6	0.00	72.5	72.5	0.00	64.3	64.3
0.15	45.7		0.23	50.2		0.11	64.0	64.0
0.25	66.7	71.0	0.52	8.4	67.0	0.22	64.0	64.0
0.39	59.9	70.1	0.78	8.4	65.9	0.32	61.8	61.8
0.48	45.7	69.2	0.94	8.4	60.6	0.43	61.4	61.4
0.59	45.7	68.0	0.96	7.0	59.1	0.53	60.1	60.1
0.68	45.7	66.9	0.97	8.4	57.7	0.63	59.8	59.8
0.79	45.7	65.1	0.99	8.4	54.1	0.72	57.2	57.2
0.85	45.7	63.6	1.00	8.4	8.4	0.82	52.9	52.9
0.937	45.7	60.0				0.91	53.2	53.2
0.955	45.7	58.4				1.00	54.5	54.5
0.975		56.4						
0.980	45.7	56.1						
0.983		54.6						
0.988	53.4	53.4						
0.993	51.6	51.6						
0.995	47.6	47.6						
1.000	46.4	46.4						

PPP-LLL			SSS-SES			SSS-SSE		
X	Solidus	Liquidus	X	Solidus	Liquidus	X	Solidus	Liquidus
0.00	65.1	65.1	0.00		72.2	0.00	72.2	72.2
0.12	63.9	64.9	0.10		71.7	0.10	69.8	71.9
0.17	59.7	64.2	0.20		71.2	0.20		71.2
0.25	56.0	63.8	0.30		70.6	0.2	68.0	71.5
0.31	55.6	63.5	0.40	69.9	0.3	67.3	71.2	
0.32	53.6		0.50		69.5	0.30		70.6
0.33	46.1		0.60		69.0	0.40		70.0
0.36		63.1	0.70		68.3	0.4	65.6	70.9
0.37	45.7	62.9	0.80		67.5	0.50		69.2
0.44		62.4	0.90		66.6	0.5	64.6	70.2
0.46		61.9	1.0		65.5	0.60		68.4
0.49	45.7	61.7				0.6	64.1	68.6
0.66	45.7	59.6				0.69	63.1	66.5

(*Continued*)

Appendix 4 Continued

0.75	45.7	
0.80		56.5
0.82		55.7
0.84		55.1
0.89		52.8
0.92	45.7	
0.94		50.1
0.95		49.6
0.967		47.1
0.970		46.7
0.973	45.7	45.7
0.989		46.3
0.995		46.4
1.000	45.7	45.7

SSS-SEE		
X	Solidus	Liquidus
0.00		72.2
0.20		71.2
0.30		70.6
0.40		70.0
0.50		69.2
0.60		68.4
0.70		67.4
0.80		66.2
0.90		65.8
1.00		63.4

0.70		67.4
0.80	62.5	65.5
0.80		66.2
0.89	62.1	64.6
0.90		65.8
0.94	62.1	63.4
1.00	62.1	62.1

PPP-SSE		
X	Solidus	Liquidus
0.00	65.8	65.8
0.05	60.8	64.5
0.10	59.5	64.2
0.14		63.0
0.21	57.6	62.9
0.29	56.4	62.3
0.41	55.6	61.3
0.50		59.8
0.54	56.2	58.7
0.56		58.3
0.59	55.7	58.6
0.61		59.3
0.64	56.2	59.8
0.67	56.1	60.4
0.70	56.0	
0.76		61.3
0.81	56.0	
0.87	57.1	61.6
0.92	59.3	61.9
1.00	61.9	61.9

PPP-EEE		
X	Solidus	Liquidus
0.00	65.4	65.4
0.05	64.2	65.1
0.09	64.2	65.0
0.14	63.7	65.1
0.19	62.9	64.7
0.23	61.6	64.5
0.28	61.4	64.2
0.33	61.0	64.3
0.38	60.0	65.0
0.43	59.0	64.6
0.48	55.9	64.6
0.53	55.4	64.7
0.58	52.2	64.4
0.63	50.6	63.0
0.68	46.9	62.5
0.73	43.9	61.3
0.78	40.3	61.2
0.84	40.0	60.0
0.89	39.8	58.0
0.95	39.3	55.0
1.00	40.3	40.3

LLL-EEE		
X	Solidus	Liquidus
0.00	46.0	46.0
0.05	44.8	46.0
0.15	43.5	46.0
0.21	42.6	45.9
0.30	41.5	44.8
0.36	40.4	45.1
0.40	39.3	44.3
0.45	38.9	44.1
0.50	38.9	44.1
0.55	38.1	43.3
0.60	40.0	42.5
0.67	37.7	42.6
0.70	37.3	39.6
0.74	37.1	38.2
0.80	37.8	39.1
0.84	37.8	39.7
0.89	38.4	40.2
0.95	38.9	40.0
1.00	39.5	40.3

(*Continued*)

Appendix 4 Continued

SSS-SOS			PPP-SOS			PPP-POP		
X	Solidus	Liquidus	X	Solidus	Liquidus	X	Solidus	Liquidus
0.00	72.8	72.8	0.00	65.8	65.8	0.00	65.9	65.9
0.06	65.5		0.09	61.6	65.5	0.06		65.4
0.17	53.6		0.19	54.5	64.7	0.10	58.4	65.0
0.23	44.3		0.26	50.0	64.2	0.13	49.6	64.6
0.27		70.9	0.35	44.0	63.7	0.25	44.8	63.6
0.51	44.3	69.3	0.47	40.6	62.6	0.35	35.2	62.7
0.61	44.3	68.3	0.57	41.0	61.1	0.45		61.6
0.75	44.3	66.1	0.69	41.2	59.0	0.56	35.2	60.5
0.83	44.3	64.5	0.79	41.0	56.1	0.63	35.2	59.5
0.91	44.3	61.3	0.88	41.6	49.5	0.80	34.5	56.4
0.95	44.3	57.8	0.93	41.0	44.0	0.85		53.6
0.97	44.3	52.0	0.94	41.6	41.3	0.88	34.7	50.7
0.99	44.3	44.8	0.97	41.8	41.8	0.95		43.0
1.00	44.3	44.3	1.00	42.3	42.3	0.97		39.5
						0.98		37.9
						0.99		37.1
						1.00	34.6	34.6

PPP-POO			SES-SSE			SOS-POS		
X	Solidus	Liquidus	X	Solidus	Liquidus	X	Solidus	Liquidus
0.00	65.7	65.7	0.00	65.4	65.4	0.00	36.5	36.5
0.06	65.3	65.3	0.10	65.3	65.3	0.10	34.2	36.5
0.08	64.5	64.5	0.20	65.2	65.2	0.20	34.2	37.0
0.15	13.6	64.7	0.30	65.0	65.0	0.30	34.5	38.5
0.32	14.7	63.3	0.40	64.9	64.9	0.40	35.0	39.0
0.49	17.1	61.3	0.50	64.7	64.7	0.50	35.5	40.5
0.68	17.7	58.1	0.60	64.5	64.5	0.60	35.5	41.8
0.83	17.9	54.5	0.70	64.2	64.2	0.70	36.5	42.5
0.92	18.5	50.0	0.80	64.0	64.0	0.80	38.0	43.0
1.00	18.6	18.6	0.90	63.6	63.6	0.90	40.5	43.5
			1.00	63.3	63.3	1.00	44.0	44.0

(*Continued*)

Appendix 4 Continued

SOS-POP			POS-POP			POP-PEP		
X	Solidus	Liquidus	X	Solidus	Liquidus	X	Solidus	Liquidus
0.00	44.0	44.0	0.00	36.5	36.5	0.00	33.0	33.0
0.10	38.5	43.5	0.10	34.0	36.2	0.08	31.1	41.7
0.20	35.5	43.0	0.20	32.0	36.0	0.16	31.5	45.3
0.30	35.0	42.5	0.30	31.0	35.5	0.25	31.1	47.1
0.40	35.0	41.5	0.40	31.8	35.2	0.50	31.1	52.9
0.50	34.0	40.0	0.50	31.5	34.0	0.75	36.0	54.4
0.60	34.0	39.0	0.60	31.5	34.5	1.00	57.0	57.0
0.70	33.5	37.0	0.70	31.5	35.5			
0.80	33.5	36.0	0.80	31.5	35.5			
0.90	33.5	36.5	0.90	34.0	37.0			
1.00	37.2	37.2	1.00	37.2	37.2			

PPO-POO			PPO-OPO			POO-OPO		
X	Solidus	Liquidus	X	Solidus	Liquidus	X	Solidus	Liquidus
0.00	32.6	32.6	0.00	34.7	34.7	0.00	19.3	20.0
0.17	11.8	32.7	0.11	28.9	33.1	0.04	18.7	19.8
0.29	12.3	32.0	0.25	25.3	31.1	0.08	17.6	19.4
0.40	12.2	31.0	0.40	22.7	29.6	0.23	14.0	18.4
0.47	12.1	29.7	0.50	21.1	29.1	0.38	12.0	17.6
0.62	12.8	28.0	0.55	19.3	28.7	0.52	11.2	15.6
0.78	13.1	26.3	0.60	18.2	28.0	0.62	11.1	16.3
0.84	14.6	18.3	0.70	17.8	26.2	0.77	11.6	18.4
1.00	18.6	18.6	0.80	18.2	23.1	0.91	14.0	18.9
			0.85	17.8	20.2	1.00	19.8	19.8
			0.87	17.6	19.8			
			0.90	17.6	18.7			
			0.95	17.8	19.1			
			0.98	18.2	19.2			
			1.00	19.3	19.3			

(*Continued*)

Appendix 4 Continued

SSS-OOO			PPP-OOO			SOS-OOO		
X	Solidus	Liquidus	X	Solidus	Liquidus	X	Solidus	Liquidus
0.00	73.9	73.9	0.00	64.5	64.5	0.00	42.8	42.8
0.01		72.5	0.10			0.12	42.4	42.4
0.11		71.9	0.20			0.33	41.3	41.3
0.29		70.3	0.30			0.52	40.3	40.3
0.33	5.4	68.9	0.40			0.81	35.3	35.3
0.51		68.4	0.50			0.90	32.1	32.1
0.54		64.5	0.60			0.96	30.0	30.0
0.58		64.2	0.70			0.98	28.2	28.2
0.62		65.4	0.80			1.00	5.4	5.4
0.71		64.9	0.83		54.3			
0.80		64.1	0.88		52.3			
0.83	5.4	65.4	0.90					
0.84		62.7	0.91		50.3			
0.84		60.7	0.93		49.0			
0.85		66.1	0.942		47.3			
0.88		60.0	0.956		44.7			
0.89	4.9	62.4	0.971		42.7			
0.89		66.6	0.978		41.0			
0.899		61.9	0.989		38.0			
0.907		57.3	0.991		35.7			
0.920		56.0	0.993		34.3			
0.920		54.0	0.996		32.7			
0.947		54.7	1.000	6.7	6.7			
0.949		57.8						
0.960		52.0						
0.960		51.3						
0.974		47.3						
0.974		44.7						
0.975		55.0						
0.980		50.0						
0.987		41.3						
1.000	5.4	5.4						

(x in mol fraction, solidus and liquidus in °C)

REFERENCES

1. Poot C, Biernorth G. In: The Lipids HandbookGunstone FD, Harwood JL, Padley FB, eds. London: Chapman and Hall, 1986.
2. Larsson K. In: The Lipids HandbookGunstone FD, Harwood JL, Padley FB, eds. London: Chapman and Hall, 1986.
3. Duffy P. J Chem Soc 1853; 5:197.
4. Chapman D. Chem Rev 1962; 62:433.
5. Larsson K. Arkiv Kemi 1964; 23:35.
6. Simpson TD, Hagemann JW. JAOCS 1982; 84:349.
7. Hernqvist L, Larsson K. Anstrichmittel 1982; 84:349.
8. Hagemann JW, Rothfuss JA. JAOCS 1983; 60:1123.
9. Sato K. Food Microstructure 1987; 6:151.
10. Sato K, et al. JAOCS 1989; 66:664,1614.
11. Gibon V. Thesis. Universite Notre Dame de la Paix, Namur, 1984.
12. Kellens M, Meeussen W, Riekel C, Reynaers H. Chem Phys of Lipids 1990; 52:79.
13. de Jong S. Thesis. Rijksuniversiteit Utrecht, 1980.
14. Cebula DJ, McClements DJ, Povey MJW. JAOCS 1990; 67: 76.
15. Hagemann JW, Rothfus JA. JAOCS 1988; 65:1493.
16. Timms RE. Prog Lip Res 1984; 23:1.
17. Hernqvist L. Thesis. University of Lund, 1984.
18. Nyvlt J. J Chem Prum 1967; 18:260.
19. Perron R. Rev Fr Corps Gras 1986; 33:195.
20. Wieske T. Internal Unilever report BAH D7019 (1970).
21. Wieske T, Brown K. Private communication, 1986.
22. Prausnitz JM. Molecular thermodynamics of fluid phase equilibria. New York: Prentice Hall, 1986.

23. Zief M, Wilcox WR. Fractional solidification. New York: Marcel Dekker, 1967.
24. van Putte K, Bakker B. JAOCS 1987; 64:1138.
25. Knoester M, de Bruijne P, van den Tempel M. J Crysal Growth 1968; 3:776.
26. Norton IT, Lee-Tuffnell CD, Rowlands DW. Unilever Research Colworth 1985; 85:1175.
27. Norton IT, Lee-Tuffnell CD, Ablett S, Bociek SM. JAOCS 1985; 62:1237,1261.
28. Gautam R, Seider WD. AIChE J 1979; 25:991,999.
29. Shah VB. Thesis. University of Toledo, 1980.
30. Asselineau L, Jacq J. Fifth Annual Conference on Fluid Properties and Phase Equilibrai. Banff. Canada, 1989.
31. Michelsen M. Fluid Phase Eq 1982 9:1, 1982; 9:21, 1989; 16.
32. Swank DH, Mullins JC. Fluid Phase Eq 1986; 30:101.
33. Crowe CM, Nishio M. AIChE J 1975; 21:528.
34. Murray W, Gill PE, Wright M. Practical Optimization, London: Academic Press, 1981.
35. Knoester M, de Bruijne P, van den Tempel M. Chem Phys Lipids 1972; 9:309.
36. Wesdorp LH, Struik M. European Patent EP 0264149, 1990.
37. Juriaanse AC. Butterlike margarines. Unilever Research Report VD 85 6003, 1985.
38. Christophersen MJN. Study of some fat blends with DCS. Unilever Research Report 1986; 86:3274.
39. Busfield WK, et al. JAOCS 1990; 67:171.
40. Smith K. Unilever Research Colworth. Private communication. 1988.
41. Norton IT, et al. JAOCS 1985; 62:1237.
42. Yap PH, de Man JM, de Man L. JAOCS 1989; 66:693.
43. Broadhurst MG. J Res NBS-A 1962; 66:241.
44. Wurflinger A. Thesis. University of Bochum, 1972.

45. Perron R. Rev Fr Corps Gras 1984; 31:171.

46. Flory PJ, Vrij A. JAOCS 1963; 85:3548.

47. Billmeyer FW. J Appl Phys 1975; 28:115.

48. Bommel M. Thesis. Rijksuniversiteit Utrecht, 1986.

49. Timms RE. Chem Phys Lipids 1978; 21:113.

50. Dollhopf W, Grossmann HP, Leute U. Colloid and Polymere Sci 1981; 259:267.

51. Zacharis HM. Chem Phys Lipids 1977; 18:221.

52. Bailey AN. Melting and solidification of fats. New York: Interscience, 1950.

53. de Bruijne P, Eedenburg J. Unilever Research Report PVD 83 3062, 1983.

54. Hagemann HW. JAOCS 1975; 60:1123.

55. Zacharis HM. Ad X-ray Anal 1975; 18:535.

56. Gray MW, Lovegren NV. JAOCS 1978; 55:310,601.

57. Lovegren NV. JAOCS 1976; 53:519.

58. Norton IT. Unilever Research Report PCW 84 1065, 1984.

59. Ollivon M, Perron R. Thermochimicia Acta 1982; 53:183.

60. Ollivon M, Perron R. Chem Phys Lipids 1979; 25:395.

61. Hagemann HW. Crystallization and polymorphism of fats. In: Surfactant Science. Garti N, Sato K, eds. New York: Marcel Dekker, 1988.

62. Garti N, Schlichter J, Sarig S. Fat Sci Technol 1988; 90:295.

63. Gibon V. Thesis. Universite de Namur, 1986.

64. de Jong S, van Soest TC. Acta Cryst 1978; B34:1570.

65. Birker PJMWL, de Jong S, Roijers EC, van Soest TC. JOACS 1991; 68:895.

66. de Bruijne P, van den Tempel M, Knoester M. Chem Phys Lipids 1972; 9:309.

67. Hannewijk J, Haighton AJ, Hendrikse PW. Analysis and characterization of oils, fats, and fat products. London: Interscience, 1964.
68. Hendriske PW. Dilatation of fats. Unilever Research.
69. Fredenslund A, Gmehling A, Rasmussen P. Vapor-liquied equilibria using UNIFAC. Amsterdam: Elsevier, 1977.
70. Fifth International Conference on Phase Equilibria for Chemical Process Design, 1989.
71. Desty DH, et al. Gas chromatography. London: Butterswoth, 1962.
72. Grob RL. Modern practices of gas chromatography. New York: J Wiley, 1985.
73. Smith JM, van Ness HC. Introduction to chemical engineering theromodynamics, 4th edition. New York: McGraw-Hill, 1987.
74. Desphande DD, Patterson D, Schreiber HP, Su CS. Macromolecules 1974; 7:530.
75. Gandasasmita I. Thesis. Technische Universiteit Delft, 1987.
76. Muller A. Proc Roy Soc 1932; 138:514.
77. Small D, et al. The physical chemistry of lipids: handbook of lipid research 4. New York: Plenum Press, 1984.
78. Human H, Ende J, Alderliesten L. Poster at AOCS meeting Masstricht. Netherlands, 1989.
79. Luzatti V, Mustacchi H, Skoulios A, Husson F. Acta Cryst 1960; 13:660.
80. van den Tempel M. Physicochimie des Composes Amphiphiles. Colloques Nat 1979; 938:261.
81. Pamplin BR. Crystal Growth. New York: Pergamon Press, 1980:526–530.
82. Grootscholten PAM. Jancic: industrial crystallization, 1986.
83. Kitaigorodskii AI. Molecular crystals and molecules. London: Academic Press, 1973.
84. Haget Y, et al. Second codata symposium on prediction of phase equilibria in mulitcomponent systems, 1985.
85. Won KW. Fourth international conference on fluid properties and phase equilibria for chemical process design. Helsingor. Denmark, 1986.

86. Won KW. Fifth international conference on fluid properties and phase equilibria for chemical profess design. Banff. Canada, 1989.

87. Hansen HA, Fredenslund A, et al. A thermodynamic model for predicting wax formation in crude oils. Danmark: Tekniske Hojskole, 1987.

88. Null HR. Phase equilibria in process design. New York: Krieger, 1980.

89. Fischer J, Moeller D. 1985; 1:246.

90. Morancelli M, Strauss HL, Snyder RG. J Phys Chem 1985; 89:5260.

91. Rossell JB. Adv Lip Res 1967; 5:353.

92. de Bruijne P, Reckweg F. P VD 71:3637.

93. Grootscholten PAM. Unilever Research Vlaardingen, private communication, 1987.

94. Kerridge R. Unpublished work. Private communication to J.B. Rossel. 1952.

95. Lutton ES. JAOCS 1955; 32:49.

96. de Bruijne P, Reckweg F. P VD 72:3275.

97. Perron R, Petit J, Matthieu A. Chem Phys Lipids 1971; 6:58.

98. De Smedt A, Gibon V. Private communication, 1990.

99. Krautwurst J. Keiler Milchw Forsch Ber 1972; 22:255.

100. Barbano P, Sherbon JW. JAOCS 1977; 55:478.

101. Grootscholten PAM. Calculation of solid liquie equilibria in fats. LP VD 3074; 84.

102. Janelli L. 1985; 1:246.

103. Hagemann HW. JAOCS 1975; 52:204.

104. Brumbaugh EE, Johnson ML, Huang C. Chem Phys Lipids 1990; 52:69.

105. Vetterling W, Teukolsky S, Press W, Flannery B. Numerical Recipes. Cambridge: Cambridge University Press, 1990.

106. Kung HC. Internal Unilever Report LB 113. 1950.

107. Clements MS, Rossell JB. Internal Unilever Report P WN 660044. 1966.

108. Freeman IP. Internal Unilever Report, Port Sunlight Program. Spring 1957:45.

109. Vazquez Ladron R, Castro Ramos R. Gracas y Aceites 1971; 22:401.

110. Malkin T, Carter MGR. J Chem Soc 1947:554.

111. Kitaigorodskii AI. Mixed crystals: solid state sciences 33. Berlin: Springer Verlag, 1984.

112. Keulemans K. Unilever Research Vlaardinger: Private communication, 1986.

113. Hernqvist L, Larsson K, et al. J Sci Food Agric 1981; 32:1197.

114. Hernqvist L, Anjou K. Fette Seife Anstrichmittel. 64; 85.

115. Chanh NB, Haget Y. Acta Cryst 1972; 28:3400.

116. Chanh NB, Haget Y. J Chem Phys 1975; 72:760.

16

Imaging of a Model Plastic Fat System by 3-Dimensional Wide-Field Transmitted Polarized Light Microscopy and Image Deconvolution

JERROLD W. LITWINENKO
Department of Food Science
University of Guelph
Guelph, Ontario, Canada

1. BACKGROUND

1.1. Introduction

Food lipids, such as butter, margarine, cocoa butter, vegetable shortenings, and lard are widely used as functional ingredients in foods high in fat [1–8]. The primary role of fats in foods is to impart sensory attributes such as creaminess, mouthfeel, spreadability, melting profile, cohesiveness, and structure [3,4,7,9–12]. In many food applications, the fat component ex-

ists in a semisolid state, in the form of a fat crystal network [4,12–14].

Because fats are composed of a wide variety of triglycerides (i.e., they are multicomponent systems), they exhibit a wide range of melting and crystallization temperatures. This property of fats results in a high degree of variability of crystallization behavior when subjected to various crystallization conditions. Variables such as the rate of cooling, the degree of supercooling, the presence of shear and storage time can all result in different microstructures [1,2,5,7,8,10,14–23]. Altering crystallization conditions results in differences in the properties of the network on the microstructural level, which can include changes in crystal size, morphology, number, and degree of crystal distributional order [7,8,14]. These changes on the microscopic level result in changes in the interactions between the particles that make up the network, which in turn influence macroscopic properties [4,12–14,24]. Therefore, it is important to further our understanding of the relationship between microstructure and rheologic properties.

Of particular interest is the fractal scaling behavior demonstrated by fat crystal networks. Two-dimensional (2D) fractal analyses on images of thin film networks have been extensively studied, which suggest that the relative degree of order and fill in the networks can be quantified and used to make predictions pertaining to mechanisms of network formation and macroscopic rheologic properties [4,7,12–14,24]. These analyses have been compared to three-dimensional (3D) fractal dimensions determined by rheologic methods with intermediate success [4,7,12]. This has led to many questions related to the fundamental differences between 2D and 3D crystallization conditions and their resulting fractal dimensions. Imaging and fractal analysis of fat crystal networks in 3D would therefore be of high value.

Imaging of fat crystal networks in three dimensions, however, is far from trivial. Many efforts have involved 3D imaging techniques, such as confocal, electron, and atomic-force microscopies, and have resulted in successful but limited interpretations of the 3D structure of bulk fats [25–27]. Although all of these techniques are highly valuable in their own respects, limi-

tations inherent to these methodologies hinder the ability to resolve and view the internal structures of thick sections or volumes of bulk fats. For this reason, a novel 3D imaging technique capable of viewing thick sections of bulk fats was pursued.

Three-dimensional imaging using fluorescence and brightfield light microscopies and confocal laser scanning microscopy has been well established [28–36]. Optical sections through a volume are acquired by using a z-stage motor, and contain both in-focus and out-of-focus detail. The process of image deconvolution reassigns unfocused pixels to their most likely location by means of complex 3D algorithms [33,34]. The main objective of this study was to adapt and assess the validity of this optical–sectioning, 3D imaging and deconvolution technique to a transmitted polarized light imaging modality. On doing so, a new means of observing fat crystal networks in unconfined space would be established, and a greater understanding of the effects of confinement on network formation and fractal dimensionality could be pursued.

1.2. Objectives

The overall aims of this work were:

1. To develop and assess the validity of a new 3D imaging technique. This involved the design of a sample holder that would allow for volumetric imaging of fat crystal networks. Three-dimensional volume data sets were then obtained by wide-field polarized light microscopy. These data sets were then to be deconvolved by two different methods (nearest neighbors and blind algorithms) and their relative successes compared.
2. To further our understanding of the crystallization of fats in three dimensions and make comparisons to the results of traditional 2D thin film crystallization conditions. This included an examination of crystal morphology, particle sizes, and distributions of mass in both volume and thin film conditions to investigate possible mechanisms or network formation and influences of confinement on network properties and growth.

3. To further our understanding of the fractal nature of fat crystal networks. This involved the determination of fractal dimensions of 2D slices from a 3D volume, as well as 2D projections of a 3D volume. Also, the development of a novel means of determining a relative degree of order from images was pursued. These studies aimed to further our understanding of the factors that influence fractal dimensions determined by particle-counting and by box-counting methods (D_f and D_b) as well as comparison to those determined from 3D rheologic methods.
4. To offer insight into future developments of this new 3D imaging technique. This included an investigation into the assumptions and limitations inherent to the technique being developed. Suggestions for further experiments and verifications of the validity of the new method were also an aim of this research.
5. To determine if changing imaging systems has any impact on image analysis fractal dimension parameters D_f and D_b. This involved comparison of results from this study to results obtained in the past, using an older microscope and camera system.

1.3. Literature Review

1.3.1. The Fractal Nature of Fat Crystal Networks

1.3.1.1. The Concept of Fractality

Fractal geometry was first proposed by Benoit Mandelbrot in 1982 as a means of quantifying objects of complex structure that defy classical Euclidean geometry [37].

In order for an object or distribution of objects to be fractal in nature, the following conditions must be met:

- It must have a dimensionality of noninteger (non-Euclidian) value
- It must display self-similarity
- It must exhibit scaling behavior within the range examined

The concept of fractality is difficult to understand without first referring to a few examples that demonstrate the concept.

Classical Euclidean geometry deals with objects that possess dimensionalities of integer values. These objects fill Euclidean space or their "embedding" space of dimension d. Examples that fall into this category include a line ($d = 1$), a plane ($d = 2$), and a cube ($d = 3$) [4]. Fractal geometry, on the other hand, serves as a means to quantify objects of intermediate, or noninteger values, and is assigned a fractal dimension D [38]. For example, if kinks were introduced in a line or plane, or an object of approximate cubic shape contained voids, these objects would no longer exist as classical Euclidean objects with integer dimensions [4].

1.3.1.1.1. Self-Similarity and Scaling Behavior: Perfect fractal objects are objects that display scale invariance (i.e., they display exact self-similarity). Simply put, this means that fractal objects appear the same at various scales [38]. Natural systems, however, do not occur as perfect fractals, but rather display statistical self-similarity within a finite range of length scales because randomness is introduced by the complexity of structure formation [4,12]. A common example of statistical self-similarity is the tree analogy: a small branch of a tree closely resembles a large branch of the tree, which closely resembles the tree. Although (by comparison to perfect fractals) the range of fractal scaling behavior exhibited by natural systems is narrow, this does not mean that natural systems are not fractal [12]. For example, it has been demonstrated in colloidal gels that scaling behavior exists within the range the size of primary particles to the size of the clusters of particles [4,12,38–40]. Knowledge of a materials structure allows for fractal analyses to be performed within the range of scaling behavior [12].

1.3.1.1.2. Fractal Dimension Determination: Fractal dimension determination is often demonstrated with a classical example. If one were to closely examine a map of the coast of England, which is approximately a plane, ($d = 2$) by iteratively measuring its perimeter with rulers of decreasing size, its fractal dimensionality ($D < 2$) could be determined [38]. This is an example of the fractality of an object determined by

the scaling relationship between perimeter and length, and is just one of many methods that can be used to determine an object's fractal dimension.

Determining the fractal dimensions of an object or distribution of objects in space can also be performed by examining mass–distance relations [4,38,41–43]. Typical mass–radius techniques involve the iterative computation of a property of the object (which can be mass, area, length, density, etc.) as a function of the decreasing radius of a circle placed on the object [43]. The general relationship examined by mass–distance techniques is as follows:

$$P(R) \approx R^D \tag{1}$$

where the measured property (P) is proportional to the radius of the circle (R) containing the measured property raised to the exponent D, which is the objects fractal dimension. Plotting P(R) as a function of R in a log-log fashion results in a linear relationship with a slope equal to D [38,41,43]. Mass–distance methods are usually preformed on objects in a 2D embedding space, or projections of 3D objects onto a 2D space. This is the case when examining fractal dimensions from images of microstructures formed in thin films, and 2D projections of 3D volumes, respectively.

Additional methods for determining fractal dimension involve the scaling behavior exhibited by physical properties of fractal systems [38a,44–50]. One pertinent example is the 3D scaling behavior observed between mechanical properties and solids volume fraction, which will be discussed in more detail later. Before referring to this specific example, however, a short discussion on the mechanisms of fractal network formation is appropriate.

1.3.1.1.3. Diffusion-Limited Aggregation: The rate of growth of larger structures that make up fractal networks (including colloidal gels and fat crystal networks) is believed to be dictated by heat and mass transfer (diffusional) processes [4,43]. In the case of fat crystal networks, primary particles (about 2–6μm in size) formed by nucleation and growth diffuse to the surface of other primary particles and aggregate to form larger microstructures (approximately 100–200μm), which

then aggregate to form a solid 3D network [4]. This theory suggests that network formation may be due to both particle-cluster and cluster-cluster aggregation processes, which may confound the fractal dimension determination [38]. Computer simulations have been performed to predict the fractal dimensions of structures formed by various diffusional mechanisms including particle-cluster aggregation and cluster-cluster aggregation [38,41,43].

1.3.1.1.3.1. Particle-Cluster Mechanism: In the simplest of cases, DLA occurs when drifting particles irreversibly adhere to existing clusters, leading to a branched, wispy structure with $D = 1.7$ in 2D embedding space and $D = 2.5$ in 3D embedding space [38,43].

1.3.1.1.3.2. Cluster-Cluster Mechanism: In more complicated cases of DLA, rather than particles diffusing and adhering to existing clusters, a process of irreversible cluster-cluster aggregation occurs leading to the formation of single large clusters. In this instance, computer simulations result in a predicted fractal dimension $D = 1.7–1.8$ in 3D embedding space [43].

1.3.1.1.4. Reaction-Limited Cluster-Cluster Aggregation: As is implied by its name, for reaction-limited cluster-cluster aggregation (RLCA) the rate of aggregation depends not on diffusional processes (as in DLA) but on the reaction rate of cluster-cluster aggregation. This implies that when clusters come together they may be reversibly unattached [38,43]. It is therefore highly unlikely that fractal analysis of irreversible colloidal gels or fat crystal networks would reveal RLCA behavior. Computer simulations predict a mass fractal dimension of $D = 1.53$ and $D = 1.98–2.11$ for reaction-limited growth in 2D and 3D embedding spaces, respectively [38,43].

1.3.1.1.5. Rules of Fractal Scaling: As will be discussed later, efforts to determine the fractal dimension of fat crystal networks have been performed by both 2D and 3D analyses (image analysis of thin films and rheologic scaling methods respectively) and their values compared [4,7,12]. This

being the case, there are a number of "rules" related to fractal scaling that are relevant to our studies. In particular, rules related to fractal dimensions in varying Euclidean spaces are of interest. Viscek states the following [38]:

1. Many times it is the projection of a fractal that is of interest or can be experimentally studied (e.g., a picture of a fractal embedded into $d = 3$). In general, when projecting a $D<d\text{-}m$ dimensional fractal onto a d-m dimensional surface results in a structure with the same fractal dimension $D_p = D$. For $D \geq d\text{-}m$ the projection fills the surface, $D_p = d\text{-}m$.
2. Cutting out a d-m dimensional slice (cross-section) of a D dimensional fractal embedded into a d dimensional space usually leads to a D-m dimensional object.

Interpretation of rule 1 would suggest that a fractal object of dimensionality of $D<2$ in 3D space, when projected onto a 2D plane, would retain its fractal dimension ($D<2$). If, on the other hand, the object in 3D embedding space had a fractal dimension of $2 \leq D \leq 3$ when projected onto a 2D plane, it would fill the plane and result in a $D = 2$.

Rule 2 suggests that if a 2D cross-section were taken of a fractal with dimensionality D embedded in 3D space its fractal dimension would be reduced to $D-1$. This rule has also been interpreted in reverse, with a value of 1 added to D when translating a fractal measured on a 2D plane into 3D space. Little in the way of experimental evidence can be found to verify the validity of such an interpretation; however, in some cases, this translation has been found to be satisfactory [7,12,51].

A clearer understanding of these complex fractal scaling principles and their relevancy to our studies can be attained following a discussion on how these principles were first developed by Brown and Ball [52,53] and later demonstrated for the analysis of colloidal aggregates [38a]. For the sake of simplicity and relevancy, discussions on fractal scaling theory to follow will focus on the theory introduced by Brown and Ball and the techniques demonstrated by Shih et al., followed by their adaptation to fat crystal networks. Continuing efforts to determine the fractal dimension of fat crystal networks by image analysis of microstructure will also be discussed.

1.3.1.2. Fractality as It Pertains to Colloidal Gels

Brown and Ball demonstrated that colloidal aggregates behave as 3D mass fractals [52,53]. In colloidal gels that are composed of a disordered distribution of mass containing statistical self-similar patterns, the observed power–law relationship between the elastic modulus and the solid volume fraction was discovered [52,53]. These findings formed the basis for continued studies by Shih et al., who developed a scaling theory explaining the elastic properties of colloidal gels via the fractal flocculation within two distinct rheologic regimes: the weak-link and the strong-link regime [38a].

1.3.1.2.1. The Strong-Link Regime: At low particle concentrations, clusters grow large and act as weak springs, and, as a result, the elastic constant of the gel (K) is dominated by the elasticity of the flocs themselves, and follows the relationship:

$$K \sim \phi^{(d\,+\,x)/(d\,-\,D)} \tag{2}$$

where Φ is the volume fraction, d the Euclidean dimension, D the fractal dimension, and x is the backbone fractal dimension [38a]. However, this relationship does not apply to fat crystal networks because, at low volume fractions, a solid 3D network is not formed [4].

1.3.1.2.2. The Weak-Link Regime: At high particle concentrations, small flocs act as strong, hard springs, and, as a result, the elastic constant of the gel (K) is dominated by the interfloc links. This can be expressed in a system of size L:

$$K \sim \left[\frac{L}{\xi}\right]^{d-2} K_l \sim \xi^{-(d-2)} \tag{3}$$

where K_l is the elastic constant of the interfloc links, and ξ is the average size of the flocs.

If the fractal dimension of the microstructures is D, assuming that the volume fraction within flocs is equal to the volume fraction of the system [38a,54], then the scaling relationship between the average floc size and the volume fraction can be expressed as:

$$\xi \sim \Phi^{1/(D\ -\ d)} \tag{4}$$

Combining equations 2 and 3, it follows that:

$$K \sim \Phi^{(d\ -\ 2)/(d\ -\ D)} \tag{5}$$

and for an object in 3D Euclidean space:

$$K \sim \Phi^{1/(3\ -\ D)} \tag{5a}$$

Consequently, a log-log plot of the elastic constant (K) vs. the volume fraction (Φ) is linear with the slope being -D. The value of D is the fractal dimension of the colloidal gel.

Since the initial discovery of the fractal nature of colloidal gels, much research has verified the validity of the model. In 1992, Wessel and Ball used fractal scaling properties to examine fractal aggregation in gels under applied shear [45]. Colloidal aggregation experiments employing light scattering techniques have been successful in assessing cluster structure and the arrangement of clusters in gels [46] and in determining internal dynamics and elastic moduli of very weak gels [47]. Recent work has also examined the concentration dependence of the cluster fractal dimension in colloidal aggregation [48].

1.3.1.3. The Adaptation of Fractal Scaling to Fat Crystal Network

Vreeker et al. were the first to suggest that the fractal scaling behavior observed in whey protein gels could hold true for fat crystal networks becuase the structure of fat crystal networks closely resembles that of a flocculated colloidal system [55,56]. In 1996, Rousseau and Marangoni applied the model developed by Shi et al. to fat crystal networks at high volume fractions (in the weak-link regime) [57]. They found that the shear elastic modulus of fat systems varied with the solid volume fraction as a power–law relationship, similar to that observed previously in colloidal gels. Since microstructures are the closest level of structure to the macroscopic network, it stood to reason that the application of small deformations on the network could be related to the fractal dimension as adapted from the model proposed by Shih et al. (equation 5) as follows:

$$G' \sim \lambda \Phi^{1/(3\ -\ D)} \tag{6}$$

where G′ is the shear elastic modulus determined within the linear viscoelastic region, Φ is the volume fraction (solid fat content/100), and *D* is the fractal dimension, and

$$\lambda \sim \frac{A}{6\pi a d_o^2 \gamma_o} = \frac{2\delta}{a} \tag{7}$$

where *A* corresponds to Hamaker's constant, a to the diameter of the primary particles, d_o to the intercluster separation distance, γ_o to the shear strain at the limit of linearity, and δ to the crystal-melt interfacial tension [4,12–14,58]. It must be noted, however, that the value of λ only remains constant within a certain range of solids' volume fraction. At higher volume fractions and following the formation of the network structure, coarsening may affect the value of λ [12]. A representative schematic of a fat crystal network is presented in Figure 1.

1.3.1.3.1. Weak-Link Rheologic Method for the 3-Dimensional Fractal Dimension Determination: To determine an estimate of the 3D fractal dimension of fat crystal networks, the shear elastic modulus is measured at varying

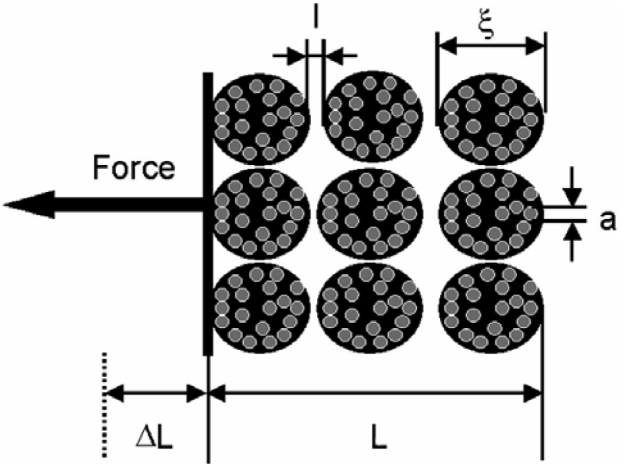

Figure 1 An idealized schematic of a fat crystal network under an applied stress.

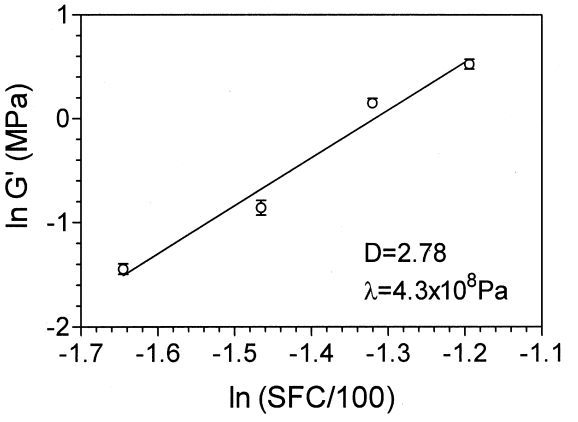

Figure 2 Log-log plot of the storage modulus (G′) vs. the solids volume fraction (solid fat comtent/100) used to determined the three-dimensional fractal dimension of a lard crystal network.

volume fractions [4,12–14,57]. This is performed by creating dilutions of the material in a solvent that does not solubilize the material in the temperature range at which rheologic measurements are to be preformed [4,12–14]. This has typically been performed by diluting the fat system in canola oil and crystallizing the dilutions at 5°C [4,12–14]. The slope of the linear relationship between the storage modulus (G′) and volume fraction (SFC/100) determines the fractal dimension of the fat system [4,12–14]. A representative plot depicting results for lard is presented in Figure 2.

Because self-similarity is observed in polarized light images of fat crystal networks, many efforts to determine the fractal dimensions of fat systems on the basis of microstructure have also been pursued and will be addressed in the following section.

1.3.1.4. Fractal Dimensions by Microscopy and Image Analysis

1.3.1.4.1. Particle-Counting Fractal Dimension (D_f): Assuming a statistically constant microstructural ele-

ment (or particle) size, the relationship between radius and mass can be altered (equation 8) to determine the fractality of crystal networks from 2D PLM images [5,7,13].

In this case, the scaling relationship between the number of discrete particles (N) and the length of the square region of interest containing the particles (L) can be expressed as:

$$N = cL^D \tag{8}$$

where c is a constant, and N is the number of distinct particles within a region of interest of length L. It has been demonstrated that the use of a square region of interest (in lieu of a circle) allows for the computation of the mass fractal dimension [42]. Much like equation 1, this method involves an iterative measurement of the number of particles as a function of the size of the decreasing regions of interest (ROI). To begin, the number of particles is first counted within the entire image. At 5% increments, the image is cropped thereby making a new, smaller length L, and the number of particles in each new image counted. This process is repeated until the length of the image is 35% of the original size [12,59].

Caution must be taken to avoid the occurrence of artIfacts in this method. First, the effect of the contribution of small boxes is a skewing of the D value to elevated values. This occurs because, as the box size gets small, a tailing off occurs on the log-log plot of N(L) vs. L. Once the box sizes become very small, the length of the box sizes decreases faster then the areas of the ROIs. This is especially problematic if the features falling on the edges of the ROI are large, since they will be greatly included and excluded in their respective counts. For this reason, performing the counts on ROIs representing 100–35% of the original box size is more accurate [12,59].

The number of particles counted within each box size of various lengths (L) is then plotted on a log-log scale, and the slope of the line determined by linear regression. This slope corresponds to D_f. This method for calculating D_f however, was modified from previous procedures in our laboratory in order to eliminate artefacts and improve accuracy [7,12]. Unfortunately, the image analysis macro used is not capable of count-

ing the particles touching only two of the four sides of each ROI (an adjusted count). As a result, including all particles touching all sides of each ROI results in a D value that is lower than expected, and, conversely, excluding all particles results in a higher than expected D value. To compensate, the average of the D values obtained by including and excluding counts in the 100–35% range is taken. This is analogous to counting just those features touching two of the four sides of each ROI, eliminates the skewing effect of small boxes, and results in an accurate D_f value [7,12]. The particle-counting method will be discussed in more detail in sections 2.1.3. and 3.2.11.

1.3.1.4.2. Box-Counting Fractal Dimension (D_b): Another method used to examine microstructure is the box counting or "grid dimension" analysis. This dimension is referred to as a grid dimension because for mathematical convenience the boxes are usually part of a grid that is laid over the image [38,41,43,60,61]. The box dimension is defined as the exponent D_b in the relationship:

$$N(L) \sim \frac{1}{L^{D_b}} \tag{9}$$

where N(L) is the number of boxes of linear size L necessary to cover a data set of points distributed in a 2D plane. If the network is indeed fractal, plotting the logarithm of N(L) vs. the logarithm of L results in a linear plot with a negative slope equal to $-D_b$ [38,41,43,60,61]. This analysis appears to be sensitive primarily to the degree of fill of the solids in a crystal network. It can be expected that a network that is more empty (many large void spaces) will result in a lower proportion of full boxes counted, and thus will result in a lower fractal dimension and vice versa [62]. This type of analysis has been used extensively to examine the fractal dimensions of food protein gels [24,51] and fat crystal networks [6,8,12,59] and is empirically useful despite the fact the growth of the network is limited to two dimensions [12]. The effects of confined growth on the fractal dimension is, therefore, one of the aims of the research in this study.

It is important to note that, in some cases, the fractal dimensions estimated by different methods are not the same.

This is exemplified by the recent studies by Martinez-Lopez et al and by Quevedo et al who found different values of D by number different image analysis techniques [40,63]. Values of the fractal dimensions for fat crystal networks determined by the particle-counting and box-counting methods are not equivalent, even though both methods are sensitive to the degree of order and amount of mass in the network [62]. Therefore, it is necessary that one be aware of the particular method used and its interpretation; this is mandatory for comparisons of dimensions of different data sets [61,64].

1.3.2 Traditional Two-Dimensional Polarized Light Microscopy of Fats

1.3.2.1. Polarized Light Microscopy

The polarized light microscope (PLM) has been the most widely used form of microscopy in the study of fat crystal networks. PLM involves the manipulation of light in such a way that it allows us to observe crystal structures. In general, light travels from a point source in a propagational or "ray" direction, while having different vibrational directions perpendicular to the wave-front [65,66]. When passed through a sheet of polarizing film, it becomes plane polarized because all of the lights vibrational directions are reduced to a single plane [65,66]. Figure 3 demonstrates this concept.

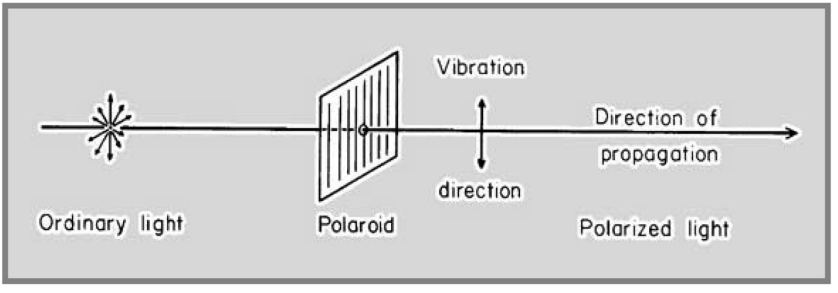

Figure 3 Diagram demonstrating the plane polarization of light.

When polarized light interacts with the specimen by double-refraction, the term *birefringence* is used. In the case of observing fat crystal networks, cross-polarization is used, which means that a second polarizer (called the analyzer) is positioned above the sample. When cross-polarization is used, anisotropic crystal structures that doubly refract are observed as various shades of grey, depending on their density and orientation. On the other hand, the liquid portion of the network is isotropic, does not refract polarized light, and appears stark black [65,66]. These criteria form the basic means of observing the complex particles and aggregated flocs of particles that make up the fat crystal network, and will be discussed in more detail later.

1.3.2.2. What is a ''Particle''?

The majority of quantitative microstructural analyses employed in our laboratory involve the characterization of features that make up the crystal network. Put simply, the thresholding of polarized light micrographs results in the isolation of network components that are of the brighter pixel intensities. This means that the network features that impart ample birefringence are those features that appear as light "flecks," which are retained upon thresholding. However, because the network can consist of various sizes of crystals and clusters of agglomerated crystals, the concept of individual particle isolation is somewhat confounded. Networks that are more granular in appearance tend to be more easily thresholded and their discrete particles retained. Networks that consist of large clusters of particles become more difficult to threshold for individual crystallites because some merging of particles (both in reality and due to the thresholding process) can occur. This loose definition of a particle leads to criticism worthy of addressing.

Furthermore, not all crystal mass in the network appears as birefringent features that are subsequently retained upon thresholding. This has been demonstrated through the comparison of network features under polarized light and phase contrast (see DVD in Appendix 2 → "Miscellaneous" image gallery, and "Polarized Light-Phase Contrast" movie gallery).

In examining these different views of the fat crystal network, it becomes evident that not all mass is represented by PLM imaging. Nonetheless, those birefringent features that are retained following thresholding represent a subset of sampled features that have been shown to be representative of the mass present during early network formation, which dictates the final network properties. The number and distribution of subsampled features that are observed in the early stages of crystallization have a profound influence on the final structure, number, and distribution of features as the network continues to reach an equilibrium state [67]. This indicates that, although the appearance of the crystal network may change significantly as it develops, the number of flecks determined by image analysis remains relatively constant, and, hence, the counting of birefringent features in a fully set network corresponds well to the fundamental particle distribution established in the early stages of crystallization (preceding the occurrence of agglomeration and merging). Recent work by Rodrigo Campos addresses this issue and will be discussed briefly here.

Figure 4 displays the number of particles as a function of time in an experiment studying the effects of shear on cocoa butter microstructure. Corresponding micrographs are presented in Figure 5. Note that the number of particles present following storage for extended periods of time remains relatively constant despite changes in the network appearance, and also that the relative difference in the counts under shear and statically remains nearly unchanging in time.

Hence, operating with this flexible definition of a particle is justified and allows us to perform further analyses, including particle size and fractal dimension determinations, with greater confidence.

1.3.2.3. Thin Film Crystallization Studies

Polarized light microscopy of thin films has been successfully employed to assess the effects of processing conditions on microstructure. Extensive and numerous studies have demonstrated effects on microstructure due to altered rates of cooling [7,10,22,59,68], the degree of supercooling [7,8,15,23,69],

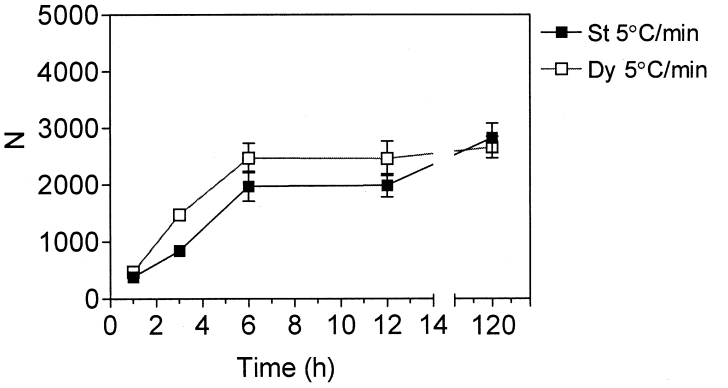

Figure 4 The number of particles (N) as a function of time (h) in a developing cocoa butter crystal network following cooling at 5°C and storage at 24°C. One sample was cooled in static conditions (St), while the other was subjected to shearing (Dy). Data courtesy of Rodrigo Campos.

the presence of shear [59], and storage time [59]. Altering crystallization conditions results in differences in the properties of the network on the microstructural level, which can include changes in the size, morphology, number, and degree of order [7,22,59,68]. These changes on the microscopic level have been shown to result in changes in the interactions between the particles that make up the network, which in turn affect macroscopic mechanical properties [7,12,59].

Of particular interest is the fractal scaling behavior demonstrated by fat crystal networks. Two-dimensional fractal analyses on images of thin film networks have been extensively studied and suggest that the relative degree of order

Figure 5 Polarized light micrographs of cocoa butter cooled at 5°C/min to 24°C statically followed by crystallization and storage at 24°C following (**A**) 1 h, (**B**) 3 h, (**C**) 6 h, (**D**) 12 h, (**E**) 24 h, and (**F**) 120 h. Also shown are image cooled in the presence of shear under the same cooling conditions and following storage for (**G**) 1 h, (**H**) 3 h, (**I**) 6 h, (**J**) 12 h, (**K**) 24 h, and (**L**) 120 h. Images courtesy of Rodrigo Campos.

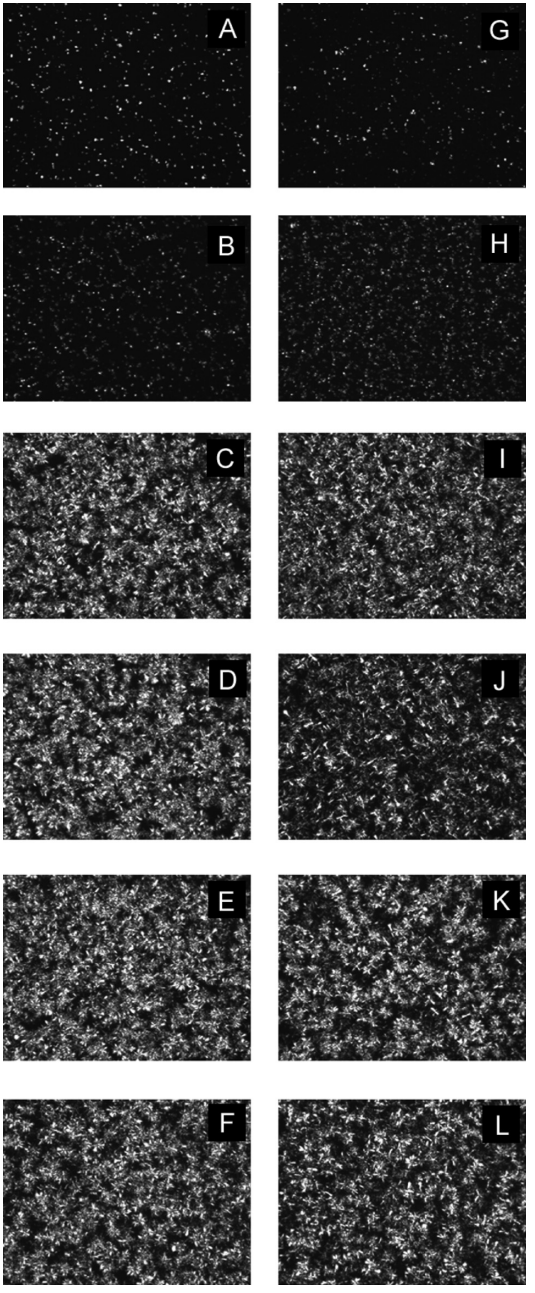

and fill in the networks can be quantified and used to make predictions pertaining to mechanisms of network formation and macroscopic rheologic properties [7,12,59]. These analyses have been compared to 3D fractal dimensions determined by rheologic methods with intermediate success [4,7,12]. This has lead to many questions related to the fundamental differences between 2D and 3D crystallization conditions and their resulting fractal dimensions. Imaging and fractal analysis of fat crystal networks in 3D would, therefore, be of high value.

1.3.3. Three-Dimensional Microscopy of Fats—Previous Efforts

Although polarized light microscopy of thin samples of fats has been of great value in the examination of microstructure, little information about the actual internal 3D structure of fat crystal networks can be attained by this method. The following discussion briefly highlights some of the significant efforts made to acquire 3D images of fat crystal networks.

1.3.3.1. Scanning Electron Microscopy

Scanning electron microscopy (SEM) uses a condensed stream of monochromatic electrons that scan the specimen and interact with the sample, and various backscattering electrons that are detected and displayed on a cathode ray tube to form an image. Of the efforts to image 3D fat crystal networks by electron microscopy the most significant were pursued by Heertje et al. at Unilever Research [2,26]. Efforts prior to Heertje et al.'s were inefficient because thin sections suitable for imaging required freeze fracturing. In preparing samples for fracturing, the freezing process results in the crystallization of the liquid phase of the network, confounding the ability to observe the original solid network structure prior to freezing [25]. In 1987, Heertje et al. developed a novel sample preparation technique that aimed to remove the liquid phase from the semisolid 3D fat crystal network while leaving the solid matrix intact [26,70]. Sample preparation required the use of a specially crafted sample holder through which system specific deoiling of the liquid phase was preformed using mixtures of butanol and methanol at various temperatures and for various

treatment times [26]. Upon subsequent freezing and fracturing, the remaining solid matrix was then observed by SEM. While images obtained by this method successfully demonstrated 3D fat network features, much criticism resulted because in many cases partial stripping of the solid matrix (30–50%) coupled with partial retention of the liquid phase (10–20%) may have resulted in image artifacts [26]. Despite this problem, the work of Heertje et al. was successful in demonstrating the general 3D structure of a variety of fat-based food products such as margarines, butter, shortenings, and other fat spreads consisting of oil-in-water emulsions [2,26,27]. Further efforts by Heertje and Leunis involved removal of the liquid phase using detergents on the surface of bulk crystallized fats, followed by carbon fixation and transmission electron microscopy (TEM) [27]. Other significant efforts to image bulk fats by SEM were carried out by Rousseau et al. and involved solvent extraction of solid crystals as well as freeze-fracturing techniques [71]. This work was successful in demonstrating the presence of both amorphous and defined crystalline regions in tempered milk fat; however, in many cases, the crystal structure is not well defined and the network appeared spongelike in nature [72]. While these techniques were successful in observing differences in crystal structure due to different processing conditions and composition, their limitations and potential for artifacts limited the use of these techniques.

1.3.3.2. Fluorescence Confocal Scanning Laser Microscopy

Unlike electron microscopy, which requires complex sample preparations, confocal scanning laser microscopy (CLSM) allows for 3D observation of a system's interior without disturbing the internal structure [73,74]. The principle of confocal microscopy is: light emitted from a source is focused on an imaging pinhole and is reflected by a dichroic mirror on a single point within the specimen. Mirrors on scanning devices then focus the beam in X and Y directions within the sample. Excitation light within the specimen is emitted, passes through the dichroic mirror and is focused on the detector pin-

hole to form an image of the plane in focus [75]. Focusing at various depths can be facilitated by moving the sample or the sample stage in the z-direction, and, hence, multiple 2D scans can be used to recreate 3D volume renderings [30,35,76].

The use of confocal fluorescence microscopy has been successful as a means of observing fat globules in cheese [77], as well as in oil-in-water emulsions [78]. In bulk fat systems, however, attempts to image thick sections ($>50\mu m$) are met with limited success due to limitations in the ability to image at greater depths. This occurs when emitted light at deep focusing planes is absorbed and scattered and is insufficiently transmitted back through the sample to the detector [79]. In addition, the level of structural detail attained by CLSM of fat networks is inherently low, so finer detail within clusters is often indiscernible. Also, speckling can occur to do the presence of residual fluorescent dyes, even after filtering. Due to these limitations, imaging bulk fat systems by confocal microscopy has not been extensively pursued. Figure 6 depicts selected slices from a fluorescence confocal z-series that demonstrate these points.

Recent work by Balberg et al., who have developed a method to extend focus depth in scattering media by use of volume halographic filters, may be of value in the future [79].

1.3.3.3. Atomic-Force Microscopy

Atomic-force microscopy (AFM) is a relatively new technique that can be used to acquire 3D topographical images.

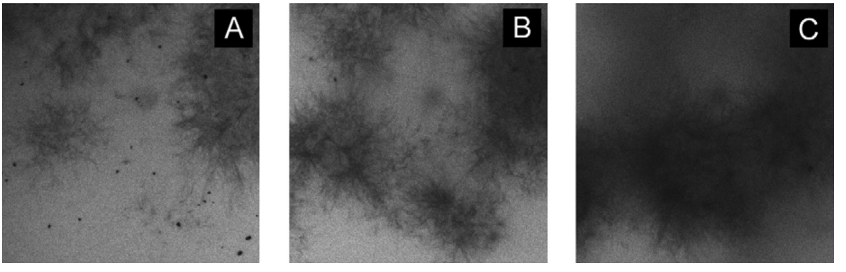

Figure 6 Confocal images of anhydrous milk at depths of (**A**) 0 μm (the top of the sample), (**B**) 20 μm, and (**C**) 40 μm. Images by Alejandro Marangoni used with permission.

The basic principle of AFM is as follows: a cantilevered tip scans the surface of a sample, and, through various measurements of tip deflection and oscillation, images can be acquired on the basis of height, amplitude, and phase [80].

AFM was recently used to study the effects of cocoa butter bloom on the microstructure of the surface of chocolate [81]. However, the use of AFM to image semisolid fat crystal networks is difficult due to the presence of liquid oil, which tends to coat the tip of the probe and interfere with signal measurement. Because this method measures surfaces, information pertaining to the interior structures is limited. For this reason, AFM has not been extensively pursued as a means of imaging bulk fats, although some successes in imaging fat crystal networks have been attained, as demonstrated for cocoa butter and for the high-melting fraction (HMF) of milk fat, discussed later (Figs. 7 and 8).

All of the aforementioned 3D imaging techniques are valuable in their own respects, but fail to provide sufficient information about the 3D structures in bulk fat systems. The desire to image the interior structures of bulk fat systems in three dimensions was the driving force of this study, and the technique developed was based on the concept of transmitted light optical z-series imaging and deconvolution.

1.3.4 Imaging and Deconvolution

1.3.4.1. The Deconvolution Principle

The term "deconvolution" encompasses a wide range of filtering operations that aim to recover the essential information from a signal degraded by blur and noise [82,83] and is not exclusive to image restoration. In fact, deconvolution principles have been extensively studied and implemented in a wide variety of signal processing applications including seismology, acoustics, wireless communications, and noninvasive medical signal analysis [83–90]. The commonalities in all of these applications are the desires to undo the convolution (or blurring) observed in a measured signal, and reconstruct the signal close to its original state. The following discussions will focus only on the use of deconvolution in imaging applications.

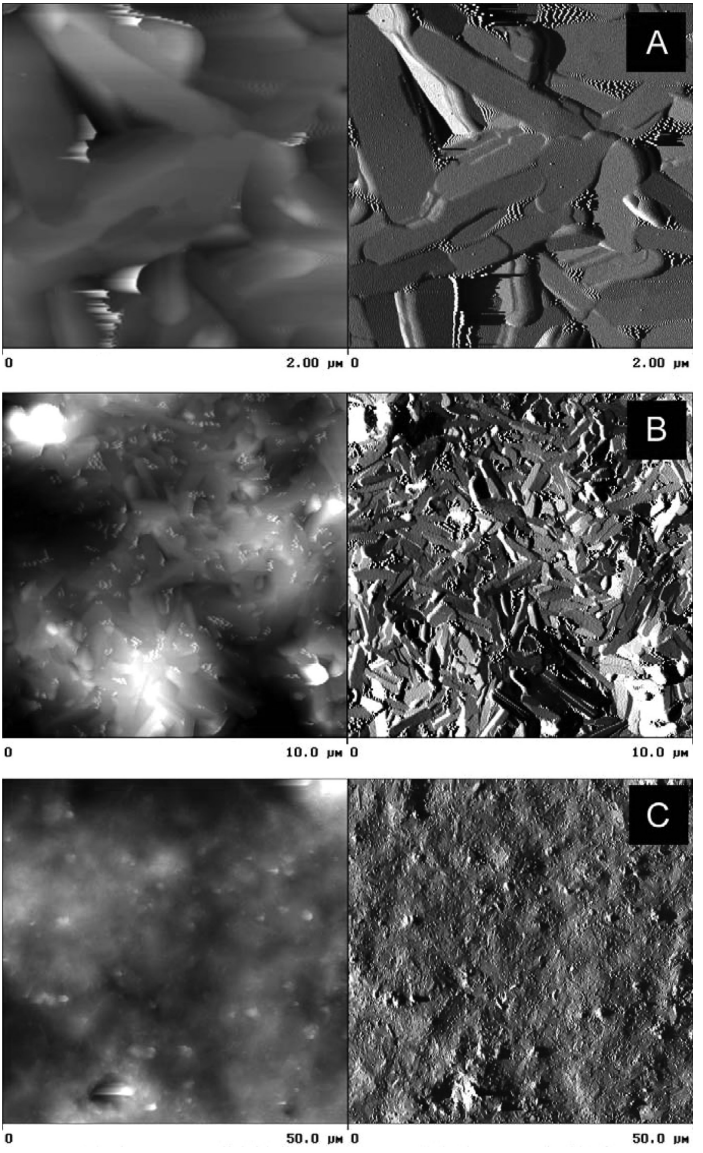

Figure 7 Atomic-force micrographs of cocoa butter at multiple magnifications. The width of each image corresponds to (**A**) 2 μm, (**B**) 10 μm, and (**C**) 50 μm. Images on the left correspond to the height signal, and those on the right correspond to the phase signal. Images with permission by Alejandro Marangoni (Marangoni FRI2002).

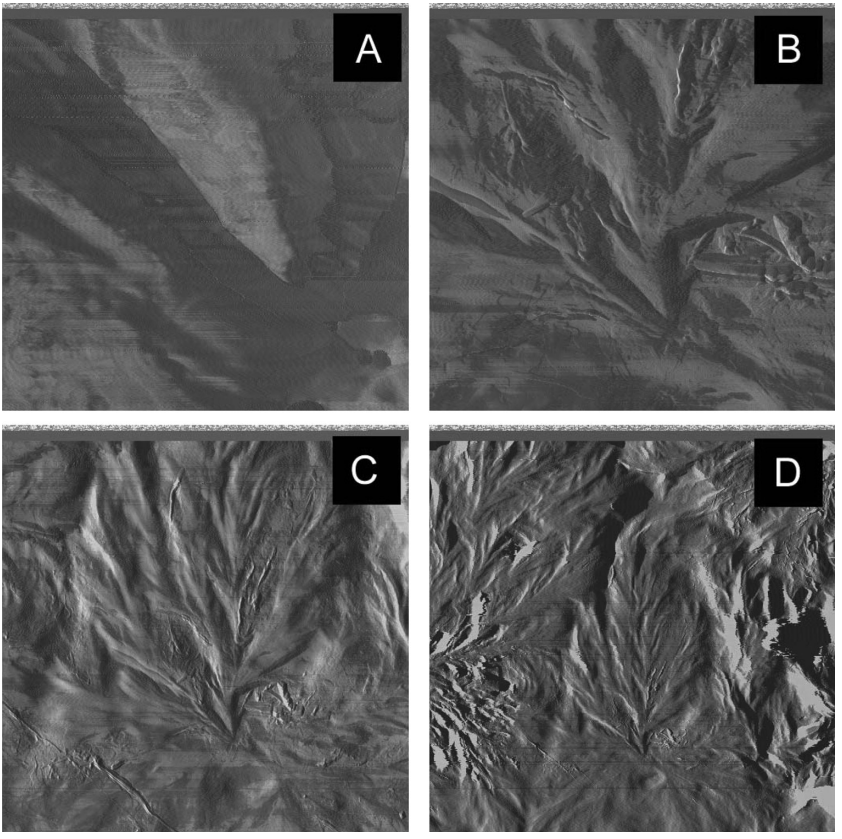

Figure 8 Atomic-force micrographs (a 50/50 overlay of the amplitude and phase signals) of high-melting fraction (HMF) at multiple magnifications. The width of each image is corresponds to (**A**) 2 μm, (**B**) 10 μm, and (**C**) 25 μm, and (**D**)50 μm.

1.3.4.2. Applications of Deconvolution in Two-Dimensional Imaging

In most 2D imaging applications, the observed image g(x,y) is a function of the true image f(x,y) and a shift-invariant blur h(x,y), which is also known as the point spread function (PSF):

$$g\,(x,y) = f(x.y) * h(x,y) + n(x,y) \tag{10}$$

where * is the convolution operator and n(x,y) represents all contributions due to additive noise [83]. The aim of deconvolution is to remove blur and perform a restoration that best represents the true image f(x,y) having only measured the degraded image g(x,y) and having limited knowledge of the point-spread function (PSF) h(x,y) and noise contributions n(x,y) [91,92]. The model for blur that has evolved in theoretical optics is based on the concept of the PSF. The PSF is based on an infinitely small point source of light originating in the specimen. Imaging systems collect just a fraction of the light emitted by this point, and, therefore, cannot focus the light into a perfectly sharp image of the point [34]. Instead, the point appears widened and spreads into an XY diffraction pattern. Thus, the PSF is formally defined as the diffraction pattern generated by an ideal point source of light. Figure 9 depicts a flow chart for the concept of image formation and deconvolution.

A wide variety of image deconvolution algorithms have been developed and applied, some of which are highlighted next.

1.3.4.2.1. Classical Two-Dimensional Deconvolution Algorithms: Inverse filters were the first deconvolution algorithms to be employed in imaging applications and are com-

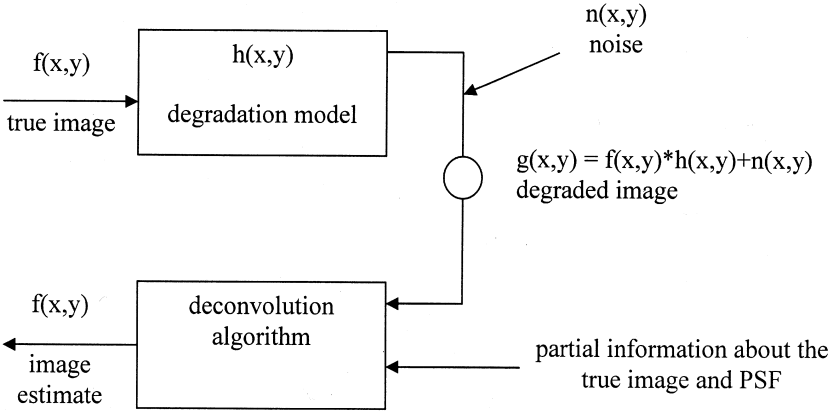

Figure 9 Flow chart depicting the concept of two-dimensional image formation and deconvolution principles.

monly referred to as "Wiener deconvolution," "regularized least squares," "linear least squares," and "Tikhonov-Miller regularization" [34]. In these instances, the PSF is known explicitly prior to deconvolution [83], which allows for accurate knowledge of the convolution process. The algorithm works by taking the Fourier transform of the image and dividing it by the Fourier transform of the explicit PSF, which, because division in Fourier space is equivalent to deconvolution in real space, represents the simplest means of reversing the convolution operator [34,93]. Inverse filtering methods have been used extensively for image deconvolution, with a popular example being images acquired by the Hubble space telescope and other astronomic speckle-imaging systems [82,83]. Other common applications include image deconvolution by remote sensing, various medical systems, imaging of the Earth's underlying surface, and standard photography [83,88,94,95]. Inverse filters have also been applied to 2D slices of 3D data sets, which will be described in more detail to follow, to improve spatial discrimination in 3D fluorescence imaging [36].

1.3.4.2.2. Two-Dimensional Deblurring Algorithms: Deblurring algorithms include techniques referred to as "nearest neighbor," "no-neighbor," and "unsharp-masking" and are another class of 2D deconvolutions. For 2D images, these methods operate under the principle that out-of-focus blurs tend to be "flatter" and composed of lower spatial frequencies than in-focus light. Removing lower spatial frequencies and boosting higher spatial frequencies constitutes blur removal [34,96]. No-neighbor and unsharp-masking are commonly used as artifical focusing operations in image-processing software for digital imaging and can be used to enhance poorly focused 2D photographs, for example [97]. Nearest neighbor techniques use some, but not all, of the 3D information in the 3D data sets to perform plane by plane deconvolution by using information from only adjacent planes to subtract estimated blur [34,96,98]. These algorithms are useful when quick deblurring is desired or when computation power is not available but are often riddled with artifacts due to relative changes in pixel intensities, additive noise from neighboring planes, and,

because some features may have PSFs, overlapping in the z-direction [34].

1.3.4.2.3. Two-Dimensional Blind Deconvolution Algorithms: In many cases, knowledge of the PSF is limited, unknown, or difficult, sometimes even impossible, to measure. Examples of 2D images where this is the case include aerial and astronomic imaging, where fluctuations in the PSF due to the atmosphere are common [83]. Satellite and ground-based telescopes also inherently result in PSFs that are difficult to quantify [92,99,100]. In addition, some imaging scenarios also render measurement of the PSF impossible, such as medical video-conferencing and x-ray imaging (where high-intensity beams required for PSF measurement would be hazardous to patients' health) [83]. In these cases, the use of blind deconvolution algorithms is beneficial because they do not require knowledge of the PSF because the algorithm facilitates both blur identification and image restoration concurrently [83]. Therefore, Blind deconvolution is an inverse process of obtaining the best estimate of the true image f(x,y) while concurrently estimating the degradation model or PSF g(x,y) and noise contributions n(x,y) [83,91,92,94,99,101,102]. Several variations of algorithms and approaches are used for blind deconvolution, including zero sheet separation, *a priori* blur identification, nonparametric deterministic constraints, autoregressive moving average, and high-order statistic algorithms [83]. Each operates slightly differently, but their functions are similar in that they use the image data to compute the blur function and restore the image.

1.3.4.3. Applications of Deconvolution to Three-Dimensional Imaging

In the early 1990s, and with great advances in computing power, deconvolution of 3D data sets became more feasible and is now commonly used to remove out-of-focus blur in 3D confocal and fluorescence microscopies [30,103]. These methods, also referred to as computational optical sectioning microscopy (COSM), involve optical sectioning of 3D volumes by taking a series of 2D (XY) slices at multiple depths within the sample (the Z axis). A representative diagram of this process is depicted in Figure 10.

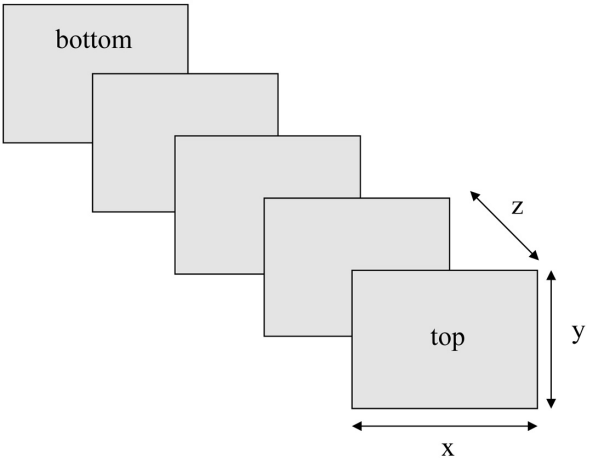

Figure 10 Schematic diagram representing the acquisition of 3D data sets, also called stacks. XY image planes (also called slices) are acquired at known z-increments by use of a motorized microscope stage and contain both in and out of focus features.

Because each optical plane contains both focused features and out-of-focus blur from features above and below each plane, the aim of 3D deconvolution is to either remove this blur, or, in more complex algorithms, to reassign out-of-focus pixels to their original position within the specimen [29,34,96,104–108].

In 3D imaging applications, the observed image g(x,y,z) is a function of the true image f(x,y,z), the 3D PSF h(x,y,z) and contributions by noise n(x,y,z) [106,107]:

$$g\,(x, y, z) = f\,(x, y, z) * h\,(x, y, z) + n\,(x, y, z) \qquad (11)$$

In the case of 3D deconvolution, the PSF takes on a more complicated form, and role. When describing the point spread function in three dimensions, it is useful to apply an x, y, z coordinate system, where x and y are parallel to the focal plane of the specimen and z is parallel to the optical axis of the microscope. The PSF appears as a set of concentric rings in the x-y plane, and resembles an hourglass in the x-z and y-z planes

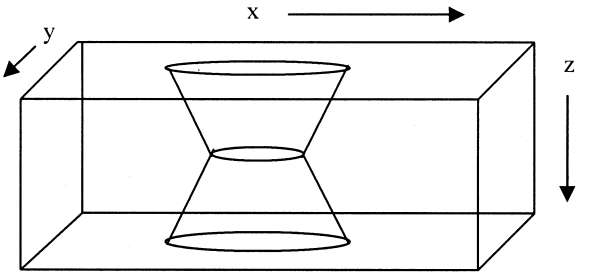

Figure 11 Schematic diagram illustrating the concept of the three-dimensional point-spread function (PSF) (From Ref. 112).

[34,96,107]. A representative diagram of the PSF in 3D imaging is depicted in Figure 11. Almost all 3D deconvolution algorithms (the exception being blind deconvolution) require knowledge of the PSF. As will be discussed for specific algorithms, the PSF can either be measured experimentally or theorized on the basis of the imaging optics used [34,96]. To determine the PSF for an optics system experimentally, a subresolution fluorescent microsphere (that emulates a point light source) is imaged by taking optical sections starting above the point source and ending below the point source [96].

In addition, the imaging conditions used during PSF determination should best approximate the conditions that will be used to image the actual specimen. To determine the PSF theoretically, software can be used. The information usually required for the computation of a theoretical PSF is as follows: objective lens numerical aperture and working distance, the wavelength of the emitted light, the XYZ image dimensions, the pixel size, the z-spacing, the refractive index of the immersion medium, and the coverslip thickness [96].

Aside from the differences in the PSF, the overall process of 3D deconvolution is no different than that of 2D deconvolution, depicted in Figure 9, except images in 3D are also a function of depth (z).

1.3.4.3.1. Two-Dimensional Deblurring Algorithms for Three-Dimension Data Stacks: Deblurring algorithms techniques, referred to as "multiple neighbor" (which

was one of the methods used in this study), are essentially 2D deconvolutions that are performed on 2D slices of 3D stacks of images [34]. Multiple nearest-neighbors techniques use some, but not all, of the 3D information in the data to perform plane–by-plane deconvolution by using information from only a select number of planes above and below each plane to subtract estimated blur [34,96]. Most commercial deconvolution software, such as the one used in this study, employ a theoretical PSF.

1.3.4.3.2. Classical Constrained Iterative Methods: Jansson-Van Cittert, Nonlinear Least Squares: To reduce artifacts that can arise by linear deconvolution methods, such as inverse filters and nearest neighbors algorithms, constraints are imposed that ensure image intensities remain positive [29,34,96]. These complex algorithms operate iteratively on the entire 3D data set by first convolving with the input PSF and acquiring a "blurred estimate," which is then compared to the raw images [34]. An error criterion is computed via this comparison, which is then used to alter the estimate in such a way that error is reduced. A new iteration is performed, the new estimate convolved, a new error criterion calculated, and so on until the solution is reached at convergence by minimizing the error criterion [34]. As a result, the time required to deconvolve is sufficiently greater; however the advantages of artifact reduction may improve results.

1.3.4.3.3. Statistical Image Restoration: Maximum Likelihood Estimation (**MLE**): The most common type of statistical deconvolution employs a maximum likelihood estimation (MLE) algorithm, which in addition to imposing positivity constraints, also incorporates information about the statistics of noise [33]. As a result, these algorithms are more computationally intensive than the classical algorithms, but are better suited to images that are perturbed by appreciable levels of noise [34]. Since these methods are also iterative in nature, and more complex, some data sets may require several hours to deconvolve [33]. These algorithms also require the knowledge of either an empirical or theoretical PSF for the system.

1.3.4.3.4. Blind Deconvolution: Modified MLE: As was mentioned in the discussion on 2D blind deconvolution, there are many instances where knowledge of the PSF of the system is either difficult or impossible to acquire. The same applies to 3D microscopy. The main advantage to blind deconvolution is that it obviates the need to have knowledge of the PSF because it simultaneously computes the blur function and restores the image by using all information in the 3D data set [29,34,96,104]. Blind deconvolution is essentially a modified version of the MLE algorithm, with PSF estimation added [34,99]. The algorithm starts with a theoretical PSF, but, through, iteration it adjusts the PSF according to the specific data being deconvolved, handles noise, and, to a certain extent, can also correct for spherical aberration [34,109]. The use of blind deconvolution is, therefore, an attractive option in many cases, and has been used extensively in various applications using both 3D reflected fluorescence microscopy and confocal [29,33,34,106,108]. Some commercially available blind deconvolution software packages now even include algorithms that correct noise and artifacts inherent to charge coupled device (CCD) cameras prior to deconvolving [105].

1.3.4.3.5. A Note on Deconvolution and the Potential for Vendor-Driven Biases: The choice of empirical or theoretical PSF use is often a point of contention among users and developers on deconvolution algorithms. While some believe that the empirically measured PSF is easy to acquire and gives superior results compared to the use of a theorized PSF, others believe that empirical measurement of the PSF is rigorous and, if done incorrectly, can impair the images more than improve them. Others believe that, for various imaging scenarios, the empirical PSF may differ significantly from the PSF that occurs when imaging the actual specimen and that, in some cases, the use of a theoretical PSF may be preferred since it is noise free.

Another point of contention among deconvolution users and software developers is the use of a blind deconvolution algorithm in lieu of measuring and using an empirical PSF and nonblind algorithm. While some believe that an accurately obtained empirical PSF is best, others would argue that blind

deconvolution is a better alternative since any inaccuracies in the empirical PSF would be expressed in the deconvolved images. Since deconvolution users are also involved in the development and sale of expensive deconvolution software, the potential for bias arises; therefore, it is important that this be considered when looking for a deconvolution solution. In many instances, the right choice of algorithm or software is dependent on the intended use. In some cases, several algorithms may perform equally well. Ideally, a number of algorithms should be explored. For this reason, many vendors of deconvolution software offer temporary demo software and/or encourage the submission of experimental data for demonstration purposes prior to purchase. These discussions can be found by searching the archives of the University of Buffalo Confocal Listserv [110].

1.3.4.4. Adaptation of Deconvolution Techniques to Three-Dimensional Transmitted Brightfield (TLB) Microscopy

The adaptation of a blind deconvolution algorithm for use in 3D transmitted light brightfield (TLB) microscopy was first proposed by Holmes et al. in 1995, and was especially attractive because, until then, there were no robust means to image in three dimensions by transmitted light [111]. Because TLB is also one of the most widely used imaging modalities in a number of scientific disciplines, and because blind deconvolution can be used pervasively, this development has the potential for great impact [112].

The deconvolution algorithm proposed for TLB is based on the MLE blind approach discussed previously, with a number of added components. These include an estimate of the 3D optical density distribution (also positively constrained), and a "guardband" which constrains the bulk of the energy within the PSF to lie within an hourglass-shaped 3D region (which serves to eliminate artifacts caused by circular convolution) [112]. During the development of this algorithm, an image montage and an acceleration scheme were also devised as a means of reducing the number of required iterations to convergence [112]. Another important aspect of this recent develop-

ment was that it demonstrated the possibility for 3D imaging and deconvolution by a modality that has a partially coherent optics model [112]. Preliminary applications of the algorithm on stained pyramidal neurons resulted in identifying dendrite features by TLB that were not easily observed by 3D fluorescence or confocal microscopies [112]. This recent deconvolution development, in addition to preliminary discussions with Dr. Tim Holmes, served as a major source of inspiration and confidence that the adaptation of optical sectioning and deconvolution to transmitted polarized light microscopy should be pursued [107].

2. METHODS AND MATERIALS

This section addresses the methodologies employed in this study. This includes the preparation, imaging, image processing, and image analysis of 2D and 3D systems. The model fat system used in all studies was the high-melting fraction of milk fat (HMF) diluted in triolein at a 30:70 (w/w) ratio.

2.1. Conventional Two-Dimensional (Thin Film) Methods and Materials

2.1.1. Conventional Two Dimensional (Thin Film) Slide Preparation

The following method is the standard procedure for preparing samples for imaging, and has been employed in our laboratory for many years and for many fat systems for various crystallization experiments [5,7,8,10,12,13,23,59].

A small, representative sample of the fat was first melted and held at 80°C in an oven for a period of 30 minutes to ensure that all crystal memory was erased. Using a preheated, thin, glass disposable micropipette and plunger (Drummond Scientific Company, Broomall, PA, USA), molten fat was drawn from the mixed, molten sample. Working in the oven, the plunger was held perpendicular to a preheated 25 × 75 × 1mm glass slide (Fisher Scientific, Pittsburgh, PA, USA) and the plunger was slowly depressed until a small droplet (approximately 10 μL) of molten fat fell onto the slide. A 22 × 22mm preheated glass coverslip (Fisher Scientific, Pittsburgh,

PA, USA) was then carefully placed over the sample to produce a film of uniform thickness. If this is performed carefully, no excess liquid fat should be expelled from under the coverslip, thereby ensuring a consistent thickness within the sample, and in repeated slide preparations.

The slide was then quickly transferred to a thermostatically controlled microscope stage (Model LTS 350, Linkam, UK), which was preheated to 80°C (Fig. 12).

Figure 12 The Linkam LTS 350 microscope heating/cooling stage. The temperature of the sample is maintained by the use of a heating coil and liquid nitrogen, which are controlled by an external programmer and pump system (not shown).

Each sample was immediately viewed under the microscope to confirm that it remained in a completely molten state (no birefringence observed) during transfer from the oven to the imaging system. The sample was then held at 80°C for 10 minutes to ensure a consistent initial temperature, and cooled at a controlled rate of 10°C/min (mediated by the temperature-controlled stages external pump and programmer, which uses liquid nitrogen as a cooling medium) to 28°C and held isothermally for 15 minutes prior to imaging. This process was repeated for three slides.

2.1.2. Conventional 2D (Thin Film) Imaging

Imaging of the thin films was performed on a microscope using polarized light (Leica Microsystems: DM-RXA2/CTR-MIC—Richmond Hill, ON, Canada). The polarizer was set to 90° (full extinction) relative to the analyzer (crossed-polarization). The light source was set at 10.5 volts and the aperture was wide open. The objective lens used had a numerical aperture of 0.55 and magnification of 50X. The aperture was closed down until it was visible in the field of view, centered, and then opened to just beyond the field of view in order to ensure even and efficient illumination. A green filter (Hoya: G[X1]—Japan) was used to provide monochromatic light and enhance contrast [78].

A cooled CCD camera (Q-Imaging: Retiga 1300—Burnaby, BC, Canada) was used to view the magnified sample on a cathode ray tube (CRT) monitor (LaCie: Electron 19 blue III—Hillsboro, OR, USA) on a personal computer (Apple: Macintosh G4—Cupertino, CA, USA). Exposure was set to ensure a proper distribution of greys (i.e., the features were visible, but no saturation of pixels occurred). This was confirmed by viewing the live camera image histogram, which displayed all pixels frequencies within the range of 0–255 grayscales. The lighting conditions and camera exposure were kept constant during imaging to avoid introducing variables.

Focused images were acquired as uncompressed 8-bit (256 grays) grayscale .TIFF files, with a spatial resolution of 1280×1024. Three slides were prepared as previously de-

scribed (section 2.1.1), and three random, representative fields were imaged from each slide.

In various past studies in our laboratory a different microscope (Olympus: BH—Japan), video CCD camera (Sony: XC-75—Japan), and image-capture board (Scion: LG-3—Frederick, MD, USA) with on-board 16-frame averaging were used as our primary imaging system [5,7,8,10,23]. This setup resulted in 8-bit greyscale images with a spatial resolution of 640 $\times$ 480 pixels (and, hence, a smaller field of view acquired in each image, relative to the newer imaging system). Therefore, it was in our interest, to compare, qualitatively and quantitatively, both results of imaging experiments from the old and new microscope and camera imaging systems. In particular, our interests lay in determining whether or not the change to newer optics and image resolution had any affect on the image analysis parameters D_b and D_f, which are fractal dimensions that describe the order and fill of the crystal networks (to be explained in more detail in section 3.1.2). This comparison will be addressed as a brief note in the results section (section 3.2.11).

2.1.3. Conventional Two-Dimensional (Thin Film) Image Processing and Analysis

2.1.3.1. Thresholding

Grayscale images of the network must be converted to a binary format prior to image analysis. The discriminatory conversion of grayscale images to binary format, requires a process termed "thresholding." Images of fat crystal networks are typically obtained as 8-bit (256 color) images and consist of a histogram of pixel values that span the range of 0 (pure white) to 255 (pure black). Thresholding involves the selection of a particular pixel value within the range of 0 and 255 that will result in a binary image that best isolates the features of the network. This process is subject to much controversy because the selection of the cutoff pixel value can often be subjective. To minimize subjectivity, an autothresholding algorithm can be used that often provides accurate and reproducible results (performed on a Macintosh computer using the public

domain NIH Image program, developed at the U.S. National Institutes of Health and available on the internet at http://rsb.info.nih.gov/nih-image). This algorithm works by scanning the histogram to find an intensity value where the average moments of the histogram counts about an intensity value are balanced. This means that a threshold value is chosen where the average pixel intensities are equal above and below the threshold [78a]. The general process of thresholding can be seen in Figure 13.

When autothresholding fails to result in a binary image that accurately represents the features in a grayscale image, manual and somewhat subjective thresholding can be performed. Manual thresholding is subject to much criticism be-

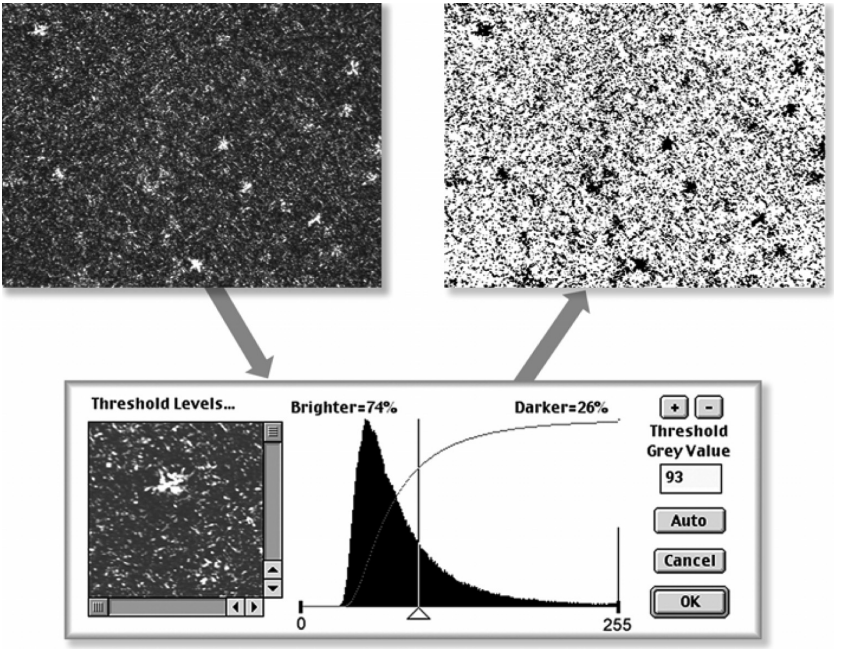

Figure 13 The conversion of an 8-bit (256-grayscale) micrograph to a binary (pure black and white) image suitable for image analysis. A threshold value is manually chosen to isolate the features that will be measured.

cause it introduces variability in the user's subjective determination of threshold. In order to reduce this subjectivity as much as possible, the following procedure is performed in Adobe Photoshop (Adobe Systems Inc, CA, USA): the image is opened, inverted, and an exact copy is overlaid on a layer above the original. This top, duplicated layer is then thresholded. By toggling the opacity of this thresholded layer, a scrupulous comparison to the underlying original grayscale image can then be made, and the threshold value adjusted accordingly (if the first chosen value does not accurately represent the features of the original image).

This procedure was followed for all required manual thresholding operations in this study. Once the image is converted to binary and the features isolated, it can be subjected to image analysis. Features are measured, and result in data, which can then be interpreted and related to structure. A flow chart outlining the general process from start to finish is depicted in Figure 14 [113]. Emphasis is put on acquiring initial images that are of high quality (high distribution of pixel values, no saturation of white features, and evenly distributed lighting) in order to avoid unnecessary image processing to enhance features thereby altering pixel values.

2.1.3.2. Image Calibration

Brightfield images of a 1000 μm stage micrometer (Fisher Scientific, Pittsburgh, PA, USA) were acquired and used to create an image calibration file prior to performing all analyses. The Image Processing Toolkit (IPTK) processing and analysis filter/plug-ins package (Reindeer Graphics, Asheville, NC, USA) automates various imaging tasks, and works within the framework of the graphics software Adobe Photoshop (Adobe Systems Inc, San Jose, CA, USA). Using the IPTK's IP-Measure → calibrate filter, two points on the image of the micrometer (of known distance apart) were marked and the corresponding known length input. This filter results in a calibration file that saves the μm/pixel ratio and subsequently allows all further quantitative imaging filters to output calibrated results in units of μm.

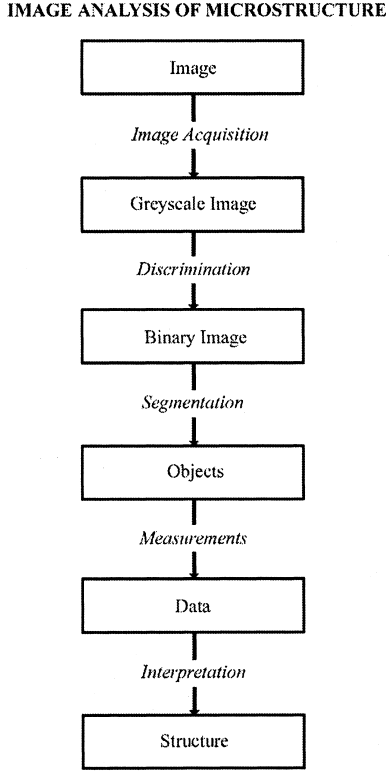

Figure 14 Flowchart depicting the steps involved in obtaining and evaluating the microstructure of materials from digitally acquired images (From Ref. [113).

2.1.3.3. Fractal Dimensions

Assuming a statistically constant microstructural element (or particle) size, the relationship between radius and mass (equation 12) can be used to determine the fractality of crystal networks from 2D PLM images [4,12].

In this case the scaling relationship between the number of discrete particles (N) and the length of the region of interest containing the particles (L) can be expressed as:

$$N = cL^D \tag{12}$$

The first method used was a particle counting algorithm performed using NIH-Image (analysis performed on a Macintosh computer using the public domain NIH Image program, developed at the U.S. National Institutes of Health and available on the Internet at http://rsb.info.nih.gov/nih-image) as follows: c is a constant, the number of distinct particles (N) are first counted within the entire image of known length (L). At 5% increments, the image is cropped thereby making a new, smaller length L and the number of particles in each new image counted. This process is repeated until the length of the image is 35% of the original size. A diagram depicting the overlaying of the boxes of decreasing size can be appreciated in Figure 15.

The number of particles counted within each box size of various lengths (L) is the plotted on a log-log scale, and the slope of the line determined by linear regression. This slope corresponds to D_f. This method for calculating D_f was modified from previous procedures in our laboratory in order to eliminate artifacts and improve accuracy. This was accomplished by performing these iterative counts twice on each image—once

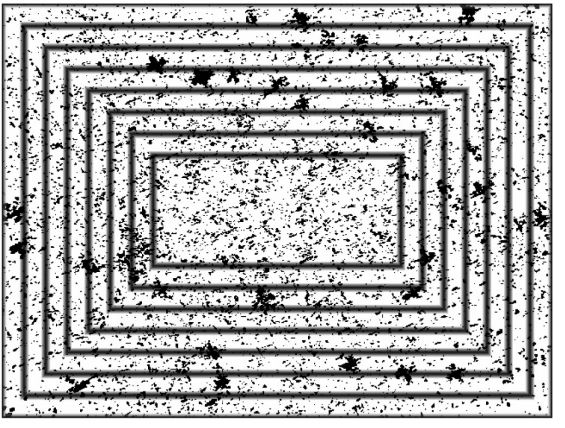

Figure 15 Schematic diagram showing the incremental decreases in box size (or region of interest [ROI]) used for the particle counting method for the determination of the fractal dimension D_f.

including all particles touching the edge of each region of interest, and once excluding those that touch the edges. By taking the average of these two counts, a D_f that best represents the spatial distribution of mass is obtained [5,7,12]. This improved method is equivalent to well-established methods that involve counting features that touch two sides of the region of interest [114]. A brief discussion of the effects of edge and image resolution on the particle-counting fractal dimension will be included in greater detail in the results (section 3.2.11).

The fractal dimension arrived at by this method reveals information on the degree of order in the packing of the microstructural elements within the microstructures. Systems that display a high degree of disorder have characteristically lower fractal dimensions than those of a more ordered network [7,12,38,43]. Another method used to examine microstructure is the box counting or "grid dimension" analysis. This dimension is referred to as a grid dimension because for mathematical convenience the boxes are usually part of a grid that is laid over the image [38,41,43,60,61]. The box dimension is defined as the exponent D_b in the relationship:

$$N(L) \sim \frac{1}{L^{D_b}} \tag{13}$$

where N(L) is the number of boxes of linear size L necessary to cover a data set of points distributed in a 2D plane. If the network is indeed fractal, plotting the logarithm of N(L) vs. the logarithm of L results in a linear plot with a negative slope equal to $-D_b$ [38,41,43,60,61]. This analysis appears to be sensitive primarily to the degree of fill of the solids in a crystal network. It can be expected that a network that is more empty (many large void spaces) will result in a lower proportion of full boxes counted, and thus will result in a lower fractal dimension and vice versa [62]. A screen capture depicting the software interface is included in Figure 16.

It is important to note that in some cases the fractal dimensions estimated by different methods are not the same. It is therefore necessary that one be aware of the particular method used and its interpretation; this is mandatory for comparisons of dimensions of different data sets [61,64].

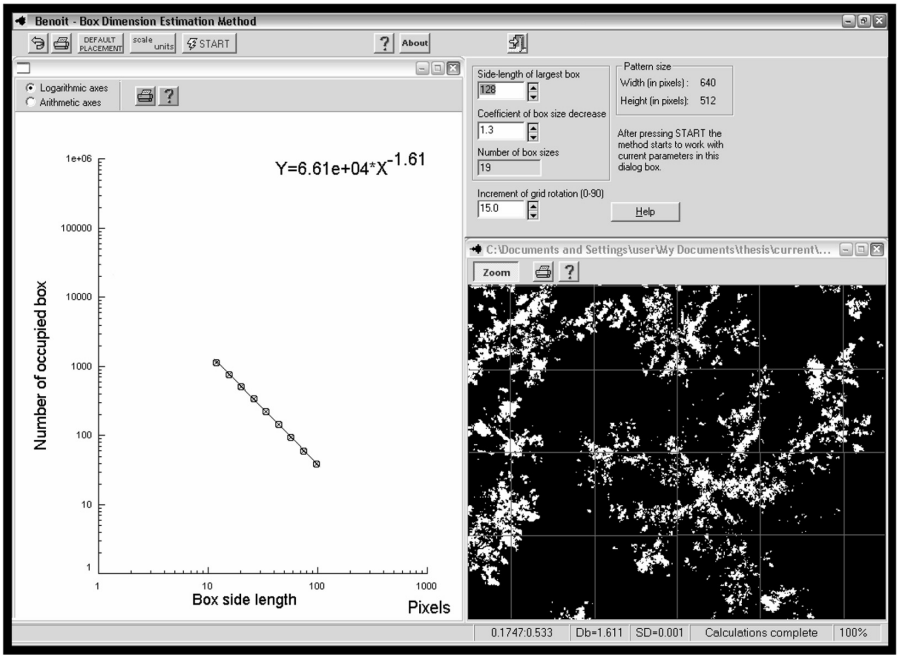

Figure 16 Screen capture depicting the box-counting fractal dimension (D_b) determination in TruSoft's Benoit software application. Box size is iteratively reduced and the number of occupied boxes counted. Results are plotted on log-log axes, and the resulting slope is D_b.

2.1.3.4. Area Fraction

Area fraction was determined from binary images by using the IPTK's IP-measure → global filter (Reindeer Graphics, NC, USA). This filter works by simply counting the number of black pixels which represent crystal mass. The number of black pixels divided by the total number of pixels in the entire image represents the area fraction, which is an indication of the quantity of crystal mass.

2.1.3.5. Number of Particles and Microstructural Element Size

The number of particles, N, (as was defined in section 1.3.2) within each 2-dimensional image was computed using

NIH-image (analysis performed on a Macintosh computer using the public domain NIH Image program, developed at the U.S. National Institutes of Health and available on the Internet at http://rsb.info.nih.gov/nih-image). The first step of the particle counting fractal dimension determination involves the counting of discrete features within the full image dimensions. This count is performed twice, once ignoring all features that touch the edge of the region of interest, and a second time including these edge touching features in the count. The number of particles was taken as the average of these two counts, and is equivalent to ignoring the particles that touch two of the four edges of the region of interest. Alternatively, and with greater ease, the number of particles can be computed using the IPTK's IP-features → distribution filter. This filter can be used to count all particles in the image, neglecting edge effects (less accurate), or can be used to perform an "adjusted count" which takes into account the number of edge-touching features on the basis of their size distribution (more accurate) [114]. Results from the NIH Image and Photoshop methods are nearly equivalent, but since the data for number of particles were already produced within the data used to compute the particle-counting fractal dimension, there was no need to repeat counts in Photoshop.

Mean microstructural element size (MES) was determined concurrently with the IPTK's IP-features → distribution → size (based on area) filter, and makes no assumptions regarding geometry. By counting the number of pixels a feature occupies, and referencing the μm/pixel calibration, it outputs the result as an area in μm^2.

2.1.3.6. Mean Nearest-Neighbor Distance (NND)

In order to lend support to the belief that fractal dimension analyses reveal information about the degree of order in the network, mean nearest-neighbor distances (NND) were calculated. Of particular interest is not necessarily the value of the NND (which would be indicative of the relative "compactness" of the network particles), but rather the standard deviation of the NND, which would indicate the variation in

distances between particles. If the variation in the calculation of the mean NND is high, it would be indicative of a more disorderly distribution of particles, whereas a lower relative variation would indicate a more orderly distribution.

2.2 Novel Three-Dimensional (Volume) Methods and Materials

2.2.1. Three-Dimensional Slide Preparation

Initial attempts to create a volume suitable for imaging were performed in the following manner: A metal washer of approximately 300 μm in thickness was placed on a glass slide. The slide and the mental washer were preheated to 80°C and the molten fat sample was poured into the ring-shaped washer. A preheated class coverslip was then placed on top of the ring and slight pressure was applied to ensure good contact between the coverslip and the washer. Excess molten fat was therefore forced out by this pressure. The sample, still in the melt, was then transferred to the temperature controlled stage apparatus which was at a temperature of 80°C. Preliminary experiments with a cooling rate of 10°C per minute to 28°C followed by isothermal crystallization for 15 minutes yielded a highly birefringent fat crystal network, capable of being imaged slice by slice all the way through the volume. However, within a very short period of time, the network became excessively birefringent and it became difficult to discern individual crystal agglomerates.

Further attempts to create a volume that was suitable for imaging involved a reduction in the volume thickness. An attempt to source slides with wells of known depth that weren't curved in shape was unsuccessful. Slides with manufactured wells also presented a further difficulty since the depth was variable at any XY position.

A sample preparation that resulted in a suitable volume was performed in the following manner: a standard glass slide formed the base of the sample holder. Two glass coverslips were glued to the glass slide using liquid Krazy Glue leaving a gap of 8 mm between them. Molten fat sample was then placed within this gap and a third preheated glass coverslip

was placed over the gap. Access molten fat sample was forced to out by applying slight pressure. In order to be certain of sample thickness, a small scratch was etched onto the surface of the glass slide, and on the underside of the final coverslip. These small scratches could be viewed under the microscope, and the position of the z controlled stage recorded. This established the top and bottom of the sample, and the overall sample thickness was determined to be 207 μm. This depth is greater than that of a standard glass slide (170 μm) likely due to small contributions in height added by the thin layer of supporting glue and any remaining liquid fat that may have been present between the fixed bottom coverslips at the third coverslip that bridged them from above. A representative schematic drawing is presented in Figure 17.

When a sample in this apparatus was crystallized in the same manner as the washer apparatus, a birefringent crystal fat network was established and could be imaged for an ex-

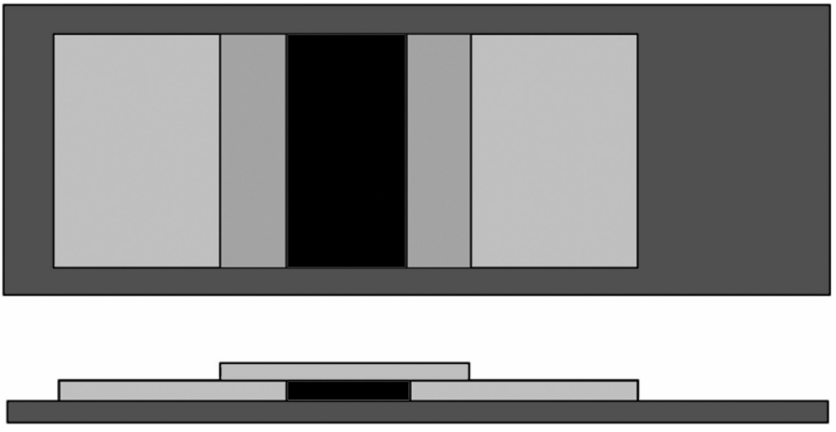

Figure 17 Top view and profile view of the apparatus used to create a 207-μm-thick sample suitable for imaging as a stack. Two standard glass slides (light gray) were glued to a standard glass slide (dark gray). Molten fat (black) was poured into the gap between the two glued slides, and a third glass slide (light gray) was placed on top with slight pressure. Note: components are not shown to scale.

tended period of time without becoming too birefringent, and without changing appreciably in time.

2.2.2 Three-Dimensional Imaging

Imaging of thick sections was performed using the same imaging apparatus as previously described for thin films (section 2.1.2). The only modification to the imaging technique was a change in the aperture setting, which in the case of thick sections, was opened to a wider extent in order to achieve a reduced focusing depth [65].

Prior to imaging, the sample apparatus was viewed under brightfield conditions in order to establish the z-stage position representing the top and bottom of the actual sample. This was achieved by recording the position of the stage when the finely scratched glass surfaces were in focus.

All imaging was performed within the Openlab software module (Improvision Software and Scientific Imaging, Inc, UK). The software includes automations that allow for user input of the following parameters: the stage position at the top and bottom imaging planes, and the number of optical slices desired between these two stage positions. The top and bottom focus planes were set in accordance to the positions of the scratches on the sample holder glass surfaces, as described in section 2.2.1.

The camera and computer interface used were the same as described for the imaging of thin films (section 2.1.2.). Once again, the exposure level was appropriately set to ensure a proper distribution of pixel intensities and the histogram was consulted in order to confirm the appropriateness of the selected exposure time.

The z-series automation (macro) was loaded and started. A total of 150 optical slices were acquired between the top and bottom set-points, and the resulting z-increment was 1.38 μm per slice. The sample thickness was a total of 207 μm. Images were acquired as 8-bit grayscale (256 greys) with an image resolution of 1280 $\times$ 1024 pixels. Each resulting slice was 1.3 Mb in size, and the total imaged volume approximately 192 Mb.

Upon completion of the z-series acquisition, the entire data set was then saved in Openlab's proprietary "LIFF" format, which saves all image and layer information in one file. By selecting all imaged layers, and accessing the file drop-down menu, the entire stack of 2D slices was output as individual numerically ordered 8-bit .TIFF files, which were later analyzed. A 2D projection of the entire stack was prepared, as will be discussed in section 2.2.3. This image was then saved as a separate 8-bit .TIFF file.

2.2.3 Three-Dimensional Image Processing

2.2.3.1. Image Deconvolution—Nearest-Neighbors Algorithm

Image deconvolution was preformed by two different algorithms. The first deconvolution technique used was a component of an image processing application called Openlab 3.1.4, which was developed by Improvision (Improvision Software and Scientific Imaging Inc, UK) and distributed by Quorum Technologies (Quorum Technologies Inc, Guelph, Canada). The deconvolution was performed on the same Macintosh computer system used for the imaging (section 2.1.2). The Openlab deconvolution algorithm employs a "multiple neighbors" technique, for which the background theory was described previously in more detail in section 1.3.4 of the literature review, and briefly reiterated here. In this case, a theoretical point spread function is used to perform the deconvolution [34,96].

Following acquisition of the raw 150-slice volume stack, all layers were selected, and the volume deconvolution option in the image drop-down menu was chosen. Figure 18 depicts the working interface for performing the deconvolution. In order to apply the algorithm to 3D data sets obtained using a polarized light modality (which to date has not been presented in literature) the theoretical point spread function was input as a fluorescence modality. This assumption will be addressed in more detail in section 4.2.

Input requirements include a value for the number of nearest neighbors. Increasing the number of nearest neighbors increases the accuracy of the deconvolution but concur-

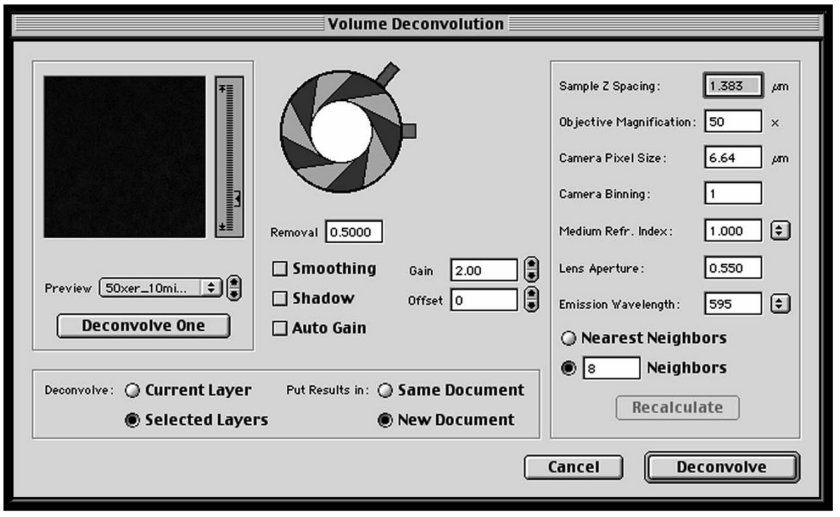

Figure 18 Screen capture depicting the deconvolution dialogue box in the Openlab Volume Deconvolution software application. Input requirements for nearest neighbors (8 in this case) deconvolution include: sample Z-spacings; microscope lens magnification, numerical aperture, medium refractive index, and emission wavelength. Camera pixel size and binning values are also required. A magnified preview image, and navigation within the stack assess the effects of the chosen haze removal, gain, and offset values.

rently increases the time required to perform the deconvolution. Preliminary efforts on images of dimension 1280 × 1024 × 150 employing four nearest neighbors required approximately 1 hour to deconvolve and resulted in mediocre results (not shown). Increasing the number of nearest neighbors to a value of 8 (which means that each slice is deconvolved by referencing four slices above and four slices below each layer) required approximately 3 hours for deconvolution and yielded significantly better results. This value was therefore deemed appropriate.

Input requirements related to the computation of the theoretical point spread function included the sample z-spacing (1.38 μm), microscope lens magnification (50X), numerical

aperture (0.55), immersion medium refractive index (air = 1), emission wavelength (595 nm), camera pixel size (6.64), and binning value [1].

A magnified preview image and slider bar, which allowed for navigation within the stack, gave a real-time assessment of the effects of the chosen haze removal, gain, offset, smoothing, and shadow values. The gain and offset values are analogous to controlling the deconvolved images brightness and contrast values, and were set to values that best represented the refocused structures and avoided pixel saturation [115]. Smoothing reduces the contrast, especially at the edges of features, and was therefore not used. Shadows introduce artificial edge effects, and hence were not used [115].

By altering the degree of haze removal, a subjective decision as to what value is appropriate must be made. In other words, by toggling the haze removal value, the user has the ability to alter pixel values, thereby including or excluding haze on the basis of a visual preview. Since the haze removal is not perfect, by toggling the haze removal value to too great an extent, it appeared to remove actual focused features. This is a well-known and characterized problem with several deconvolution techniques [34]. In order to address this issue, it was decided that a strategy must be implemented to avoid removing features that should be retained. By navigating into various depth positions within the stack, where focused features were present, and toggling the haze removal value to a maximum for each layer, a global "threshold haze removal value" could be determined. This value was such that it did not result in the removal of any actual focused features within the entire 150 slice stack. As a consequence of meeting this requirement, all unfocused haze could not be eliminated; however, enough was removed to produce an improvement in focus at each optical imaging plane.

2.2.3.2. Image Deconvolution—Blind Algorithm

The second deconvolution technique used was an adaptive blind algorithm found within the application called AutoDeblur & AutoVisualize 9.1, which was developed by Auto-

Quant (AutoQuant Imaging Inc, New York, USA). A 30-day full access trial version was downloaded free of cost from http://www.aqi.com. Deconvolution was performed on a Toshiba Satellite 2450 laptop PC with a 2.6 GHz processor and 512 Mb of RAM. Unfortunately, repeated attempts to deconvolve a 3D data set of size $1280 \times 1024 \times 150$ (192 Mb) were unsuccessful due to computer failure, even with what was assumed to be ample processing power and memory. To solve this problem, the size of the data set was reduced to $640 \times 512 \times 150$ (48 Mb) by batch resizing using "constrained aspect ratio" and "smooth bicubic interpolation" in Photoshop. It must be noted that this stepdown in size is not lossless, but rather is analogous to a minor image compression, since groups of pixels are grouped into single pixels by interpolation [116].

The AutoQuant deconvolution algorithm employs an "adaptive blind" technique, for which the background theory was described previously in more detail in section 1.3.4 of the literature review, and briefly reiterated here. In this case, an empirically determined point spread function, computed from the actual data set is used to perform the deconvolution [109].

The numerically sequenced raw 150 slice volume stack was opened in the AutoQuant software. By default, the software displays the stack as one 2D brightest point merge projection image. To view the stack as slices, the slice viewer icon need be accessed. The deconvolution is performed by accessing the "Deconvolution" drop-down menu and selecting "Start 3D Deconvolution" tab. Figure 19 depicts the working interface for performing the deconvolution.

Once again, in order to apply the algorithm to 3D data sets obtained using a polarized light modality the initial estimated point spread function was input assuming a fluorescence optics modality. This included the sample z-spacing (1.38 μm), microscope lens magnification (50X), numerical aperture (0.55), immersion medium refractive index (air = 1), emission wavelength (595 nm). From this initial information, and from the scattering detected from the actual 3D data set, the empirical point-spread function is automatically generated [109]. The automatic deconvolution settings were used, which incorporates an iteration and save interval of 10, file output as

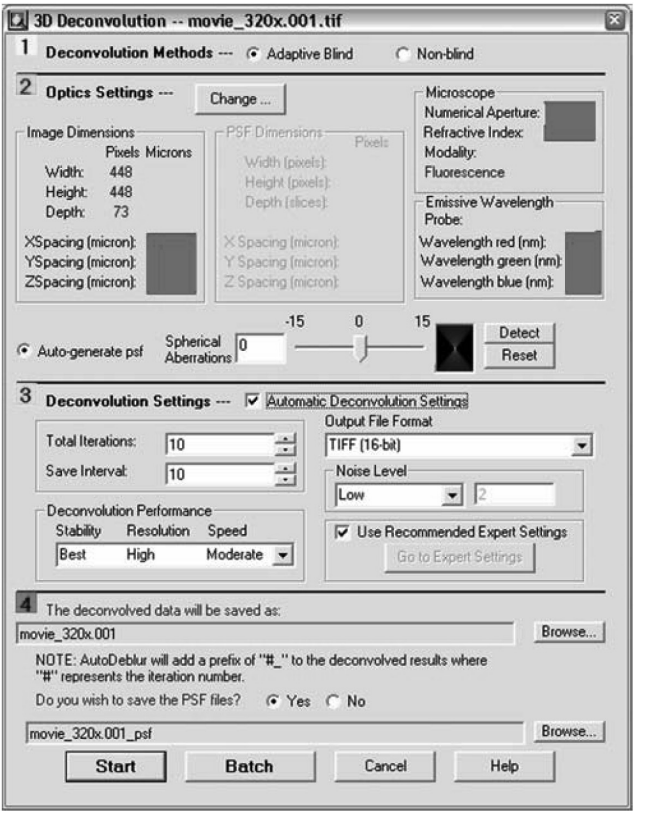

Figure 19 Screen capture depicting the deconvolution dialogue box in the AutoQuant AutoDeblur software application. Input requirements for blind deconvolution include: image X, Y, and Z-spacings; microscope lens numerical aperture, medium refractive index, and modality; and emission wavelength. Spherical aberration can also be input and/or detected. Deconvolution iteration and output format options, and point spread function output are also presented.

16-bit .TIFF, and low noise level. This resulted in the best stability, high resolution, and moderate speed. The resulting PSF was saved as a proprietary .DEB file (630 Mb). This saved PSF file could potentially be used in future nonblind constrained iterative deconvolutions, if deemed appropriate as a

representative theoretical PSF for other specimens. Spherical aberration was assumed to be negligible, and hence was not incorporated into the deconvolution process. For the sake of interest, however, spherical aberration detection was run, and resulted in a value of -0.87 on a scale spanning the range of -15 to 15, indicating little to no influence. Deconvolution required approximately 1.5h for completion, after which the deconvolved 3D data set was then saved as individual 8-bit .TIFF files.

2.2.3.3. Two-Dimensional Projections of Three-Dimensional Data Sets

Two-Dimensional projections of the entire 150 slices of each stack were prepared in order to examine the effects of projection of 3D features onto 2D Euclidean space. The technique employed was a "brightest point merge" or "maximum projection." Each projection was prepared in its respective software bundle. The NN data set was projected in the Openlab software by selecting all 150 layers simultaneously and dragging them onto the "new layer" icon in the layers palette. The software examines each XY coordinate or pixel along the Z direction or "rays," and displays a new layer which represents the 2D projection of the full stack [117]. By projecting the brightest point encountered along each z-oriented ray, the brightest objects are displayed. In the AutoQuant software package, when a stack of images is opened, it by default displays the maximum point projection. To save this projection as a single image, one must simply "save the current view" under the file drop-down menu. In all cases, the output image format was 8-bit TIFF.

Each 2D projection was then analyzed in the same manner as all other 2D images. Images were manually thresholded to isolate discrete features. This required a threshold value of 220 for the NN data set, and a value of 228 for the blind.

2.2.3.4. Three-Dimensional Renderings and Animations

Three-dimensional volume renderings were prepared as a means of visualizing the stack of 2D images, and were not

meant to be used for quantification. Qualitative comparisons of the effects of the nearest neighbors and blind deconvolution on the 3D structure could, however, be made.

A 3D rotating volume rendering was prepared for each of the three data sets (raw, NN, and Blind) using the Autovisualize module in the AutoQuant software bundle (AutoQuant Imaging Inc, New York, USA). Preparing 3D renderings of the full resolution images ($1280 \times 1024 \times 150$) was not possible because of the intense computing power required (this was attempted, but computer crashing/hanging resulted). Images were resized to 640×512, but the same problems occurred. Images resized to 320×256, were however, of suitable size for the rendering to proceed. Images were batch-resized by creating an automation in Adobe Photoshop 7.0 (Adobe Systems Inc, San Jose, CA, USA). Sequentially numbered images were each opened and resized to 320×256 with the "constrain proportions" and "smooth bicubic resampling" options activated. This operation reduced the XY resolution and the size of each image to 82 kb (which in turn made the full 150-slice stack a workable 12 Mb). This step-down in size is analogous to image compression, since groups of pixels are grouped into single pixels by interpolation [116]. This significant step-down in image size also justifies the use of resulting 3D renderings for qualitative purposes only.

The entire stack of sequentially numbered images was opened in the AutoQuant application, and the appropriate X, Y, and Z aspect ratio was input. The "make movie" option in the AutoVisualize drop-down menu was then selected. The software automatically creates a series of 2D projections of the 3D data at various observation angles. To customize the 3D volume rendering, the options drop-down menu in the 3D viewer window was chosen, and the control panel accessed. The rendering mode chosen was "volume rendering—hardware" which is preferred over the "software" option since it creates smoother rotational transitions [109]. The maximum projection mode was selected since it resulted in the best visual representation of the structure. Under the "movies" tab in the 3D viewer control panel, a rotation about the Y-axis from the initial XY starting position to 360° was applied. A step angle of

5° and frames/sec value of 40 were chosen to ensure reasonably smooth rotation and movie quality. The display perspective angle was set to 40° and the hardware volume projection quality setting set to highest. A preview window allowed the user to see the resulting movie file and the "create movie" button created the full rotating series as an AVI file (compatible with most media players).

All movies (raw, NN, and blind) were prepared in the same manner, using the same rendering options. A fourth, anaglyphic movie was created from the blind deconvolved data set, and included the addition of stereoscopic effects to further enhance the 3D depth qualities. Within the movie control panel settings/stereo tab, a red/cyan filter was applied at a +/− angle of 5°. This digital image filter adds a shifted red and cyan color channel to the image features, which when viewed through actual red/cyan filters, creates a perception of added depth [114].

Since 3-D volume renderings cannot be fully appreciated and evaluated in the form of 2D printed images, they are included in digital format on the DVD in the Appendix. To access them, the HTML file entitled "index" should be opened in any web browser on a Macintosh of PC computer capable of viewing AVI file types. By following the "Movies" link, the 3D rendered movie files should be readily located within.

2.2.4 Three-Dimensional Image Analysis

Without the acquisition and use of very expensive 3D analysis software, information about the 3D dimensional fat crystal network can still be obtained. This was attained by two methods: firstly by performing analysis on each slice as an independent image, and secondly by creating a 2D representation or "projection" of all the slices that made up the 3D volume.

2.2.4.1. Two-Dimensional Slices from Three-Dimensional Data Sets

The 2D images that made up the raw 3D z-series contained too much haze and out of focus features to confidently and accurately segment true features via thresholding. For this reason, analysis of the raw 3D data sets was not performed.

Two-dimensional images that resulted after deconvolution by both the nearest neighbors and blind algorithms, however, were suitable for thresholding because ample haze was removed to allow for discrete feature isolation. Automatic thresholding (see section 2.1.3) was not an option for converting these data sets to binary images prior to analysis, since the resulting binary images did not adequately or accurately represent the features present. Manual thresholding was preformed in the same manner as it was in the binarization of thin section images in section 2.1.3.

For consistency, a constant threshold value was used for all images within each 3D stack. After performing the procedure for determining an accurate thresholding value in a subjective manner (see section 2.1.3) in every tenth slice in each stack, the same threshold was applied to all images in each stack. The nearest-neighbor data set was thresholded at a value of 220 and the blind stack was thresholded at a value of 250. All binary images were analyzed by the same methods described for thin films (section 2.1.3). The XY μm/pixel ratio was assumed to be independent of position in the Z direction, and the same calibration file used in thin film studies was therefore used for all slices in the 3D volume.

2.2.4.2. Two-Dimensional Projections

Each set of 2D binary images was then analyzed in the same manner as conventional 2D images of thin sections, including the area fraction, number of discrete particles, mean particle size, and fractal dimensions D_b and D_f (section 2.1.3).

In addition to these analyses, a quantitative fast Fourier transform (FFT) image analysis technique was used to qualitatively demonstrate the degree of haze removal in projections following NN and blind deconvolutions. After selecting a 512×512 pixel region of interest from each image 2D projection (raw, NN, and blind), the IPTK filter IP-FFT → forward FT was applied. This filter converts the spatial domain to the frequency domain, and replaces the original image with the power spectrum [114]. The resulting patterns in the power spectrums were then examined for the presence of characteristic banding which is indicative of focus quality and in this case the presence of haze [114].

2.2.4.3. Pearson Linear Correlation Analysis

Pearson correlation calculations are based on the assumption that both X and Y values are sampled from populations that follow a Gaussian distribution, at least approximately [118]. When two variables vary together, a high correlation between these variables occurs. A significant correlation is characterized by a p-value of less than 0.05.

This correlation analysis was carried out on all parameters studied, following blind deconvolution. When performing correlation on these parameters as a function of depth, the range of data was limited to the range corresponding to the top of the sample to the peak value of the parameter observed within the volume. Correlation analysis of various parameters to particle size was preformed after removing two outlying points. This will be addressed further in section 3.2.8.

3. RESULTS AND DISCUSSION

3.1. Qualitative Results

3.1.1. Crystallization in a Thin Film (Two-Dimensional, Confined Space)

When viewed under cross-polarized light, solid crystal mass was observed in the form of bright distributions of particles. The anisotropic nature of solidified crystals (seen as various shades of white and gray) differentiates them from the isotropic liquid phase (which remains stark black in color) [65,66]. Grayscale micrographs of the networks produced under thin film conditions are presented in Figure 20. Corresponding binary images, which were used for further quantitative analyses, are depicted in Figure 21.

Each nucleation event is believed to result in an individual primary particle of approximately 500 nm in size [4,12]. These particles then clustered to form significantly larger aggregates in the range of 100–300μm (Figs. 20 and 21). On average, there were 10 large clusters within the field of view. When compared to images of focused planes of the same mate-

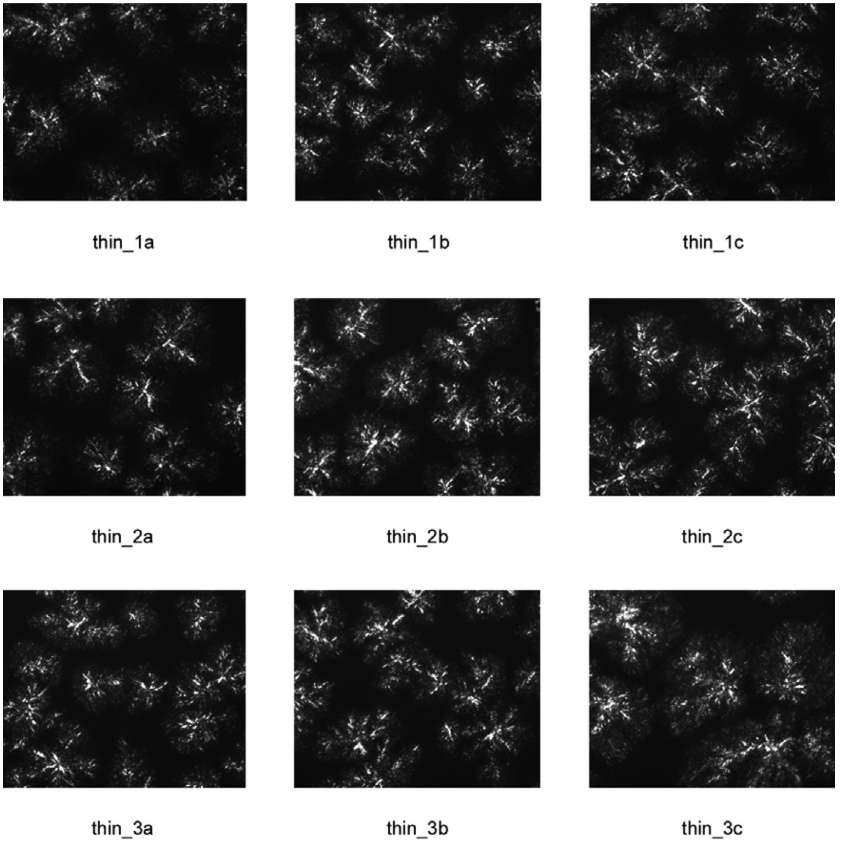

Figure 20 Polarized light micrographs (8-bit grayscale) of the model fat system crystallized for 15 minutes at 28°C in a thin film (approximately 20-μm thick). Image names indicate slide number [1–3] and repetition (a–c) [76].

rial growing in three dimensions (Fig. 22), it appears that the large clusters growing in two dimensions are similar in radial diameter and general 2D shape, but are more numerous than in any given focused optical slice in 3D.

This observation intuitively suggests that the growth of clusters to these large sizes is strongly influenced by the volume available for growth. Since the thickness of the sample is lim-

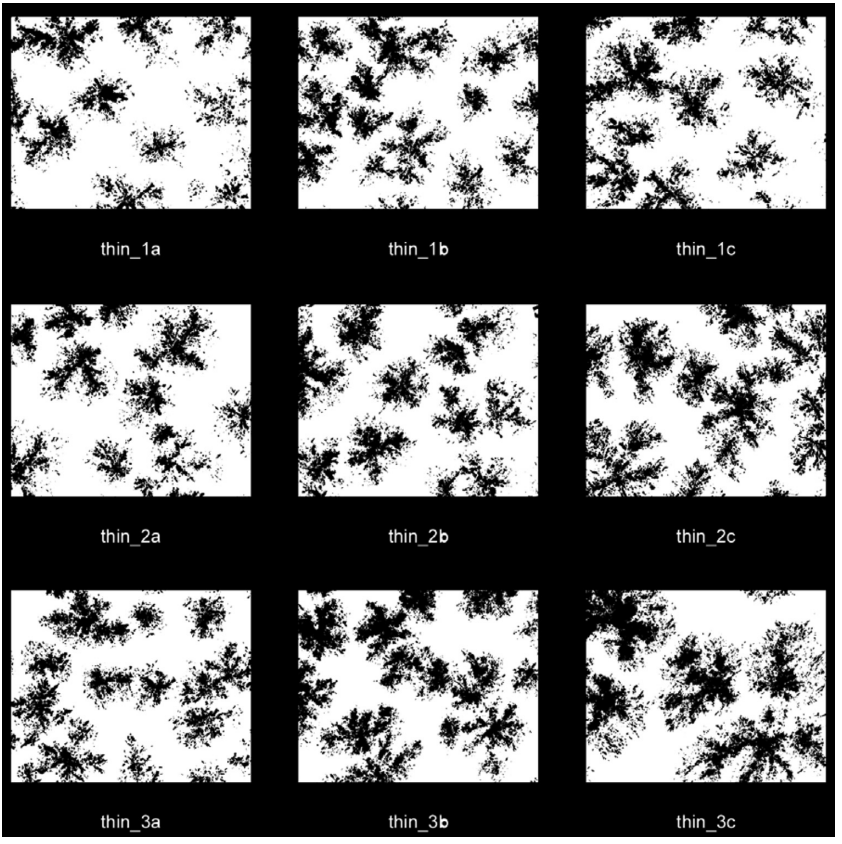

Figure 21 Manually thresholded polarized light micrographs (binary) of the model fat system crystallized for 15 minutes at 28°C in a thin film (approximately 20-μm thick). Image names indicate slide number [1–3] and repetition (a–c).

ited to approximately 20 μm, spherulitic growth beyond a critical radius of 20 μm is hindered. Since these clusters continue to grow as crystallization progresses, the only possible subsequent circumstances would be: (a) continued, true spherulitic growth; (b) forced, continued lateral growth; or (c) some combination of the former two behaviors. Within the area of lipid crystallization, there is a void in the literature, and these issues have not been sufficiently investigated nor addressed.

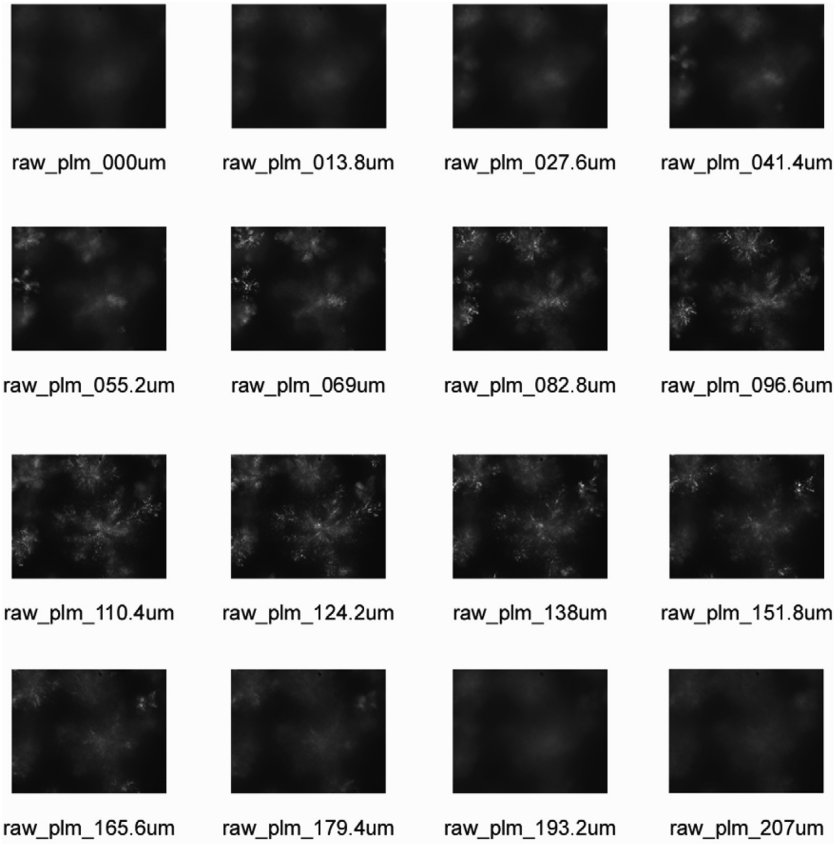

Figure 22 Raw polarized light microscopy images of the 207-μm thick sample. Shown here is every tenth slice, which represents a step size of 13.8 μm into the sample. The actual experiment contains 150 images at 1.38-μm increments.

Many crystallization conditions (such as slow cooling and /or crystallization at low degrees of supercooling) result in large clusters that exceed the sample thickness by several fold [1,2,5,7,8,10,14–16,18–21,23,68]. These resulting structures have often been referred to erroneously in the literature as large "spherulites" when in fact simple geometric arguments would suggest that they are actually disc or plate-shaped with

thicknesses of just a fraction of their lateral diameters. In theory and in practice, continued, unabated growth of large spherulites beyond the sample thickness is highly unlikely. The growth of large structures capable of physically "lifting" the coverslip and thereby increasing the overall sample thickness is not plausible. In practice, this behavior would be easily detected, because conventional polarized light imaging would then be problematic. Difficulties in imaging would arise, since large clusters would exceed the depth of focus for the objective lenses used, and create multiple, focal planes. In practice, this is not observed to any appreciable extent; however in some very specific, rare instances the growth of large clusters does increase the sample depth by a small amount [119].

Despite the seemingly imminent influence of confinement on the growth of crystal networks, extensive empirical experimentation has demonstrated that valuable and credible information can still be harvested from images of networks growing under these conditions [1,2,5,7,8,10,14–16,18–21,23,68]. These analyses were carried out on the images of networks growing in two dimensions and on deconvolved 2D slices taken from 3D data sets and will be presented in section 3.2.

3.1.2. Crystallization in a Volume (Three Dimensions, Unconfined Space)

3.1.2.1.Raw Polarized Light Microscopy (PLM) at Multiple Imaging Planes

Thick samples, when viewed under cross-polarized light, demonstrated birefringence similar to that of thin films, but because crystallization occurred at various depths in the sample, any given optical plane within the volume contained both in and out-of-focus features. Features that fell above or below the focusing depth for a particular objective lens appeared as scattered light or haze. Micrographs depicting raw polarized light optical planes at various depths within the 207-μm-thick sample are presented in Figure 22.

At the first optical plane (Fig. 22—0 μm), which is the upper boundary, a significant amount of haze was observed, while no discernable features appeared to be in focus. As the

motorized z-stage moved up, the focal plane moved incrementally deeper into the sample, and the hazy areas became progressively more crystal-like in appearance. It wasn't until a depth of approximately 40μm that features became in-focus. However, while some features appeared in focus, additional features that presumably lay at deeper points in the sample still contributed haze (see Fig. 22—41.4 μm). Stepping further into the sample, some of the larger clusters remained in focus at multiple focal planes, indicating that these features had geometries that spanned the z-axis. In other words, aggregated crystal masses were of sufficient size and appropriate shape to occupy 3D space. When stepping further into the sample, features in various XY positions appeared more in and out of focus in the z-direction, until a point deep within the sample where, similar to shallow depths in the sample, features no longer in focus were present (see Fig. 22—193.2 μm). Beyond this depth, an appreciable amount of haze was again present. The presence of great amounts of haze at the top and bottom of the sample made it difficult to conclusively determine whether material was crystallizing on the top and bottom glass surfaces, or whether all mass was centralized in the middle of the volume confines.

After stepping through the sample from top to bottom, a "mentally mapped" rendering of the network could be predicted. The imaged volume consisted of six large clusters of crystalline material (almost half the number of clusters observed in thin film growth), each having different centres in 3D space (Fig. 23*D*). Some of these 3D clusters appeared to be of similar diameter to those disc-shaped clusters observed in thin film crystallization (Fig. 20), however much of the crystallized mass was in the form of one very large branched cluster (Fig. 23*D*—1). This large 3D cluster was not generally of spherical shape, but was larger in XY dimensions (about 300 μm at its greatest length) than in its depth in the Z dimension (about 100 μm at its greatest length).

The presence of haze from planes above and below each optical slice also confounded the identification of the outer edges of the large clusters of particles. Moreover, small particles that made up the larger clusters were also difficult to

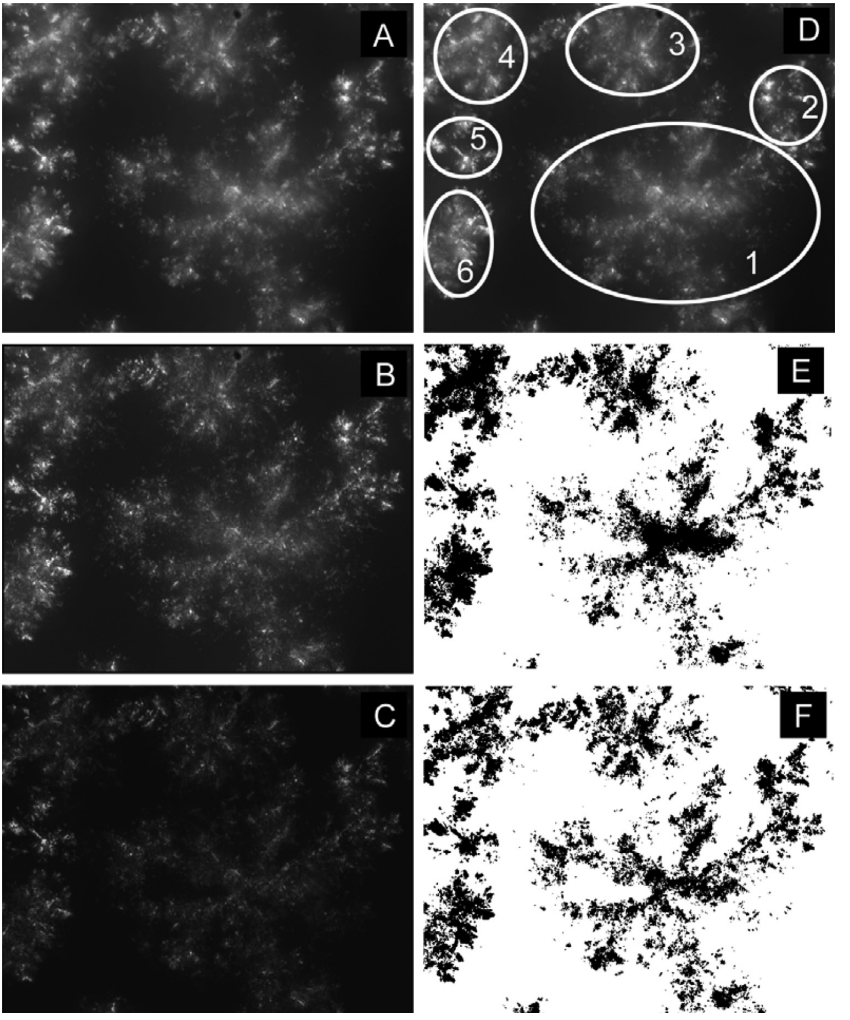

Figure 23 Two-dimensional projections of three-dimensional stacks of the 20-μm-thick sample: (**A**) raw polarized light, with (**D**) major features labeled; (**B**) following deconvolution by the nearest neighbors algorithm, and (**E**) subsequent thresholding; and (**C**) following deconvolution by the adaptive blind algorithm and (**F**) subsequent thresholding. Projections were obtained by the brightest point merge technique.

identify discretely. The aim of deconvolution was to remove haze from out of focus planes, and therefore, improve this situation in order to be able to observe features and their locations with greater accuracy.

3.1.2.2. Nearest Neighbors Deconvolved Images of Multiple Planes

All 150 slices in the stack were deconvolved by the nearest neighbors (NN) algorithm. Every tenth slice within the stack (at 13.8 μm increments in depth) is shown in Figure 24 and their corresponding thresholded features shown in Figure 25. These images, when compared to their corresponding original raw PLM images (Fig. 22), demonstrate a small degree of success in terms of haze removal and feature sharpening.

When comparing the uppermost slice in the NN deconvolved volume to the raw PLM image at the same Z-position much but not all out of focus haze was removed. When progressing deeper into the stack the presence of less haze was still noted at depths that did not include in-focus material (Fig. 24–13–55.2 μm). Some of this haze was retained upon subsequent thresholding (Fig. 24—13–55.2 μm). Marked improvements in the ability to observe discrete crystallites could be noted at depths that included in-focus features (Fig. 24—69–165.6μm), however, some residual haze was also retained upon thresholding for feature isolation (Fig. 24—69–165.6 μm). In slices at greater depths yet, where no in-focus features existed (193.2–207 μm) significant haze was observed but a slight improvement over the raw slices was observed in all slices.

Qualitatively, NN deconvolution was successful in removing only a portion of the out of focus haze present, and therefore wasn't as efficient as anticipated.

3.1.2.3. Blind Deconvolved Images of Multiple Planes

The raw PLM stack was deconvolved by the blind algorithm, and every tenth slice within the stack (at 13.8 μm increments in depth) is shown in Figure 26 and their corresponding thresholded images in Figure 27. These images demonstrate

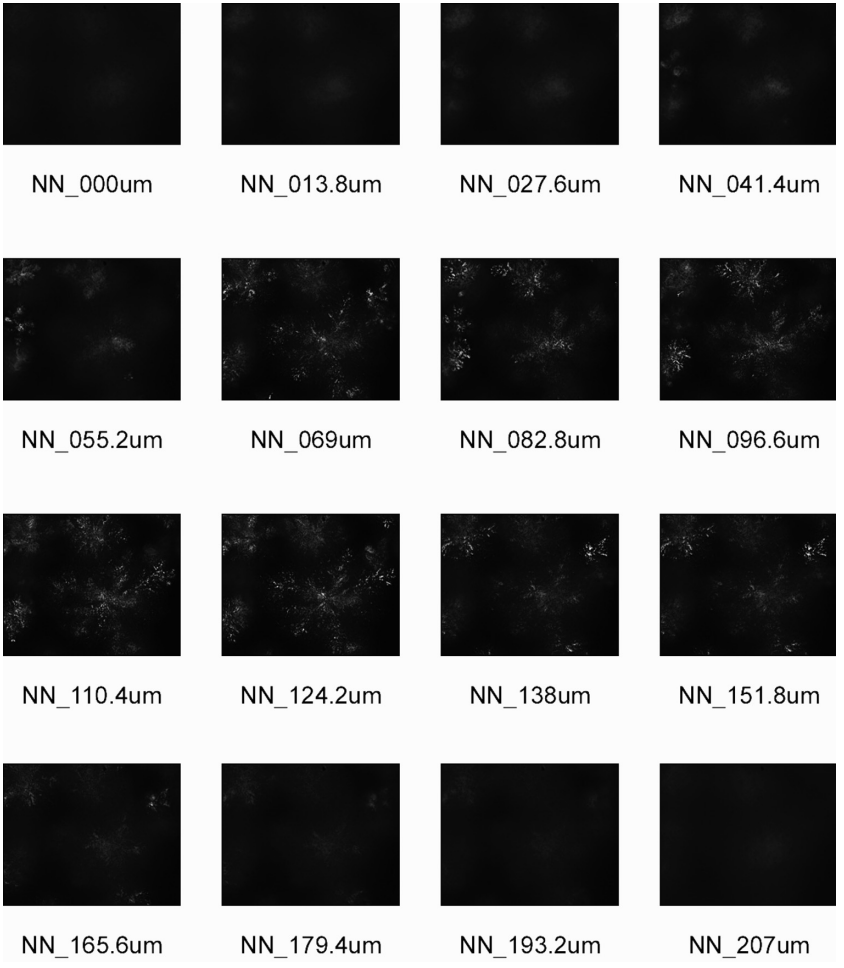

Figure 24 Polarized light microscopy images of the 207-μm-thick sample following deconvolution with the nearest neighbors algorithm. Shown here is every tenth slice, which represents a step size of 13.8 μm into the sample. The actual experiment contains 150 images at 1.38 μm increments.

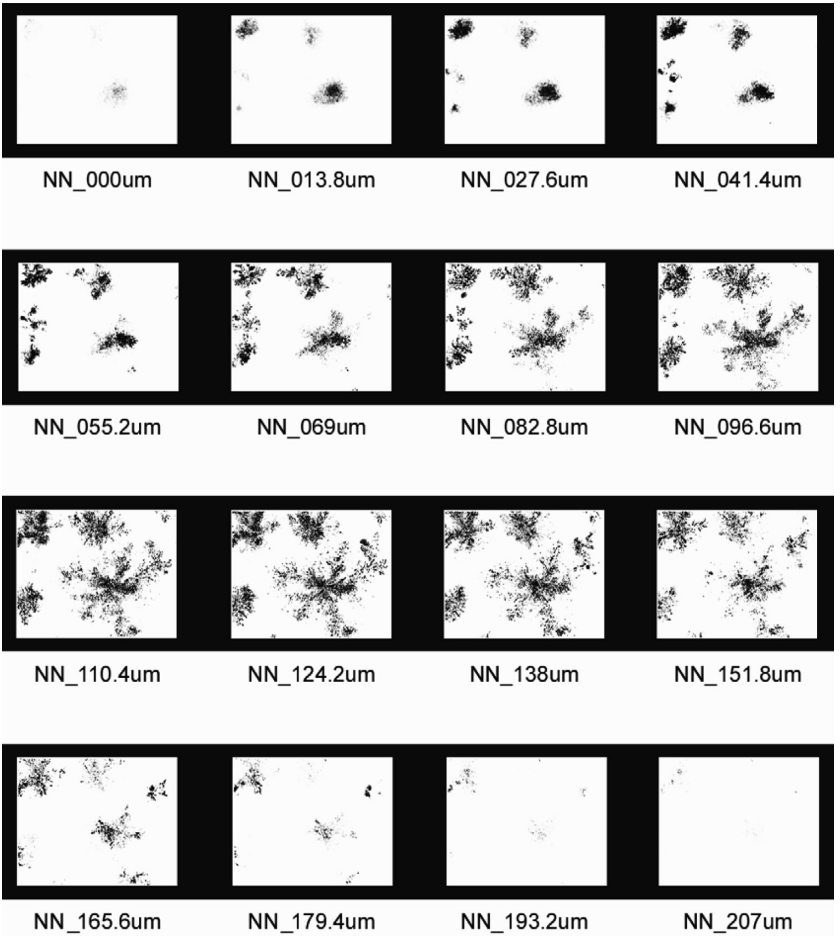

Figure 25 Thresholded polarized light microscopy images of the 207-μm-thick sample following deconvolution with the nearest neighbors algorithm. Shown here is every tenth slice, which represents a step size of 13.8 μm into the sample. The actual experiment contains 150 images at 1.38 μm increments.

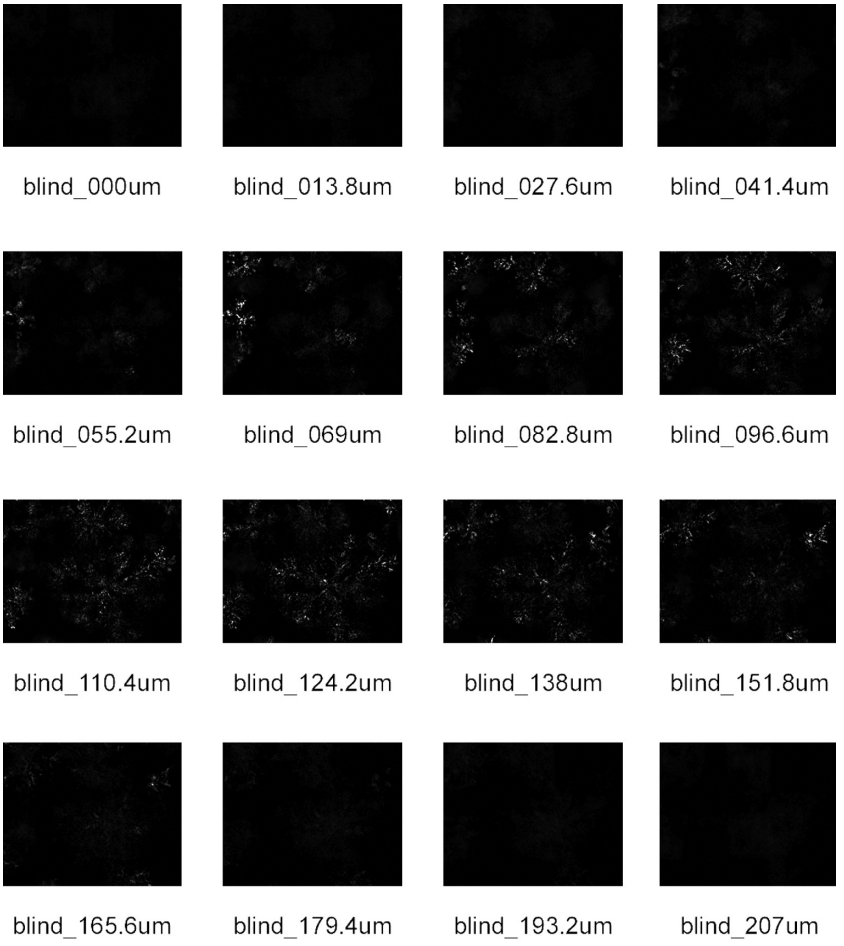

Figure 26 Polarized light microscopy images of the 207-μm-thick sample following deconvolution with the adaptive blind algorithm. Shown here is every tenth slice, which represents a step size of 13.8 μm into the sample. The actual experiment contains 150 images at 1.38 μm increments.

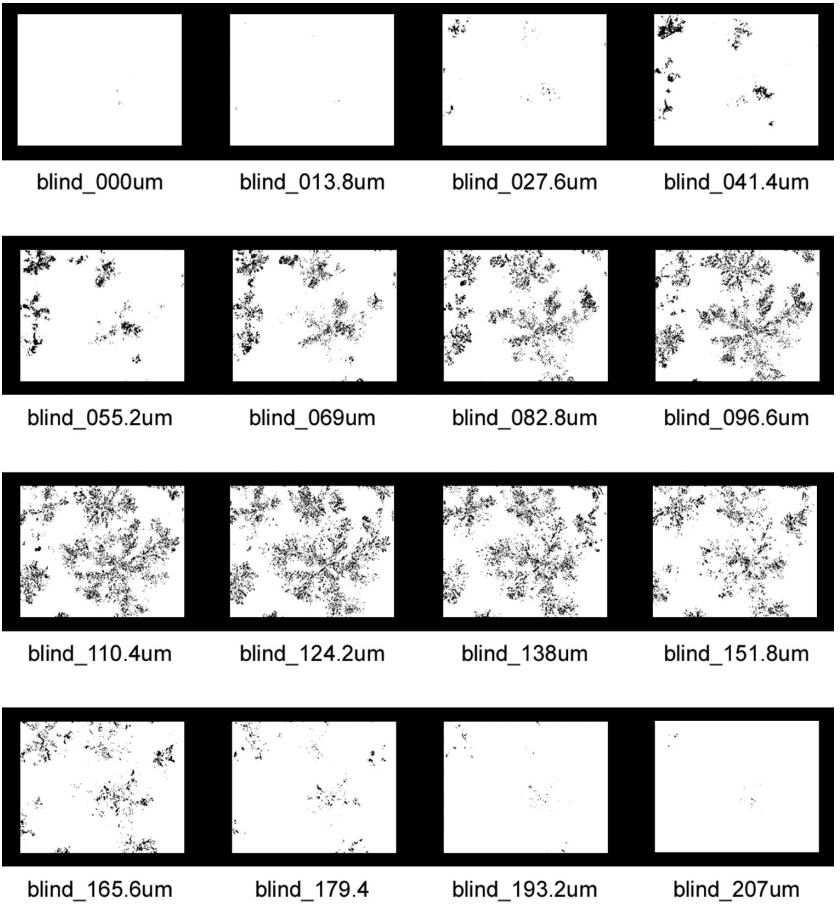

Figure 27 Thresholded polarized light microscopy images of the 20-μm thick sample following deconvolution with the adaptive blind algorithm. Shown here is every tenth slice, which represents a step size of 13.8 μm into the sample. The actual experiment contains 150 images at 1.38 μm increments.

a significant improvement in haze removal and feature sharpening when compared to their corresponding original raw PLM images (Fig. 22), and demonstrate much better results than those arrived at by NN deconvolution (Fig. 24). The presence of a small amount of focused material on the top and bottommost slices may have been an indication that a small amount of the sample crystallized on the glass surfaces. Following deconvolution by the blind algorithm, no detectable haze was present in all slices within the stack. For this reason, the images deconvolved by the blind algorithm are believed to be most representative of the actual crystal network.

Another observation that could be made from qualitative examination of the micrographs was the apparent presence of more crystal mass in the lower half of the volume, which may have resulted from an uneven distribution of cooling of the sample, and can be attributed to the construction of the cold stage apparatus. This hypothesis will be addressed in more detail in a following discussion on quantitative results (section 3.2.1).

3.1.3. Two-Dimensional Projections of a Three-Dimensional Volume

3.1.3.1. Raw PLM Two-Dimensional Projection

The 2D projection of the 3D data set provided a means of observing all of the network features (Fig. 23*A*,*D*). Since this technique was a projection, all information regarding the third dimension was lost, however, it allowed us to see all of the network features on one representative, collapsed 2D image. Since this projection contained the brightest pixels at all XY coordinates within the full raw PLM stack, it retained much of the haze that was described earlier. This haze contribution rendered the image unfit for reliable thresholding and quantitative analyses since any thresholding value chosen either retained much haze, or completely eliminated pertinent structures.

Examination of the 2D projection confirmed the presence of six large clusters of crystals, which are identified in Figure

23D. Comparison of the raw PLM 2D projection of the 3D volume to images of the same material crystallizing under the same cooling conditions in a thin film (Fig. 20) demonstrate major differences in overall network structure and cluster properties. Crystal growth in unconfined space appeared to result in larger, less numerous crystal aggregates compared to the smaller, more numerous crystals resulting from growth in a thin film. This observation corresponds well to expectation: the same amount of material crystallizing in an unconfined space would have the innate ability to grow to larger proportions. In addition, the rate of heat transfer in a thin film would be greater than that of a larger sample. This would potentially lead to enhanced nucleation, which may have lead to the formation of a higher number of clusters. Also, within a thin film, crystallization of clusters with centers at greater distances from one another would be promoted by highly localized heat evolution occurring during the phase transition from liquid to solid. This is likely the cause for a greater number of clusters observed in the thin film compared to less, larger clusters that were present in the volume sample.

A final qualitative observation lay in the amount of apparent mass in both scenarios. Even though the 2D projection may result in merging of mass at similar XY coordinates but varying depths, the overall mass occurring appears to be similar to the amount of mass observed in thin films under the same crystallization conditions. This hypothesis will be addressed quantitatively in section 3.2.1.

3.1.3.2. Deconvolved Two-Dimensional Projections

2-Dimensional projections of 3D image stacks following deconvolution by the nearest neighbors and blind algorithms are presented in Figures 23*B* and 23*C*, respectively. Deconvolution and subsequent 2D projection revealed a small degree of haze removal by the nearest neighbors technique. While some features were enhanced, the presence of residual haze still confounded the ability to clearly identify small crystals within the larger clusters. This is more evident when examining the thresholded image in Figure 23*E*.

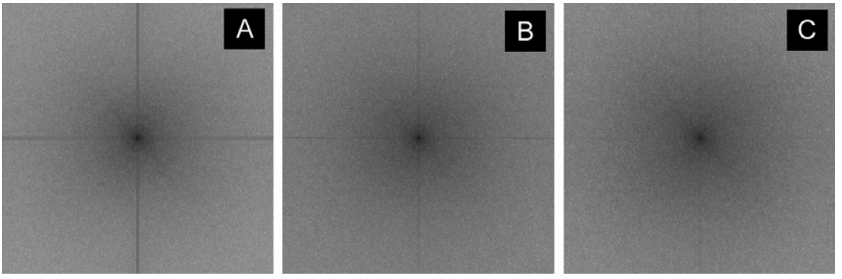

Figure 28 Forward Fourier transforms of 512 × 512 cropped areas of two-dimensional projections of 3-dimensional stacks of the 207-μm thick sample: (**A**) raw polarized light, (**B**) following deconvolution by the nearest neighbors algorithm, and (**C**) following deconvolution by the adaptive blind algorithm.

Following blind deconvolution, on the other hand, the 2D projection shows a distinct improvement in the ability to clearly identify discrete crystals, since most, if not all of the haze due to scattering was removed (Figs. 23*C*,*F*). Examination of the FFT power spectrums of 2D projection images revealed the relative amounts of poorly focused or hazy features (Fig. 28). The cross pattern observed in the power spectrum of the raw 2D projection indicates significant presence of haze (Fig. 28*A*). Following NN deconvolution, the relative amount of haze is reduced, and can be seen as a narrowing of the cross-pattern in its power spectrum (Fig. 28*B*). Finally, the high degree of haze removal by the blind deconvolution technique results in just a faint trace of the banding in the power spectrum (Fig. 28*C*). This qualitative examination of the power spectrum serves as a semi-quantitative proof of the relative efficiencies of the two deconvolution algorithms used.

3.1.4. Three-Dimensional Volume Renderings

Because 3D volume renderings cannot be fully appreciated and evaluated in the form of 2D printed images, they are included in digital format on the DVD in the Appendix. To access them, the HTML file entitled “index” should be opened in any

web browser on a Macintosh or PC computer capable of viewing. AVI file types.

By viewing the 3D rotating movie files, comparison of the raw PLM rendering ("raw_3Drender.avi") to those created from NN ("8n_neigh_3Drender.avi") and blind deconvolution ("blind_3drender.avi") reveal dramatic differences in the level of efficiency of haze removal and improved feature recognition. As was the case in the examination of deconvolved 2D slices and 2D volume projections, the nearest-neighbors algorithm removed only a small portion of the out-of-focus haze. The blind algorithm, on the other hand, demonstrated a high degree of haze removal and feature sharpening.

Qualitative information about the structure of the crystal network in 3D space can also be taken from these renderings. For example, the localization of almost all of the crystal mass within the center of the volume, and not at the upper and lower boundaries is clearly evident. The locations of the large clusters relative to the embedding space and relative to other clusters in the volume can also be qualitatively observed.

One observation of particular significance can be made when observing the network in the YZ plane (by pausing the rendering video, this plane can be observed without the burden of motion). Crystals appear to be somewhat stretched in the z-direction. This may be due to a number of causes including: an artefact of the 3D rendering process; improper calibration of the z-stage; or crystals actually tend to grow in this manner. Calibration of the z-stage is far from trivial, but might rule out any of the proposed causes for this observed stretching behavior. One possible calibration procedure is discussed in more detail in the section on recommendations for future research (section 6).

3.2. Quantitative Results

3.2.1. Area Fraction (% black)

The amounts of crystal mass present, determined by computing the area fraction of binary images of 2D slices from each deconvolved volume, their 2D projections, and the structures that resulted from growth in thin films are presented in Figure 29.

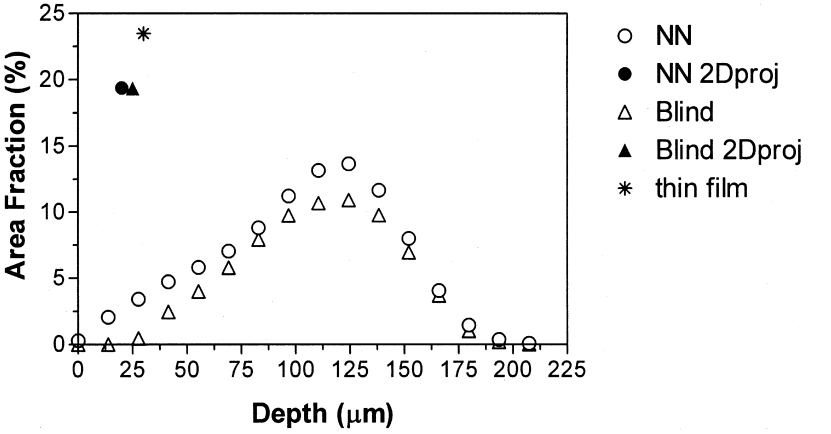

Figure 29 Area fraction (%) vs. depth (μm) in a 207-μm- thick sample. Every tenth slice (or 13.8μm) within the deconvolved 3D stack (nearest neighbors and blind algorithms) was analyzed. 2D projections (by brightest point merge) of each 3D stack and a 20-μm-thin film sample are also included for comparison.

3.2.1.1. Two-Dimensional Slices of the Three-DimensionalVolume

An immediately evident trend is observed for results of the area fraction of deconvolved stacks as a function of slice depth. In both cases, results suggest that there is a higher concentration of solid crystal mass in the middle portions of the volume, with progressively less mass residing in the upper and lower portions of the sample. These results also suggest that crystal growth had not taken place to an appreciable extent at the upper and lower sample boundaries. This also suggests that the growth mode of the clusters is of a radial nature, with early crystallization events occurring centrally and subsequent growth occurring in all directions. As noted in section 3.1.2, many of the clusters were of nearly spherical geometry, but one predominant large cluster was significantly larger in XY plane than Z plane (Fig. 23D-1) and contributed greatly to these measured results.

Another observed trend was the shift in peak mass to slightly below the middle depth. This shift in mass concentration to depths below center may mean that the earliest nucleation conditions of under-cooling and molecular compatibility were satisfied below center. This may also be supported by the hypothesis that this downward shift in mass localization may have been in part influenced by the nature of the cooling apparatus used. The construction of the Linkam cold stage is such that the greatest driving force for cooling may be located directly beneath the sample, creating a gradient in heat transfer that is in theory greater toward the bottom of the sample. Liquid nitrogen is pumped into the stage apparatus, and is circulated through a high heat capacity (copper) block that supports the sample slide. As a result, the overall sample temperature may not be evenly distributed in the z-direction, and enhanced conditions for nucleation and crystal growth may be created in a location below the center of the sample. It is also possible that sedimentation due to gravity occurred prior to imaging.

Comparison of the results for the two deconvolution algorithms used yielded quantitative results that confirmed qualitative observations. Since more haze was removed by the blind technique, the area occupied by remaining thresholded features was slightly lower in all slices studied. However, the peak area occurred at the same depth in both cases, indicating that both methods result in highly similar indications of mass relative to depth. The exception to this finding is that the residual haze in the NN data resulted in a gross overestimation of the amount of crystal mass present in the uppermost and lowermost slices (on the glass surfaces). On the other hand, values of near zero area fraction at the top and bottom slices following blind deconvolution correspond to the visual inspection of slices and belief that just a very small amount of crystal was actually present at these locations.

A significant linear correlation coefficient between area and depth ($r = 0.98$, Table 1) indicated that as the sample was analyzed from the top to the peak value (near the middle) more mass was progressively present.

Table 1 Pearson Linear Correlation Coefficients for Various Network Parameters Determined by Image Analysis of Polarized Light Micrographs of 2D Slices of a 3D Volume Following Blind Deconvolution. Negative Correlations Indicate an Inverse Relationship. Correlations that are Statistically Significant are Bolded

	Depth[b]	Area Fraction	D_f	D_b	N	Standard Deviation of NND
Area Fraction	**0.98**					
D_f	**0.92**	**0.79**				**−0.72**
D_b	**0.96**	**0.98**	**0.84**			**−0.73**
N	**0.96**	**0.98**	**0.84**	**0.97**		
MES[a]	**0.87**	**0.86**	0.26	**0.81**	**0.85**	

Bolded: $p < 0.05$
[a]Outliers removed.
[b]From top of sample to peak value.

3.2.1.2. Two-Dimensional Projections of Three-Dimensional Volumes

Comparison of the 2D projections following both deconvolution methods revealed no appreciable differences in the area fraction upon thresholding. Since the majority of haze results from scattering directly above crystal mass at lower depths, much of the haze retained following the NN deconvolution would have been obscured by the lower laying crystal mass. Therefore, the haze in the 2D projection did not contribute to an increase in the area fraction upon thresholding. Both 2D projections values, however, are greater than the peak value within the volume because the projections include the contribution of all the clusters present. Also important to note is that the area fraction for the 2D projections are not equal to the cumulative contribution on the slices that make up the 3D stack. This is due to two factors: (a) the occurrence of masking and merging of features from separate clusters that share XY coordinates but are located in various different locations in the Z direction, and (b) some features within clusters extend into multiple planes in the Z-direction. Visual examination

and interpretation of the 3D renderings in the Appendix DVD support both of these claims.

3.2.1.3. Thin Film Conditions

The area fraction of crystal networks that resulted from growth under confinement in thin films are also shown in Figure 29. After observing these networks (Fig. 20) and knowing that the clusters are forced to grow laterally, the fact that they possess a higher area fraction relative to any given 2D slice from a volume set and relative to the 2D projections can be expected. Although differences in the amount of crystalline material that resulted in both the volume and thin film samples were assumed to be negligible, the nature of the growth of the material differed and was detectable via differences in the area fraction.

3.2.2. Fractal Dimension (D_f)—Degree of Order and Fill

Fractal analyses of polarized light micrographs revealed characteristics of the crystal networks growing in a volume and in thin film conditions. In particular, information pertaining to the spatial distribution of mass and in the network and the degree of fill (via D_f and D_b) was obtained. These analyses also yielded new-found experimental evidence related to fractal scaling theory in 2D and 3D Euclidean space.

The particle-counting fractal dimension (D_f) is sensitive to both the degree of order and fill displayed by the particles that make up the network [4,12–14,24]. As stated previously, a high value for D_f is associated with a network that results from a more space-filling network and/or more orderly distribution of particles in space, and often is the result of slow cooling or cooling to lower degrees of supercooling for example [4,7,12–14,24]. On the other hand, lower relative values for D_f can be expected when particle distribution is more disorderly in nature, and/or less space-filling, such as under faster cooling or cooling to a higher degree of supercooling. Empirically, D_f is believed to be more sensitive to order than to space-filling properties [62]. This analysis has been used extensively in thin film studies, and only now is being used to examine volumes. Fractal dimension

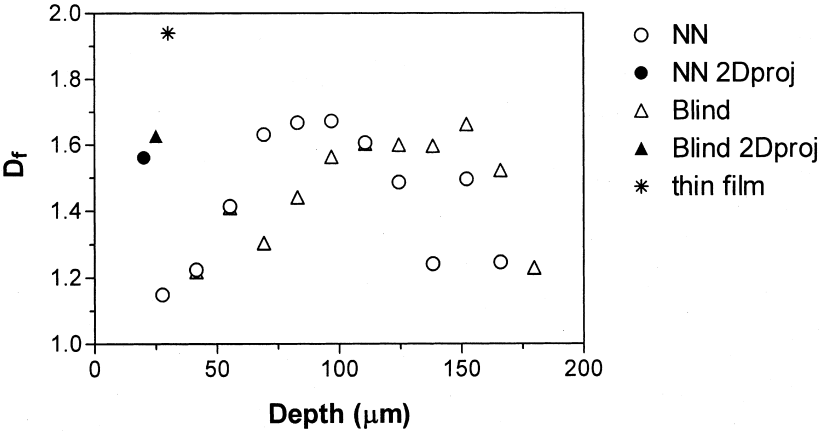

Figure 30 Particle-counting fractal dimension (D_f) vs. depth (μm) in a 207-μm-thick sample. Every tenth slice (or 13.8 μm) within the deconvolved 3D stack (nearest neighbors and blind algorithms) was analyzed. 2D projections (by brightest point merge) of each 3D stack and a 20-μm-thin film sample are also included for comparison.

determinations by the particle-counting method of 2D slices of 3D volume stacks, 2D projections of 3D volumes, and 2D thin film conditions are depicted in Figure 30.

3.2.2.1. Two-Dimensional slices of the Three-Dimensional Volume

Much like the trends observed for the area fraction for 2D slices of the 3D volume, D_f values were highest ($D_f \sim 1.6$) at depths in more central portions of the sample. This experimental value corresponds well with the predicted value of particle-cluster diffusion-limited aggregation ($D = 1.7$, $d = 2$) by computer simulation and is an indication of the growth mode of the large clusters of particles [33,38]. This also intuitively makes sense since the slices that demonstrated this value of 1.6 consisted primarily of a cross-section of one large cluster. This also indicates that the spatial distribution of mass in this general location was more orderly compared to the upper and lower regions of growth where values were much lower ($D_f = 1.10–1.40$). Intuitively, if the large clusters are growing

in a somewhat spherical fashion (section 3.1.2) then it stands to reason that the distribution of mass near the centers of such clusters would be of higher order, simply because they have had more time and ability to set. Changes in crystal habit that involve molecular transitions to more stable polymorphs can occur within minutes of the onset of crystallization [8,17,120–123], but transitions to more stable structures at the mesoscale level are not as easily demonstrated. Since crystallization in the case of this study was conducted at a relatively low degree of supercooling, it is conceivable that diffusion and molecular mobility may be high enough to allow for restructuring. Also, some experimental evidence from literature suggests that in thin films, large discs formed by slow cooling or cooling to low degrees of supercooling can result in more compact or orderly crystal structure in their interiors relative to their outermost regions [8].

The degree of order was found to be significantly correlated with depth, when analyzed from the top of the sample to the peak value, below the middle of the sample ($r = 0.92$, Table 1). This would indicate that the sample was fuller and/or more orderly as a function of depth in this range.

3.2.2.2. Two-Dimensional Projections of Three-Dimensional Volumes

The values of D_f for the 2D projections were similar following deconvolution by both techniques (Fig. 31). This indicates that differences in the degree of haze removal due to the two deconvolution methods, when presented as 2D projections, did not result in a detectable difference in spatial distribution of mass. An experimental D_f value of 1.63 for the blind 2D projection corresponds well with the predicted value for cluster-cluster diffusion-limited aggregation ($D = 1.7–1.8$, $d = 3$) [38,43]. This intuitively makes sense, since we are observing a projection of a group of clusters in 3D embedding space that could quite conceivably be part of a larger cluster. More interesting, however, is the finding that the experimental particle-counting fractal dimension of the 2D projection of the 3D volume ($D_f = 1.63$) corresponds to the peak value observed within the 2D slices of the 3D volume ($D_f = 1.66$). This result provides

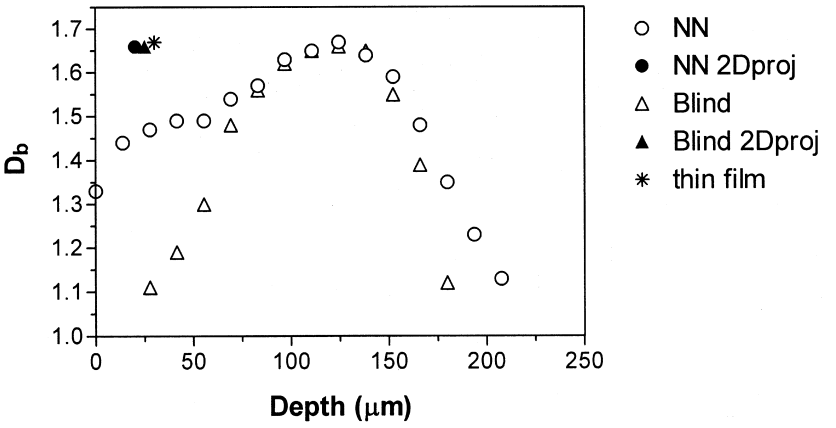

Figure 31 Particle-counting fractal dimension (Df) vs. area fraction (%) in a 207-μm-thick sample. Every tenth slice (or 13.8 μm) within the deconvolved 3D stack (nearest neighbors and blind algorithms) was analyzed. 2D projections (by brightest point merge) of each 3D stack and a 20-μm-thin film sample are also included for comparison.

newfound experimental evidence for fractal scaling properties that have long been theorized but have not to date been demonstrated in the literature. Theory states, as a "rule," that an object in 3D Euclidean embedding space, that has a fractal dimension less than 2, when projected onto a 2D Euclidean plane, will retains its fractal dimension [38]. This result for the system studied offers preliminary evidence in the form of an actual experimental system.

Also, it is believed that if the object in 3D space has a dimensionality of greater than 2, when projected onto a 2D plane, will completely fill that space and the fractal dimension would collapse to a value of 2 [38]. This fractal scaling property suggests that the distribution of mass in unconfined volumes has a fractal dimension less than 2, since when collapsed to 3D it is not space-filling. This finding does not correspond, however, to rheologic determinations of D_f, in which case values between 2 and 3 are the norm, perhaps due to much higher degrees of supercooling used for rheologic methods. This may,

on the other hand, suggest that perhaps the growth of networks prepared for rheologic determinations of D_f are truer volumes, and that perhaps a network grown in a sample of 207μm in thickness is still influenced by confinement. Since large clusters with radial diameters greater than the total sample thickness were observed, a small yet substantial effect of confinement may still occur, and confound the fractal dimension determinations. Furthermore, it may be possible that rheologic methods are sensitive primarily to particle cluster interactions (which correspond to a $D = 2.5$ in 3D space) [38,43] while 2D projection image analysis techniques are confounded by the inability to disseminate the crossover between particle-cluster and cluster-cluster aggregation processes.

3.2.2.3. Thin Film Conditions

The particle-counting fractal dimension of networks grown in thin film conditions resulted in a characteristic value of 1.94. This result, when compared to the values obtained for the 2D projections of slices in 3D space offers some fresh perspective. In this instance, new-found information pertaining to the effects of confined growth is demonstrated. The much higher value for D_f resulting from growth in a thin film ($D_f = 1.94$) relative to the peak value and 2D projection values of deconvolved stacks ($D_f \approx 1.60$) and predicted values by simulation ($D_f = 1.7$) provides further evidence that growth under confinement is in fact creating conditions for more orderly, nearly homogeneous network formation ($D = 2$).

3.2.3. Fractal Dimension (D_b)—Degree of Fill and Order

Empirically, the box-counting fractal dimension (D_b) is sensitive primarily to the degree of fill or space occupancy of particles that make up the network [8,62]. A high value for D_b is associated with a network that results from a more space-filling network, and often is the result of fast cooling or cooling to higher degrees of supercooling [8]. On the other hand, lower relative values for D_f can be expected when the network is less space-filling, such as under slower cooling conditions or cooling to a lower degree of supercooling [8]. Little in the way of experi-

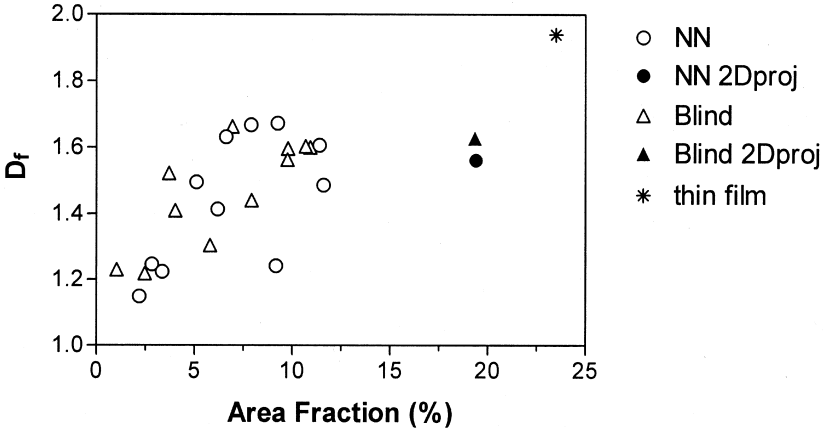

Figure 32 Box-counting fractal dimension (D_b) vs. depth (μm) in a 207-μm-thick sample. Every tenth slice (or 13.8 μm) within the deconvolved 3D stack (nearest neighbors and blind algorithms) was analyzed. 2D projections (by brightest point merge) of each 3D stack and a 20-μm-thin film sample are also included for comparison.

ment evidence has demonstrated conclusively that D_b is influenced by the spatial distribution of mass of fat crystal networks. Fractal dimension determinations by the box-counting method of 2D slices of 3D volume stacks, 2D projections of 3D volumes, and 2D thin film conditions are depicted in Figure 32.

3.2.3.1. Two-Dimensional Slices of the Three-Dimension Volume

Analyses of the blind deconvolved 2D slices of the 3D volume revealed increasing values for D_b with increasing depth, up to a peak value ($D_b = 1.66$) which occurred below the middle of the sample ($r = 0.96$, Table 1). Much like was revealed by D_f, the box-counting fractal dimension D_b corresponds well to predicted values arising from diffusion-limited particle-cluster aggregation ($D = 1.7$, $d = 2$). This also indicates a tendency for a higher degree of space-filling near the center of the sample relative to the upper and lower regions.

This also corresponds to results for area fraction (section 3.2.1; Fig. 29), and with qualitative observations described in section 3.1.2. Once again, the shift in peak value to a depth slightly below center may be attributed to the nature of the apparatus used for temperature control. Further evidence of the failure of nearest neighbors deconvolution to remove all scattered light is clearly observed here, since in the upper and lower regions of the volume, where residual haze was present, space-filling tendencies are detected in regions where little to no crystal mass was actually present.

3.2.3.2. Two-Dimensional Projections of Three-Dimension Volumes

Values of D_b for the 2D projections were similar following deconvolution by the NN and blind methods ($D_b = 1.66$). This indicates that the differences in the degree of haze removal due to the two deconvolution methods, when presented as 2D projections, did not result in a detectable difference in the degree of fill in the network. Since the majority of haze results from scattering directly above crystal mass at lower depths much of the haze retained following the NN deconvolution would have been hidden amongst the lower laying crystal mass in the 2D projection, and hence would not contribute enough to heighten space-filling tendencies upon thresholding. This also is observed qualitatively as slight blurring of small crystals that make up the larger clusters (Fig. 23B).

Once again, the fractal dimension of the 2D projection of the 3D clusters in the volume ($D_b = 1.66$) corresponds well to predicted values that arise from diffusion-limited cluster-cluster aggregation ($D = 1.7–1.8$, $d = 3$) [38,43]. These values are very similar to the peak value observed within the 2D slices of the 3D volume. This result once again provides further novel experimental evidence for the theorized rule that an object in 3D space that has a fractal dimension less than 2, when projected onto a 2D plane, retains its fractal dimension [38].

3.2.3.3. Thin Film Conditions

The box-counting fractal dimension of networks grown in thin film conditions resulted in a characteristic value 1.67.

This result shows strong agreement with the values obtained for the deconvolved 2D projections of slices in 3D space (D_b = 1.66) despite differences in area fraction (23.5% in thin films as opposed to 19.3% in deconvolved 2D projections). This finding suggests that perhaps other network characteristics in addition to space-filling tendencies may have an influence on D_b. This will be further addressed in section 3.2.9.

3.2.4. The Relationships between Fractal Dimensions and Area Fraction

Since D_f and D_b are both believed to be sensitive to the degree of fill in the network (more is the case for D_b), plots of these parameters as a function of area fraction were examined (figs. 32 and 33).

The particle-counting fractal dimension D_f did not display a direct linear relationship with area fraction, although linear correlation analysis of the blind deconvolved data indicated a significant positive relationship (r = 0.79) between these two

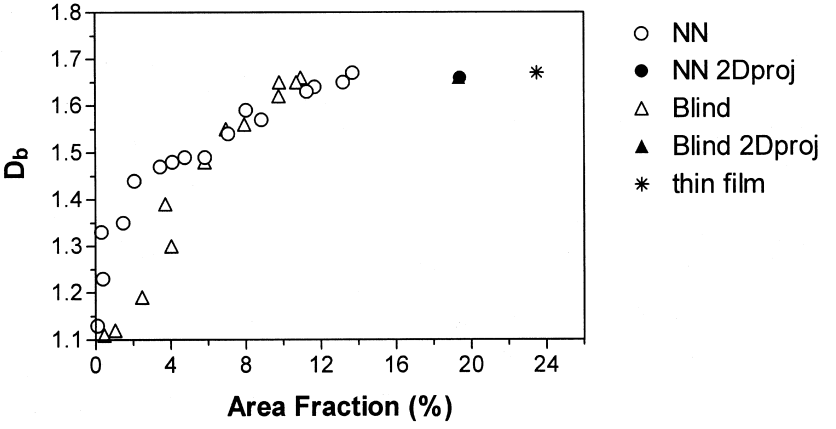

Figure 33 Box-counting fractal dimension (D_b) vs. area fraction (%) in a 207-μm-thick sample. Every tenth slice (or 13.8-μm) within the deconvolved 3D stack (nearest neighbors and blind algorithms) was analyzed. 2D projections (by brightest point merge) of each 3D stack and a 20-μm-thin film sample are also included for comparison.

variables (Fig. 32 and Table 1). This supports our understanding that D_f is influenced in part by the amount of crystalline mass in the network, and in part the spatial distribution of mass [4,7,12–14,24]. Once again, it can be observed that 2D projections of the 3D slices of the volume retain their peak value, and the much higher values for D_f and area fraction in thin films suggest that cluster growth is affected by confinement.

The box-counting fractal dimension D_b displayed a linear relationship with area fraction, and linear correlation analysis of the blind deconvolved data indicated a significant positive relationship ($r = 0.96$) between these two variables (Fig. 33 and Table 1). This lends further novel support to our belief that D_b is more highly influenced by amount of crystalline mass in the network than D_f ($r = 0.71$) [62]. Since the 2D projection and thin film values of D_b remain constant despite having heightened area fractions, this suggests that D_b is in part influenced by some factor other than the quantity of crystalline mass. This will be further addressed in section 3.2.9.

3.2.5. Number of Particles (N)

3.2.5.1. Two-Dimensional Slices of the Three-Dimension Volume

The number of particles, as defined in section 3.2.1, was computed for all micrographs that made up the volume element (Fig. 34). Results following blind deconvolution displayed trends similar to those found in area fraction, with a gradual increase to a peak near the middle of the sample followed by a subsequent decrease. Linear correlation analysis of particle number revealed a significant positive relationship to both depth (from the top of the sample to the peak within, $r = 0.96$) and area fraction ($r = 0.98$), as would be expected (Table 1). The granular morphology of the crystallites that make up the clusters, in this case, means that a higher number of particles results in more overall mass (detected as area fraction), which is shown to occur near the middle of the sample (Fig. 29).

The much higher number of particles observed following deconvolution by the NN technique is yet another consequence of incomplete haze removal by the NN technique. Some of this

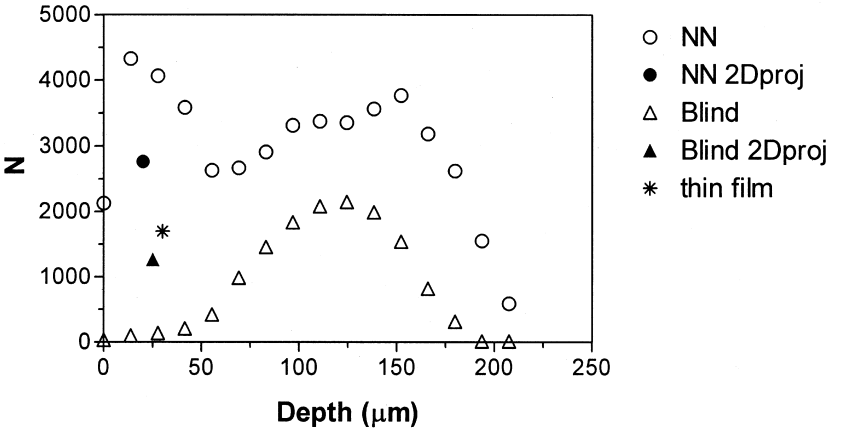

Figure 34 Number of particles (N) vs. depth (μm) in a 207-μm-thick sample. Every tenth slice (or 13.8 μm) within the deconvolved 3D stack (nearest neighbors and blind algorithms) was analyzed. 2D projections (by brightest point merge) of each 3D stack and a 20-μm-thin film sample are also included for comparison.

residual haze was retained following thresholding (Fig. 24), resulting in small artefactual features which subsequently resulted in higher than actual particle counts for NN slices, especially near the upper portion of the sample. A return to the thresholded images in the upper slices reveals clearly the presence of this artefact (Fig. 25—000–41.4 μm).

3.2.5.2. Two-Dimensional Projections of Three-Dimension Volumes

The number of particles observed in 2D projections of the 3D volumes reveals a number of qualities worthy of note. First, the values of N for the projections are not equivalent to the cumulative contribution of the slices that make up the stack, but in fact are even lower than the values observed with a given slice (near the middle, for example). This is easily explained by commenting on the nature of the projection method. Inherent to the brightest point merge projection technique, loss in feature isolation or detail occurs when features are of similar brightness in a particular shared XY coordinates but

originate from different Z coordinates. The consequence of this loss, which does inevitably occur (and would with any alternative projection technique chosen), is the masking and merging of features, and a value for N that is less than that of the 3D volume. A much higher number of particles present in the 2D projection following NN deconvolution (relative to the blind counterpart) was again attributable to partial retention of haze contribution upon thresholding and can be observed in the 2D projection image (Fig. 23*E*).

3.2.5.3. *Thin Film Conditions*

The number of particles observed in thresholded images of thin films is similar to that of the 2D projection following blind deconvolution. Although, in theory, the thinner sample would result in a network with a greater number of particles, the effect of confinement (which earlier was shown to increase order) may also result in denser, more compact clusters. The higher density of small crystals that make up the large clusters may result in the inability to resolve individual crystallites. Once again, this behavior, and its affects on quantitative image analysis, is not well established in the literature. This behavior is observed qualitatively in micrographs (Figs. 20 and 21).

3.2.6. The Relationships between Number of Particles (N) and Area Fraction (%)

The number of particles that make up the network following blind deconvolution is significantly correlated with the amount of space occupied by the particles ($r = 0.98$, Table 1) and is depicted in Figure 35. Artefacts resulting from incomplete haze removal after NN deconvolution (especially in the uppermost and lowermost slices) result in unreliable data for the number of particles and area fraction (more so N). Projections and thin films display a lower N value due to same reasons previously described in section 3.2.4.

3.2.7. The Relationships between Number of Particles (N) and Fractal Dimensions (D_f and D_b)

The number of particles that make up the network following blind deconvolution is significantly correlated with the deg-

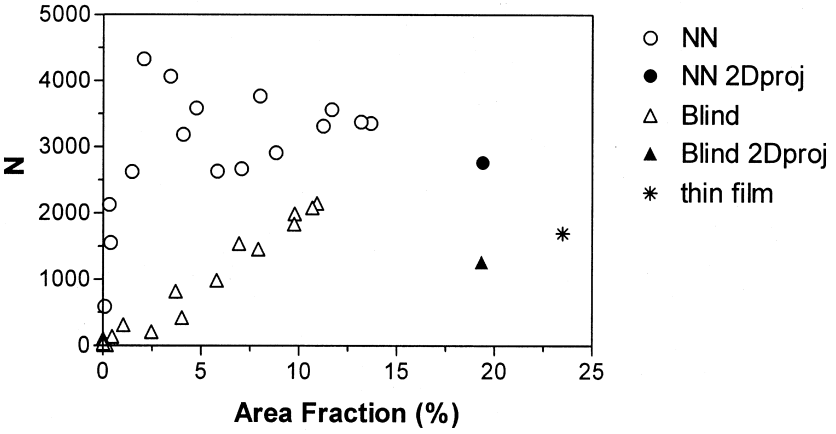

Figure 35 Number of particles (N) vs. area fraction (%) in a 207-μm-thick sample. Every tenth slice (or 13.8 μm) within the deconvolved 3D stack (nearest neighbors and blind algorithms) was analyzed. 2D projections (by brightest point merge) of each 3D stack and a 20-μm-thin film sample are also included for comparison.

ree of fill and order displayed by the network (D_b: $r = 0.97$, D_f: $r = 0.79$, Table 1) and is depicted in Figures 36 and 37. This would be expected, since both D_b and D_f are both highly correlated with area fraction as well. Once again, artifacts resulting from inefficient haze removal by NN deconvolution resulted in unreliable data for the number of particles and D_b, especially relevant in the upper and lower regions of the sample. Projections and thin films display a reduced N value due to same reasons previously described (section 3.2.4.). A constant D_b value in these cases demonstrates the influence of more than simply fill, and will be addressed in section 3.2.9.

3.2.8. Microstructural Element Size

In all cases, particle distribution analysis resulted in microstructural element size (MES) values that corresponded to visual examination of slices within the volume stack. However, in two instances (blind results for slices at 41.4 μm and 55.2 μm, see Fig. 27) a very low number of large clusters were pres-

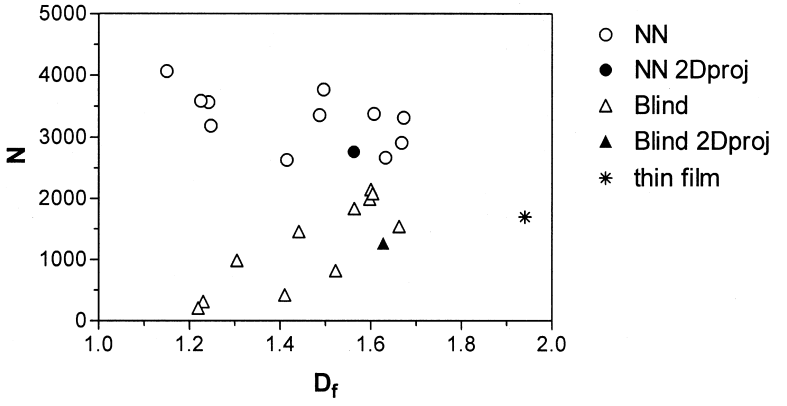

Figure 36 Particle-counting fractal dimension (D_f) vs. the number of particles (N) in a 207-μm-thick sample. Every tenth slice (or 13.8 μm) within the deconvolved 3D stack (nearest neighbors and blind algorithms) was analyzed. 2D projections (by brightest point merge) of each 3D stack and a 20-μm-thin film sample are also included for comparison.

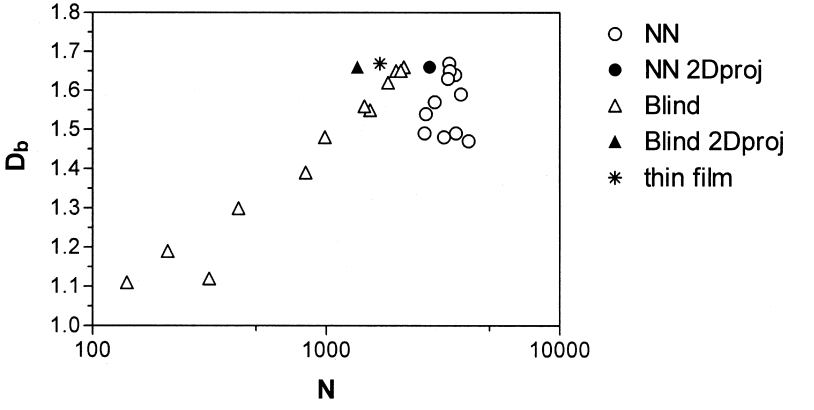

Figure 37 Box-counting fractal dimension (D_b) vs. the number of particles (N) in a 207-μm-thick sample. Every tenth slice (or 13.8 μm) within the deconvolved 3D stack (nearest neighbors and blind algorithms) was analyzed. 2D projections (by brightest point merge) of each 3D stack and a 20-μm-thin film sample are also included for comparison.

ent, and were not representative of the particles observed in the volume as a whole. For this reason, these two points skewed results and were excluded from correlation analysis.

3.2.8.1. Microstructural Element Size and Depth

The size of particles that make up the network following blind deconvolution was significantly correlated with the depth within the sample from the top to the location at peak MES ($r = 0.87$, Table 1) and is depicted in Figure 38. This indicated that mean size of particles making up the network increased as a function of depth in the range studied, and may indicate that growth originated near the center and at the time of imaging those particles near the center had simply had more time to grow to larger proportions. Once again, residual haze artifacts resulting from nearest-neighbor deconvolution led to unreliable data for the mean size of particles. Projections and thin film display increased MES due to masking and merging of particles as previously described in section 3.2.4.

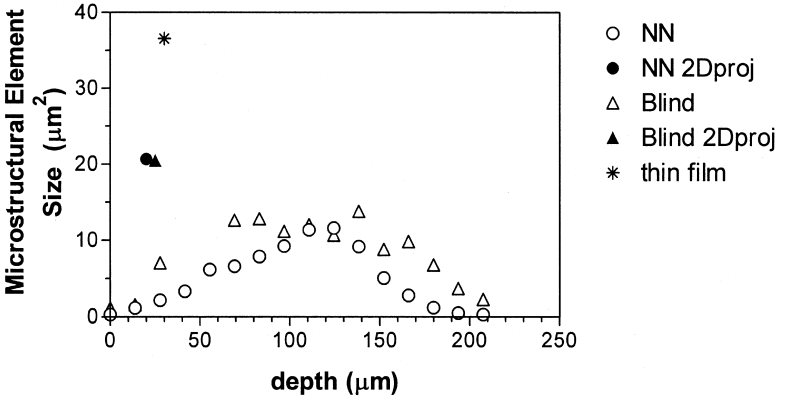

Figure 38 Microstructural element size (μm^2) vs. depth (μm) in a 207-μm-thick sample. Every tenth slice (or 13.8 μm) within the deconvolved 3D stack (nearest neighbors and blind algorithms) was analyzed. 2D projections (by brightest point merge) of each 3D stack and a 20-μm-thin film sample are also included for comparison.

3.2.8.2. Microstructural Element Size and Area Fraction (%)

The size of particles that made up the network following blind deconvolution was significantly correlated with the area fraction (r = 0.86, Table 1) and is depicted in Figure 39. This indicates that slices composed of larger particles also covered more area, and once again corresponds to the belief that the earliest and more progressive crystal growth occurred near the center of the sample. Results from nearest-neighbor deconvolution do not give reliable data for the size of particles due to residual haze. Projections and thin film display increased MES and area fraction due to same reasons previously described in section 3.2.4.

3.2.8.3. Microstructural Element Size and Degree of Fill (D_b)

The size of particles that make up the network following blind deconvolution is significantly correlated with the degree of fill (r = 0.81, Table 1) and is depicted in Figure 40. Artefacts resulting from nearest-neighbor deconvolution do not give reli-

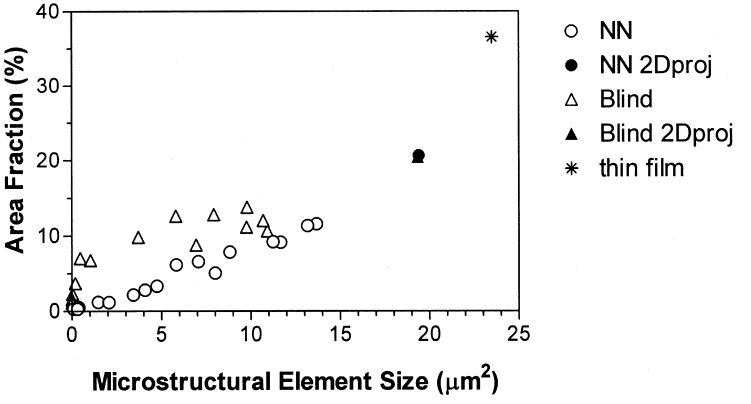

Figure 39 Area fraction (%) vs. microstructural element size (μm^2) in a 207-μm-thick sample. Every tenth slice (or 13.8 μm) within the deconvolved 3D stack (nearest neighbors and blind algorithms) was analyzed. 2D projections (by brightest point merge) of each 3D stack and a 20-μm-thin film sample are also included for comparison.

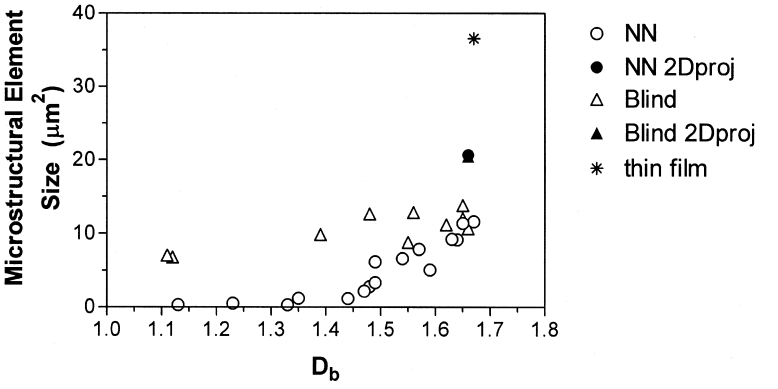

Figure 40 Microstructural element size (μm^2) vs. box-counting fractal dimension (D_b) in a 207-μm-thick sample. Every tenth slice (or 13.8 μm) within the deconvolved 3D stack (nearest neighbors and blind algorithms) was analyzed. 2D projections (by brightest point merge) of each 3D stack and a 20-μm thin film sample are also included for comparison.

able data for the size of particles. Projections and thin film display increased MES while D_b remains constant due to same reasons previously described.

3.2.8.4. Microstructural Element Size and Number of Particles (N)

The size of particles that make up the network following blind deconvolution is significantly correlated with the number of particles in the network ($r = 0.85$, Table 1) and is depicted in Figure 41. Artefacts resulting from nearest-neighbor deconvolution do not give reliable data for the size nor the number of particles. Projections and thin film display increased MES and while N is less than the max in the volume due to same reasons previously described (masking and merging, and confinement, respectively).

3.2.9. Standard Deviation of Mean Nearest-Neighbor Analysis as an Indicator of Order

The influence of area fraction or degree of fill on the fractal dimensions D_f and D_b was demonstrated by high correlation

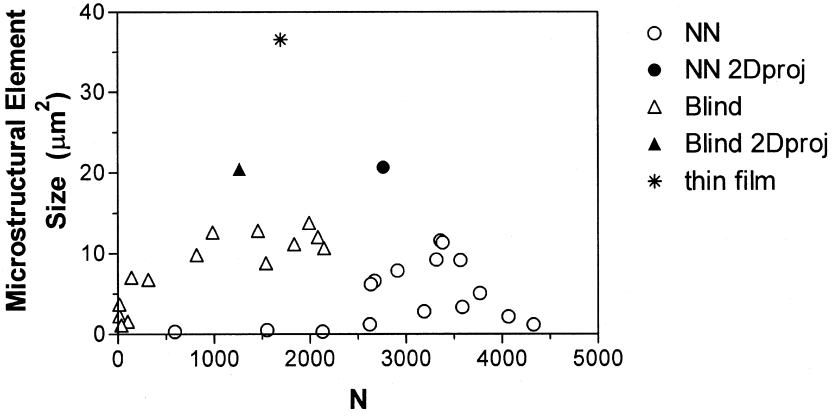

Figure 41 Microstructural element size (μm^2) vs. number of particles (N) in a 207-μm-thick sample. Every tenth slice (or 13.8 μm) within the deconvolved 3D stack (nearest neighbors and blind algorithms) was analyzed. 2D projections (by brightest point merge) of each 3D stack and a 20 μm thin film sample are also included for comparison.

with area fraction (section 3.2.5), however, theory predicts that the fractal dimensions D_f and D_b are also influenced by the degree of order in the distribution of mass [7,12]. Therefore, an attempt was made to reveal an alternative indicator of order from polarized light microscopy. This was performed by examining the variation (or standard deviation) in the determination of mean nearest-neighbor distance (NND). Figure 42 demonstrates the relationships between the standard deviation of the mean NND and D_f and D_b following blind deconvolution. In both cases, significant negative correlation coefficients were found (D_f: $r = -0.72$, and D_b: $r = -0.73$, Table 1). This means that a higher fractal dimension occurs in images of the network that show lower variation in the distribution of particles, which is analogous to a more orderly particle distribution. Conversely, a low fractal dimension is associated with a larger variation in NND, which indicates a more disorderly particle distribution. Both fractal dimensions thus demonstrate a dependence on both order and fill.

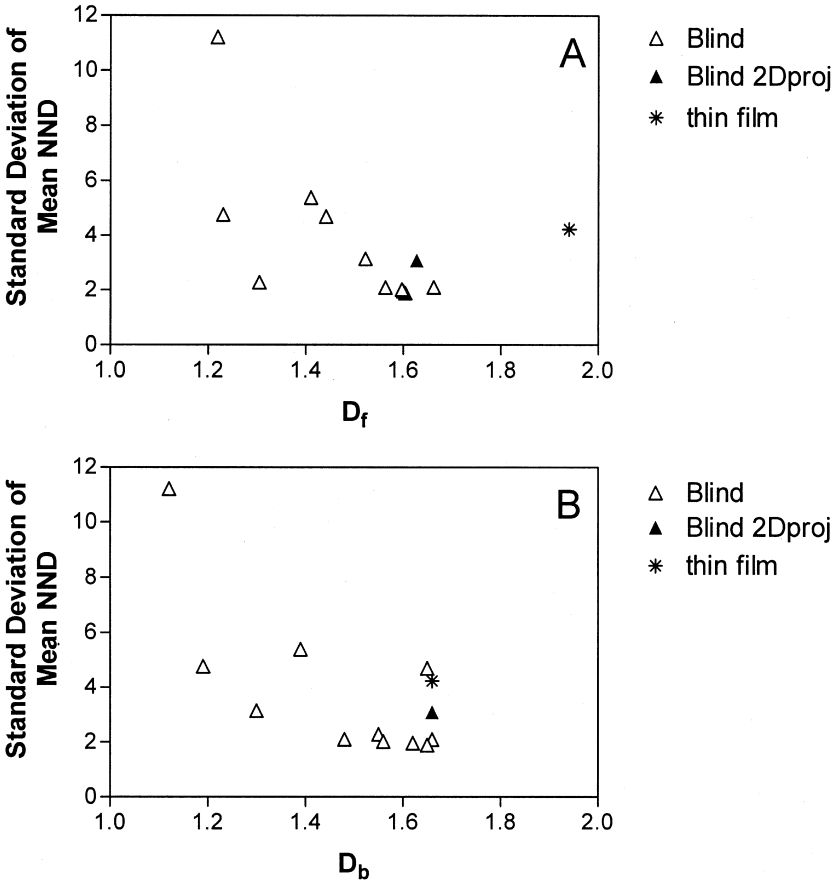

Figure 42 The standard deviation of the mean nearest-neighbor distance (NND) as a function of the fractal dimensions (**A**) D_f, and (**B**) D_b following blind deconvolution. Every tenth slice (or 13.8 μm) within the deconvolved 3D stack was analyzed. The 2D projection (by brightest point merge) of the 3D stack and a 20-μm-thin film sample are also included for comparison.

The differences observed for the D values for thin film growth provide further evidence for the relative contributions of order and fill. While the D_f value is much higher in thin films than in a volume (and thus demonstrates the effect of confinement on order and fill), the D_b value is not elevated in

thin film conditions (despite having a higher area fraction and higher apparent order). This suggests that the box-counting method is not as sensitive to order (relative to fill) in thin film conditions. This finding corresponds to previous studies where D_f and D_b have been found to be inversely proportional [62].

3.2.10. Pearson Linear Correlations of Blind Deconvolved Data

Table 1 highlights the Pearson linear correlation coefficients for various network parameters determined by image analysis of the 2D slices of a 3D volume following blind deconvolution. Correlations that are statistically significant are bolded. High correlation indicates that the variables studied vary well together [118], and are thus statistically associated. Significant correlation between most of the studied parameters was observed, and suggests a high level of interrelatedness between network characteristics. The number and location of particles influences the size of the particles, which in turn influences the area fraction. The area fraction influences the fractal dimensions which are also correlated with the apparent degree of order in the spatial distribution of mass. These correlations may be system and condition specific, however. Further studies on various systems and crystallization conditions one of the many recommendations for future work (section 6).

3.2.11. Note on the Effects of Edges, Optics, Magnification, and Image Resolution on Fractal Dimensions

3.2.11.1. Edge Effects on Fractal Dimension Determination

Recent investigations into the effects of including and excluding of features that fall on the edges of the region of interest (ROI) in the particle-counting procedure have revealed important cautions that must be heeded in order to avoid artifacts [7,12]. Further artifacts also occur when the size of the ROI gets small. This issue will be addressed only briefly here.

Figure 43*A* depicts the results of the particle-counting method (both including and excluding features that touch the edges of each ROI) for an image of cocoa butter, courtesy of Tarek Awad. In this case, the ROI was iteratively reduced from 100–5% of the original image size. Figure 43*B* depicts results from the same image but only the ROIs representing 100–35% of the original image size are included. The number

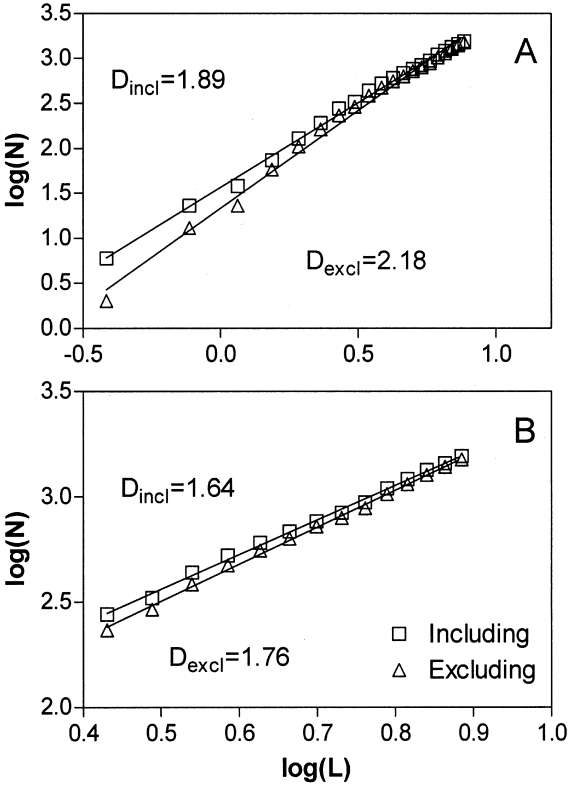

Figure 43 Log-log plots of the number of particles (N) vs. the length of the box (L) used to determine the particle-counting fractal dimension D_f. In (**A**) counts corresponding to regions of interest spanning 100–5% of the original image length are included, whereas in (**B**) the region used is 100–35% of the original image length. Data courtesy of Tarek Awad.

of particles is plotted against the length of the ROI in a log-log fashion. The resulting slope in each case is an uncorrected D_f.

Two artifacts related to the effects of counting features at the edges of the ROIs are observed. Firstly, the effect of the contribution of small boxes is a skewing of the D value to elevated values. This occurs because as the box size gets small, a tailing off occurs on the log-log plot. Once the box sizes become very small, the length of the box sizes decreases faster then the areas of the ROIs. This is especially problematic if the features falling on the edges of the ROI are large, since they will be greatly included and excluded in their respective counts. For this reason, performing the counts on ROIs representing 100–35% of the original box size is more accurate.

Secondly, if the particles that touch the edge of each ROI are excluded from the counts, the resulting slope is elevated due to an overexclusion. Conversely, if the particles on the edges of the ROI are all included in the counts, a lower than true value results because of an underinclusion artefact.

Unfortunately, the image analysis macro used is not capable of counting the particles touching only two of the four sides of each ROI (an adjusted count). To compensate, the average of the D values obtained by including and excluding counts in the 100% to 35% range is taken. This is analogous to counting just those features touching two of the four sides of each ROI, eliminates the skewing effect of small boxes, and results in an accurate D_f value [7,12]. For the image data portrayed in Figure 43, the corrected D_f has a value of 1.70.

3.2.11.2. Effects of Optics, Magnification, and Image Resolution on Fractal Dimension Determination

Previous to the recent implementation of the Leica system used for imaging thin films and the volume in this study (see section 2.1.2.) another older system was used. This older system consisted of a polarizing microscope (Olympus model BH, Tokyo, Japan), a CCD video camera (Sony model XC75), and 640 × 480 video capture board (Scion, Frederick, MD, USA). These two systems differ in terms of the quality of the optics,

the type of camera, the magnification used, and spatial resolution of the images acquired. It was therefore of interest to verify results of image analysis parameters, particularly the fractal dimensions D_f and D_b, from images obtained using both systems. Soon to be published microstructural data from a separate study on the same model fat system crystallized by the same cooling conditions in thin film form were obtained from images obtained on this older imaging system. These results are presented here as an indication of the effects of differences due to the use of two unique imaging systems.

Figure 44 depicts a representative thresholded thin film image acquired on both systems. The relative sizes of the images were kept constant in order to demonstrate the differences in the actual sampling size. Note the differences in the sampling sizes and feature appearance obtained by imaging using a 50X objective and pixel resolution of 1280 $\times$ 1024 (Fig. 44*A*) and that obtained by using a 10X objective and pixel resolution of 640 $\times$ 480 (Fig. 44*B*).

Quantitative results for the fractal dimensions D_f and D_b determined on both imaging systems are presented in Table 2. Despite the many differences in imaging scenarios, both fractal dimensions were statistically similar (verified by a t-test, assuming equal variances). This comparison suggests that the image analysis parameters are not influenced by differences in imaging and that in both cases, the imaged field is within the region of structure that exhibits fractal scaling properties.

4. ASSUMPTIONS AND LIMITATIONS

Since the methods employed in this study were unique, a number of assumptions were made that warrant further discussion. Perceived limitations inherent to the methods used are also discussed in the section that follows.

4.1. Z-Stage Calibration

For all 3D imaging experiments conducted on the imaging system in our laboratory, it has been assumed that the z-stage

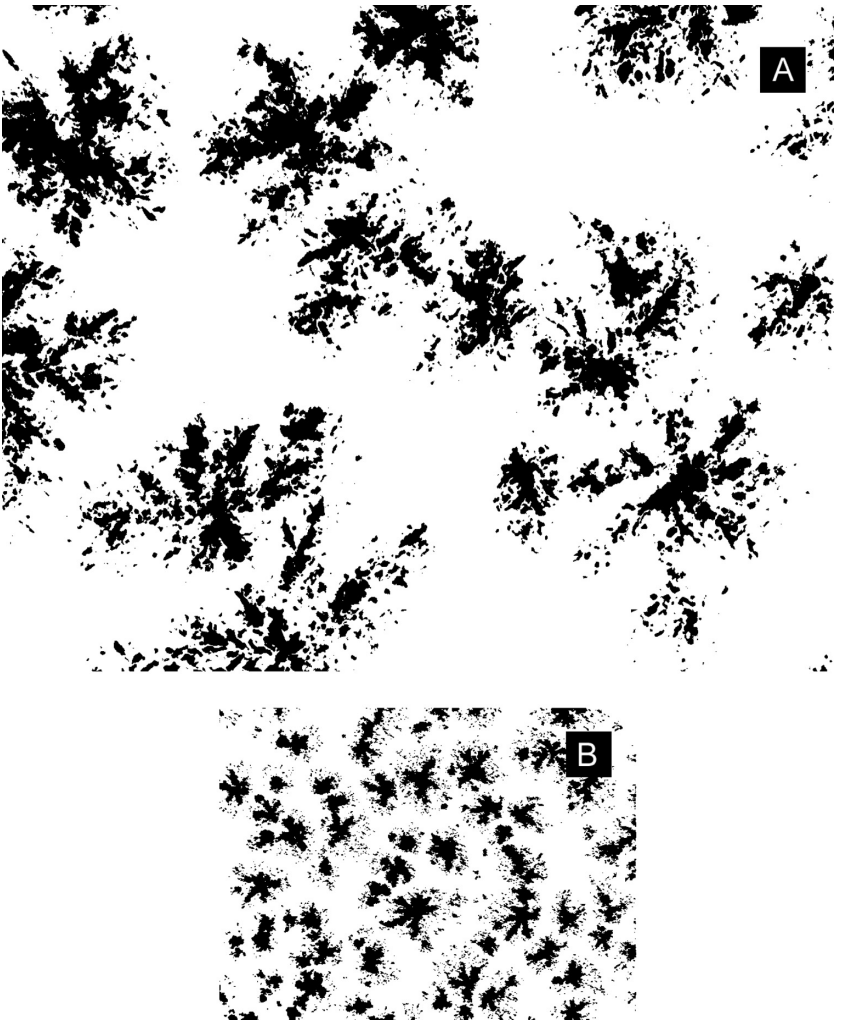

Figure 44 Representative thresholded polarized light micrographs from (**A**) the more recent Leica microscope system, and (**B**) the older Olympus microscope system. Images acquired on the Leica system have pixel dimensions of 1280 × 1024 and were taken using a 50X objective lens. Images on the older Olympus system were 640 × 480 and the 10Xobjective used.

Table 2 Fractal Dimensions D_f and D_b and their Standard Deviations Determined on Two Different Microscopes, Using Different Magnifications, and Image Spatial Resolutions (n = 7)

	Imaging System	
	Old	New
D_f	1.91 ± 0.13	1.94 + 0.12
D_b	1.67 ± 0.03	1.67 ± 0.03

motor is properly calibrated. This is of utmost relevance if absolute 3D morphological measurements are desired (which has not been the case to date). If the z-stage stepping motor is out of calibration, it can be assumed that the drift from calibration is consistent at all depths. A recommendation for z-stage calibration and one possible method for performing this calibration are addressed in section 6.1.

4.1.1. Standardization Attempt: Bright-field Vs. Polarized Light Microscopy

Blind deconvolution of transmitted light bright-field (TLB) volumes has been recently developed [111,112]. The same is not true, however, for volumes imaged using polarized light. In order to assess the validity of imaging volumes for deconvolution using transmitted polarized light, comparisons of the z-series of an object that could be viewed under both conditions was performed.

A cylindrical fiber (believed to be nylon) was cut into small fragments, and embedded in triolein (the same medium that made up the liquid fraction of the fat system studied). When viewed by TLB, the fragments appeared as semi-translucent rods, with a dark center, which is consistent with the appearance of nylon and other synthetic fibres [124]. When viewed under polarized light the outer layer of the fibre was birefrin-

gent, and the rod size and shape appeared to be the same as when viewed by TLB. Z-series were then taken on the sample field of view, using both TLB and PLM, with the same Z-increments. Examining the XY and ZX slices of the raw image stacks demonstrated that under both lighting conditions, the fibres features and dimensions remained unchanged. Images of the fibre can be observed in Figure 45. This finding validated the technique of 3D z-series imaging of PLM images, however, an apparent stretching of the object (when examining the ZX profile) may be an indication the z-stage is improperly calibrated (see section 6.1).

4.2. The Use of Fluorescence Settings in Deconvolution Procedures

Since no commercially available software is designed to handle 3D images obtained under polarized light conditions, deconvolution was carried out assuming a fluorescence model.

In the case of nearest-neighbors deconvolution (which did not perform very well), it is not possible to conclude that deficiencies in haze removal were due to differences in the input theoretical fluorescence based PSF and the actual PSF on the sample. Incomplete haze removal may have simply been a result of deficiencies in the nearest-neighbors algorithm itself, since noise from multiple planes is added together [34].

In the case of blind deconvolution, it can be safely assumed that the use of a fluorescence based theoretical PSF (which merely serves as an initial estimate of the experimental PSF) has no profound influence on the results of deconvolution. Inherent to the blind technique is the construction of an experimental PSF from the data itself [29,34,96,104], in which case the use of a fluorescence-based PSF as an initial estimate seems to be appropriate based on the quality of the results.

4.3. Limitations Related to Properties of Fat Crystal Networks

While performing various preliminary experiments using samples of greater depth, to higher degrees of supercooling, and following extended crystallization times, it became evi-

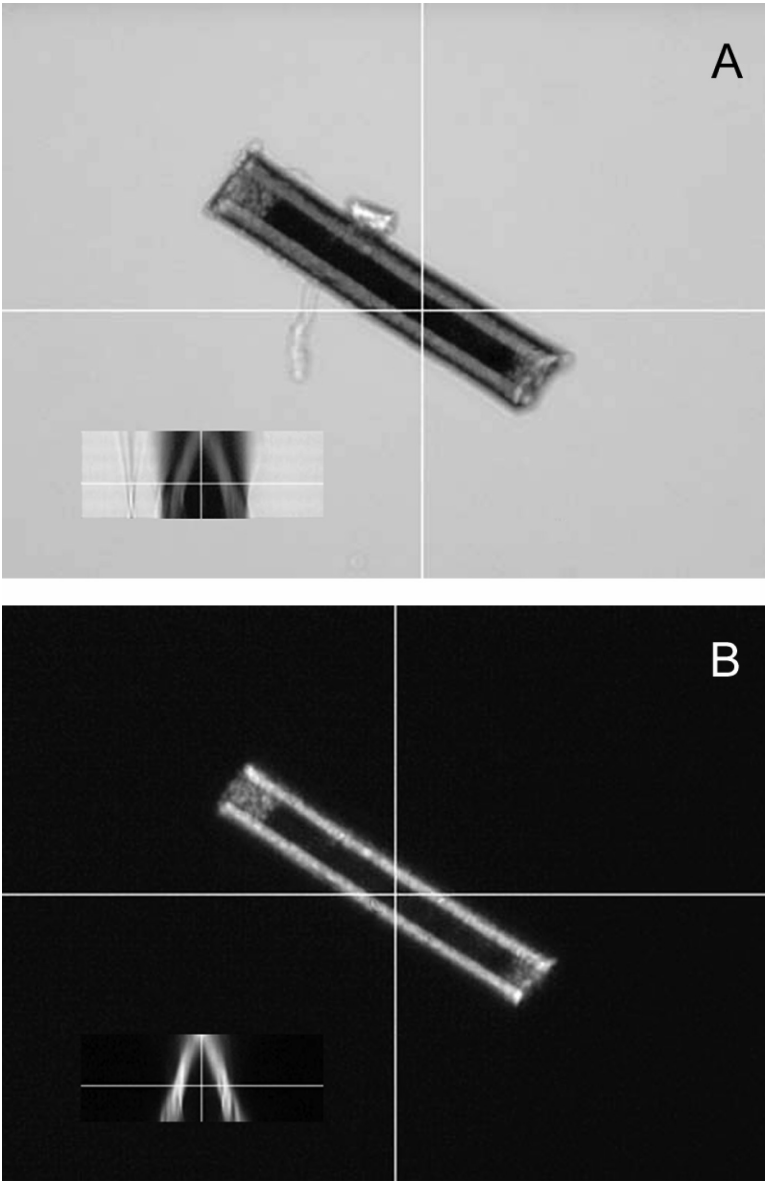

Figure 45 Images of a nylon fiber under (**A**) transmitted brightfield and (**B**) polarized light. The XY planal view, and the coronal (ZY) views are shown for each.

dent that there is an ill-defined limit to the amount of birefringent material that can be present that still allows for successful volume imaging. When an excessive amount of birefringent crystal mass is present (dictated by solid fat content), volume imaging is confounded because it becomes increasingly difficult to differentiate crystals and clusters of crystals in both the XY direction and the Z direction. This limitation means that various compromises in crystallization conditions may be required. Compromises in the depth may be required if higher degrees of supercooling are desired, for example. Imaging of a sample at an earlier stage of crystallization may allow for higher degrees of supercooling, faster cooling rates, or increased depth conditions to be employed. The limitations of the technique will be highly system specific, and hence cannot be addressed in great detail at this time (see section 6.2). At the time of imaging, the SFC of the model fat system in this study was approximately 20% (determined by pulsed nuclear magnetic resonance).

5. CONCLUSIONS

Preliminary results from volumetric imaging of fats by wide-field deconvolution microscopy with polarized light suggest that this novel method is feasible. Deconvolution employing an adaptive blind algorithm is more suited to this technique than is a nearest neighbors algorithm because the blind method obviates the need to measure the point spread function under experimental conditions. Blind deconvolution also outperforms the nearest neighbors technique in terms of out-of-focus haze removal and feature isolation.

Novel 3D analyses of blind deconvolved images of the fat system studied were successful in demonstrating several previously theorized characteristics of fractal scaling properties. This included experimental evidence for diffusion-limited cluster aggregation, and evidence for fractal dimension retention upon collapsing of an object in 3D onto a 2D plane. Furthermore, results of a novel quantitative measure of order, along with measurement of area fraction, provided evidence the sup-

ports the belief that the fractal dimensions D_f and D_b are influenced by both the degree of fill and the degree of order of particle distribution in space. However, the relative contributions of fill and order to fractal dimension values still remains to be conclusively determined.

Comparison of network features in a volume to those in thin films was successful in demonstrating dramatic effects of confinement in thin film growth. This included an increase in area fraction, and the fractal dimension D_f, suggesting that confinement greatly increases the degree of order and fill in thin films, relative to growth in a volume.

For the system studied, many significant correlations were found for a number of network properties. These relationships suggest that growth of large clusters in a volume is 3D in nature, with a large proportion of mass found near the center of the sample. Relationships between these characteristics suggest that the areas with more mass consisted of a higher number of larger particles that displayed higher fractal dimensions.

Three-Dimensional volume reconstructions of blind deconvolved polarized light images provided a new means of visualizing fat crystal networks grown in volume conditions. Qualitative assessment of the size of 3D clusters and the relative locations of clusters in 3D space could be made from these renderings, thereby offering a never-before-seen perspective.

Lastly, the results for fractal dimensions D_f and D_b obtained for thin films were shown to be equivalent to those determined under varying experimental conditions including the use of different microscope, camera types, magnifications, and image spatial resolutions.

6. RECOMMENDATIONS FOR FUTURE RESEARCH

The preliminary work in this study suggests that wide-field blind deconvolution of fat systems viewed under polarized light is feasible. However, a number of recommendations for further research are suggested.

6.1. Verification of the Z-stage Calibration

The z-stage controller used in this study was assumed to be accurate at the time of purchase and drift from its calibrated state was assumed to be negligible. Since 3D polarized light microscopy is not traditionally performed, obtaining a calibration specimen is difficult if not impossible. There are other methods, however, to assess the accuracy of the z-stage motor. One such method was proposed by Barry Burbach and shared by Martin Wessendorf [125] and involves the use of spherical glass beads around 10–30 μm in diameter. Beads are mounted in the mounting medium that is doped with a fluorescent dye. Z-series are acquired and their XZ profiles acquired. If the microscope is correctly calibrated in XY and assuming that the beads spherical, the z-calibration can be deduced from the average of the ratio of the bead diameter in the x-direction to that in the z-direction. If the z-stage is properly calibrated the cross-section of a sphere should appear to be a circle. By verifying the z-stage calibration, the cause of the appearance of elongated crystals in the XZ profile could be better assessed (3.1.4). Alternatively, the use of a bead coated with fluorescent dye may be used [33].

6.2. Various Systems, Crystallization Conditions, and Degrees of Confinement

Since this study was conducted on one model fat system, under specific crystallization conditions, it is highly recommended that future efforts aim to validate the findings within, and determine the limitations discussed in section 4.2. By repeating this study with various fat systems, under similar conditions, support for the findings within and benchmarking of limitations would be of great value. In addition, studies employing the same model fat system with altered crystallization conditions may reveal differences due to crystallization conditions. It is well known that the crystallization of fats is highly influenced by factors including the rate of cooling, the degree of supercooling, and the presence of shear (refs) and learning more about the effects of these parameters on the crystallization of fats in volumes would be advantageous. Furthermore,

by altering the thickness of the volume sample, studies may reveal differences in network formation resulting from various degrees of confinement.

6.3. Other Deconvolution Algorithms

Although blind deconvolution has obvious great benefits over methods that require knowledge of the point spread function, and although it has been demonstrated as a successful means of imaging 3D volumes, investigations of other algorithms may be of value. Such other methods may include classical iterative algorithms (Agard's modification of the Jansson-Van Cittert algorithm for example), and statistical iterative algorithms (the Maximum Likelihod Estimation, for example) [34]. While these methods require a measured PSF, they may or may not produce better deconvolution results. The only way to be certain would be to try them, although obtaining an accurate PSF will admittedly be difficult.

6.4. Four-Dimensional Imaging

This study was successful in investigating network characteristics in 3-dimensions (X, Y, and Z). By including time as a fourth variable, it may be possible to perform multiple z-series acquisitions thereby allowing us to observe the growth of 3D networks as a function of time [76,126,127]. This would be of great value and would address many unanswered questions related to the growth of network features. For example, the locations of early crystal growth, the nature of secondary growth, and the evolution and changes that occur in crystal morphology would be observed. These findings would be of great importance in furthering our understanding of the nature and mechanisms of crystallization and network formation in bulk fat systems.

6.5. Development of a Three-Dimensional Imaging-based Fractal Dimension Method

The development of a 3D imaging-based fractal dimension determination would be far from trivial and would include a

number of assumptions. The following is one conceivable approach that may be appropriate for pursuit in the future.

If the 3D volume imaging technique reaches a level of stereological accuracy that allows for high confidence in the ability to quantitatively determine the exact locations of individual particles in 3D space, an iterative particle-counting procedure could be pursued. Particles embedded in iteratively reduced cube sizes could be counted using an adjusted count that includes features touching three of the six cube faces. Applying these counts to the fractal scaling model, a log-log plot of the number of particles as a function of cube length may result in a 3D fractal dimension. This would admittedly be far from trivial, but in theory, it could be performed. This analysis would be particularly interesting when compared to the existing model for the determination of 3D fractal dimensions by rheologic methods.

ABBREVIATIONS

Φ solids' volume fraction
ξ average floc size
δ crystal-melt interfacial tension
° degrees
°C degrees Celsius
°C/min degrees Celsius per minute
2D 2-dimensional
3D 3-dimensional
4D 4-dimensional
a primary particle size
A Hamacker's constant
AFM atomic force microscopy
CCD charge coupled device
COSM computational optical sectioning microscopy
CSLM confocal scanning laser microscopy
D fractal dimension
d Euclidean dimension
d_o intercluster distance
Db box-counting fractal dimension
Df particle-counting fractal dimension
DLA diffusion-limited aggregation
DVD digital video disc

Dy dynamic (shear present)
EM electron microscopy
FFT fast Fourier transform
G' shear elastic modulus
GHz gigahertz
h hours
HMF high-melting fraction of milk fat
IPTK image processing toolkit
kb kilobytes
K elastic constant
L length
Mb megabytes
MES microstructural element size
MLE maximum likelihood estimation
N number of particles
NIH National Institute of Health
nm nanometres
NN nearest neighbors (deconvolution)
NND nearest neighbor distance
PC personal computer (Windows OS)
PLM polarized light microscopy
PSF point spread function
R Pearson linear correlation coefficient
RAM random access memory
RLCA reaction-limited cluster aggregation
ROI region of interest
St static (no shear present)
SEM scanning electron microscopy
SFC solid fat content
TEM transmission electron microscopy
TLB transmitted light brightfield
UK United Kingdom
w/w weight to weight proportion
x backbone fractal dimension
X times (magnification)
μL microliters
μm micrometers

REFERENCES

1. de Man J. Physical properties of milk fat II. Some factors influencing crystallization J Dairy Res 1961; 28:117–122.

2. Heertje I, van Eendenburg J, Cornelissen J, Juriaanse A. The effect of processing on some microstructural characteristics of fat spreads Food Microstructure 1988; 7:189–193.

3. Shukla A, Rizvi S. Relationship among chemical composition, microstructure, and rheologic properties of butter Milchwissenschaft 1996; 51(3):144–148.

4. Narine S, Marangoni A. Relating structure of fat crystal networks to mechanical properties: a review Food Research International 1999; 32:227–248.

5. Campos R, Narine S, Marangoni A. Effect of cooling rate on the structure and mechanical properties of milk fat and lard Food Research International 2002; 35:971–981.

6. Campos R, Litwinenko J, Marangoni A. Fractionation of milk fat by short-path distillation J Dairy Sci 2003; 86:735–745.

7. Litwinenko J, Rojas A, Gerschenson L, Marangoni A. Relationship between crystallization behavior, microstructure, and mechanical properties in a palm oil-based shortening J Am Oil Chem Soc 2002; 79:647–654.

8. Marangoni A, McGauley S. Relationship between crystallization behavior and structure in cocoa butter Crystal Growth & Design 2003; 3:95–108.

9. Sato K. Solidification and phase behavior of food fats—a review Fett/Lipid 1999; 101:467–474.

10. Wright A, McGauley S, Narine S, Willis W, Lencki R, Marangoni A. Solvent effects on the crystsallization behavoir of milk fat fractions J Agric Food Chem 2000; 48:1033–1040.

11. Sato K. Crystallization behavior of fats and lipids—a review Chemical Engineering Science 2001; 56:2255–2265.

12. Marangoni A. The nature of fractality in fat crystal networks Trends in Food Science & Tehnology 2000; 13:37–47.

13. Narine S, Marangoni A. Fractal nature of fat crystal networks Physical Review E 1990; 59:1908–1920.

14. Narine S, Marangoni A. Factors affecting the texture of plastic fats Inform 1990; 10(6):566–570.

15. de Man J. Effect of cooling procedures on consistency, crystal structure and solid fat content of milk fat Dairy Industries 1964; 29(4):244–246.

16. Grall D, Hartel R. Kinetics of butterfat crystallization J Am Oil Chem Soc 1992; 69:741–747.

17. Kellens M, Meeussen W, Reynaers H. Study of polymorphism and the crystallization kinetics of tripalmitin: a microscopic approach J. Am. Oil Chem. Soc. 1992; 69:906–911.

18. Heertje I. Microstructural studies in fat research Food Structure 1993; 12:77–94.

19. Fairly P, Krochta J, German J. Crystal morphology of mixtures of tripalmitin and butterfat J Am Oil Chem Soc 1995; 72:693–697.

20. Kawanari M. Butter's characteristics: effects of processing Inform 1996; 7(10):1104–1110.

21. Blaurock A. Fundamental understanding of the crystallization of oils and fats. In: Physical properties of fats, oils, and emulsifiers Widlak N, Ed. Champaign. IL: AOCS Press, Inc., 1999.

22. Herrera M, de Leon Gatti M, Hartel R. A kinetic analysis of crystallization of a milk fat model system Food Research International 1999; 32:289–298.

23. Wright A, Marangoni A. Effect of DAG on milkfat TAG crystallization J Am Oil Chem Soc 2002; 79:395–402.

24. Marangoni A. Elasticity of high-volume-fraction fractal aggregate networks: a thermodynamic approach Physical Review B 2000; 62(21):13951–13955.

25. Manning D, Dimick P. Crystal morphology of cocoa butter Food Microstructure 1985; 4:249–265.

26. Heertje I, Leunis M, van Zeyl W, Berends E. Product morphology of fatty products Food Microstructure 1987; 6:1–8.

27. Heertje I, Leunis M. Measurement of shape and size of fat crystals by electron microscopy Lebensm-Wiss u-Technol 1997; 30:142–146.

28. Abbott D, Nugent K. Characterization of imaging from a three-dimensional optical microscope SPIE—The International Society for Optical Engineering 1992; 1660:148–157.

29. Krishnamurthi V, Liu Y, Holmes T, Roysam B, Turner J. Blind deconvolution of 2D and 3D fluorescent micrographs SPIE—The International Society for Optical Engineering 1992; 1660:95–102.

30. Stevens J. Introduction to confocal three-dimensional volume investigation. Three-dimensional confocal microscopy: volume investigation of biological specimens Stevens J, Mills L, Trogadis J, Eds. San Diego. CA: Academic Press, Inc., 1994.

31. Ancin H, Roysam B, Chestnut M, Ridder G, Szarowski D, Turner J. Advances in automated 3-D image analysis of cell populations imaged by confocal microscopy Cytometry 1996; 25:221–234.

32. Barta P, Dhingra L, Royall R, Schwartz E. Improving stereological estimates for the volume of structures identified in three-dimensional arrays of spatial data J Neurosci Meth 1997; 75:111–118.

33. McNally J, Markham J, Conchello J. Comparing methods for 3D microscopy SPIE—The International Society for Optical Engineering 1998; 3261:108–1.

34. Wallace W, Schaefer L, Swedlow J. A working person's guide to deconvolution in light microscopy BioTechniques 2001; 31(5):1–16.

35. Verbeek F, Boon P. High resolution 3D reconstruction from serial sections. Microscope instrumentation, software design and its implementation SPIE—The International Society for Optical Engineering 2002; 4621:65–76.

36. Verveer J, Squire A, Bastianes P. Improved spatial discrimination of protein reaction states in cells by global analysis and deconvolution of fluorescence lifetime imaging microscopy data J of Microscopy 2001; 202:451–456.

37. Mandelbrot B. The fractal geometry of nature. New York: W. H. Freeman & Co., 1982.

38. Vicsek T. Fractal growth phenomena. Singapore: World Scientific Publishing Co, 1992.

38a. Shih W, Shih W, Kim S, Liu J, Aksay I. Scaling behavior of the elastic properties of colloidal gels Physical Review A 1990; 42(8):4772–4779.

39. Marangoni A, Hartel R. Visualization and structural analysis of fat crystal networks Food Technology 1998; 52(9):46–51.

40. Martinez-Lopez F, Cabrerizo-Vilchez M, Hidalgo-Alvarez R. On the self-similarity of fractal colloidal aggregates in two dimensions Journal of Physics A: Mathematical and General 2001; 34:7393–7398.

41. Barnsley M. Fractals everywhere. San Diego. CA: Academic Press, Inc., 1988.

42. Solecka-Cermakova K, Vlckova B. Structural characteristics of ag colloid-adsorbate films determined from transmission electron microscopic images: fractal dimensions, particle size and spacing distributions and their relationship to formation and optical responses in films J Phys Chem 1996; 100: 4954–4960.

43. Rothchild W. Fractals in chemistry. New York: John Wiley & Sons, Inc., 1998.

44. Liu J, Shih W, Sarikaya M, Aksay I. Fractal colloidal aggregates with finite interparticle interactions: energy dependance of the fractal dimension Physical Review A 1990; 41: 3206–3213.

45. Wessel R, Ball R. Fractal aggregates and gels in shear flow Physical Review A 1992; 46:3008–3011.

46. Haw M, Poon W, Pusey P. Structure and arrangement of clusters in cluster aggregation Physical Review E 1997; 56: 1918–1933.

47. Krall A, Weitz D. Internal dynamics and elasticity of fractal colloidal gels Physical Review Letters 1998; 80:778–781.

48. Gonzalez A, Lach-Hab M, Blaisten-Barojas E. On the concentration dependance of the cluster fractal dimesnion in colloidal aggregates Journal of Sol-Gel Science and Technology 1999; 15:119–127.

49. Tather M, Erdem-Senatalar A. Method to evaluate the fractal dimension of solid adsorbents J Phys Chem B 1999; 103: 4360–4365.

50. Cipelletti L, Manley S, Ball R, Weitz D. Universal ageing features in the restructuring of fractal colloidal gels Physical Review Letters 2000; 84:2275–2278.

51. Hagiwara T, Kumagai H, Masunaga K. Analysis of aggregate structure in food protein gels with the concept of fractals Bioscience, Biotechnology, Biochemistry 1997; 61:1663–1667.

52. Brown W, Ball R. Computer simulation of chemically limited aggregation J Phys A 1985; 18:L517–L521.

53. Brown W, Ball R Department of Physics, Cambridge, UK, 1987.

54. Witten T. Polymeric solutions: a geometric introduction. In: Soft matter physics Daoud M, Williams C, Eds. Triltsch. Germany: Springer-Verlag Inc., 1999.

55. Vreeker R, Hoekstra L, den Boer D, Agertof W. Fractal aggregation of whey proteins Food Hydrocolloids 1992; 6:423–435.

56. Vreeker R, Hoekstra L, den Boer D, Agertof W. The fractal nature of fat crystal networks Colloids and Surfaces 1992; 65: 185–189.

57. Rousseau D, Marangoni A. Restructuring butter fat through blending and chemical interesterification. 3. Rheology J Am Oil Chem Soc 1996; 73:983–989.

58. Marangoni A, Rogers M. Structural basis for the yield stress in plastic disperse systems Applied Physics Letters 2003; 82: 3239–3241.

59. Rye G. The effects of processing conditions and storage time on the physical properties of anydrous milk fat. Guelph. Canada: University of Guelph, Department of Food Science, 2003.

60. Daoud M, van Damme H. Fractals. Soft matter physics Daoud M, Williams C, Eds. Triltsch. Germany: Springer-Verlag Inc., 1999.

61. TruSoft International, Inc. Benoit Fractal Analysis System. St. Petersburg, FLA (Florida), 2000.

62. Marangoni A, Awad T. Personal communications. Guelph. Canada: University of Guelph, Department of Food Science, 2003.

63. Quevedo R, Carlos L, Aguilera J, Cadoche L. Description of food surfaces and microstructural changes using fractal image texture analysis J Food Engineering 2002; 53:361–371.

64. Russ J. Fractal surfaces. New York: Plenum Press, 1964.

65. McCrone W, McCrone L, Delly J. Polarized light microscopy. Ann Arbor. MI: Ann Arbor Science Publishers Inc., 1978.

66. Robinson P, Bradbury S. Royal microscopical society. 09. Quantitative polarized light microscopy. New York: Oxford University Press, 1992.

67. Marangoni A, Campos R. Personal communications. Guelph. Canada: University of Guelph, Department of Food Science, 2003.

68. Herrera M, Hartel R. Effect of processing conditions on crystallization kinetics of a milk fat model system J Am Oil Chem Soc 2000; 77:1177–1187.

69. Foley J, Brady J. Temperature-induced effects on crystallization behavior, solid fat content and the firmness values of milk fat J of Dairy Research 1984; 51:579–589.

70. de Man J, Beers A. Fat crystal networks: structure and rheologic properties J of Texture Studies 1987; 18:303–318.

71. Rousseau D, Hill A, Marangoni A. Restructuring butter fat through blending and chemical interesterification. 2. Microstructure and Polymorphism J Am Oil Chem Soc 1996; 73: 973–981.

72. Rousseau D, Marangoni A. On deciphering the fat structure-functionality mystery: the case of butter fat. Physical properties of fats, oils, and emulsifiersWidlak N, Ed. Champaign. IL: AOCS Press, Inc., 1999.

73. Brakenhoff G, van der Voort J, van Spronsen E, Nanninga N. Imaging of biological structures by high resolution confocal scanning laser microscopy Scanning Microscopy 1988; 2(1): 22–40.

74. Brooker B. The study of food systems using confocal laser scanning microscopy Microscopy and Microanalysis 1991; 27: 13–15.

75. Bacallo R, Garfinkel A. Three-dimensional volume reconstruction in confocal microscopy: pratical considerations. In: Three-dimensional confocal microscopy: volume investigation of biological systems Stevens J, Mills L, Trogadis J, Eds. San Diego. CA: Academic Press, Inc., 1994.

76. Thomas C, White J. Four-dimensional imaging: the exploration of time and space Tibtech 1988; 16:175–182.

77. Ding K, Gunasekaran S. Three-dimensional image reconstruction procedure for food microstructure evaluation Artificial Intelligence Review 1998; 12:245–262.

78. Van Dalen G. Determination of the water droplet size distribution of fat spreads using confocal scanning laser microscopy Journal of Microscopy 2002; 208:116–120.

79. Balberg M, Barbastathis G, Fantini S, Brady D. Confocal imaging through scattering media with a volume halographic filter SPIE—The International Society for Optical Engineering 2000; 3919:69–74.

80. Weisendanger R. Scanning probe microscopy analytical methods. Triltsch. Germany: Springer-Verlag Inc., 1998.

81. Rousseau D. Atomic force microscopy in fats and oils research, Inform March, 2003. Champaign. IL: AOCS Press, Inc., 2003.

82. Bones P, Satherly B, Parker C, Watson R. Non-iterative methods for image deconvolution SPIE—The International Society for Optical Engineering 1993; 2029:2–13.

83. Kundar D, Hatzinakos D. Blind image deconvolution IEEE Signal Processing Magazine 1996; 13(3):43–64.

84. Lanteri H, Barilli M, Beaumont H, Aime C, Gaucherel P, Touma H. Comparison of several algorithms for blind deconvolution. Analysis of noise effects SPIE—The International Society for Optical Engineering 1995; 2580:275–287.

85. Lee G, Gelfand S, Fitz M. Bayesian techniques for blind deconvolution IEEE Transactions on Signal Processing 1996; 44(7): 826–835.

86. Amari S, Cichocki A. Adaptive blind signal processing—neural network approaches Proceedings of the IEEE 1998; 10: 2026–2048.

87. Yu T, Chen D, Pottie G, Yao K. Blind deconvolution and deconvolution algorithm for multiple-input multiple-ouput system I: theorum derivation SPIE—The International Society for Optical Engineering 1999; 3807:200–209.

88. Protasov K, Belov V, Molchunov N. Image restoration with an a priori estimation of the point spread function SPIE—The International Society for Optical Engineering 1999; 3983: 160–168.

89. Inouye Y, Tanebe K. Super-exponential algortihms for multichannel blind deconvolution IEEE Transactions on Signal Processing 2000; 48(3):881–888.

90. Douglas S, Kung S. Gradient adaptive algorithms for contrast-based blind deconvolution Journal of VLSI Signal Processing 2000; 26:47–60.

91. Law N, Lane R. Blind deconvolution using a least squares minimisation Optics Communications 1996; 128:341–352.

92. Leung W, Lane R. Blind deconvolution of images blurred by atmospheric speckle SPIE—The International Society for Optical Engineering 2000; 4123:73–83.

93. Javidi B. Image deconvolution by non-linear techniques in the fourier domain SPIE—The International Society for Optical Engineering 1990; 1297:168–175.

94. Christou J, Hege K, Jefferies S, Cheselka M. Physically constrained iterative deconvolution of adaptive optics images SPIE—The International Society for Optical Engineering 1988; 3494:175–186.

95. Goudail F, Ruch O, Refregier P. Deconvolution of an image perturbed by several defocus blurs SPIE—The International Society for Optical Engineering 1999; 3808:457–468.

96. McNally J, Karpova T, Cooper J, Conchello J. Three-dimensional imaging by deconvolution microscopy Methods 1999; 19:373–385.

97. Yli-Harja O, Rustanius P, Reponen S. Image deconvolution and noise control SPIE—The International Society for Optical Engineering 2001; 4304:277–287.

98. Poon S, Ward R, Palcic B. Analysis of three-dimensional images in quantitative microscopy SPIE—The International Society for Optical Engineering 1992; 1660:178–185.

99. Dayton D, Sandven S. Hybrid blind deconvolution for high resolution satellite imaging SPIE—The International Society for Optical Engineering 1995; 2580:268–274.

100. Bloemhof E, Marsh K, Dekany R, Troy M, Marshall J, Oppenheimer B, Hayward T, Brandl B. Stability of the adaptive-optic point-spread function: metrics, deconvolution, and initial polamar results SPIE—The International Society for Optical Engineering 2000; 4007:889–898.

101. Takahashi T, Takajo H, Maki H, Dainty J. Blind deconvolution by iterative Fourier transform algorithms SPIE—The International Society for Optical Engineering 1996; 2778:517–518.

102. Yap K, Guan L, Liu W. A recursive soft-decision approach to blind image deconvolution IEEE Transactions on Signal Processing 2003; 51(2):515–520.

103. Richardson M. 3D deconvolution of microscope data SciTech Journal 1997; 7(9):20–21.

104. Bhattacharyya S, Szarowski D, Turner J, O'Connor N, Holmes T. The ML-blind deconvolution algorithm: recent developments SPIE—The International Society for Optical Engineering 1996; 2655:175–186.

105. Wang C, O'Connor N, Wang M, Turner J, Holmes T. Data correction methods for 3D light microscopy SPIE—The International Society for Optical Engineering 1998; 3261:93–107.

106. Markham J, Conchello J. Parametric blind deconvolution of microscopic images: further results SPIE—The International Society for Optical Engineering 1998; 3261:38–49.

107. Holmes T. Personal communications. Guelph. Canada: University of Guelph, Department of Food Science, 2002.

108. Hiesinger P, Scholz M, Meinertzhagen I, Fischbach K, Obermayer K. Visualization of Synaptic markers in Optic Neuropils of Drosophila using a new constrained deconvolution method J of Comparative Neurology 2001; 429:277–288.

109. AutoQuant Imaging, Inc. AutoQuant Imaging Webite FAQs Section. 2003. http://www.aqi.com/support.asp?type=faqs.

110. University of Buffalo. 2003. http://listserv.buffalo.edu/archives/confocal.html.

111. Holmes T, Battacharyya S, Cooper J, Hanzel J, Krishnamurthi V, Lin V, Roysam B, Szarowski D, Turner J. Light microscopic images reconstructed by maximum likelihood deconvolution. Handbook of biological confocal microscopyPawley J, Ed. New York: Plenum Press, 1995.

112. Holmes T, O'Connor N. Blind deconvolution of 3D transmitted light brightfield micrographs J of Microscopy 2000; 200(2): 114–127.

113. Russ J. Image analysis of the microstructure of materials. Images of materialsWilliams D, Pelton A, Gronksy R, Eds. New York: Oxford University Press, Inc., 1991.

114. Russ J. The image processing handbook. Boca Raton. FL: CRC Press & IEEE Press, 1999.

115. Improvision IPVCL. Openlab Deconvolution Manual. England: Image Processing & Vision Company Limited, 2000.

116. Adobe Systems, Inc. Adobe Photoshop 7.0 help files, Adobe Systems, Inc.. San Jose. CA, 2002.

117. NIH-Image. NIH-Image Online Manual for Version 1.61. 2003. http://rsb.info.nih.gov/nih-image/manual/contents.html.

118. GraphPad GraphPad Prism help files. San Diego. CA: GraphPad Software, Inc., 2002.

119. Singh A. Personal communication. Guelph. Canada: University of Guelph, Department of Food Science, 2002.

120. van Malssen K, Peshar R, Brito C, Schenk H. Real-time X-ray powder diffraction investigations on cocoa butter. III. Direct beta-crystallization of cocoa butter: occurrence of a memory effect J Am Oil Chem Soc 1996; 73(10):1225–1230.

121. Breitschuh B, Windhab E. Parameters influencing cocrystallization and polymorphism in milk fat J Am Oil Chem Soc 1988; 75(8):897–904.

122. ten Grotenhuis E, van Aken G, Maki H, Dainty J. Polymorphism of milk fat studied by differential scanning calorimetry and real-time x-ray powder diffraction J Am Oil Chem Soc 1999; 76(9):1031–1039.

123. van Langevelde A, Driessen R, Molleman W, Peshar R, Schenk H. Cocoa-butter long spacings and the memory effect J Am Oil Chem Soc 2001; 78(9):911–918.

124. McCrone W, Draftz R, Delly J. The particle atlas. Ann Arbor. MI: Ann Arbor Science Publishers, Inc., 1967.

125. Wessendorf M. Calibrating scanners/stages, Confocal Listserve. http://listserv.buffalo.edu/, 2003.

126. Mohler W, White J. Stereo-4-D Resconstruction and Animation from Living Fluorescent Specimens BioTechniques 1998; 24(6):1006–1012.

127. Kriete A. 4D image processing in microscopy by combined methods SPIE—The International Society for Optical Engineering 2000; 3919:110–117.

Fat Crystal Networks

about the book . . .

The first authoritative source on the subject, this reference offers comprehensive discussions of the various levels of structure that influence the macroscopic physical properties of fat crystal networks—summarizing 50 years of structural research in the field, as well as a wealth of information on fat crystal networks pertinent to real-world challenges in industry.

Features a digital library containing ***8000 high-resolution images*** *of crystallized fats including cocoa butter, milkfat, milkfat fractions, and palm oil.*

Richly illustrating a wide range of analytical methodologies, this detailed source provides pioneering studies on the use of 3-dimensional microscopy and the microanalysis of fat crystal networks…the most in-depth research available on the phase behavior of triacylglycerols…an introduction to the use of fractal analysis in the natural sciences…state-of-the-art advancements gleaned from the author's personal research in the field…recent methods to alter fat functionality through blending and physical manipulation…and coverage of formulation problems currently affecting the food industry.

about the author . . .

ALEJANDRO G. MARANGONI is Professor and Canada Research Chair, University of Guelph, Ontario, Canada. He is the author, coauthor, or editor of numerous professional publications, including *Physical Properties of Lipids* and *Soft Materials* (both titles, Marcel Dekker). He is a member of the American Physical Society, the American Chemical Society, the American Oil Chemists' Society, Sigma Xi, and the Institute of Food Technologists. He is the recipient of numerous awards, including the first Young Scientist Research Award and the T.L. Mounts Award from the American Oil Chemists' Society, as well as an E. W. R. Steacie Fellowship from the Natural Sciences and Engineering Research Council of Canada. He received the B.Sc. degree (1987) from McGill University, Montreal, Quebec, Canada, and the Ph.D. degree (1990) from the University of Guelph, Ontario, Canada.

Printed in the United States of America

DK1243

ISBN 0-8247-4075-0

90000

9 780824 740757

MARCEL DEKKER
NEW YORK